UAB
Universitat Autònoma de Barcelona

Time constraints and dynamics of the Eaux-Chaudes nappe (West-Central Pyrenees):
A study combining new tectonothermal data and thermo-mechanic simulations

Marc Guardia Alen

**PhD Thesis
2024**

Supervisors:

Dr. Albert Griera

Dr. Antonio Teixell

UAB

Universitat Autònoma de Barcelona

Facultat de Ciències

Departament de Geologia

UAB

Universitat Autònoma de Barcelona

Facultat de Ciències

Departament de Geologia

Time constraints and dynamics of the Eaux-Chaudes nappe (West-Central Pyrenees):

A study combining new tectonothermal data and thermo-mechanic simulations

Memòria presentada per Marc Guardia Alen per optar al títol de Doctor en Geologia

Gener, 2024

Tesi doctoral dirigida per:

Dr. Albert Griera Artigas, Departament de Geologia de la Universitat Autònoma de Barcelona

Dr. Antonio Teixell Cácharo, Departament de Geologia de la Universitat Autònoma de Barcelona

Dr. Albert Griera Artigas   Dr. Antonio Teixell Cácharo

Marc Guardia Alen

A la meva família i amics

«Lo que sabemos es una gota de agua, lo que ignoramos es el océano»

Isaac Newton

En la Ciencia la única verdad sagrada, es que no hay verdades sagradas

Carl Sagan

Index

Abstract

Fold nappes and thrust nappes are found either in the internal and external parts of orogenic belts worldwide and are geometrically and kinematically well constrained after more than a century of studies. However, the mechanics favouring ones vs. the others are still incompletely understood due to the uncertainty and variability of pre-contractional configurations.

The Eaux-Chaudes massif is a recently described Alpine south-verging fold-and-thrust structure located in the western Axial Zone (French Pyrenees) affecting the Paleozoic rocks and Upper Cretaceous carbonates. It consists of a basement-cored recumbent fold nappe with a large recumbent limb in the Upper Cretaceous carbonates which are ductilely deformed, passing to the east of the massif to an imbricate thrust fan also showing strong ductile deformation. Based on the field natural example of the Eaux-Chaudes fold nappe, this thesis presents a systematic numerical modelling study of the variability in the initial mechanical, geometrical and temperature conditions on the development of recumbent fold nappes and their transition to thrust nappes.

The occurrence of this singular structure and the observed deformation style makes necessary to put an age constraint on the ductile event within the history of the massif and its successive evolution until the present day, to further advance in the knowledge of the Pyrenees. During the structural development of the massif, foliation with a strong stretching lineation, asymmetric intra-foliation folds, and S-C structures strongly evidence south-directed tectonic transport in this part of the northern Axial Zone. Also studied are calcite veins parallel to the foliation developed in the Upper Cretaceous carbonates (registering the main deformational event) as well as orthogonal to it (post-dating it). The cross-cutting relationships between them allowed to stablish relative chronologies that were then dated by U-Pb geochronology to constraint a minimum and maximum age for the main deformation in the massif. Finally, to complete the history of the Eaux-Chaudes massif, a systematic low-temperature thermochronologic and thermal-modelling study has been performed (zircon (U-Th)/He) within the different structural units of the Eaux-Chaudes massif and its surroundings, giving additional information on the tectonic and exhumation history of the area.

Resum

Els mantells d'encavalcament i els mantells de plegament són estructures presents tant a les parts internes com externes dels oròens arreu del món, i després de més d'un centenar d'anys d'estudi es pot considerar que estan ben caracteritzats a nivell cinemàtic i geomètric. A nivell mecànic, però, les condicions que afavoreixen els uns vs. els altres romanen no del tot enteses degut a les incerteses lligades gran variabilitat de configuracions pre-contraccionals.

El massís d'Eaux-Chaudes és un sistema de plecs i encavalcaments d'edat Alpina situat a la part oest de la Zona Axial (Pirineus Francesos) que afecta les roques Paleozoiques i els carbonats del Cretaci Superior. L'estructura consisteix en un plec recumbent de nucli Paleozoic (basament) amb un flanc invers que presenta deformació dúctil als carbonats del Cretaci Superior, i que cap a l'est del massís fa una transició lateral cap a un mantell d'encavalcaments imbricats, també deformat dúctilment. Prenent com a base l'exemple de camp del plec d'Eaux-Chaudes, aquesta tesi presenta un estudi sistemàtic mitjançant modelització numèrica de la variabilitat en les condicions inicials a nivell de mecànica, geometria i temperatura en el desenvolupament de mantells de plegament i la seva transició cap a mantells d'encavalcament.

La presència d'aquesta singular estructura i la deformació dúctil associada fa necessària la seva datació i l'estudi de la seva evolució fins l'actualitat per a seguir avançant en el coneixement de la serralada dels Pirineus. Durant la constitució del massís, la deformació registrada per les roques del Cretaci Superior (foliació amb lineació d'estirament, plecs asimètrics intra-foliació i foliacions S-C) indiquen una forta vergència cap al sud. He estudiat també venes de calcita paral·leles (enregistrant el principal esdeveniment de deformació) i ortogonals (postdatant la deformació) a la foliació. Les relacions de tall entre aquestes han permès establir cronologies relatives que han estat datades mitjançant geocronologia d'U-Pb. Finalment, per conèixer l'evolució recent del massís s'ha realitzat un estudi sistemàtic de termocronologia de baixa temperatura (U-Th/He en zircons) combinat amb modelització tèrmica en les diferents unitats estructurals del massís d'Eaux-Chaudes i els seus voltants, i que aporta més informació sobre la història tectònica i d'exhumació de la zona.

Glossary of terms

- **_ECM_**: Eaux-Chaudes massif

- **_ECFN_**: Eaux-Chaudes fold nappe

- **_E-C nappe_**: Eaux-Chaudes nappe

- **_ECRFN_**: Eaux-Chaudes recumbent fold nappe

- **_UC layer_**: Upper Cretaceous layer

- **_ECP_**: Eaux-Chaudes pluton

- **_UCD level/panel/layers_**: Upper Cretaceous – Devonian level/panel/layers

- **_PFV_**: Veins parallel to the foliation

- **_OFV_**: Veins orthogonal to the foliation

- **_AHe_**: Apatite Helium system

- **_ZHe_**: Zircon Helium system

- **_AFT_**: Apatite fission track system

- **_APRZ_**: Apatite partial retention zone

- **_ZPRZ_**: Zircon partial retention zone

- **_APAZ_**: Apatite partial annealing zone (AFT system).

Chapter 1: Introduction

The evolution of fold and thrust belts resulting from inversion tectonics in collisional orogens is strongly controlled by the pre-orogenic mechanical and geometrical architecture of the collided margins, which in turn strongly depends on the previous geodynamic evolution within the Wilson cycle (e.g., Manatschal et al., 2021). Depending on the previous history (i.e. ancient collisions, rifting processes, thermal subsidence, basin evolution, margin geometry and distribution, etc.) the resulting configuration will be determined by the existence of mechanical heterogeneities due to the diverse rheology of the rocks involved, or to inherited faults that can nucleate further deformation (e.g., Welbon, 1988; Butler et al., 2006; Bellahsen et al., 2012; Zerlauth et al., 2014; Butler et al., 2018; Fig. 1.1).
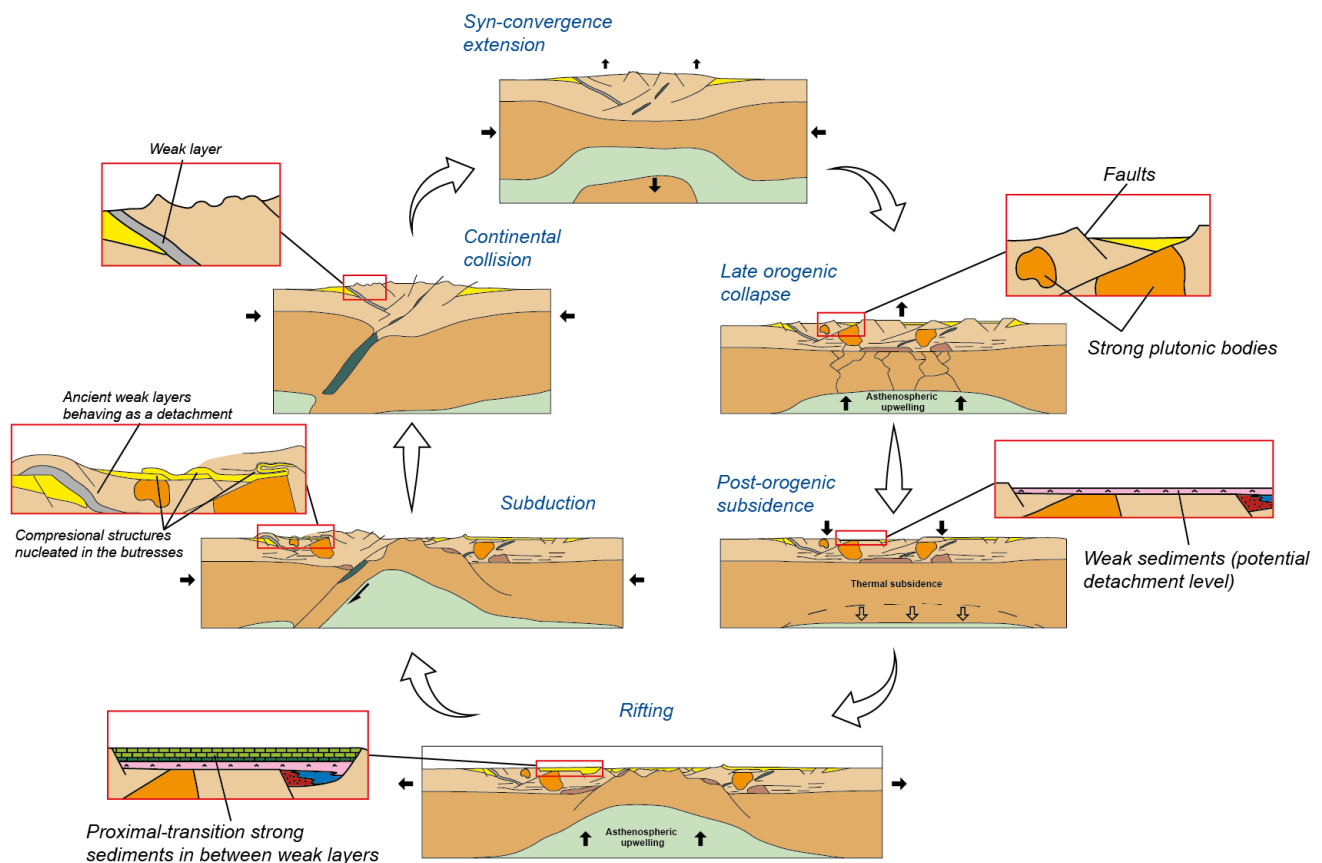
Figure 1.1: A) Simplified sketch (modified from Manatschal et al., 2021) of the main stages within the Wilson cycle showing the main geometric and mechanic features that could exercise control and determine the final geometry of the tectonic structures formed.

High-strength heterogeneities can play an important role during rift inversion processes by localizing strain (e.g., Wissing and Pfiffner, 2003; Bauville and Schmalholz, 2017; Kiss et al., 2020; Spitz et al., 2020). On the other hand, weak layers such as shales or evaporites are of great relevance due to their ability to act as detachment horizons for the contractional structures, facilitating the strong layers (e.g., limestones, sandstones) to travel relatively long distances over autochthonous terrains (e.g., Pfiffner, 1993). They can also determine the preferential occurrence of thrust- or fold-nappes accommodating the orogenic shortening (e.g., Pfiffner, 1993; Epard and Escher, 1996; Erickson, 1996; Costa and Vendeville, 2002).

Examples of these two end-members (thrust and fold nappes) have been long recognized in orogenic belts worldwide (e.g., Fig 1.2). On one hand, thrust nappes are usually found in the external parts of orogens, where there are relatively shallower burial conditions and the rocks involved show a dominance of the brittle/frictional behaviour (e.g., Hatcher, 1981; Belhassen et al., 2014; Martínez-Catalán et al., 2020). Conversely, nappe stacks found in the internal or transitional zones are usually associated with tectonic burial and temperature increases, allowing the activation of the ductile/viscous behaviour which favours the development of fold nappe structures (e.g., Hatcher, 1981; Ramsay, 1981; Dietrich and Casey 1989; Fernández et al 2007; Belhassen et al., 2012, 2014; Boutoux et al., 2014; Martínez-Catalán et al., 2020; Fig. 1.2).

A) **Western Alps**

Deep internal (folding)

Shallower external/transitional (thrusting)

Mont Blanc

Aiguilles Rouges

Préalpes

Internal units

Jura

Molasse basin

10 km

B) **Appalachians**

Shallower external/transitional (thrusting)

Deep internal (folding)

Valley and Ridge

Blue Ridge

Inner

Piedmont

Charlotte Belt

Carolina Slate Belt

Coastal Plain Overlap

Chauga Belt

Kings Mtn Belt

KIOKEE BELT

NW

SE

SL

SL

Horizontal and Vertcal Scales

10   0   10   20   30 Miles
10   0   10   20 30 40   50 Kilometers

C) **Iberian massif (NE Spain)**

Deep internal (folding)

Shallower external/transitional (thrusting)

GTMZ   CIZ   WALZ   CZ

km   WNW   MALPICA-TUI
50   COMPLEX   A'   A"   CABO   OLLO DE SAPO
                                                          ORTEGAL ANTIFORM   MONDOÑEDO   LET   A'''   ESE
40   COMPLEX   VF   NAPPE

30   ÓRDENES COMPLEX

      PADRÓN DOME   LUGO DOME
20   Reequilibrated and collapsed   Basement of the West
      crust of the Central Iberian Zone   Asturian-Leonese Zone   Basement of the Cantabrian Zone
            ESCIN-3.2   ESCIN-3.3
10   a   Root of the West Asturian-Leonese Zone
                                          Root of the Cantabrian Zone   ESCIN-1.2   ESCIN-1.1
0   0 10 20 30 40 50 60 70 80 90 100 km

*Figure 1.2: Examples of the change in structural style between the internal and external parts of characteristic orogens. Brittle/frictional behaviour (i.e., thrusting) is common in the external parts while viscous/ductile behaviour is favoured closer to the internal areas, where recumbent folding is more common. **A)** Cross-section of the Western Alps from Belhassen et al. (2014). **B)** Cross-section of the Appalachians (Hatcher, 1981). **C)** Cross-section of the Iberian massif (Martínez-Catalán et al., 2020).*

1.1. Folding vs. thrusting

Thrust nappes (or thrust sheets) and fold nappes could be considered as the two end-member forms of tectonic superposition driven by compression. According to Dennis et al. (1981), thrust nappes are allochthonous sheets over a localized, thin basal thrust surface showing a short or absent reverse limb (Fig. 1.3A and 1.4), and commonly associated with shallow and brittle/frictional conditions. On the other hand, fold nappes are defined as allochthonous units showing large-scale overturned or recumbent limbs (km-scale), often developed deeper in the crust (e.g., Ramsay, 1980; Epard and Escher, 1996; Bastida et al., 2014; Figs. 1.3B and 1.4). Fold nappes are associated with more distributed deformation, dominated by ductile-viscous behaviour, and exhibit sub-horizontal axial planes and usually long and stretched recumbent limbs that may be sheared out into basal thrusts or shear zones. As pointed out by Bastida et al. (2014), there is still controversy regarding the length of the overturned limb to be considered as a fold nappe since some authors (e.g., Dennis et al., 1981; France, 1987; Ramsay and Huber, 1987) consider a minimum length of 5 to 10 km for the overturned limb to qualify as such. In agreement with Bastida et al. (2014), this study considers a fold nappe any recumbent fold with a km-scale overturned limb, without the restriction of a minimum length of 5km.
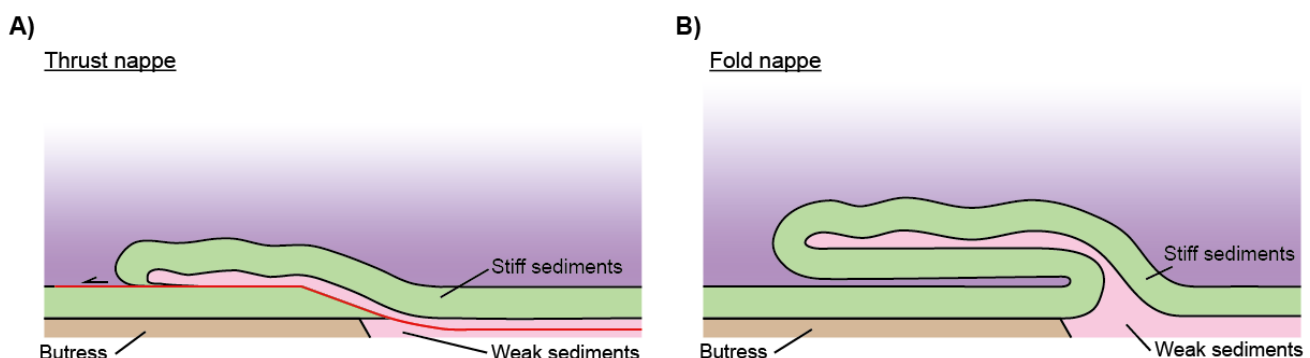
Figure 1.3: *Simplified sketch of the geometrical features of idealized thrust nappe **(A)** and recumbent fold nappe **(B)** end-members resulting from tectonic shortening.*

1.2. Folding mechanisms: rigid rotation vs. limb stretching

Recumbent folds are usually interpreted as developed in wide zones of simple shear in compressional settings (Bastida et al., 2014). A determinant parameter to their development is the original orientation of strong marker layers with respect to the shear zone margins (e.g., Ramsay et al.,1983; Dietrich and Casey, 1989; Carreras et al., 2005; Llorens et al., 2013). If the layer orientation is parallel to the shear zone (that is, an orientation without shortening parallel to the layer in simple shear) and is surrounded by weaker rocks (i.e. such as a stiff single-layer in a weak matrix), an initial buckling instability is required in order to develop folds. Once nucleated, folds start with an axial plane at high angle to the layer and the shear direction, and can evolve into recumbent folds as the shearing advances with time (e.g., Ez, 2000; Fig. 1.4). This case requires a large amount of deformation before attaining a large fold amplification, and the strain could be reduced if the initial angle between the strong layer and the shear zone is oblique (Bastida et al., 2014). Subsequent kinematic evolution within the simple shear zone can determine the stretching of the reverse limb of the fold structure (Bastida et al., 2014). However, in this situation, the fold hinges are fixed in the material (or non-mobile hinges) after the buckling process, and the length increase of fold limbs could only be done by stretching during the late phases (e.g., Mancktelow, 1999; Frehner, 2011), which can evolve to the shearing out of the recumbent limb (e.g., Fig. 1.4). A good example of this situation is the Morcles fold nappe in the Alps, which displays a clearly stretched recumbent limb (e.g., Figs. 1.4 and 1.5B).

Alternatively, Perrin et al. (2013) proposed from analogue models that relatively large, overturned limbs of fold nappes could form by progressive migration of fold hinges (i.e., material particles are travelling with time between structural positions within the fold nappe). In their analogue models, the growth of an overturned fold limb was controlled by progressive shift and unfolding of the syncline formed during the early stages of a paired fold system (an

anticline-syncline pair with a reverse limb in between). This situation leads to rigid rotation of the strong layer and preserve their original thickness (e.g., Fig. 1.3B and 1.4). The setup of Perrin et al. (2013) models was aimed to model the thrust and fold propagation in front of a backstop in foreland basins with erosion and little burial with a backstop.
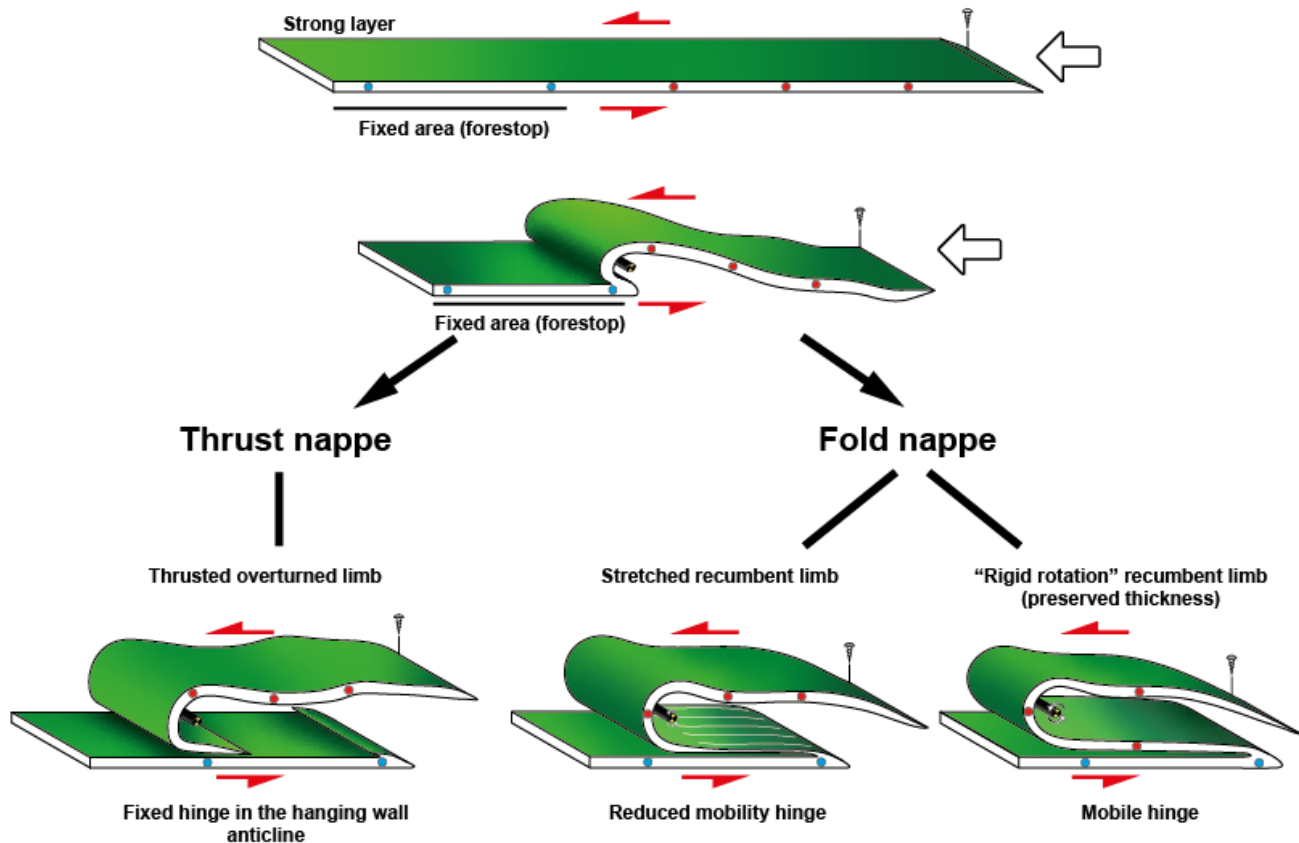
Figure 1.4: Sketch of the principal mechanisms under which a thrust nappe or a fold nappe end-members can evolve from an initial flat layer. A sedimentary panel with a fixed area (blue dots) is subjected to layer-parallel compression and shear is developed. The fixed area acts as a buttress, nucleating a buckling anticline and the structure is then translated to foreland. Progressive deformation can derive to an idealized thrust nappe (blocked hinge) or to an idealized recumbent fold nappe, in which the thickness of the recumbent limb is preserved (mobile hinge). Mobility of the hinge is defined by the material particles transport (red dots) through the different structural elements of the different developed structures. Between both end-members, a potential type is defined by stretching of the recumbent limb and the possibility of hinge migration.

However, in settings with moderate burial conditions and effective detachment levels, the migration of anticline hinges seems to be favoured if a forestop condition is present, because the syncline is fixed by the strain shadow created by the stiff forestop; otherwise, buckle folds will be produced by the progressive migration of the syncline hinge (e.g., Epard and

Groshong, 1995; Homza and Wallace, 1995, 1997; Poblet and McClay, 1996; Perrin et al., 2013; Poblet, 2020). However, with the increase of burial (and temperature) the ductile and viscous behaviour of rocks becomes enhanced, and the formation of long overturned limbs maintaining a constant thickness (i.e., low stretching) is unlikely. Recently, Caldera et al. (2023) described the case of the Eaux-Chaudes recumbent fold nappe in the Axial Zone of the western-central Pyrenees, a km-scale fold nappe in which the thickness of the recumbent limb is preserved (e.g., Fig. 1.5A) and represents the motivation of this thesis.
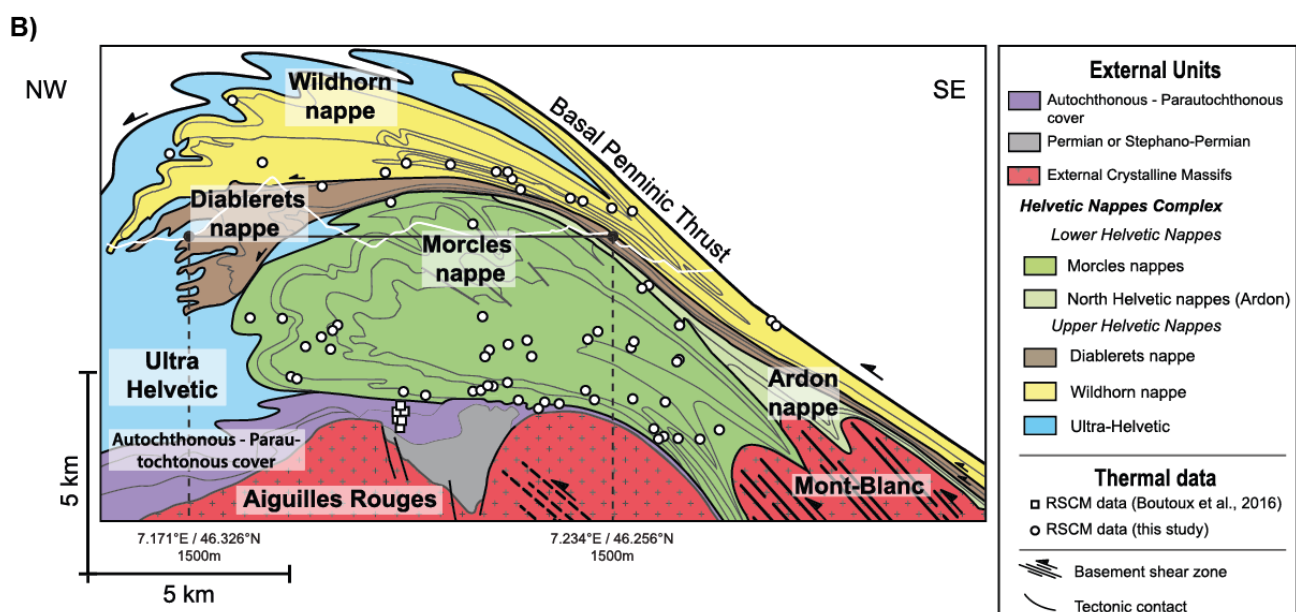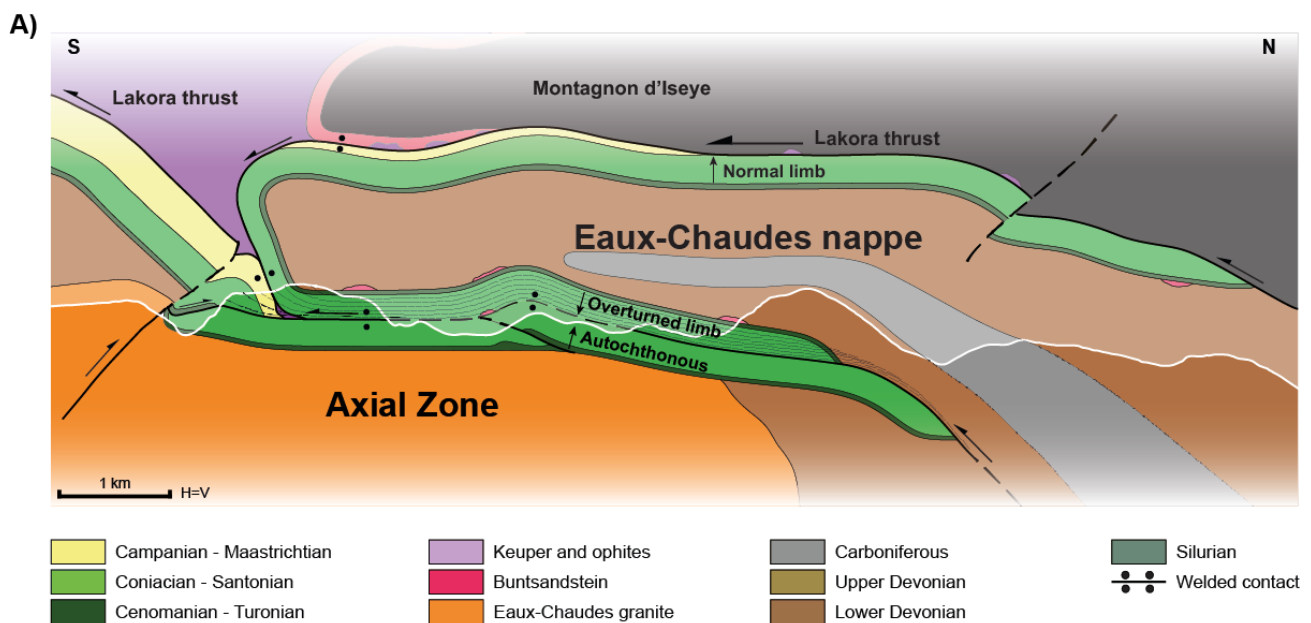
Figure 1.5: A) Geological cross-section from the western Eaux-Chaudes massif from Caldera et al. (2021). B) Geological cross-section of the Helvetic nappe complex from Escher et al. (1993) after Girault et al. (2020). Both cross sections show similar features such as the presence of sub-horizontal recumbent limbs and fold axial planes, the overthrusting of allochthonous units, or the presence of stiff crystalline massifs in the footwall of the structures.

1.3. Geological setting of the western-central Pyrenees

The Pyrenean massif is an asymmetric doubly-verging orogenic wedge (e.g., Choukroune et al., 1989; Muñoz, 1992; Teixell, 1998) developed during the late Cretaceous-early Miocene Alpine orogeny (Fig. 1.6) from the inversion of a hyperextended rift system, involving the collision of the Iberian and Eurasian rifted margins (Clerc and Lagabrielle, 2014; Jammes et al., 2009; Teixell et al., 2016). It consists of a large thick-skinned thrust system developed in the Iberian basement that links to the north and the south to thin-skinned imbricate thrusts affecting the Mesozoic-Cenozoic sedimentary cover. After the Variscan orogeny (late Paleozoic), rifting occurred in the Pyrenean domain in two main episodes during the Permian-Triassic and the early Cretaceous, culminating in mantle exhumation during the Albian-Cenomanian (Jammes et al., 2009; Lagabrielle et al., 2010), subjecting to high temperatures and fluid circulation the Mesozoic sedimentary rocks of the rift basin (e.g., Clerc, 2012; Clerc et al., 2015, 2016; Chelalou et al., 2016; Menant et al., 2016; Villard, 2016; Corre, 2017; Ducoux, 2017; Espurt et al., 2019; Izquierdo-Llavall et al., 2020; Saspiturry et al., 2020; Ducoux et al., 2019, 2021). The Late Cretaceous encompassed a short post-rift stage, followed by initial orogenic inversion starting in the mid Santonian times (ca. 84 Ma).

As for the orogenic evolution, Teixell et al. (2016) and Labaume and Teixell (2020), proposed a model for the west-central Pyrenees in which during the first stages of the Pyrenean orogeny the deformation in the west-central Pyrenees was mostly accommodated by thin-
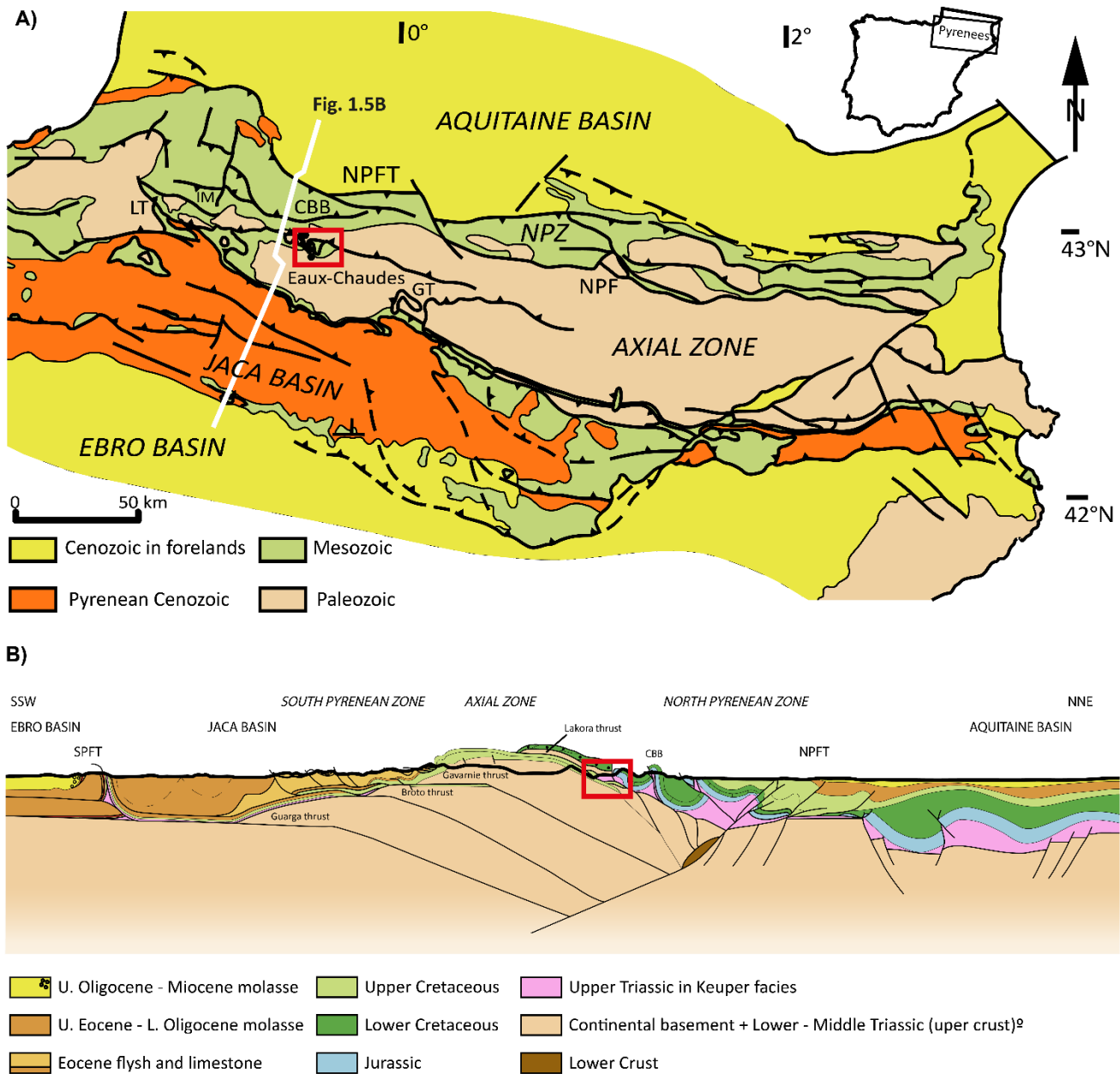
Figure 1.6: A) Geologic sketch of the Pyrenees showing the location of the Eaux-Chaudes massif, mapped in Fig. 1.7. B) Crustal cross-section of the west-central Pyrenees (simplified from Teixell et al., 2016) indicating the structural setting of the Eaux-Chaudes structure (red square), here projected in the subsurface; CBB: Chaînons Béarnais Belt; NPFT: North-Pyrenean Frontal Thrust; SPFT: South-Pyrenean Frontal Thrust.

skinned thrusting detached from the continental and upper mantle basement, favoured by weak layers (mainly Triassic evaporites and shales) (e.g., Lakora thrust and Chaînons Béarnais Belt). Later convergent deformation progressively involved the basement, as the exhumed mantle domain was shortened and closed and the continental margins collided

(e.g., Teixell et al., 2016). An alternative model, based on the existence of a strong positive anomaly in the western French Pyrenees, considers that the upper mantle remained at a shallow position from the rifting to the Pyrenean orogeny and acted as a rigid backstop guiding the deformation of the Iberian margin (Wang et al., 2016; Garcia-Senz et al., 2019; Saspiturry et al., 2020).

The Eaux-Chaudes massif (ECM) is an Upper Cretaceous inlier surrounded by Paleozoic basement rocks in the northwestern Axial Zone in the west-central Pyrenees (Ternet, 1965; Fig. 1.6A). In the western part of the massif, in the Ossau Valley, the Eaux-Chaudes structure consists of a km-scale south-verging, basement-cored recumbent fold outlined by Upper Cretaceous carbonates (Caldera et al., 2021; Fig. 1.8A). To the east, the structure changes abruptly through a transfer zone (the Gourzy transfer zone, GTZ in Fig. 1.7) to a simple thrust structure, and much of the deformation is transferred to the autochthonous footwall (Caldera et al., 2023; Fig. 1.8B). Due to the shallow-water carbonate nature of the pre-orogenic Upper Cretaceous rocks, the Eaux-Chaudes massif is thought to have been located in the upper Iberian margin (the Iberian shelf) before the Pyrenean collision. Compressional deformation of the Eaux-Chaudes massif and related shear zones east of the massif is inferred to have happened before the emplacement of the underlying Gavarnie thrust, during the early and mid-Eocene (Wayne and McCaig, 1998; Jolivet et al., 2007; Labaume et al., 2016b) (Fig. 1.5B).

The stratigraphic succession of the Eaux-Chaudes massif consists of Upper Cretaceous platform limestones resting directly on top of Paleozoic low-grade metasedimentary rocks or granodiorites (Fig. 1.9). The Paleozoic metasedimentary sequence (Fig. 1.9) starts with the Silurian weak unit mainly composed of black slates (Mirouse, 1962), which is considered a regional decoupling level within the Axial Zone of the Pyrenees (e.g., Garcia-Sansegundo et al., 2011, and references therein). The Silurian is followed by ~400 m of pelites, limestones,
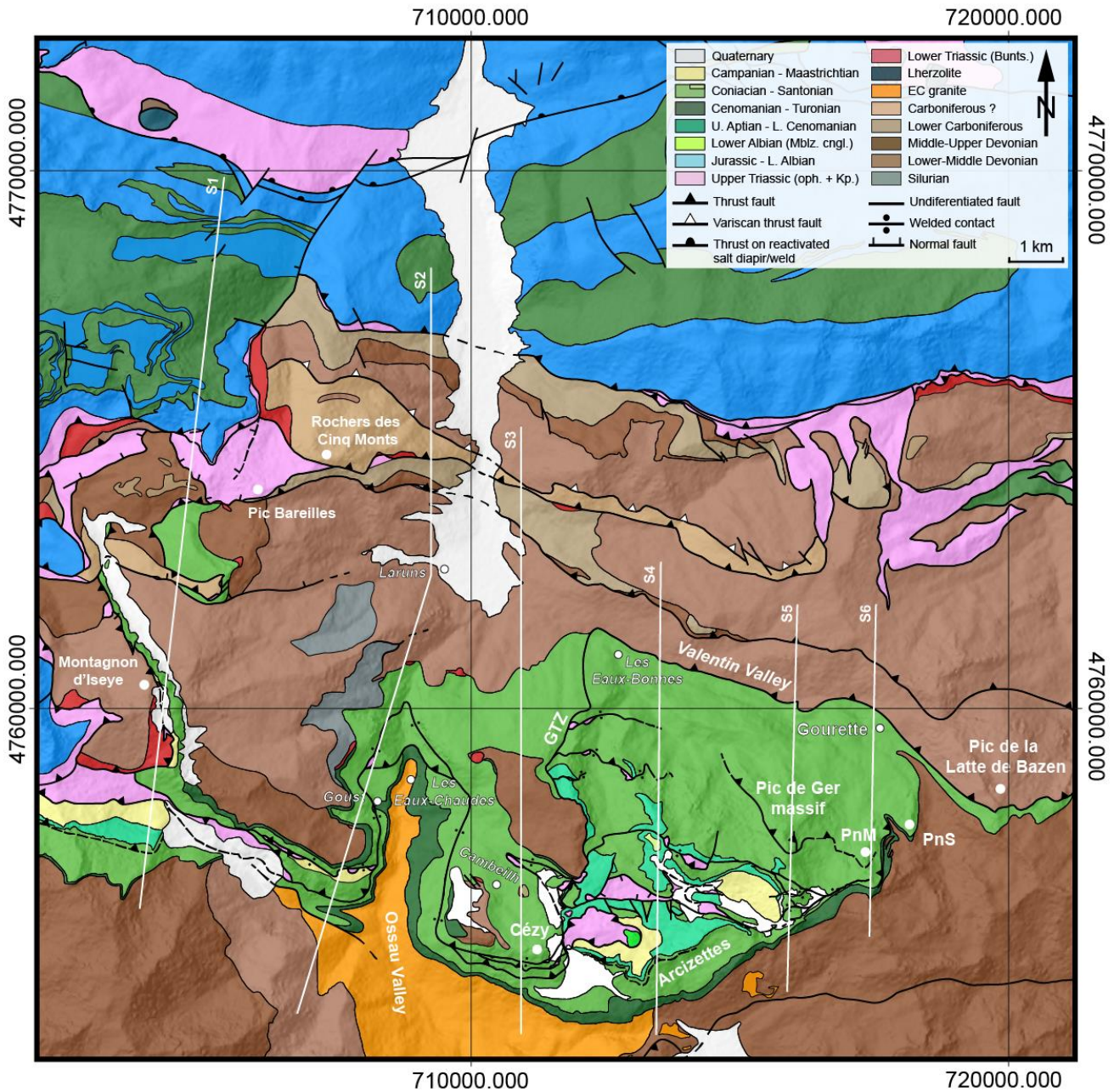
Figure 1.7: *Geological map of the Eaux-Chaudes massif and surrounding areas modified from Caldera et al. (2023) (location in Fig. 1.6A). Cross sections S2 and S5 are shown in Fig. 1.7 and are representative of the change in the structural style between the western and the eastern sectors of the ECM. PnM: Pêne Médaa ridge; PnS: Pêne Sarrière ridge; GTZ: Gourzy transfer zone.*

sandstones, and quartzites Devonian of age (Ternet et al., 2004), culminating with turbidites and limestones of the Carboniferous Culm facies (Delvolvé, 1987). These rocks were folded during the Variscan orogeny and are intruded by a late Carboniferous granodiorite (301±9

Ma; Guerrot, 2001) known as the Eaux-Chaudes pluton (ECP), which together with the Upper Cretaceous autochthonous succession immediately above, shows little deformation during the Alpine orogeny (Fig. 1.8A; Caldera et al., 2021). Along the unconformity between the Paleozoic basement and the Upper Cretaceous, occasionally Lower Triassic Buntsandstein sandstone to conglomerate pods are preserved (Ternet, 1965), allowing to constraint the polarity of the Paleozoic-Mesozoic succession wherever deformed (Fig. 1.9).

The middle-upper Triassic Keuper in the Eaux-Chaudes massif and vicinity is composed of a melange of claystone and cargneule, enclosing Muschelkalk limestones, and ophites. Although Keuper evaporites are not observed at the surface, these are commonly described in adjacent Pyrenean pre-orogenic basins, essentially in the subsurface (e.g., Biteau et al., 2006; Ortí et al., 2017; Soto et al., 2017). In the Eaux-Chaudes massif ss., Caldera (2022) and Caldera et al. (2023) interpreted the Keuper exposures to belong to an allochthonous sheet carried by the Lakora thrust.

The Upper Cretaceous carbonates, of Cenomanian to Santonian age, represent a shelf in the proximal margin of the Iberian plate during the Pyrenean post-rift stage (Casteras, 1956; Casteras and Souquet, 1964; Ternet, 1965; Alhamawi, 1992). The Cenomanian consists of a quartz-rich microconglomerate to coarse sandstone at the bottom that pass vertically to packstones and mudstones (Conard and Riuolt, 1977; Caldera, 2022). The thickness of the Cenomanian is ~25m and it lies on top of any Paleozoic unit (Figs. 1.7-1.9). A Turonian limestone is highly variable in thickness (maximum of 80m) and is shown partly dolomitized at the base. The transition to the Coniacian is usually recognized by a ~40m pack of dolomitized grainstones and packstones (Alhamawi, 1992; Ternet et al., 2004).

The Santonian limestone is the most visible and recognizable unit along the massif (Fig. 1.7-1.9). It consists of a widespread, white-coloured massive limestone with a thickness of 250m
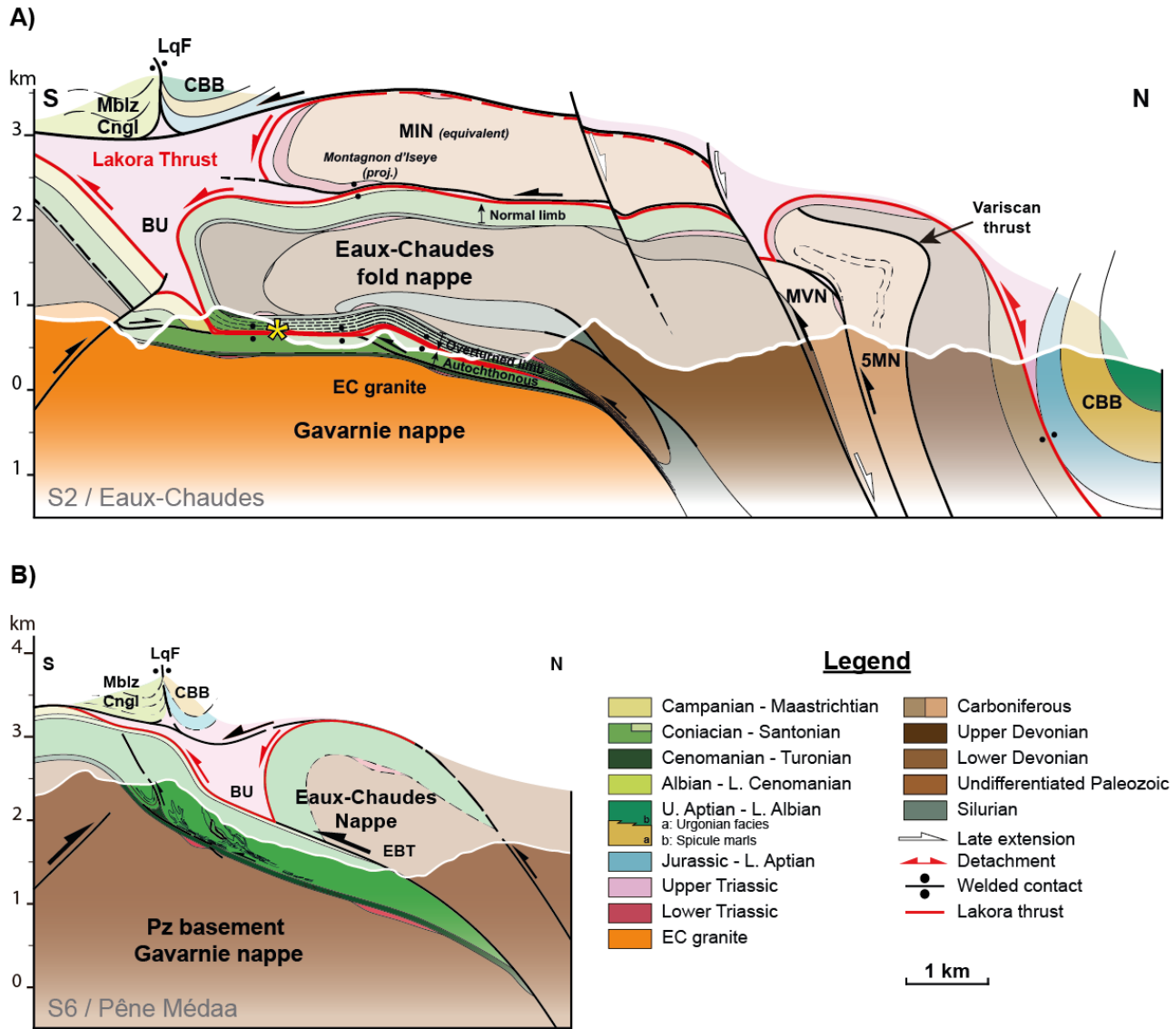
Figure 1.8: A) *Representative cross-section of the western sector of the ECM from Caldera et al. (2023) in the Ossau valley displaying the main geometrical features of the Eaux-Chaudes recumbent fold nappe (S2 in Fig. 1.7). Yellow asterisk indicates the location of a pinched allochthon Keuper in the welded syncline of the recumbent fold. The Paleozoic autochthon is represented by the Eaux-Chaudes pluton, little deformed during the Alpine compression.* **B)** *Representative cross-section of the eastern sector of the Eaux-Chaudes massif from Caldera et al. (2023) (S6 in Fig. 1.7). The recumbent fold nappe is no longer observed, and the Eaux-Chaudes nappe is interpreted to be replaced by a simple fold-thrust structure, eastward of the Gourzy transfer zone, transferring much of the deformation to the Upper Cretaceous autochthon, which is characterized by ductile features. In contrast with the western section, the Paleozoic autochthon is represented by Devonian metasedimentary rocks. Mblz Cngl, Mendibelza Conglomerates; LqF, Licq Fault; CBB, Chaînons Béarnais Belt; MIN, Montagnon d'Iseye nappe; 5MN, Cinq Monts nappe; MVN, Montagne Verte nappe; BU, Bedous Unit (carried by the Lakora thrust); EBT, Eaux-Bonnes Thrust.*

(Ternet, 1965) that forms the highest reliefs. This unit ends with ~6-30m of limestone with silex nodules, commonly developed in the cover of the western Axial Zone (Souquet, 1967; Teixell, 1992).

The Santonian limestones are followed by sandstone-shale flysch deposits of Campanian-Maastrichtian age (Ternet, 1965), recording the first stages of the flexural subsidence related to the Pyrenean orogeny (Teixell, 1992). This unit could reach several hundreds of meters in thickness in the Eaux-Chaudes massif (Ternet et al., 2004), but its top is not exposed.

The structure of the Eaux-Chaudes massif along the Ossau valley consists of ~9 km long recumbent fold nappe detached on the Silurian shales, with a large overturned limb showing ductile deformation in the Upper Cretaceous carbonates (Caldera et al., 2021). Raman Spectroscopy of Carbonaceous Material (RSCM) paleothermometry in these carbonates indicates maximum temperatures of ~350°C for the overturned limb of the Eaux-Chaudes structure (equivalent to greenschist facies conditions), consistent with observed mylonitic foliation and lineations in the Upper Cretaceous carbonates (Caldera et al., 2023). In the normal limb, which is comparatively little deformed, temperatures of ~310°C were reached, which led Caldera (2022) to deduce a relatively moderate geothermal gradient of ~30-45°C/km based on the Upper Cretaceous rocks. The recumbent fold is in tectonic contact over an autochthonous Upper Cretaceous cover with similar stratigraphy, attached to the Eaux-Chaudes pluton underneath (Fig. 1.8A). Small Buntsandstein remnants are pinched in the tectonic contact between the overturned limb and the autochthonous succession (yellow asterisk in Fig. 1.8A). The fold structure shows a marked strain increase towards the recumbent limb, and from the south to the north (Caldera, 2022; Fig. 1.10A).
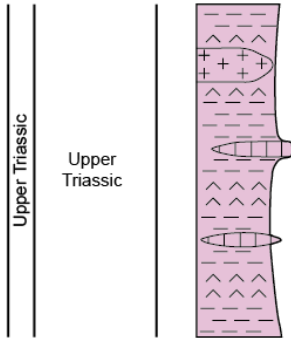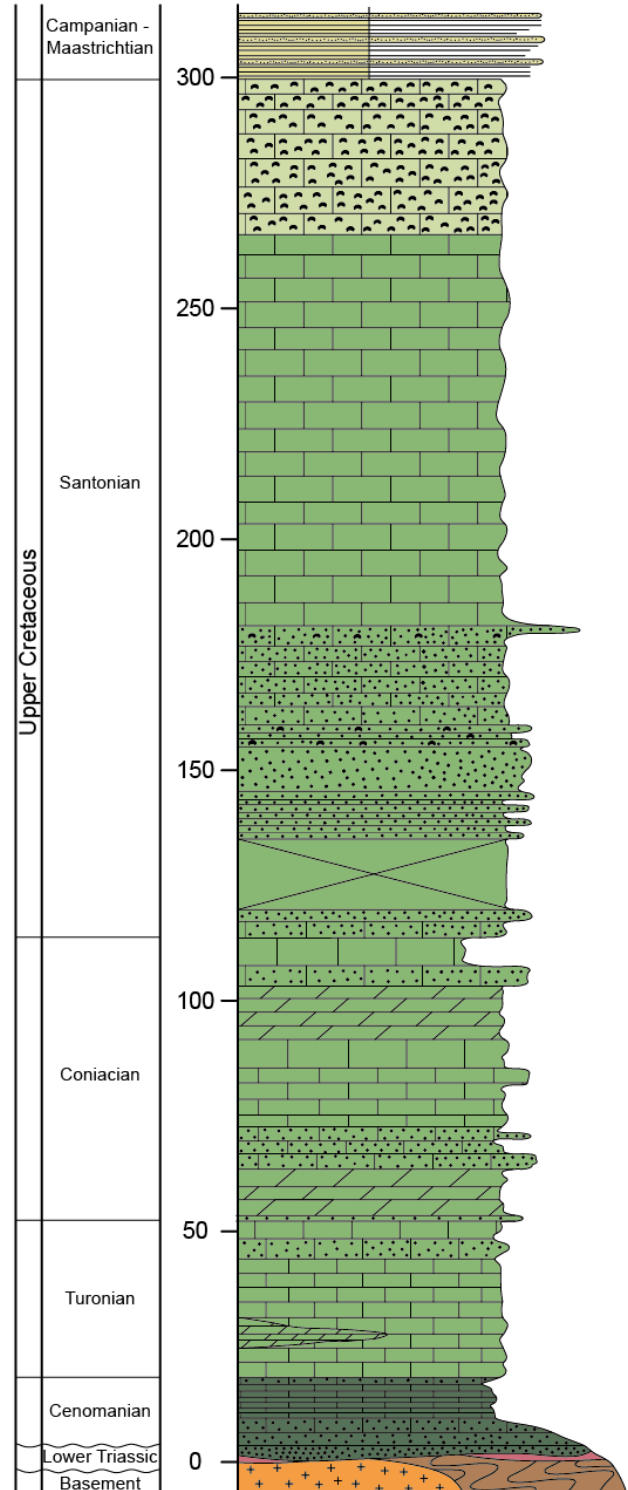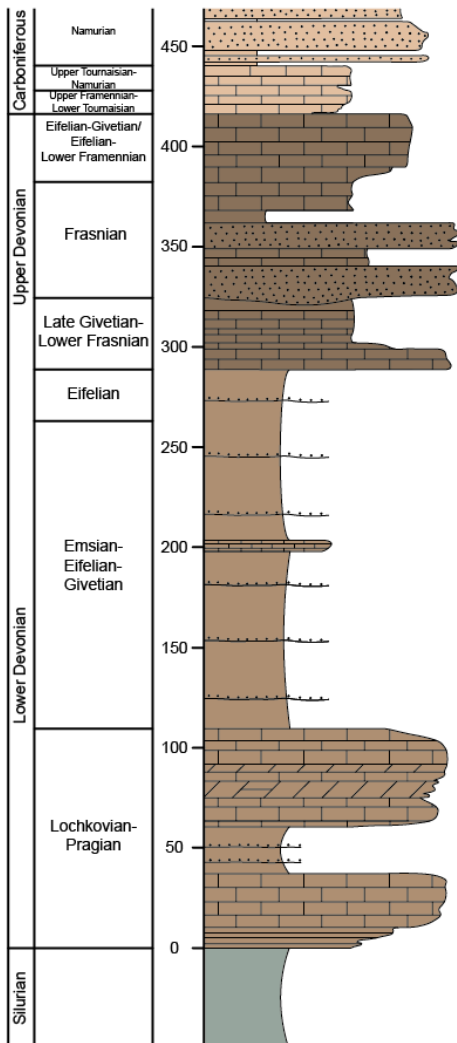
Figure 1.9: *Synthetic stratigraphic columns modified from Caldera (2022) of the different lithostratigraphic units outcropping in the Eaux-Chaudes massif and surrounding units.*

To the east, the structural style changes abruptly through the Gourzy transfer zone to a fold-thrust fan in the Upper Cretaceous carbonates (including the Eaux-Bonnes thrust, Fig. 1.8B, equivalent to the basal thrust of the fold nappe described in the west). The upper Cretaceous in this area also registered elevated temperatures (~350°C), consistent with the observed ductility of the limestones (Caldera et al., 2023; Fig. 1.11). In this area, the strain increase from north to south (Fig. 1.10B), and the autochthonous succession is attached to the metasedimentary Devonian limestones and slates just below (e.g., Fig. 1.8B). The latter are intensely deformed and reworked in the Alpine times, and so is the unconformity between them.
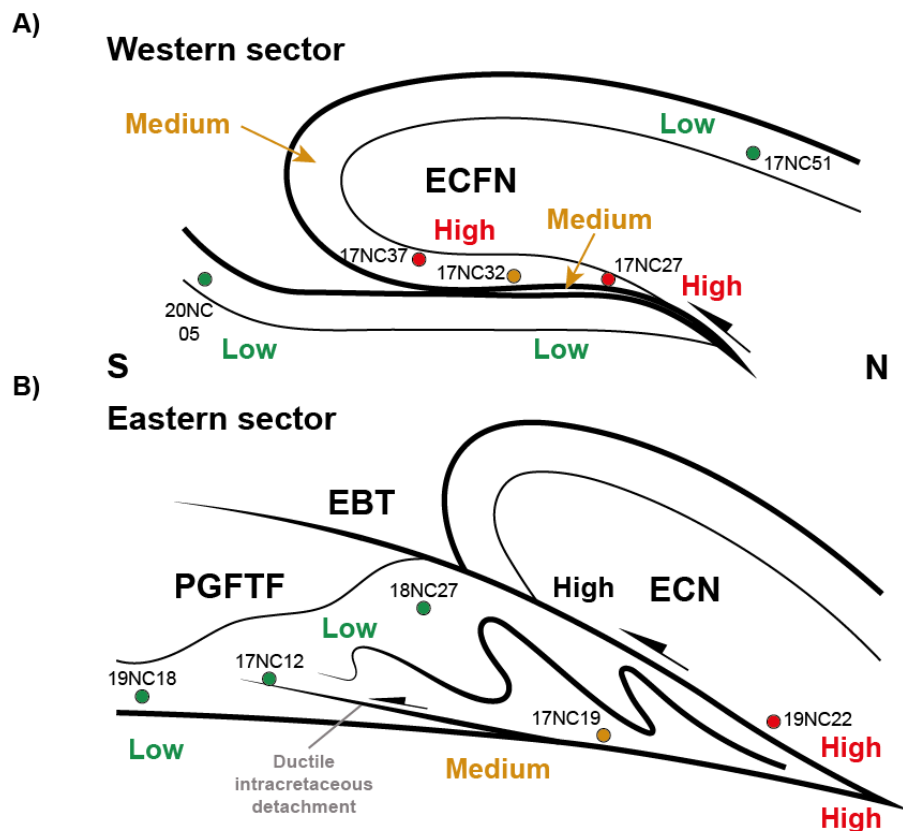
Figure 1.10: Sketch from Caldera (2022) highlighting the domains of strain using the fabric intensity as a proxy in the A) western sector or Eaux-Chaudes recumbent fold nappe domain and B) eastern sector or deformed autochthon domain. ECFN: Eaux-Chaudes Fold Nappe; EBT: Eaux-Bonnes thrust; PGFTF: Pic de Ger fold-thrust fan; ECN: Eaux-Chaudes Nappe.
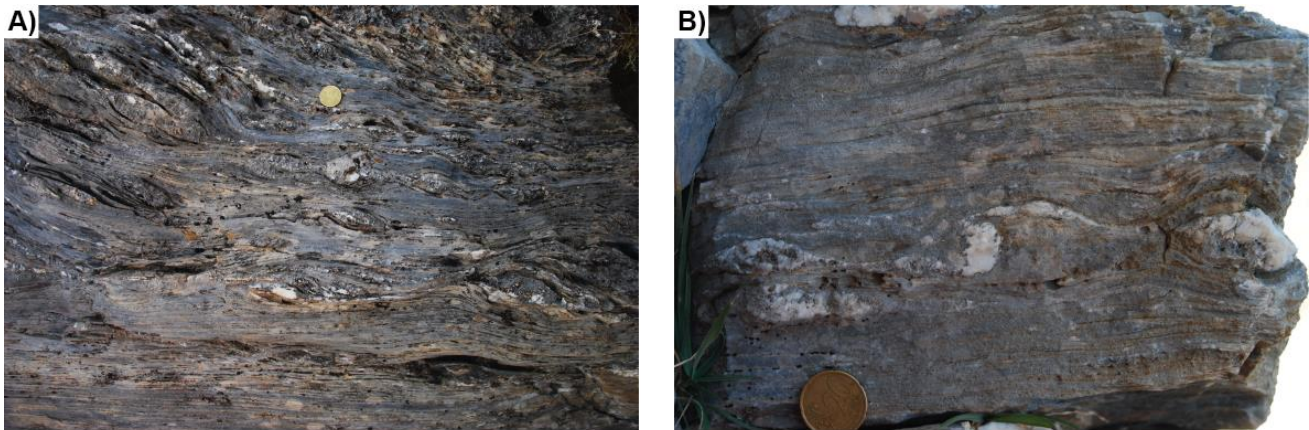
Figure 1.11: Examples from the ductility displayed by the Upper Cretaceous carbonates of the Eaux-Chaudes massif.

Both the recumbent fold nappe and the folds of the eastern deformed autochthon display a moderate plunge to the west. On the western hillsides of the Ossau valley the fold nappe disappears cartographically under the Lakora thrust sheets, a series of allochthonous units that carry Palaeozoic metasediments and Triassic (Buntsandstein, and Keuper facies of the Bedous unit, Fig. 1.8A), as well as Albian conglomerates (Mendibelza unit) (Figs. 1.7 and 1.8). To the north, these units are in turn overridden by the Chaînons Bearnais belt (CBB), a fold-thrust system involving Jurassic to Aptian carbonates and Upper Cretaceous flysch detached on the Keuper, affected by widespread diapirism (Teixell et al., 2016; Labaume and Teixell, 2020). The estimated burial for the Eaux-Chaudes massif from field observations by Labaume et al. (2016b) and Caldera et al. (2023) encompass from 8 to 12 km, although there is a large uncertainty in this estimation.

The whole system was uplifted in the hanging wall of the Gavarnie and Guarga thrusts during mid-late Eocene to Oligocene times, during fast exhumation and the tilting of the Axial Zone arch (Bosch et al., 2016; Labaume et al., 2016b). This produced a gentle northward tilt of the ECM, and small, north-verging back-thrusts, backfolds, and a steep foliation in the southern part of the massif (Caldera et al., 2023).

1.4. Motivation and objectives of the study

As aforementioned, the mechanical properties of rocks and the mechanical variations are key factors in the deformation style acquired in a particular region (e.g., Figs. 1.1 and 1.8). In the case of the Pyrenees, inherited extensional structures from the hyperextension (e.g., Chevrot et al., 2018), crustal-scale transfer zones (e.g., Saspiturry et al., 2022) or tear faults delimiting areas with marked different structural style (e.g., Caldera et al., 2023) highlighted the non-cylindricity of the northern Pyrenees.

The Eaux-Chaudes massif constitutes a unique starting-point natural laboratory to investigate the variables favouring the occurrence of thrust nappes or fold nappes, and to gain insight into the meaning of structural variations in terms of rheology and mechanical stratigraphy (e.g., Fig. 1.12). Moreover, the preservation of the Upper Cretaceous in this part of the Axial Zone is a key factor because it is a marker of the ductile deformation suffered during the Alpine orogeny, not easy to characterize in other areas of the Pyrenean Axial Zone. The presence of a stiff plutonic body, the alternance of weak and stiff layers and their initial geometrical configuration are among the key variables during the Alpine deformation of the Pyrenees which will be investigated (e.g., Fig. 1.12).

The main objective of this thesis is to reveal how to reconcile the high-temperature and ductile conditions observed in the Eaux-Chaudes massif reported in the regional study of the structure carried out by Caldera (2022) and determine the sequential timing of events that produced the Eaux-Chaudes fold nappe, including the age of the deformation and the exhumation of the structure.
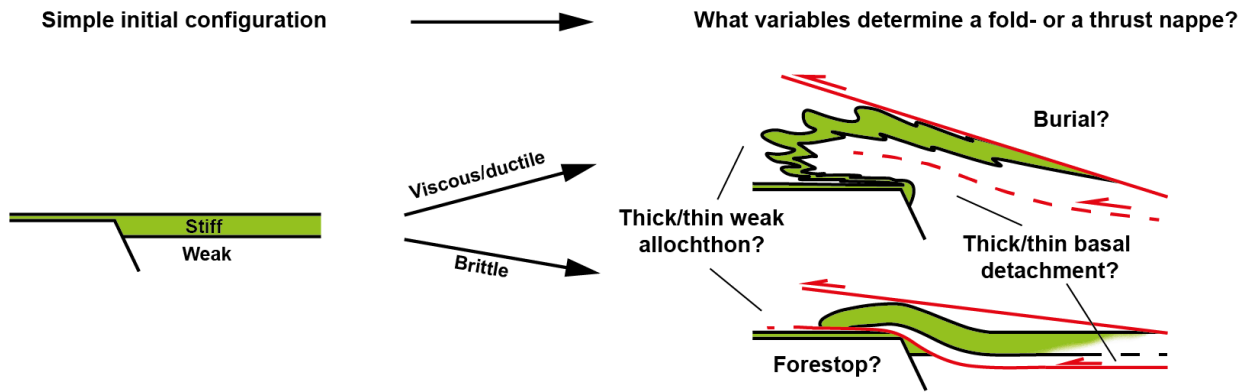
Figure 1.12: *Sketch of an alternance of stiff and weak layers within a thick shear zone and the variables that could determine the dominant frictional-plastic/brittle or viscous/ductile behaviour, therefore, the structural style developed.*

The specific objectives of this study are summarised as follows:

- To model under which geometric and mechanic conditions in terms of mechanical stratigraphy (plasticity vs. viscosity) a thrust- or a fold nappe with a long recumbent limb are favoured, based on the Eaux-Chaudes fold nappe natural example and applicable to other orogens worldwide.

- Related to the latter point and to the paleotemperature record provided by Caldera (2022), to model under which range of thermo-mechanical and rheological conditions one of the two types of nappes is favoured.

- To constrain the sequence of events and the age of folding in the Eaux-Chaudes massif, to better understand the timing of the inversion process in the upper Iberian margin in the west-central Pyrenees.

- To provide information on the timing of exhumation of the Upper Cretaceous of the Eaux-Chaudes recumbent fold nappe and the autochthonous of the eastern sector (the low-temperature thermochronology performed by Bosch et al. (2016) was exclusively focused in the Eaux-Chaudes pluton), as well as of the overlying upper nappes (i.e., Montagnon d'Iseye, Cinq-Monts and Chaînons Béarnais units).

- To model the thermal history of the Eaux-Chaudes massif from the exhumation data to better understand the thermicity observed in the area and its timing.

1.5. Thesis structure

This thesis is divided into 9 chapters. It constitutes the work I have done at the Department of Geology of the Universitat Autònoma de Barcelona (UAB) to obtain the degree of PhD, with collaboration with the Johannes Gutenberg University Mainz and the University of Texas at Austin. The chapters of this thesis are organised as follows:

- **Chapter 2** describes the methodology used to achieve the main objectives proposed.
- **Chapter 3** contains an analysis by means numerical modelling simulations (LaMEM numerical code) of the role of the inherited geometry and the mechanical stratigraphy on the development of thrust and fold nappes under linear viscosities, non-dependent on temperature.
- **Chapter 4** extends the modelling study by including the influence of the temperature and non-linear rheologies on the numerical simulation of thrust and fold nappes, by means of thermo-mechanical modelling.
- **Chapter 5** presents the results of a study of calcite veins in the Eaux-Chaudes massif as kinematic indicators of the deformation, and shows the geochronological results obtained in vein calcite and their implications.
- **Chapter 6** presents the thermochronology (ZHe) results to constraint the exhumation and late thermal evolution of the Eaux-Chaudes massif by the obtention of central ages of cooling and by inverse thermal modelling results (QTQt software).
- **Chapter 7** contains a general discussion of the results presented in chapters 3, 4, 5, and 6.

– **Chapter 8** presents the main conclusions of this work.

– **Chapter 9** contains the references cited.

– **Annex A.3** shows complementary mechanical simulations in addition to those shown in Chapter 3

– **Annex A.4** contains the complementary thermo-mechanical simulations in addition to those of Chapter 4

– **Annex A.5** contains the geochronology data repository from Chapter 5 and also the complete series of Tera-Wasserburg age plots of all the analysed samples.

– **Annex A.6** includes the complete series of QTQt model runs performed in this work.

Chapter 2: Methodology

Chapter 2 describes the workflow used to achieve the proposed objectives. This thesis is based on a multi-method approach combining classical field work, numerical simulations to generate prediction models, novel and recently developed instrumental techniques (*in-situ* LA-ICP-MS U-Pb dating in calcite), and classical instrumental methods (low temperature (U-Th)/He thermochronology).

2.1. Fieldwork

This thesis is based on 66 days of fieldwork in the Eaux-Chaudes Massif and the surrounding structural units from October 2018 to October 2022. Due to high mountain weather conditions, the Eaux-Chaudes massif is covered by snow from November to June, and field campaigns (each from 5 to 12 days) had to be scheduled in the summer. The characteristic high relief of the Eaux-Chaudes massif makes it difficult to access the study area by car outside the main roads (where the Upper Cretaceous outcrops are scarce), and access to elevated areas via the few off-roads was only possible prior to municipal permit demand. Hence, most of the effort and time was inverted in hiking to access remote areas for sampling, recognizing, and describing the geology or taking panoramic photos of the outcrops.

Field structural data acquisition (bedding and foliation dips, calcite vein orientation, stretching lineation, and fold axes) was performed using a tablet (IPAD model Air A1566) and FieldMove application for structural data. These data were later processed in the office with the MOVE software using an academic license provided by Petroleum Experts and plotted using the Stereonet© software (Cardozo and Allmendinger, 2013).

Since the mapping and recognition of the structure at the macro- and microscale was performed by Caldera (2022), the main objective of the fieldwork focused on the search for

kinematic indicators registered by the Upper Cretaceous rocks (i.e., calcite veins). These are very useful for constraining relative chronologies at the outcrop scale, which could then be extrapolated to a larger scale and susceptible to be dated by LA-ICP-MS U-Pb in calcite, allowing us to put a precise age on the deformational event. Another objective of the fieldwork was the sampling of the Upper Cretaceous rocks at different structural positions of the Eaux-Chaudes Fold Nappe (ECRFN) and also the Paleozoic structural units (i.e., Montagnon d'Iseye nappe, Cinq-Monts nappe and Bois de la Traillère nappe) to obtain suitable apatite and zircon grains to analyse by low temperature (U-Th)/He thermochronology.

During fieldwork, a total number of 220 samples were collected from the Eaux-Chaudes massif, including calcite veins (125 samples) and bedrock samples for facies identification and petrographic recognition of the metamorphic and tectonic processes recorded by the rocks (60 samples). In addition, 5–10 kg were collected for each sample intended for the low-temperature thermochronologic study because of the calcareous nature of the massif (35 samples).

2.2. Laboratory work

Petrographic and geochemical analyses were performed on samples collected in the field. The methods used included classical petrography and cathodoluminescence from thin sections, major element analysis (ICP-MS), zircon separation, (U-Th)/He thermochronology, and *in-situ* LA-ICP-MS U-Pb geochronology in calcite. These methods are described in detail below.

2.2.1 Petrography from thin sections

A total number of 144 thin sections were made from the 220 samples collected in the ECM area and surrounding units (i.e., Montagnon d'Iseye nappe, Cinq-Monts nappe and Bois de la Traillère nappe). Most of the thin sections belong to calcite veins of the Upper Cretaceous

carbonate rocks, but they also include Triassic (Buntsandstein) sandstone and Paleozoic metasedimentary rocks.

The samples were oriented in the field, and thin sections were made normal to the foliation and parallel to the stretching lineation (where identified) to observe the fabrics and symmetry. Some samples were cut multiple times in the regions of interest (i.e., porphyroclasts, rods, etc.). Petrographic observations of the thin sections were made using a Nikon Eclipse E400 Polarizing Light microscope connected to a Nikon DS-F/3 12V camera.

2.2.2. Cathodoluminiscence

Cathodoluminescence (CL) is a non-destructive imaging technique that can be used to distinguish crystal growth zonation and mineral generation from different fluids. If applied to fracture-filling carbonates (calcite and dolomite), it can provide clues to different fracture opening events, which is especially useful because it allows us to date different tectonic processes using the *in-situ* LA-ICP-MS U-Pb technique (if there is enough [U] and low common [Pb]). The intensity of the CL is a function of the trace elements present in the calcite and dolomite structures (Roberts et al., 2020), where Mn^{2+} is the main brightness activator and Fe^{2+} is the principal suppressor (e.g., Machel, 1985, 2000; Savard et al., 1995; Hiatt and Pufahl, 2014; Roberts et al., 2020). Although U is a trace element in carbonate minerals, the luminescence is not specifically related to it (Roberts et al., 2020), and in some cases, it can also be activated by rare earth elements (REEs) and Pb^{2+} (Richter et al., 2003).

To identify the possible different fracture-filling calcite and dolomite cements that potentially register different fluid events related to recumbent folding or thrusting in the ECM, petrographic observations of 25 selected and polished thin sections were made under a cathodoluminescence microscope. A Technosyn Cold Cathode Luminescence model 8200 MkII at Universitat de Barcelona (Spain), with operating conditions of 15-18 kV and gun

current of 300-350 µA was used to distinguish different types of cements susceptible to dating using the LA-ICP-MS technique.

2.2.3. Element analysis (ICP-MS)

Prior to the geochronological analyses of calcite veins by *in-situ* LA-ICP-MS U-Pb in calcite, major element analyses (Ca, Mg, Mn, Fe, Sr, Na, U, and Pb) by mass spectrometer inductively coupled plasma (ICP-MS) were performed to provide information about the availability of U to address the dating of the veins. Samples were analyzed using the Thermo Scientific mode Element XR in the Geochemical Laboratory labGEOTOP of the GEO3BCN-CSIC. A second batch of samples was analyzed using Agilent ICP-MS, model 7900, at the chemical analytics service facility (SAQ) of the Universitat Autònoma de Barcelona.

Representative calcite veins from different domains of the ECM were sampled from trims using a 400/500 µm-diameter dental drill at the petrographic laboratory of the Universitat de Barcelona. Up to 100 mg of each powdered sample was dried at 40°C for 24h and acid digested in closed vessels with a combination of HNO_3, HF, and $HClO_4$ (2.5 mL : 5 mL : 2.5 mL v/v). These were then evaporated and 1 mL HNO_3 was added for double evaporation. Finally, the samples were re-digested and diluted with MilliQ water (18.2 $M\Omega cm^{-1}$) and 1 mL of HNO_3 in a 100 mL volume flask.

2.2.4. In situ LA-ICP-MS U-Pb geochronology in calcite

The applied method was similar to that described in Palacios-Garcia et al. (2023). The U-Pb analyses were carried out at the UTChron Laboratory of the University of Texas at Austin in four fully automated sessions in a period between 24-09-2021 and 29-11-2021. Samples were ablated with a Teledyne Analyte G2 193 nm Excimer laser, with a Helex dual volume sample cell. The ablated material was transported by helium carrier gas to a Thermo-Element 2, High-Resolution Single Collector Magnet Sector (HR-ICP-MS). Laser conditions included an

energy of 6 mJ, a repetition rate of 10 Hz and a fluence between 2.79 J/cm2 and 4.04 J/cm2 depending on the session (Table 2.1).

Session	Date	Sample	Spot ⌀	Fluence (J/cm²)
1	24/09/2021	19MG21	110 µm	2.79
		19MG74A		
		19MG74B		
		19MG79		
2	08/10/2021	19MG21	85 µm	3.80
		19MG46		
		19MG74A		
		19MG79		
3	05/11/2021	19MG20	85 µm	3.59
		19MG21		
		19MG43		
		19MG46	135 µm	
4	29/11/2021	19MG20	85 µm	4.04
		19MG32		
		19MG67		
		19MG43	65 µm	

Table 5.2: *Detailed laser conditions during each performed session at the UTChron Lab*

Different spot sizes were used depending on the thickness of particular veins. Some samples were revisited in successive sessions to focus on the zones with the highest [U]. The laser conditions were optimized to maximize the signal strength and stability, while ensuring that no melting occurred at the ablation site. The samples were analysed with *in-situ* LA-ICP-MS in polished billets (0.5 cm thick). The individual spot analysis consisted of 10 pre-ablation shots for surface cleaning followed by 25 seconds of baseline data collection, and then 300 ablation shots were fired finally followed by 27 seconds of washout. Between 15 and 75 spots were ablated in each cement, counting a total of 100-150 spots per sample and approximately 1606 spots in total (including WC-1 and NIST-614 standards). The repository of the obtained data grouped per session is presented in Appendix A.5 (Tables A5.1, A5.2, A5.3, and A5.4).

The age calculations were performed with the Iolite v3.5 software (Paton et al., 2011) and VisualAge_UcomPbine program of Chew et al. (2014). Elemental and isotopic fractionation were corrected by interspersed analysis of the primary calcite reference material WC-1 (Roberts et al., 2017). Analyses were performed in a repeated series of two standards followed by ten unknowns, with NIST-614 measured periodically to monitor the Pb isotopic fractionation (Hollocher and Ruiz, 1995). As explained in Palacios-Garcia et al. (2023), the primary reference material, WC-1, was corrected for common Pb by using the ^{207}Pb isotope (^{207}Pb/^{206}Pb = 0.85; Roberts et al., 2017). Time-integrated data were exported from the Iolite as entire 30-s ablation windows when isotopically homogenous or broken up into several shorter ablation windows when exhibiting isotopic variation to maximize spread in common Pb composition. When calcite precipitate in the veins it incorporates ^{238}U and ^{235}U to the crystal lattice, which decays to ^{206}Pb and ^{207}Pb respectively. However, it also can incorporate initial or "common Pb", which refers to any non-radiogenic source of Pb (usually calculated as the ^{238}U/^{204}Pb). In an ideal U-Pb geochronometer, the amount of common Pb is zero, and all daughter Pb is product of the parent U decay if it remains in a closed system. However, if the system becomes open, variable amount of common Pb can be incorporated into the calcite or part of the U can be lost, restarting the geochronometer or adding imprecision to the age (e.g., Roberts et al., 2020).

The ^{207}Pb/^{206}Pb and ^{238}U/^{206}Pb isotopic ratios, together with the associated absolute 2σ errors, were plotted on Tera-Wasserburg diagrams (Tera and Wasserburg, 1972), and lower intercept ages were calculated using IsoplotR (Vermeesch, 2018). Data showing large error ellipsoids (>25% error) off the regression line and/or spots hitting two types of cement or the host rock were excluded from age determination according to the recommendations of Roberts et al. (2020).

2.2.5 Zircon (U-Th)/He Thermochronology

The laboratory work consisted of obtaining suitable zircons and apatites of the study area samples for low-temperature (U-Th)/He thermochronology. From the 220 total samples of this thesis project, 35 were collected in the different structural units recognized, conforming vertical profiles where possible.

The heavy mineral fraction of the samples was obtained following standard separation methods based on the methodologies proposed by Mange and Maurer (1992) and Andò (2020) at the Thin Section Laboratory and Petrographic and Geochemical Laboratory of the Department of Geology of the Universitat Autònoma de Barcelona. Samples were crushed with a Retsch Disc Mill DM 200 and submitted to Struers Metason 200 for 5 minutes to disaggregate the well-cemented sand and clay coatings, and then sent to a digital electromagnetic sieve shaker BA-200 (dry sieving) to obtain the <500μm fraction. Then, the recovery of the heavy fraction was performed first using a Holman-Wilfley laboratory shaker table and then by the centrifuging method (using nontoxic dense liquid Na-polytungstate; 3.00 – 3.05 g/cm3) and partial freezing with liquid nitrogen (Andò, 2020). Zircon and apatite were obtained using a Slope Frantz isodynamic magnetic separator at the Universitat de Barcelona and the UTChron laboratory of the University of Texas at Austin.

The (U-Th)/He analyses were performed at the UTChron Laboratory at the University of Texas at Austin. Mineral grains from the selected samples (11) belonging to the different structural units were handpicked and screened for inclusions using a Nikon SMZ-U/100 stereomicroscope with a rotating stage at the University of Texas at Austin. Zircons with fluid inclusions and fractures were excluded to be picked. All the grains were digitally photographed and archived using a Nikon camera. The grains were morphometrically measured using LabVIEW-based custom codes and imported to LabView routine to calculate

alpha-ejection correction. These values were uploaded and archived to the UTChron database. After morphometric characterization, the mineral grains were packed in Pt tubes and step-heated and degassed for He under ultrahigh vacuum. The total He concentration was measured using a quadrupole mass spectrometer (e.g., Brennan et al., 2020). After degassing, the zircons were unpacked from Pt tubes and dissolved with a combination of HF and HNO_3, which was analyzed using a Thermo Scientific Element2 ICP-MS for the absolute concentrations of U, Th, and Sm (Wolfe and Stockli, 2010). Incompletely dissolved grains were discarded from analysis. Fish Canyon zircons were used as reference material for monitoring data quality (Reiners, 2005), and an 8% standard error was applied to all zircon data measurements.

2.3. Office work

2.3.1. Numerical modelling

Mechanical and thermomechanical simulations were performed to study the constraints for thrust/fold nappe development and reproduce field observations of the Eaux-Chaudes recumbent fold nappe and gain understanding on the rheological, mechanical, geometrical and temperature conditions under which a determinate structural style (i.e., thrust nappe vs. recumbent fold nappe) is favoured over the others, so that the results could be extrapolated to similar setups or situations found in other orogens.

The 3-D thermomechanical staggered finite differences code LaMEM (Kaus et al., 2016) was used to perform 2D parametric simulations to investigate the controlling factors and changes in the deformation style between thrust nappes (plastic/brittle-localization) and recumbent fold nappes (viscous/ductile-distributed). The LaMEM code is based on the concept of continuum mechanics (e.g., Mase and Mase, 1970; Turcotte and Schubert, 2014) to solve partial differential equations describing the deformation of rocks.

We applied the conservation of mass, linear momentum, and energy using the following equations:

$$\frac{\partial v_i}{\partial x_i} = 0, \tag{2.1}$$

$$-\frac{\partial \mathrm{P}}{x_i} + \frac{\partial \tau_{ij}}{\partial x_j} = \rho g_i, \tag{2.2}$$

$$\rho C_p \frac{\partial \mathrm{T}}{\partial \mathrm{t}} = \frac{\partial}{\partial x_i}\left(\lambda \frac{\partial \mathrm{T}}{\partial x_i}\right) + H_R + H_S, \tag{2.3}$$

where x_i is the Cartesian coordinate system (1 is for x-direction, 2 for y-direction and 3 for z-direction), v_i is the component of the velocity vector, P is the pressure, $\tau_{ij} = \sigma_{ij} + P\delta_{ij}$ represents the components of the deviatoric Cauchy stress tensor (δ_{ij} is the Kronecker delta), ρ is density, $\vec{g_i}$ is the gravity vector with a value of [0 0 9.8], C_p is the specific heat, λ is the thermal conductivity, H_R is the radiogenic heat production and H_S the shear heating.

The simulations were performed using visco-elasto-plastic rheology with linear viscosities in the case of the purely mechanical simulations:

$$\dot{\varepsilon}_{ij} = \dot{\varepsilon}_{ij}^{el} + \dot{\varepsilon}_{ij}^{vs} + \dot{\varepsilon}_{ij}^{pl} = \frac{\tau'_{ij}}{2G} + \frac{\tau_{ij}}{2\eta_{eff}} + \dot{\varepsilon}_{II}^{pl} \frac{\tau_{ij}}{\tau_{II}}, \tag{2.4}$$

where $\dot{\varepsilon}_{ij}$ is the deviatoric strain rate tensor; $\dot{\varepsilon}_{ij}^{el}, \dot{\varepsilon}_{ij}^{vs}, \dot{\varepsilon}_{ij}^{pl}$ are the elastic, viscous and plastic components of the deviatoric strain rate tensor; $\tau'_{ij} = \frac{\partial \tau_{ij}}{\partial t} + \tau_{ik}\omega_{kj} - \omega_{ik}\tau_{kj}$ is the Jaumann objective stress rate; $\omega_{ij} = \frac{1}{2}\left(\frac{\partial v_i}{x_j} - \frac{\partial v_j}{\partial x_i}\right)$ is the spin tensor; G is the elastic shear modulus; η_{eff} is the effective viscosity; and τ_{II} is the square root of the second invariant of the stress tensor; $\tau_{II} = \left(\frac{1}{2}\tau_{ij}\tau_{ij}\right)^{1/2}$. In the case of the thermo-mechanical simulations, the temperature-dependent viscosity is governed by the equation:

$$\eta_{eff} = 2 \left[B_n \, e^{-\frac{En + P \, Vn}{RT}} \right]^{1/n} \dot{\varepsilon}_{II}^{\left(1 - \frac{1}{n}\right)}, \tag{2.5}$$

where η_{eff} is the viscosity; B_n is the creep constant, E_n is the activation energy, R the universal gas constant, n is the stress exponent and $\dot{\varepsilon}_{II}$ is the square root of the second invariant of the strain rate tensor ($\dot{\varepsilon}_{II} = \left(\frac{1}{2}\dot{\varepsilon}_{ij}\dot{\varepsilon}_{ij}\right)^{1/2}$).

The magnitude of the plastic strain rate ($\dot{\varepsilon}_{II}^{pl}$) is determined by applying the Druker-Prager criterion for plasticity:

$$\tau_{II} \leq \tau_Y = \sin(\phi)\, P + \cos(\phi)\, c, \tag{2.6}$$

where τ_Y is the yield stress; ϕ is the friction angle, P is the pressure and c the cohesion.

The systems equation is solved with LaMEM using a discretization of the continuum based on a staggered-grid finite-difference approach. Material properties were advected using the marker-in-cell method, and a free surface was implemented using the sticky air approach.

In the initial setup, a free-slip boundary condition was applied to the left and right sides of the models to allow free vertical displacements and a constant strain rate of 10^{-15} s^{-1} from both sides of the model.

2.3.2. Thermal modelling

Thermochronometric data obtained in this study (see sections 2.2.5 and 6.2) was modelled using the QtQt software (Gallagher, 2012), which performs inverse thermal histories using the Bayesian transdimensional Markov Chain Monte Carlo (MCMC) (Gallagher et al., 2009). During the inversion, the QTQt software first defines random time-temperature paths to approximate a thermal history, allowing the modeling of the observed data, which is limited by user-defined constraints. Subsequently, the thermal history is altered to produce a

proposed model that is compared to the data. If the data fit the model well, it is accepted and statistically contributed to the overall collection of models; otherwise, it is rejected. Following the recommendations of Abbey et al. (2023), this process was repeated 300.000 times each model run. The acceptance of the proposed model is done as a function of the data fit (likelihood functions). The output released by the QTQt software is a probabilistic ensemble of all accepted thermal history models, where the maximum likelihood model is the one which most fits the data, although it could be complex because it can include features that may not be justified by the data. Nevertheless, the software also releases the weighted mean model (expected model), which contains the most relevant features of the posterior (i.e., accepted) models, averaging out less certain features. The ZHe and AHe ages were modelled using spherical diffusion, where α-ejection and diffusion during the thermal history were also simulated.

The software includes the radiation models of Flowers et al. (2009) and Gautheron et al. (2009) for apatite, and Guenthner et al. (2013) for zircons. The software can use resampled ages instead of the observed ages by using a normal distribution based on the observed age with a standard deviation equal to the input error, which allows for the uncertainty in the ages. The same process can be done with the error (resampling error), which consists of introducing a scaling factor in the observed error to treat the data as more precise (low scaling) or less precise (high scaling). This approach assumes that there is no major disruption between samples; therefore, they have experienced similar thermal histories. Modelled thermal histories for the uppermost and lowermost samples are simulated together with the temperature offset in every iteration, and the thermal histories of the samples in between both are linearly interpolated (Gallagher et al., 2009; Gallagher, 2012, 2021).

2.4. Glossary of terms and definitions used in this manuscript

To facilitate the comprehension and the easy-reading of this thesis memoir, a short glossary of terms and abbreviations which are used is presented in this section.

- ***Linear behaviour***: This term is used in the numerical modelling to describe a linear relationship between the deviatoric strain-rate and stress tensors (i.e., $\dot{\varepsilon} \propto \sigma$). It implies that the stress exponent *n* is equal to 1. For this condition the viscosity is constant.

- ***Non-linear behaviour***: This term is employed to describe non-linear relationship between deviatoric strain-rate and stress tensors $\dot{\varepsilon} \propto \sigma^n$, where *n*>1. It implies that viscosity is strain-rate dependent.

- ***Mechanical models***: The mechanical models are those simulations in which the employed rheologies (linear or non-linear behaviour) are non-temperature-dependent.

- ***Thermo-mechanical models***: Refers to those simulations made using LaMEM software in which the rheologies (linear or non-linear elasto-viscoplastic) are temperature-dependent.

- ***Media (chapter 4)***: This term is restricted to chapters 4 and 7 and is utilized to englobe the Silurian, the Eaux-Chaudes granite and the Keuper layers in the thermomechanical simulations.

- ***Plastic vs. ductile strain***: Following the common usage in modelling studies, plastic strain is used to describe deformation under dominantly brittle conditions (after yield defined by frictional criteria). On the other hand, ductile strain is employed to describe deformation under dominantly viscous behaviour (i.e., with no plasticity developed).

- ***Bulk natural strain***: The natural logarithm of the ratio between final and original length.

- ***Second invariant of the strain-rate ($\dot{\varepsilon}_{II}$)***: it is a physical quantity of the strain-rate tensor independent of the reference coordinate system and provides a quantification of the

intensity of the deformation. The $\dot{\epsilon}_{II}$ is one of the real roots of the characteristic equation of the strain rate tensor and is expressed as $\dot{\epsilon}_{II}^2 = \frac{1}{2}\left(\dot{\epsilon}_{ii}\,\dot{\epsilon}_{jj} - \dot{\epsilon}_{ij}\,\dot{\epsilon}_{ji}\right) = \dot{\epsilon}_{xx}\dot{\epsilon}_{yy} + \dot{\epsilon}_{yy}\dot{\epsilon}_{zz} + \dot{\epsilon}_{xx}\dot{\epsilon}_{zz} - (\dot{\epsilon}_{xy}^2 + \dot{\epsilon}_{yz}^2 + \dot{\epsilon}_{xz}^2)$, where $\dot{\epsilon}_{ij}$ are the components of the strain rate tensor in the system of reference (*x,y,z*).

- **(strain) localization levels**: this term refers to zones in the numerical simulations with high values of the second invariant of the strain rate tensor.

Chapter 3: Fold vs. thrust nappes: insights from numerical modelling using linear elastoviscoplastic rheology

3.1. Introduction

Fold and thrust belts resulting from basin inversion in orogenic belts are mainly controlled by pre-existing geometrical factors (e.g., basin geometry, orientation of inherited structures and sedimentary layers, variations in cover/basement relationships, etc) and by the mechanical behaviour of the rocks involved in the deformation (i.e., brittle frictional sliding vs. ductile viscous creep) (e.g., Pfiffner, 1993; Bellahsen et al., 2014; Lacombe and Bellahssen, 2016).

Thrust nappes (or thrust sheets) and fold nappes could be considered as the two end-members of the so-called tectonic nappes, which are recognized in orogenic fold-and-thrust belts worldwide (e.g., Price and McClay, 1981). Although the geometry and kinematics of fold nappe structures are well documented after more than a century of studies (e.g., Lugeon, 1902; Heim, 1906, 1919-1922, Termier, 1906; Argand, 1916; Ramsay, 1980; Escher et al., 1993; Epard and Escher, 1996, Fernández et al., 2007; Bastida et al., 2014, Pfiffner, 2014), their mechanical controls are still being under discussion (e.g., Bauville and Schmalholz, 2017; Spitz et al., 2020; Kiss et al., 2020).

As pointed out by previous studies based on field observations, geometrical factors such as the alternation of weak and strong sedimentary layers and their relative thickness play a mechanical key role in the thrust or fold nappe development. Thus, the overall folding of strong layers is promoted over thrusting when the weak levels are relatively thick in comparison to the strong layers (e.g., Pfiffner, 1993; Epard and Escher, 1996, Erickson, 1996, Costa and Vendeville, 2002).

Tectonic inheritance is a key feature that must be considered in orogenic belts, not only due to the precursor geometry but also because of its influence on the mechanic behaviour of the system (e.g., Butler et al., 2006; Bellahsen et al., 2012; Zerlauth et al., 2014; Butler et al., 2018). The presence of stiff plutonic bodies or faults that can potentially act as buttresses can also exercise a control on the structural style developed in a region, by focusing the deformation (e.g., Wissing and Pfiffner, 2003; Bauville and Schmalholz, 2017; Kiss et al., 2020, Spitz et al., 2020).

In recent years, numerical modelling has become a powerful tool to unravel the influence of mechanical properties and initial geometry on the final configuration of fold-and-thrust nappes. Studies have been carried out particularly with application to the Helvetic nappes of the Alps, endorsing field observations and highlighting the relevance of the mechanical stratigraphy (e.g., Beaumont et al., 2000; Wissing and Pfiffner, 2003; Jaquet et al., 2014; Bauville and Schmalholz, 2015; Lafosse et al., 2016; von Tsharner et al., 2016; Bauville and Schmalholz, 2017; Spitz et al., 2020; Kiss et al., 2020).

In this sense, the infra-Helvetic nappes of the Alps (i.e., Morcles, Diablerets, Wildhorn) are interpreted as result of ductile closure of former extensional basins along thick basement shear zones, and the accompanying extrusion of the weak sedimentary cover infilling these basins (Belhassen et al., 2012; Spitz et al., 2020). In the Axial Zone of the Pyrenees, Caldera et al. (2021) recently described a basement-involved fold nappe structure affecting the strong Upper Mesozoic sedimentary lid in the Eaux-Chaudes area (western Axial Zone, France; Fig. 1.6 and 3.1). For this case, the ductile closure and extrusion of deep rifting Mesozoic basins cannot be invoked given that the fold structure was formed after a tabular carbonate platform deposited during the post-rifting stage. In general, Alpine deformation in the Pyrenean hinterland is interpreted as produced by thick-skinned thrust stacking of the basement rocks (i.e., Axial Zone) (e.g., Choukroune et al., 1989; Muñoz, 1992; Teixell, 1998; Beaumont et al.,

2000; Mouthereau et al., 2014; Teixell et al.,2018). The observation of a fold nappe structure affecting the Upper Cretaceous sedimentary cover in the hinterland of the Pyrenean orogen offers insights that can be compared to other orogens where similar ductile structures in sedimentary cover rocks are observed (e.g., the Helvetic Alps).

The objective of this chapter is to study the influence of the tectonic inheritance (i.e., initial configuration), mechanical stratigraphy (i.e., material properties and their constrasts), and rheology (e.g., brittle/frictional vs. viscous) on thrust or fold nappe development, based on the Eaux-Chaudes example. Additionally, I also try to explain and quantify the mechanisms under which a km-scale overturned recumbent limb can be developed (i.e., fixed hinge and stretching of the overturned limb vs. hinge migration and rigid limb rotation).

3.2. The mechanical modelling method

3.2.1. Model configuration

The structure of the Eaux-Chaudes fold nappe proposed by Caldera et al., 2021 is shown in Fig. 3.1. Restoration of the cross-section was done assuming plane strain, transport parallel to the cross-section and line-length balancing. Being aware of the uncertainty of the implicit assumption of the latter, the uncertainties in the amount of ductile deformation experienced by the recumbent limb (e.g., Caldera et al., 2023), two end-member options were used for the restoration to constrain the minimum/maximum length of the Upper Cretaceous cover. One option assumed no stretching of the recumbent limb (Fig. 3.1C and E), which gave an Upper Cretaceous panel 21.3 km long and 12.8 km of shortening (60%). The second extreme option was to assume that all the recumbent limb was formed by ductile/brittle simple shear (Fig. 3.1D and F), implying a discrete shear zone and offset between layer cut-offs, giving a restored Upper Cretaceous of 16.3 km long and 7.8 km of shortening (48%).

The geometrical features of the reference model to start the simulations is shown in Fig. 3.2. Based on the Eaux-Chaudes nappe restoration, it consists of 85 x 11 km model box with a numerical resolution of 256 x 136 (X x Z) elements, and a refinement of the mesh in the Z direction in the bottom part of the model (128 elements between -8 km < Z < -0.5 km). The model is divided in two main domains separated by the Lakora thrust detachment level of the allochthonous nappes. The hanging wall represents the allochthonous nappes of the Lakora and the North Pyrenean nappes (i.e., allochthonous Paleozoic-bearing upper thrust sheets and Mesozoic rocks of the CBB) while the footwall includes two subdomains representing the future Eaux-Chaudes nappe and its autochthonous footwall (Fig. 3.2B). The Lakora detachment was prescribed as a weak mechanical layer with a flat-ramp-flat geometry (Fig. 3.1 and 3.2). For the reference model, the angle of this ramp was defined to be β=10º. The
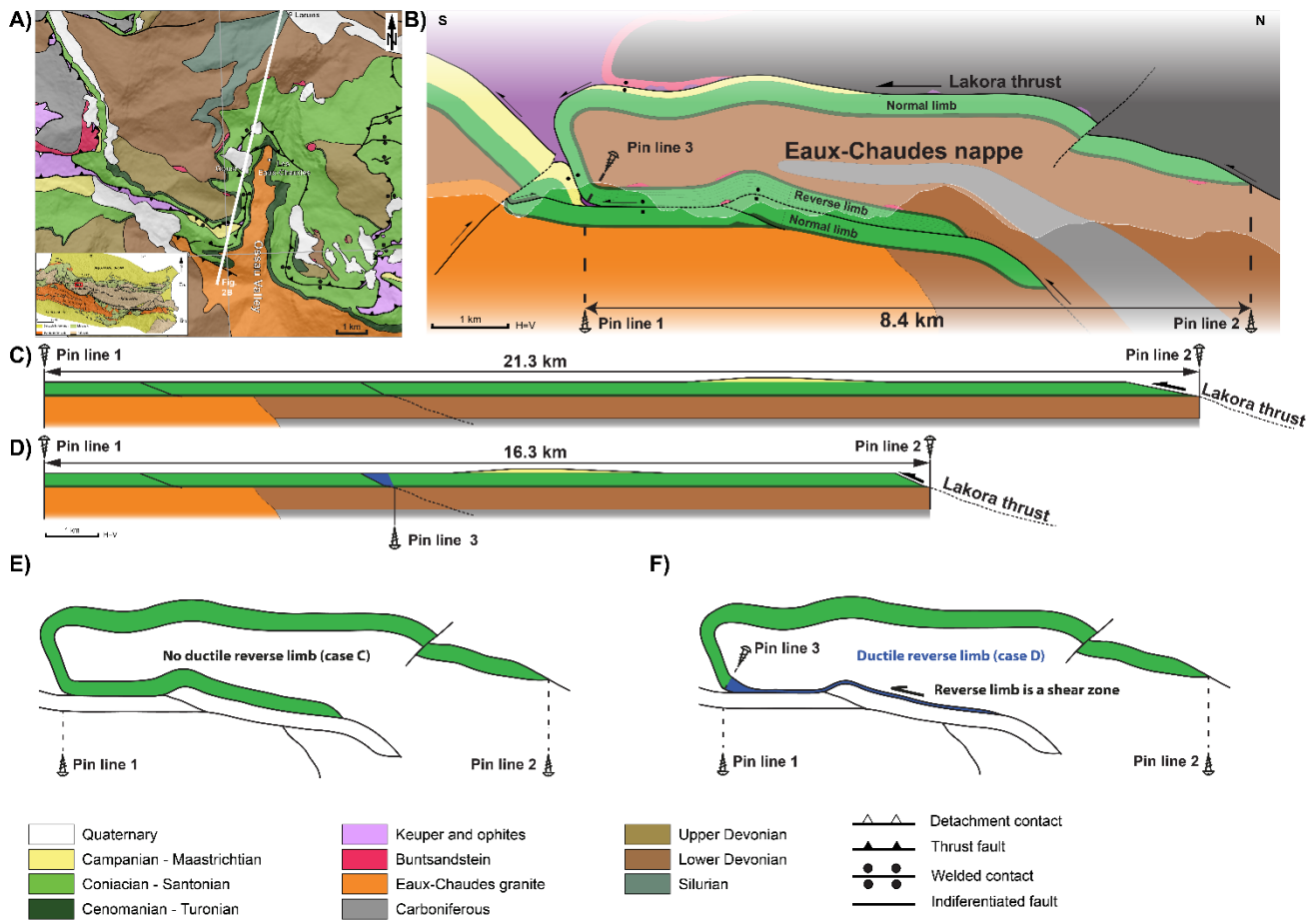
Figure 3.1: A) *Geological map of the western Eaux-Chaudes massif in the Ossau valley (Caldera et al., 2021).* **B)** *Cross section of the Eaux-Chaudes recumbent fold nappe in the western side of the Ossau valley (see Figs. 1.6 and 1.7 for location) (Caldera et al., 2021).* **C)** *Restored section of the Eaux-Chaudes fold nappe assuming no ductile stretching of the reverse limb (i.e., migrating fold hinge).* **D)** *Alternative restored version considering the entire reverse limb as a product of ductile stretching (i.e., blocked or reduced-mobility hinge).* **E)** *Sketch of the non-ductile reverse limb end-member case shown in C, assuming that there is no ductile stretching in the recumbent limb.* **F)** *Sketch of the entire-ductile recumbent limb end-member case shown in D, assuming that the whole reverse limb (blue path) is product of the ductile stretching.*

upper and lower allochthonous nappes (AN) were defined as moderate mechanical units between 8 and 6.6 km of maximum and minimum thicknesses (Fig. 3.2) to simulate the North Pyrenean Nappes. Both are mechanically similar (Table 3.1) and the sole purpose of having two units is to have a reference point for the advance of the upper allochthonous. The Paleozoic rocks of the Eaux-Chaudes nappe were defined as a pile of layers with inherited
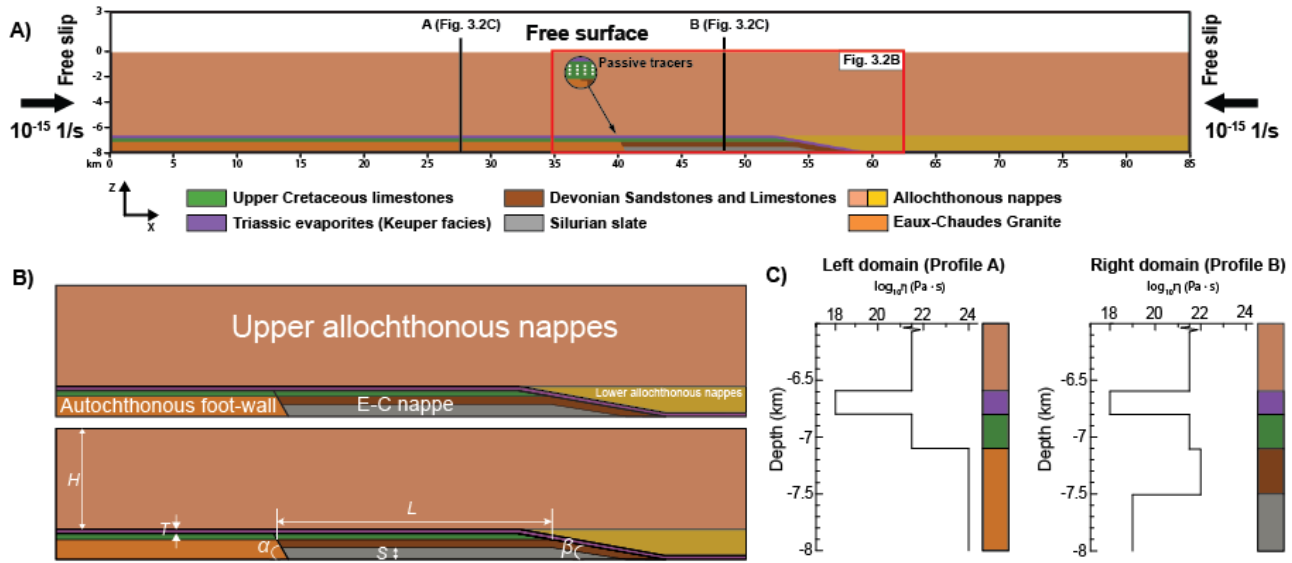
Figure 3.2: A) *Initial setup of the reference simulation. Numerical resolution is 256x136 (X x Z) grid points and a mesh refinement of 128 grid points between Z=-0.5km and Z=-8km and 8 grid points for Z>-0.5km. A free slip boundary conditions has been applied in the left and the right sides and a free surface at the top of the initial setup.* ***B)*** *Structural units of the Eaux-Chaudes massif represented in the reference model.* ***C)*** *Viscosity vertical profiles showing the vertical and horizontal mechanical contrasts for the domains on the left and the right sides in the simulations.*

gentle arching (i.e., simplified to a north-dipping kink, Fig. 3.2A and B; Caldera et al., 2023) composed of a basal weak material of 0.5 km thick to represent the Silurian black slates (grey colour Fig. 3.2B), and a layer of 0.4 km thickness to represent the Devonian-Carboniferous metasedimentary rocks (dark brown). The autochthonous footwall was defined as a stiff unit of 0.9 km thickness mimicking the Eaux-Chaudes granitic pluton. The boundary between both basement subdomains is assumed to be steeply dipping (α = 60º). Finally, on top of both subdomains a layer of 0.3 km thickness is defined to represent the unconformably overlying Upper Cretaceous limestones (green). On top of this initial setup, there is a 3 km thick low viscosity air layer with a free surface condition. A total of seven distinct mechanical units are thus used (eight considering the low viscosity air unit). The different units are defined as internally mechanically homogenous, and their mechanical properties are summarized in detail in Table 3.1.

Unit	ρ (kg/m³)	G (GPa)	η (Pa·s)	c (MPa)	ϕ (°)
Granite	2800	10	10^{24}	50	30
Silurian shale	2500	10	10^{19}	1	5
Devonian sandstone and limestone	2700	10	10^{22}	1	30
Keuper	2500	10	10^{18}	1	5
Upper Cretaceous	2700	10	5×10^{21}	10	30
Upper North Pyrenean nappe	2700	10	5×10^{21}	1	30
Lower North Pyrenean nappe	2700	10	5×10^{21}	1	30

Table 3.1: *List of the mechanical properties used for each unit represented in the simulations, based on the geology of the Eaux-Chaudes massif. ρ: density; G: shear modulus; η: Viscosity; c: cohesion; ϕ: friction angle.*

Variable	Reference
H (km)	6.6 (3-10)
T (m)	200 (0-400)
L (km)	14 (10-22)
β (°)	10 (20-90)
S (m)	500 (300-700)
η_{UC} (Pa·s)	5×10^{21} ($1 \cdot 10^{22}$)
ϕ_{UC} (°)	30 (5-30)
η_{AN} (Pa·s)	$5 \cdot 10^{21}$ ($1 \cdot 10^{22}$)
c_{UC} (MPa)	10 (1-100)

Table 3.2: *List of geometrical and mechanical variables and values used in each simulation. A sketch of the geometrical variables listed can be found in Fig. 3.2B. Geometrical variables: H: thickness of the overburden; T: thickness of the upper weak layer; L: length of the Upper Cretaceous panel; β: angle of the Lakora footwall ramp; α: angle of the authochthonous E-C granite; S: thickness of the lower Silurian weak layer. Mechanical variables: η_{UC}: Viscosity of the Upper Cretaceous panel; ϕ_{UC}: Friction angle of the Upper Cretaceous panel; c_{UC}: Cohesion of the Upper Cretaceous panel; η_{AN}: Viscosity of the allochthonous nappes.*

In order to investigate the conditions favouring the development of fold nappes or thrust nappes, several mechanical and geometrical variables have been tested from the reference model (namely "*Rs*"; Fig. 3.2). The geometrical setup of the reference model is shown in Table 3.2, together with the range of studied values for the different parameters indicated between parentheses.

With respect to the reference simulation, the viscosity (η_{UC}), cohesion (C_0) and friction angle (ϕ) of the Upper Cretaceous unit, and the viscosity (η_{AN}) of the upper allochthonous thrust sheets were varied. In addition, the influence of the tectonic inheritance has also been tested by varying the thickness (*T*) of the Lakora weak detachment layer (Keuper), the stiffness of

the autochthonous basement unit (i.e., the Eaux-Chaudes granite), the thickness of the overburden (H) by allocthonous nappes, the thickness of the Silurian weak layer (S), the angle of the Lakora foot-wall ramp (β), the angle of the contact between Paleozoic subdomains (α) and the length (L) of the Upper Cretaceous cover overlying the Eaux-Chaudes nappe (Fig. 3.2B). Detailed values for the geometrical and mechanical parameters of each simulation are listed in Tables 3.1 and 3.2, in which the subscript indicates the value of the modified property.

3.2.2. Evaluation of the grade of localization

In order to better constraint the geometrical differences between thrust and fold nappes, the deformation of the Upper Cretaceous layer has additionally been assessed by tracking the position of a passive tracer grid defined by 400 x 3 markers (Figs. 3.2A and 3.3A). For the simulations with variable L, the total number of passive tracers was modified to maintain constant the initial distance between consecutive tracers for all models.

The degree of strain localisation in the Upper Cretaceous layer was carried out using a localisation index (I_{Loc}) defined as follows:

$$s = \frac{l}{l_0}, \tag{3.1}$$

$$I_{Loc} = 1 - \left[\left(\frac{\sum s \cdot \sum s}{\sum s^2} \right) \cdot \frac{1}{N} \right], \tag{3.2}$$

where l is the length between two consecutive passive tracers, l_0 is the initial length (fixed in 0.13 km for all simulations), s is the stretching and N the number of tracers. In order to define the same structural interval for calculations, the number of tracers considered was defined between two reference points defined by 1) the cut-off of the E-C nappe and autochthonous zone (orange point in Fig. 3.3B) and the Lakora thrust cut-off (NL in Fig. 3.3B). The I_{Loc} was

systematically evaluated every 10 timesteps, between a range of bulk shortening from 21.5% (7.6 Ma of simulation time) to 46.2% (19.6 Ma of simulation time).

On the other hand, the variation of fold limb length and position of hinges were also tracked during simulations in order to test potential migration of fold hinges, as proposed by Perrin et al. (2013) (see results section).
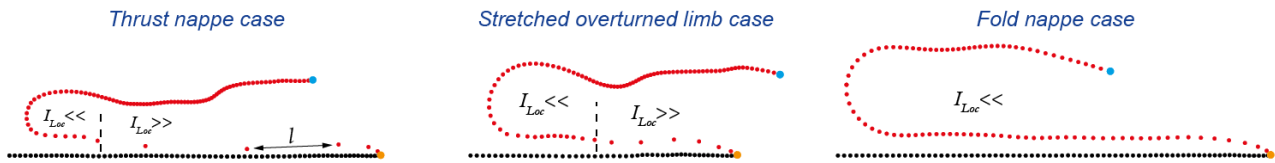
Figure 3.3: *Passive tracers extracted from the thrust nappe and fold nappe end members and from an intermediate between both (stretched reverse limb). The longitude l between tracers is increasing from the fold nappe to the thrust nappe as is the I_{Loc} parameter, which can be used as a tracker for quantifying the localization.*

3.3. Modelling Results

Firstly, the results of the reference simulation based on the initial configuration described above are exposed (Fig. 3.4). After that, a systematic description of the results obtained by varying the mechanical and geometrical parameters (Table 3.1 and 3.2) is presented (Fig. 3.5, 3.6 and 3.7). The focus is centred on the differences between variables enhancing thrust- or those favouring fold nappes.

The results are evaluated in order to reproduce the first-order features of fold nappes, with application to the case of the Eaux-Chaudes nappe, which are: (1) a flat-lying, kilometric scale overturned limb with its thickness approximately preserved, (2) a normal limb with second-order structures (i.e., folds with a vertical axial plane), (3) a sub-horizontal axial plane and (4) a tight syncline between the overturned limb and the autochthonous succession.

A total number of 67 simulations were carried out varying mechanical and/or geometrical variables. During the first stages, all the simulations share certain common features during their development. With the onset of the shortening, a thickening of the upper units (i.e., allochthonous nappes in Fig. 3.4) occurs and the units below are increasingly buried as the simulation progresses (Fig. 3.6A and B). A low-angle high strain-rate zone is observed through the upper weak layer (i.e., the allochthonous Keuper) due to the displacement of the upper nappes over the E-C nappe towards the foreland (i.e., left side of the simulation) (Fig. 3.6E). The E-C granite unit exerts a strong mechanical heterogeneity in the shortening direction and triggers a concentration of the stress within the modelled Devonian and Upper Cretaceous layers near the contact (Fig. 3.6C). During the initial stages of shortening, this heterogeneity results in the nucleation and growth of a gentle, foreland-verging asymmetric fold. The initial vertical amplification of its frontal part results in the squeezing of the upper weak layer (Fig. 3.6A). The thinning of this layer reduces the efficiency of the decoupling in this upper localization level at the base of the upper thrust sheets, indicated by a one-to-two orders of magnitude drop in the second invariant of the strain rate (i.e from 10^{-12}-10^{-13} s^{-1} to 10^{-14}-10^{-15} s^{-1}) until the end of the simulations. At the same time, a low-angle strain localization zone becomes active within the lower weak unit until the end of the simulation (Fig. 3.6E and F).

3.3.1. Reference model

The results of the reference simulation are presented in Fig. 3.4 in two steps, after a 22.7% of bulk shortening (Fig. 3.4A) and 41.6% of bulk shortening (late stage; Fig. 3.4B). Posterior simulations (Figs. 3.5, 3.6, and 3.7) were performed by varying one variable or a combination of two variables (see Table 3.2).

As described above, the displacement of the allochthonous nappes over the E-C nappe enables an upper localisation level in the early stage of the simulation (Fig. 3.4E), and the
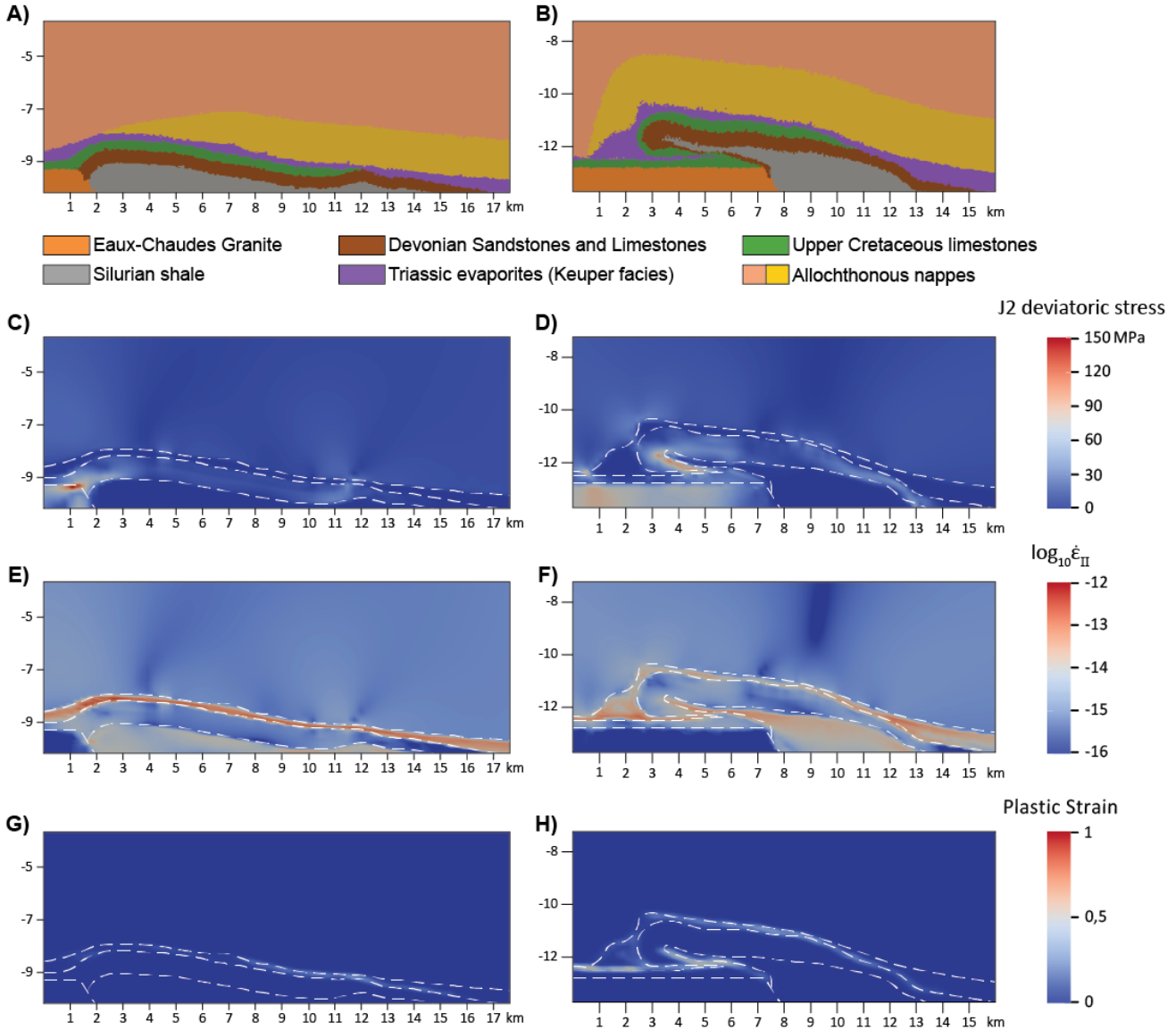
Figure 3.4: A, B) *Geometrical configuration after 22% bulk shortening (early stage) and 41.6% shortening (late stage). (C, E, G) Variation of the deviatoric stress, the total second invariant of the strain-rate tensor ($\dot{\varepsilon}_{II}$ in log scale) and the accumulated plastic strain for 22% of bulk shortening. For this early stage, the maximum deviatoric stresses are observed in the footwall of the structure, and the maximum $\dot{\varepsilon}_{II}$ and plastic strain along the upper weak level. D, F, H) Plots of the deviatoric stress, the second invariant strain-rate and accumulated plastic strain for 41.6% bulk shortening. The maximum stresses are located in the overturned limb, the maximum strain rates are in the lower weak level and the top of the autochthonous footwall while the strain localization in the upper weak level is partially deactivated, causing the coupling between the allochthonous and the lower E-C nappes. The accumulated plastic strain is observed mainly in the reverse limb and in front of the structure, with values relatively low to moderate compared to the bulk natural strain (i.e., the natural logarithm of the ratio between final and original length of the model) of approx. e=0.89.*

within the lower weak unit (i.e., Silurian shale; Fig. 3.4F). As the simulation progresses, the rotation of the reverse limb of the structure is increased until it becomes sub-horizontal and completely overturned. The larger stresses are now concentrated in the stiff basement units (dark brown; "Devonian sandstones and limestones" unit) localised in the reverse limb (Fig. 3.4D) which causes its thinning and stretching (Fig. 3.4B) after its rotation and overturning.

The resulting structure at the late stage of the reference simulation (Fig. 3.4B) resembles a fold nappe structure with a sub-horizontal and thinned overturned limb and underlain by a tight synform, where the upper weak layer has been nearly squeezed out and there is a "welding" between synform limbs. Although the geometry of the overturned limb appears continuous, strong thinning is observed and a high strain-rate zone is visible within it (Fig. 3.4F). This is pointing to a change from dominantly viscous behaviour in the overturned limb in the early to mid-stages of the simulation (Fig. 3.4G) to a greater plasticity component during the late stages (Fig. 3.4H).

3.3.2. Intrinsic mechanical controls on nappe development

To explore the influence of mechanical parameters on fold/thrust nappes, further simulations has been run (i) increasing the viscosity of the Upper Cretaceous layer (model η_{UC}; Fig. 3.5A, D and G), (ii) reducing the friction angle to 15° of the Upper Cretaceous unit (model ϕ_{UC}; Fig. 5B, E and H) and (iii) increasing the viscosity of the allochthonous nappes to 10^{22} Pa·s (model η_{AN}; Fig. 5C, F and I).

A common feature observed in all the intrinsic mechanical models (i.e., varying η_{UC}, η_{AN} and ϕ_{UC} variables) is that the upper weak layer (i.e., Keuper allochthon) was almost squeezed out along the footwall ramp of the Lakora (Fig. 3.5A, B and C). The reduction of the thickness of the upper weak layer enhances the coupling between the E-C nappe and the upper allochthonous nappes, reducing the transport of the latter over the E-C nappe and facilitating

the decoupling in the lower weak layer (i.e., Silurian unit). This is documented by drops of the second invariant of the strain rate tensor within the upper weak layer with shortening, which point to the solidary translation of both units (Fig. 3.5D-F). Note that this situation leads to a subtractive contact between the hanging wall and footwall series.

The results of the simulations increasing η_{UC} and decreasing ϕ_{UC} are very similar, and there is a positive enhancing of the fragile/plastic behaviour over the viscous/ductile behaviour of the Upper Cretaceous unit, especially for ϕ_{UC} =15° (Fig. 3.5E and H). Compared to the reference simulation, the Upper Cretaceous unit loses its continuity in both cases over a thin and localized level marked by high strain rate values (10^{-13}-10^{-12} s^{-1}) which is cross-cutting the reverse limb of the structure (Fig. 3.5D and E). The E-C nappe is transported over this level without changing the length of neither the reverse nor the normal limb, and qualitatively pointing to the absence of migration of the anticline hinge after yielding. The resulting structure shows relatively short overturned limb and gently-to-moderately dipping axial plane, being akin to a cut-off hanging wall anticline as in natural thrust tectonics (Fig. 3.5A and B).

The increase of the viscosity of the allochthonous nappes with respect to the reference model (*Rs*) also results to an increase of the (frictional) plasticity affecting the E-C nappe, but in a minor scale compared to the previous η_{UC} or ϕ_{UC} variables (Fig. 3.5G-I). Shearing of the Upper Cretaceous is also observed, and the E-C nappe is then transported over a thin and strong localized level, also cross-cutting the reverse limb (Fig. 3.5F and I). The structure developed is thicker and possesses a larger overturned limb than those for variables η_{UC} and ϕ_{UC}, probably induced by the extrusion and migration of the Silurian-analogue weak material towards the core of the anticline.
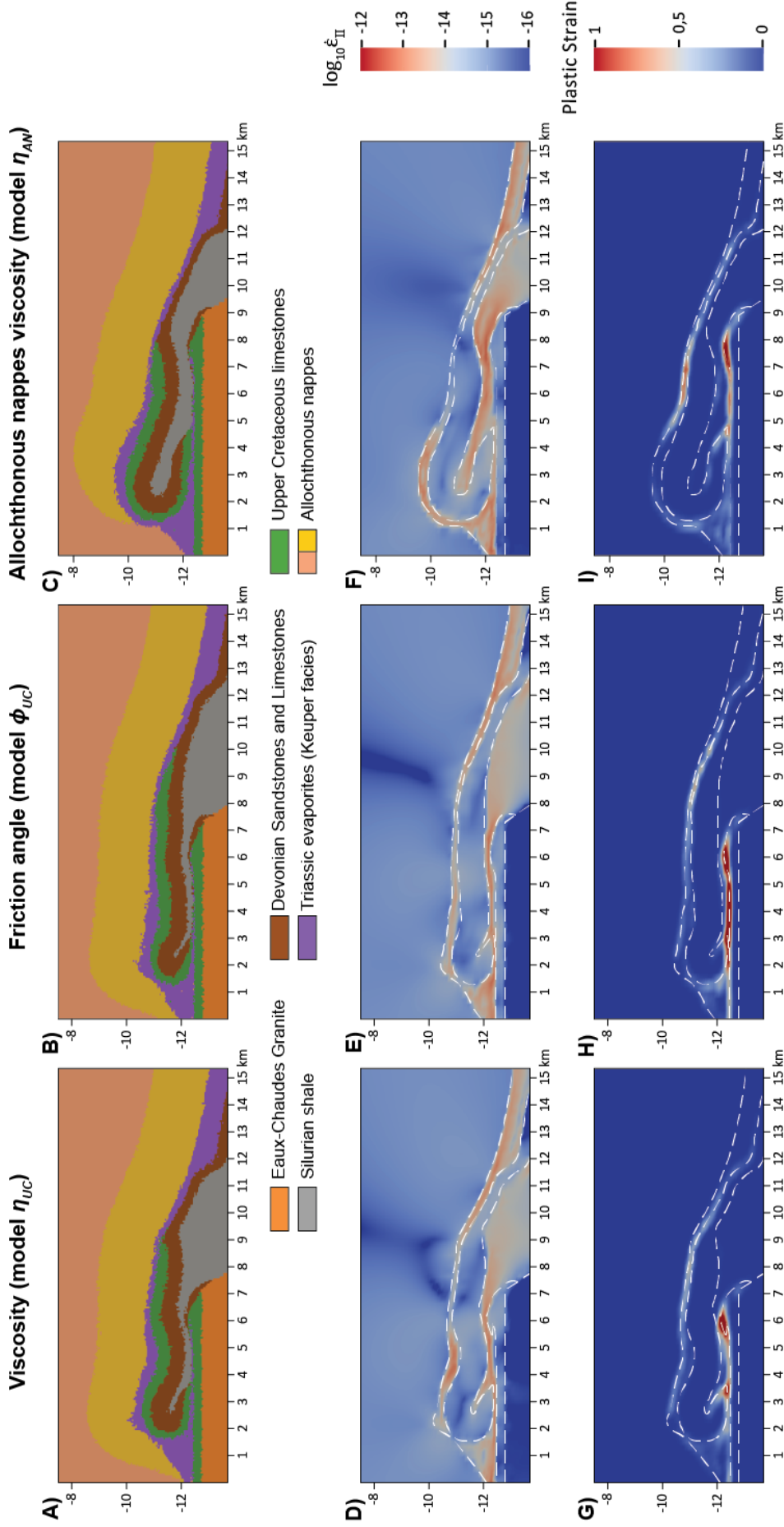
Figure 3.5: *Effect of the mechanical parameters (see text for explanation; the range of values is shown in Table 3.2). A), D) and G) Final geometry and distribution of the second invariant of the strain-rate tensor and plastic strain for the model with η$_{UC}$= 10²³ Pa·s. B), E) and H) Geometry, second invariant of the strain-rate tensor and plastic strain plots for model with φ$_{UC}$=15°. C), F) and I) Geometry, second invariant of the strain-rate tensor and plastic strain plots for the model with η$_{AN}$=10²² Pa·s, which enhances the brittle behaviour of the Upper Cretaceous level.*

3.3.3 Geometrical controls on nappe development

A series of model runs were performed modifying the initial configuration of the mechanical units (dimensions, burial, angles, etc.). The geometrical variables tested are listed in Table 3.2, and the results are presented in Figs. 3.6 and 3.7. Briefly, the tested variables were 1) the thickness of the upper weak layer (T; series of models T_{0-400}), 2) the angle of the Lakora ramp (β; series of models β_{20-90}), 3) thickness and ramp angle combined ($T+\beta$; series of models $T_{250-400}+\beta_{20-40}$), 4) the depth of burial (H; series of models H_{3-10}), 5) the length of the Upper Cretaceous panel (L; series of models $L_{9.7-21.7}$), 6) the angle of the strong granite forestop (α; series of models α_{10-90}) and 7) the thickness of the lower weak detachment layer (S; series of models $S_{300-700}$). Additionally, the potential effect caused by the absence of a strong mechanical unit such as the natural case of the E-C granite was also tested (Ng; model No Granite).

Increasing of the thickness of the upper weak layer (models T_{0-400}; Fig. 3.6A-C) promotes a major displacement of the allochthonous units over the E-C nappe due to a better decoupling. In this progression, there is a reduction of the shear transmission downwards, although without preventing it entirely, as can be deduced by the limited advance of the E-C nappe towards the foreland margin of the simulation (Fig. 3.6A-C). Additionally, this difficults the activation of the lower weak level, which also prevents an efficient detachment and the amplification of the frontal part of the nappe. In summary, the allochthonous thrust sheets and the E-C nappe are not coupled, and the displacement of the later structure is inhibited, resulting in a geometry consisting of a fold with a short reverse limb and moderately dipping axial plane. Finally, the nappe shows additional large-scale secondary upright folds. For the case of a model without an upper weak layer (model T_0; Fig. 3.6A), neither a thrust nor a fold nappe develop, and instead a long-wavelength anticline with marked thickening layers. The lower weak layer is then extruded towards the fold core.
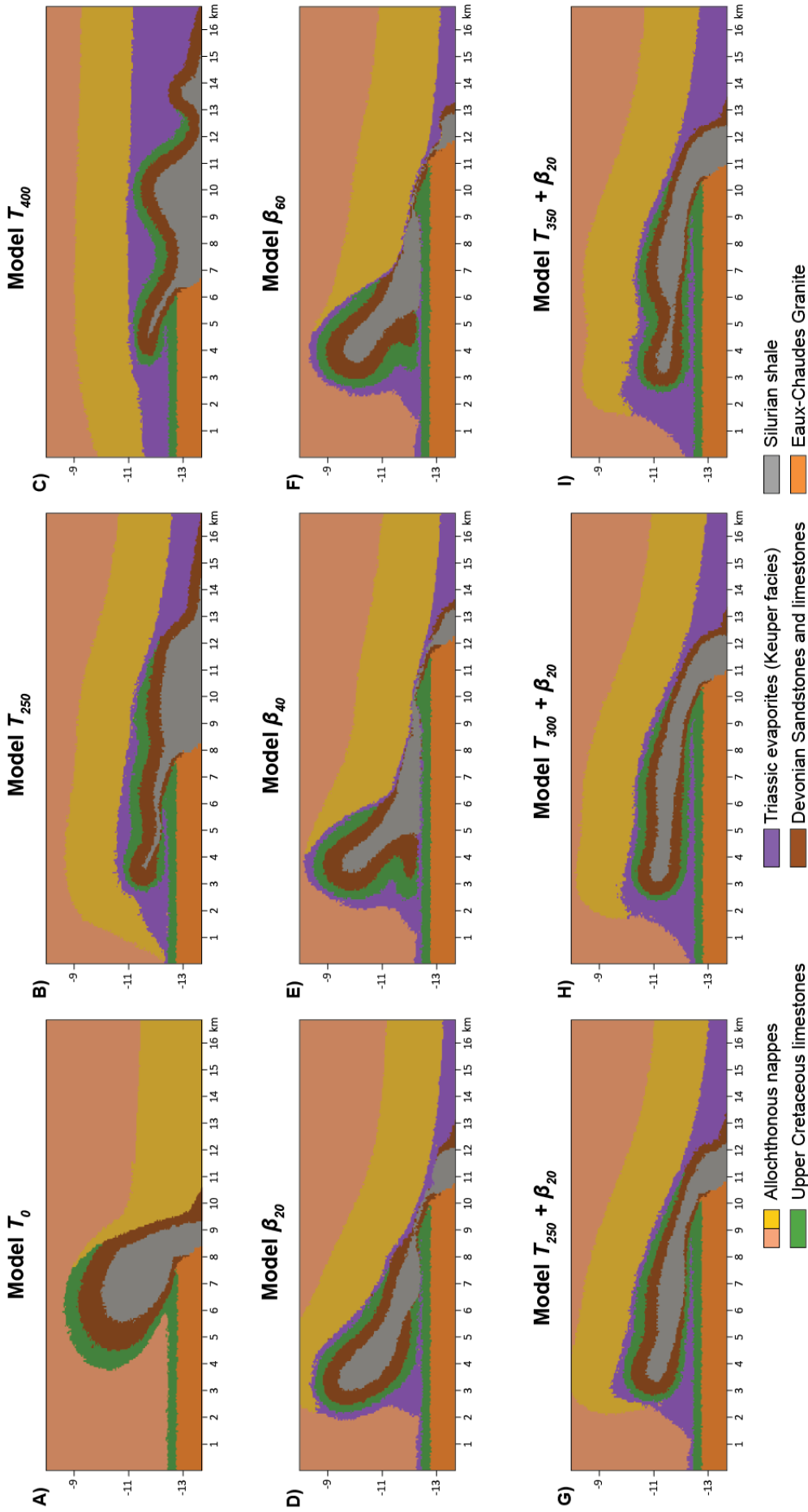
Figure 3.6: *Graphical summary of results exploring the effect of variation in the geometrical variables.* ***A)*** *T= 0m,* ***B)*** *T=250m,* ***C)*** *T=400m,* ***D)*** *β =20°,* ***E)*** *β =40°,* ***F)*** *β =60°,* ***G)*** *T= 250m + β =20°,* ***H)*** *T= 300m + β =20° and* ***I)*** *T= 350m + β =20°. Values of the parameters increase from left to right (see Table 3.2 for additional information).*

For initial settings with the Lakora footwall ramp angle larger than the reference model (i.e., $\beta > 10°$, but keeping T invariant) (model Rs; Fig. 3.4), large deformations are concentrated along the footwall ramp, promoting 1) stretching, thinning and segmentation of the Devonian layer along the normal limb, 2) shear localisation in the reverse limb, affecting Upper Cretaceous and Devonian units, and enhanced plastic deformation (Fig. 3.6D-F), and 3) thinning-out of the upper weak layer. Geometrically, the latter results in the welding of the thrust contacts of the E-C and upper nappes.

Increasing the β values (Fig. 3.6D-F) enhances the stress transmission normal to the Lakora footwall ramp which hinders the displacement of the upper nappes over the E-C nappe towards the foreland and promotes the early coupling of both structural units due to the aforementioned squeezing of the upper weak layer over the footwall ramp area. It also causes the early activation of the lower shear zone through the lower weak unit. The Upper Cretaceous and the Devonian layers are lifted vertically near the Lakora footwall ramp and also in the strong granite area, and a tall, km-scale upright fold is then developed. The E-C nappe layers are then sheared off due to the early coupling, resulting in greater displacement of the E-C nappe over a thin and localized surface on top of the autochthonous units (Fig. 3.6E and F).

However, for model with $\beta=20º$ (model β_{20}; Fig.3.6D), longer overturned limbs are promoted compared to the reference model. The overturned limb of the structure is very gently-dipping oriented, at a low angle to the autochthonous footwall. However, the limb dip increases towards the frontal part of the anticline where is moderately dipping towards the hinterland, similarly than the axial plane and the normal limb.

Simulations combining increased thickness and ramp angle (i.e., variables ($T+\beta$) combined; models $T_{250-400}+\beta_{20-60}$; Figs. 3.6G-I and A.3.2) produce final geometries with large and sub-horizontal overturned limbs and axial planes, favouring fold nappe development. In general,

the increase the angle β improves the efficiency of the transmission of the stresses and the displacement of the allochthonous units towards the E-C nappe (Fig. 3.6G-I and A.3.2). This is a remarkable difference from the observations in the series of models $T_{250-400}$ and $\beta=10$, where large, sub horizontal overturned limbs and axial planes were not reproduced (Fig. 3.6A-C). In such cases of increase β to 20°, the activation of the lower shear zone within the lower weak Silurian layer is promoted, without the shearing off the E-C nappe forelimb as happens when T is <250m (Fig. 3.6D), and this results on the large and sub-horizontal reverse limbs that resemble the Eaux-Chaudes natural example (Figs. 3.1 and 3.6G-I).

As happens in the series of models β_{20-90}, in the performed simulations with β >20° (shown in appendix), both the Upper Cretaceous and Devonian layers show thinning and boudinage in the overturned limb and in the Devonian of the normal limb, and the structure is resolved in a thin localized level (also affecting the Devonian of the normal limb) which controls the structural transport (Fig. A3.2)

In this combined $T+\beta$ simulations, the existence of a thicker weak Keuper layer (T >250 m; Fig. 3.6G-H) favours the decoupling between the upper and lower units, resulting in horizontal axial planes and overturned limb of the fold nappe due to the high flow capacity to of this low viscous layer, which can be extruded from the footwall syncline (Fig. 3.6H). For these simulations (i.e., β = 20° and T > 250 m), the overturned limbs fairly maintain the thickness of the Upper Cretaceous layer, although a bit of thinning is observed near to the footwall syncline, especially for simulations when the upper weak layer is thinner than the reference model (Fig. 3.6G). Secondary gentle folds are developed in the normal limb when $T \geq 350$ m (maintaining β = 20°) (Fig. 3.6H and I).

For this succession of models varying variables T and β, the thickness of the overturned limb does not change substantially, which qualitatively points to potential mechanism of hinge migration and rigid rotation of the overturned limb, instead of stretching and shearing. In any
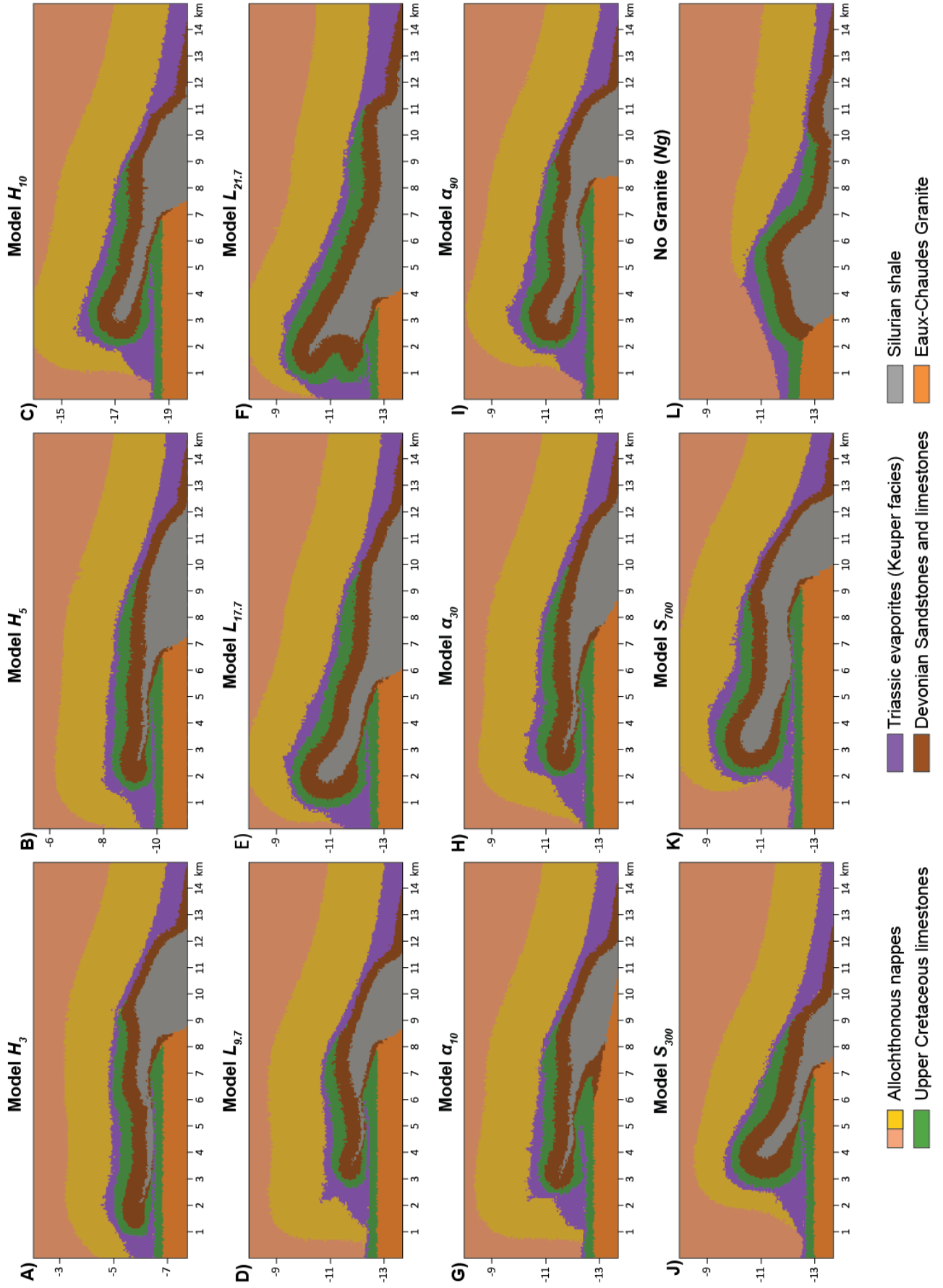
Figure 3.7: *Final geometry for models varying:* **A-C)** *the burial thickness (H),* **D-L)** *the initial length of UC basin (L),* **G-I)** *the angle of the of the E-C foot-wall (α),* **J-K)** *the thickness of the Silurian weak layer and L) the non-presence of a strong fore-stop (or granite with similar properties than basement layers). Sub-indexes indicate the value of the parameters. (see additionally Table 3.1 for more information).*

case, all these geometries for models with $T + \beta$ appear to indicate dominantly viscous rather than plastic behaviour.

Varying the depth of burial (series of models H_{3-10}; Fig. 3.7A-C) leads to significant variation of the structural patterns. The simulation with an initial H<5 km (shallower conditions; Fig. 3.7A) results in a cut-off of the Upper Cretaceous short reverse limbs, producing a thrust ramp anticline. The E-C nappe appears as a thrust nappe displaced over a localized detachment in the Silurian weak level, like previously observed in η_{UC} and ϕ_{UC} simulations (Fig. 3.5A and B). The original thickness of the UC layers is rather conserved (Fig. 3.7A) (despite there is a small thinning in the reverse limb of the structure), which points to a dominantly plastic/frictional behaviour.

Conversely, for H> 5 km the resulting structures always have a continuous overturned limb. Higher burial values favour the conservation of the thickness of the UC layer and larger overturned limbs, pointing to a dominantly viscous behaviour of the Upper Cretaceous layer (Fig. 3.7B and C).

For series of models varying the initial length of the UC layer (L), shorter layer lengths (L) produce structures resembling thrust nappe structures (models $L_{9.7-21.7}$; Fig. 3.7D). On the other hand, larger original layers (Fig. 3.7E and F) increase the dip of the structural elements (i.e., reverse and normal limbs and fold axial plane) towards the hinterland. In addition, for such cases the reverse limb of the structure is also relatively short, and the Silurian weak level was thickened in the core of the fold (Fig. 3.7E). Furthermore, for L>17.7 km, secondary folds can be observed in the hinge and normal limb and result in an increases structural relief of the E-C nappe.

The angle of the boundary of the granite or stiff autochthonous E-C footwall (model α_{10-90}; Fig. 3.7G-I) also allows to differentiate between different structures. For $\alpha \leq 60°$ (model *Rs*; Fig. 3.4 and 3.7G and H), the simulated nappes show a thinned and stretched reverse limb. On the other hand, for $\alpha = 90°$ (Fig. 3.7I) there is a promotion of the early coupling of the upper allochthonous nappes and the E-C nappe due to the amplification of an upright fold in the contact between stiff granite and lower detachment layer level due to the high angle of the mechanical contact between both, which causes the weaker level to extrude. The E-C nappe is sandwiched in between the pushing of the upper nappes and the granite, which triggers the shearing off of the Devonian and Upper Cretaceous layers in the forelimb (Fig. 3.7I). The results for models varying the initial thickness of the lower weak layer, simulating the Silurian in the natural case, are shown in Fig. 3.7J and K (simulations S_{300} and S_{700}). For S_{300} model, with thickness lower than the reference model, the E-C nappe panel shows a less advance towards the foreland than the reference model. The Silurian detachment was not activated until late steps of the simulation because of there is no nappe coupling until then, which results on a fold exhibiting a short reverse limb, with thickness constant due to the limb rotation (Fig. 3.7J). On the contrary, an increase of the lower weak thickness (model S_{700}; Fig. 3.7K) results on longer what and shearing off the the Upper Cretaceous and Devonian layers. Furthermore, the weak layer is thickened in the fold core, which produces an increase of the structural relief.

Finally, the absence of the strong footwall body, which in this simulation was replaced by a deformable basement with mechanical properties similar to the Devonian (model *Ng*; Fig. 3.7L), produces the development of large-scale upright buckle folds and prevented the development of thrust/fold nappes. This highlights the importance of the autochthonous granite in the development of the natural Eaux-Chaudes structure.

3.4 Discussion

In order to perform a more quantitative analysis of the structural transition between fold and thrust nappes, the mechanical simulations presented in this chapter were analysed and categorized using several geometrical and mechanical variables.

3.4.1 Quantification of the strain localisation factor (I_{Loc})

The UC layer was used to constrain the evolution of the degree of strain localisation (I_{Loc}). The term I_{Loc} (see section 3.3.2 for its definition) allows to distinguish quantitatively the distribution of deformation between cases in which deformation is highly localised in thin levels (I_{Loc} near 1) from cases in which deformation is distributed or poorly localised (I_{Loc} tends to 0). In the current simulations, the region expected to achieve the higher strain localisation is the reverse/overturned limb, and hence, the I_{Loc} factor permits to quantitatively discriminate between cases with uniform thickness (low I_{Loc} values) to cases with strongly heterogeneous thinning of the reverse/overturned limb (I_{Loc} near 1). In order to keep a similarity in the procedure of calculation of the I_{Loc} between simulations with different geometrical setting, the I_{Loc} was calculated between the reference points defined by the footwall cut-off of the Lakora thrust (pin point "NL" in Fig. 3.9) and the hinge of the syncline formed in the footwall of the E-C structure (pin-point "IS" in Fig. 3.9).

The results of the analysis are shown in Fig. 3.8, for all simulations and a series of selected models. The general trend of the I_{loc} is to increase with time. Three main types of evolution are observed:

1) Simulations that evolve with a fast increase of I_{Loc} up to stabilise at high values (I_{Loc} > 0.7). This type of trend is observed in models with a tendency towards thrusting, with high plastic strain accumulated, and strong shearing and thinning of the reverse fold limb. Examples of this type are the simulations with low initial burial (e.g., H_3; Fig. 3.7A),

high viscosity of the allochthonous nappes (e.g., η_{AN}; Fig. 3.5C), low frictional angles (e.g., ϕ_{UC}; Fig. 3.5B) or moderate to short dimension of the UC panel (e.g., $L_{9.7}$; Fig. 3.7D). This type corresponds to the category labelled as "thrust nappes".

2) Simulations with a flat distribution in time and low values of I_{Loc} (<0.15). This type corresponds to models displaying fold nappe geometries, with the UC level displaying a homogenous thickness without significant stretching, and overall dominated by viscous flow. Examples of simulations displaying this trend are usually those linked to the presence of a thick upper weak layer (e.g., model $T_{300} + \beta_{20}$; Fig. 3.6H and 3.8A). There are few simulations displaying this trend (Fig. 3.8B). This type corresponds to the category labelled as "fold nappes".

3) Simulations with an initial flat trend but displaying moderate increase of the I_{Loc} after some deformation. This type corresponds to simulations resulting in geometries hybrid between fold and thrust nappes, showing gradual stretching and thinning of the overturned limb, without losing its continuity, and low plastic deformation. Most of the models correspond to this type, such as the reference simulation (e.g., Rs model; Figs. 3.4 and 3.8A). This type corresponds to the category labelled as "fold nappes with stretched recumbent limbs".

An attempt to define the boundaries between these three main categories was calibrated using as a reference the last step of the simulations, in which the amount of shortening is maximum. The first category labelled as "fold nappe" was defined when $I_{Loc} < 0.15$ and corresponds to idealized fold nappes in which the thickness of overturned limb is constant, the stretching of the overturned limb is very low, and the deformation was accommodated in a dominant viscous behaviour; a second type labeled such as "fold nappes with stretched reverse limbs alludes to fold nappes with I_{Loc} between 0.15 and 0.6, where the overturned limb is continuous but shows moderately to strong thinning and stretching; and finally, a third

A)

Localisation index (I_{Loc})

$$I_{Loc} = 1 - \left[\left(\frac{\sum s \cdot \sum s}{\sum s^2} \right) \cdot \frac{1}{N} \right]$$

Thrust nappes

Fold nappes with stretched recumbent limbs

Fold nappes

Reference	$H = 3$ km	$T = 250$ m	$\beta = 20° + T = 350$ m
$\phi = 15°$	$H = 5$ km	$L = 11.7$ km	$\beta = 20° + T = 300$ m
$\eta_{AN} = 1e22$ Pa·s			

B)

Evolution of (I_{Loc}) for all variables tested
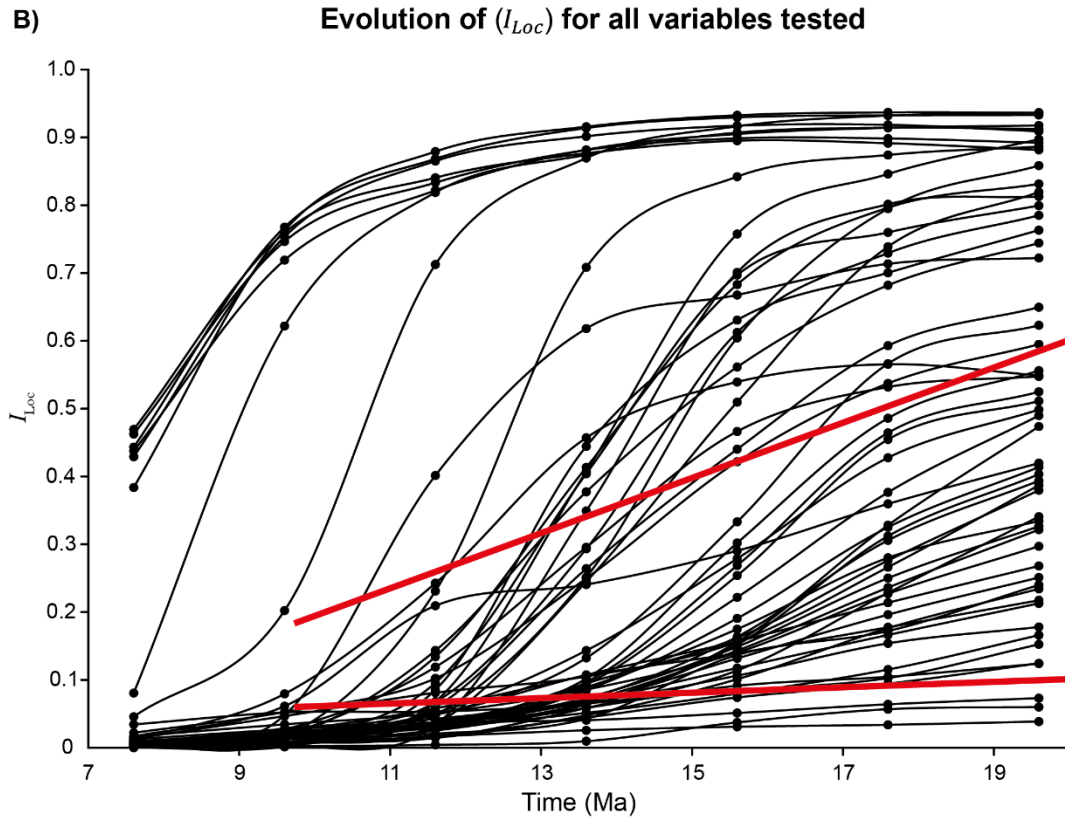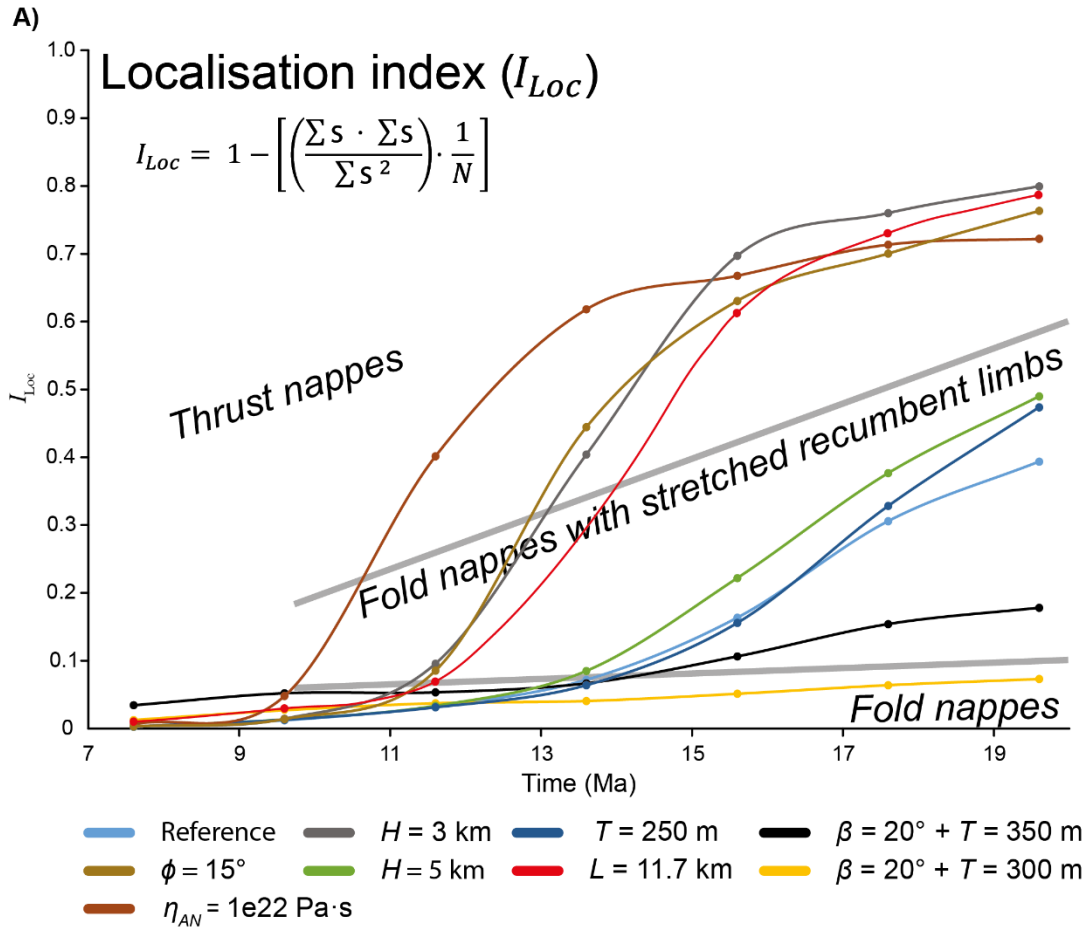
Figure 3.8: A) *Evolution of the I_{Loc} with respect to the simulation time for the reference simulation and for selected parameters varied from it as shown in Tables 3.1 and 3.2. This illustrates recumbent fold nappe (β = 20° + T = 300) and thrust nappe (H = 3 km) end members. Thrust nappes exhibit a fast rise of the index of localisation and fold nappes show low and stable behavior of the index of localization through time. The fold nappes with stretched reverse limbs possess features from fold nappes (initial stable slope) and thrust nappes (moderate rise), attesting for the stretching of the recumbent limb.* **B)** *Evolution of the I_{Loc} with respect to time plotted for all simulations undistinguished. The most observable trends correspond to "thrust nappe" and "fold nappe with stretched limb", and only in three cases we can observe homogenous thickness and little localisation corresponding to a "fold nappe" case.*

type represents I_{Loc} > 0.6 and makes reference to thrust nappes, where the reverse limb is not continuous and the dominant behaviour is plastic (Fig. 3.8). Because there is a general tendency to increase I_{Loc} with time, these boundaries cannot be defined as a strictly straight line in the diagram and were defined using a positive slope.

3.4.2 Quantification of the fold hinge migration

The assessment of potential migration of the fold hinges during deformation was measured using passive tracers in selected units. By hinge migration we understand the travelling of material particles between different structural elements in a fold (i.e., fold limbs). The simplest case is a migration of the hinge along the normal limb, producing the increase of the length of the reverse limb. This mechanism could help explaining the observation of long recumbent limbs with preserved thicknesses, a feature that is in general difficult to explain by a fixed-hinge mechanism and limb stretching.

To constrain the hinge migration, a method based on the relative distance between the inflexion position of the fold and a series of key reference points was used. Using the last step of each simulation, the inflexion point of the curvilinear recumbent anticline was defined as the point with maximum dip angle (IA; green dot in Fig. 3.9), taken to mark the transition from the normal to the reverse limb. The material position of the final point IA was tracked during all the deformation steps (Fig. 3.9B).

For each increment of deformation, the current inflexion point (IAc; red dot in Fig. 3.9B) was identified and three distances were measured: 1) the horizontal distance between the IAc and the Lakora footwall cut-off (NL; blue dot in the Fig. 3.9), representing the length of the normal limb, 2) the horizontal distance from the IAc to the syncline hinge in the footwall of the E-C nappe (IS; yellow dot in Fig. 3.9), representing the length of the reverse limb, and finally, 3) the horizontal distance between the IAc and IA. Note that during progressive fold growth, the IA represents a material point located in the normal limb that in the last step of the simulations is the inflection point of the anticline fold. To graphically represent the evolution of these distances, the location of the IAc for each time step was defined as the coordinate origin (Fig. 3.10).

In order to quantify the effect of plastic deformation in the reverse limb, the degree of strain localisation was used to divide the reverse limb into two segments (labelled by RL and P, and $IS = P + RL$; Fig. 3.9) according to the segments with I_{Loc} higher or lower than 0.15. Segment RL was defined as the distance between the IAc and the first marker which implies a bulk I_{Loc} higher than 0.15 (always using as the first marker the NL point and increasing the number of markers up to overcome the threshold). The segment P was defined as the distance between the tracer with $I_{Loc} > 0.15$ and the syncline inflexion tracer.
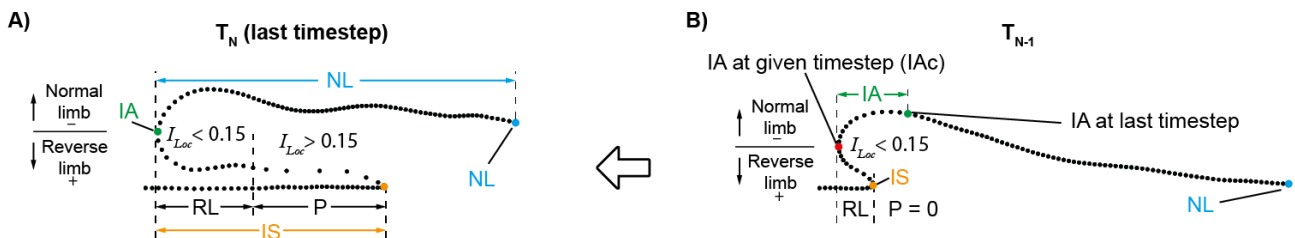
Figure 3.9: Quantification of the hinge migration for a fold nappe end member from passive tracers. Tracers in the normal limb are traveling towards the inflection while the passive tracers in the reverse limb are moving away of it. The sign of tracers is changed as a function of its position in the reverse or the normal limb taking as a reference the tracer located in the hinge inflection of the fold (tracer IA).

Fig. 3.10 illustrates several examples of hinge migration evolution in the framework of the three main categories distinguished by the localization index (section 3.5.1; Fig. 3.8A).

For the case of the "thrust nappe" category (e.g., model H_3; Fig.3.7A) the evolution is characterized by a trajectory of the IA tracer (green curve) that migrates during the early fold growth stages but quickly it becomes fixed with respect to material particles (approx. 11.0 Ma), up to the end of the simulation. This indicates that for this category the hinge of the fold is blocked and cannot migrate. On one hand, the normal limb NL always shows a positive tendency with time, with a reduction of its distance respect to the IA and thus indicating that part of deformation was accommodated by progressive shortening of the normal limb. On the other hand, the IS during the early stages was located relatively near the IA, but relatively soon (approx. 9.2 Ma), the relative distance between both markers starts to increase. An analysis using the $I_{Loc} > 0.15$ condition shows that the major increase in distance is due to plastic deformation (P) and the length of the "little deformed" reverse limb was relatively short and constant during all time.

For the case of the "fold nappe" category (e.g., model $T_{300} + \beta_{20}$; Fig. 3.6H), the trajectory of the IA tracer describes a continuous positive tendency, with displacement of the material particle from the normal limb towards the inflection (reached in the last step by the definition of the IA). The NL and IS curves show also similar trend, with a tendency to increase their relative distances respect to the IA. Analysis of strain localisation indicates that the I_{Loc} threshold was never exceeded (i.e., $I_{Loc} > 0.15$), and hence, the deformation was mainly accommodated by distributed viscous flow and very low plastic behaviour. For the example shown in the Fig. 3.10C, there was a migration of the hinge equivalent to 4 km.
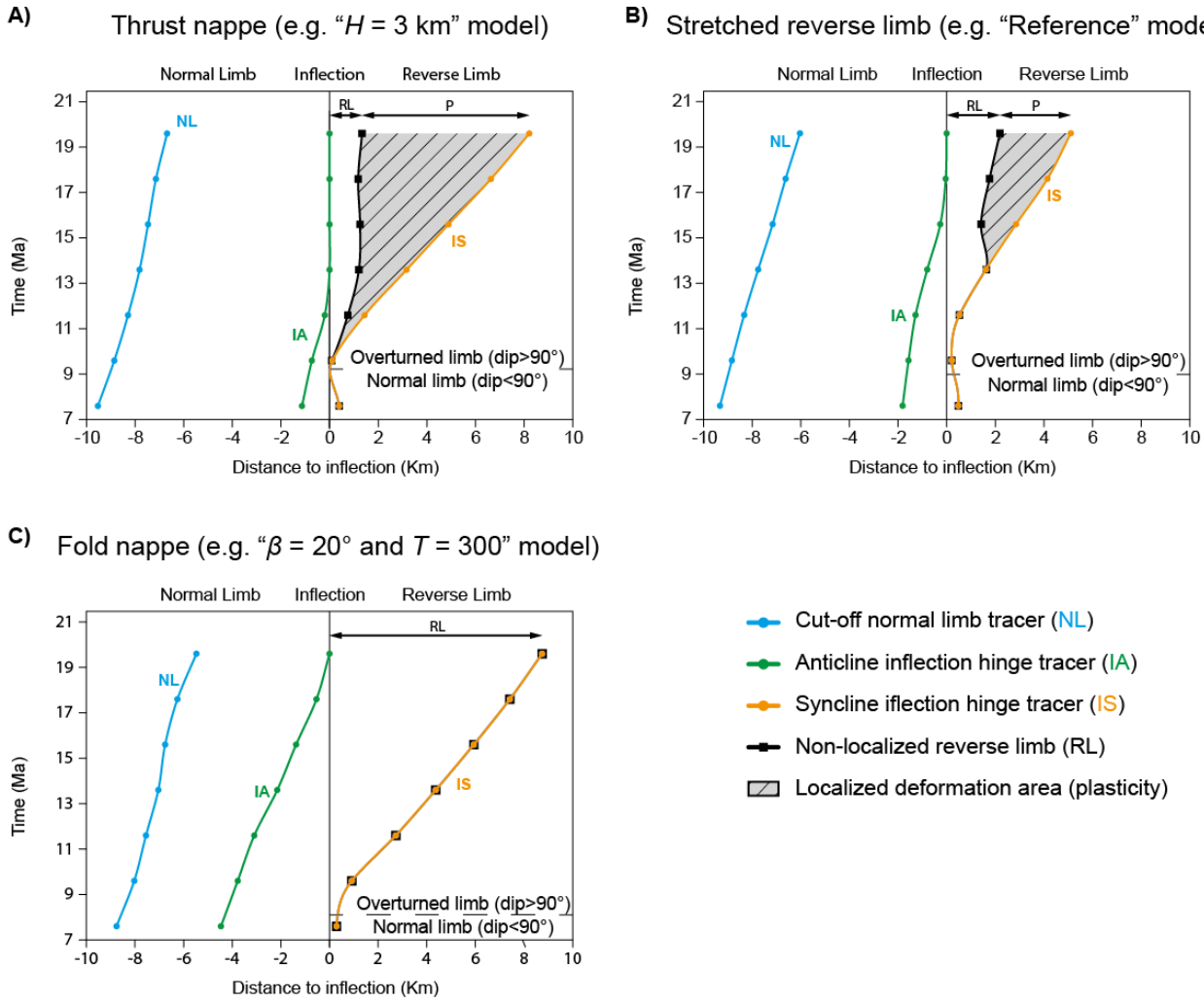
Figure 3.10: *Plot of the variation of the position of the three passive tracers with respect to the fold inflection. A) Thrust nappe end member, where the hinge migration is locked from 13 Ma onwards and the plasticity (P) is increasing (I_{Loc} > 0.15) from the early simulation time, causing the extreme stretching and thrusting of the reverse limb at the end of the simulation. B) Fold nappe end member. Hinge migration is active until the end of the simulation and there is no plasticity in the reverse limb (P=0 and I_{Loc} < 0.15). C) Stretched reverse limb (0.15 < I_{Loc} < 0.6) showing mixed features between the fold nappe and thrust nappe end members, where the migration of the hinge is active until 13Myr and then it is not as intense, which results in the stretching of the reverse limb.*

Finally, for the case of "fold nappe with stretched reverse limb" category (e.g., *Rs* model; Fig. 3.6), the IA, NL and IS trajectories show trends between the previous two cases. The IA displays a large time interval with hinge migration until approx. 17.7 Ma of simulation time, when it became fixed and remained blocked until the end of the simulation (Fig. 3.10B). Pre-stage before blocking of the fold hinge causes the I_{Loc} to rise over 0.15 (approx. 13.7 Ma),

resulting in the stretching of the reverse limb by viscous and plastic flow until the end of the simulation.

3.4.3 On the influence of geometrical and mechanical variables in the nappe geometry

The effect of varying the different variables tested using the numerical modelling (Fig. 3.2; Table 3.1 and 3.2) is summarized in Fig. 3.11. The same three main categories (thrust nappes, fold nappes with stretched reverse limb and fold nappes) are used.

On one hand, from Fig 3.11, thrust nappe geometries are sighted when there is an increase of mechanical variables such as the viscosity of the upper allochthonous nappes (η_{AN}) or the viscosity of the Upper Cretaceous (η_{UC}), or when there is a decrease of the frictional angle of the Upper Cretaceous layer (ϕ_{UC}). The geometrical variables that promote thrust nappes are short L and H, thin detachment levels (T) and, in general, moderate/large angles of the Lakora ramp (β) or the forestop (α). On the other hand, the variables promoting fold nappe geometries preserving layer thickness of the recumbent fold are very restricted. From the systematic series of models, there is a positive enhancement of fold nappe occurrence only for moderate values of the viscosity of the upper allochthonous nappes (η_{AN}) or when there is an increase of the thickness of the upper detachment level (T). In general, the most likely situation in the series of performed models is the development of fold nappes with stretched limbs and very heterogenous distribution of strain.

From a kinematic and mechanical perspective, the development of thrust vs. fold nappes is relevant for the spatial distribution of stress and strain rate (Fig. 3.12). In summary, a common feature of all the simulations showing a thrust-nappe geometry is a highly deformation band cross-cutting through the Upper Cretaceous layer (e.g., Fig. 3.12A or 3.5D-F) and elevated plastic strain in the reverse limb (e.g., Fig. 3.5G-I and 3.12G) indicating predominant plastic-brittle conditions. From a geometrical point of view, this causes the development of short or

very short reverse limbs, hanging-wall anticlines, and overall a small structural relief. Using the localization index I_{Loc}, the process is observable by a "fast" increase of the I_{Loc}, passing from conditions of distributed strain (low I_{Loc}) to moderate/high values >0.4-0.6. Additionally, this is also coincident with the blocking of the fold hinge migration, which enhances the early plastic yield of the material and the extreme stretching of the overturned limb (Fig. 3.8A and 3.10). The spatial transition from low deformed to highly deformed is rapid (e.g., Fig. 3.5B and Fig. 3.10A).
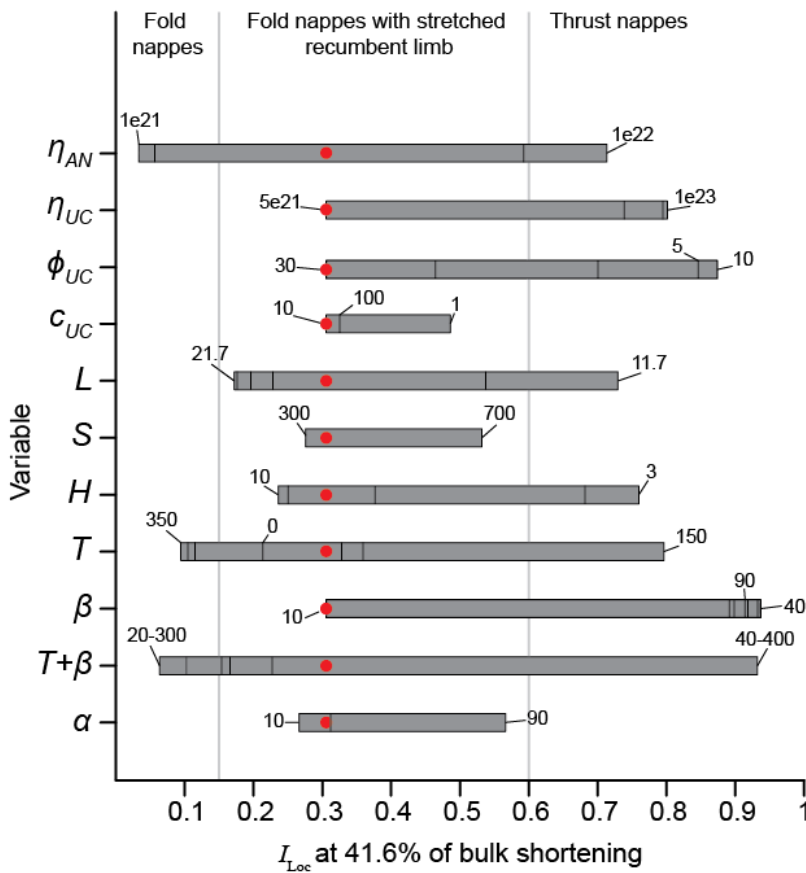
Figure 3.11: Range of variation of the index of localization for each variable tested and structural style developed. The red point indicates the reference simulation, while the numbers indicate the range of values used for each variable.

On the other hand, the fold nappe end member (Fig. 3.12B) can be summarized by the continuity of the reverse limb and moderate structural relief. In contrast to thrust nappes, plastic strain is very low, stresses and strain rates are moderate/low high strain zones cross-cutting the overturned limb are not formed (Fig. 3.10C and 3.12F and H). The fold nappes exhibit km-scale overturned limbs without significant heterogeneous stretching and strain

localisation and dominated by viscous flow (I_{Loc} <0.15; Fig. 3.8A and 3.10C). However, this end member must be considered as an idealized or very restrictive structure, and probably the more usual cases in nature are with I_{Loc} > 0.15 with stretched overturned limbs (Fig. 3.8B).

More realistic recumbent folds are those presented in Fig. 3.6G and 3.6I or in Fig. 3.7B, where the reverse limbs are stretched, but without attaining the yielding of the materials during early/intermediate stages of deformation. Accordingly, the I_{Loc}, never overcomes the thrusting boundary (Fig.3.8A). Overturned limbs show continuous thinning, and during last stages the plastic condition can be achieved, producing the progressive localisation of deformation. Such localisation may represent the basal thrust observed in some natural fold nappes. The resulting structures in the modelling show many of the first-order features observed in natural examples (i.e., a flat-lying reverse limb of kilometric scale, a normal limb with second-order structures, a sub-horizontal axial plane and a tight syncline between the recumbent limb and an autochthonous succession), as in the Helvetic nappes of the Alps (e.g., Ramsay et al., 1983, Pfiffner, 1993;).

3.4.4 Application to the Eaux-Chaudes fold nappe and comparison with other cases

The numerical results of this thesis highlight the importance of the role of the mechanical and geometrical controls of the stratigraphic succession and the tectonic inheritance during the Alpine deformation of the Pyrenean hinterland. For the specific case of study, two main factors arise to first-order control the development of structures such as the E-C fold nappe: (1) the presence of a stiff forestop in the shortening direction to produce a buttress condition (in the natural case constituted by the Eaux-Chaudes granite), and (2) the existence of two weak layers (i.e., Keuper and Silurian at Eaux-Chaudes) that favoured the structural decoupling and localisation of the deformation.

In accordance with previous numerical models of the Helvetic Alps by Kiss et al. (2020) and Spitz et al. (2020), a viscosity contrast of about three orders of magnitude between the strong key levels (Upper Cretaceous, Devonian) and the upper and lower weak detachment levels (Keuper, Silurian) are required to develop nappe structures with large-scale stratigraphic inversion or/and displacement, and in coherence with the fold nappe definition by Dennis et al. (1981) (cf. section 1.2). In situations with lower viscosity contrast or without an upper weak level, fold nappe structures with large displacement did not form.

The presented results show that tectonic inheritance in the form of a basement forestop is controlling the nappe initiation by concentrating stress in the contact between the strong layers, immersed between weak layers, and the forestop (Fig. 3.4C). Similar results have been obtained by Bauville and Schmalholz (2017), Kiss et al. (2020), and Spitz et al. (2020) with application to the Helvetic nappes, which points to the same mechanism of nappe initiation. If the mechanical heterogeneity of the viscous contrast between the granitic and metasedimentary basement was absent (Fig. 3.7L), neither a fold nor a thrust nappe was produced, but large scale upright buckle folds are formed instead. The push and shear stress provided by the Lakora thrust and the upper allochthonous nappes (e.g., the Ultrahelvetc nappes in the case of the Alps) focus stress concentration in the contact between the E-C pluton and the Upper Cretaceous limestone interface as suggested by the reference simulation (Fig. 3.4C), producing the activation of the Silurian lower detachment of the E-C nappe and the growth of the structure. Hence, the Eaux-Chaudes pluton (with apparently no signs of significant ductile deformation during the Alpine compression) played an essential role for recumbent folding. This example highlights the role of mechanical heterogeneities arising from pre-alpine rocks during the Pyrenean orogeny, such as also documented for the Alps (e.g., Wissing and Pfiffner, 2003; Kiss et al., 2020). However, in contrast to the infra-Helvetic nappes of the Alps, in the case of the Eaux-Chaudes massif I cannot only invoke the
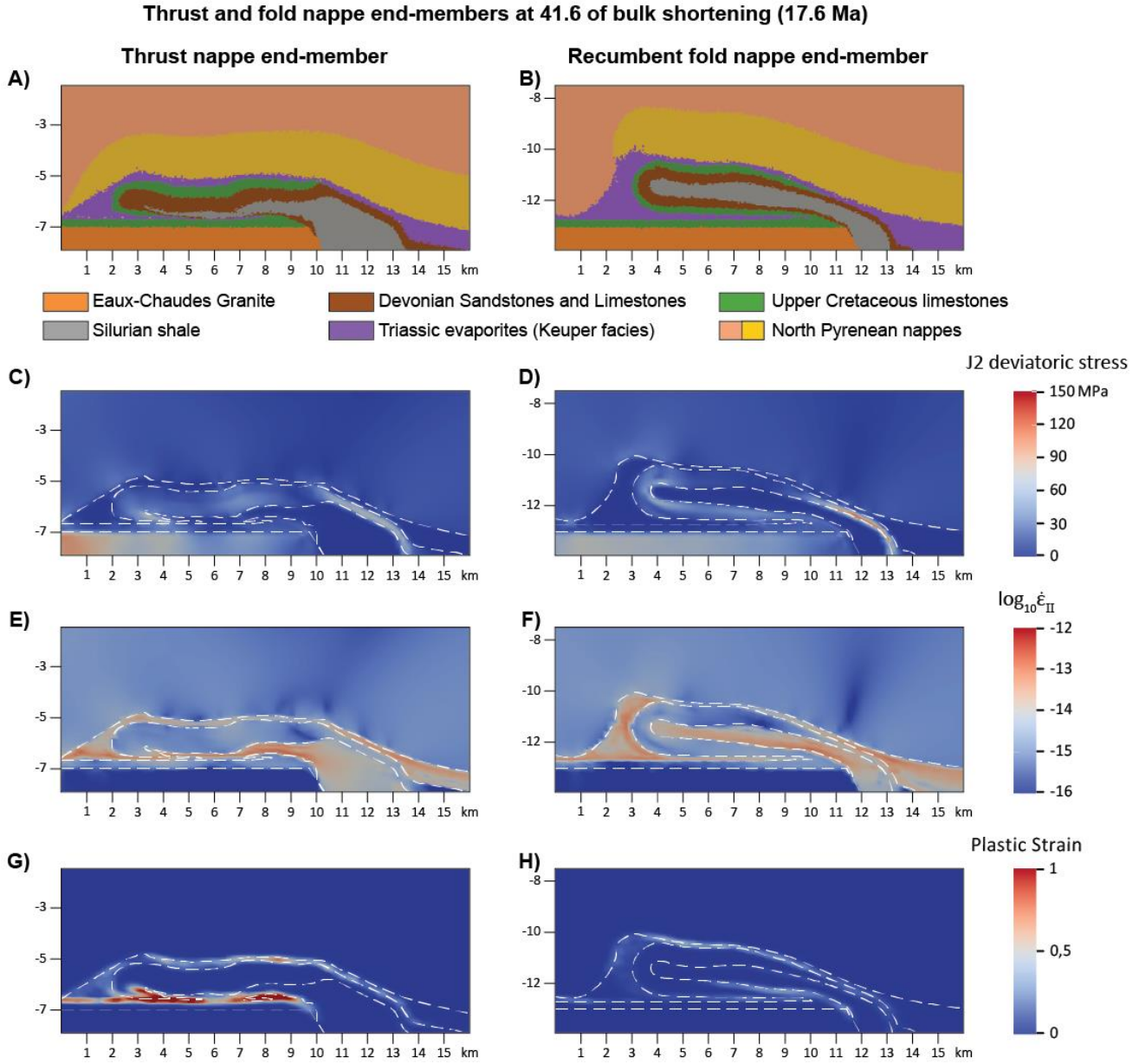
Figure 3.12: *Final geometry (**A** and **B**), second invariant of the differential stress (**C** and **D**), second invariant of the strain rate tensor (**E** and **F**) and plastic natural strain (**G** and **H**) after 41.6% of shortening for a typical example of a thrust nappe (left; model H_3) and recumbent fold nappe (right; model $T_{300} + \beta_{20}$).*

ductile closure of precursor extensional basins and the extrusion of their sedimentary infill. Indeed, according to the results a minimum initial burial condition of ~5 km in depth is needed to mechanically develop a fold nappe (Fig. 3.7A-C), which is in accordance with the emplacement conditions proposed by Caldera et al. (2021) ranging 8-10 km. Our results also emphasize the role of the upper Keuper allochthonous weak layer, enabling the decoupling

between structures but also allowing the growth of the recumbent fold given its capacity to flow and migrate.

The multilayered character of the models with weak rocks such as slates, shales or evaporites between stiffer layers triggered the development of upper and lower shear zones (Fig. 3.4E and F), which are necessary for the development of the fold nappe structure. In addition, recumbent fold structures are favoured for settings with thicker upper detachment level (T ~250-350m) because such settings allow the decoupling from the allochthonous nappes since the early steps of the convergence (e.g., Fig. 3.4E). However, the thickness of the upper weak layer must allow the shear stress transmission downwards (becoming more effective as the upper weak layer is reduced in thickness) to permit the activation of the Silurian basal detachment, which is hindered for $T > 350m$ (Fig.3.6C). On the other hand, an excessive thinning of the upper weak layer reduces the efficiency of decoupling between this weak layer and the E-C nappe (e.g., Fig. 3.4F) positively enhancing the shear transmission downwards, and the low angle shear zone within the lower weak level become the only active level until the end of the simulation (Fig. 3.4E-F). Similar observations were pointed out by Pfiffner (1993), where high ratios between the thickness of the weak to the stiff layers favoured the development of fold nappes. From a qualitative interpretation based on the final geometry, the simulations with I_{Loc} displaying moderate to low values (<<0.6 Fig. 3.6G-I, 3.8A and 3.10C) are the cases that most closely resemble to the E-C natural example.

Furthermore, the cases where the upper allochthonous sheets and the E-C nappe are relatively coupled and the lower shear zone is active, are optimum for the mechanism of fold hinge migration and limb rotation as ways to overturn the forelimb during the early deformation steps. Even though both fixed hinge-limb stretching and hinge migration coexist in all our simulations, geometries approaching recumbent fold nappes similar to the E-C field example are those formed by a dominant mobile hinge mechanism (Fig. 1.4, 3.6G-I and 3.10B-C).

However, a direct comparison of the E-C or other natural examples with the model kinematics is challenged because of the scarcity of markers confirming mobile hinges, as previously pointed out by Mercier et al. (2007).

Therefore, the interpretation proposed here is that the Eaux-Chaudes fold nappe results from an asymmetric detachment fold developed by limb rotation, with limb overturning during the early deformational steps and later amplified by progressive hinge migration with only moderate stretching of the overturned limb. Similar scenarios were also invoked by Epard and Groshong (1995), Homza and Wallace (1997), Poblet and MClay (1996), Perrin et al (2013) and Poblet (2020), to describe the migration of fold hinges, but focused on the migration of the forelimb synclines. In the study case, the presence of the strong footwall granitic forestop blocked the migration of syncline hinge, and forced the migration of the anticline hinge.

3.5. Conclusions

The presented mechanical simulations are reproducing the first order features, structural elements and the scale of the Eaux-Chaudes and other natural fold nappes. Modelling results emphasize the need of weak layers above and below the Eaux-Chaudes fold nappe, as well as the need of stiff footwall forestop to localize the deformation, represented by the Eaux-Chaudes pluton.

The E-C recumbent fold nappe was developed under a double weak layer geometry within a low angle shear zone regime. The thickness of both layers are very relevant to allow the detachment of the structure (Silurian) but also to permit the fold growth (Keuper) due to the migration of the hinge and the shear transmission from the Lakora and overlying nappes. The upper weak level must also allow enough coupling of the structures to develop a fold nappe with a large reverse limb. An increase of the upper weak layer thickness is favouring the

viscous/ductile behaviour of the stiffer layers (Upper Cretaceous and Devonian) making longer, stretched and horizontal reverse limbs and axial planes (with welded synform limbs). On the other hand, the ECP in the footwall is acting as a forestop localizing the deformation, without which distributed deformation along the Upper Cretaceous and Devonian layers would have been favoured over fold or thrust nappe localisation, resulting instead in large-scale upright buckle folds.

The migration of the hinge (1) and the rotation of the forelimb followed by the translation of the E-C nappe (2) are the end-member mechanisms under which the modelled structures are developed. (1) is characterized by the continuity of the key layers (Upper Cretaceous and Devonian) and moderate to low values of I_{Loc} (<0.6), while (2) can be identified by an interrupted key layer (cross-cutted by a low angle shear zone) and high values of I_{Loc} (>0.6), which is a reflex of an extreme stretching process. It is also evidenced that the intrinsic mechanical properties (ϕ, η_{UC}) of the Upper Cretaceous layer can determine thrusting over folding. In addition, the mechanical properties of the surrounding upper nappes (η_{AN}) can also be determinant in the same way, so that the presence of stiffer basement nappes just above the Eaux-Chaudes fold nappe (without significant weak layer) would have resulted in a thrust nappe structure.

The model variability suggests that nappe development does not depend on only one factor, but on the concurrence of different variables.

The main features regarding the initial geometrical configuration and also the mechanical properties of the rocks involved in the deformational process are suggesting that both the mechanical and geometrical inheritance are key factors that must not be ignored to gain understanding on the development of thrust nappes and fold nappes.

The concepts here discussed may be applicable to other natural examples of recumbent fold nappes well described in the literature (e.g., Helvetic Alps: stiff granite footwall, weak supra-nappe cover, etc.).

Chapter 4: Thermo-mechanical simulations of fold/thrust nappes

Chapter 3 focused on a systematic study of the geometrical and mechanical factors that facilitate the development of recumbent folds. The rheology used in those simulations was based on simple linear viscous materials, without a dependency on the temperature or the strain rate. In this chapter, the favorable conditions under which a recumbent fold could be formed are explored using a non-linear viscous approach dependent on the temperature and strain rate, and therefore, using rheologies closer to the expected for rocks.

For low strain rate tectonic processes, rocks can be considered as viscous and the behavior could be defined by a non-linear relationship between the deviatoric stress (σ) and the strain-rate ($\dot{\varepsilon}$) (e.g., Gerya, 2019). The mechanical response of rocks to applied stress has been investigated for several decades in laboratory conditions. From these studies, a general viscous power law was proposed in which the temperature dependence is mainly introduced using an Arrhenius term (i.e., an exponential term controlled by an activation constant and inverse to the temperature):

$$\eta_{eff} = 2 \left[B_n \, e^{-\frac{En + P\,Vn}{RT}} \right]^{1/n} \dot{\varepsilon}_{II}^{\left(1 - \frac{1}{n}\right)}, \qquad \text{(c.f. section 2.3.1).}$$

where n_{eff} is the effective viscosity (Pa·s); B_n is the pre-exponential rheological factor (Pa^{-n}/s); E_n and V_n are the activation energy per mol (J/mol) and the activation volume (J/Pa/mol), which are experimentally determined; R is the gas constant (m^3·Pa·K^{-1}·mol^{-1}); T is the temperature (K); P is the pressure (Pa); n is the stress exponent and ε_{II} is the second invariant of the strain rate tensor (s^{-1}) (e.g., Schmid et al., 1977; Schmid et al., 1980; Wawersik and Zeuch, 1986; Shea and Kronenberg, 1989, 1992, 1993; Kronenberg et al., 1990; Walker et al., 1990; Mares and Kronenberg, 1993; Wang et al., 1996; Arndt et al., 1997; Renner et al.,

2002; Niemeijer and Spiers, 2005). The parameters obtained from laboratory experiments for minerals and rock aggregates are then used as input parameters in geodynamic numerical modelling addressed to small and large-scale tectonic processes (e.g., Bauville and Schmalholz, 2015; Kiss et al., 2020; Spitz et al. 2020), thereby providing a powerful geodynamical tool to complement field/experimental observations.

This chapter aims to explore the effects of 1) the grade of non-linearity of the system and 2) the temperature dependence on the development of the transition between thrust and fold nappes, focusing specifically on the conditions favorable for large-scale recumbent folding. As previously introduced, the reference case study is the Eaux-Chaudes (E-C) recumbent fold nappe and the paleotemperature conditions deduced by Caldera et al. (2021) and Caldera (2022), mainly between 310-350°C, which will be used to constraint the numerical simulations.

A handicap is the lack of rheological data on the rocks exposed in the E-C area. For this reason, published experimental data will be used as a reference for material properties. This approach is similar to that in recent numerical simulations studying the development of thrust/fold nappes in the external western Alps (i.e., Helvetic and infra-Helvetic units) (Bauville and Schmalholz, 2015; Kiss et al., 2020; Spitz et al., 2020).

A priori, the geometrical and rheological set-up of the simulations of the Eaux-Chaudes and the infra-Helvetics (i.e., Morcles nappe) could be very similar, with predominant influence of factors such as the mechanical contrast between units, the overthrust burial due to the tectonic emplacement of the upper Helvetic nappes (e.g., Pfiffner, 1993) or the temperatures recorded during the deformation (e.g., Girault et al., 2020). However, several differences are expected, such as the absolute scale difference between the Morcles nappe and the Eaux-Chaudes fold nappe or the role of the highly anisotropic behaviour of the detachment level in

the Silurian slates in the Eaux-Chaudes case, that will need to be addressed in a simplified way.

4.1. Initial set-up and model configuration

The initial set-up for the thermo-mechanical simulations is shown in Fig. 4.1. The set-up is similar than the simulation labelled "*T*=300m and *β*=20°" in chapter 3, a configuration that resulted in the development of recumbent fold nappes (see Fig. 3.6H).
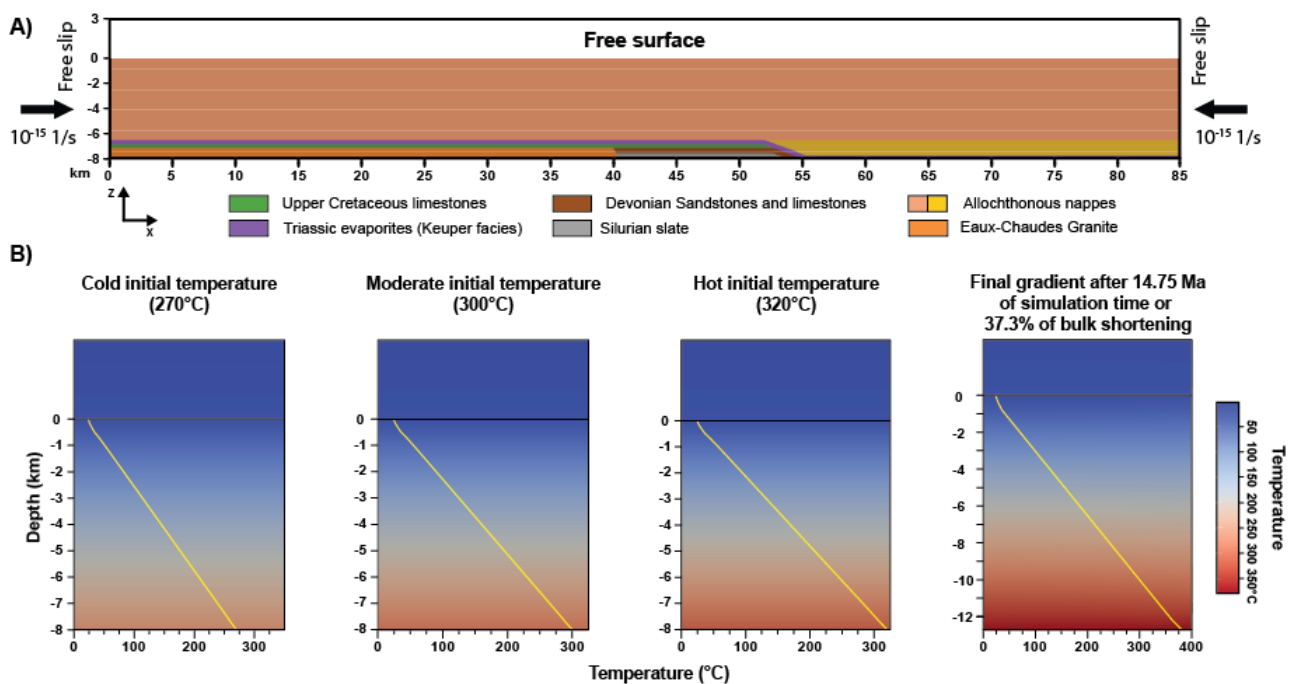
Fig. 4.1: A) Initial set-up used for the thermomechanical simulations from model β=20° and T=300m (c.f. Chapter 3). Numerical resolution is similar to that of the mechanical simulations in Chapter 3, including the mesh refinement and boundary conditions. B) Initial temperature profiles of 30.4, 34.1 and 36.5°C/km applied to the initial set-up in the case of variable temperature (Table 4.1), together with the temperature profile at 37.3% of bulk shortening, which coincides with that of the figures shown in this chapter.

The simulations are defined using the same numerical grid resolution and boundary conditions as those used in Chapter 3 (Fig. 4.1A). The model was divided in three large mechanical entities: 1) Upper Cretaceous (UC) and Devonian, 2) an entity labeled as "media" formed by the Silurian, Keuper and E-C granite units and 3) the allochthonous upper nappes (Fig. 4.1A). In all the simulations, the UC/Devonian entity was modelled using linear or power-

law temperature-dependent rheology (see Table 4.1), while for the allochthonous nappes a linear viscous non-temperature dependent rheology was used in order to simplify the simulations, optimize the simulation time and focus on the key layers (i.e., Keuper and below). The media was simulated using linear/power-law rheologies, and attending the set-up of the temperature profile, the simulations can be divided into two main groups (Table 4.1):

1) Linear/power-law viscous media with constant temperature: in order to explore the effects of the temperature in the effective viscosity for linear/power-law materials, a series of models were run using constant temperature in the entire profile (i.e., geothermal gradient $gr = 0°C/km$), spanning between 250°C and 300°C.

2) Linear/power-law viscous media with temperature gradient: to test the influence of temperature gradients, different initial geothermal gradients of 30.4, 34.1, and 36.5°C/km were applied. These gradients are equivalent to initial temperatures of 270, 300, and 320°C at the bottom of the model, respectively. To simulate the heating effect due to the progressive increase of the tectonic burial, the temperature at the bottom of the model was increased by 6.1, 4.4, and 3.3°C respectively each 0.75 Ma until a maximum of 380°C at 14.25 Ma of the simulation time (Fig 4.1B). From this point onwards, the temperature remained fixed at the bottom of the model until the end of the simulation (25 Ma). In this manner, the effect of inherited abnormally high temperatures from the preorogenic hyperextension stage could be also tested. After deformation, the final geothermal gradient was 25.80 °C/km for all simulations.

As previously explained, a linear/power-law viscous elastoplastic rheology was used to simulate the mechanical behaviour of materials. For power-law materials, temperature-dependent dislocation creep flow laws derived from laboratory experiments were preferently used. The viscosity and temperature-dependent properties were recalculated for viscous linear materials using flow laws from laboratory experiments.

UC/Devonian	Media	Allochthonous	Temperature	
Linear/power-law, *T* dependent, *n* =1,2, 3 and 4.7	Linear	Linear, non-dependent *T*	Constant	250 to 300°C
	Power-Law			
	Linear		Variable	T_i = 270; T_f=380°C
				T_i = 300; T_f=380°C
				T_i = 320; T_f=380°C
	Power-Law		Variable	T_i = 270; T_f=380°C
				T_i = 300; T_f=380°C
				T_i = 320; T_f=380°C

Table 4.1: *List of model variables tested for different temperature scenarios. The values of the experimental parameters and their range of variability can be found in Table 4.2. In the case of constant profile temperature, a model run was performed each 10°C from 250 to 300°C. The allochthonous nappes are viscous-linear and non-temperature dependent in all simulation cases. T_i: Initial temperature at the bottom of the model. T_f: final temperature at the bottom of the model, reached at 14.25 Ma of simulation time and preserved from then until the end of the simulation.*

The brittle frictional behaviour was modeled using the Drucker–Prager yield criterion and defined by the cohesion and friction angle parameters. The list of material properties is presented in Table 4.2.

To test the influence of the stress exponent *n* and the temperature dependence in the deformation of the Upper Cretaceous and Devonian units, the material parameters (pre-exponential constant B_n and activation energy E_n) for different stress exponents were recalculated from the original calcite power-law of Schmid et al. (1977) with *n* = 4.7. Taking into account the reference strain rate of 10^{-15} s^{-1} of the simulations and assuming a temperature of *T*=300°C, the pre-exponential constant was calculated maintaining the assumption of similar effective viscosity of $10^{21.5}$ Pa·s as the original flow law. The activation energy constant was modified to show the same viscosity variation with a temperature gradient, independent of stress exponent. This was done to keep the same range of viscous variation similar for all non-linear behaviors (Table 4.1, 4.2, and Fig. 4.2).

The Silurian flow law

From a mechanical point of view, a problematic level is the Silurian slates. In chapter 3, the Silurian slate unit was shown to be a key element for the development of the Eaux-Chaudes recumbent fold nappe acting as the lower, ductile detachment level.

Model unit	ρ (kg/m^3)	η (Pa $\cdot$ s)	Rheology	f (Pa^{-n}/s)	B_n (Pa^{-n}/s)	N	E_n (J/mol)	λ (W m^1 K^{-1})	φ	C (MPa
Granite	2800	10^{24}	Granite[1]	1	2.6×10^{-27}	2.9	2.19×10^5	3	30°	50
Silurian	2500	10^{19}	Mica[2]	10^{18}	2.04×10^{-134}	18	5.1×10^4	2.5	5°	1
Devonian	2700	-	Calcite[3]	1	1.69×10^{-24} to 2.04×10^{-13}	1 to 4.7	1×10^5 to 2.98×10^5	2.5	30°	1
Keuper	2500	10^{18}	Salt[4]	1	7.26×10^{-36}	5	5.39×10^4	2.5	5°	1
Upper Cretaceous	2700	-	Calcite[3]	1	1.69×10^{-24} to 2.04×10^{-13}	1 to 4.7	1×10^5 to 2.98×10^5	2.5	30°	10
Upper allochthonous nappe	2700	5×10^{21}	Viscous linear	1	-	-	-	-	30°	1
Lower allochthonous nappe	2700	5×10^{21}	Viscous linear	1	-	-	-	-	30°	1

Table 4.2: List of the simulated units and their material properties, where ρ is the density, η is the linear viscosity, B_n is the pre-exponential factor, f is a custom pre-factor applied to the B_n, n is the stress exponent, E_n is the activation energy, λ is the thermal conductivity, φ is the friction angle, and C is the cohesion. For all simulations, the heat capacity (C_P) is set constant at 1050 J/K. The creep flow laws are from (1) Arndt et al. (1997), (2) Kronenberg et al. (1990), (3) Schmid et al. (1977) and (4) Wawersick and Zeuch (1986).

In the area of study, the Silurian slates are majorly composed of phyllosilicates (biotite, white mica, and chlorite) in approximately 70-80% (from thin-section observations; Fig. 4.3A and B), but also contain small amounts of siliciclastic grains (mainly quartz), graphite and opaque minerals. Few flow laws for mica-single minerals have been published. In this study, we use the flow law proposed by Kronenberg et al. (1990) and obtained from laboratory experiments using a single biotite crystal. To generalize to a polycrystalline aggregate, several mixing laws and approaches have been reported in the literature (e.g., Tullis et al., 1991; Huet et al., 2014; Wallis et al., 2015), and these are here considered for the Silurian slates.
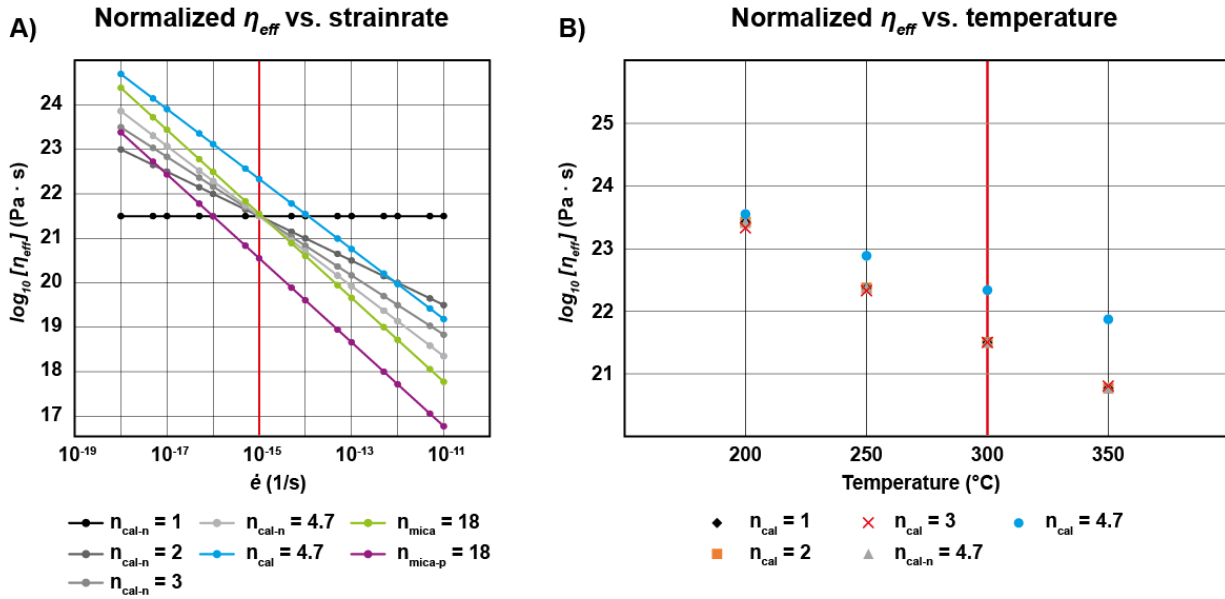
Figure 4.2: *Variation of effective viscosity with **A)** strain rate and **B)** temperature for UC/Devonian and Silurian units. The subindexes "cal" and "mica" indicate the original creep laws of Schmidt et al. (1977) and Kronenberg et al. (1990) for calcite and mica, respectively. For the simulations comparing the influence of non-linearity (subindexes "cal-n"), the effective viscosity of the power-law materials was normalized to $10^{21.5}$ Pa·s, for a reference strain-rate of 10^{-15} s^{-1} (vertical red line in A) and a temperature of 300ºC (vertical red line in B). Additionally, the activation energy was selected to show similar values of effective viscosity with temperature, independent of the stress exponent. For the Silurian unit, a pre-factor was applied to the original mica law and indicated by "mica-p".*

Recently, Rast and Ruh (2021) combining experimental flow laws and numerical simulations of quartz-mica aggregates proposed a graphical way to estimate the effective stress exponent (n) and B_n for a polycrystalline aggregate using relative proportion between biotite and quartz.

Considering the 70- 80% mica content of field samples and the Rast and Ruh (2021)'s diagram, the range of n and B_n for the polycrystalline aggregate are indicated in orange in Fig. 4.3C-D, and within the range of the flow law proposed by Kronenberg et al. (1990). The viscosity contrast between the power-laws of calcite (Schmidt et al., 1977) and mica of Kronenberg et al. (1990) is approximately one order of magnitude (Fig. 4.2A). To maintain the same order of magnitude in viscosity contrast (which is key to avoid homogeneous deformation; cf. chapter 3), applying the normalized calcite power-laws with different stress exponents, a custom pre-factor $f = 10^{18}$ Pa^{-n}/s multiplying the B_n of the Silurian was used.
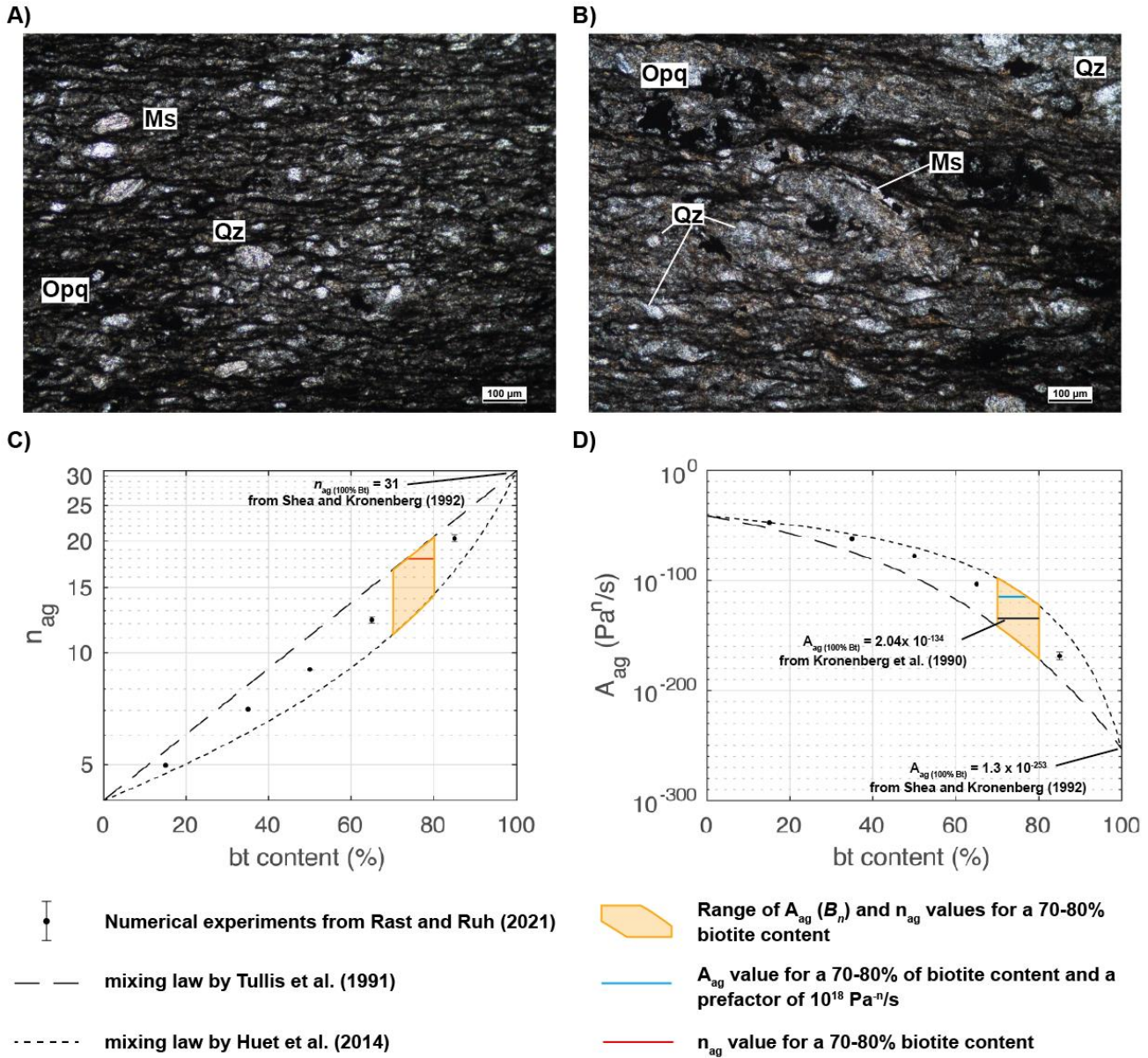
Figure 4.3: *A)* and *B)* PPL photomicrographs of the Silurian slates which are mainly composed by phyllosilicates with small amounts of quartz grains, graphite and opaque minerals. *C)* and *D)* Relationship between the % of biotite content in a polymineralic aggregate and the bulk values of n and A (equivalent to Bn) of the viscous power-law of the aggregate (from Rast and Ruh, 2021).

4.2. Results: on the influence of the stress exponent

As previously mentioned, to test the influence of the stress exponent (i.e., the linearity or non-linearity of the rheological behavior) in the evolving structures and the transition between fold and thrust nappes, a series of models with constant-temperature profiles were performed (Table 4.1). The range of geometrical variability in function of the stress exponent and temperature is shown in Fig. 4.4 for a series of representative simulations. The strain-rate field and plastic strain distribution for these simulations are shown in Figs. 4.5 and 4.6.

Two distinct geometries can be identified from this series of models. (1) On the one hand, models that show a long and continuous Upper Cretaceous-Devonian panel (UCD onwards), with low values of plastic strain and therefore without brittle/frictional localization (e.g., Figs. 4.4C and 4.5C). The UCD level shows an overturned and flat limb in all cases (i.e., models in Fig. 4.4C, $n=1$ and $T=280°C$; Fig. 4.4H, $n=4.7$ and $T=260°C$; Fig. A4.1C, $n=1$ and $T=280°C$; and Fig. A4.1E, $n=2$ and $T=260°C$), so does the axial plane of the fold. However, the overturned limbs usually display signs of stretching in the syncline hinge zone (e.g., Fig. 4.4C), where the UCD panel can be extremely thinned (e.g., Fig. 4.4H). Moreover, the normal limb of the structure is typically flat with second-order large wavelength gentle folds (e.g., Fig. 4.4C). The plasticity recorded in these structures is usually very low, which points to a dominant viscous/ductile behavior (e.g., Fig. 4.4H and 4.6H). This can be observed at temperatures above 260°C, especially for $n \leq 2$ (e.g., Figs. 4.4C, 4.6C), despite viscous-dominated recumbent folding can also be identified at lower temperatures (e.g., 260°) and n ≥ 3 (e.g., Figs. 4.4H and 4.8). With linear media, recumbent folding is more restricted to stress exponents below 3, sharing the same temperature range than those simulated using non-linear media (Figs. 4.9 and A4.1, A4.2 and 4.3).
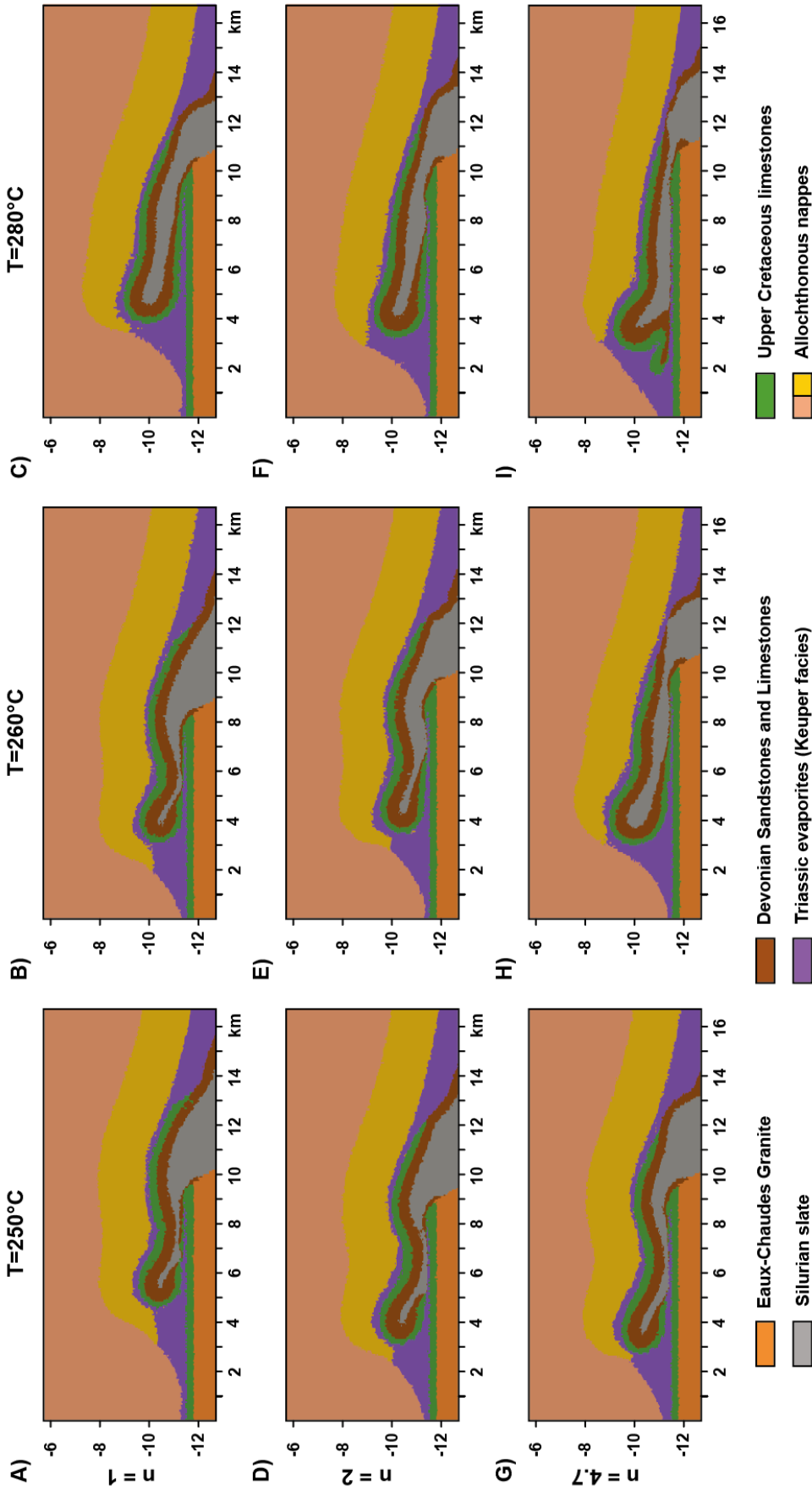
Figure 4.4: *Comparative chart on the influence of stress exponent (n=1, 2 and 4.7) and temperature (T= 250, 260 and 280°C) in the final geometry for models with a non-linear media. All pictures at 37.3% of bulk shortening. Brittle deformation of the overturned limb (i.e. thrusting) is present below 270°C and n ≤ 3 (see Figs. 4.6 and 4.8). Ductile localization is favored in a wide range of temperatures and at n ≥ 2 (see Figs. 4.6 and 4.8). In between, a range of situations where recumbent folding (with constant or stretched recumbent limb) are produced.*
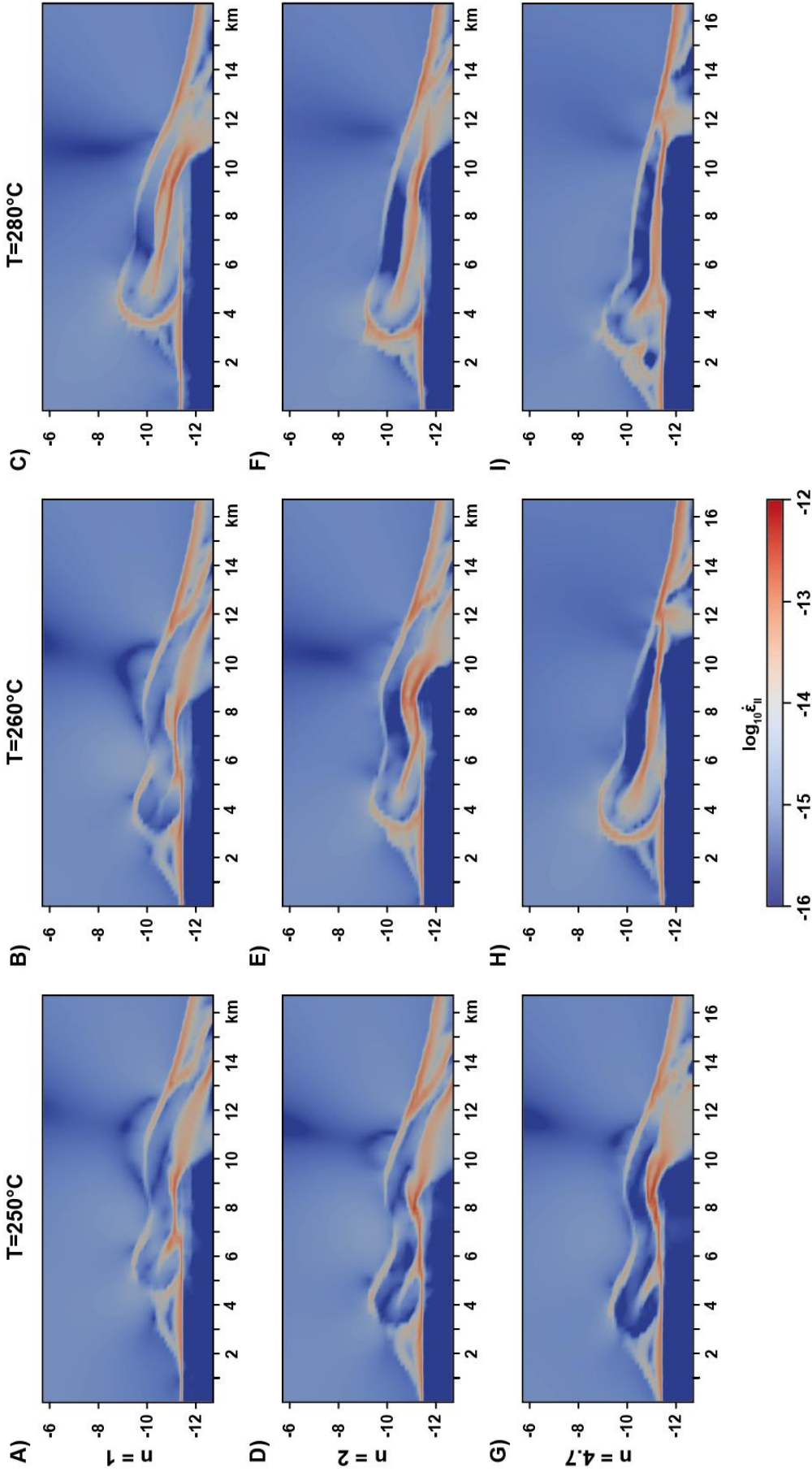
***Figure 4.5**: Selected simulations of the second invariant of the strain rate tensor ($\dot{\varepsilon}_{II}$) of the systematic model runs under non-linear media at different constant temperature profiles for different stress exponents (n) at 37.3% of bulk shortening. Each simulation picture correspond to the same interval and area to those shown in Figs. 4.4 and 4.6. Flat localization surfaces are detected by the elevated strain rate values through the overturned limbs in simulations where no recumbent folding is occurring, showing geometries much resembling a thrust nappe.*
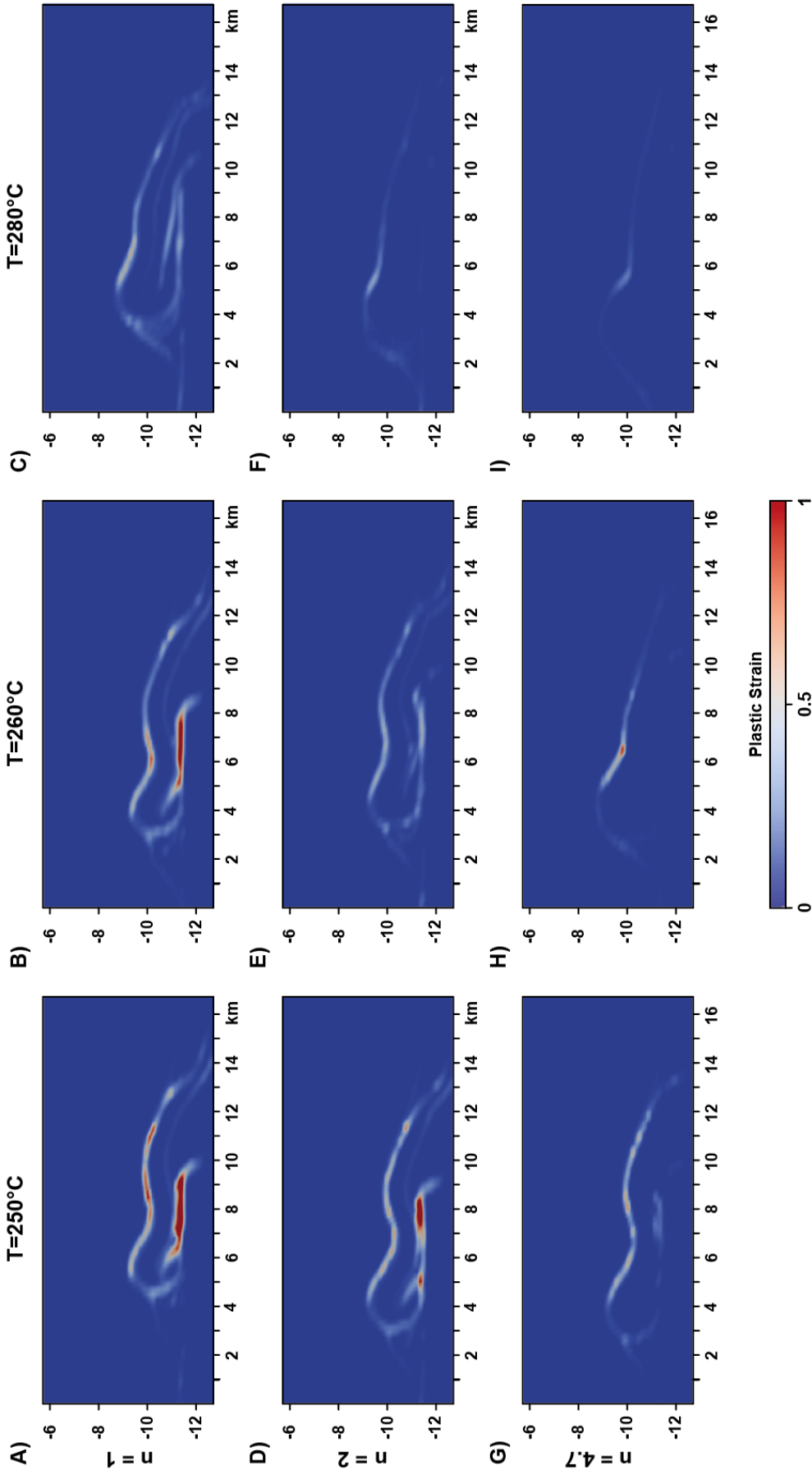
Figure 4.6: *Selected simulations of the natural plastic strain of the systematic model runs under non-linear media at different constant temperature profiles for different stress exponents (n) at 37.3% of bulk shortening. Each simulation picture corresponds to the same interval and area to those shown in Figs. 4.4 and 4.5. Plasticity is favored at low temperatures and stress exponents while the viscous behaviour is dominant at high stress exponent and*

(2) On the other hand, the geometry most commonly obtained in the simulations consists of non-continuous UCD panel, which occurs in a wider range of situations. These are characterized by moderate-to-short and truncated overturned limbs, usually flat or dipping towards the hinterland (i.e., the right side of the models) (e.g., Fig. 4.4D-F). The final structure shows preferent strain localization in the lower weak level (i.e., the Silurian), allowing detachment along a thin and flat level with large transport of the units over the autochthonous (e.g., Fig. 4.5D). These localization levels can be identified by high strain rates of ~10^{-13} s^{-1}, and in most cases, cross-cutting the overturned limb (e.g., Figs. 4.5G and 4.6G). The normal limb displays upright folds with shorter wavelengths than those observed in the simulations where there was no localization in the recumbent limb (e.g., Fig. 4.4D), and for $n = 4.7$ and $T \geq 260°C$ the Devonian phase is extremely stretched in the normal limb (e.g., Fig. 4.4H and I). In contrast to the continuous fold structures described in (1), frictional plasticity is well developed at low temperatures and moderate-to-low stress exponents (e.g., Figs. 4.4A and 4.6A). However, similar geometries without plasticity are also observed at higher stress exponents and temperatures (e.g., Fig. 4.4I and 4.6I). This indicates a duality in the strain localization according to the dominant behavior regime (brittle vs. ductile) under which qualitatively similar geometries could be developed on a large scale (e.g., Figs. 4.4A and 4.6A vs. Figs. 4.4I and 4.6I), which has implications in the expected rocks to be found at the field-scale (brittle – cataclasite vs. ductile – mylonite).

In fact, the enhancement of frictional plasticity is not only linked with the decrease of temperature (as intuitively expected), but also with the decrease of the stress exponent (Fig. 4.6). High stress exponents promoted stress weakening between the UCD level and the surrounding media, producing a more heterogeneous distribution of the effective viscosity within the UCD panel in the areas with higher strain-rate values (i.e., the overturned limb).
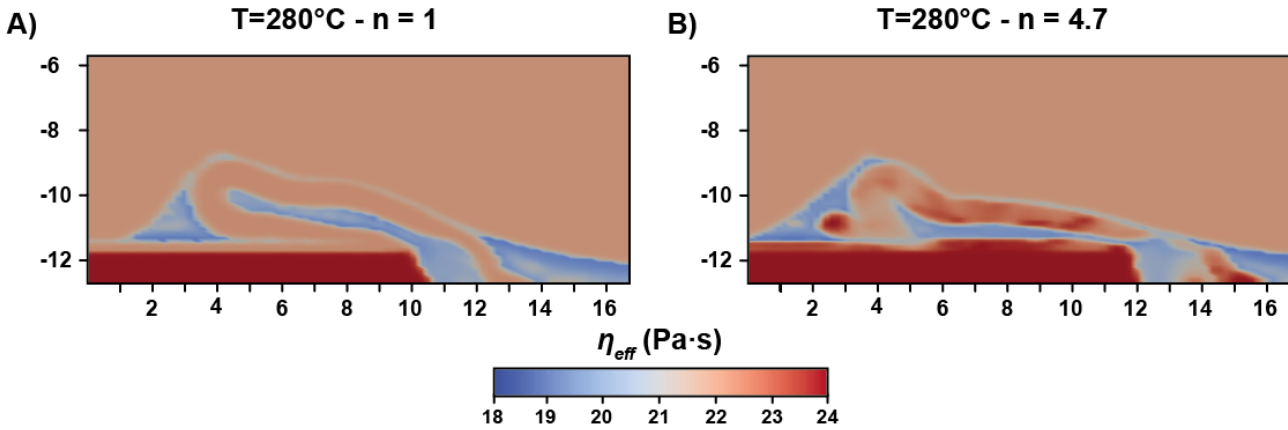
Figure 4.7: Example of the effect of an increase of the stress exponent on the viscosity of the UCD panel, increasing the internal viscosity heterogeneities and reducing the effective viscosity in the high strain areas.

This results on a reduction of the effective viscosity of the panel, thus hindering the frictional plasticity in favor of a dominant viscous/ductile behavior (e.g., Fig. 4.7).

In general, the viscous/ductile structures (1) described in this chapter are geometrically characterized by slightly taller structural heights (i.e., the distance between the top of the autochthonous Upper Cretaceous layer and the highest marker at the top of the Upper Cretaceous of the normal limb) than the frictional-plastic ones (2) (averages of ~2.4 km vs. 2.2 km respectively).

Finally, it is necessary to mention that for all the thermomechanical simulations, the allochthonous upper nappes and the UCD panel are mechanically coupled, independently of the structure developed (Fig. 4.5; c.f. chapter 3). In general, the displacement of the upper nappes over the UCD panel is slightly larger in the cases of where there is strain localization in the recumbent limb (e.g., Fig. 4.4A and 4.5A vs. 4.4C and 4.5C). The coupling of the allochthonous nappes and the UCD panel is in all cases (also in the simulations presented in chapter 3) coinciding with the pass of the allochthonous nappes (i.e., the contact between the two allochthonous nappes units) over the basement stiff block (simulating the Eaux-Chaudes pluton), because is where the nappe is initiated (as an upright fold; e.g., Fig. 3.6A) due to the stiffness of the granite. Deformation is transmitted from the upper weak level (Keuper) to the

lower weak level (Silurian), producing a migration of the intensity of the strain localization from the upper weak level to the basal weak level during initial steps, and finally shifting to focus deformation in the recumbent limb, provoking its lengthening, stretching and yielding depending on the case (Figs. 4.4 and 4.5).

Qualitative summary diagrams of the conditions under which the resulting end-member structures (i.e., thrust nappes and fold nappes) are observed and the dominant conditions under which they were developed are displayed in Figs. 4.8 and 4.9.
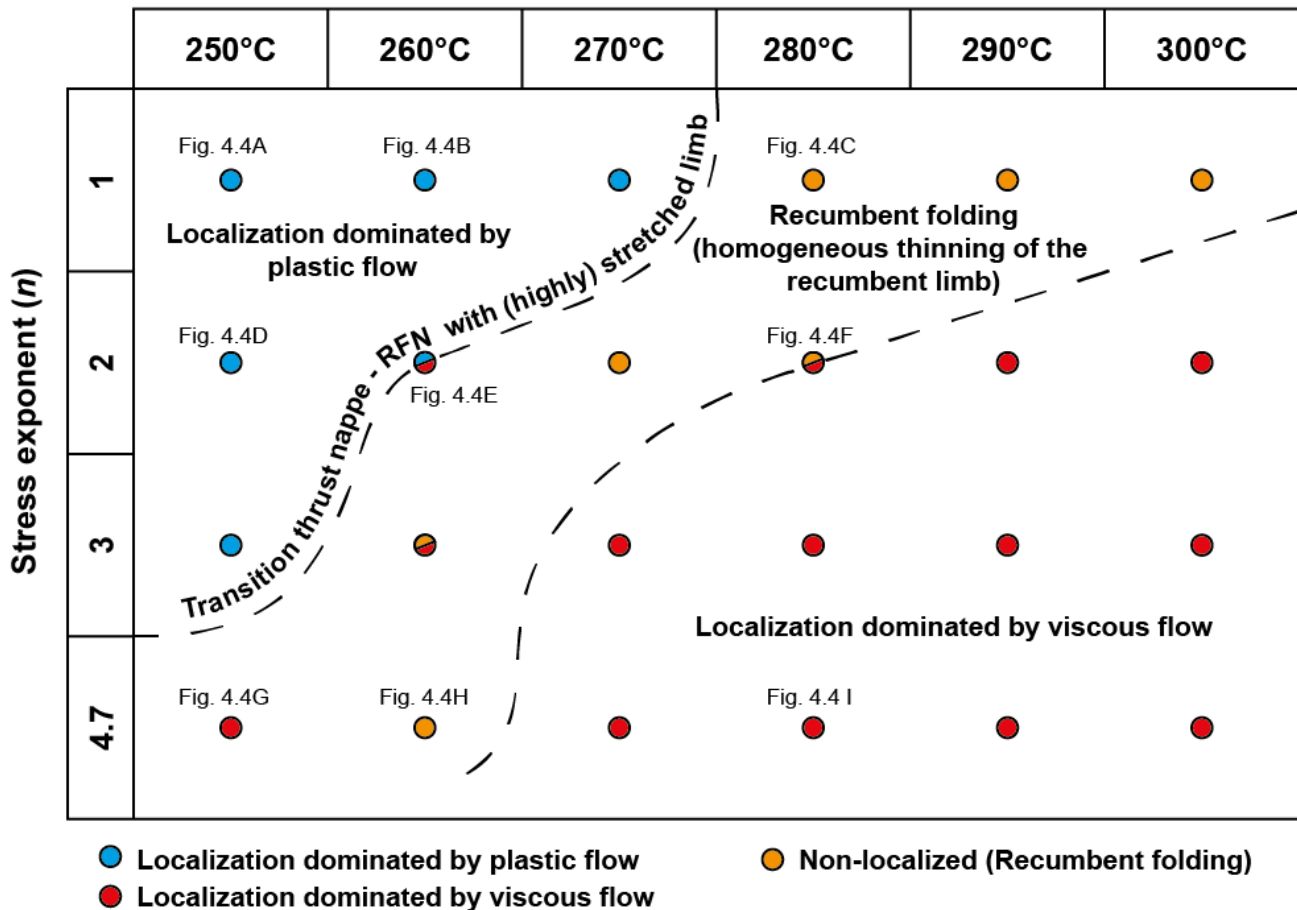
Figure 4.8: *Qualitative summary diagram of the resulting structures obtained in thermomechanical modelling under nonlinear media for different stress exponents and constant temperature profiles and the dominant regime under which they were developed. RFN: Recumbent fold nappe.*
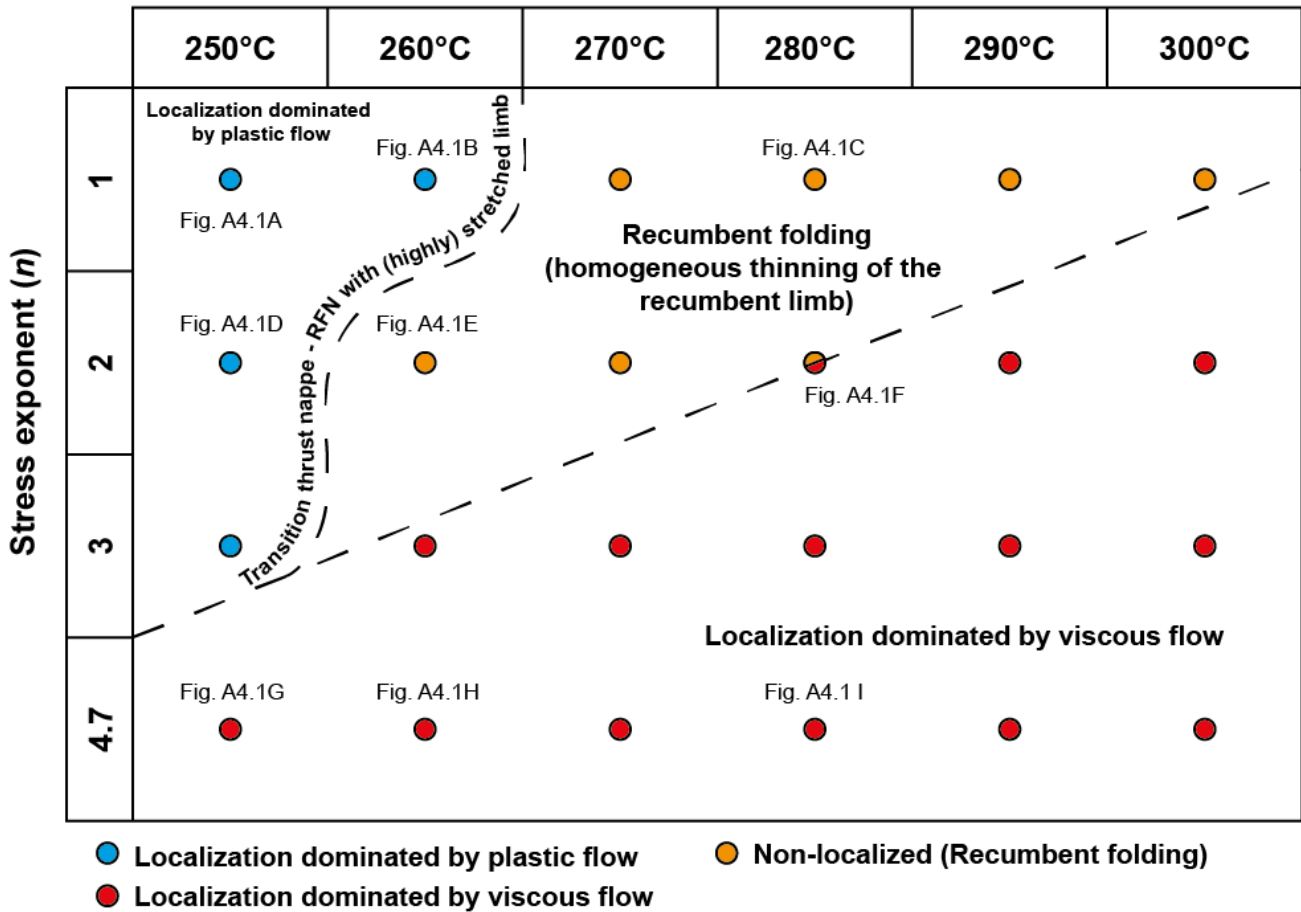
Figure 4.9: *Qualitative diagram of the resulting structures obtained in thermomechanical modelling under linear media for different stress exponents and temperatures and the dominant regime under which they were developed. RFN: Recumbent fold nappe.*

4.3. The effect of the temperature gradient

As mentioned above, different temperature gradients (24.5, 27.2, and 29.1°C/km) were tested to investigate the influence of the initial temperature. The results for stress exponents of 1, 2, and 4.7 of the UCD level and temperature- and strain-rate-dependent media are shown in Figs. 4.10, 4.11, and 4.12, respectively. The results for the same simulations under linear and non-temperature-dependent media can be found in the annexes (Figs. A4.4, A4.5, and A4.6), which display the same general features as those of the simulations for nonlinear media shown in Figs. 4.10-4.12. A qualitative diagram of the conditions under which the resulting structures (i.e., thrust/fold nappes) are observed and the dominant conditions where they

were developed (brittle/ductile) are displayed in Fig. 4.13, including nonlinear and linear media simulations.

End-member geometries like those described in section 4.2 (i.e., thrust nappes and fold nappes) are obtained using the temperature gradients. However, when the temperature profile is applied, the occurrence of recumbent folds is restricted to conditions where the stress exponent is 1 (Fig. 4.10).
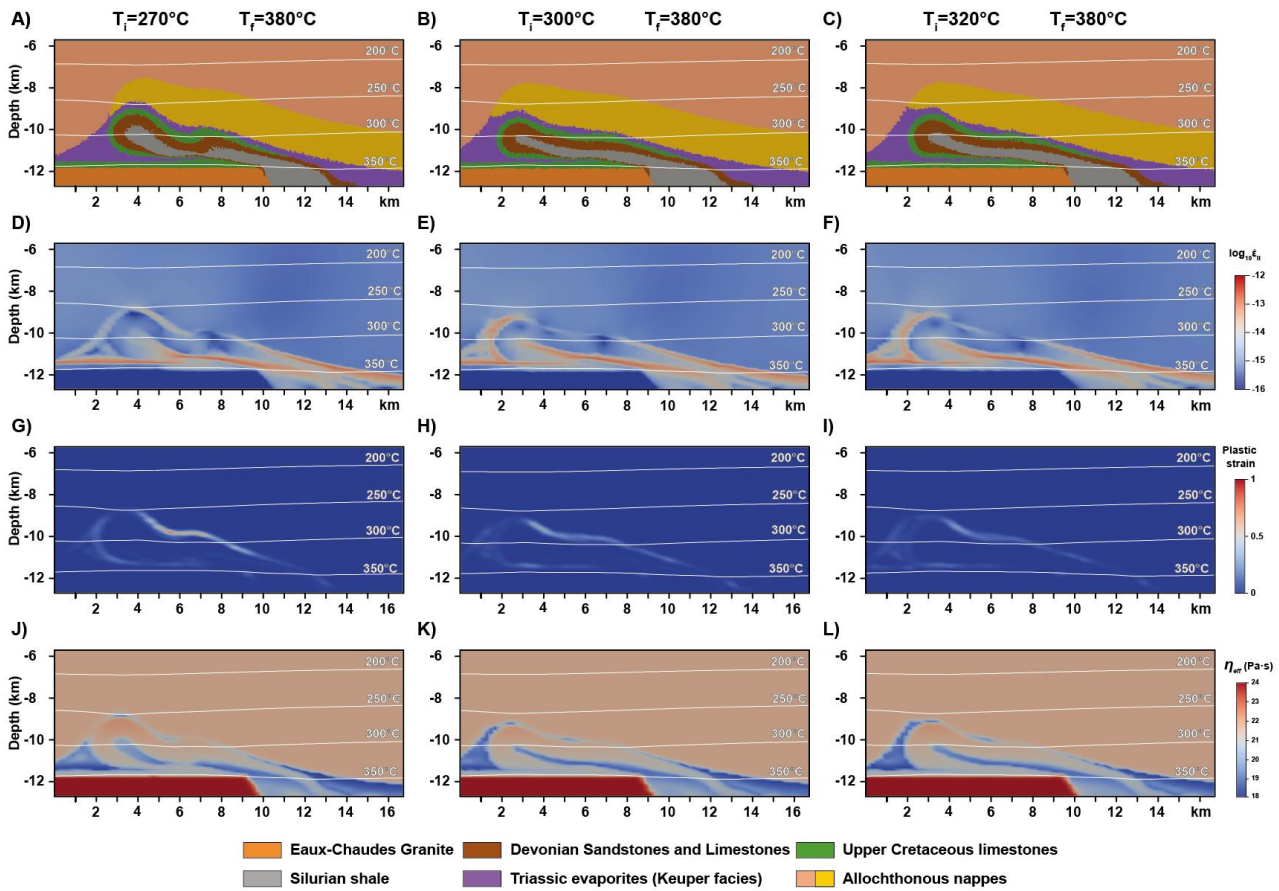
Figure 4.10: Thermo-mechanical simulation results for n = 1 (UCD panel) at different applied temperature profiles and non-linear media (dependent on temperature and strain rate), including the phase (*A*, *B* and *C*), second invariant of the strain rate tensor (*D*, *E*, and *F*), natural plastic strain (*G*, *H* and *I*) and effective viscosity (*J*, *K* and *L*) plots. Ti : initial temperature at the bottom of the model; Tf : final temperature at the bottom of the model.

For a final temperature of T=~350°C in the autochthonous Upper Cretaceous layer, the overturned limb of the UCD panel shown a flat and continuous trend, despite being extremely stretched in all cases (Fig. 4.10A-C) and exhibiting no signs of plastic strain (Fig. 4.10G-I). Although high strain rates are observed in the stretching area of the syncline hinge, the development of a discrete, continuous localization level is not observed (Fig. 4.10D-F). The autochthonous reached temperatures about 350°C too. For simulations with an initial $T \geq$ 300°C, the normal limb of the structures displayed second-order gentle folds, similar to those observed in the models using constant temperature profiles (Fig. 4.10B-C). Below 300°C, open upright folds were produced in the normal limb, just as happened in the simulations
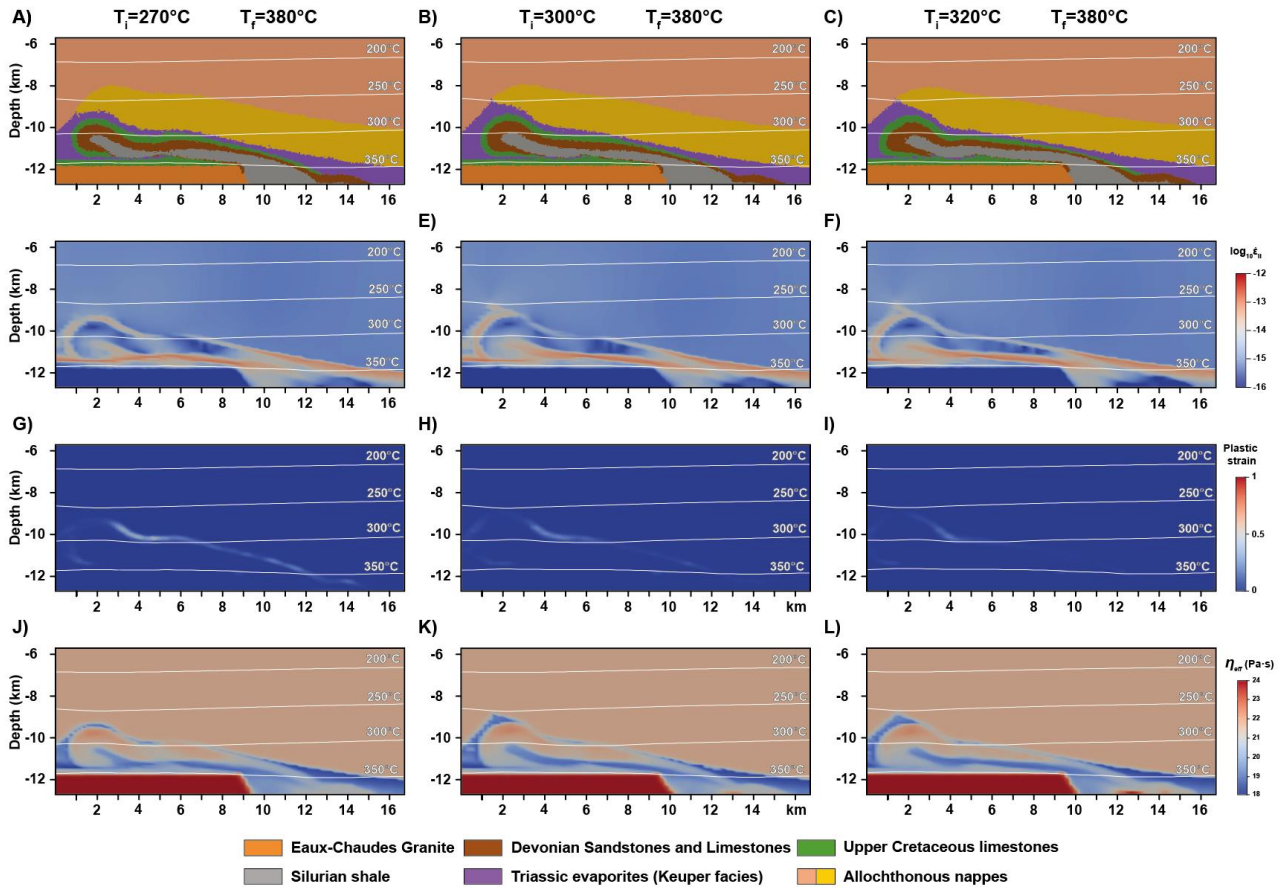
Figure 4.11*: Results from thermo-mechanical simulations with n = 2 (UCD panel) for different applied temperature profiles and non-linear media (i.e., dependent of temperature and strain rate). Final geometry of phases (**A, B** and **C**), second invariant of the strain rate tensor (**D, E,** and **F**), natural plastic strain (**G, H** and **I**) and effective viscosity (**J, K** and **L**) plots. Ti, Tf: initial and final temperature at the bottom of the model, respectively.*
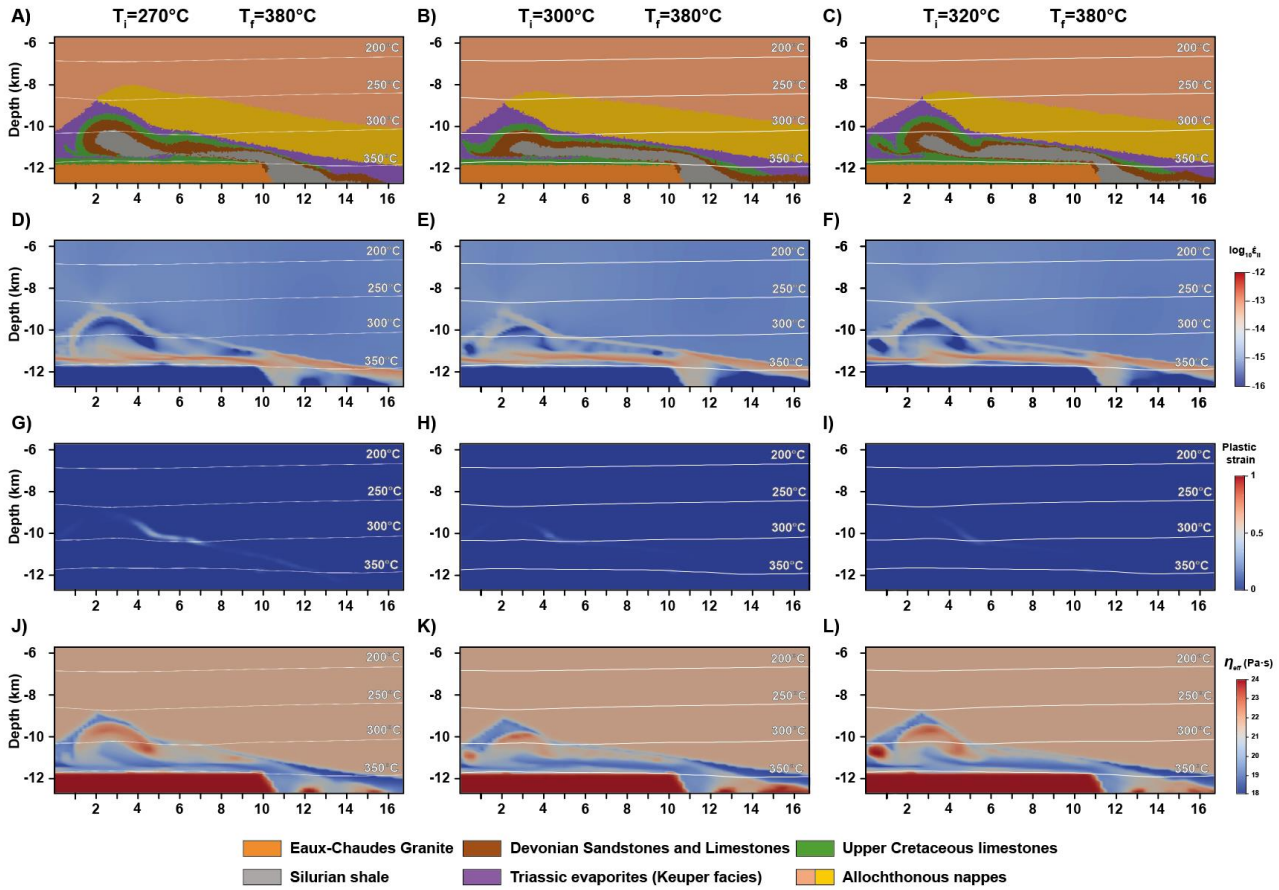
Figure 4.12*: Thermo-mechanical simulation results for n = 4.7 (UCD panel) at different applied temperature profiles and non-linear media (dependent on temperature and strain rate), including plots of the phase (**A**, **B** and **C**), second invariant of the strain rate tensor (**D**, **E**, and **F**), natural plastic strain (**G**, **H** and **I**) and effective viscosity (**J**, **K** and **L**). Ti : initial temperature at the bottom of the model; Tf : final temperature at the bottom of the model.*

using constant temperature profiles where the structures resembled geometrically thrust nappes (e.g., Fig. 4.4 and 4.10).

In any case, the temperatures reached by this structural domain (i.e., normal limb) are around ~300°C, although in the hinge of the anticline they are usually lower (e.g., Fig. 4.10A-C).

Regardless of the initial temperature gradient, the final distribution of the effective viscosity is approximately homogeneous at a given depth within the UCD panel, and is observed a vertical gradient due to the increase in temperature with depth. In addition, the viscosity contrast between the UCD panel and the surrounding weak levels is approximately 2 orders

of magnitude, slightly less at ~12 km depth due to the higher temperatures (Figs. 4.2 and 4.10J-L).

For non-linear stress exponents ($n > 1$) of the UCD panel, no recumbent folding was observed under the applied temperature profiles, even in simulations using linear and non-temperature-dependent media (e.g., Fig. 4.11, 4.12, A4.4 and A4.6). The resulting structures displayed short and truncated overturned limbs that reached 350°C with no signs of plasticity (decreasing with n), and geometrically resembling thrust nappes (cf. chapter 3; Figs. 4.11 and 4.12). Moreover, the autochthon was thinned and tectonically eroded, especially at $n > 2$ and elevated temperatures (e.g., Fig. 4.11C and 4.12C). At $n = 4.7$, the modelled Upper Cretaceous displayed secondary tight folds in the frontal part of the anticline (Fig. 4.12B and C) or small thrust slices of Upper Cretaceous (Fig. 4.12C). Moreover, the normal limb is progressively stretched with the increase of n (especially) and T (in lesser proportion) (e.g., Figs. 4.11 and 4.12).

Thin and flat high-strain-rate levels are developed through the overturned limb, over which the UCD panel is translated (e.g., Figs. 4.11D-F and 4.12D-F). These levels even affect the normal limb, which is increasingly stretched with the increase of the stress exponent, close to being beheaded (e.g., Figs. 4.11C, F and 4.12C and F). The range of temperature for the normal limb is approximately 300°C for the n, with colder areas in the anticline hinge (Figs. 4.11 and 4.12).

In contrast to simulations with $n = 1$, the effective viscosity within the UCD level for non-linear conditions is heterogeneous, not only because of the effect of the temperature but also because of the strain-rate weakening inherent to power-law flow. These heterogeneities are more pronounced with increased stress exponent, and lower effective viscosities are observed in the high-strain-rate areas (e.g., Figs. 4.12J-L vs. 4.13J-L). Moreover, as a

contraposition to the n = 1 (UCD panel) results, the viscosity contrast between the UCD panel and the surrounding weak levels is being progressively reduced with the increase of the n from ~2 orders of magnitude (n = 1) to near the same order of magnitude (~10^{19} Pa· s), especially in those areas with elevated strain rates (e.g., Figs. 4.12J-L and 4.13J-L).
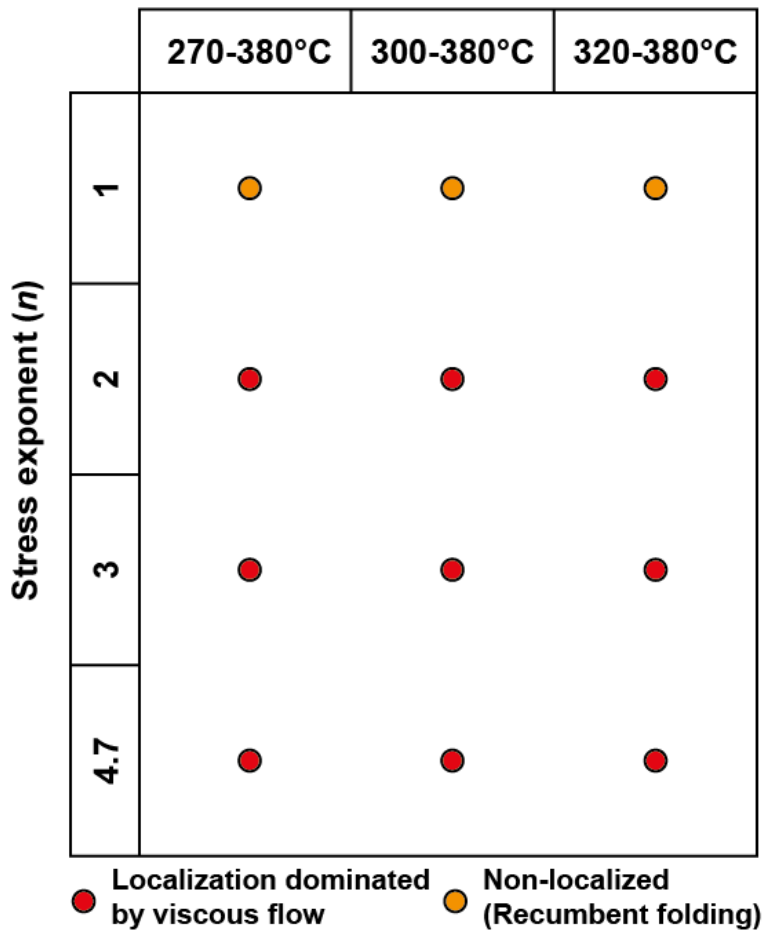
Figure 4.13: Qualitative summary diagram of the resulting structures obtained in thermo-mechanical modelling under non-linear media for different stress exponent and initial temperature gradient.

4.4. Summary and discussion of parameters and results

Thermomechanical simulations confirmed that the viscosity contrast between units is a key factor in the development of recumbent folds (c.f. Chapter 3). An increase of T and n makes the viscosity contrast between the UCD panel and the surrounding weak levels drop to near the same order of magnitude, which results on viscous flow dominated strain localization surfaces because of the absence of frictional plasticity (e.g., Figs. 4.11 and 4.12). Despite

these modelled structures are geometrically resembling thrust nappes, ductile features should be expected to be found in the field (such as shear zones and mylonites), which Caldera et al. (2023) reported in the ECM area.

The experimental power-law by Kronenberg et al. (1990) fits within the mixing power-laws for quartz-biotite aggregates from Rast and Ruh (2021), in agreement with the mineral content observed in the Silurian of the Eaux-Chaudes massif (Fig. 4.3A and B). However, the parameters of Kronenberg et al. (1990) were obtained from single-crystal, oriented biotite experiments. Although the preferent basal slip due to the crystallographic anisotropy of micas was taken into account, the law does not address the anisotropic mechanical behavior of a polycrystalline aggregate. Silurian slates show a well-developed and penetrative foliation which was probably developed in Variscan times before the onset of the Alpine orogeny (e.g., Garcia-Sansegundo et al., 2011, and references therein), defining a strong mechanical anisotropy in the rock. Therefore, we propose the use of a prefactor (*f*) in a manner similar that Spitz et al. (2020) used it to facilitate the brittle-ductile transition at depth, but in our case additionally to calibrate the viscous behavior of the Silurian phase to be in the same range of values as in the purely mechanical simulations (c.f. Chapter 3). A moderate viscosity contrast between units is required to activate detachment horizons within rocks involved in deformation (e.g., Pfiffner, 1993; Bauville and Schmalholz, 2015; Kiss et al., 2020; Spitz et al., 2020) and without a prefactor, the Silurian no longer acts as a detachment level because the viscosity contrast with surrounding units is insufficient (e.g., Fig. 4.14).

Temperature (*T*) and stress exponent (*n*) produce variation of the effective contrast between units and affect the deformation style causing the development of heterogeneities within the UCD panel that favors strain localization within it (e.g., Figs. 4.4-4.7 and 4.10-4.12).
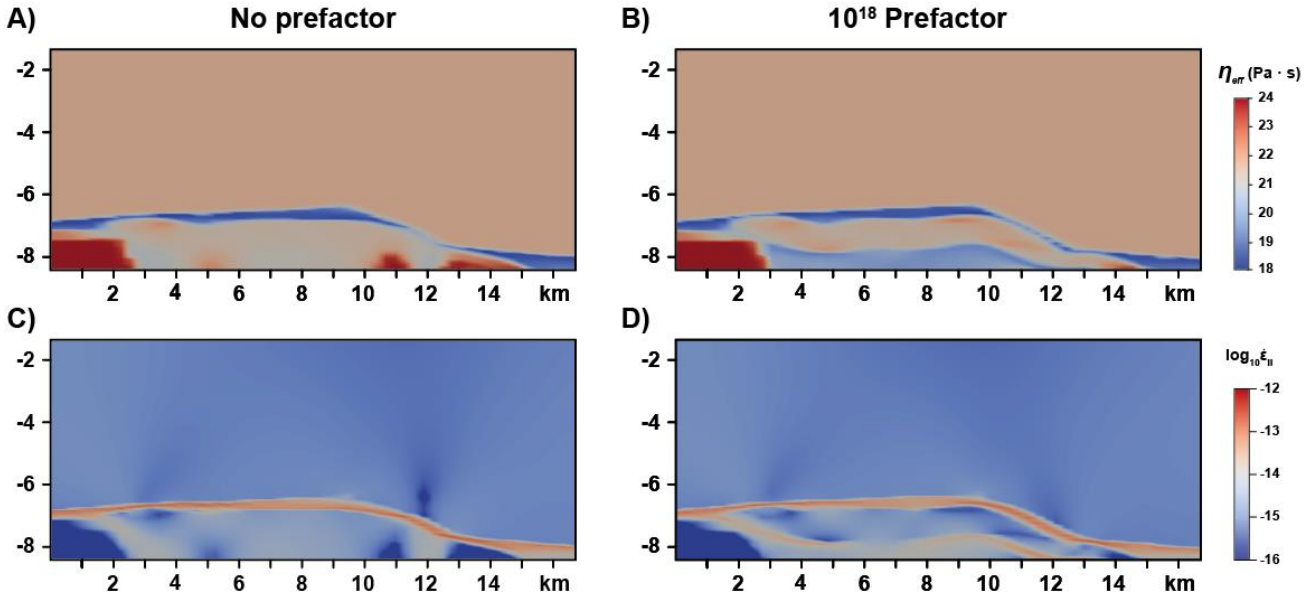
Figure 4.14*: **A and B)** η_{eff} plots from equivalent simulation examples with no prefactor (left) and adding a 10^{18} prefactor (right) from the early steps of a simulation (9.2% of bulk shortening or 3.6 Ma of simulation time). **C and D)** Equivalent plots of the second invariant of the strain rate tensor, showing the development of localization surfaces when a prefactor is used. Without a prefactor, the viscosity contrast between the U. Cretaceous and Devonian panel and the Silurian slates is insufficient such that the latter no longer acts as a detachment level.*

For model runs using a linear viscous law for the UCD panel ($n = 1$), the simulations reproduce part of the first-order geometrical features of the Eaux-Chaudes recumbent fold nappe observed in the field. These simulations tend to preserve the thickness of the recumbent limb (e.g., Fig. 4.4C), a feature that is also observed when the media (i.e., the Silurian, E-C granite, and Keuper units) is also linear and purely viscous (i.e., independent of T) (e.g., Figs. 4.4C vs. A4.1E and F).

For $n > 2$, the effective viscosity heterogeneities within the panel are more pronounced at a given temperature because the UCD level is more sensitive to the partitioning of the strain rate and a dominant viscous/ductile behavior of the panel is observable at lower temperatures (e.g., Figs. 4.6 and 4.7), which favors the development of localization levels (e.g., Figs. 4.4G and 4.5G). This effect (i.e., the appearance of effective viscosity heterogeneities) was accentuated when temperature gradients were applied to the initial set-up of models. Indeed, no recumbent fold with constant limb thickness was observed for models with $n > 1$, although

deformation was dominantly accommodated by viscous/ductile flow, but the strong ductile strain deformation produced recumbent limbs with extremely stretched limbs (Figs. 4.10 and 4.12). Moreover, the viscosity contrast is progressively reduced with the increase of n (i.e., stress weakening) which contributes to the prevalence of the viscous/ductile behaviour of the UCD panel and increases its internal heterogeneous behaviour .

In all cases, the isotherms crosscut the structure, showing a relationship that could induce an interpretation of the heating as post-tectonic, but in the case of the simulations was synchronous with deformation. This result is basically related with the thermal properties used for the different units and the low rate of amplification of the structure that it was unable to produce heat advection (i.e., the heat diffusion is faster than mechanical structural growth).

In general, the range of initial temperatures used in the simulations where a temperature gradient was applied does not significantly affect the development of a recumbent fold nappe, although only for $n = 1$ a structure conserving the continuity of the recumbent limb was observed. For models with initial low temperatures ($T < 300°C$), upright gentle folds are amplified in the normal limb of the modeled structures (Fig. 4.10). At $T > 300°C$, the normal limb of the structure is shown with large wavelength upright folds, which resemble the Eaux-Chaudes recumbent fold nappe described by Caldera et al. (2023), which may point to slightly hot conditions to initiate recumbent folding.

4.5. Main conclusions on thermomechanical modelling

The viscosity contrast between units is a key factor in the development of recumbent folds, without which the deformation tends to be accommodated more homogeneously between units with similar viscosities. A handicap in LAMEM and the experimental and mixing power laws is that they do not consider the effect of internal mechanical anisotropies of the rocks in the range of effective viscosities. Because anisotropy is common in natural systems,

especially in those involved in multiple orogenic processes, the effective viscosity under applied strain rates could be over- or underestimated depending on the case (i.e., in general underestimating the effective viscosity in a direction normal to the anisotropy, while it tends to be overestimated in directions parallel to anisotropy).

Recumbent folding in layered successions such as the natural case of the Eaux-Chaudes massif is particularly favored when strong sedimentary rock (here represented by the Upper Cretaceous-Devonian panel) tends to behave rheologically linearly (i.e., $n = 1$). The combined effect of temperature (T) and stress exponent (n) induces stress weakening between units causing variation of the effective viscosity contrast and development of heterogeneities. These heterogeneities could trigger the development of localized levels in the brittle/plastic regime at low n and T or in the viscous/ductile regime at high n and T. In such cases recumbent folding will be hampered, favoring the localization under dominantly viscous flow (i.e., ductile shear zones) or under dominantly plastic/brittle flow (i.e., thrusting).

Chapter 5: Sequential timing of the Eaux-Chaudes massif from the structure and U-Pb geochronology of calcite veins

During the construction of fold and thrust belts, secondary porosity develops within rocks involved in the deformation generating pathways for fluid circulation and precipitation (e.g., Travé et al., 1997; Nemcok et al., 2005; Cosgrove, 2015; Crognier et al., 2018; Cruset, 2019). At the outcrop scale, the most visible and common evidence of this interaction are the network of veins, which can provide valuable information to depict the history of the fluid flow evolution in terms of composition and origin (e.g., Roure et al., 2005; Cruset et al., 2023), but also can serve as potential tracers of the paleostress field evolution acting as relative chronology markers (e.g., Bons et al., 2012; Ring and Gerdes, 2016; Cruset, 2019). Two of the most common minerals precipitated from fluids within veins are calcite and dolomite, which are susceptible to dating by U-Pb geochronology, which is utilized in a wide range of applications (e.g., Hopley et al., 2019; Nicholson et al., 2020; Holdsworth et al., 2019, 2020; Kreissl et al., 2018; Drake et al., 2017; Incerpi et al., 2020; Methner et al., 2016; Coogan et al., 2016; Lawson et al., 2018; Drost et al., 2018). Whether the veins can be linked to deformational episodes, absolute ages could in principle be given, providing a high value to the study of the structures and/or the events linked to vein precipitation (e.g., Roberts and Walker, 2016; Ring and Gerdes, 2016; Goodfellow et al., 2017; Hansman et al., 2018; Parrish et al., 2018; Beaudoin et al., 2018; Nuriel et al., 2017, 2019; Smeraglia et al., 2019).

The Eaux-Chaudes Massif experienced a complex deformation history, first documented by Ternet (1965) and more recently revisited and reinterpreted by Caldera (2022) and Caldera et al. (2023), who applied concepts arisen from the tectonic exploration of rifted margins and novel instrumental techniques (e.g., Raman Spectroscopy in Carbonaceous Material and Electron Backscatter Diffraction). His work unraveled a km-scale, recumbent folding, and

ductile deformation at maximum temperatures of ~350 ± 25°C within the Upper Cretaceous platform carbonates of the massif. The onset of the inversion of the hyperextended rift basin in the area was documented by Teixell et al. (2016) and Labaume and Teixell (2020) in the Mid-Santonian times (ca. 84Myr), recorded by the deepening of the platform (late Cretaceous flysch sedimentation) and the southward displacement of the salt-detached Chaînons Béarnais fold-and-thrust belt (CBB) on the Lakora thrust.

With the onset of the inversion, layer-parallel shortening and nappe stacking occurred, deforming the Upper Cretaceous sediments within a thick shear zone between the weak detachment layers of the Silurian and the allochthonous Keuper (cf. Chapter 3 and 4; Fig. 5.1). The age of the eastern termination of the Eaux-Chaudes basement thrust was first documented in the Néouvielle basement massif by Wayne and McCaig (1998) using Rb-Sr method on mylonite veins and later by Jolivet et al. (2007) using $^{40}Ar/^{39}Ar$ in K-feldspar in the same area. Both studies obtained an age of thrusting in the Early Eocene (48 ± 2 Ma and 50 Ma, respectively). In mid Eocene-Oligocene times, the entire system was uplifted and partially exhumed on top of the active Gavarnie basement thrust (cf. Chapter 6; Bosch et al., 2016).

Associated with the inversion of the Iberian rifted margin and the posterior exhumation, pre/sin- and post-deformational polymineral calcite-dolomite-quartz veins precipitated in the ECM within secondary porosity. The aim of this chapter is to decipher the nature and time sequence of the fracture network and vein precipitation in the ECM and its relationship with the deformation of the Upper Cretaceous carbonates from the macro- (map scale) to micro-scale (thin section scale).
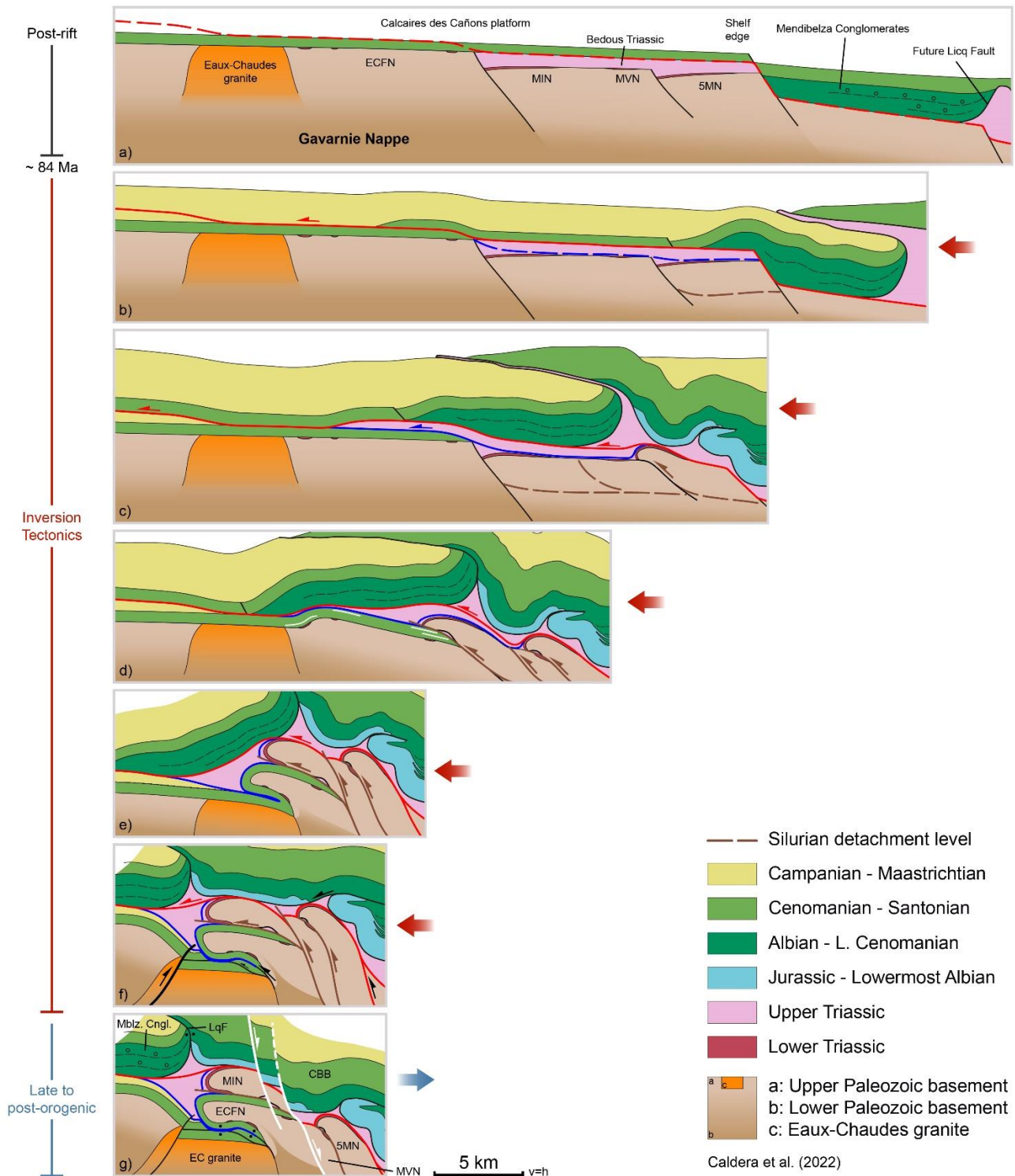
Figure 5.1: *Sequential evolution of the ECM taken from Caldera et al. (2023) comprising from the late post-rift times to the post-orogenic stage. The blue line corresponds to the branch of the Lakora thrust that carries the allochthonous Keuper sheet (horse) on the ECFN. The dashed lines show the locations of the future faults in the following steps: ECFN: Eaux-Chaudes Fold Nappe; MIN: Montagnon d'Iseye Nappe; 5MN: 5 Monts Nappe; MVN: Montagne Verte Nappe; CBB: Chaînons Béarnais Belt; Mblz. Cngl: Mendibelza Conglomerates.*

5.1 Strain domains of the Eaux-Chaudes massif from EBSD analysis

The Upper Cretaceous carbonates of the ECM are heterogeneously deformed depending on their position within the regional structure and on the rheological properties of the rocks. Caldera (2022) defined four main domains of deformation (Fig. 5.2) based on microstructural EBSD analysis:

1. Deformed autochthon domain (DA)

2. Overturned limb domain (OL)

3. Weakly deformed autochthon domain (WDA)

4. Normal limb domain (NL)
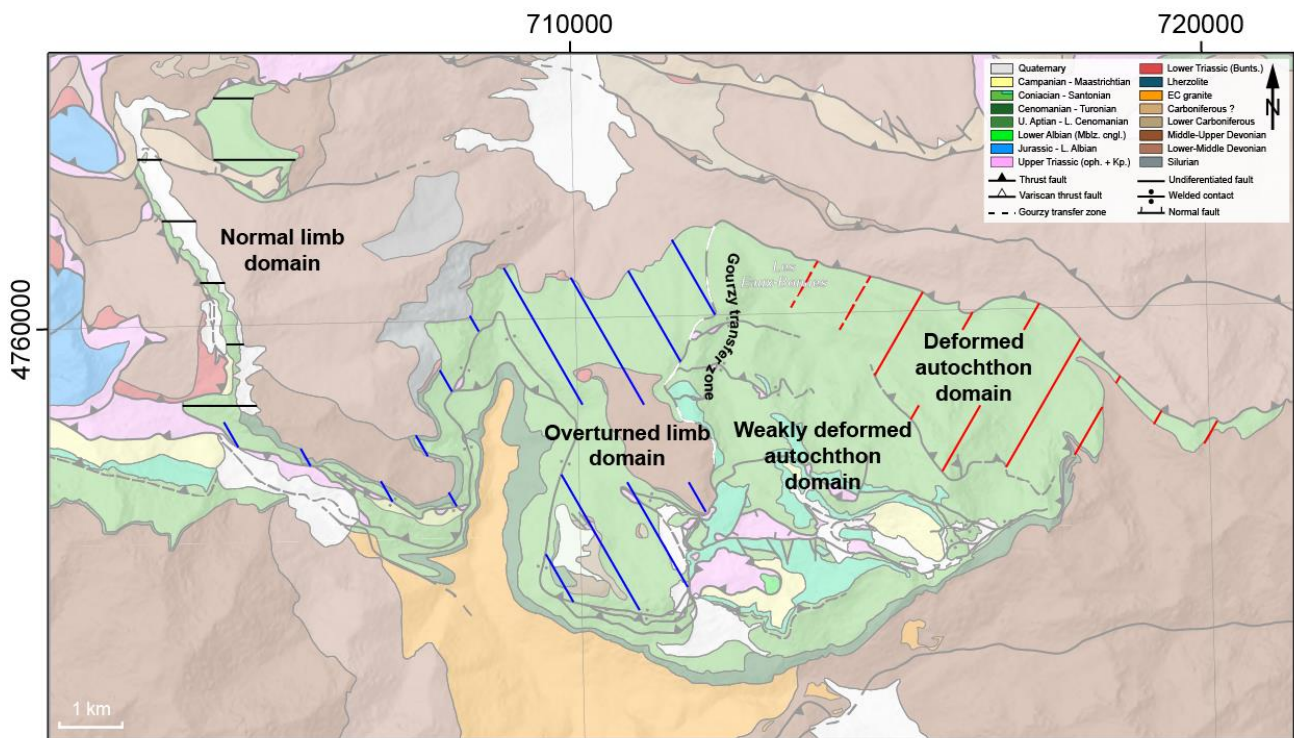
Figure 5.2: *Strain domains proposed by Caldera (2022) for the ECM, which do not coincide exactly with the macroscale structure boundaries.*

Summarizing from Caldera (2022), strong deformation was observed in the eastern autochthon and overturned limb domains (DA and OL; 1 and 2). These are characterized by strong ductile deformation and dynamic recrystallization, erasing any sedimentary or fossil

feature within the Upper Cretaceous carbonates. Well-developed schistosity (often qualified as mylonitic foliation) parallel to stratification (S_{0-1}), S-C fabrics, mineral orientation (stretching lineation), and asymmetric porphyroclasts in sedimentary quartz and dolomite-rich aggregates are observable structures in these domains, showing evidence of top-to-the-south shear (Fig. 5.3A and B). On the other hand, both the weakly deformed autochthon and the normal limb domains (WDA and NL; 3 and 4) are observed unstrained or low deformed in a brittle-ductile regime (small-scale faults and pressure-solution features), and most of the fossil remains and sedimentary structures are well preserved (Fig. 5.3C and D).
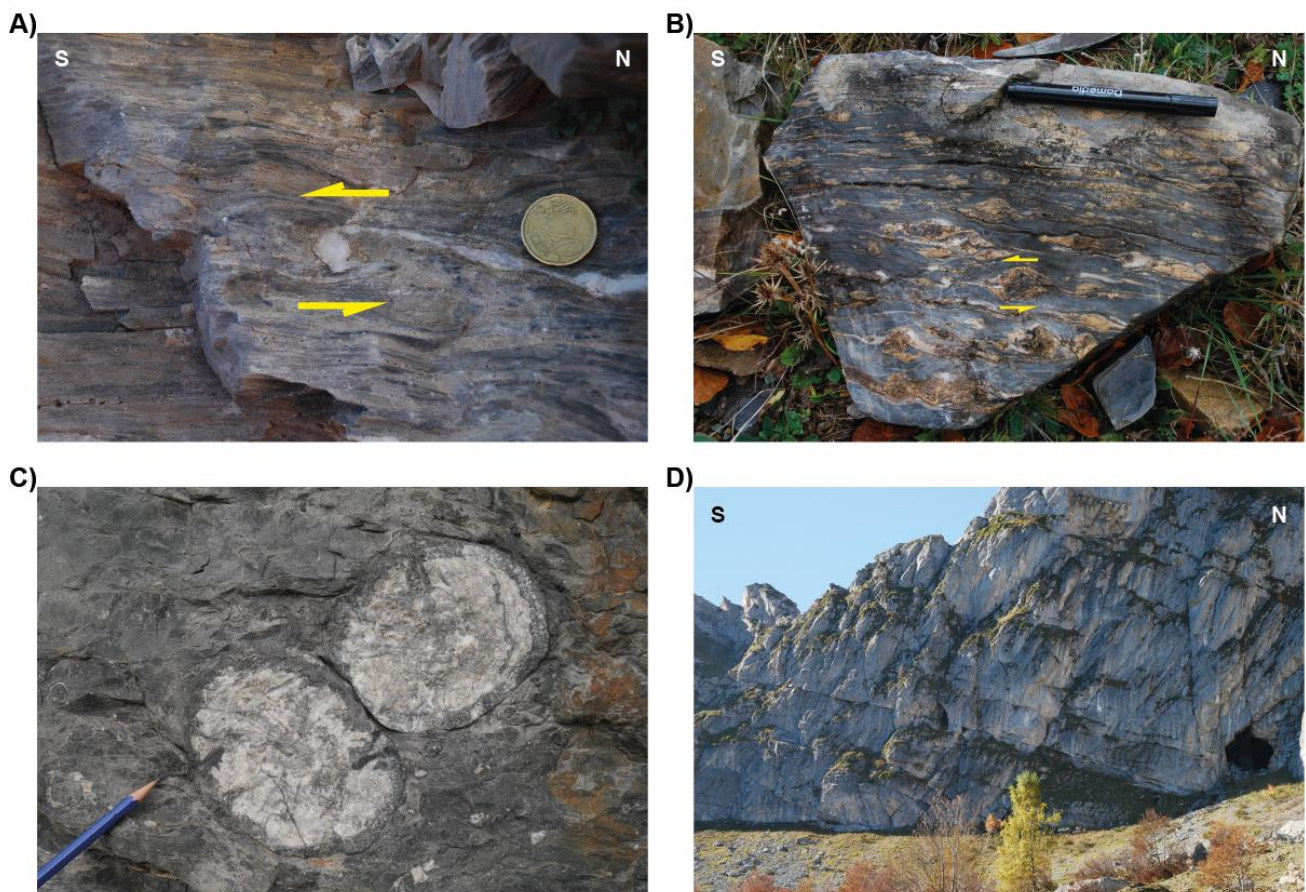
Figure 5.3: *Examples of heterogeneous strain regimes from each strain domain. **A)** δ-shaped calcite vein from the deformed autochthon domain showing a top-to-the-south sense of shear. **B)** Asymmetrical folded dolomite from the overturned limb in the Cambeihl area indicating top-to-the-south sense of shear. **C)** Undeformed fossils (rudists) from the weakly deformed autochthon domain near Goust village. **D)** Late brittle fractures developed in the normal limb domain.*

In addition, the boundary between the western weakly deformed autochthon domain and the eastern deformed domain (overturned limb) is accommodated by the so-called Gourzy transfer zone, which at the same time marks the transition between the recumbent fold nappe and the Eaux-Bonnes thrust, and coincides with the sharp end of the EC granite in the autochthon domain (Fig. 5.2; Caldera, 2022).

5.2. Vein network of the Eaux-Chaudes massif

Multiple veins are observed within the different lithostratigraphic units of the Upper Cretaceous carbonates, which constitute the host rocks. The individual veins have thicknesses in the 0.1-20 cm range and lateral extents up to a few meters. Geometrically, three main vein families can be identified for which a relative timing can be established: 1) veins parallel to the S_{0-1} foliation (namely PFV veins), and two cross-cutting conjugate sets of steeped veins, oriented 2) NW-SE to WNW-ESE and 3) NE-SW to NNE-SSW, orthogonal to S_{0-1} (namely OFV veins). To track their occurrence at the scale of the massif, a total number of 671 veins were measured at 19 sites (see location in Fig. 5.4) within the strain domains above defined.

5.2.1. Field data

The orientation of the poles to the bedding and foliation is displayed in Fig. 5.5, together with stretching lineation and fold-axis data, grouped according to the four domains.

The average dip of the bedding planes is to the north, with moderate to gentle dip angles for the DA, OL, and WDA domains (Fig. 5.5). However, deviations are common, particularly in the OL and WDA domains, where vertical or WSW dips are observed. On the other hand, the normal limb shows a clear dip trend to the W with moderate dips (Fig. 5.5). The foliation and
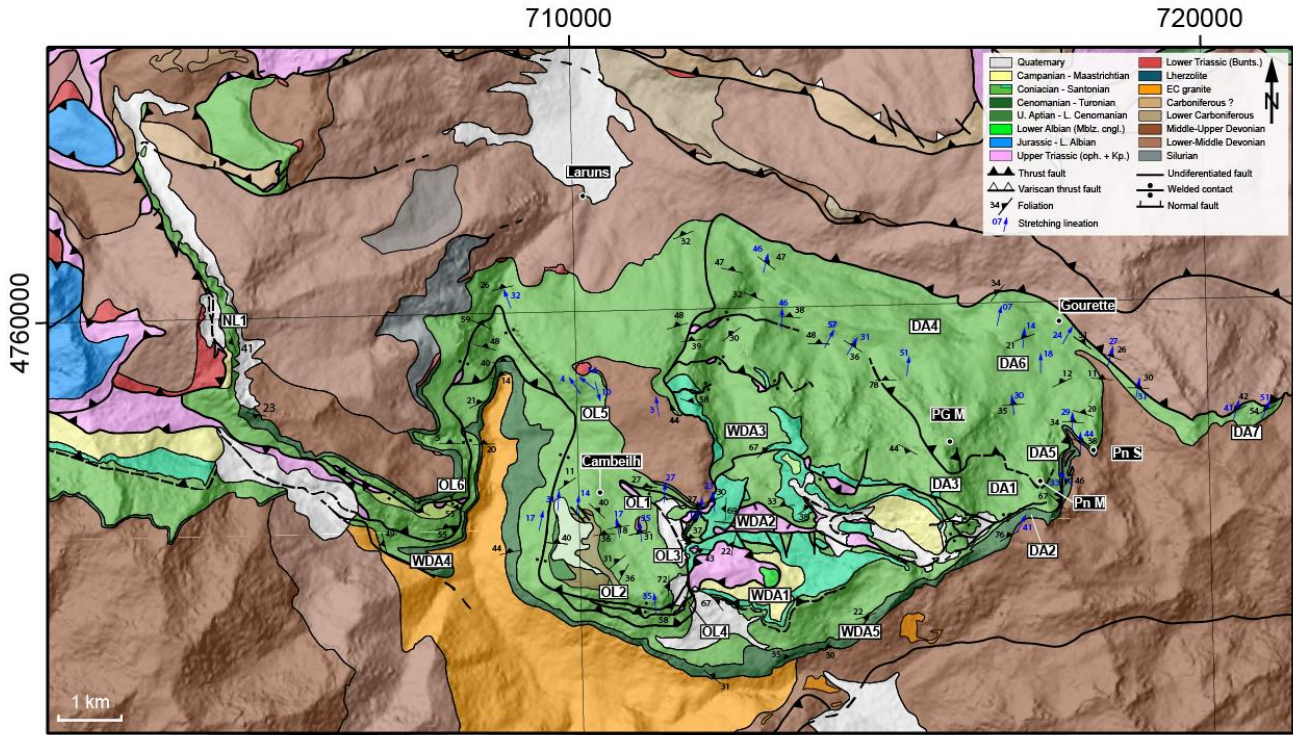
Figure 5.4: *Geological map of the ECM showing a representative selection of foliation and stretching lineation data and the location of the calcite veins measurements and sampling sites. PG M: Pic de Ger Massif; Pn M: Pêne Médaa; Pn S: Pêne Sarrière. The structural data displayed in this map corresponds to the published dataset by Caldera (2023).*

S_{0-1} show a similar pattern to the bedding, except for the NL domain, which has no foliation developed because of its low deformation (e.g., Caldera, 2022). The foliation and S_{0-1} in the overturned limb show a concentrated northward dip (mean 352/30) (Fig. 5.5).

Stretching lineation was only observed in the high-strain deformed domains. In the DA domain it strongly points to the north, with very gentle-to-moderate plunges (mean 010/37). However, anomalous values showing vertical plunges and/or some northwest trends were observed in this area (Fig. 5.5). On the other hand, the stretching lineation in the OL is less dispersed and north-oriented (mean 354/23) (Fig. 5.5).

Finally, small scale isoclinal fold hinges and boudin necks affecting the PFV veins (e.g., Figs. 5.7B and C) or the host rock were identified and measured in the DA domain (Fig. 5.5),
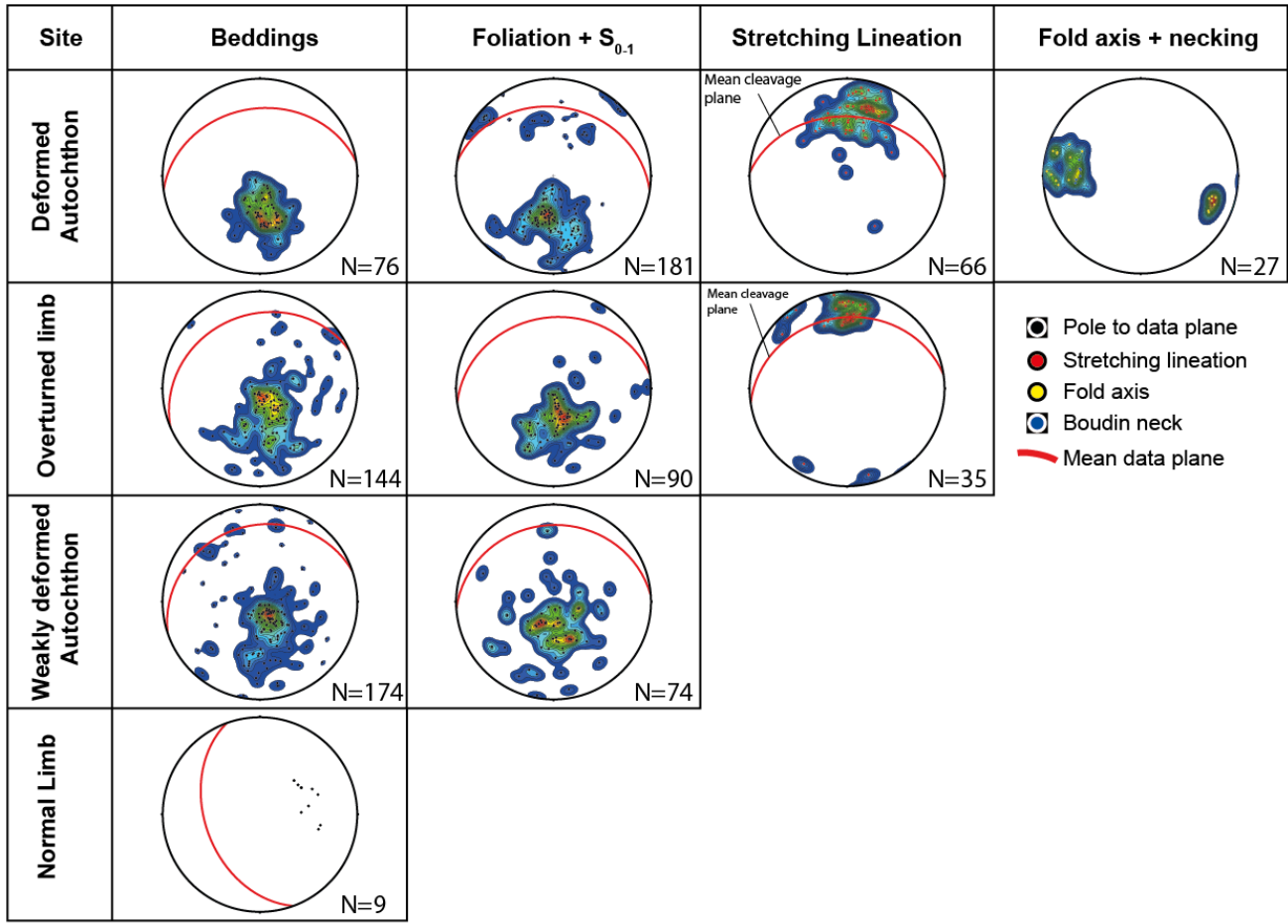
Figure 5.5: *Results of structural data measured in the ECM (Schmidt lower hemisphere, equal area stereoplots). Contoured density diagrams are calculated at 1% of area on lines (stretching and fold axis/boudin necks) or poles (bedding and foliation + S$_{0-1}$) with N ≥ 25. The mean data plane is calculated from the pole of the mean Fisher vector of the data at 95% level of confidence. Data contours represents the percent of data per 1% area.*

showing a clear west-east orientation of these structural elements (mean 269/43), which is compatible with the foliation and stretching lineation observed in the domain (Fig. 5.5), and their asymmetry indicates top-to-the-south shear (e.g., Fig. 5.7C).

5.2.2. Calcite vein orientation data.

The orientation of the calcite veins in the ECM is shown in Fig. 5.6 according to the four deformation domains. The two main types of calcite veins described above can be clearly distinguished from structural data. The early set of veins parallel or at low angle (<30°) to the foliation are common in the high strain domains (i.e., OL and DA) but also present in the

weakly deformed autochthon (foliation-parallel veins in Figs. 5.6 and 5.7). On the other hand, the conjugate sets of calcite veins striking NE-SW to NNE-SSW and NW-SE to WNW-ESE, which cut at a high angle the main foliation (>30°) exist in all strain domains (foliation-orthogonal veins in Figs. 5.6 and 5.7).
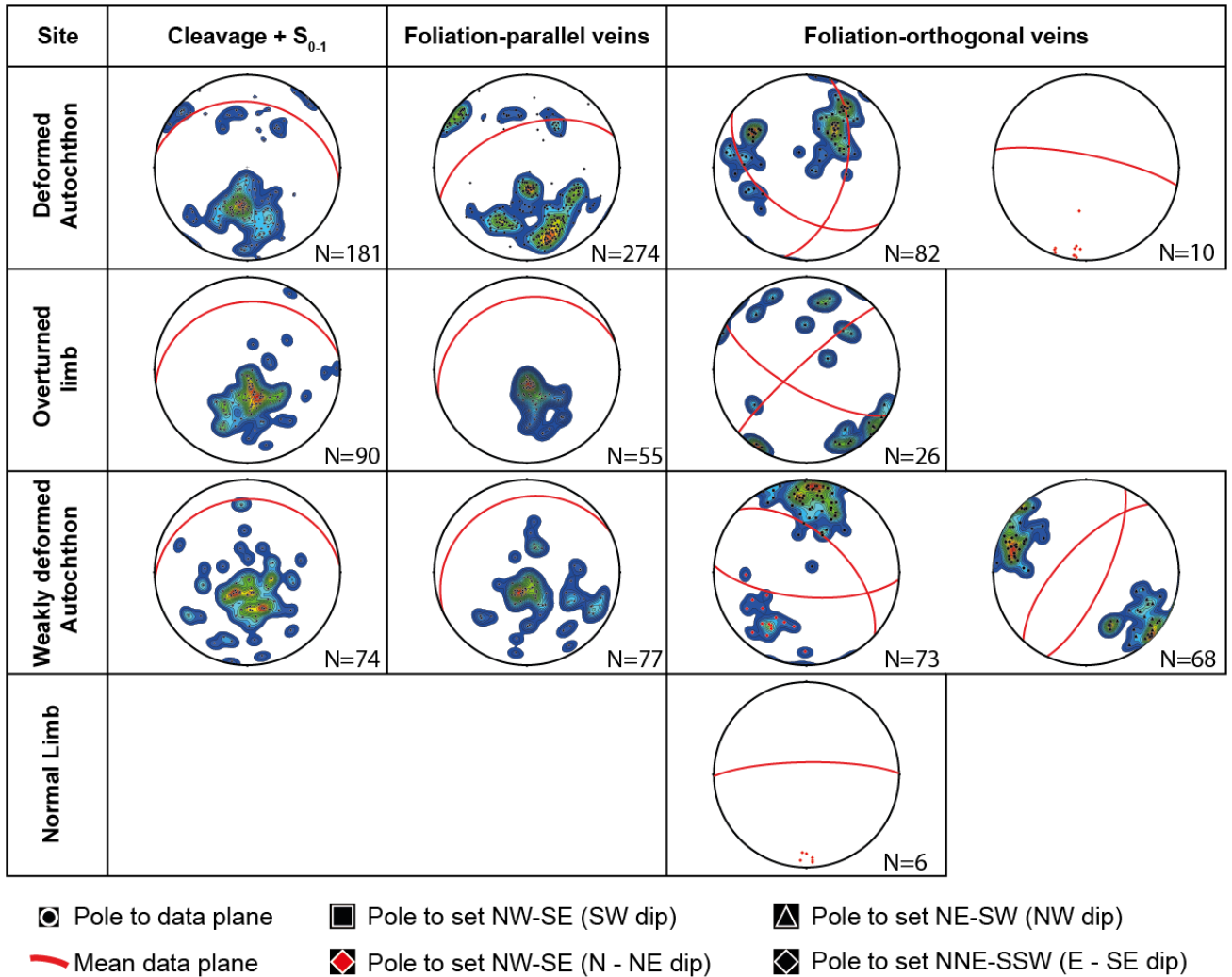
Figure 5.6: *Results of the calcite vein orientation data measured in the ECM (Schmidt lower hemisphere, equal area stereoplots) displaying the poles to each vein set. The foliation parallel veins encompass those veins parallel or at low angle to the foliation of the outcrop (<30°), whether the orthogonal veins are those that cross-cuts at high angle (>30°) the foliation of the outcrop where it was measured. The data is also grouped in each EBSD strain domain proposed by Caldera (2022). Contoured density diagrams are calculated at 1% of area on data poles (vein bedding and foliation + S$_{0-1}$) with N ≥ 25. The mean data plane is calculated from the pole of the mean Fisher vector of the data at 95% level of confidence. Data contours represents the percent of data per 1% area.*
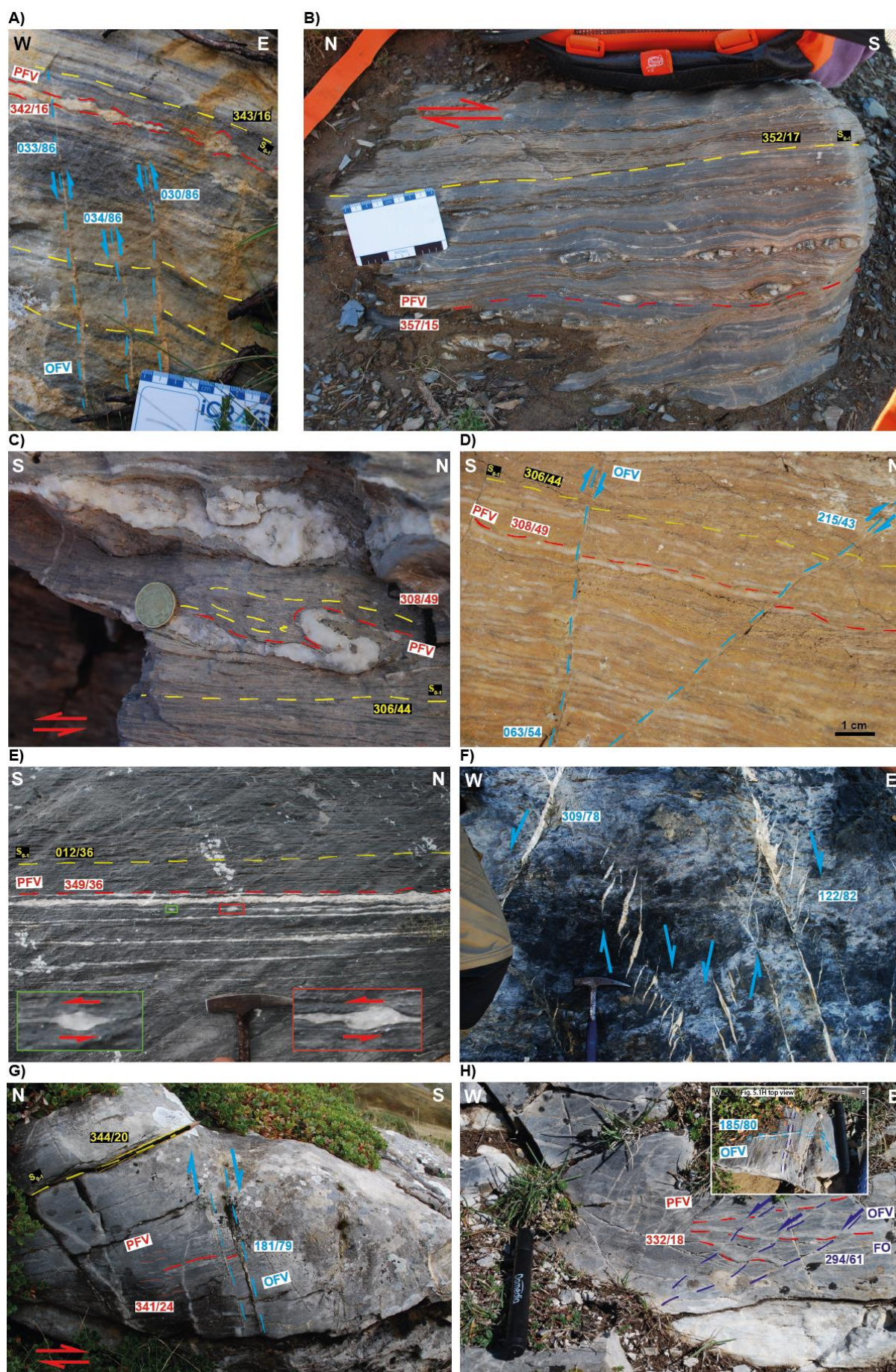
Figure 5.7: *Examples of calcite veins parallel and orthogonal to the foliation. **A) and B)** Boudinaged calcite veins (PFV) belonging to the overturned limb, parallel to the N dipping foliation (S$_{0-1}$), cross-cut and displaced by straight fractures filled with calcite (blue). A belongs to the locality OL5 and B to OL1 **C)** Intramylonitic folds affecting the foliation (S$_{0-1}$) and the calcite veins showing top-to-the-south sense of shear in the deformed autochthon domain (locality DA5). **D)** Dense stack of S$_{0-1}$-parallel calcite veins cross-cut by thin shear fractures filled with calcite in the deformed autochthon domain (locality DA1). **E)** Boudinaged calcite veins parallel to the foliation in the Gourette area (deformed autochthon domain) with asymmetry indicating top-to-the-south shear (locality DA6). **F)** En-échelon calcite veins from the weakly deformed autochthon indicating vertical displacement (i.e., normal-sense) in the unconformity between the metasedimentary Paleozoic and the Upper Cretaceous (locality WDA5). **G) and H)** OFV calcite veins cross-cutting relationships with respect to the PFV but also between the WNW-ESE to NW-SE and the NE-SW sets (dark and light blue in inset, Figure H; locality WDA1).*

Most of the calcite veins present in the DA domain are parallel to the main foliation (Fig.5.6). A slight obliquity between the mean foliation (352/30) and mean calcite vein planes (340/52) is observed. The orthogonal conjugate veins are clearly defined, and a scarce subvertical vein set trending near to E-W (mean dip 011/78) is also observed.

Similar features were observed in the OL domain. A set of veins parallel to the main foliation is common in this domain, less dispersed than in any other domain of the ECM (Fig. 5.6). In contrast to the DA the mean plane of the foliation (352/30) and calcite veins (343/23) are nearly parallel (Fig. 5.6).

The OL also has two conjugate sets of veins at a high angle to the main foliation. The first identified set is striking NW-SE (mean 210/71) and compatible in orientation to the set NW-SE set of the DA domain. A second high-angle set with a NE-SW strike (mean 317/84) was also observed and measured in the OL (Fig. 5.6).

Veins parallel to the foliation are also present in the WDA domain with a comparable mean dip (335/21) to the DA and OL domains. In this domain, in contrast to the other ones, two sets of conjugate veins at high angle to the foliation (Fig. 5.6) are identified. The first set has a common WNW-ESE to NW-SE strike and steep dips of the two subsets. It could be correlated with the NW-SE veins observed in the DA and OL domains. On the other hand, a second set

of conjugate veins with NE-SW strike and high dip angles (mean 313/68 and 115/73, respectively) can be identified in this domain (Fig. 5.6).

Finally, the NL domain only a set of vertical calcite veins with a W-E strike (mean 359/79) was observed, and comparable to a similar set observed in the DA (Fig. 5.6). The scarce data prevents us from doing a quantitative analysis in this domain. It is worth noting that this
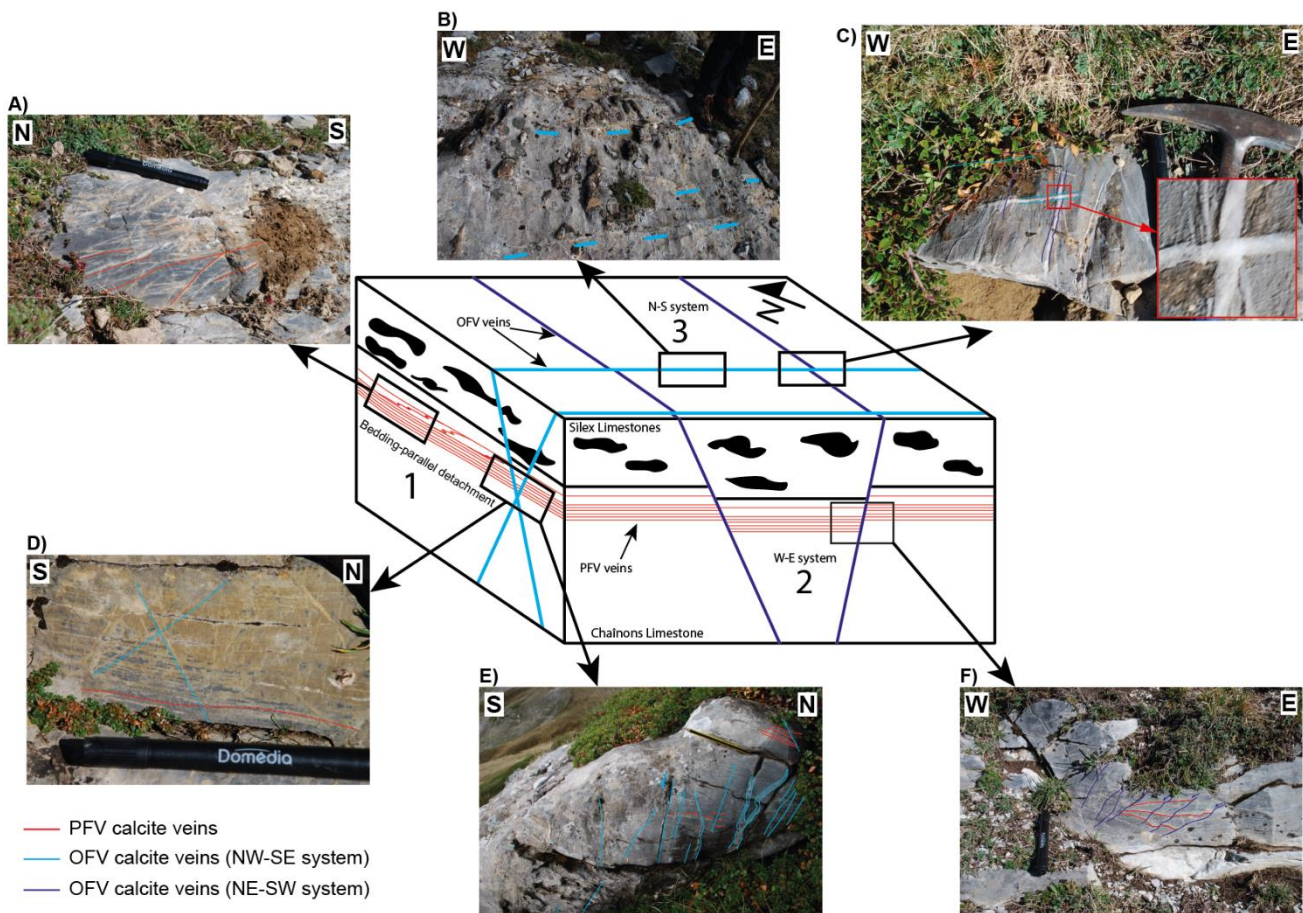
Figure 5.8: Interpretative three-dimensional sketch using vein data from the WDA1 site (Fig. 5.4), where cross-cutting relationships between the bedding, foliation, S$_{0-1}$ and calcite veins allow us to unravel the relative chronology of the fracture/vein network events. A) PFV calcite veins near a bedding-parallel detachment at the top of the Santonian carbonates parallel or at a low angle (folded) to the S$_{0-1}$. B) Top view of the NW-SE to WNW-ESE dipping OFV vein set (blue) within the Santonian silex limestone, cutting the silex nodules. C) Top view of the NW-SE to WNW-ESE dipping OFV vein sets showing that the NE-SW vein set system formed first. D) Dense network of the NE-SW OFV vein sets (blue) cross cutting the PFV (red) in the bedding-parallel detachment at the top of the Santonian carbonates. E) PFV veins displaced by the OFV NE-SW vein sets. F) NE-SW OFV veins cross-cutting and displacing (normal sense) the top Santonian PFV calcite vein set.

orientation is parallel to a set of map scale W-E normal faults that are characteristic of the normal limb of the Eaux-Chaudes fold nappe (e.g., Caldera, 2022).

5.2.3. Relative chronology of veins from field observations

The studied outcrops in the ECM domains allowed us to constrain the relative chronology of the vein sets described above. The summarized relationships between the vein sets observed at the WDA1 site (see location in Fig. 5.4) are shown in Fig. 5.8. In fact, the calcite veins parallel to the bedding, foliation, or S_{0-1} (where developed) (PFV) are always cut by either set that has a high angle relationship between these elements and the calcite vein (OFV), regardless of the strain domain (Fig. 5.7A, D, G and H). Across the study area, the PFV veins are occasionally affected by small displacements along the OFV veins, but these are not always consistent, despite most of them displays normal component (e.g., Fig. 5.7A, D, G, and H).

A particular feature of WDA1 site is that it constitutes the only outcrop where a relative chronology between the different OFV sets can be deduced. In this site, both the NW-SE and NE-SW vein sets can be observed (Figs. 5.6 and 5.8). The sequence of events can be inferred from the outcrop in Fig. 5.8C, where the calcite vein belonging to the NW-SE system (outlined in light blue) postdates the NE-SW system (outlined in dark blue).

Therefore, the NW-SE to WNW-ESE calcite vein system is superimposed on the NE-SW veins, all cutting the PFV vein network, thus establishing the relative chronology of fracture network events. Out of outcrop WDA1, all the cross-cutting relationship examples concerned only one of the OFV sets (either NW-SE or NE-SW) and the PFV vein set.

Other sites where the OFV are observed to post-date PFV are the DA1 and DA5 (see Fig. 5.4 for location). In the DA1 (Figs. 5.7D and 5.9A) oblique NW-SE veins cut a dense pack of PFV veins that I interpret as defining a shear zone (see discussion below). In both DA1 and
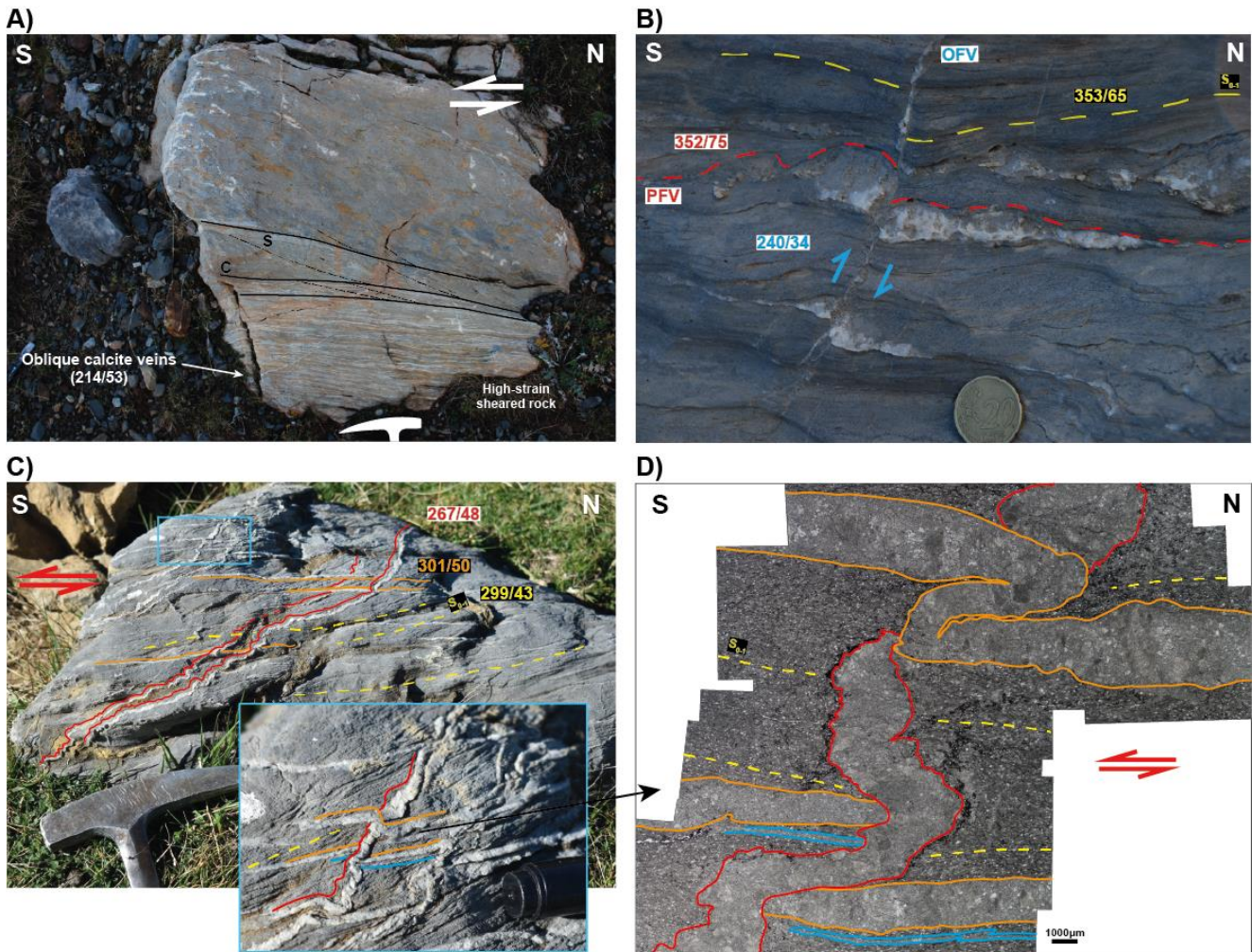
Figure 5.9: A) *High strain sheared rock from the DA1 site, characterized by a progressive shear increase and multiple PFV calcite veins. Oblique calcite veins post-dates those PFV veins.* ***B)*** *PFV and OFV veins from the DA5 site showing the WNW-ESE system post-dating the PFV and the S_{0-1}.* ***C)*** *and* ***D)*** *Straight calcite veins (orange dashed line) oblique to the foliation and parallel to the axial planes of the folds developed in the PFV calcite vein (red dashed line) in the WDA2 site near the Gourzy transfer zone. The folded PFV vein is compatible with senestral sense of shear and cross-cuts and is cross-cut at the same time by the straight veins, indicating the syn-tectonic nature of all of them.*

DA5 (Fig. 5.9D), the NW-SE vein system is represented by thin and straight calcite veins which may show a slight offset (Fig. 5.7D and 5.9B).

In the OL, the superimposition of the OFV on the PFV can also be appreciated (e.g., Fig. 5.7A). In this case, the north-dipping PFV veins of the OL1 site (location in Fig. 5.4) were interrupted by thin and straight reverse fractures filled with calcite from the vertical NW-SE set (Fig. 5.7A).

The rapid transition between the western large-scale ductile recumbent fold to eastern ductile fold-and-thrust fan led Caldera (2022) to propose that this transition was accommodated through the N-S Gourzy transfer fault. The WDA2 site is located eastward of the Gourzy transfer zone (see location in Fig. 5.4), and was also affected by fracturing and calcite vein filling (Fig. 5.9C). Two types of calcite veins can be found here, dipping to the west at low-to-high angles with respect to the main foliation (Fig. 5.9C). The first veins (orange dashed in Fig. 5.9C and D) are nearly parallel to S_{0-1} and are boudined, which is a common feature of veins observed at other sites (e.g. WDA1; DA1; Figs. 5.7, 5.8 and 5.9A). The second veins (red dashed line in Fig. 5.9C) are shown folded at high angle with respect to the main foliation of the outcrop, which is nearly parallel to the axial planes of the vein folds. Although it may reasonably appear that the parallel veins (orange dashed in Fig. 5.9C) occurred after the folded veins, the cross-cutting relationship between both sets is more complex, by which the veins parallel to the S_{0-1} are cut and at the same time cross-cut the veins at high angle to the S_{0-1} (Fig. 5.9D). This, together with the orientation and the observed deformation features, suggests that these veins belong to the progressive evolution of the Gourzy transfer zone in a sinistral sense of shear.

5.2.4. Structure, microstructure, and petrology of the calcite veins

Samples of calcite veins belonging to deformed and non-deformed limestone domain were analyzed using optical (110 samples) and cathodoluminescence (28 samples) petrography (Fig. 5.10). In addition, samples 18NC16, 18NC20, and 19NC37 of the normal limb domain, and 19NC13 and 19NC14 of the WDA domain from Caldera (2022) were included in this study.

Apart from the veins parallel to S_{0-1} (PFV) and the orthogonal steeped veins (OFV), calcite veins associated with pressure shadows of rigid clasts, with boudinage necking and en-
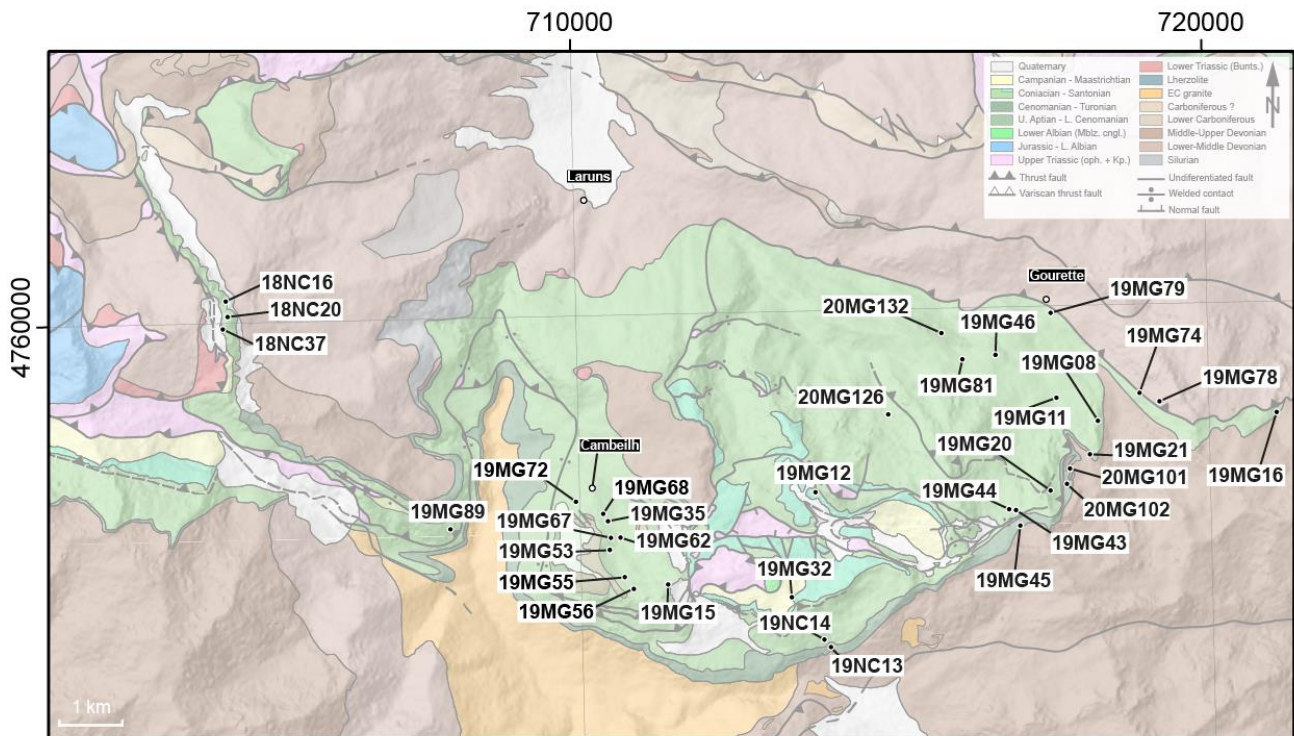
Figure 5.10: *Location of the vein samples analyzed by cathodoluminiscence.*

échelon vein arrays were also observed (e.g., Fig. 5.7, 5.8, 5.9, and 5.11). Most veins are composed by blocky or stretched-blocky calcite crystals (e.g., Fig.5.11 A-C), although fibrous calcite could also be observed usually associated with extensional fractures in competent layers related to boudinage necking (e.g. 5.11C) or OFV veins (e.g., Fig. 5.11D). Additionally, veins are also observed in pressure shadows of rigid clasts related to sedimentary quartz grains or coarse pyrite from the host rock (e.g., Fig. 5.11E and F), or in the vein walls of thick veins mainly composed by blocky or stretched-blocky calcite (e.g., Fig. 5.14C). Dolomite and quartz (both sometimes euhedral) are associated minerals that are always present, regardless of whether they are PFV or OFV (e.g., Fig. 5.11G and H).
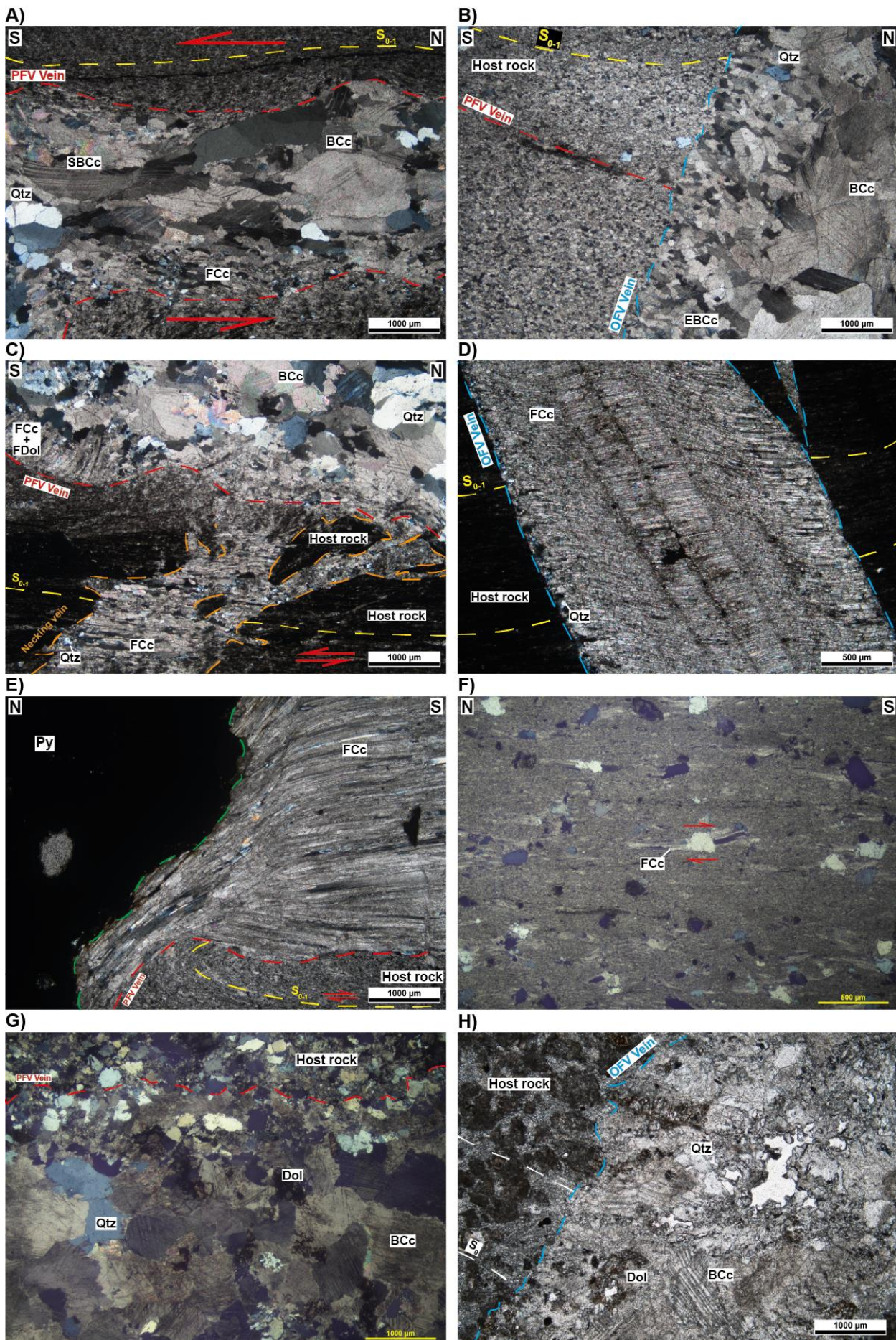
Figure 5.11: *Petrographic microscope images from representative examples of the different calcite veins outcropping in the deformed autochthon domain.* *A)* *Crossed polarized light image (XPL) of blocky and stretched blocky calcite grains and anhedral brittle quartz from a PFV boudinaged calcite vein of sample 19MG20 (DA5 site). The calcite crystals are twinned and sometimes with brittle fractures, and the grain boundaries are sutured. The tilted fibrous calcite from the lower vein wall (FCc) indicates top-to-the-south shear sense.* *B)* *XPL image of from the DA3 site showing the NW-SE to WNW-ESE trend OFV system post-dating the PFV and the S_{0-1}. The PFV vein is shown recrystallized and almost vein walls are erased at thin section scale. The OFV vein is composed of coarse blocky calcite grains in the center of the vein and smaller grains of slightly elongated-blocky calcite and euhedral quartz near the vein wall.* *C)* *XPL image of PFV calcite vein associated with boudinage necking (orange) from sample 19MG20 (DA5). Fibrous calcite parallel to the S_{0-1} indicates the sense of opening of the vein. The thick PFV vein (shown in A) also has fibrous calcite and dolomite in the vein wall, perpendicular to it.* *D)* *XPL image of an antitaxial OFV vein composed by fibrous calcite and quartz parallel to S_{0-1} from a Campanian flysch sample (sample 19MG32; WDA1 site).* *E)* *XPL image of strain fringes in pyrite crystals from the basal Cenomanian limestone outcropping in the base of the Pêne Sarriere (sample 19MG21; DA6 site) indicating top-to-the-south sense of shear.* *F)* *XPL image of quartz rigid clast of the Cenomanian sheared carbonate from Cambeilh (OL1 site) with fibrous calcite in the strain shadows that indicates top-to-the-south sense of shear (sample 19MG68).* *G)* *Plain polarized light image (PPL) of blocky calcite, dolomite and anhedral quartz from a vein in sample 19MG35 from the OL1 site.* *H)* *PPL image of an OFV calcite vein composed of blocky calcite, dolomite, and quartz in a dolomite-rich host rock from the WDA1 site. BCc: blocky calcite; SBCc: stretched blocky calcite; EBCc: elongated-blocky; FCc: fibrous calcite; Dol: dolomite; FDol: fibrous dolomite; Qtz: quartz; Py: Pyrite.*

Deformed autochthon

At outcrop scale, most of the PFV veins are organized in discontinuous lenticular to tabular and continuous bodies that are in the thickness range of 0.1-20 cm (e.g., Fig. 5.7C and E; 5.9B; 5.12A; 5.14A). These veins are ductile (i.e., folded or boudined) or brittle-ductile deformed, sometimes showing geometries resembling pull-apart veins. Occasionally they contain top-to-the-south sense-of-shear indicators (e.g., Fig. 5.7C and E, 5.12A and 5.14A). Pyrite grains with associated strain shadows where calcite precipitated are also characteristic of this DA domain and indicate the same southward sense of shear (Fig. 5.11E and 5.16A). In addition, we can recognize PFV veins organized in a densely packed stack of S_{0-1}-parallel calcite veins related to intense shear in the Upper Cretaceous carbonates (e.g., Fig. 5.9A).
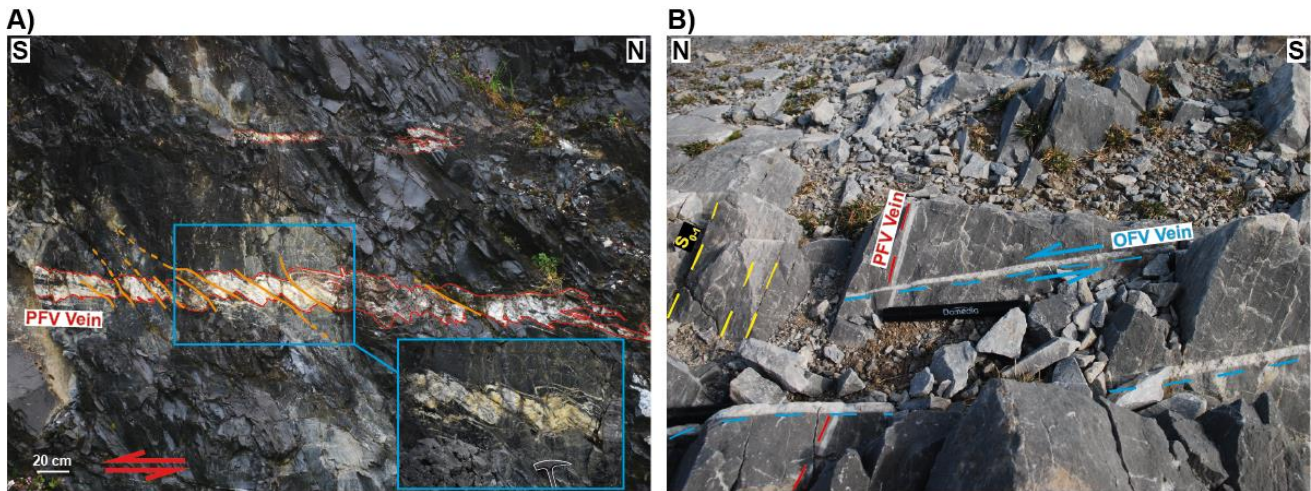
***Figure 5.12:** **A)** Folded and brittle imbricated thick calcite vein from the DA4 site. **B)** PFV calcite vein slightly displaced by an OFV vein in the DA3 site in the Pic de Ger massif. A thin section of this cross-cutting relationship is presented in Fig. 5.11B.*

On the other hand, OFV veins are also present in the domain, which are straight and thin, mostly on the mm-scale, but can also be found at the cm-scale (e.g., Fig. 5.7D; 5.9B and 5.12B).

A densely packed calcite vein level 1-5 m thick is located in the base of the Upper Cretaceous (Cenomanian), a few meters above the Upper Cretaceous-Paleozoic unconformity, just to the west of the Pene Médaa (DA1 site; see Fig. 5.4 for location). Internally it is composed of a ~ 1–5 mm thick host rock-calcite vein sequence. Under transmitted light the PFV veins that form it are almost indistinguishable from the micritic host rock and are mainly composed of fine-grained calcite and small quartz grains in a minor proportion (Fig. 5.13E and F); relicts of coarse twinned calcite grains can sometimes be observed (e.g., Fig. 5.13E and F). Under the CL, the host-rock and PFV veins are shown with a fairly homogenized dull-yellow color (Fig. 5.13B and D).

The OFV veins (NW-SE) in this sector are mainly composed of coarse blocky calcite grains with multiple twins and sutured grain boundaries (Fig. 5.13E and F).

118
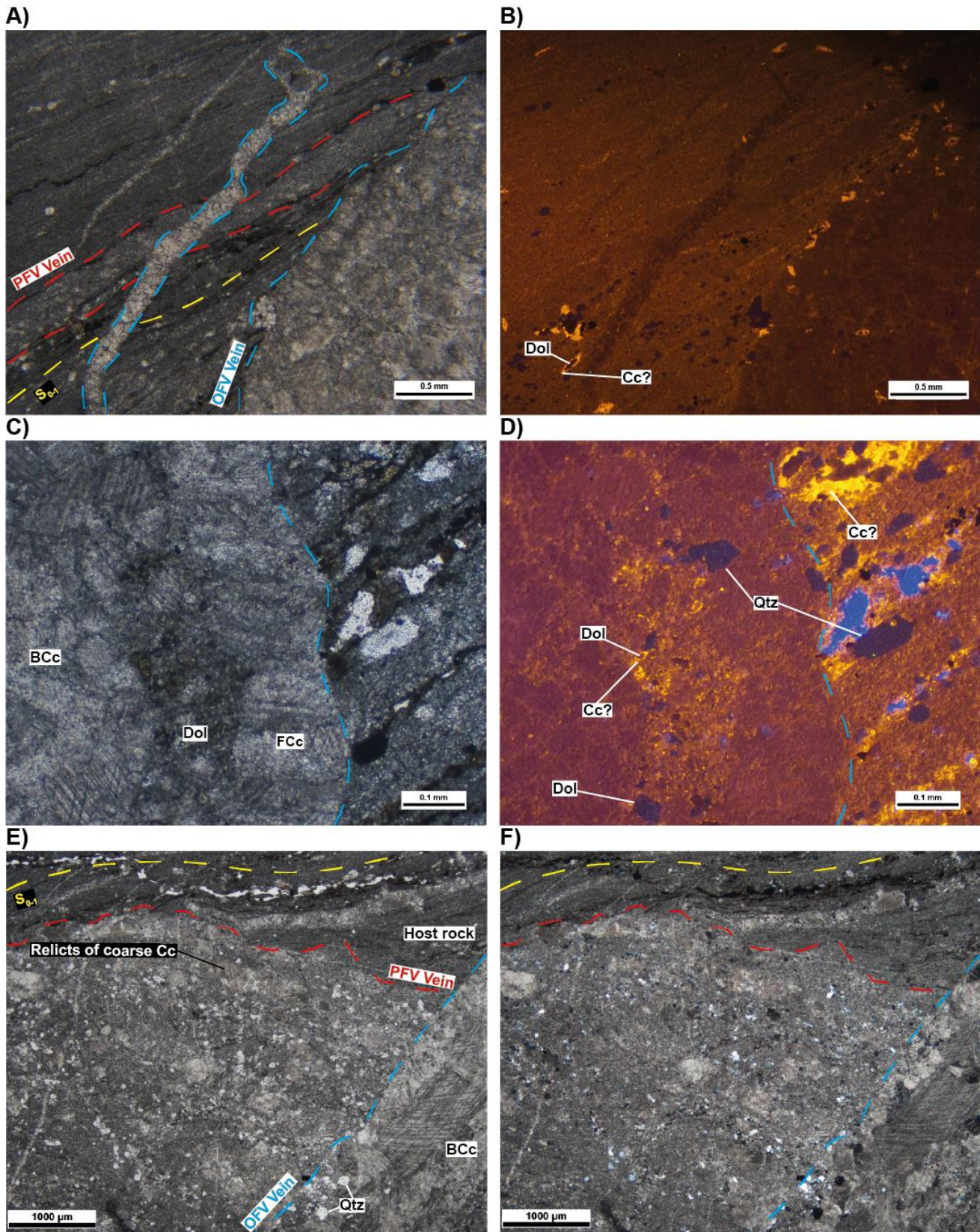
Figure 5.13: A-D) *Transmitted (left) and cathodoluminiscence (right) light images from the densely packed PFV calcite veins associated with shear zones and from the OFV veins from the DA1 site (sample 19MG43). The dolomite from the host rock and the PFV and OFV veins has a second cement with bright yellow rims. It is*

*probably composed of calcite because it has its typical CL color and sometimes it is fully replacing the dolomite. The quartz from the vein and the matrix is euhedral, precipitated in the host rock and vein porosity. **E** and **F)** PPL (left) and XPL images of the PFV and OFV calcite veins. Relicts of blocky calcite are observed in the PFV vein. The calcite from the OFV vein has undulose extinction, twins, and sutured grain boundaries. BCc: blocky calcite; FCc: fibrous calcite; Dol: dolomite; Qtz: quartz.*

Under CL, the calcite grains from these veins exhibited dark yellow/brownish colors (Fig. 13B and D). Dolomite is an accessory mineral of the veins with a dark brown to non-luminescent color signal under the CL. Most of the dolomite crystals have a bright yellow rim, which could be replacing calcite (which can occasionally fully replace the dolomite) (Fig. 5.13B and D). Finally, the disperse euhedral to anhedral quartz is also observed as an accessory mineral in the OFV veins with a dark blue CL signal (Fig. 5.13D).

Boudinaged PFV calcite veins are observed at the base of the Pêne Médaa (DA5 site; Fig 5.4 for location), structurally just above the densely packed calcite vein level, which could represent the Cenomanian detachment level reported regionally by Caldera (2022). Most of these boudinaged veins are between 0.1 and 5 cm thick, although thicker ones can also be observed (e.g., Fig. 5.14A). They are typically folded following the top-to-the-south intrafoliation folds developed within the host rock (e.g., Fig.5.7C and 5.3A). Indeed, in some cases the veins acted as rigid bodies during the ductile deformation, displaying asymmetrical features serving as sense-of-shear indicators (e.g., Fig. 5.3A and 5.7C). Nevertheless, low-angle obliquities between the boudinaged vein and S_{0-1} can be locally observed (Fig. 5.14A).

The veins from this DA domain are principally composed by coarse blocky and stretched blocky calcite grains, although fibrous calcite is observed perpendicular to the walls of the thicker veins (e.g., Fig. 5.11A and C). The latter is shown at high angles to the vein wall in the boudins and at a lower angle in the boudin necks, indicating top-to-the-south shear (e.g., sinistral in the thin section in Fig. 5.11A). The blocky and stretched blocky calcite grains show undulose extinction, sutured grain boundaries, sings of dynamic recrystallization (GBM), and
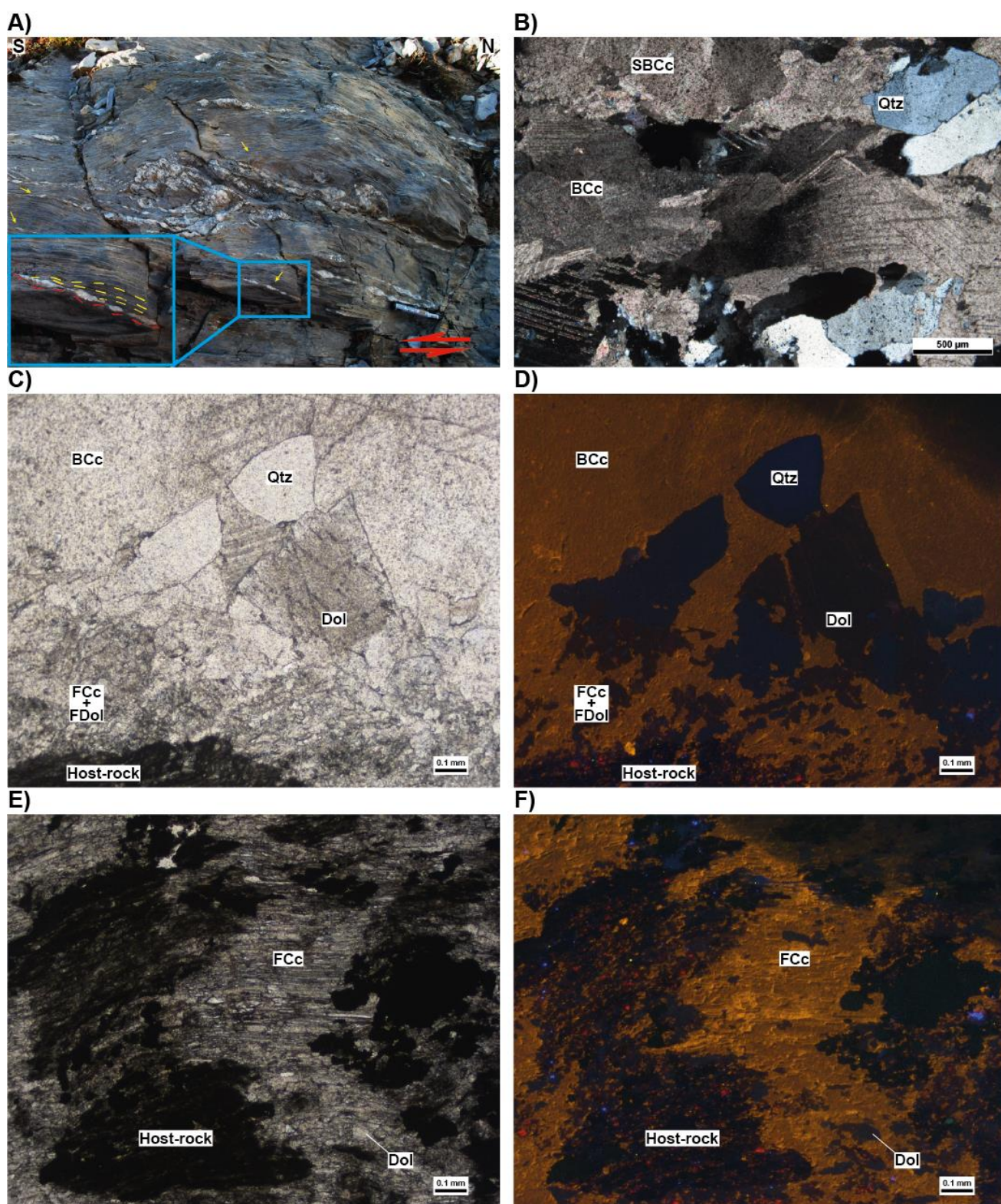
Figure 5.14: A) *Field image of the boudinaged calcite veins in the DA5 site indicating top-to-the-south sense of shear (red arrows). The veins are usually folded following the intrafolial folds of the host rock (e.g., Fig. 5.7C). Most veins acted as rigid bodies developing complex sigma/delta porhyroclast structures. Yellow arrows indicate*

most of them show type III-IV twins in the sense of Burkhard (1993) and Ferrill et al. (2004) indicating elevated temperatures during the deformation (e.g., Fig. 5.11A, C, and Fig. 5.14B). In both cases, the calcite grains gave homogenized dull to dark yellow colors under CL (Fig.5.14C and D).

Coarse dolomite and quartz showing brittle features are present in the veins in a larger proportion than in other samples of the ECM (e.g., Fig. 5.14C and D). Dolomite sometimes shows straight crystalline grain boundaries in the center of the vein (sometimes with euhedral shapes) and a fibrous texture perpendicular to the vein wall. As observed with calcite, fibrous dolomite crystals are present in the walls of thicker veins (e.g., Fig. 5.14D). Regardless of the texture or the position of the crystal, the dolomite of the veins always yields dark brown colors under the CL (Fig. 5.14D and F). An interesting point to mention is that the dolomite crystals from the host rock have a rim that gives the same CL color as the dolomite from the vein. However, the cores of these dolomites from the host rock have bright magenta colors under the CL, evidencing multiphase growth, as also reported by Caldera (2022).

Fibrous calcite infilling small extensional boudin necking fractures is also observed in the thin sections from this domain but not at the outcrop scale (e.g., Fig. 5.11C and 5.14E). Calcite fibres are parallel to S_{0-1}, indicating that the fractures opened parallel to it (e.g., Fig. 5.11C). Calcite belonging to these veins has bright to slightly yellow CL colors (Fig. 5.14F). Dolomite
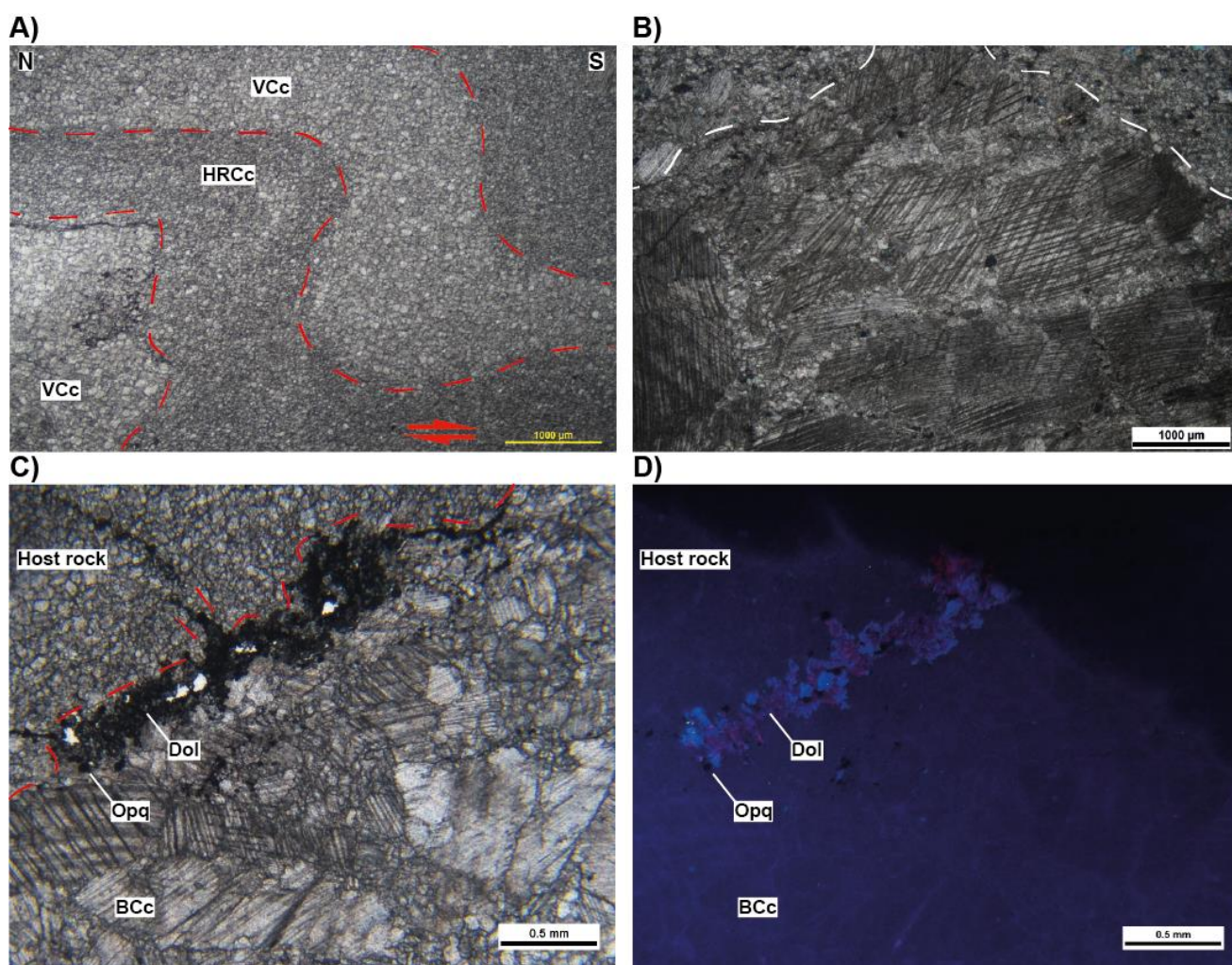
Figure 5.15: *A) PPL image of the PFV veins from sample 19MG46 (DA6 site). The veins and the host rock share similar grainsize, making them almost undistinguishable. B) Very coarse calcite grain (>0.5 cm) from sample 19MG81, with undulose extinction, twins and brittle fractures. Note the fine grains of calcite recrystallized between the fractures that compartmented calcite grain. White dashed line indicates the coarse grain boundary, located within a calcite vein. C) and D) PPL (left) and cathodoluminiscence (right) images of sample 19MG46 from the DA6 site. Dolomite (magenta in CL) and opaque minerals precipitated in the vein wall. VCc: calcite from the vein; HRCc: calcite from the host-rock; BCc: blocky calcite; Dol: Dolomite; Opq: opaque minerals.*

and quartz are present in these veins in a minor proportion compared to the former, giving dark brown and dark blue CL colors, respectively (Fig. 5.11C and 5.14F). Also, dolomite and quartz are present in these veins in a minor proportion than the former, giving dark brown and dark blue CL colors, respectively (Fig. 5.11C and 5.14F).

At the outcrop scale, the PFV veins from the DA6 site (Fig. 5.4) are not different from those from the DA5 site, showing also top-to-the-south sense of shear (e.g., Fig 5.7E and Fig.5.12A). However, at the thin section scale and under the CL, they are completely different (e.g., Fig. 5.15). Veins from DA6 are composed by dynamically recrystallized calcite with a grain size similar to that of calcite host rock in most of the samples (e.g., Fig. 5.15A). The contact between the vein and host rock is not always evident, and sometimes it can be identified by the presence of opaque minerals or by dolomite with a dull to dark magenta CL response (e.g., Fig. 5.15A and D). However, we can observe relicts of coarse calcite crystals (>0.5 cm) which show type III-IV calcite twins, undulose extinction and also signs of recrystallization (GBM) and brittle deformation (e.g., Fig. 5.15B and C). Under CL, the calcite from the samples from this area is shown to be non-luminescent or have bright blue luminescence (e.g., Fig. 5.15C and D).

Finally, asymmetric and displacement-controlled strain fringes beside pyrite crystals from the base of the Pêne Sarrière (sample 19MG21 at the DA6 site; Fig. 5.4) are excellent kinematic indicators, evidencing again the top-to-the-south sense of simple shear as well as a component of pure shear (Fig. 5.16A). In the external domain of the fringes, the calcite is folded and appears to draw an S_2 crenulation (Fig. 5.16A). Small shear bands with antithetic shear-sense (equivalent to P' fractures) are also developed in the external part of the fringe, also detected with EBSD by Caldera (2022) (Fig. 5.16A and B). The foliation affecting the host rock is shown folded close to the strain fringe, and is cut by the pyrite and the calcite fibers from the fringes (Fig. 5.16A and D). Several authors have proposed methods to constrain incremental strain from the shape and orientation variation of crystal fibers (e.g., Ramsay and Huber, 1983 ; Müller et al., 2000; Koehn et al., 2001; Aerden and Sayab, 2017). However, these methods assume low strain and rigid rotation of fringes, a condition that is

A)

B)

C)

D)

E)
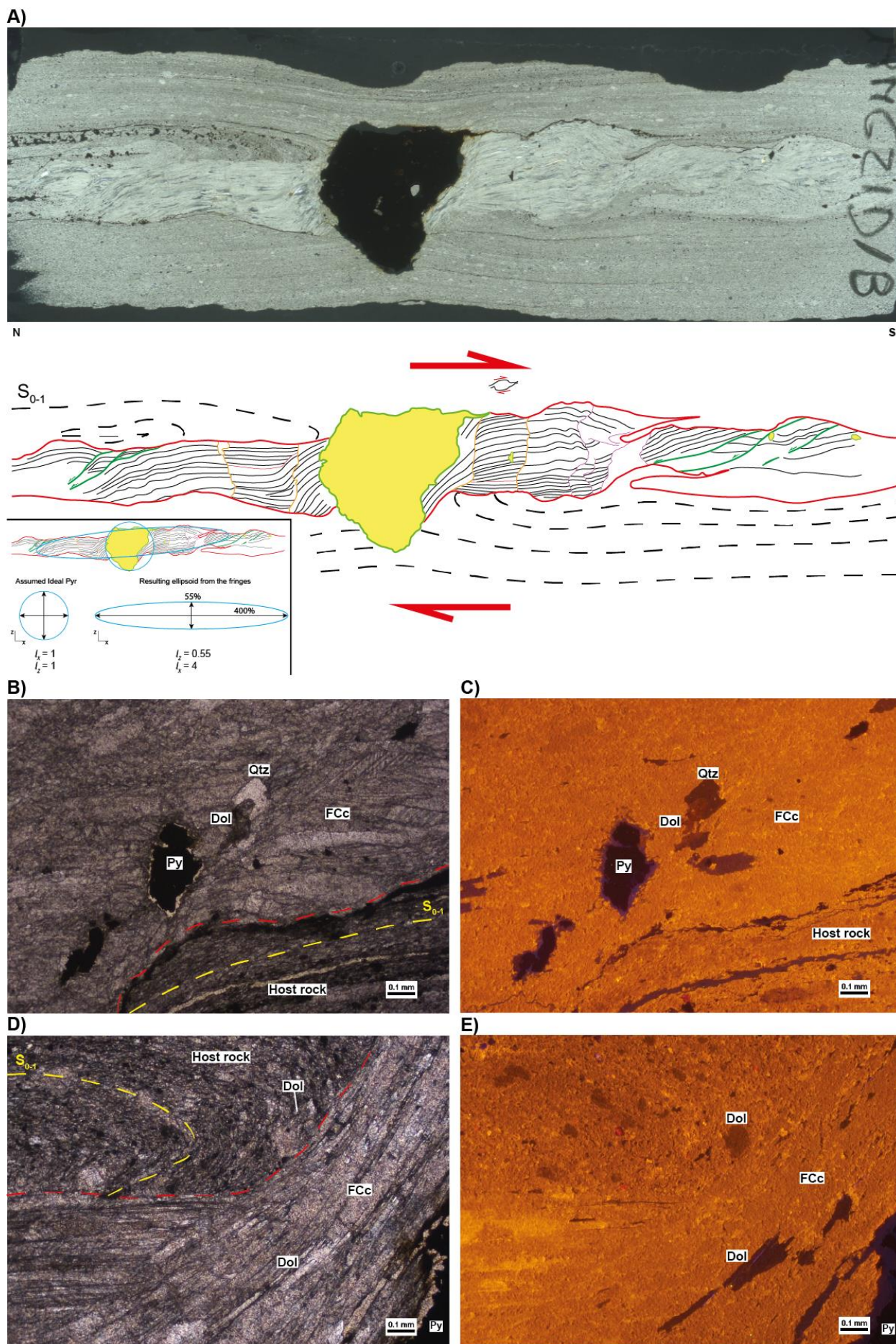
Figure 5.16: *A) XPL scanned thin section image and line drawing of a ductile deformed strain fringe in a pyrite grain of sample 19MG21 from the DA6 site, showing top-to-the-south sense of shear. Assuming an idealized circular pyrite, a minimum of 400% of stretching and minimum of 55% of shortening has been inferred. B) and C) PPL (left) and cathodoluminiscence (right) images of the strain fringes from sample 19MG21. Euhedral quartz and related dolomite precipitated within the strain fringes. D) and E) PPL (left) and cathodoluminiscence (right) of the host rock and the strain fringes from sample 19MG21. Dolomite from the host rock is shown reddish under CL with dark brown CL color in the rim. Fibrous dolomite is also present in the fringes. FCc: fibrous calcite; Dol: dolomite; Qtz: quartz; Py: pyrite.*

not possible to assume in the field examples where large ductile deformation of calcite fibers is observed (e.g., width of calcite fringe is smallest than the inclusion size).

Due to these complexities and uncertainties, it was not possible to calculate the strain increments from the fringes in a way than previous studies However, assuming a circular shape for the rigid pyrite and considering the limits of the fringes, the observed shape indicates a minimum stretch of ca. 400% in the extensional direction and a minimum shortening of ca. 55% perpendicular to it (Fig. 5.16A). Stiff dolomite crystals are present in the host rock also acting as rigid bodies (Fig. 5.16A).

The calcite from the fringes gives bright yellow colors under the CL, which are similar to the calcite CL colors from the host rock (Fig. 5.16C and E). We can also identify fibrous dolomite crystals in the fringes, which gives a brown CL color (Fig. 5.16E). Dolomite grains in the matrix has the same CL color (brown) in the rim of the grains as those of the fringes (Fig. 5.16E). Intergrowing with dolomite crystals, there are sometimes euhedral quartz crystals with dark blue to non-luminescent CL color (Fig. 5.16C).

Overturned limb

The Upper Cretaceous of the OL domain is mainly characterized by PFV calcite veins ranging from 0.1 to 4-5 cm in thickness, which are often boudinaged (Figs. 5.7A and B). Also, pressure

shadows associated with stiff quartz or dolomite grains belonging to the Cenomanian siliciclastic facies are observed, showing a top-to-the-south sense of shear (e.g., Fig. 5.11F).

The fibrous calcite crystals associated with rigid grains are rarely twinned under optical microscope and have a dull-yellow color response under cathodoluminescence (CL), which is similar to the CL signal of the calcite in the host rock (e.g., Fig. 5.17). CL response of the dolomite grains is variable in colors and intensities, generally characterized by heterogeneous overgrowths (e.g., Fig. 5.17D). A second bright yellow CL phase is observed precipitating in the external rims of the dolomites, which is probably calcite substituting the dolomite (e.g.,
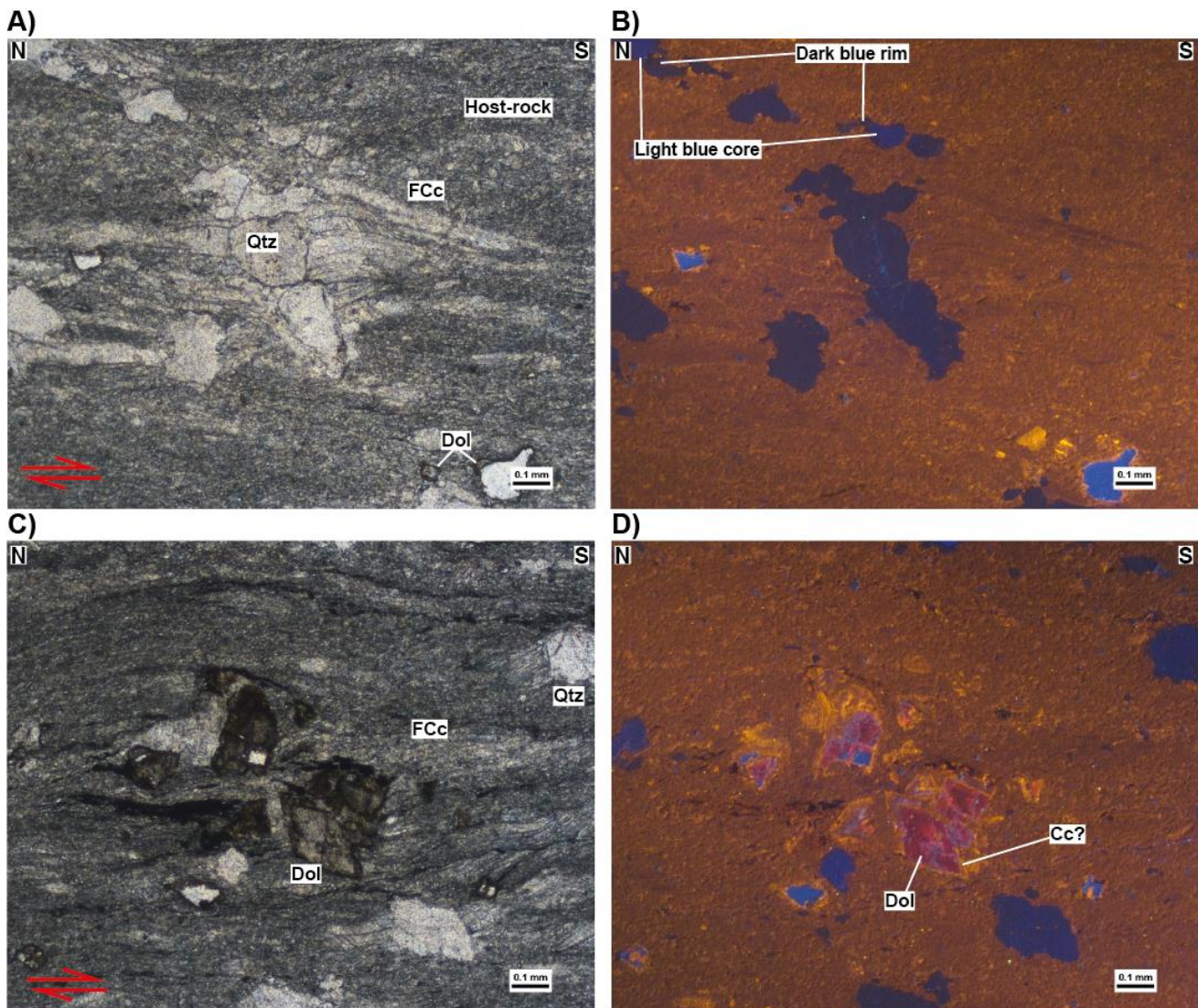
Figure 5.17: *PPL (left) and cathodoluminiscence (right) images of sample 19MG67 from the Cambeilh area (OL1 site).* **A)** *and* **B)** *Fibrous calcite precipitated in the strain shadows of sedimentary quartz grains, which sometimes develops dark blue rims under CL. Small dolomite is totally replaced by calcite that gives bright yellow colors under CL.* **C)** *and* **D)** *Calcite fibers precipitated in the strain shadows of dolomite and quartz grains. The dolomite gives a heterogeneous response under CL and presents bright yellow calcite(?) in the crystal rims, which could respond for a calcite replacement in a dedolomitization process as inferred by Caldera (2022). FCc: fibrous calcite; Dol: dolomite; Qtz: quartz*

Fig. 5.17D). Further information on the paragenetic processes (i.e., dedolomitization) suffered by the host rock can be found in Caldera (2022).

The quartz crystals of the host rock are rounded to angular in shape and commonly have opaque mineral rims (e.g., Fig. 5.17A and 5.18A). When the host rock is grain-supported, the quartz grain boundaries are sutured by pressure-solution, and opaque minerals are common near them (e.g., Fig. 5.18A). Under CL, most crystals show a light blue signal in the core and a dark blue signal in the rim of the grain (e.g., Fig. 5.17B, D and 5.18A).

The PFV veins have irregular contacts with the host rock, most likely due to the boudinage (e.g., Fig. 5.7A). In thin sections, the veins are composed of dominant coarse blocky and stretched-blocky crystals parallel to the vein wall, giving similar dull-yellow colors under the CL (e.g., Fig. 5.18B and D). Both textures developed type III-IV calcite twins and present sutured grain boundaries, undulose extinction and signs of dynamic recrystallization (e.g., Fig. 5.18C and D). Fibrous calcite perpendicular to the vein wall is sometimes observed, indicating the sense of opening and giving similar dull-yellow color as the coarser calcite crystals (e.g., Fig.5.19B).

Associated anhedral and stretched dolomite (parallel to the vein walls) and anhedral to euhedral quartz crystals are observed in these veins (e.g., Fig. 5.19A-C). Fibrous dolomite is also present perpendicular to the vein walls (e.g., Fig. 5.19B). Dolomite within the vein gives a dull magenta to dark magenta color under the CL. Bright yellow colors can sometimes be
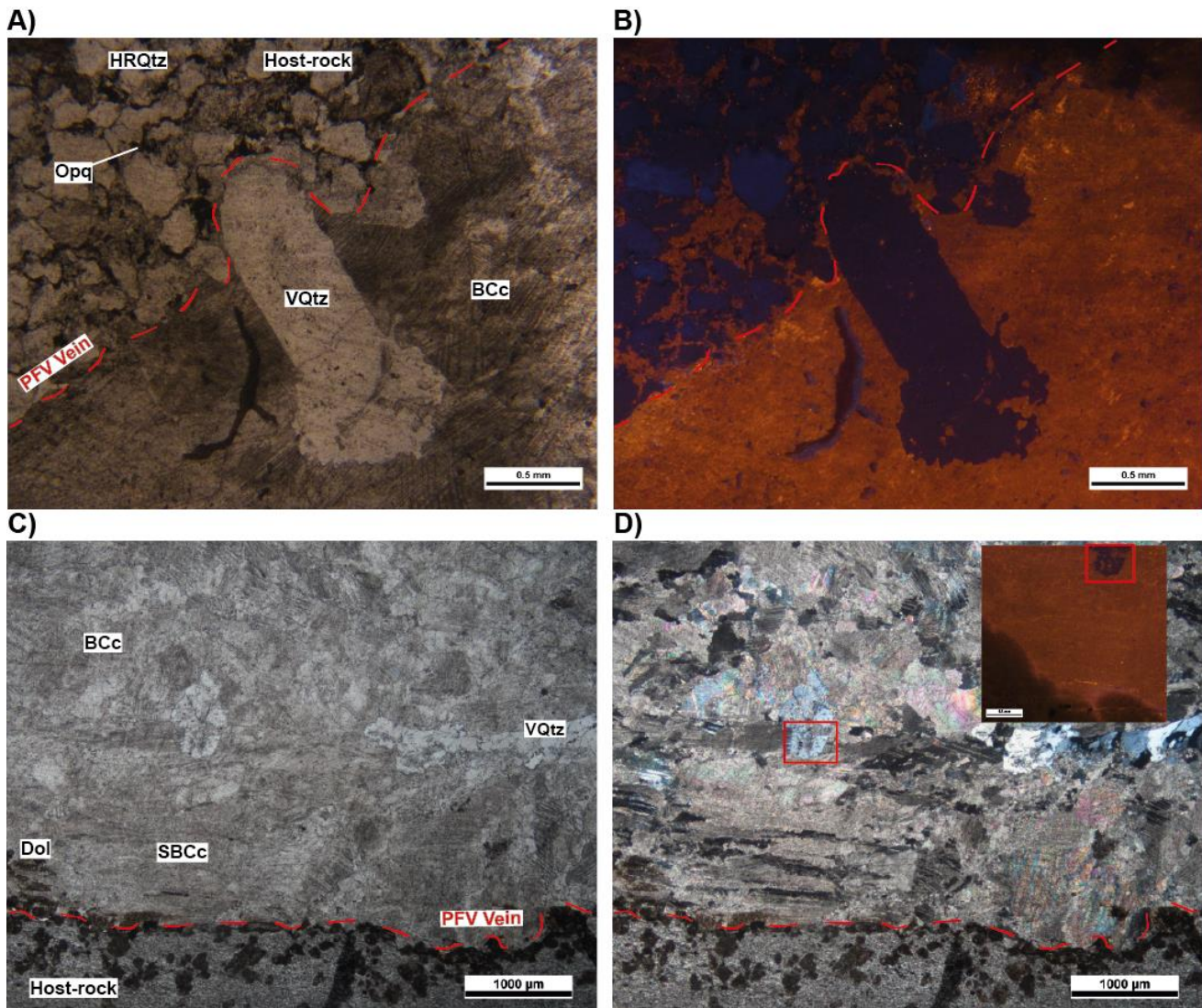
Figure 5.18: A) *and **B)** PPL (left) and cathodoluminiscence (right) images of PFV calcite veins from sample 19MG68 in the OL1 site. The CL color from the rims of the sedimentary quartz differs from those of the core and are similar than those of the anhedral quartz from the vein. The quartz from the vein has an irregular contact with the quartz from the host rock, attesting to the deformation of the vein-host rock boundary. **C)** and **D)** PPL (left) and XPL (right) images of sample 19MG68 where the blocky and elongated-blocky calcite grains show the same dull-yellow CL response. HRQtz: host rock quartz; Opq: opaque minerals; VQtz: quartz from the vein; BCc: blocky calcite; SBCc: stretched-blocky calcite; Dol: dolomite.*

observed in mineral grains resembling dolomite in PPL, but they are probably related to OFV calcite veins that provoked partial or total dedolomitization in the host rock and within the vein (e.g., Fig. 5.19E and F; Caldera, 2022). Euhedral dolomite is also present in the host rock,

showing a heterogeneous CL response of magenta to dull magenta, with overgrowth rims and dedolomitization processes, as described by Caldera (2022) (e.g., Fig. 5.17D and 5.19D).

The quartz from the veins, associated with dolomite (e.g., Fig.5.19C, E, and F), is shown dark blue under CL, similar to the rims of the siliciclastic grains in the matrix (e.g., 5.17B and 5.18B).

On the other hand, thin (0.1-0.2 cm thick) and straight OFV (NE-SW) veins can also be observed, although they are scarce in this domain (e.g., Fig. 5.5 and 5.7A). These veins are composed of calcite (bright yellow under the CL) and dolomite (dark magenta under the CL) (Fig. 5.19D).

Weakly deformed autochthon

The Upper Cretaceous host rocks from the WDA domain are little deformed, with preserved sedimentary textures and fossil shapes (e.g., Fig. 5.3; Caldera, 2022). However, 0.1 to 2 cm thick bedding- and S_{01}-parallel calcite veins are also observed, similar than OFV veins (Fig. 5.6 and 5.8). At the outcrop scale, PFV veins are mostly straight with regular contact with the host rock, although it is not rare to identify folded PFV veins (Fig. 5.8A). In addition, a relatively dense pack of calcite vein arrays is also observed in the WDA1 at the level of the top of the Santonian (e.g., Fig. 5.8A), but not that dense as in the DA1 site (which was at the Cenomanian detachment level, Caldera et al. 2023). The OFV veins are thin (0.1-2 cm thickness) and appear straight in the contact with the host rock (e.g., Fig. 5.8C and D).

Under the microscope, the PFV veins from the WDA1 site (Fig. 5.4 for location) are developed at the top of the Santonian limestone and are almost undistinguishable from the host rock at the thin section scale (e.g., Fig.5.20A and B). These belong to the top Santonian densely packed array (Fig. 5.8A, E and F) and are composed of very fine-grained calcite, although relicts of highly deformed coarse and twinned calcite grains can sometimes be identified. In
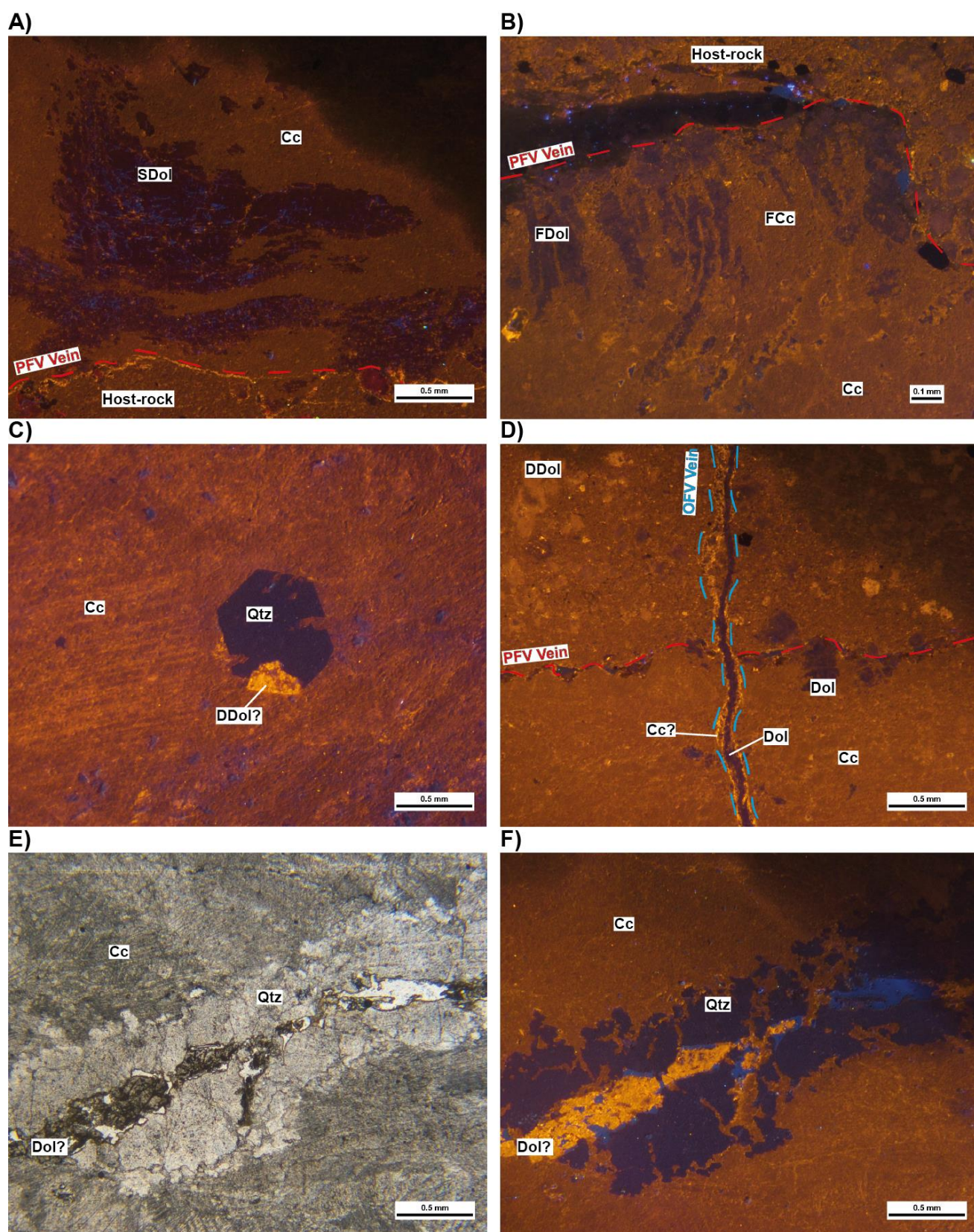
Figure 5.19: A) and *B) Cathodoluminiscence images of PFV veins from sample 19MG68 in the OL1 site. A)* *shows stretched dolomite and B) calcite and dolomite fibers orthogonal to the vein wall. Bright yellow calcite is also present just in the vein wall, and in the rims of the euhedral dolomite of the host rock. C) Cathodoluminiscence image of euhedral quartz and originally dolomite grains totally replaced by calcite with bright yellow CL color (sample 19MG35 from site OL1). The exhibited texture points to a fluid sub-saturated in Si. D) OFV calcite (bright yellow)-dolomite (dark magenta) vein cross cutting PFV vein from sample 19MG68. Note the good development of dedolomitization in the host rock by the presence of originally dolomite replaced by calcite which gives slight yellow CL response. E) and F) PPL (left) and cathodoluminiscence (right) of dolomite and quartz from the center of the PFV vein of sample 19MG67. The dolomite preserves its PPL texture, but seems totally replaced by calcite under CL, which gives bright yellow color. The quartz is also corroded by calcite. Cc: calcite; FCc: fibrous calcite; Dol: dolomite; FDol: fibrous dolomite; SDol: Stretched dolomite; DDol: dedolomite (dolomite replaced or partially replaced by calcite); Qtz: quartz.*

addition, solution seams marked by of opaque minerals are visible oriented (012/26), usually surrounding the relicts of coarser calcite or the vein wall. Little deformed quartz is also present in the PFV veins from this domain (e.g., Fig. 5.20A and B).

The PFV veins from site WDA2 (Fig.5.4 for location) are essentially composed of coarse blocky calcite grains, which have type III-IV twins and sutured grain boundaries. Smaller crystals formed by recrystallization are also observed, which are rarely twinned (e.g., Fig. 5.20C and D). Coarser grains have undulose extinction and sometimes evidence of brittle fracturing (e.g., Fig. 5.20D). Under the CL, the calcite from the vein gives dark yellow colors (Fig.5.20F). In addition, calcite with a bright yellow CL color is also observed following the host rock-vein contact (Fig. 5.20F).
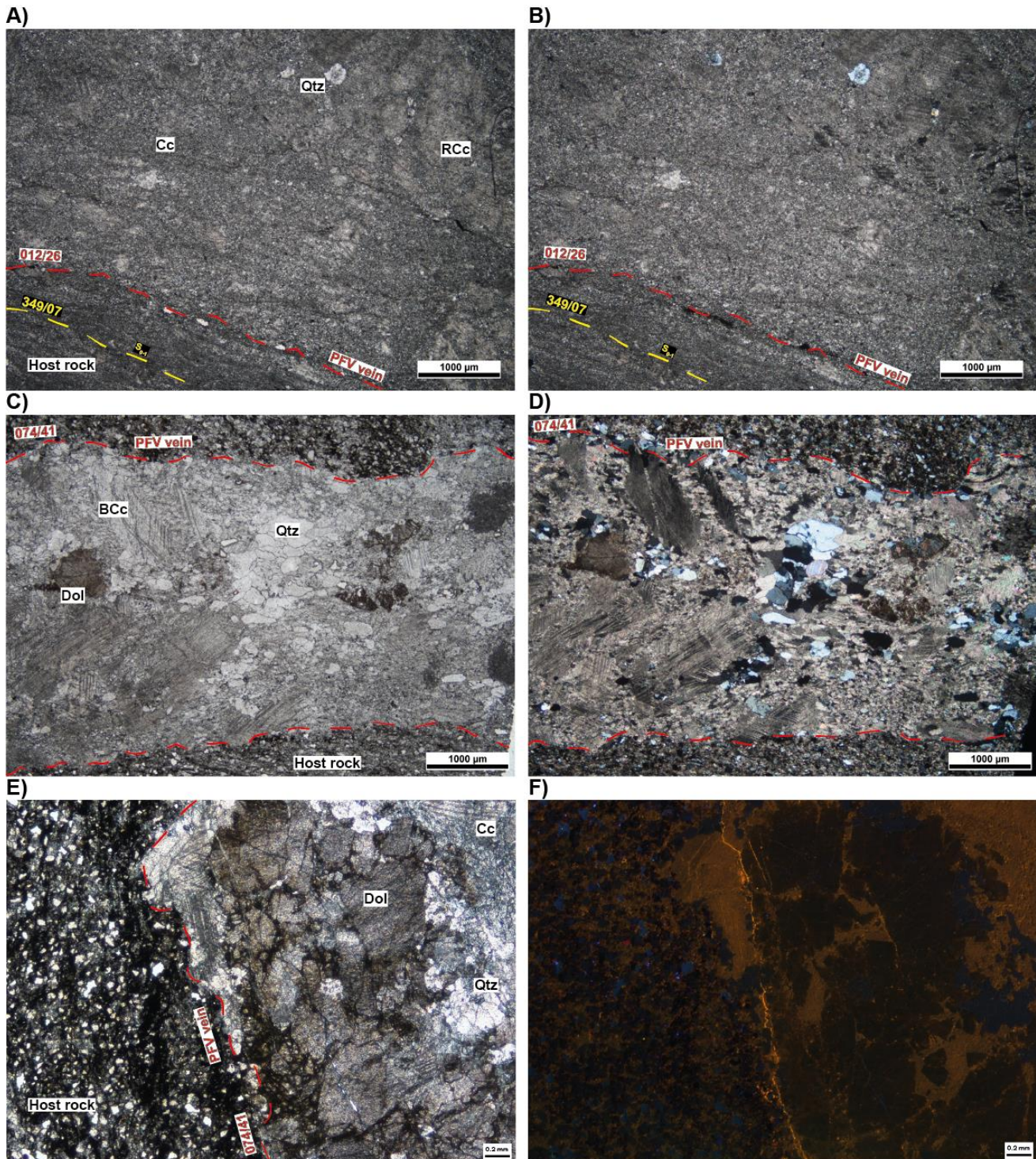
***Figure 5.20: A)** and **B)** PPL (left) and XPL (right) images of PFV calcite veins from site WDA1. **C)** and **D)** PPL (left) and XPL (right) images of PFV calcite vein from sample 19MG12 from site WDA2. **E)** and **F)** PPL (left) and cathodoluminiscence (right) images from sample 19MG12 shown in C) and D). Cc: calcite; BCc: blocky calcite; RCc: relict calcite; Qtz: Quartz; Dol: Dolomite.*
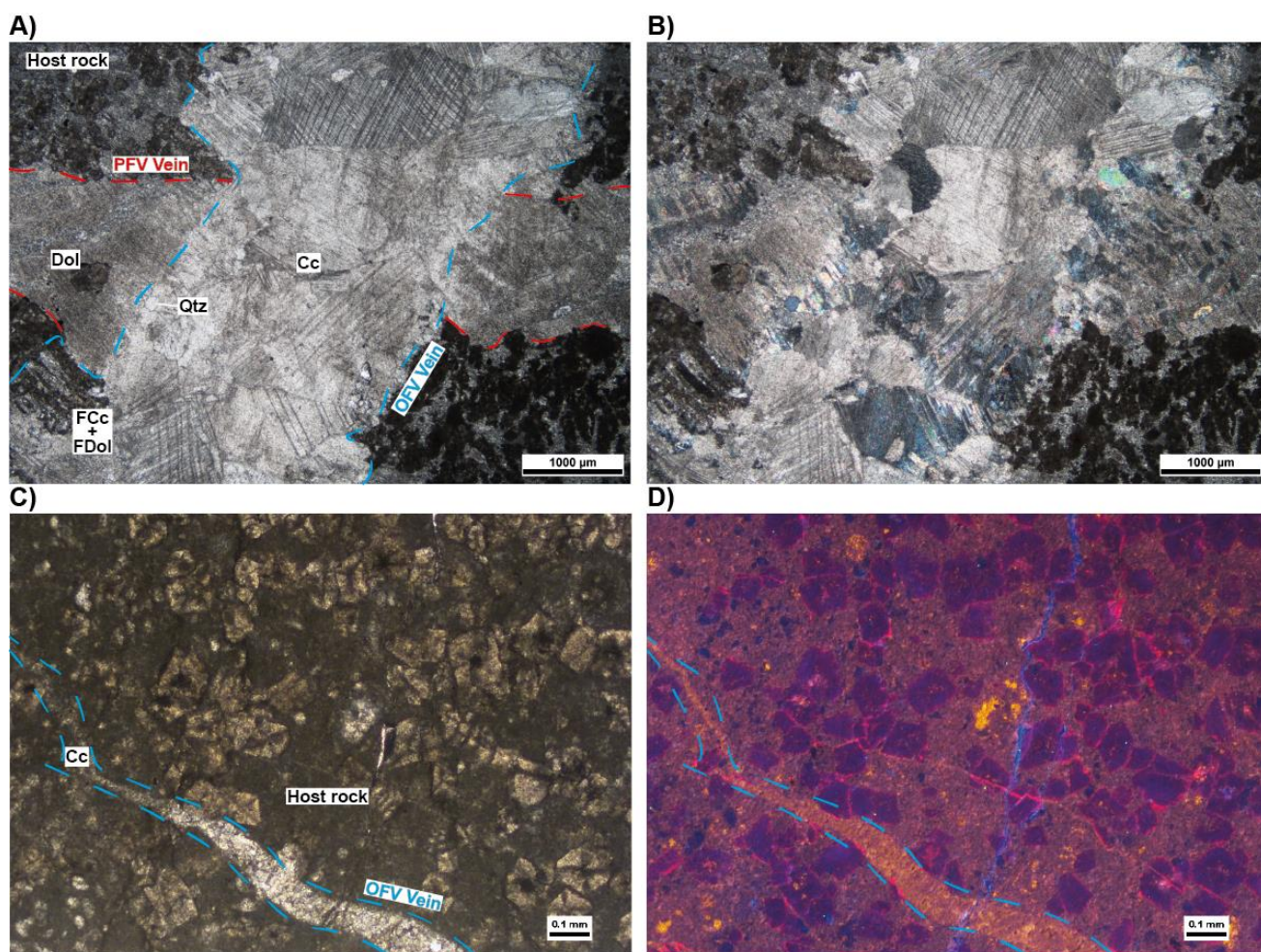
Figure 5.21: A) *and **B)** PPL (left) and XPL (right) images from PFV vein with relicts of coarser calcite grains cross-cut by an OFV vein (blue dashed lines) composed by coarse twinned calcite grains. **C)** and **D)** PPL (left) and cathodoluminiscence of OFV calcite vein in sample 19NC13 from Caldera (2022). The host-rock is composed by dolomite grains with violet to dark-dull luminescence in the core and brighter violet borders or dissolved nuclei. Calcite with bright yellow CL color precipitated in the porosity of the host-rock. Cc: Calcite; Dol: Dolomite; FCc: fibrous calcite; FDol: fibrous dolomite; Qtz: quartz.*

As in the other domains, dolomite and quartz are associated minerals within the veins. Dolomite, coarse in grain size, shows brittle fracturing and undulose extinction (e.g., Fig. 5.20D-F). Under CL, it gives dark brown colors similar to those of dolomite of the host rock (e.g., Fig.5.20F). On the other hand, the quartz in the veins, with smaller grain sizes than the other phases, has sometimes sutured contacts with the other grains and solution seams, but this is less evident than in other domains with higher strain (Fig. 5.20B and C). It gives dark blue color in CL (Fig. 5.20E and F).

In contrast, the OFV veins of this domain are characterized by coarse blocky calcite grains, most of which are twinned (e.g., Fig. 5.21A and B). Fibrous calcite can appear in the vein walls (e.g., Fig. 5.21A and B). The grain boundaries are generally sutured, despite the identification of some straight crystalline boundaries (e.g., Fig. 5.21A and B). Under CL, calcite from the veins gives bright to slightly yellow colors (e.g., Fig. 5.21C and D).

As observed in the other domains, dolomite and quartz are always accompanied by calcite within the vein (e.g., Fig.5.21A and B).

Normal limb

Finally, in the normal limb domain, only calcite veins at high angle to the bedding were observed, which at the outcrop scale ranged from 0.1 to 2 cm thick and has straight contact with the U. Cretaceous host rock (e.g., Fig. 5.22A).

In thin section, these veins are composed of coarse blocky calcite, which is sometimes twinned and brittle fractured (e.g., Fig. 5.22B). The grain boundaries are mostly straight, although some boundaries are sutured, with a rim attesting for pressure-solution (e.g., Fig.5.22B). Smaller calcite crystals are observed in the vein walls (Fig. 5.22B). In this domain, the only accessory phase is dolomite (Fig. 5.22B).

Under CL, calcite from veins and the host rock matrix displays a broad homogeneous dull-yellow color, although bright yellow is also detected principally in the host rock matrix (e.g., Fig. 5.22C and D). No dolomite was observed within the vein under the CL (Fig. 5.22C and D).
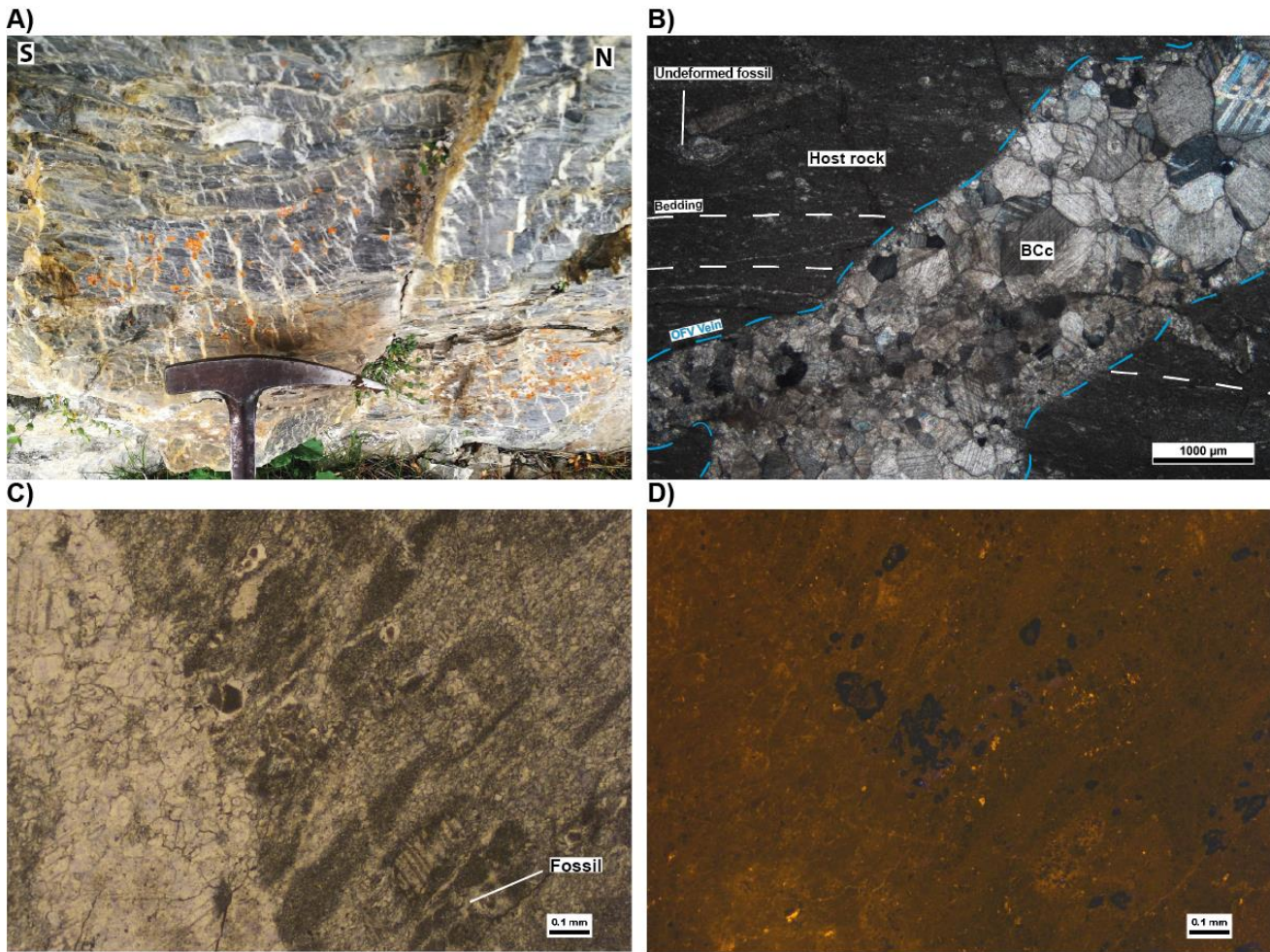
Figure 5.22: A) *Field image of the OFV en-échelon vein array from site NL1 in the Normal Limb domain cross-cutting the bedding which is oriented 260/42 (out-of-plane). Occasionally, calcite from the same network precipitated parallel to the bedding planes.* **B)** *XPL image from blocky calcite cement of a OFV vein from site NL1. Note the undeformed fossil from the host rock attesting for low strain in this domain.* **C)** *and* **D)** *PPL (left) and cathodoluminiscence images of a OFV vein from sample 18NC37 of site NL1 from Caldera (2022) showing homogenous dull-yellow CL color.*

5.3. Vein timing from U-Pb in calcite cements

5.3.1. Composition of the calcite veins of the ECM

Prior to the *in-situ* LA-ICP-MS U-Pb geochronological analysis in calcite, 16 vein samples from the different strain domains were analyzed by inductively coupled plasma mass spectrometry (ICP-MS) to obtain information about the amount of U and Pb as a strategy to address the dating. The results of these analyses are shown in Table 5.1.

Sample	Lat(°)	Long(°)	Domain	Ca	Mg	Mn	Fe	Sr	Pb	U
19MG11	42.950016°	-0.331300°	DA	396000	6800	41	405	224	1.9	0.15
19MG12	42.934762°	-0.382872°	WDA	330000	6000	240	21000	500	4.1	0.075
19MG20	42.933456°	-0.333141°	DA	330000	6600	290	38000	300	5.4	0.19
12MG21	42.940222°	-0.325987°	DA	350000	5600	380	3900	350	1.5	0.17
19MG32	42.921712°	-0.386888°	WDA	310000	2800	490	11000	780	1.9	0.10
12MG35	42.933333°	-0.419167°	OL	360000	3100	210	7800	210	1.6	0.017
19MG43	42.932952°	-0.341588°	DA	380000	3900	190	9600	340	1.3	0.10
19MG45	42.927628°	-0.343861°	DA	370000	3400	72	310	410	0.90	0.070
19MG46	42.958108°	-0.339688°	DA	370000	3500	14	100	240	<0.25	0.10
19MG56	42.925669°	-0.417581°	OL	370000	3600	260	6300	230	2.5	0.021
19MG66	42.933154°	-0.418932°	OL	360000	3200	200	15000	220	1.9	0.018
19MG68	42.934982°	-0.422567°	OL	380000	4800	88	2000	170	2.1	0.045
19MG74	42.953336°	-0.321682°	DA	360000	4000	88	1600	360	1.1	0.18
19MG78	42.950321°	-0.317892°	DA (Pz)	390000	2500	170	1200	2100	2.6	0.014
19MG79	42.955487°	-0.327027°	DA	410000	3900	78	330	300	0.72	0.18
20MG126	42.953479°	-0.360887°	DA	320000	48000	170	6100	140	4.8	0.020

Table 5.1: *Major element ICP-MS results in ppm (µg/g) for the calcite veins from the DA, WDA and OL strain domains of the ECM. Na was also analyzed giving quantities below detection limit (0.5 ppm). The type to which each vein belongs can be found in Table 5.2.*

The calcite veins analyzed from the different strain domains are principally composed of Ca, Fe, and Mg, with accessory concentrations of Sr and Mn (Table 5.1). Regarding the elements important for dating (i.e., U and Pb), the major concentrations are very low (Table 5.1). Pb concentration is always one or two orders of magnitude higher than that of U, which is most

likely in the ppb range. Hence, the U/Pb ratios are below 0.1, despite that samples 19MG74, 19MG79, and 19MG46 have ratios over 0.1 (Table 5.2).

It should be mentioned that the U/Pb ratio from sample 19MG46 has been calculated assuming a [Pb] = 0.25 ppm, but the actual value may be much lower than that (Table 5.1 and 5.2).

5.3.2. Age results from in-situ LA-ICP-MS U-Pb in calcite

A total number of 9 calcite vein samples (principally PFV but also some OFV; Table 5.3) from the different ECM strain domains were analyzed for U-Pb ultimately to constraint the age on the main folding and thrusting events on the basis of the vein-macrostructure relationships. The locations of the samples are shown in Fig. 5.10. These were chosen as a function of the U/Pb ratio principally and then on the concentration of U, regardless of the Pb concentration. Before programming the automated sequence, a few testing shots measuring the $^{238}U/^{206}Pb$ and $^{207}Pb/^{206}Pb$ ratios were fired to find U-rich areas. In places where high U was found, a laser shot was programmed to measure the U and Pb isotopic compositions within a fully automated sequence overnight. The analyses were performed in four different sessions at the University of Texas at Austin; further information on the procedure can be found in Chapter 2.

From the total of 45 calcite cement crystals analyzed within the different vein samples, only 4 yielded possible ages to the deformation of the ECM (Table 5.4). The Tera-Wasserburg age plots with the main results of dated samples 19MG20 and 19MG43 are shown in Figs. 5.23 and 5.24, and the rest of the analyzed samples can be found in the annexes together with the data repository of the LA-ICP-MS isotopic composition (Tables A5.1–A5.4 and Figs. A5.1 – A5.6). The summarized age results for each vein analyzed are displayed in Table 5.4.

Sample	Domain	Vein	U/Pb
19MG11	DA	PFV	0.075
19MG12	WDA	PFV	0.018
19MG20	DA	PFV (boudin necking)	0.035
12MG21	DA	PFV	0.113
19MG32	WDA	OFV	0.053
12MG35	OL	PFV	0.011
19MG43	DA	OFV	0.077
19MG45	DA	PFV	0.078
19MG46	DA	PFV	0.400*
19MG56	OL	PFV	0.008
19MG66	OL	PFV	0.009
19MG68	OL	PFV	0.021
19MG74	DA	PFV	0.164
19MG78	DA (Pz)	OFV	0.005
19MG79	DA	PFV	0.250
20MG126	DA	OFV	0.004

*Table 5.2: Major element U/Pb ratios from the ICP-MS analyses showing generalized elevated [Pb] with respect to the [U]. *U/Pb ratio from sample 19MG46 has been calculated assuming the detection limit displayed for Pb in Table 5.1 (i.e., 0.25) but it is much probably lower than the expected.*

Sample	Lat (°)	Long (°)	Domain	Type
19MG20	42.933456°	-0.333141°	DA	PFV and OFV
19MG21	42.940222°	-0.325987°	DA	PFV
19MG32	42.921712°	-0.386888°	WDA	OFV
19MG43	42.932952°	-0.341588°	DA	OFV
19MG46	42.958108°	-0.339688°	DA	PFV
19MG67	42.933069°	-0.418863°	OL	PFV
19MG74A	42.953336°	-0.321682°	DA	PFV
19MG74B				
19MG79	42.955487°	-0.327027°	DA	PFV

Table 5.3: Location, domain and type of calcite vein samples attempted to be dated by in situ LA-ICP-MS in calcite.

The samples from the ECM exhibit a high non-radiogenic isotope composition, with $^{207}Pb/^{206}Pb$ following planar trends mainly in the common Pb side of the diagrams (e.g., Fig. 5.23D and F; 5.24A and B and Annex 5). Most of the ages suffer from large uncertainties, which are related to the very low concentrations of U (<1ppm in most cases) and radiogenic Pb, and the generally limited spread in $^{238}U/^{206}Pb$ ratios. However, up to four exceptions to

Sample	Analyzed ID	Vein	Cement	Age	error (±2σ)	MSWD
19MG20	SH1	PFV (Strain shadow)	Fibrous	0.000021	0.064	2.9
	SH2	PFV (Strain shadow)	Fibrous	54.0	13.0	2.2
	T1	OFV	Fibrous	73.8	36.7	1.6
	T2	OFV	Fibrous	48.87	5.66	1.4
	T3	OFV	Fibrous	93.0	16.0	4.0
	V1	PFV	Fibrous (vein wall)	36.0	42.4	1.6
19MG21	1	PFV (Strain fringe)	Fibrous	115	103	1.3
	1B	PFV (Strain fringe)	Fibrous	104.5	26.8	1.2
	1C	PFV (Strain fringe)	Fibrous	31.9	18	1.7
	2	PFV (Strain fringe)	Fibrous	37.8	330.6	1.4
	3	PFV (Strain fringe)	Fibrous	3.4	90.35	1
	4	PFV (Strain fringe)	Fibrous	12.1	21.8	0.82
	4B	PFV (Strain fringe)	Fibrous	37.2	18.2	0.99
	5	PFV (Strain fringe)	Fibrous	81.8	242	0.75
	6	PFV (Strain fringe)	Fibrous	12.8	145.2	1.1
19MG32	1	OFV	Fibrous	0.00012	0.41672	1.3
	2	OFV	Fibrous	0.00011	1.42622	1.6
	3	OFV	Fibrous	62.4	100.1	1.3
19MG43	1	OFV	Fibrous	24.5	23.7	1.5
	2	OFV	Blocky	3.08	15.86	4.2
	3	OFV	Blocky	56.99	9.35	2.3
	3B	OFV	Blocky	39.5	15.4	1.1
	4	PFV	Micritic cement	38.14	5.99	1.4
19MG46	1	PFV	Blocky	0.00011	0.11027	2.2
	2	PFV	Blocky	0.00011	0.12654	2.5
	3	PFV	Blocky	0.00012	0.1004	2.7
	4	PFV	Blocky	0.00013	0.08691	1.9
	4B	PFV	Blocky	6.91	14.14	2.2
	5	PFV	Blocky	0.00011	0.03474	2.9
	5B	PFV	Blocky	15	19.6	3.5
	6	PFV	Blocky	1.89	18.81	3.3
	6B	PFV	Blocky	0.00013	0.05095	2.8
19MG67	1	PFV (Strain shadow)	Fibrous	0.000018	0.14966	2.1
	2	PFV	Blocky	0.00012	0.04247	2.5
	3	PFV	Blocky	14.7	52.5	1.4
19MG74A	1	PFV	Blocky	358	466	1.1
	2	PFV	Blocky	101	193	1.2
	3	PFV	Blocky	2.4	17.27	1.4
	4	PFV	Blocky	0.00012	0.09556	1.7
	4B	PFV	Blocky	10.5	34.3	1.2
	5	PFV	Blocky	0.00012	0.08729	1
	5B	PFV	Blocky	0.00012	0.109	1.3
	6	PFV	Blocky	0.00012	0.11162	1.1
	6B	PFV	Blocky	0.00012	0.05604	1.9
19MG74B	-	PFV	Blocky	4.65	13.58	1.4
19MG79	1	PFV	Blocky	0.00012	0.06312	2.1
	1B	PFV	Blocky	0.00012	0.0441	1.7

Table 5.4: *Summarized age results obtained by LA-ICP-MS U-Pb in calcite cements of the ECM. Reported ages that do not belong to the samples 19MG20 or 19MG43 have not been purged for large ellipse error (section 2.2.3) due to the large amount of common Pb.*

this general trend can be observed in samples 19MG20 and 19MG43, which show a higher spread in the $^{207}Pb/^{206}Pb$ and $^{238}U/^{206}Pb$ ratios (Figs. 5.23B, E and 5.24C and D). From these four ages, those belonging to the necking vein T2 (Fig. 5.23B), and the vein 4 (Fig. 5.24D), are shown statistically and internally consistent.

The results obtained from the T2 fibrous calcite of the OFV vein from sample 19MG20 yield an age of 48.87 ± 5.66 Ma (MSWD = 1.4) and exhibits larger $^{207}Pb/^{206}Pb$ spread than the general trend of the whole ECM massif (Fig. 5.23B). A second slightly similar age of 54.0 ± 13.0 Ma (MSWD=2.2) has been obtained from the fibrous calcite precipitated in the strain shadow SH2, showing small dispersion in both $^{207}Pb/^{206}Pb$ and $^{238}U/^{206}Pb$ isotopic compositions (Fig. 5.23E).

The PFV calcite vein 4 from sample 19MG43 yielded an age of 38.14 ± 5.99 Ma (MSWD = 1.4) showing most of the data in the common Pb side of the Tera-Wasserburg diagram, although a trend to the radiogenic composition can be observed (Fig. 5.24D and G). On the other hand, an age of 39.5 ± 15.4 (MSWD = 1.1) has been obtained from the thin OFV vein 3B, which is similar to that of the vein 4, which suggest that the isotopic system may have been re-equilibrated (Fig. 5.24C and F).
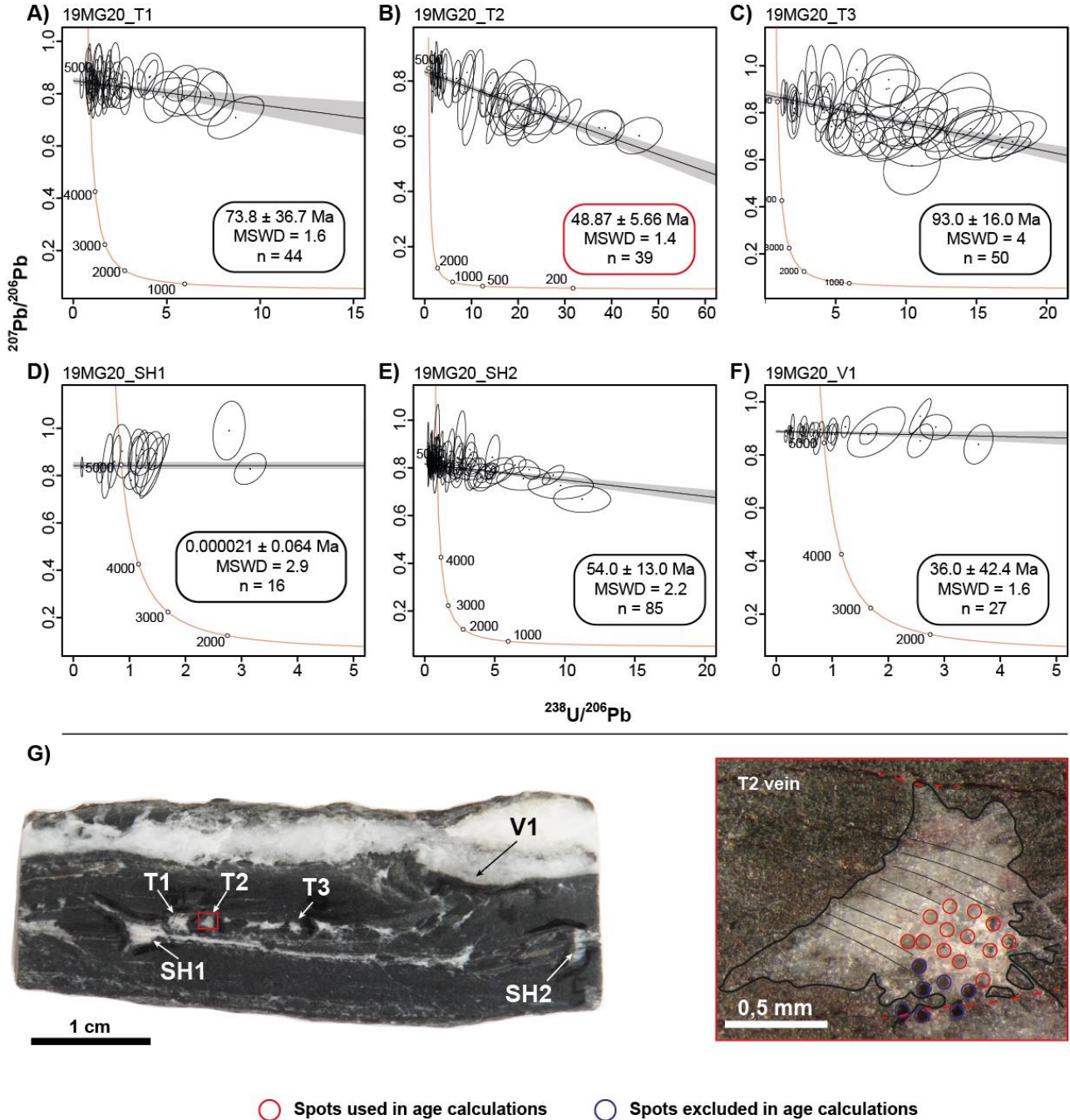
Figure 5.23: A-F) *Tera-Wasserburg plots from the analyzed calcite cements from sample 19MG20 (Age±2σ). Lower intercept ages were calculated using IsoplotR (Vermeesch, 2018). T1, T2 and T3 corresponds to OFV tensional fractures filled with fibrous calcite shown in Fig. 5.11C and 5.14E and F. V1 are the fibrous calcite cement from the PFV vein wall shown in Fig. 5.11A and 5.14C and D. SH1 and SH2 are the calcite precipitated in strain shadows developed in stiffer host-rock areas.* ***G)*** *Billet which contains the analyzed veins and detailed image from regular microscope of the T2 vein. Blue spots correspond to the excluded LA-ICP-MS laser shots from age calculation because they totally or partially impacted in the host rock.*
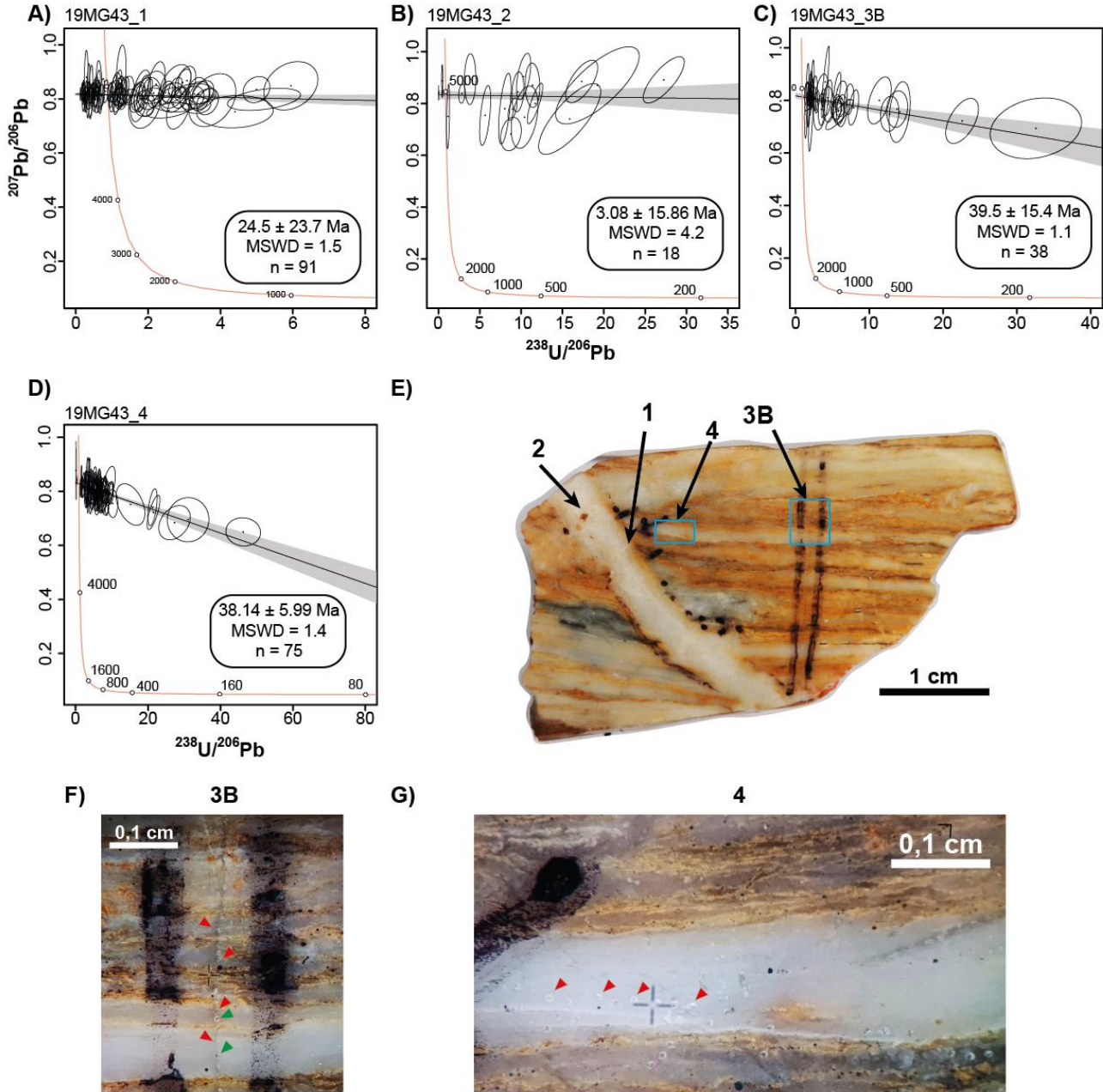
Figure 5.24: A-D) *Tera-Wasserburg plots of the analyzed calcite cements from sample 19MG43 (age±2σ). Lower intercept ages were calculated using IsoplotR (Vermeesch, 2018). The numbers correspond to the different analyzed areas of the sample. 1: fibrous calcite of the OFV vein wall shown in Fig. 5.13C and D. 2: blocky calcite crystals of the OFV thick vein also shown in Fig. 5.13C and D. 3B: calcite precipitated in thin calcite OFV vein. 4: analyzed PFV calcite vein similar to that shown in Fig. 5.13A and B. **E)** Billet from sample 19MG43 which contains the analyzed veins. **F and G)** Detailed image from regular microscope of the OFV thin vein and the PFV vein, which gave an Eocene age. Green arrows points to old spots corresponding to ø 85 μm spot laser that exceeded the thickness of the vein and impacted the host rock. The red arrows points to the thinner spots (ø 65 μm) used for the age calculation.*

5.4. Discussion: timing and significance of veins and implications for the tectonic evolution of the Eaux-Chaudes massif

5.4.1. The calcite veins as kinematic indicators

Calcite veins found in the ECM constitute an excellent kinematic indicator of the different tectonic processes that occurred in this area during the early constitution of the Pyrenean orogenic belt. Veins precipitated parallel or at low angles to the foliation or to S_{0-1} (PFV) are present in the DA, OL, and WDA domains (Fig. 5.2 and 5.6) and register the deformation suffered by the Upper Cretaceous carbonates during the main thrusting and folding event (e.g., Fig. 5.7, 5.11, and 5.12). The consistency in orientation with the foliation and their progressive deformation (e.g., folding, stretching and boudinage, sense-of-shear record, etc.) suggests that they are genetically related. (Fig. 5.5 and 5.6).

The complex cross cutting relationships observed in the veins from the Gourzy transfer zone (WDA2 site, Fig. 5.4) indicates that they are syn-tectonic because veins with similar orientations (i.e., orange labelled in Fig. 5.9C and D) cross cuts and are either cut by veins at high angle to they (i.e., red labelled in Fig. 5.9C and D) and at the same time the whole set is shown deformed (folded and boudined), indicating multi event of vein precipitation and evolution of vein orientation during the progressive deformation in this site. The observed orientation features of both type of veins indicates sinistral sense of shear for the Gourzy transfer zone, which is consistent with the folds (and axial plane foliation) developed in the red dashed veins and the extensional (boudinage) features displayed by the orange-labelled veins, which are in the extensional field with respect to the shear zone. Moreover, the offset and the folding displayed by the orange labelled veins (Fig. 5.9C and D) is compatible with the kinematics of R' fractures in the sense of Cloos (1928) and Riedel (1929), also supporting the sinistral sense of shear. Therefore, the Eaux-Chaudes fold nappe was translated over the

autochthonous succession far south than the eastern thrust-fan attending the veins from the WDA2 site, confirming the solution proposed by Caldera (2022) and Caldera et al. (2023) to accommodate the different structural styles developed in the Eaux-Chaudes massif.

The vein cements probably precipitated in mode-I or mode-II fractures (e.g., Pollard and Segall, 1987; Scholz, 2002; Bons et al. 2012), where fibrous and blocky calcite crystals grew, as indicated by the fibers observed in the vein walls (e.g., Fig.5.11C and 5.19B). However, owing to the observable combination of simple and pure shear registered by the veins and the host rocks, it is sometimes difficult to decipher the original orientation and geometry of the crystals (e.g., Fig. 5.7 and 5.16A).

In general, PFV veins displays ductile deformation at the outcrop scale, similar to that observed and described by Caldera (2022) in the Upper Cretaceous host carbonates. As introduced just above, most of these veins are asymmetrically boudinaged and folded following the top-to-the-south intrafolial folds of the host rock or acted as rigid δ-shape porphyroclats especially in of the eastern DA sector (e.g., Figs. 5.3A; 5.7C and 5.14A). The most common cases are boudinaged veins that simply follow the foliation or S_{0-1}, usually found in both the DA and OL domains (e.g., Figs. 5.7A, B, E and 5.23G). Linked to the boudinage, tensional necks were observed where fibrous calcite precipitated (e.g., Figs. 5.14E, F, and 5.23G), which should be considered as syn-tectonic veins. Moreover, similar fibrous calcite is observed in the SH1 and SH2 near to the tensional T1, T2 and T3 veins, indicating the sense of shear (Fig. 5.23G).

Despite the observed ductility, the PFV veins also register evidence of late brittle fracturing during the main deformation event, since the folded veins are sometimes brittle-thrusted (e.g., Fig. 5.12A); therefore, they probably formed during a protracted period including late brittle-ductile conditions.

In singular outcrops such as DA2 (Fig. 5.4 for location), the PFV veins form nearly 100% of the rock and define the foliation within outcrop-scale shear zones (e.g., Fig. 5.9A), much similar to the bedding-parallel Larra detachment level outcropping further west and interpreted as a product of brittle-ductile multi-event enhanced by fluid pressure (Teixell et al., 2000). At the thin section scale, the calcite from the veins from this area presents similar features (twins, dynamic recrystallization, etc.) than those described by the same authors in the Larra massif. This 5-10m level could represent the Cenomanian detachment level from the eastern DA sector described by Caldera (2022), although it is sometimes misoriented with respect to the general trend, probably affected by late retro thrusting and folding, which is common in this sector (e.g., Caldera et al., 2023; Figs. 5.4 and 5.7D).

Ductile features in the calcite veins are also observable at the thin-section scale. Mechanical twinning, dynamic recrystallization, and pressure-solution are combined with the fracturing that opened the cracks where coarse blocky calcite precipitated. Stretched calcite crystals at boudin necks are also indicative of crystalline plasticity after vein formation. Most of the observed twins in the PFV veins are type-III and IV in the sense of Burkhard (1993) and Ferril et al. (2004) (e.g., Figs. 5.11A, 5.14B, 5.20D, and 5.21B), suggesting relatively high-temperature during the deformation, as also corroborated by the paleotemperature record registered by the Upper Cretaceous host rocks of the ECM (~350°C, Caldera, 2022). Grain-size refinement by dynamic recrystallization of calcite (e.g., Fig. 5.15A-C), occasionally blurred the veins completely in thin sections (Figs. 5.11B and 5.12B at the outcrop scale). Relicts of coarse deformed blocky crystals attest for the grain-size reduction (e.g., 5.13A, E, and F; 5.20A ad B), even in the WDA domain (Fig. 5.21A and B).

Brittle cracks are sometimes developed in the coarser blocky crystals from the veins (e.g., 5.11A and 5.15B). These brittle features are especially developed in quartz and dolomite (e.g., Figs. 5.11A, 5.14C and 5.20E) and in the rigid grains of the host rock (Fig. 5.17C). Coexisting

brittle and ductile deformation features were also observed in the host rocks by microstructural EBSD analysis (Caldera, 2022).

Two main OFV conjugate vein sets have been identified in the ECM post-dating those PFV: NE-SW to NNE-SSW and NW-SE to WNW-ESE (e.g., Figs. 5.6, 5.7A, D, G, H; Fig. 5.11B; Fig. 5.19D; Fig. 5.21A and B). At the macroscopic scale, the ECM and Cauterets granite (just south of the ECM, in the footwall of the Eaux-Chaudes allochtons) are affected by a fracture network displaying similar orientations (e.g., Fig. 5.25). In addition, in the Larra massif (westward of the ECM), the NE-SW and WNW-ESE sets can be identified (e.g., López-Martínez, 1987; Teixell, 1992). Although a relative chronology can be established between these sets in a particular outcrop (e.g., Fig. 5.8C), it is not safe to attribute this sequence of events to the history of the massif without a systematic and statistical study. Therefore, for convenience, both sets are considered to belong broadly to the same process. From the Late Eocene, the emplacement of the Gavarnie thrust induced a change in the deformation style through the accretion of a footwall sequence of thick-skinned thrusts, resulting in the Axial Zone antiformal structure (Teixell, 1996; Jolivet et al., 2007; Labaume et al., 2016; Teixell et al., 2016), producing also minor north-verging back-thrust/fold systems. This vertical thrust accretion could have produced extension in the hanging wall, being responsible of the observed normal offsets therefore producing a change in the stress regime by which OFV veins precipitated at high angles producing normal offsets in the PFV veins (e.g., Fig. 5.7F, G and H). Normal faulting and veining in the Larra area were also attributed to the broad Gavarnie deformation by arching and tangential longitudinal strain over the thrust (Teixell et al., 2000).

Cauterets granite macroscopic fractures   **Eaux-Chaudes macroscopic fractures**

Cauterets granite main fracture orientation   **Eaux-Chaudes main fracture orientation**
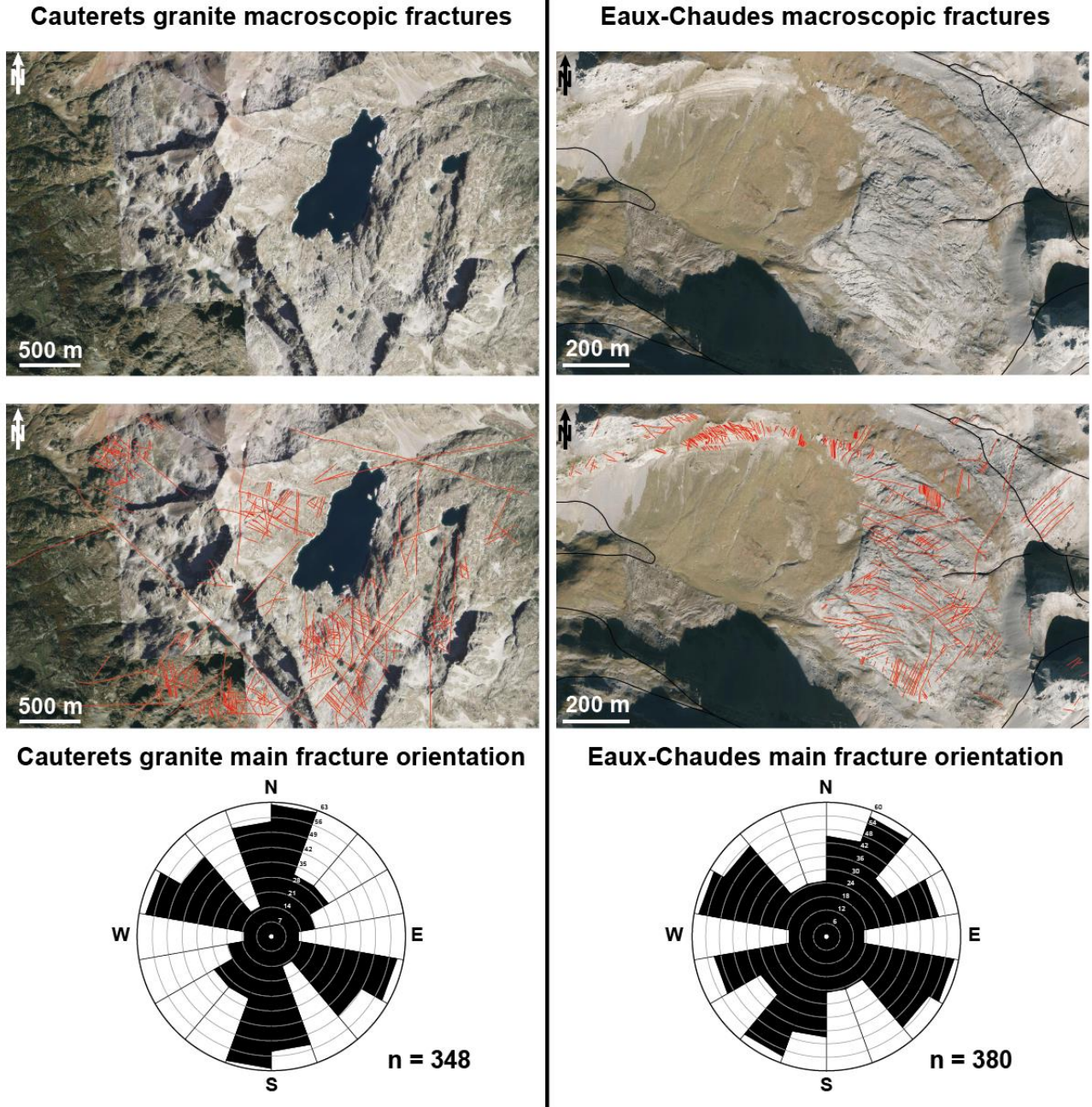
Figure 5.25: Macroscale fracture network from selected areas belonging to the Cauterets granite (left) and the Eaux-Chaudes massif (right, southwards to the DA3 site in Fig. 5.4) showing similar fracture orientation. Coordinates of the Cauterets measurement area are 42°52'58.83"N, 0°18'13.50"W and for the Eaux-Chaudes area 42°55'53.60"N, 0°21'44.47"W. Data has been grouped in intervals of 20°.

Therefore, the OFV veins are probably related to the onset of the exhumation of the ECM during the emplacement of the Gavarnie thrust (cf. Chapter 6) and I consider them to be post-

tectonic concerning the main shortening event that produced the ECRFN (western sector) and the imbricate thrust fan (deformed eastern sector) to which the PFV veins are related.

Moreover, the calcite veins from the OFV are also shown deformed, affected by pressure-solution, and many of them have twins that can often be attributed to type II (occasionally type III) of Burkhard (1993) and Ferrill et al. (2004) classification (e.g., Figs. 5.11B; 5.13C, E, and F; Fig 5.21A and B), especially those from the WDA, DA, and OL domains (Caldera et al., 2021). Since these are considered to post-date the PFV veins (which have type III and IV twins), this indicates a decrease in temperature with respect to the metamorphic peak. In addition, coarse and little deformed blocky and elongated blocky crystals are always preserved in the OFV veins (also indicating a decrease in the tectonic activity) as a contraposition to the recrystallized and blurred calcite from most of the PFV veins (e.g., Figs. 5.11B, 5.13E and F, 5.15 and 5.21A and B).

5.4.2. Fluid evolution in the ECM

In addition to calcite, the polymineralic nature of the PFV and OFV veins indicates that Si- and Mg-rich fluids circulated along the fractures in the ECM. These fluids produced dolomite and quartz precipitates within the veins, probably simultaneously because they are usually associated (e.g., Figs. 5.19C, E and F). Considering the quartz texture from the veins, the fluid was probably subsaturated in Si (e.g., Fig. 5.18). Although deformed, these mineral phases preserved euhedral textures in most cases, even in the high-strain domains (e.g., Figs. 5.13D, 5.14D and 5.19C) because they are mechanically more resistant. Therefore, these should be interpreted post-dating the main calcite phase precipitation. In addition, the magenta dolomite from recrystallized and non-luminescent PFV calcite veins also indicates the late precipitation of this phase (e.g., Fig. 5.15D).

The general dark and dull CL intensities of the phases present in calcite veins are related to the Mn^{2+} and Fe^{2+} concentrations in the calcite, which constitute the main activators (Mn^{2+}) and quenchers (Fe^{2+}) of luminescence (e.g., Fig., 5.26; Machel, 1985, 2000; Savard et al., 1995). Concentrations above 17 ppm can cause luminescence (Mason and Mariano, 1990), and other elements are not required to activate luminescence in calcite (ten Have and Heijnen, 1985; Habermann et al., 1998). On the other side, Fe^{2+} constitutes the main quencher element (e.g., Long and Agrell, 1965; Sippel and Glover, 1965), which requires concentrations >200 ppm to be effective. Mn concentrations in the ECM samples (Table. 5.1) are in the range of 14-490 ppm, which is sufficient to activate luminescence in the veins from the ECM, which would give bright yellow and orange to red colors (Mason and Mariano, 1990). However, the elevated quantities of Fe, ranging from 100 to 38000 ppm (Table 5.1), are high enough to mask the luminescence caused by Mn^{2+}, turning it into very dark red, red-brown, or non-activated (Budd et al., 2000).
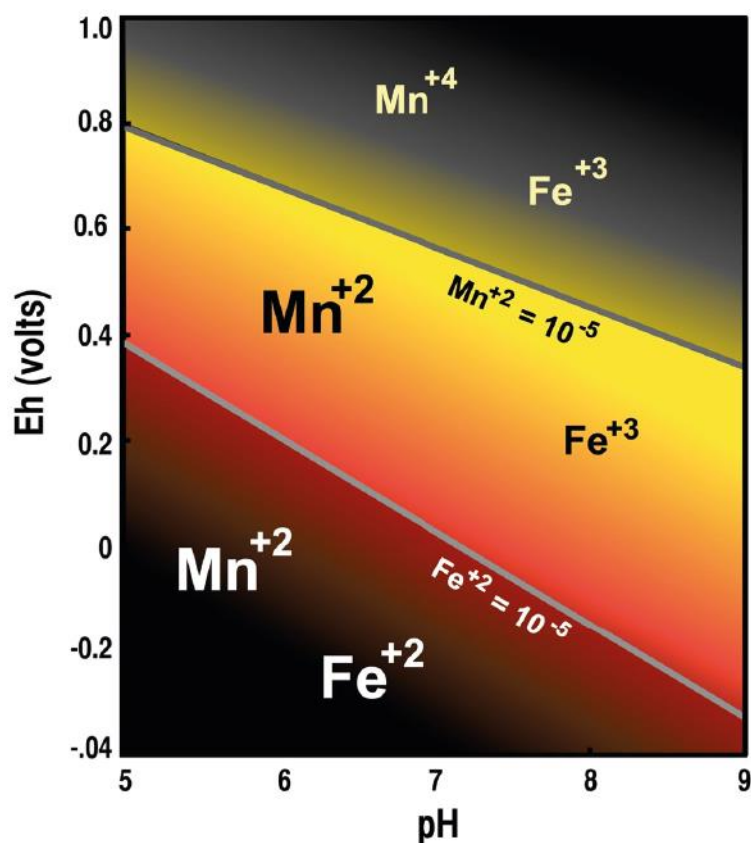
Fig. 5.26: Eh / pH diagram for the aqueous species of Mn and Fe and the expected color signal of calcite under cathodoluminiscence (from Hiatt and Pufahl, 2014).

The broadly homogeneous dark to dull yellow CL color of the calcite of the PFV veins tells that there is no evidence of multiple Ca-rich fluid events that precipitated multiple calcite cements in the original veins (e.g., Figs. 5.13 – 5.22; Cruset, 2019; Muñoz-López et al., 2023). Another possibility is that the calcite from the veins and the host rocks suffered an extended compositional homogenization due to recrystallization and dedolomitization (e.g., Fig. 5.19D), which is more likely attending the intense recrystallization suffered by the rocks, the fluid circulation observed by Caldera (2022) and the observed deformation in the veins. In addition, dedolomitization was extensive in the massif (Caldera, 2022), as was also observed in sample 19MG68 (Fig. 5.19D), probably also affecting the calcite veins.

A late fluid must have circulated through the OFV veins and parallel to the vein walls of the PFV calcite veins (e.g., Figs. 5.19A and D; 5.20F), giving a bright yellow color under the CL which is characteristic and extensive along all strain domains. The petrography (calcite vs.
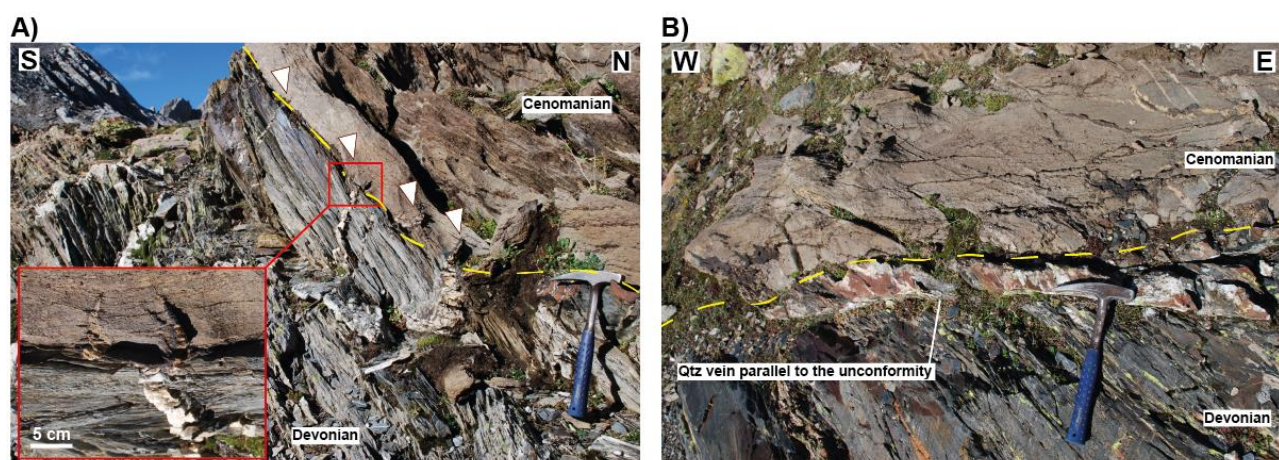
Figure 5.27: *A) Quartz vein from the Devonian basement slightly penetrating the Upper Cretaceous (Cenomanian) sedimentary cover. B) Quartz vein from the Devonian basement parallel to the Paleozoic-Upper Cretaceous unconformity (yellow dashed line).*

dolomite) of the precipitated phases associated to this fluid is unknown due to the small grainsize, but attending the bright yellow CL color it may be most probably calcite rich, which in most cases replaces the dolomite from the veins (e.g., Fig. 5.19E and F).

Finally, both quartz and dolomite from the veins are related to those of the host rock: the same fluid that precipitated the dolomite in the veins also precipitated a dark brown rim in the bright red dolomites of the host rock (e.g., Fig. 5.14 D and F), and similarly, the quartz crystals from the host rock have a dark blue rim with the same color as the quartz from the veins (e.g., Fig. 5.17B and 5.18B). The lack of stable isotope data makes it difficult to decipher the origin of these fluids (e.g., Cruset, 2019; Cruset et al., 2023; Herlambang and John, 2023; Muñoz-López et al., 2023). Usually, burial fluids provide darker colors or dull intensities, while meteoric fluids produce brighter responses (e.g., Stoppa et al., 2021). One option is that the fluids that precipitated the calcite and quartz came from the basement (hydrothermal) owing to the presence of quartz, but there is no evidence of penetrative and extensive fluid transfer between the basement and sedimentary lid; rather, quartz veins existing in the basement only penetrate in the cover for a short distance or become parallel to the unconformity (e.g., Fig. 5.27; Caldera, 2022). The abundant pressure-solution evidence in the Upper Cretaceous carbonates could be a more likely mechanism for fluid release to precipitate in both the rims of host-rock quartz and dolomite rims, but also in the porosity of the calcite veins. In addition, the brighter CL response of late fluids from the OFV veins points to late meteoric origin.

5.4.3. The age of the deformation in the ECM

The vast majority of U-Pb ages obtained from the vein samples of the ECM (41 of 45) are on the non-radiogenic Pb side of the Tera-Wasserburg diagrams (Tera and Wasserburg, 1972), and show no mixing between common and radiogenic Pb (e.g., Fig. 5.23D, 5.24A and annex 5). Hence, the U-Pb analyses from the ECM calcite samples are mainly dominated by the common Pb (Roberts et al., 2020), and hence have little geochronological significance. However, up to four ages from samples 19MG20 and 19MG43 (Fig. 5.10 for location) could be acceptable to be interpreted as maximum and minimum ages of deformation for the ECM, two of them showing statistically and internally consistent (Figs. 5.23B, E and 5.24C and D)

(e.g., Ring and Gerdes, 2016). The T2 necking vein from sample 19MG20 gave an age of 48.87±5.66 Ma showing pretty good correlation between the data, attested by a MSWD=1.4 (Fig. 5.23B), and it is the vein with the most elevated radiogenic Pb. A second and less robust age of 54.0±13.0 Ma (MSWD=2.2) arises from the strain shadow SH2, which has higher uncertainty (Fig. 5.23E). These cements are composed by fibrous calcite that precipitated in the boudinage neck areas, and should be considered syntectonic, hence recording the age of the main folding event in the ECM. Under CL, the fibrous calcite from T2 vein appears with slightly higher yellow brightness than the thick PFV vein from the same 19MG20 (Fig. 5.14D and F), maybe indicative of its slightly different composition.

Wayne and McCaig (1998) dated in 48 ± 2 Ma a series of syntectonic polymineralic veins and its altered wall rock in shear zones of the eastern termination of the Eaux-Chaudes thrust by Rb-Sr, and Jolivet et al. (2007) used $^{40}Ar/^{39}Ar$ in K-feldspar to date it in about 50 Ma, which are similar to those obtained for the syntectonic calcite veins in this study, placing the main deformation in the lower Eocene.

Younger ages were obtained from veins 3B and 4 from sample 19MG43. The clearly OFV thin 3B vein gave a not very precise but good data correlation age of 39.5 ± 15.4 Ma (MSWD=1.1) while the PFV vein (labelled as 4) arises a more precise age of 38.14 ± 5.99 (MSWD=1.4) (Fig. 5.24C and D), even though we cannot discard certain remobilization of the U homogenizing and partially re-equilibrating of the isotopic U-Pb system. Labaume et al., (2016b) discussed using tectono-sedimentary arguments that the Eaux-Chaudes thrust activity ended at ca. ~38 Ma, by which the age obtained, taking into account the error margin, is certainly close.

The mobility of Pb is considered inexistent for temperatures <300°C but could be higher if the rocks are subjected to temperatures over 400°C for long periods (>20Ma). On the other hand, the mobility of U is mainly assisted by fluids due to its solubility, enhanced at high

temperatures (Roberts et. al., 2020). The rocks from the ECM were heated at temperatures of about 300-360°C (Caldera et al., 2021; Caldera, 2022), but it is unlikely to have persisted for more than 20Myr in the Upper Cretaceous of the massif, and maybe the main reason of the high content of common Pb in all samples. The recrystallization process at moderately high temperatures that affected the Upper Cretaceous carbonates from the ECM (e.g., Fig. 5.15; Caldera, 2022) probably re-distributed the U and isotopically re-equilibrated it, a process that could be assisted by fluids hence behaving as an open system (e.g., Figs. 5.12, 5.13 and 5.24). However, in some areas where fluid was not pervasively circulating, the U-Pb system could have behaved locally as a closed system, registering the age of deformation of the ECM (e.g., Fig. 5.23B). In areas with evidence of fluid circulation (such as in DA1 site), it may deplete the PFV veins re-distributing the U (e.g., Fig. 5.24C and D). Maybe our analyzing strategy was unlucky to find U-rich areas to date because the U is known to be heterogeneously distributed across veins, vein phases and individual crystals (e.g., Drost et al., 2018; Roberts et al., 2020). Perhaps a of previous acquisition of compositional maps (e.g., Drost et al., 2018; Chew et al., 2021; Hoareau et al., 2021), it was possible to locate areas with higher U content and increase the effectivity of dating, but the large quantity of spots done in a same sample indicates that common Pb and U content is very high and very low, respectively, in our samples, and probably below the threshold sensibility of the U-Pb calcite geochronology method. Undoubtedly compositional maps could help us to know more about the U and Pb mobility in the carbonates of the ECM.

5.5. Main conclusions on the evolution of the deformation in the ECM

The calcite veins from the ECM registered the main thrusting and folding deformation event in the massif during the alpine orogeny under brittle-ductile conditions between the late Ypresian (48.87±5.66 Ma) and the early Bartonian (38.14 ± 5.99 Ma), constrained by the LA-ICP-MS U-Pb calcite geochronology.

As a kinematic indicator, the PFV calcite veins show a strong top-to-the-south sense of shear at the outcrop scale and microscale, especially in those veins where calcite precipitated in pressure shadows from the rigid grains of the host rock.

The Gourzy transfer zone accommodated the deformation between the western (recumbent fold) and the eastern (thrusting) sectors of the Eaux-Chaudes massif through a sinistral shear zone by which the recumbent fold domain was translated far south over the autochthonous than the structures developed in the eastern domain.

Veins in the Eaux-Chaudes massif are composed principally of blocky calcite (usually ductile deformed), although secondary quartz and dolomite that come from local fluids generated by the pressure-solution-assisted deformation of the Upper Cretaceous rocks of the massif also precipitated in the porosity of the veins. In addition, calcite is generally homogeneous under CL (dark-dull yellow), probably because of homogenization due to recrystallization. This homogenization could also be the cause of the abundance of common Pb observed in most of the geochronological analyses.

High-temperature twinning, dynamic recrystallization, and pressure solution are the main deformation mechanisms recorded by the veins in the Eaux-Chaudes massif, which are consistent with the macro- to micro-scale deformation recorded by the Upper Cretaceous that form the bulk of the massif (Caldera et al., 2021; 2023). Brittle cracking is less common to observe in calcite veins, but is better developed in the quartz- and dolomite-rich phase rocks.

I interpret that most of the veins orthogonal to the foliation (OFV) registered the onset of exhumation in the ECM on top of the Gavarnie thrust because they postdate the foliation-parallel veins (PFV) veins and mark a change in the main stress regime. Moreover, the mineral phases of these OFV veins were deformed under colder conditions than those parallel to foliation/S_{0-1}, and the evidence of brittle deformation is more common. The

cathodoluminiscence brighter yellow colors displayed by the calcite phase replacing dolomite and present in the vein walls and thin OFV veins, qualitatively point to the meteoric origin of the fluid, although a stable isotope study is necessary to confirm this hypothesis.

Chapter 6: Exhumation of the Eaux-Chaudes massif

Prior to Caldera et al. (2021), the Eaux-Chaudes massif (ECM) was classically interpreted as a duplex with a roof thrust carrying Paleozoic rocks over the Upper Cretaceous (Ternet, 1965; Déramond et al., 1985; Dumont et al., 2015; Cochelin et al., 2017). The previous low-temperature thermochronologic studies in the area were focused on the exhumation of the rocks outcropping in the Axial Zone culmination and its Upper Cretaceous cover, addressing the basement thrusting sequence that raised them (Bosch et al., 2016; Jolivet et al 2007; Morris et al., 1998; Labaume et al., 2016b). However, none of these studies considered the Upper Cretaceous of the ECM due to the calcareous nature of the massif that makes it difficult to obtain apatites and zircons to analyze for thermochronology. Based on apatite fission tracks and (U-Th)/He in apatites (AHe) and zircons (ZHe), Bosch et al. (2016) reported a pulse of exhumation from ~36-30 Ma (Eocene to Early Oligocene) related to the emplacement of the hanging wall of the Gavarnie basement thrust. Another pulse of exhumation from ~30-20 Ma was also defined by Bosch et al. (2016) in relation to the Guarga basement thrust.

The hot paleo-temperature record of the Iberian margin (e.g., Clerc, 2012; Cloix, 2017; Corre, 2017; Izquierdo-Llavall et al., 2020) and in particular the data obtained in the ECM by Caldera et al. (2021) suggest a complete reset of the ZHe and AHe systems. Therefore, the exhumation history could be possible to obtain from the analysis of detrital levels such as the Upper Cretaceous (mainly the Cenomanian) and Paleozoic (the Culm flysch outcropping in the Pic du Gourzy) and motivated the thermochronologic study presented in this chapter.

Furthermore, the basement-involved nappe stack and late normal faulting observed over the Eaux-Chaudes nappe (i.e., Montagnon d'Iseye (MIN), Cinq-Monts, Bois de la Traillère; Caldera, 2022) also needed the unraveling of the chronology and the temporal constraint of the nappe stack sequence. Hence, deciphering the exhumation history of the Eaux-Chaudes

massif and overlying nappe stack can provide clues to understand the collisional evolution of the West-Central Pyrenees and also of this particular structure.

6.1 Sampling methods

A total number of 35 samples were collected in the different structural units of the Eaux-Chaudes massif (s.l. autochthon, overturned fold limb, recumbent fold nappe core, normal limb, and upper sheets -MIN, Cinq-Monts and Chaînons-Béarnais Belt (CBB) units-) conforming vertical profiles where possible. From these, 11 were analyzed for low-temperature thermochronology. The location of each analyzed sample is shown in Fig. 6.1 (map view) and Fig. 6.2, Fig. 6.3 and Fig. 6.4 (section view), the results of ZHe ages are summarized in Table 6.1. Additionally, samples GPY09, GPY11 and GPY12 studied by Bosch et al. (2016) have been incorporated into this study (Table 6.2).

Four to six zircons per sample were analyzed for (U-Th)/He, which were obtained following the separation methodology described in Chapter 2. Only sample 22MG179 has 3 analyzed zircons, due to the loss of the fourth zircon during the unpacking process. After separation, we obtained no apatites suitable to perform AHe analysis, which we also intended originally. Only one apatite was found and analyzed for sample 22MG183 from the Bois de la Traillère unit.
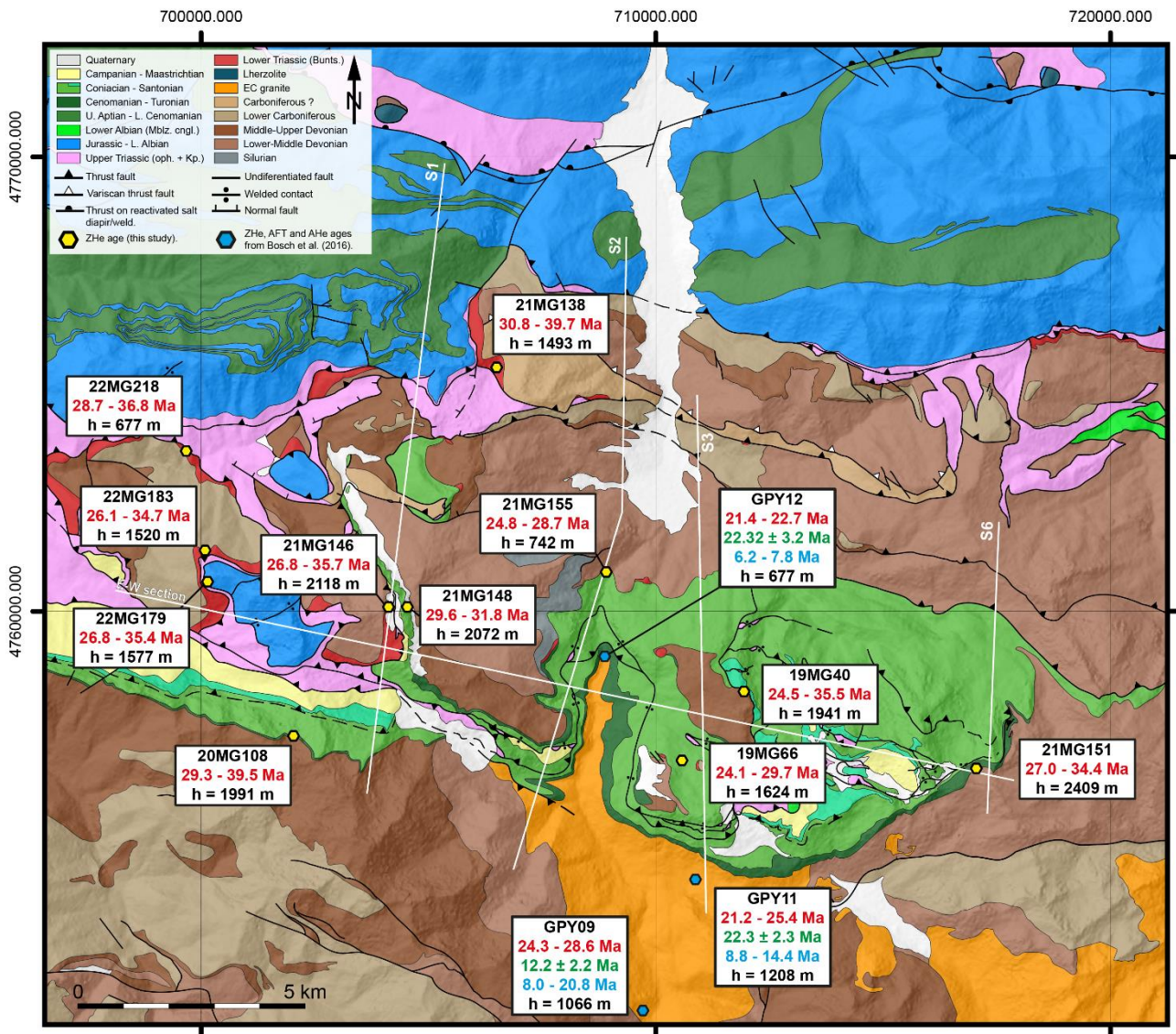
Figure 6.1. Geological map of the Eaux-Chaudes massif between the western Axial Zone (south) and the Chaînons Bearnais Belt (north), showing the location of the samples and the low-temperature thermochronological results. Zircon (U-Th)/He (ZHe) ages range are shown in red; Apatite fission track results from Bosch et al. (2016) in green; and apatite (U-Th)/He (AHe) from Bosch et al. (2016) in blue. Samples GPY09, GPY11 and GPY12 (used for QTQt modelling) were provided by Bosch et al. (2016).
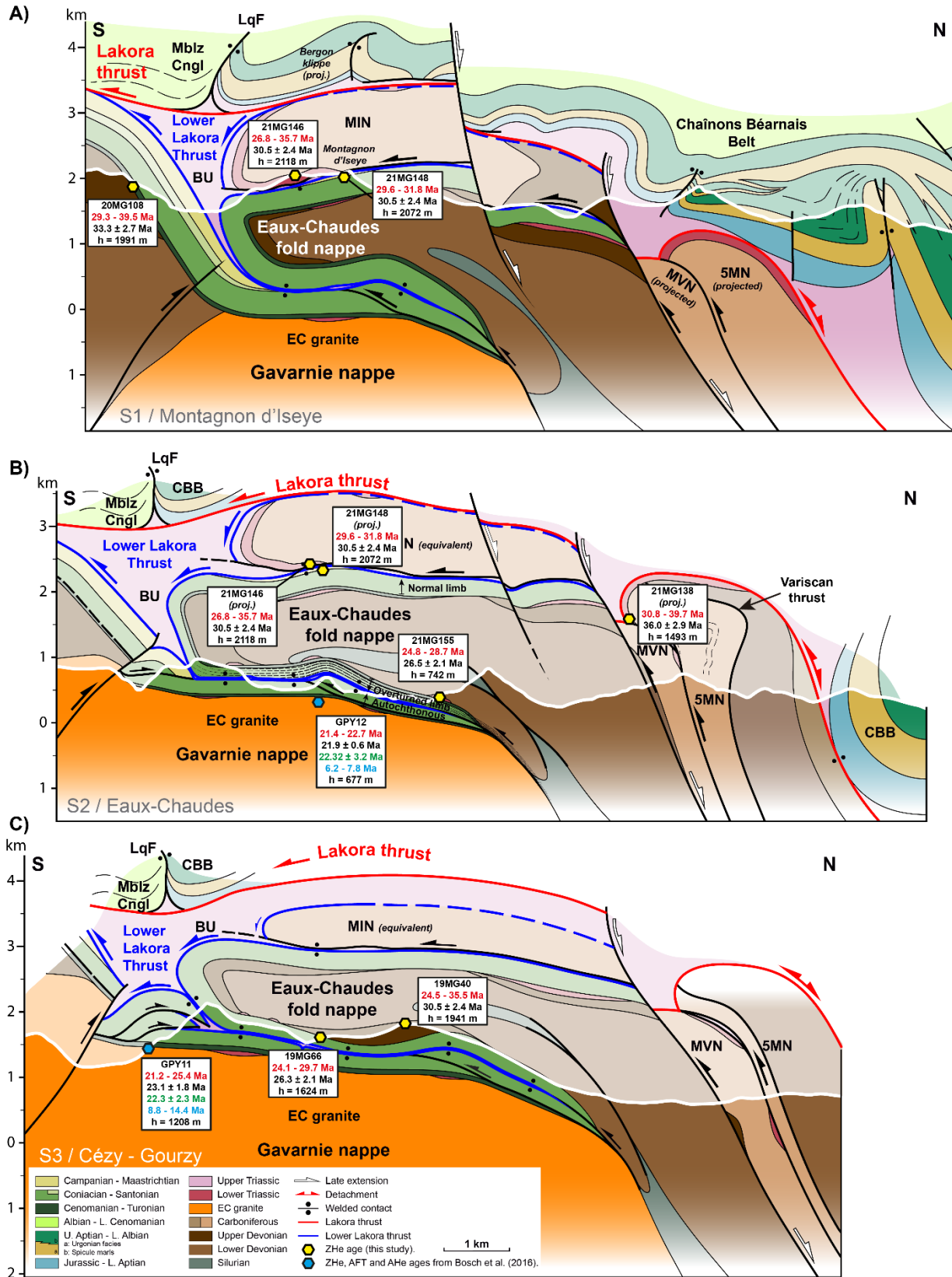
Figure 6.2: *Cross sectional projections of samples collected in the western Eaux-Chaudes massif (see location in Fig. 6.1). Sections modified after Caldera (2022). Mblz Cngl: Mendibelza Conglomerates; LqF: Licq Fault; MIN: Montagnon d'Iseye Nappe; 5MN: Cinq Monts Nappe; MVN: Montagne Verte Nappe; CBB: Chaînons Béarnais Belt; BU: Bedous Unit (carried by the Lower Lakora thrust).*
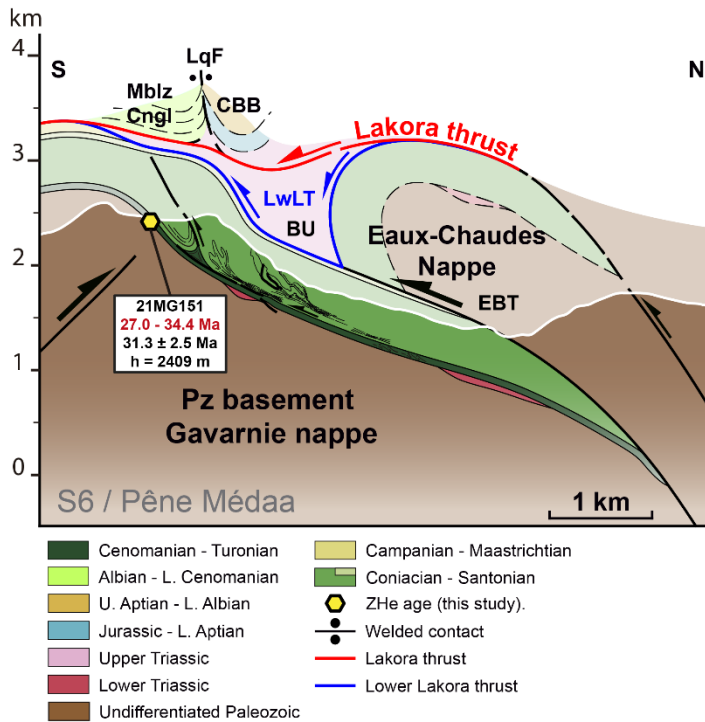
Figure 6.3: *Eastern section view of the samples collected in the ECM area.*

6.2 (U-Th)/He ages of the Eaux-Chaudes massif

6.2.1 Autochthon

Two samples of the autochthon were collected in the coarse-grained sandstones belonging to the lowermost Cenomanian, just above the Paleozoic unconformity at 1991 m (20MG108) and 2409 m (21MG151) of altitude (Table 6.1). These samples are located in the southernmost part of the ECM, which is affected by late N-S tilting and back-thrusting, probably related to the emplacement of the Gavarnie basement thrust (Dumont et al. 2015; Caldera et al. 2021) (Figs. 6.1-6.4).

Six zircon grains of sample 20MG108 were analyzed, yielding a range of uncorrected ages between 21.5 and 28.1 Ma, which correspond to a Ft corrected age (Farley et al. 1996) dispersion of 29.3 to 39.5 Ma and a mean age of 33.3 ± 2.7 Ma (Table 6.1). These observed single-grain ages could be grouped in a young population (29.3, 29.6, and 30.0 Ma) with essentially flat age-eU correlation and an older population (34.9, 36.8, and 39.5 Ma) that
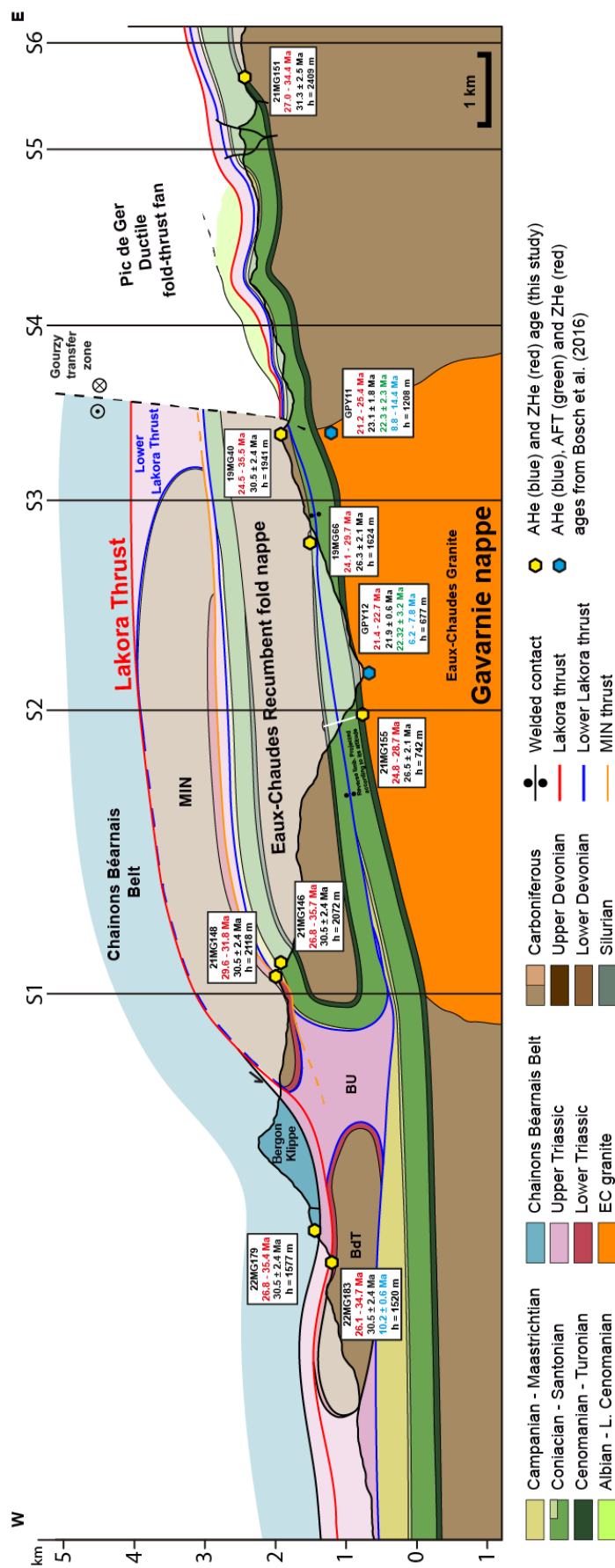
Figure 6.4: *E-W Geological cross-section of the Bois de la Traillère unit (BdT), the Eaux-Chaudes fold nappe (center), the ductile deformed Autochthon (east to the Gourzy transfer zone) and the overlying tectonic units (see location in Fig. 6.1) showing the location of samples and the thermocronological results from this study and from Bosch et al. (2016). Apatite (U-Th)/He results in blue, apatite fision track (AFT) in green and zircon (U-Th)/He in red. AHe and ZHe data are indicated by the intra-sample age range (red) and the mean together with the 1σ error (8%) in black. Sample 21MG155 is projected according to its altitude (yellow hexagon) and pointing to its structural position. S1 to S6 refer to the location of the N-S geological cross sections from Caldera et al. 2023 some of which shown in figures 6.2 and 6.3. Note the moderate west plunge of all the structure. Mblz Cngl: Mendibelza Conglomerates; MIN: Montagnon d'Iseye Nappe; BdT: Bois de la Traillère unit; CBB: Chaînons Béarnais Belt; BU: Bedous Unit (carried by the Lower Lakora thrust).*

seems to draw a sharp negative age-eU correlation. However, two single-grain ages (located around [eU] = 100 ppm; Fig. 6.5) each belonging to one of these populations could be considered to be part of the same population if we take into account the 1σ error bars (8%) (Fig. 6.5A).

On the other hand, four zircons of sample 21MG151 were analyzed giving a range of uncorrected ages of 21.4 to 26.4 Ma and a Ft corrected age dispersion of 27.0 to 34.4 Ma and a mean age of 31.3 ± 2.5 Ma (Table 6.1). Despite a slightly negative date-eU correlation is observed, the ages seem to be independent of the eU content, drawing a flat trend within the 1σ error (8%) of individual single-grain ages (Fig. 6.5A).

6.2.2 Recumbent limb

Samples 19MG66 and 21MG155 belong to the recumbent limb of the ECFN (Table 6.1). Sample 19MG66 was collected in the ductile deformed Cenomanian sandstones of the Cambeilh area, just a few meters topographically below of the Paleozoic unconformity of the fold nappe core, at 1624 m of altitude (Figs. 6.1, 6.2 and 6.4). Four zircons were analyzed, yielding an uncorrected age range of 19.7 to 25.6 Ma, an Ft corrected age dispersion of 24.1 to 29.7 Ma, and a mean age of 26.3 ± 2.1 Ma. Sample 21MG155 was collected in the conglomeratic to sandy Buntsandstein facies that delineates the contact between the recumbent limb of the structure and the Paleozoic core of the ECFN, outcropping south of Laruns at 742 m. The uncorrected ages of the six analyzed zircons range from 18.1 to 23.4 Ma, which corresponds to an Ft corrected age dispersion of 24.8 to 28.7 Ma and a mean age of 26.5 ± 2.1 Ma (Table 6.1). Neither positive nor negative correlation between single-grain ages and [eU] is observed, but flat trends for both samples are within the 1σ error (Fig. 6.5B).

Sample	Lat (°)	Long (°)	Altitude (m)	U (ppm)	Th (ppm)	^{147}Sm (ppm)	[U]e (ppm)	He (nmol/g)	Ft	Uncorrected Age (Ma)	Corrected Age (Ma±8%)	Mean Age (Ma±1σ)
19MG40 (6)	42.946839	-0.401917	1941	63.2	43.3	2.4	73.2	9.7	0.78	24.4	31.2 ± 2.5	30.5 ± 2.4
				148.9	76.9	2.3	166.6	22.4	0.81	24.8	30.8 ± 2.5	
				211.2	45.6	8.2	221.8	33.7	0.79	28.1	35.5 ± 2.8	
				67.9	30.2	2.7	74.9	10.6	0.80	26.2	32.9 ± 2.6	
				71.7	35.9	8.7	80.1	8.3	0.78	19.2	24.5 ± 2.0	
				96.4	55.8	5.2	109.3	12.7	0.77	21.4	27.8 ± 2.2	
19MG66 (4)	42.933009	-0.418792	1624	94.6	23.1	1.3	99.9	13.8	0.86	25.6	29.7 ± 2.4	26.3 ± 2.1
				154.7	39.9	1.0	163.9	18.0	0.77	20.3	26.4 ± 2.1	
				74.9	48.2	0.9	86.0	9.2	0.78	19.7	25.0 ± 2.0	
				112.6	35.7	0.0	120.8	12.9	0.82	19.8	24.1 ± 1.9	
20MG108 (6)	42.941124	-0.523648	1991	106.7	52.4	1.3	118.8	17.7	0.79	27.5	34.9 ± 2.8	33.3 ± 2.7
				50.3	37.9	5.6	59.1	8.9	0.71	27.9	39.5 ± 3.2	
				65.5	28.8	1.1	72.1	11.0	0.76	28.1	36.8 ± 2.9	
				85.0	39.0	1.6	94.0	11.3	0.74	22.1	30.0 ± 2.4	
				232.3	24.0	3.4	237.8	27.6	0.73	21.5	29.6 ± 2.4	
				169.0	40.0	1.3	178.2	21.4	0.76	22.2	29.3 ± 2.3	
21MG138 (6)	43.012381	-0.467341	1493	422.5	89.2	3.5	443.1	59.2	0.80	24.7	30.8 ± 2.5	36.0 ± 2.9
				493.4	163.3	5.1	531.0	77.6	0.79	27.0	34.0 ± 2.7	
				244.7	71.7	2.6	261.2	47.5	0.86	33.6	39.0 ± 3.1	
				270.6	85.1	3.0	290.2	51.9	0.83	33.1	39.7 ± 3.2	
				220.4	68.0	3.3	236.1	44.0	0.87	34.5	39.6 ± 3.2	
				206.4	58.5	1.0	219.8	30.3	0.77	25.5	33.2 ± 2.7	

Table 6.1 (continue)

164

Sample	Lat (°)	Long (°)	Altitude (m)	U (ppm)	Th (ppm)	147Sm (ppm)	[U]e (ppm)	He (nmol/g)	Ft	Uncorrected Age	Corrected Age (Ma±8%)	Mean Age (Ma±1σ)
21MG146 (5)	42.966044	-0.496751	2118	325.3	105.1	3.0	349.5	44.7	0.77	23.7	30.8 ± 2.5	30.5 ± 2.4
				242.1	81.9	3.0	261.0	35.8	0.80	25.3	31.5 ± 2.5	
				100.7	80.9	4.8	119.4	12.5	0.72	19.3	26.8 ± 2.1	
				134.8	74.6	2.5	152.0	17.7	0.78	21.5	27.5 ± 2.2	
				325.7	102.4	3.5	349.2	52.4	0.78	27.8	35.7 ± 2.9	
21MG148 (5)	42.968367	-0.493604	2072	176.4	34.0	0.9	184.2	23.0	0.78	23.1	29.6 ± 2.4	30.5 ± 2.4
				217.0	69.0	4.0	232.9	28.5	0.71	22.6	31.8 ± 2.5	
				43.1	21.5	1.1	48.0	6.4	0.81	24.6	30.3 ± 2.4	
				43.8	9.7	0.5	46.1	6.2	0.83	24.9	30.2 ± 2.4	
				290.9	29.4	1.7	297.6	38.6	0.79	24.0	30.6 ± 2.4	
21MG151 (4)	42.930715	-0.340270	2409	225.4	60.2	0.0	239.3	34.0	0.80	26.3	32.9 ± 2.6	31.3 ± 2.5
				364.8	113.0	1.2	390.8	52.3	0.80	24.8	31.0 ± 2.5	
				265.1	61.8	0.0	279.3	32.3	0.79	21.4	27.0 ± 2.2	
				67.6	60.7	0.0	81.6	11.7	0.77	26.4	34.4 ± 2.8	
21MG155 (6)	42.971306	-0.438404	742	352.9	81.1	1.2	371.6	37.8	0.76	18.8	24.9 ± 2.0	26.5 ± 2.1
				151.5	50.1	3.6	163.1	20.6	0.83	23.4	28.1 ± 2.2	
				439.4	108.7	1.6	464.4	50.4	0.74	20.1	27.3 ± 2.2	
				215.9	74.1	0.0	233.0	22.8	0.72	18.1	25.1 ± 2.0	
				420.5	130.2	14.9	450.5	55.4	0.79	22.7	28.7 ± 2.3	
				389.7	119.2	52.1	417.4	43.4	0.77	19.2	24.8 ± 2.0	

Table 6.1 (continue)

Sample	Lat (°)	Long (°)	Altitude (m)	U (ppm)	Th (ppm)	147Sm (ppm)	[U]e (ppm)	He (nmol/g)	Ft	Uncorrected Age (Ma±8%)	Corrected Age (Ma±8%)	Mean Age (Ma±1σ)
22MG179 **(3)**	42.973669	-0.546555	1577	179.1	83.4	0.0	198.3	19.5	0.62	18.1	29.4 ± 2.3	30.5 ± 2.4
				426.2	28.7	0.0	432.8	37.7	0.60	16.2	26.8 ± 2.1	
				876.6	602.0	0.0	1015.2	105.6	0.54	19.2	35.4 ± 2.8	
22MG183 **(4)**	42.978264	-0.545962	1520	418.0	128.6	0.0	447.7	55.2	0.67	22.8	33.8 ± 2.7	30.5 ± 2.4
				310.3	85.3	0.0	329.9	34.4	0.74	19.3	26.1 ± 2.1	
				683.5	140.6	0.0	715.9	75.2	0.72	19.5	27.2 ± 2.2	
				442.9	133.5	2.8	473.7	61.5	0.69	24.0	34.7 ± 2.8	
22MG218 **(4)**	42.996533	-0.547902	677	458.4	127.5	0.0	487.8	52.2	0.69	19.8	28.7 ± 2.3	33.2 ± 2.7
				240.4	89.1	0.0	260.9	35.0	0.67	24.8	36.8 ± 2.9	
				257.3	88.2	1.1	277.6	40.9	0.78	27.2	35.1 ± 2.8	
				513.6	118.1	0.0	540.8	64.8	0.69	22.2	32.0 ± 2.6	

Table 6.1: Zircon (U-Th)/He results. The number between parentheses in each sample identifier row is the number of zircons analyzed into an aliquot. FT is the geometric correction factor for age calculation. The age is yet corrected with FT factor and the uncertainty 1 σ was fixed at 8% of the age. The mean age is the pondered mean of the aliquot ages for each sample.

166

It should be noted that there is an altitude difference of 880 m between the last two samples, despite of this the age range is within the same time span, evidencing a N-S tilting (Figs. 6.1, 6.2 and 6.4).

Sample	Mineral	Altitude	Ft	Raw Age (Ma) ± 1σ	Corrected age (Ma) ± 1σ	Mean age (Ma) ± 1σ
GPY09	Zircon	1066	0.82	20.04 ± 1.0	24.3 ± 1.9	25.8 ± 2.0
			0.83	20.32 ± 1.0	24.4 ± 1.9	
			0.82	23.52 ± 1.2	28.6 ± 2.3	
GPY11	Zircon	1208	0.80	17.99 ±0.9	22.6 ± 1.8	23.1 ± 1.8
			0.80	16.86 ± 0.8	21.2 ± 1.7	
			0.79	19.96 ± 1.0	25.4 ± 2.0	
GPY12	Zircon	677	0.83	17.67 ± 0.9	21.4 ± 1.7	21.9 ± 0.6
			0.84	10.08 ± 0.9	21.5 ± 1.7	
			0.83	18.95 ± 0.9	22.7 ± 1.8	
GPY09	Apatite	1066	0.630	7.44 ± 0.1	11.81 ± 0.15	10.2 ± 6.1
			0.685	7.33 ± 0.11	10.69 ± 0.15	
GPY11	Apatite	1208	0.603	5.74 ± 0.08	9.52 ± 0.11	10.4 ± 3.0
			0.522	5.51 ± 0.09	9.88 ± 0.13	
			0.539	7.76 ± 0.11	14.39 ± 0.18	
			0.472	4.78 ± 0.09	10.11 ± 0.16	
GPY12	Apatite	677	0.735	4.86 ± 0.05	6.61 ± 0.06	6.56 ± 0.78
			0.673	4.17 ± 0.07	6.19 ± 0.08	
			0.675	4.43 ± 0.08	6.39 ± 0.09	
			0.538	4.22 ± 0.12	7.84 ± 0.14	

Table 6.2: *Zircon and apatite (U-Th)/He results by Bosch et al. (2016) from the Eaux-Chaudes pluton and implemented in the inverse thermal simulations (see text for explanation – section 6.2).*

6.2.3 Recumbent fold nappe core

The only sample of the core of the ECFN that provided zircons was 19MG40, collected in the Upper Devonian quarzitic sandstones of the Pic du Gourzy area at 1941 m (Fig. 6.1, 6.2 and Table 6.1). Six zircons were analyzed giving an uncorrected age span between 19.2 and 28.1 Ma and the highest Ft corrected age dispersion of 24.5 to 35.5 Ma corresponding to a mean age of 30.5 ± 2.4 Ma (Table 6.1). As it has been observed in the autochthonous samples (see section 6.2.1), an older age population (30.8, 31.2, 32.9, and 35.5 Ma) can be distinguished from a younger one (24.5 and 27.8 Ma), which seems to show an evident positive age-eU correlation (Fig. 6.5C).

6.2.4 Normal Limb

The normal limb of the Eaux-Chaudes fold nappe is represented by sample 21MG148, which was collected in the sandy limestones of Coniacian–Santonian age at an altitude of 2072 m in the Pic du Montagnon d'Iseye area (Fig. 6.1, 6.2 and 6.4). Five zircons of this sample were analyzed obtaining uncorrected ages ranging from 22.6 Ma to 24.9 Ma, which gives the less dispersed Ft corrected ages, ranging from 29.6 to 31.8 Ma corresponding to a mean age of 30.5 ± 2.4 Ma. The single-grain ages are strongly independent on the [eU] since there is no correlation between these variables, showing a flat trend (Fig. 6.5D).

6.2.5 Allochthonous upper sheets

Four allochthonous units above or in the surroundings of the ECFN were sampled with the intention to decipher their thrusting sequence (Montagnon d'Iseye nappe, Cinq-Monts, Bois de la Traillère and CBB units). They are all outcropping in the western sector of the ECM (Fig. 6.1, 6.2 and 6.4)

Just above the normal limb of the ECFN, Buntsandstein rocks of the recumbent limb of the MIN nappe (Caldera et al., 2021) were sampled at an altitude of 2118 m (21MG146). A total number of five zircons were analyzed giving an uncorrected age range of 19.3 – 27.8 Ma and an Ft-corrected age dispersion of 26.8 to 35.7 Ma, which corresponds to a mean age of 30.5 ± 2.4 Ma (Table 6.1). As observed in sample 19MG40 from the ECFN core, the single-grain ages seem to draw a positive date-eU correlation, although for the MIN sample is not that clear as for the ECFN since most of the single-grain ages could be considered as similar as they are within the 1σ error bars (Fig. 6.5E).
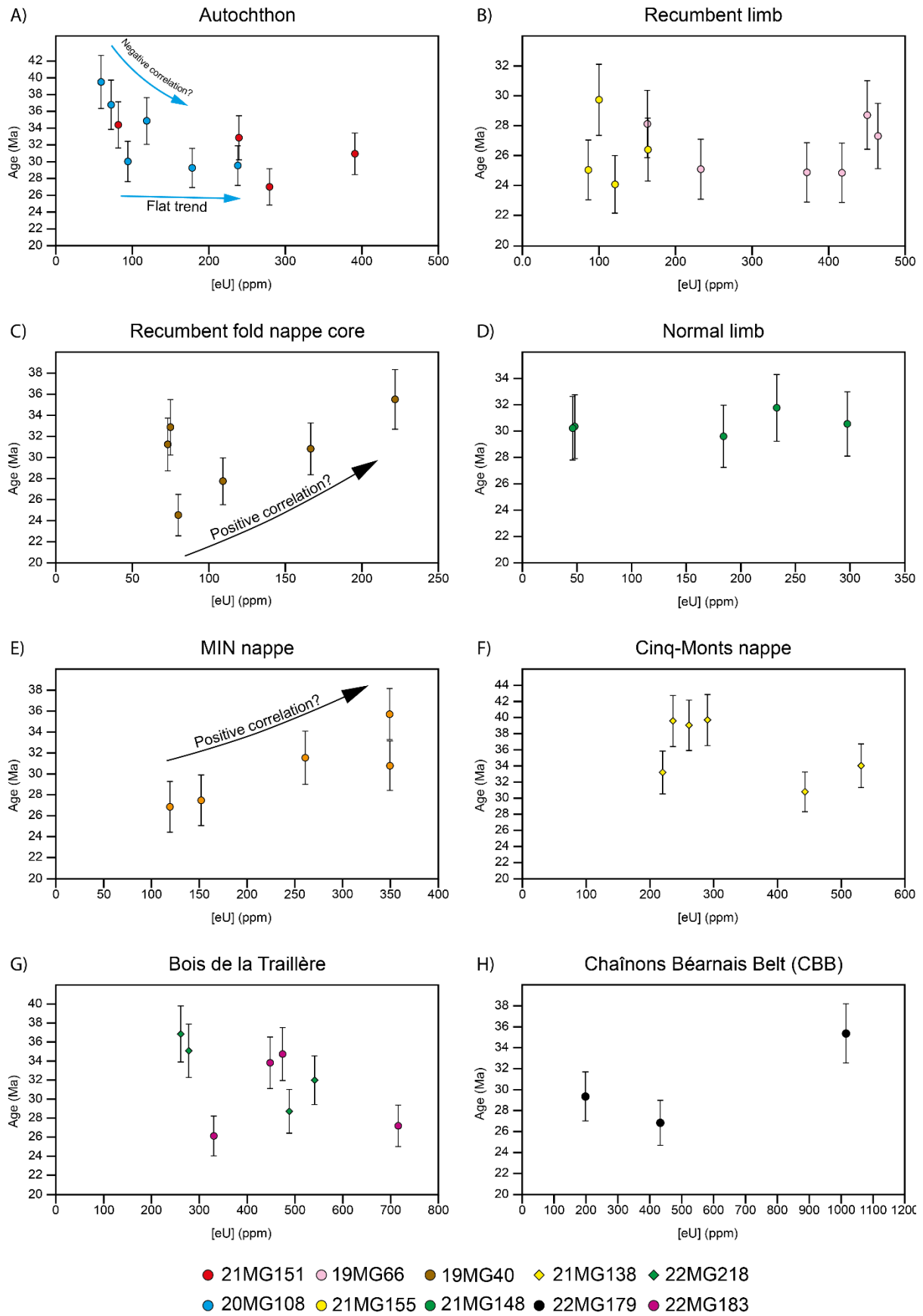
Figure 6.5: Single-grain age vs. [eU] relationship grouped for each structural unit of the ECM. The samples belonging to the Lakora (Buntsandstein) and the recumbent fold nappe core (U. Devonian sandstones) are drawing positive age-[eU] trend, while sample 20MG108 from the authochthonous seems to encompass an age population showing a negative age-[eU] trend.

Interpreted to be above the MIN nappe by Caldera (2022), the Cinq-Monts unit was also sampled (21MG138) in the Buntsandstein facies of the overturned limb at 1493 m (Figs. 6.1, 6.2 and 6.4). Six zircons were analyzed to obtain an uncorrected age span between 24.7 and 34.5, Ma that corresponds to a Ft-corrected age dispersion of 30.8 – 39.7 Ma, with no observed age-eU correlation, and a mean age of 36.0 ± 2.9 Ma (Fig. 6.5F). In addition, two well-differentiated (i.e., exceeding single-grain age error bars) age clusters are also observed, ranging from 30.8 to 34.0 Ma and a little dispersed one between 39.0 and 39.7 Ma (Table 6.1). An interesting fact to point out is that despite it is topographically below the Lakora nappe in the present day, this sample has given the oldest age (Fig. 6.2).

Westwards to the Lakora and Cinq-Monts units, two more samples were collected in the Buntsandstein facies to decipher if the Bois de la Traillère Paleozoic massif belongs to MIN unit or should be considered as independent, since this unit appears to be isolated from the Lakora by a N-S structure delineated by allochthonous Keuper rocks belonging to the CBB (Fig. 6.1). On one hand, sample 22MG183 was collected just below the CBB unit, at an altitude of 1520 m. Four zircons were analyzed yielding uncorrected ages from 19.3 to 24.0 Ma which corresponds to a Ft corrected age dispersion of 26.1 to 34.7 Ma and a mean age of 30.5 ± 2.4 Ma (Table 6.1; Fig.6.1). As it was observed in samples 20MG108 or 19MG40, an older population (33.8 and 34.7 Ma) could be isolated from a younger one (26.4 and 27.2 Ma). However, there is no clear positive nor negative relationship between the age and the [eU] content, since the 1σ error bars are overlapped between single-grain ages (Fig. 6.5G). Additionally, the only apatite of this work was found in this sample, which yielded an uncorrected age of 4.9 Ma and a Ft corrected age of 10.2 Ma. Being the only apatite in the

entire set of samples of this study, it makes a comparison difficult, but this age lies within the same range as the Bosch et al. (2016) apatite samples from the Eaux-Chaudes pluton (GPY09 and GPY11).

On the other hand, sample 22MG218 was collected in the Buntsandstein outcropping to the north to the former, at an altitude of 677 m. Four zircons were analyzed giving uncorrected ages from 19.8 to 27.2 Ma, which corresponds to a range of Ft-corrected age dispersion of 28.7 to 36.8 Ma and a mean age of 33.2 ± 2.7 Ma. The same old (32.0, 35.1, and 36.8 Ma) and young (28.7 Ma) populations are observed, but there is no clear relationship between age and [eU] since the 1σ error (8%) is overlapped, although the single-grain ages seem to draw a slight negative trend (Fig.6.5G).

Finally, the Chaînons Béarnais Belt unit (CBB) was sampled in the Jurassic carbonates materials in a small sandy level at an altitude of 1577 m (22MG179). In principle, there were little expectations to obtain zircons of this level due to the predominantly calcareous nature of the sediment. However, three zircons of this sample could be analyzed, to obtain a range of uncorrected ages between 16.2 and 19.2 Ma which gives an Ft corrected age dispersion of 26.8 and 35.4 Ma and a mean age of 30.5 ± 2.4Ma. This age is quite similar to the samples from Bois de la Traillère unit (22MG218), the MIN unit (21MG146), and the normal limb of the ECFN (21MG148) (Figs. 6.1, 6.2, and 6.4). In addition, an older population (35.4 Ma) is also distinguishable from a younger one (26.8 and 29.4 Ma) which together draws a positive age-eU trend (Fig. 6.5H), as also observed in the ECFN Paleozoic core and the MIN.

It is key to point out that sample 22MG218 is topographically below samples 22MG183 and 22MG179, which is recording a similar situation to that observed between the sample 21MG138 (Cinq-Monts unit) and the samples 21MG146 and 21MG148 (MIN and Normal Limb

structural units), where the topographically bottom samples are giving older ages than those located at higher altitudes.

In general, the range of ages obtained for the samples in this study shows a dispersion between 8-10 Ma, except for samples 19MG66 (5.6 Ma, recumbent limb), 21MG155 (3.9 Ma, recumbent limb) and 21MG148 (2.2 Ma, normal limb) (Table 6.1).

Finally, single-grain ages from all samples are independent of the grainsize, since there are no observed trends for any of them (Fig. 6.6).

6.3 Inverse thermal modelling

The collected samples from the different structural units in the ECM can be grouped in vertical profiles that provide clues to decipher the exhumation and the paleotemperature evolution of the ECM with time. In addition, the combined apatite and zircon He (AHe; ZHe) and fission track (AFT) age data from the Eaux-Chaudes pluton samples GPY09, GPY11, and GPY12 from Bosch et al. (2016) have been included in the simulations.

Because the ECM has been affected by late back-thrusting and normal faulting that disrupted the original structural position of some units, three main vertical profiles have been constructed, discarding those samples affected by this late activity. Hence, each vertical profile is considered to represent a coherent structural unit in terms of exhumation, with neither major disruptions nor internal relative displacement. In this way, the three main vertical profiles constructed in the ECM area are (some of them share samples):

- East profile (EPT): Samples 19MG40, 19MG66, GPY09 and GPY11.
- West profile (WPT): Samples 21MG146, 21MG148, 21MG155 and GPY12.
- E-W profile (GPT): Samples 19MG40, 19MG66, 21MG146, 21MG148, 21MG151, 21MG155, GPY11 and GPY12.

Although sample GPY09 may be affected by the back-thrusting, it has been initially included in the East profile because of its use in Bosch et al (2016) and also due to the availability of apatite (U-Th)/He and fission track data. It will be further discussed in section 6.3.3.

Inverse thermal modelling was performed using QTQt software (Gallagher, 2012; Gallagher et al., 2009). The (U-Th)/He ages obtained and those provided by Bosch et al. (2016) were modelled considering the diffusion of He as a spherical domain (based on the crystal's equivalent spherical radius) and eU-dependent radiation damage diffusivity for He diffusion following the models of Flowers et al. (2009) for apatite (AHe) and Guenther et al. (2013) for zircon (ZHe). In addition, the AFT data from sample GPY11 (the only with confined track lengths) was modelled following the Ketcham et al. (2007)'s multikinetic annealing model, with the D_{par} parameter as a kinetic constraint (Bosch et al. 2016). Each single model was run for 300.000 iterations and rejecting proposed models that doesn't improve the data fit option, following recommendations from Abbey et al. (2023).

The modelling results presented here are those that well represent the exhumation history of the Eaux-Chaudes massif after systematic runs presented in Figs. 6.7-6.12 and annexes, where the LA-ICP-MS U-Pb calcite age constraint of 48±5 Ma (tentatively assumed as the thermal peak; named –NCC) and the geothermal gradient between the top and bottom samples (high-low, fixed-variable) were tested. Regarding the latter, the thermal gradient in simulations was defined to a range between 15 and 35 °C/km (low geothermal gradient) or between 25 and 45°C/Km (high geothermal gradient), which can be fixed or variable with time depending on the simulation. In addition, because of the possible presence of two age populations observed in some samples (Table 6.1 and Fig.6.5), I also tested the resampling

of each single-grain age by a normal distribution based on the observed age with a standard deviation equal to the input error.

Due to the observable field geology (unconformity between the E-C pluton and the Cenomanian carbonates), all simulations were forced to be at surface in Cenomanian times and also in the present day.

6.3.1 East Vertical Profile (EPT)

Representative simulations of the forward models corresponding to the east vertical profile (EPT; samples 19MG40, 19MG66, GPY09 and GPY11, location in Figs. 6.1 and 6.2C) with the calcite age constraint (48 ± 5 Ma) are shown in Fig. 6.7. This figure uses the observed uncorrected ages for low and high variable geothermal gradients (Fig. 6.7A-D), and also the resampling of the uncorrected ages for low and high variable geothermal gradients (Fig.6.7E-H). For visualization purposes, the altitude of single-grain ages belonging to each sample is a little distorted by the QTQt software (Fig. 6.7B, D, F, and H). Simulations with fixed high and low geothermal gradients can be found in the annexes.

The QTQt software predicts the thermochronological ages of the samples coupling the (U-Th)/He data and the sample elevation within a profile. The AHe and ZHe ages are in general well predicted compared to the observed ages, with no significant differences between model runs (Fig.6.7B, D, F, and H). However, the older single-grain ages of the top sample (19MG40) are those with the worst prediction, which occurs in all simulations no matter the variable tested (Fig. 6.7 and annexes). This could be an indication that the presence of two age clusters (and also a positive age-eU correlation) could belong to different events. In addition, the AFT age from GPY09 sample is also not well predicted, as in Bosch et al. (2016).

The resampling of the ages (Fig. 6.7D and F) is not affecting significantly the age prediction, but it slightly improves the prediction of the old single-grain ages of sample 19MG40. The

modelled AHe and ZHe age-elevation profiles possess a slightly negative but essentially vertical trend, especially in the samples below 1.8 km elevation, and the single-grain ages from 1.8 km upwards are always showing a clear negative path. This observation is also observed in both low and high fixed geothermal gradient simulations (see annexes).

The time-temperature (T-t) profiles in the east of the ECM are always showing constant and precise (i.e., small 95% credible interval area) heating of ~6°C/Ma (independent on the geothermal gradient), as it is attested by the 95% credible interval. The samples overtake the apatite partial retention zone (APRZ), the apatite partial annealing zone (APAZ), and the zircon partial retention zone (ZPRZ) progressively, reaching the maximum temperatures of 300°C-340°C at ~50Ma (Lower Eocene) according to the U-Pb constraint (Fig. 6.7A, C, E and G). From this point onwards two general cooling T-t paths can be observed, also for fixed geothermal gradient (see annexes).

On one hand, simulations which trace a continuous and precise cooling path at ~8°C/Ma until ~20 Ma (Early Miocene), where the cooling is relaxed to ~2°C/Ma until the present day (e.g., model EPT_16; Fig. 6.7G), and on the other, simulations showing a more or less steady and imprecise cooling path at ~1.5-6.5°C/Ma, followed by a sudden and fast cooling path (~16-39°C/Ma) at ~30Ma (e.g., model EPT_04; Fig 6.7A). A slight variant of the latter can be identified, showing a constant and little precise cooling (~16°C/Ma) followed by a small period of faster cooling at ~30Ma (e.g., model EPT_12; Fig. 6.7E). In any case, the general trend of the latter models is considered to be the same. From this point to the present day the cooling is modelled as precise and constant at ~2-4°C/km.
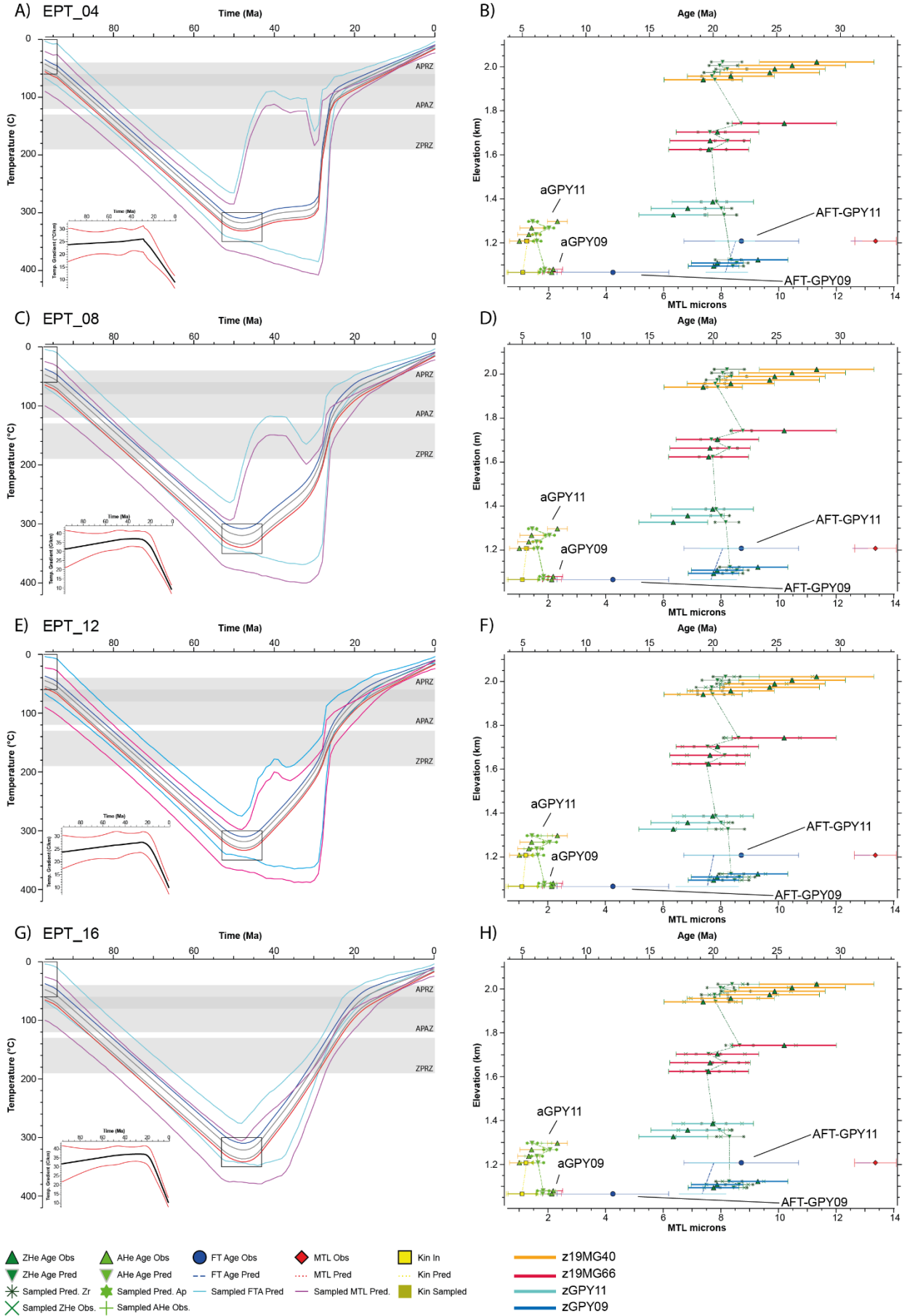
Figure 6.7: Representative thermal simulations for the East vertical profile. **A-D)** *modelled T-t path, geothermal gradient, and age-elevation profiles of the observed ages (uncorrected) for low (A and B) and high (C and D) geothermal gradients.* **E-H)** *modelled T-t path, geothermal gradient, and age-elevation profiles of the resampled ages (uncorrected) for low (E and F) and high geothermal gradients (G and H). MTL: Mean track lengths; Red and blue curves correspond to the bottom (warm) and top (cold) samples together with their 95% credible interval; APRZ: Apatite partial retention zone; APAZ: Apatite partial annealing zone; ZPRZ: Zircon partial retention zone.*

Removing the calcite age constraint (Fig. 6.8) does not significantly change the prediction of the ages, especially in what regards to the AHe ages, which show essentially the same prediction as those observed using the age constraint (Fig. 6.7). Both ZHe and AHe ages are in general well predicted, except for the top single-grain ages of the top sample (19MG40) and the AFT age of sample GPY09, as aforementioned.

In contrast, the absence of the calcite age constraint does clearly change the thermal histories, especially during the modelled burial which turns into poor unprecise paths until approx. 30Ma (Fig. 6.8A, C, E and G). The deepening (or increase of temperature) of the samples is constant in all simulations under ~3-4°C/Ma rate until ~35-40Ma, where predicted maximum temperatures of ~270-290°C are reached (above the range of the ZPRZ) no matter the geothermal gradient or the resampling of the ages.

However, maximum temperatures of 380°C could be attained due to the poor precision of the paths. In the same way, colder conditions could also be possible even until 40Ma followed by a moderate to fast burial (Fig. 6.8), which prevents the top samples from going above the ZPRZ. Once the maximum temperature (i.e., burial) has been reached, there is a quick cooling (8-12°C/Ma) between ~40Ma and ~20Ma, after which it slows down (2-3°C/Ma) until the present day (Fig. 6.8).
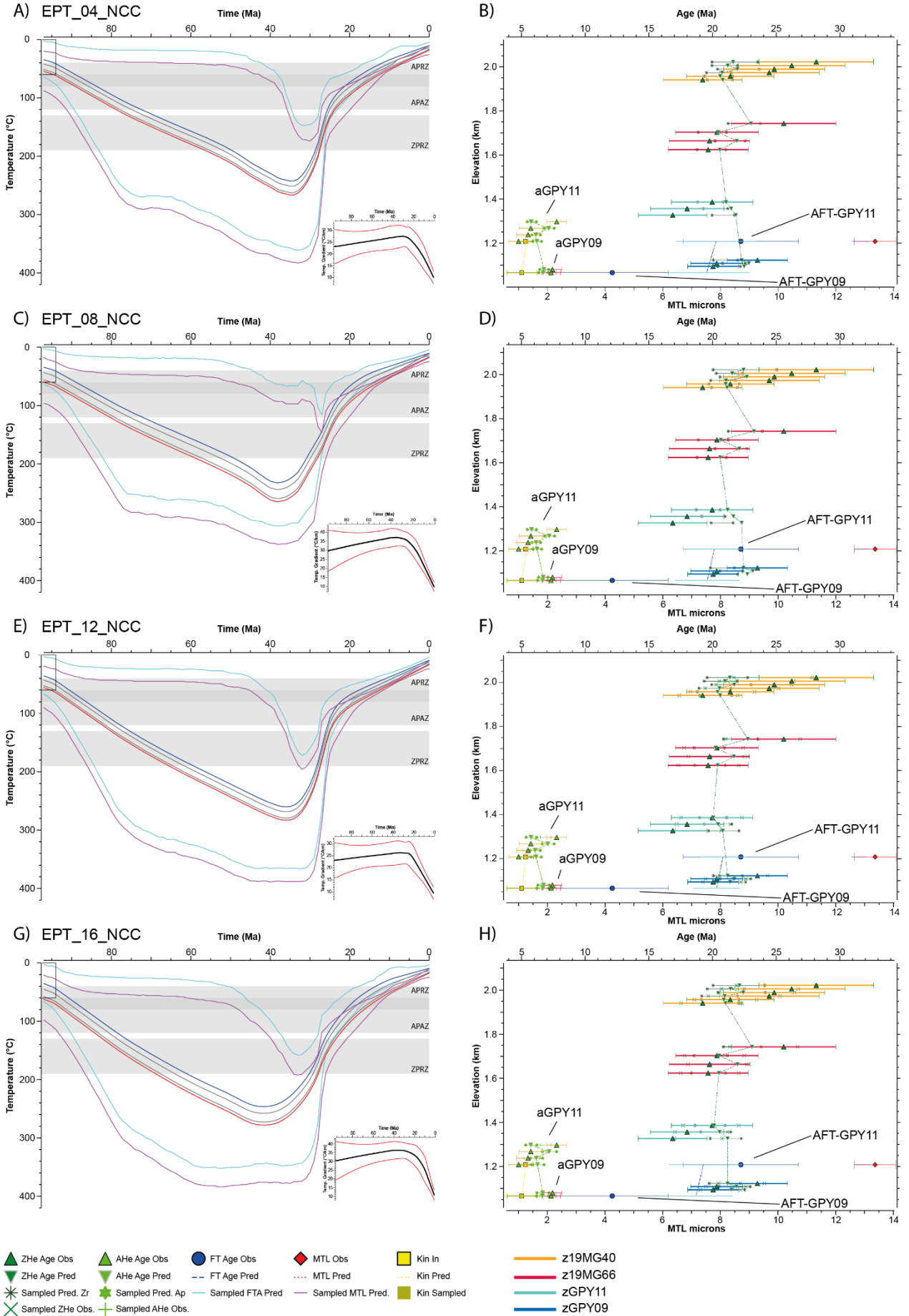
Figure 6.8: *Representative thermal simulations for the East vertical profile without the calcite age constraint.* **A-D)** *modelled T-t path, geothermal gradient, and age-elevation profiles of the observed ages (uncorrected) for low (A and B) and high (C and D) geothermal gradient.* **E-H)** *modelled T-t path, geothermal gradient, and age-elevation profiles of the resampled ages (uncorrected) for low (E and F) and high geothermal gradient (G and H). MTL: Mean track lengths; Red and blue curves correspond to the bottom (hot) and top (cold) samples together with their 95% credible interval; APRZ: Apatite partial retention zone; APAZ: Apatite partial annealing zone; ZPRZ: Zircon partial retention zone.*

Finally, in all simulation cases presented here, the variable geothermal gradient is drawing the same general path, increasing until reaching its maximum value at ~40-30Ma and then decreasing until the present day (Figs.6.7 and 6.8).

6.3.2 West Vertical Profile (WPT)

The forward modeling simulations from the West vertical profile (samples 21MG146, 21MG148, 21MG155 and GPY12, location in Figs. 6.1 and 6.2B) including the calcite age constraint (48 ± 5 Ma) are shown in Fig. 6.9. This figure uses the uncorrected ages for low and high variable geothermal gradients (Fig. 6.9A-D), and the resampling of the uncorrected ages for low and high variable geothermal gradients (Fig.6.9E-H). Simulations with high and low fixed geothermal gradients can be found in the annexes.

As observed in the East profile, the single-grain ages are in general well predicted no matter whether the geothermal gradient or the resampling method were used. Indeed, these predictions seem to be better than those of the East since the predicted ages are always within the error bars of the observed age (Fig. 6.9B, D, F, and H). Despite a slightly positive correlation that could be reasonably deduced (especially between the bottom and the top samples), these modelled AHe and ZHe profiles are essentially vertical, as the observed in the eastern profile, which could be indicative of a fast cooling of the massif (Fig. 6.9).
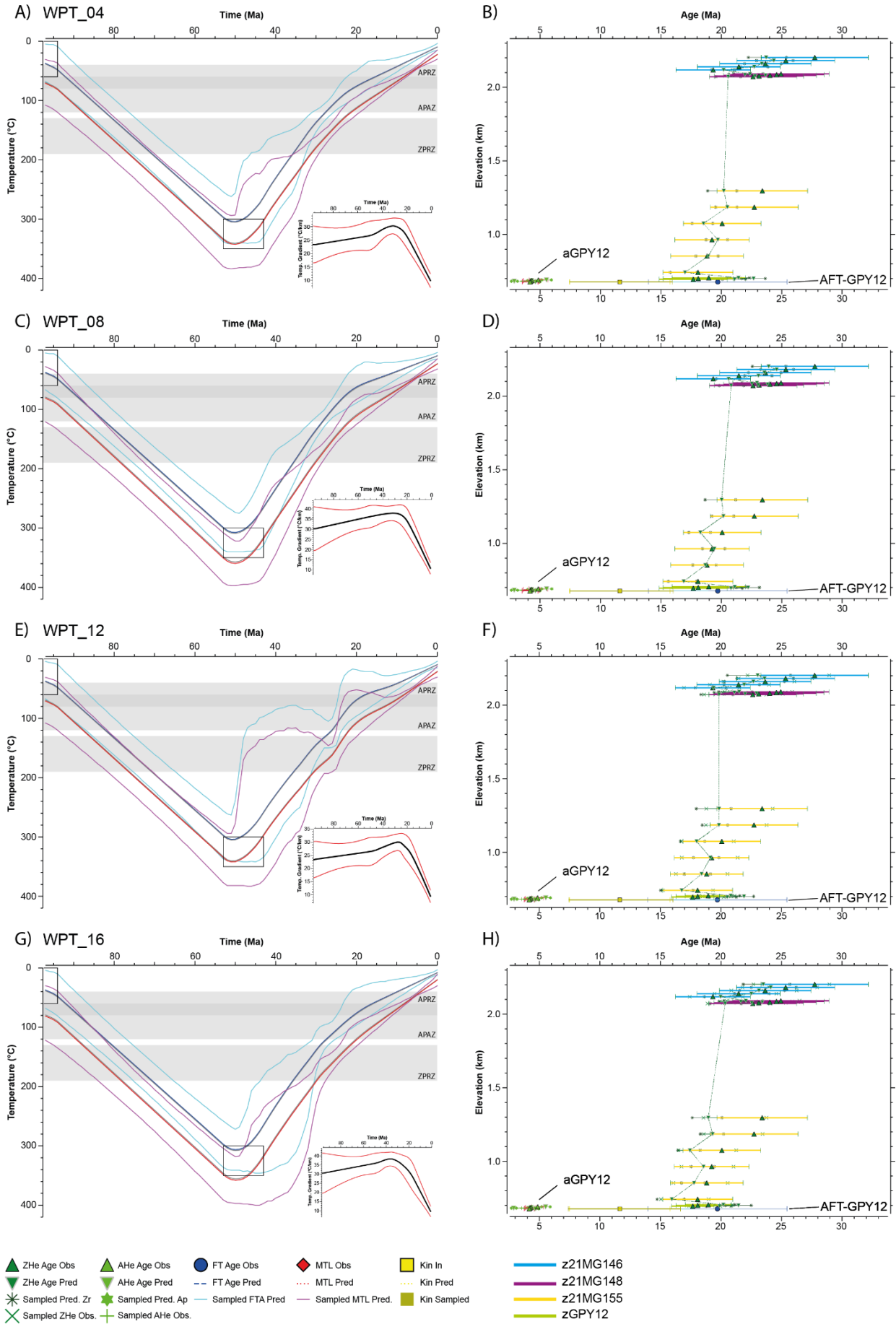
Figure 6.9: *Representative thermal simulations for the West vertical profile. **A-D)** modelled T-t path, geothermal gradient, and age-elevation profiles of the observed ages (uncorrected) for low (A and B) and high (C and D) geothermal gradient. **E-H)** modelled T-t path, geothermal gradient, and age-elevation profiles of the resampled ages (uncorrected) for low (E and F) and high geothermal gradient (G and H). MTL: Mean track lengths; Red and blue curves correspond to the bottom (hot) and top (cold) samples together with their 95% credible interval; APRZ: Apatite partial retention zone; APAZ: Apatite partial annealing zone; ZPRZ: Zircon partial retention zone.*

The heating of the samples is similar to the east profile (~6°C/Ma), no matter the geothermal gradient or the resampling, and shown as continuous and precise until maximum temperatures of 300-360°C (above the ZPRZ) depending on the sample (Fig. 6.9). What changes with respect to the east are the cooling paths, as in the western case they are continuous at ~8°C/Ma and much more precise until ~20Ma, regardless the geothermal gradient. From this point onwards the cooling rates are shown more relaxed (~3°C/Ma), but slightly less than in the east (Fig.6.8). The geothermal gradients follow the same trend than in the east, increasing until 40-30Ma and then decreasing until the present day.

Both the age-elevation profiles and thermal histories modelled without calcite age constraints are showing the same features than those of the east. The modelled age-elevation profiles do not vary significantly removing the calcite age constraint, and also draws vertical trends between samples which are well predicted in comparison with the observed (Fig.6.9B, D, F and H).

On the other hand, the thermal histories show continuous and little precise heating or burial histories at ~3-4°C/Ma, until maximum temperatures of ~260°C and ~220°C are reached by the lowermost sample (red curves in Fig. 6.10) ~by the uppermost sample (blue curves in Fig. 6.10),respectively, and always above the ZPRZ. However, maximum temperatures of 340-350°C could be possible, due to the amplitude of the 95% of credible value range (e.g., model WPT_16; Fig.6.10G). Such a thermal peak would occur at ~40-45 Ma, slightly later than the calcite age
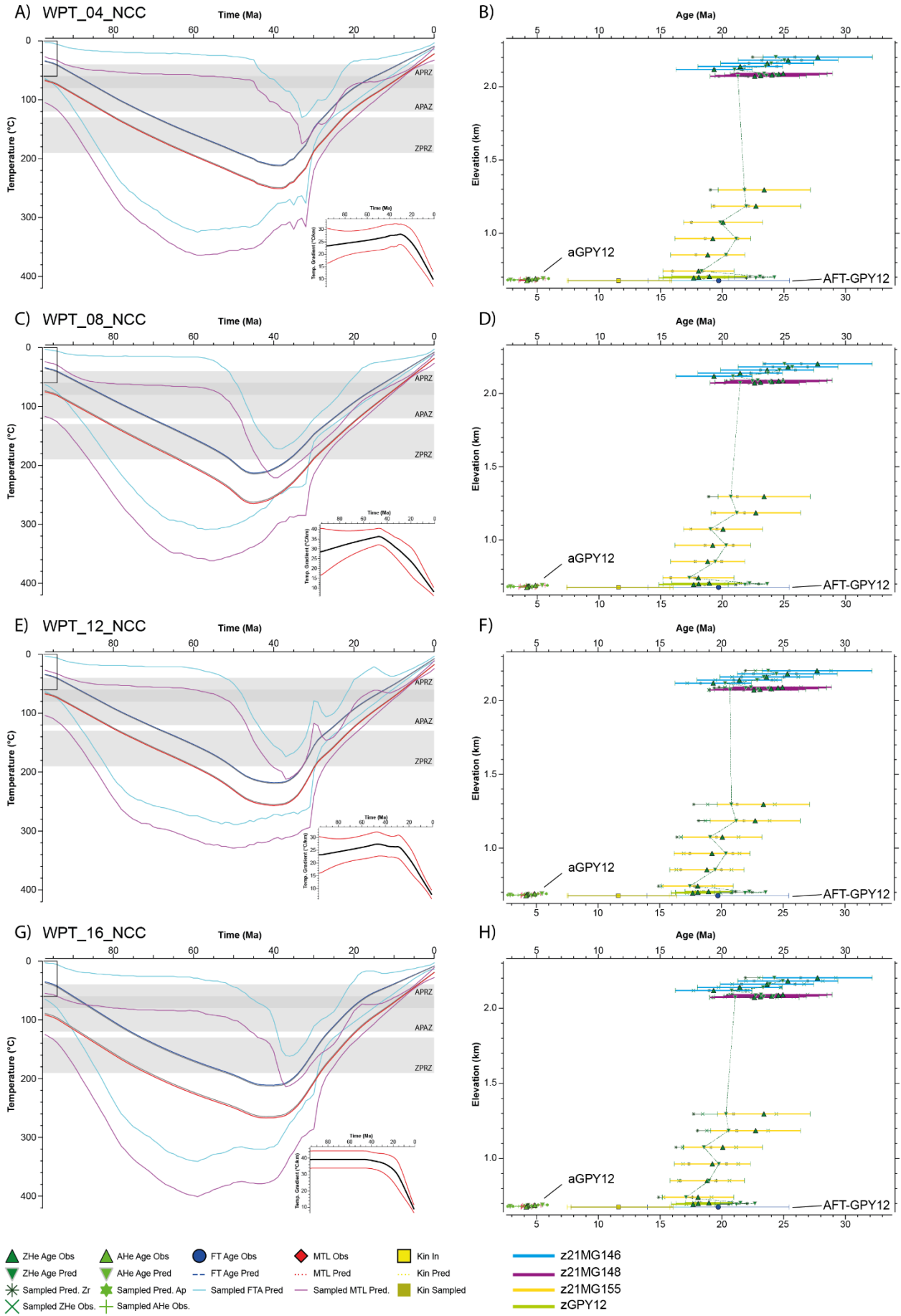
Figure 6.10*: Representative thermal simulation results for the West vertical profile without calcite age constraint.
A-D) modelled T-t path, geothermal gradient, and age-elevation profiles of the observed ages (uncorrected) for
low (A and B) and high (C and D) geothermal gradients. **E-H)** modelled T-t path, geothermal gradient, and age-
elevation profiles of the resampled ages (uncorrected) for low (E and F) and high geothermal gradient (G and
H). MTL: Mean track lengths; Red and blue curves correspond to the bottom (hot) and top (cold) samples
together with its 95% credible interval; APRZ: Apatite partial retention zone; APAZ: Apatite partial annealing
zone; ZPRZ: Zircon partial retention zone. Prefix z refers to a zircon sample, a to apatite sample, and AFT to
apatite fission track.*

constraint.

The predicted cooling histories are shown just as precise and constant as those without
calcite constraint, despite some modelled paths showing a relaxation in the cooling history at
20Ma (e.g., models WPT_04_NCC and WPT_16_NCC in Fig. 6.10)

6.3.3 E-W vertical Profile (GPT)

The last set of forward modelling simulations (including age constraint) belong to the E-W
vertical profile (samples 21MG146, 21MG148, 21MG155, GPY12, 19MG66, GPY11, 19MG40
and 21MG151; location in Figs. 6.1 and 6.4), and are presented in Fig. 6.11, using the
uncorrected ages (A-D) and the resampling of the uncorrected ages (E-H) for a low and high
variable geothermal gradient.

As observed in the east and west profiles, the single-grain AHe and ZHe ages are well
predicted regardless of the geothermal gradient or the resampling of the age. Also, the top
ZHe single-grain ages of sample 19MG40 and the bottom ZHe single-grain ages of sample
GPY11 are those with the worst prediction with respect to the observed ages, although a
significant enhancement in age predictions is observed for sample 19MG40. The key
difference with respect to the east and west vertical profiles is the trend drawn by the ZHe
and the AFT age-elevation path. While in the two former profiles, the trend is shown
essentially vertical, in the E-W profile shown in Figure 6.11 it takes on a positive trend.

The modelled thermal histories share the same features in the east and west profiles in regards to the heating histories, being continuous and precise at a heating rate of 4.5-6°C/Ma until the achievement of the maximum temperatures of 340-370°C in Early Eocene times. Then, the cooling starts with less precision up to ~30-35, Ma where it improves until the end. The whole cooling remains more or less homogeneous at a mean rate of 9°C/Ma until ~20 Ma, despite some simulations (such as for example GPT-08 or GPT-12) show a slight cooling sharpening at 30-35 Ma (Fig. 6.11). In addition, the geothermal gradients increase also until ~20Ma, where they drop until the present day. From that point onwards all thermal histories show a flat trend at cooling rates of ~1°C/Ma.

The prediction of the AHe and ZHe ages with no calcite age constraint is similar to where it was used, except for the top single-grain ages of the sample 19MG40 which it is slightly better (Fig. 6.12). Also, the ZHe age-elevation profiles show positive trends regardless of the geothermal gradient or the resampling of the ages, and the AHe age-elevation profiles are also vertical (Fig. 6.12).

The modelled thermal histories are not different from those of the west and east profiles in what concerns the heating of the samples, showing continuous and poor path heating at ~3°C/Ma up to ~40Ma, where maximum temperatures of ~270-290°C are reached.

However, the cooling histories (with better precision) are shown staggered in all simulations, which is a feature not observed in the former profiles (Figs. 6.7-6.11). This period encompassing from ~40Ma to ~20Ma is characterized by two fast cooling episodes at 11-30°C/Ma with relaxed cooling episodes in between at lower rates of 2-6 °C/Ma or 2-9°C/Ma if the simulation GPT-16-NCC is considered to belong to this group. From ~20Ma onwards the cooling is flat at a rate of ~0.5-2°C/Ma (Fig. 6.12).
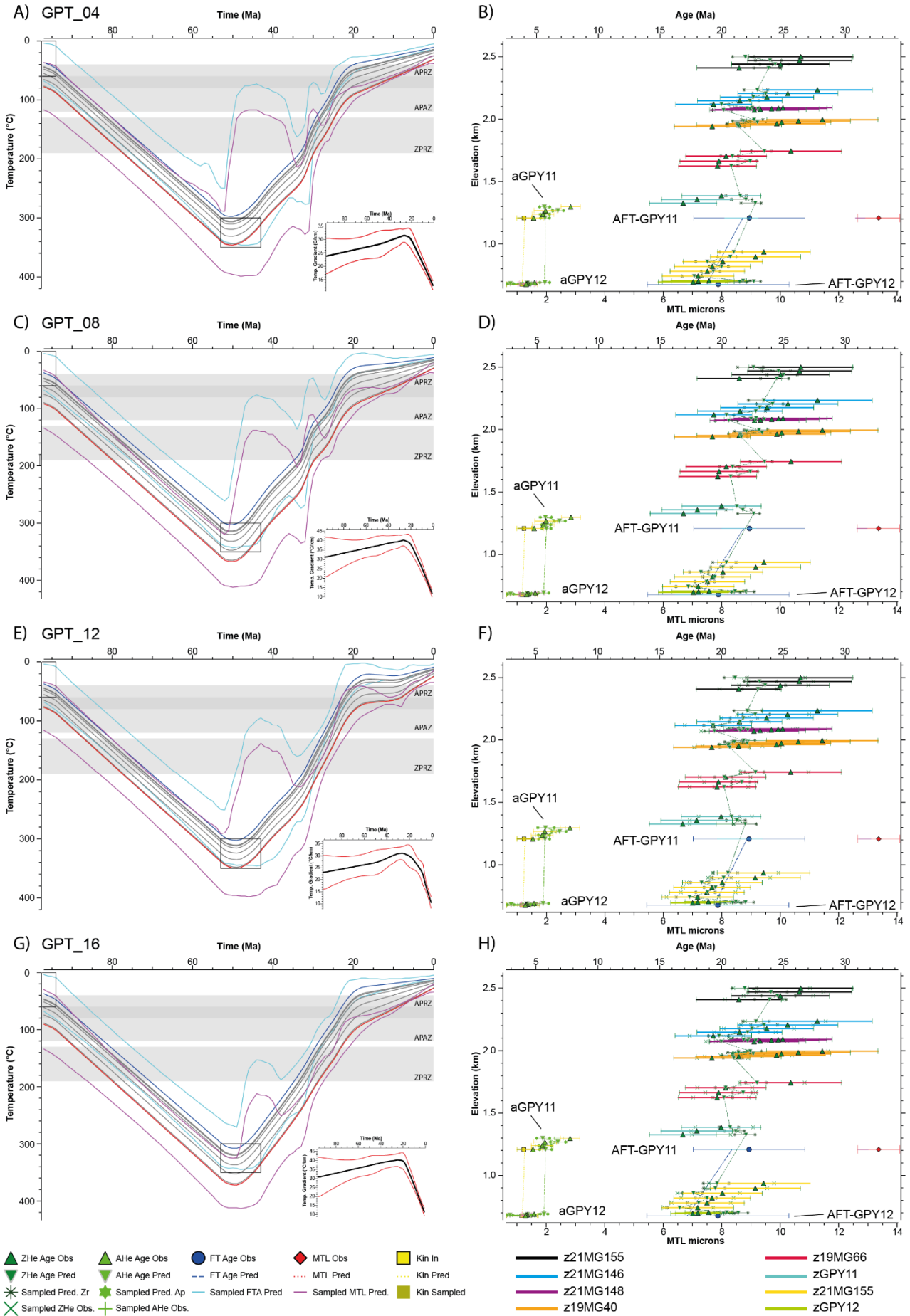
*Figure 6.11: Representative thermal simulations for the E-W vertical profile with the calcite age constraint. **A-D)** modelled T-t path, geothermal gradient, and age-elevation profiles of the observed ages (uncorrected) for low (A and B) and high (C and D) geothermal gradient. **E-H)** modelled T-t path, geothermal gradient, and age-elevation profiles of the resampled ages (uncorrected) for low (E and F) and high geothermal gradient (G and H). MTL: Mean track lengths; Red and blue curves correspond to the bottom (hot) and top (cold) samples, together with its 95% credible interval; APRZ: Apatite partial retention zone; APAZ: Apatite partial annealing zone; ZPRZ: Zircon partial retention zone. Prefix z refers to a zircon sample, a to apatite sample, and AFT to apatite fission track.*

Figure 6.12: *Representative thermal simulations for the E-W vertical profile without the calcite age constraint.* ***A-D)*** *modelled T-t path, geothermal gradient and age-elevation profiles of the observed ages (uncorrected) for low (A and B) and high (D and E) geothermal gradient.* ***E-H)*** *modelled T-t path, geothermal gradient and age-elevation profiles of the resampled ages (uncorrected) for low (E and F) and high geothermal gradient (G and H). MTL: Mean track lengths; Red and blue curves correspond to the bottom (hot) and top (cold) samples, together with its 95% credible interval; APRZ: Apatite partial retention zone; APAZ: Apatite partial annealing zone; ZPRZ: Zircon partial retention zone. Prefix z refers to a zircon sample, a to apatite sample and AFT to apatite fission track.*

6.4 Tectono-thermal evolution of the Eaux-Chaudes massif

6.4.1 Paleotemperatures and the reset of the AHe-AFT-ZHe system

The paleotemperature record of the Mesozoic of the ECM was analyzed by Caldera (2022) using the Raman Spectroscopy of Carbonaceous Matter technique (RSCM) and the calcite-dolomite geothermometer due to the observable ductile deformation of the Upper Cretaceous sedimentary rocks (Fig. 6.13). Maximum temperatures recorded by the U. Cretaceous present in the ECM area were around ~350°C for the autochthonous (deformed and non-deformed) and overturned limb units, and about ~310°C for the normal limb of the structure, which correspond to the lower green schist metamorphic facies.

Closure temperatures for AHe system range between ~40-80°C, which defines the apatite partial retention zone (Wolf et al., 1998; Farley, 2000; Stockli, 2005; Gautheron et al. 2013), between ~60-120°C for the AFT, defining the partial annealing zone (Ketcham et al., 1999), and between ~130–190°C for the ZHe system, defining the zircon partial retention zone (Reiners et al. 2002, 2004; Wolfe and Stokli, 2010). Hence, in the ECM they are far exceeded, even for the top samples of the normal limb. It is hard to constrain the Meso-Cenozoic maximum paleotemperature recorded by the Paleozoic rocks of the recumbent fold nappe core using RSCM, since the maximum temperatures of these could have been acquired

during Variscan times or during the tectonic and sedimentary burial inherent to the orogenic process, which could be assisted by abnormal gradients because of the hyperextension of the margin that brings the upper mantle to surface conditions by Mid Cretaceous times (e.g., Clerc and Lagabrielle, 2014; Lagabrielle et al., 2010; Jammes et al., 2009; Teixell et al., 2016). However, they must be at least in the same order of magnitude than those recorded by the Upper Cretaceous rocks since both are in stratigraphic contact (Cenomanian unconformity; Fig. 6.1). Hence, either ZHe, AHe and AFT systems must have been totally reset also for the Paleozoic rocks of the ECM and vicinities -especially those present in the fold nappe core of the structure- (Figs. 6.1-6.4), which was also concluded by Bosch et al. (2016) and predicted by the inverse thermal models (Fig. 6.7-6.12). In addition, the ZHe single-grain cooling ages obtained here are in a time span ranging from

Figure 6.13: Examples of the ductile deformation observable in the Upper Cretaceous rocks that indicates the high temperature conditions experienced, which is compatible with total reset of the AHe, AFT and ZHe thermochronologic systems.

39.7Ma to 24.1 Ma (Table 6.1), which is much younger than any depositional age which is also indicating of a complete reset of the apatite and zircon systems.

The reset of the low-temperature thermochronological systems is in fact a common feature of the zircons and apatites collected in the hanging-wall of the Gavarnie thrust in the west-Pyrenees, as observed further east by Jolivet et al. (2007), Labaume et al. (2016; 2016b) and Morris et al. (1998), and near the ECM and further the west by Bosch et al. (2016).

Most of the samples studied here show ZHe ages independent of the eU concentration and the grainsize (Figs. 6.5 and 6.6), also supporting complete reset. However, the samples from the upper MIN nappe (21MG146) and from the core of the ECFN (19MG40) show a positive age-eU correlation, which could be indicative of the different radiation damage accumulation between zircons, being the [eU] the proxy to measure it (e.g., Reiners et al., 2004; Reiners, 2005; Guenthner et al., 2013). In this sense, the single-grain ages with low [eU] (e.g., Fig. 6.5C) could reflect a zircon with low radiation damage and high He diffusivity, which leads to younger ages. The He diffusivity in zircons increases if the zircon has large amounts of radiation damage zones that become interconnected (Reiners et al., 2004; Reiners, 2005; Guenthner et al., 2013), but this does not seem to be the case because in the analyzed aliquots with higher radiation damage have observed the oldest ages (Fig. 6.5C and E). Precisely, the negative path observed in three single-grain ages from sample 20MG108 belonging to the autochthon could reflect this effect, where the single-grain ages with lower [eU] (i.e., radiation damage) are the oldest of the sample (Fig. 6.5A).

Taking a general view of the ZHe single-grain ages it is striking that the samples above 1520m of height (from sample 22MG183) are mostly showing two age populations above and below

~30 Ma -except for the samples 21MG138 from the Cinq-Monts unit with two age clusters older than 30 Ma, and 21MG148 from the normal limb of the ECFN with a little low-dispersed age around 30 Ma (Table 6.1; Fig. 6.1-6.4)-. However, most of the single-grain ages of the samples with positive/negative correlations which potentially possess two age clusters are within the error bars (e.g., Fig. 6.5A, E), despite the presence of these age clusters could be indicative of partial reset of the samples.

6.4.2 – Burial history of the ECM

The unconformity between the basement rocks (the E-C granite and the Paleozoic metasediments) and the Cenomanian sedimentary cover of the ECM marks the maximum age to be near-surface conditions for both before the onset of the sedimentary and tectonic burial (Fig. 6.1), which coincides with the transition from the rifting stage to the post-rifting stage (e.g., Debroas, 1987, 1990; Berastegui et al., 1990). On the other hand, both basement and Cenomanian rocks were not far from the surface until Campanian times (the youngest exposed unit) due to the relatively little thickness of the U. Cretaceous sedimentary pile (~300m; e.g., Caldera et al., 2022; Fig. 6.1).

ZHe thermochronology indicates that all samples must have been buried under the ZPRZ boundary (190-200°C) during the Pyrenean orogeny (Table 6.1). These temperatures were far exceeded to at least 310-350°C as attested by the paleotemperature record (Caldera et al., 2021; Caldera, 2022) and confirmed by the observed complete reset of the AHe, AFT, and ZHe systems (as discussed above). The inverse thermal modelling also predicts the complete reset in all cases since all the modelled profiles arrive at temperatures above the ZPRZ (Fig. 6.7-6.12 and annexes).

It is hard to interpret these temperatures in terms of burial deep due to the lack of geobarometers that constrain unequivocally the burial due to the tectonic and sedimentary

loading. A condition of more than 15 km stacking and burial was inferred for the Helvetic nappes of the Alps (Dietrich and Casey, 1989; Pfiffner et al., 1997; Herwegh and Pfiffner, 2005; Nibourel et al., 2018), where similar paleotemperatures than those of the ECM were recorded during the deformation (e.g., Girault et al., 2020 and references therein). However, this burial depth conditions are hard to conceive for the case of the Eaux-Chaudes massif because the nappe stack in this area of the Pyrenees is much thinner than in the Helvetic nappes of the Swiss Alps (e.g., Teixell, 1998; Bellahsen et al., 2019).

The hot nature of the Iberian paleomargin in the post-rift stage when the mantle was already exhumed could have induced anomalous high geothermal gradients before the onset and in the early stages of the orogeny (e.g., Clerc, 2012; Clerc and Lagabrielle, 2014; Cloix, 2017; Corre, 2017; Bellahsen et al., 2019; Caldera et al., 2021; Izquierdo-Llavall et al., 2020). However, Caldera (2022) attributed this elevated thermicity to combined tectonic burial and sedimentary burial by the syntectonic deposits associated with the orogenic flexure (e.g., Labaume et al., 2016b), and inferring a geothermal gradient in the order of ~30-45°C, which leads to burial depths of 8 to 12 km for the ECFN. A paleodepth of ~6-8 km was inferred by Jolivet et al. (2007) in the Néouvielle massif, which is in the same structural position (hanging wall of the Gavarnie thrust) further to the east of the ECM. Moreover, the range of predicted paleodepths by the thermal modelling at the thermal peak spans between 6.9 km and 13.1 km deep (Fig. 6.14B), which is fairly within this range of paleodepths although uncertainty. The geothermal gradient range from Caldera (2022) is consistent with most of the gradients predicted by the thermal modelling during the burial history, no matter if it was initially programmed to be low (25±10°C/km) or high (35±10°C/km) and also by those gradients modelled at the thermal peak, despite this range has implications on the estimated burial at the moment of maximum temperature (Fig. 6.14B). Indeed, no values lower than

A)

B)

Models with an initial gradient of 25±10 °C/km   Models with an initial gradient of 35±10 °C/km
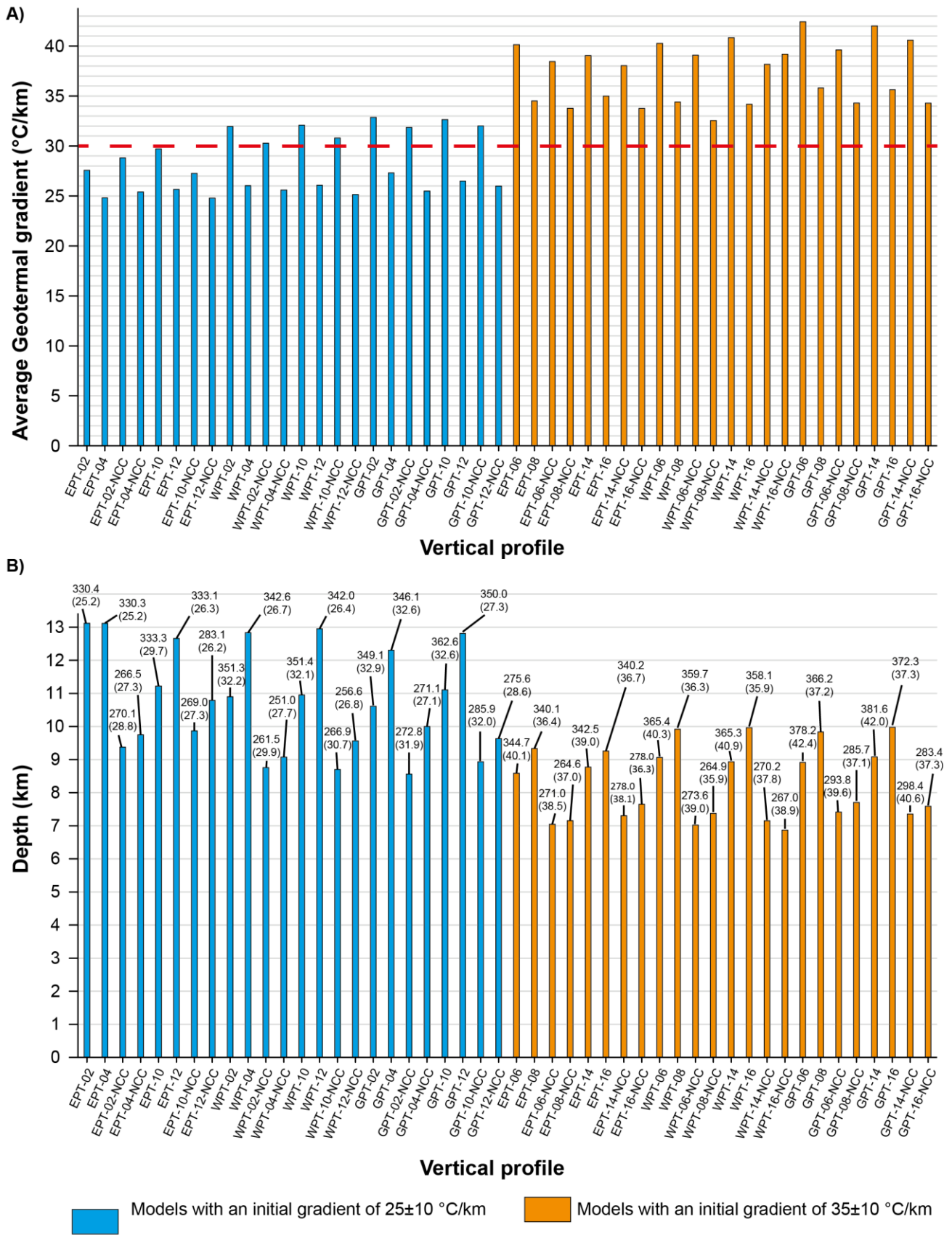
Figure 6.14: *A) Average of the forward modelling predicted geothermal gradient during burial for each profile with and without calcite constraint from the east (EPT), west (WPT) and east-west (GPT) models presented in Figs. 6.7-6.12 and annexes. The average has been calculated up to the time interval observed in the T-t path where the maximum temperature was reached. B) Forward modelling predicted paleodepths at the thermal peak for each profile with and without calcite constraint from the east (EPT), west (WPT) and east-west (GPT) models presented in Figs. 6.7-6.12 and annexes. Above the bars, the thermal peak (in °C) and the geothermal gradient at the thermal peak (in °C/km, between parentheses) are indicated.*

24.8°C/km (model EPT-12-NCC; Figs. 6.8E) were never observed for any model during the burial history (Fig.6.14A). The common cases where the burial gradients are below 30°C/km are those of initially programmed to be low and variable, no matter whether the ages were resampled or not (all models -04 and -12 in Fig. 6.14A).

Assuming the geothermal gradient of ~30°C/km inferred by Caldera et al. (2021) from samples at different elevations inside the Eaux-Chaudes recumbent fold nappe (i.e., between the normal and overturned limbs), the modelling results predicts burials between ~8.5-13 km for the ECM, which is more associated with the inverse thermal models using 25±10 °C/km of initial temperature gradient. However, this interpretation arisen from the modelled geothermal gradient should be taken with caution because the geothermal calculations from QTQt generates uncertainty as, for example, the increase of the geothermal gradient with time in an orogenic context, a feature observed in all the QTQt modelling results.

Despite that the predicted burial histories are shown continuous in all cases, two clear paths can be distinguished from the inverse thermal modelling depending on the application of the LA-ICP-MS age constraint. With the constraint, the time-temperature trend is precise and constant at heating rates of ~5-6°C/Ma (Fig. 6.15A, C, E and G). On the other hand, with no age constraint the burial path is shown imprecise, at heating rates of 3-4°C/km (Fig. 6.15B, D, F, and H). However, it is impossible know exactly the burial history due to the lack of more field constraints than the pre-Cenomanian exposure and the moderate burial by the relatively

thin Upper Cretaceous carbonate succession. Geobarometers based on chlorite systems could help to constraint maximum burial but it is outside of the goals of this study.

6.4.3 – Exhumation history of the ECM and the surrounding nappes

The Eaux-Chaudes massif and overlying units (i.e., MIN, Cinq-Monts and Bois de la Traillère) were exhumed from under the ZPRZ between 36 and 26 Ma (Late Eocene to Early Oligocene; Table 6.1), as indicated the mean ZHe ages implying totally reset of zircons (section 6.3.1). However, single-grain ages indicate that these units could be under exhumation from ~40 to 24Ma (e.g., samples 20MG108 and 19MG66; Table 6.1). These ages are consistent and correlative with ZHe ages obtained by Bosch et al. (2016) in the Eaux-Chaudes pluton (samples GPY09, GPY11, and GPY12), just below the ECFN.

The similar cooling ages of samples 21MG146 and 21MG148 strongly evidence that the MIN unit was emplaced and welded over the normal limb of the ECFN (Table 6.1). Furthermore, the juxtaposition of the hanging wall and the footwall of the Lakora thrust and their later joint exhumation is also consistent with the observations by Bosch et al. (2016) further west and confirms that the exhumation of both the MIN (carried by Lakora thrust) and the ECFN should be attributed to thick-skinned thrusting under the massif.

The similar mean ages shown by samples 21MG146, 21MG148, and 19MG40 belonging to different structural positions but at similar altitude and latitude suggests that the plunge of the ECFN towards the west was yet developed before 30.5 Ma. However, the samples from the overturned limb point to the opposite, because both 19MG66 and 21MG155 have the same mean age of 26.3 and 26.5 Ma, and are separated by a difference in elevation of 882m (Table 6.1 and Fig. 6.2). A similar situation can be derived from samples GPY11 and GPY12 from Bosch et al. (2016), which show a similar ZHe age with a difference of 531m. However, these samples are not at the same latitude, and the observed thrusting structures in the

autochthonous Upper Cretaceous and back-thrusting structures of the Axial Zone could have altered the elevation of the samples from the overturned limb (e.g., Fig. 6.2). Therefore, the ECFN was yet E-W tilted before 30.5 Ma.

The possible relevance of the two age clusters (Fig. 6.5), may also indicate thrusting sequences in the Axial Zone of the Pyrenees. In this way, the cooling age cluster of 30-39 Ma observed in samples over 1941m of altitude (from sample 19MG40) could be reflecting the activity of the Gavarnie thrust, a major south-directed basement thrust that caused a pulse of exhumation and structural relief reflected by the sedimentation of conglomerates in the Jaca basin (e.g., Puigdefabregas, 1975; Roigé et al., 2016). On the other hand, the young age cluster of 24-30 Ma could also be indicative of younger basement thrusts, which further raised the Axial Zone between the Oligocene and Miocene (Teixell, 1996; Jolivet et al., 2007; Labaume et al., 2016b). Bosch et al. (2016) also detected these pulses in both the hanging wall and the footwall of the Lakora thrust outcropping westwards. In addition, the similar AFT and ZHe ages of samples GPY09, GPY11, and GPY12 from Bosch et al. (2016) in the Eaux-Chaudes area puts a strong constraint on the fast exhumation of the massif between 30 and 20 Ma, which could also be a possible interpretation of the observed sole age cluster in samples from below 1941m. However, due to the low sampling resolution in the vertical profiles, caution is required in this interpretation.

The inverse thermal modelling -where the zircon radiation damage model from Guenther et al. (2013) is taken into account- also detects these thermal pulses (Fig. 6.5-6.12). A thermal cooling pulse at 7-15°C/Ma starting around 35-40 Ma until 20Ma was common in most of the simulations where there was not a calcite age constraint, no matter the vertical profile nor the resampling or the initially setting of the geothermal gradient (i.e., fixed or variable) (Figs. 6.8, 6.10, 6.12 and annexes). Indeed, the E-W profiles with no calcite age constraint, which are those with more sample resolution and better age prediction, are indicating two cooling pulses
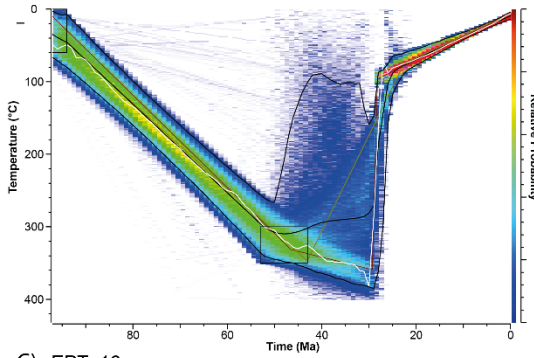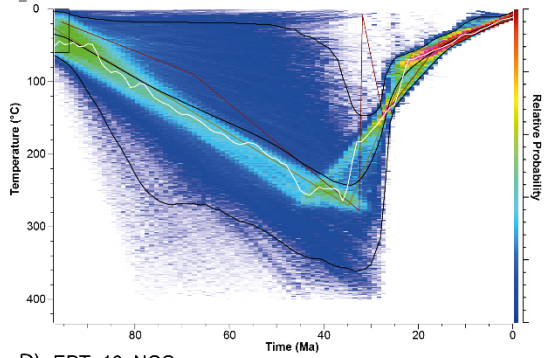
A) EPT_04
B) EPT_04_NCC
C) EPT_16
D) EPT_16_NCC
E) WPT_12
F) WPT_12_NCC
G) GPT_08
H) GPT_08_NCC
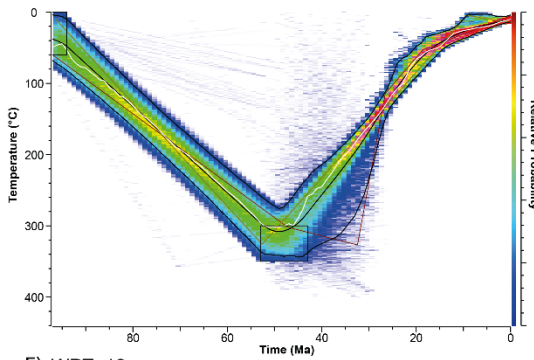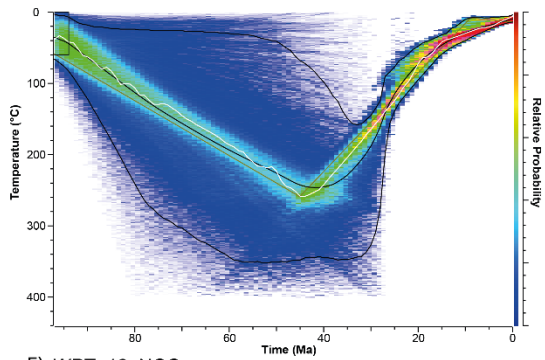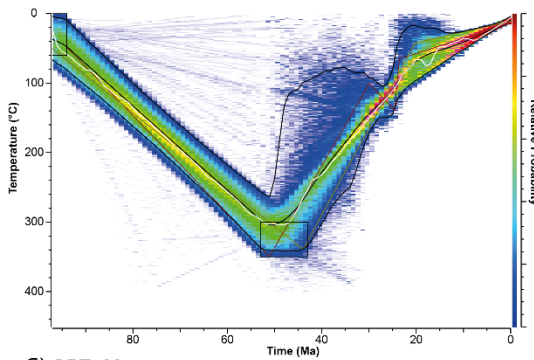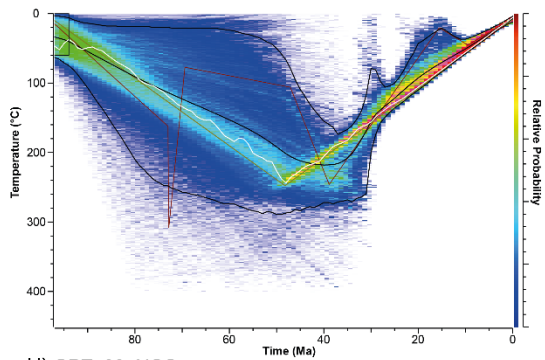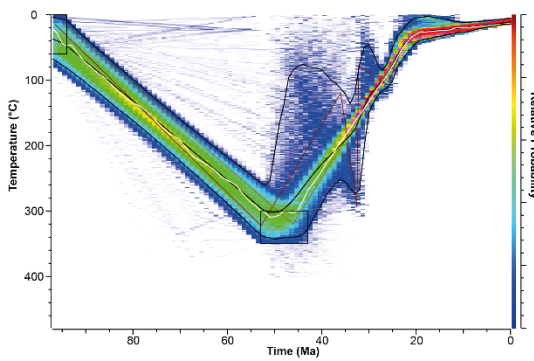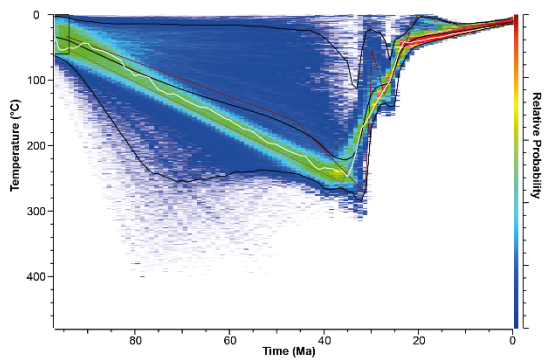
between 40 and 30 Ma (12-30°C/Ma) and between 25 and 20 Ma (11-13°C/Ma) (e.g., model GPT_08-NCC in Fig. 6.12C), which coincides with thrusting ages of Gavarnie and Guarga basement thrusts (Teixell, 1996; Jolivet et al. 2007; Labaume et al. 2016). In addition, the ending of the first cooling pulse is just predicted to happen when the samples are crossing or in the upper boundary of the ZPRZ, which could explain the presence of two age clusters in the top samples due to the partial reset of the samples (Fig. 6.12).

Nevertheless, when the condition of the calcite age is used as a constraint, several differences are observed. The cooling histories tend to show a continuous trend at 7-11°C/Ma from 50-45 Ma until 20 Ma. However, exceptions to this general tendency can be found in the East profile, where the simulations EPT_04 and EPT_08 (simulations with no resampling ages) draw a cooling pulse of 38°C/Ma and 21°C/Ma respectively between 30 and 20 Ma (Fig. 6.7A and C). Even though the no-resampling-age simulations from the E-W profile also show a sharpening in the cooling history between 30 and 20 Ma (models GPT_04 and 08; Fig.6.11A and C), the general trend is continuous at similar cooling rates than the east and west profiles.

Taking into account these two broad end-member simulations, the thermochronologic knowledge of the west-central Pyrenees favors the model of cooling pulses (e.g., Bosch et al., 2016; Jolivet et al., 2007; Labaume et al., 2016b), consistent also with the tectonic-sedimentation relationships observed in the Jaca basin. However, the probability maps from the stochastic modelling of the T-t trajectories shown in Fig. 6.15 seem to indicate just the
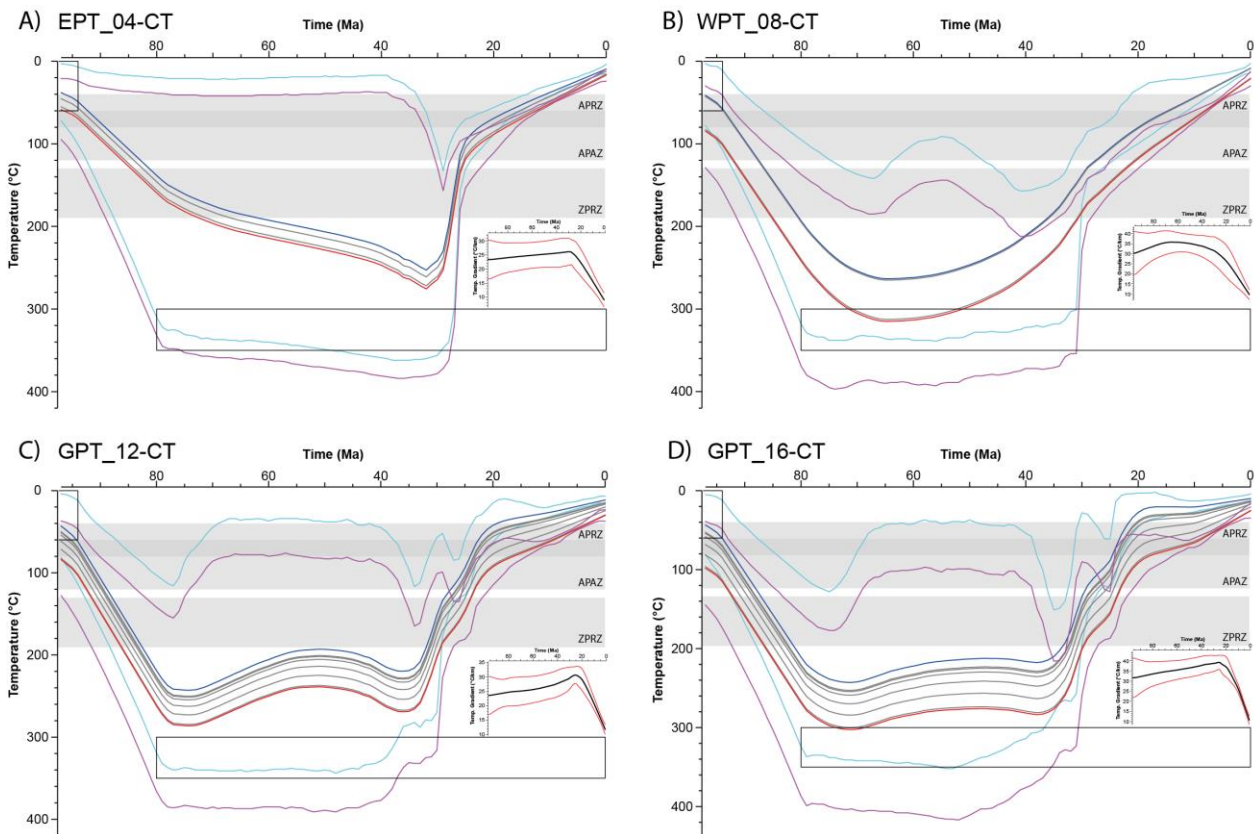
Figure 6.16: *Examples of the QTQt vertical profiles for simulations using an unconstrained age of the thermal peak of 350ºC. The simulations are equivalent to EPT_04, WPT_08, GPT_12, and GPT_16.*

opposite, being more probable a continuous exhumation model, at least for the cooling history. Indeed, the low-probability cluster of the cooling pulse model is located in the burial history, just where there are few information constraints. A big disadvantage is that, in any case, the modelling predicts the RAMAN paleotemperature of the Upper Cretaceous rocks of the ECFN, despite the latter can be considered reached taking into account the 95% credible interval. Not even when the software has the freedom to choose the timing of the thermal peak, these temperatures are reached (e.g., Fig. 6.16). Indeed, most of these models ignore the paleotemperature constraint.

The comparison of the thermochronological data of the Cinq-Monts and Bois de la Traillère units (Table 6.1) is revealing normal faulting in the surroundings of the ECM. ZHe mean age of the Cinq-Monts structural unit at 36.0±3.5 Ma, indicates older exhumation than the ECFN and MIN units (30.5±2.4 Ma), probably related to the early movement of the Gavarnie basement thrust (Teixell, 1996; Jolivet et al., 2007; Labaume et al. 2016b). However, this sample (21MG138) is located 579m below the one located in the normal limb of the ECFN (21MG148), so late faulting can be inferred between these sample localities, probably reactivating basal thrusts from the nappe stack as normal faults (Fig. 6.2B). A similar behaviour can be deduced for the Bois de la Traillère unit, since the bottom sample (22MG183) has an older mean age than the top sample.

In addition, the CBB unit was already adjacent to the Bois de la Traillère unit and both were exhumed at the same time (Table 6.1 and Fig. 6.4). The Bois de la Traillère unit has a kinematically normal relationship with respect to the ECFN and MIN units (Fig- 6.4). The ZHe ages from these units revealed the same mean age of 30.5 Ma with a difference of 561m of altitude, just in the same range than the observed between the Cinq-Monts and the ECFN. The extensional event that I deduce can also be inferred for the normal limb of the ECFN, by the existence of normal faults affecting the Upper Cretaceous rocks (Fig. 6.2).

6.5 – Main conclusions on the exhumation of the Eaux-Chaudes massif

The Eaux-Chaudes massif has a complex exhumation history spanning from ~40 to ~6.6 Ma as indicated by the ZHe, AHe and AFT systems. All Upper Cretaceous and Paleozoic rocks observed in the different structural units of the study area were totally reset.

The double cluster of ages above and below ~30 Ma observed in samples over 1520m of altitude could be manifesting different cooling pulses related to the activity of basement

thrusts during the collisional stages of the Pyrenees. A first event between ~30-40 Ma was recorded by the top samples, which coincides with the known activity of the Gavarnie thrust. A second event between ~20-30 Ma was recorded by these samples but also by those below 1520m, and was probably related to in-sequence basement thrust emplacement, probably the Guarga thrust. These cooling pulses coincide with the results of Bosch et al. (2016) in the Lakora thrust (further west) and in the ECM area. However, this double cluster could be also interpreted as influenced by the radiation damage, given that some of the samples shown positive age-[eU] correlations.

The cooling pulses are predicted by the inverse thermal modelling only in the E-W profile when the calcite U-Pb constraint is not used. In general, using the calcite LA-ICP-MS constraint blurs the cooling pulses, predicting continuous and precise cooling paths until ~20Ma, where the cooling relaxes.

E-W tilting of the ECM and surroundings must have been produced before~30Ma, due to the similar ZHe ages recorded by samples in different structural positions and with similar ages.

Late extension (probably reactivating basal thrusts from the nappe stack) provoked normal displacements in the surrounding units of the ECM, probably favored by the allochthonous Keuper carried by the underlying Lakora thrust.

Chapter 7: General discussion

7.1. Comparison between the Eaux-Chaudes massif and the infra-Helvetic nappes from the Swiss Alps.

Although the initial setup for the numerical modelling undertaken in this work is based on the case of the ECM, the concepts arising from the simulations can be applied to other orogens worldwide such as the Alps.

The classical interpretation of the Eaux-Chaudes massif (ECM) as a duplex with a roof thrust carrying Paleozoic rocks over the Upper Cretaceous (Ternet, 1965, and subsequent works) was reformulated by Caldera et al. (2021) in favour of a recumbent fold nappe structure analogous to the infra-Helvetic nappes because of their similar deformation and paleotemperatures (e.g., Ramsay, 1981; Ramsay et al., 1983; Pfiffner, 1993; Girault et al., 2020; Fig. 7.1). Additional, other common elements between these recumbent nappes are the presence of a buttressing condition due to the relief of the basement units, the alternance of stiff and weak units in the stratigraphic sequence, the existence of allochthonous units above the nappes (Fig. 7.1A), existence of flysch materials in the autochthonous unit, and the occurrence of small pieces of allochthonous units pinched between the recumbent fold limbs (e.g., Morcles-Doldenhorn nappes; Fig. 7.1; Badoux, 1971; Pfiffner, 1993; Casey and Dietrich, 1997).

However these qualitative similarities there are important differences between the ECM and Morcles-Doldenhorn nappes. The main difference is attending to the dimensions of the nappes, with ECM showing relatively modest structural relief and length of the recumbent limb (~1.5 km and ~5 km, respectively) compared to the Morcles nappe which implies approx. 5 km of structural relief and ~10km length of recumbent limb. Another difference is the distribution of paleotemperature. Although the values of the paleotemperature record in both

nappes range between 300-350ºC in the sedimentary cover, the isotherms in the Morcles nappe were interpreted as folded and oriented obliquely to the structure by Girault et al. (2020), with isotherms crossing from normal to recumbent limbs, while Caldera (2022) interpreted the isotherms in the ECM as oriented flat and sub-parallel to the normal and recumbent limbs, and hence, oblique to the fold hinge, and coherent with zircon thermochronologic record obtained in this thesis. This observation could imply that the reported thermal peak respect deformation differs between both cases or imply a difference in the heat advection during deformation. From thermo-mechanic models, a flat orientation of the isotherms was observed for conditions of increment of temperature synchronic to the deformation, indicating that heat transport by advection of the structure was relatively limited.

Another difference is in term of the materials located in the core of the nappes. While the core in the ECM includes deformed metasediments of the Variscan basement, in the case of the Morcles nappe corresponds to the Mesozoic and Cenozoic sedimentary cover and the Paleozoic basement units, such as the Mt. Blanc crystalline unit, are in general interpreted as not involved in the fold nappe structure (Fig. 7.1).

7.2. Mechanical and thermomechanical controls on recumbent folding

Crystalline rigid bodies or fault discontinuities acting as forestops or buttresses have been widely reported as effective elements to nucleate compressional structures (e.g., Bastida et al., 2014 and references therein; Bauville and Schmalholz, 2015; Spitz et al., 2020; Kiss et al., 2020), and the ECM is not an exception (e.g., Fig. 3.4). From the numerical simulations, the basement forestop strongly controls the nappe initiation due to its mechanical strength (e.g., Fig. 3.4C) by concentrating the stresses in the contact region between the forestop and
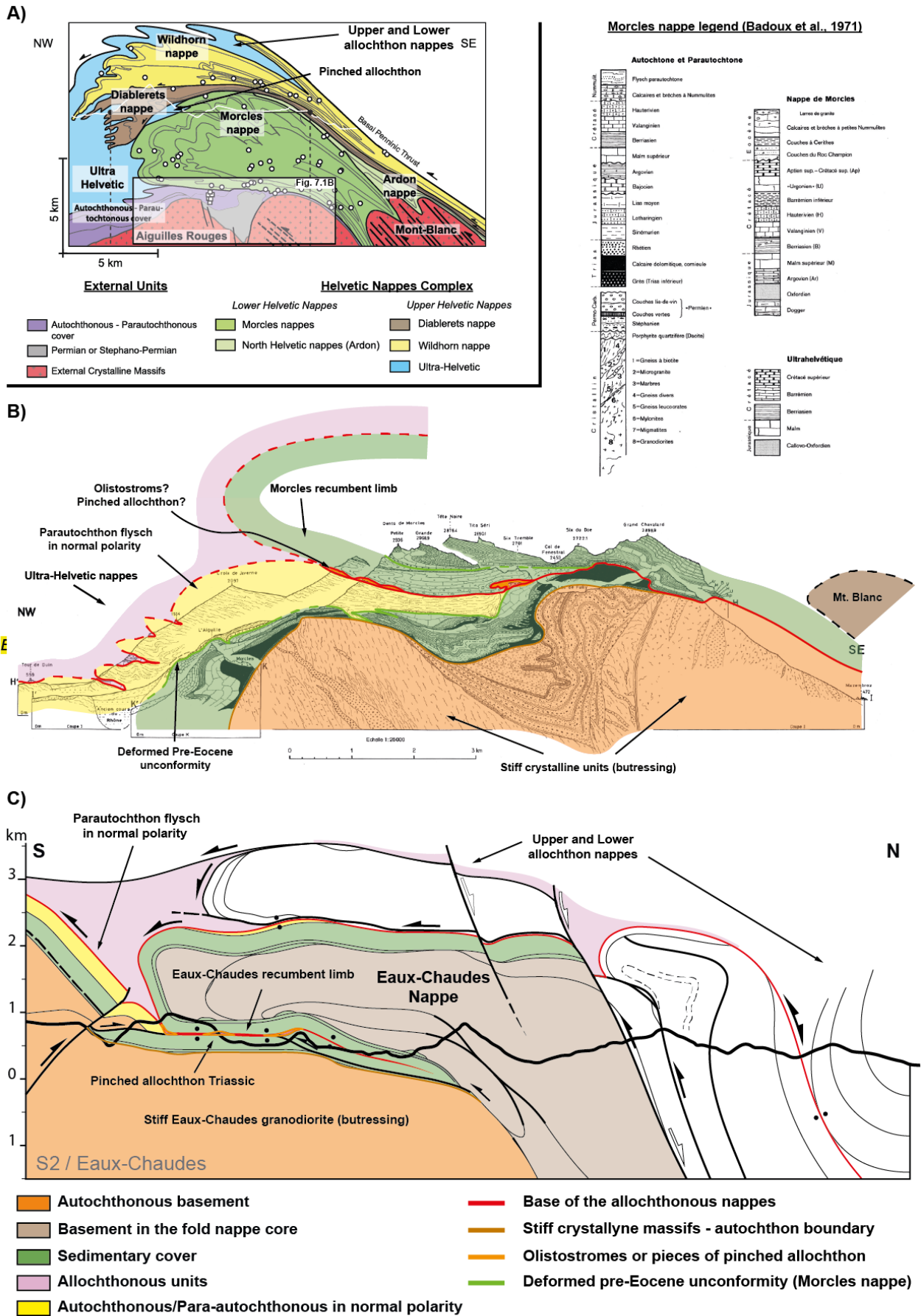
Figure 7.1: Comparison between the structural elements of the Morcles fold nappe and those of the Eaux-Chaudes massif (simplified from Caldera et al. 2023 and Fig. 1.8). A) Geological cross-section from Escher et al. (1993) after Girault et al. (2020), where the structural relationships between the Upper and lower Helvetic nappes can be compared to equivalent features observed in the Eaux-Chaudes massif. B) Geological cross-section of the western Morcles recumbent fold nappe (Badoux et al., 1971), where the relationships between the crystalline massifs of Aiguilles Rouges (to the NW) and Mont Blanc (to the SE), the autochthonous units and the recumbent fold nappe can be observed and compared to equivalent features in the Eaux-Chaudes massif. Small pieces of olistostromes are preserved in the autochthon-recumbent limb boundary could be equivalent to the pinched allochthonous pieces in the Eaux-Chaudes massif. C) Sketch of the EC fold nappe S2 section from Caldera et al. (2023) in the Ossau Valley, where similar boundaries to those observed in the Morcles nappe between the allochthonous units, the recumbent limb and the autochthon are observed.

the UC-Devonian panel. Without a forestop, the model deformation is no longer localized but distributed, and upright buckle folds develop (e.g., Fig. 3.7L). Therefore, although the presence of the Eaux-Chaudes pluton appears to have largely conditioned the development of a recumbent fold nappe in the western sector of the ECM, the observed difference in the structural style between the eastern (ductile fold-thrust-fan) and the western (recumbent fold nappe) sectors could also be attributed to other factors in addition to the forestop.

A critical result from the thermomechanical models is that developing a fold nappe preserving thickness in the recumbent limb is a strange case and was only observed in simulations using settings with linear viscous rheologies. Firstly, from a point of view of the deformation of a polycrystalline aggregate by creep mechanisms, a linear response is expected for conditions where diffusion creep is the dominant deformation mechanism (e.g., Ranalli, 1995; Karato, 2008). For situations where the deformation is accommodated by climb and glide dislocation (i.e., dislocation creep), such as the assumed in the experimental power law of calcite by Schmid et al. (1977), the stress exponents are expected in the range 3 to 5. For situations of low-temperature creep (i.e., deformation only accommodated by glide dislocation and twinning) the relationship between differential stress and strain rate is exponential and the equivalent stress exponents are still higher (i.e., $n >> 7$). Observations from microstructure analysis using optical microscopy and SEM-EBSD by Caldera (2022) indicate that calcite-rich

levels in the overturned limb show very fine grain-size (15-35 µm), and moderately preferred orientation of grains (SPO) and crystallographic axes (CPO). Piezometry using grain-size of calcite and RMSC paleotemperature by Caldera (2022) indicates that the deformation conditions were very close to the transition between diffusion and dislocation creep, conditions implying low-stress exponents (n~1-2) and conceptually in agreement with the required lineal behaviour from mechanical and thermomechanical simulations.

Secondly, lateral rheological changes within the Upper Cretaceous stratigraphic pile could also have affected changes in the bulk mechanical behavior and the deformation style. Although dolostones (or dolomite-rich rocks) are observed all along the massif, Caldera et al. (2023) reported abundant discontinuous dolomitic bodies in the eastern sector of the ECM affected by brittle-to-ductile deformation such as boudinage, folds and thrusts, clearly visible at outcrop and thin-section-scales (e.g., Fig. 7.2). The existence of these stiff bodies in the east could have increased the overall rigidity of the Upper Cretaceous in this sector, adding heterogeneities within the rocks and, therefore, enhancing the strain localization in the viscous-dominated calcite-rich levels. This process could produce a softening of material by a combination of the effect of the increasing temperature and the increasing of the strain-rate due to strain localization (e.g., Figs. 4.5-4.7).

In addition, the results reported in Fig. 3.5A, D and G also demonstrate that the increase of the viscosity of the Upper Cretaceous layer (η_{UC}) favored the brittle behaviour of the phase. These dolomitic bodies were not observed neither reported by Caldera et al. (2023) in the western sector, therefore favoring folding. Moreover, localization levels enhanced by fluid pressure (e.g., Teixell et al., 2000) (for example in the Cenomanian detachment in the ECM case; see chapter 5) are also present in the eastern sector, and could have contributed to the concentration of the deformation in the autochthonous Upper Cretaceous, hampering the required buttress conditions, one of the features needed to nucleate a recumbent folding (i.e.,
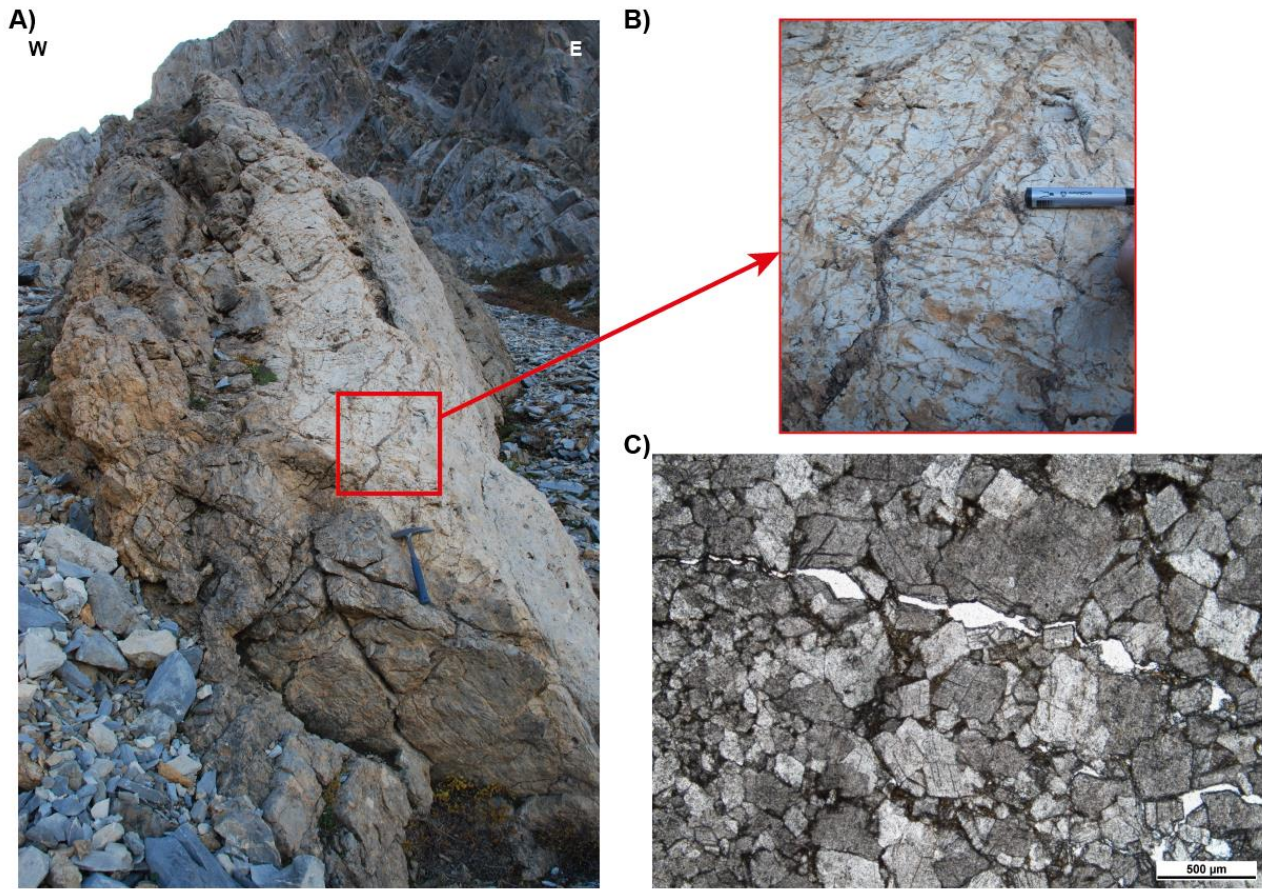
Figure 7.2: A) *Picture of a metric-scale stiff dolomite body just above the Cenomanian detachment level in the Pêne Medaà area (DA5 site in Fig. 5.4).* **B)** *Close-up of fluid-filled brittle fractures in dolomite rock.* **C)** *Thin section of the dolomite body displaying euhedral dolomite grains with brittle cracks.*

fixed surface in Fig. 1.4). These elements may have introduced mechanical, geometrical and rheological heterogeneities which prevented the recumbent folding by inducing viscosity instabilities that can result in the viscous/ductile localization, such that observed in the autochthonous Upper Cretaceous using power-law rheologies (e.g., Figs. 4.12 and 4.13).

In the western sector, no detachment levels were observed within the Upper Cretaceous succession or at the Paleozoic-Upper Cretaceous unconformity. The Upper Cretaceous autochthon forms a sedimentary lid anchored over the ECP, facilitating the buttress effect for nappe development. Both the EC granite and this sedimentary lid remained undeformed during the nappe development (Caldera, 2022; Caldera et al., 2023), which is a feature also

reproduced in my mechanical and thermomechanical simulations (e.g., Figs. 3.6, 3.7, 4.6 and 4.7).

However, to fully test more thoroughly these interpretations on the influence of lateral mechanical variations in the structural style between the eastern and western profiles of the ECM, 3D thermomechanical simulations would be desirable, which is a task to be pursued in the future.

We inferred that the weak layers in the form of slates, shales, or evaporites were key geometrical and mechanical elements allowing decoupling. Without these weak levels, the fold nappe at Eaux-Chaudes would not have been formed (e.g., Figs. 3.6A and 4.4). Either by using linear-viscous or power-law viscous rheologies, the presence of these layers triggered the development of two detachment levels (above and below the nappe) surrounding the stiff Upper Cretaceous-Devonian panel (UCD) (e.g., Fig. 3.4, 4.5 and 4.14). On one hand, the absence of an upper weak layer (i.e., Keuper) prevents the decoupling between the upper allochthonous nappes and the UCD layers, and an antiform fold is developed by the extrusion of the Silurian (Fig. 3.6), similarly to the mechanism reported by Kiss et al. (2020) and Spitz et al. (2020) for the development of the infra-Helvetic nappes. On the other hand, If the Silurian detachment was absent (or its viscosity contrast with the surrounding units was lower than approx. 2 orders of magnitude), no basal detachment was developed, hampering the translation of the UCD panel (e.g., Fig. 4.14C and D). Therefore, the double low-angle detachments within a simple shear regime is a necessary condition for nappe development in the ECM and could be extrapolated for setups where double detachment levels are observed and the ductile extrusion mechanism reported for Helvetic nappes of the Alps cannot be invoked (e.g., Bellahsen et al., 2014; Bauville and Schmalholz, 2017). Indeed, field observations by Caldera et al. (2023) prevented the Eaux-Chaudes fold nappe (ECFN) to be interpreted as a ductile extrusion of the basin infill, but as a recumbent

fold within a top-to-the-south thick shear zone surrounded by the Keuper and Silurian weak units. The numerical models presented here confirms the key role played by the basal Silurian detachment, the allochthonous Keuper, and the burial generated by the overlying upper thrust sheets (Lakora and Chaînons Béarnais). Moreover, the simulations suggest that in the case of the ECM the migration of the fold hinge by the rigid rotation of the Upper Cretaceous-Devonian panel under a thick weak layer (the Keuper) was probably the dominant nappe growth mechanism, because the recumbent limb has the layer thickness approximately preserved (respect to the normal limb), showing a general homogenous thickness. This kind of situation requires an initial thick weak unit above because otherwise, the nappe coupling favors the stretching of the recumbent limb (e.g., Figs. 3.6 and 3.8A and B). However, it is expected to observe an increase of amount of deformation and limb stretching in the modelled recumbent folds near the syncline hinge (using either linear viscous or power-law viscous rheologies), suggesting the localisation and development of a basal shear zone (or thrust) (e.g., Fig. 3.8 and 4.11). The observations of boudinaged calcite veins parallel to the S_{0-1}, the well-developed stretching lineation and the ductility observed in the Cambeilh area (OL1 in Fig. 5.4) and reported by Caldera (2022), also suggest that there is a significant stretching component in the recumbent limb of the Eaux-Chaudes nappe (e.g., Figs. 5.3B and 5.7A and B).

A review of natural examples of recumbent fold nappes (e.g., Bastida et al., 2014) shows that qualitatively there is a tendency to observe situations in which the recumbent limbs are interpreted as displaying strong ductile deformation, thinning, and development of basal thrust. There is only the example of the km-scale Courel recumbent fold nappe (North-west of the Iberian Massif; Fernández et al., 2007) in which the thickness of the normal and the recumbent limb are comparable.

Similar to the ECM case, the Courel nappe was developed in a paleozoic multilayer alternance between weak and strong levels in a basin limited by high angle extensional fault producing a high relief of basement rocks (gneiss of Ollo the Sapo; Fernández et al., 2007). During the Variscan, the metasedimentary sequence was deformed in simple shear conditions, with structural relief acting as a buttress. For the Courel nappe, the stretching direction is oriented parallel to the fold axis, and therefore, interpreted as produced by an extensional component parallel to the fold axis (i.e., transtensive conditions). For this situation, the increase of the second invariant of strain rate by the additional stretching components (compared to plane strain conditions) produces in power-law materials a homogenization of the strain rate in the strong layers, reducing the ability to localize deformation, and giving fold geometries similar to lineal cases (Fletcher, 1995). Exported this observation to the ECM case, perhaps the required linear behavior for fold nappe inferred from the thermomechanical simulations could be additionally reached by some non-plane strain conditions. However, this must be minor because stretching lineations in the field area are mainly normal to the ECM fold axis. It is a setting that could be tested in the future by means of 3D thermomechanical simulations.

Given the results obtained in this thesis and the structural similarities, it cannot be discarded that the other fold nappes such as Morcles or Doldenhord, for example, could have been grown with a small component of hinge migration (at least during early deformation), despite the reported ductility and extreme stretching in the recumbent limb of the structure (e.g., Casey and Dietrich, 1997). Nevertheless, a handicap to testing is the complexity of tracking the transient deformation from final geometry and structures

Thermo-mechanical results suggests that a recumbent fold nappe requires a moderate/large viscosity contrast between the weak detachments and the strong layers (i.e., Upper Cretaceous), in addition to the previously discussed linear behaviour of the stiff panel,

otherwise strain localization is focused favoring the development of brittle/plastic detachment levels, upright folds or deformation is distributed without nucleation of fold/fault structures.

For example, on one hand, the extreme case of a model with absence of an upper weak layer, and UCD and allochthonous nappes with similar viscosity (model T_0; chapter 3), no nappe development was observed. On the other hand, if the viscosity of the UCD is too high (i.e., 1 x 10^{22} Pa·s; Figs. 3.5A and 3.11), plastic/brittle deformation appears in the overturned limb thrusting geometries are then favored (e.g., Fig. 3.5G).
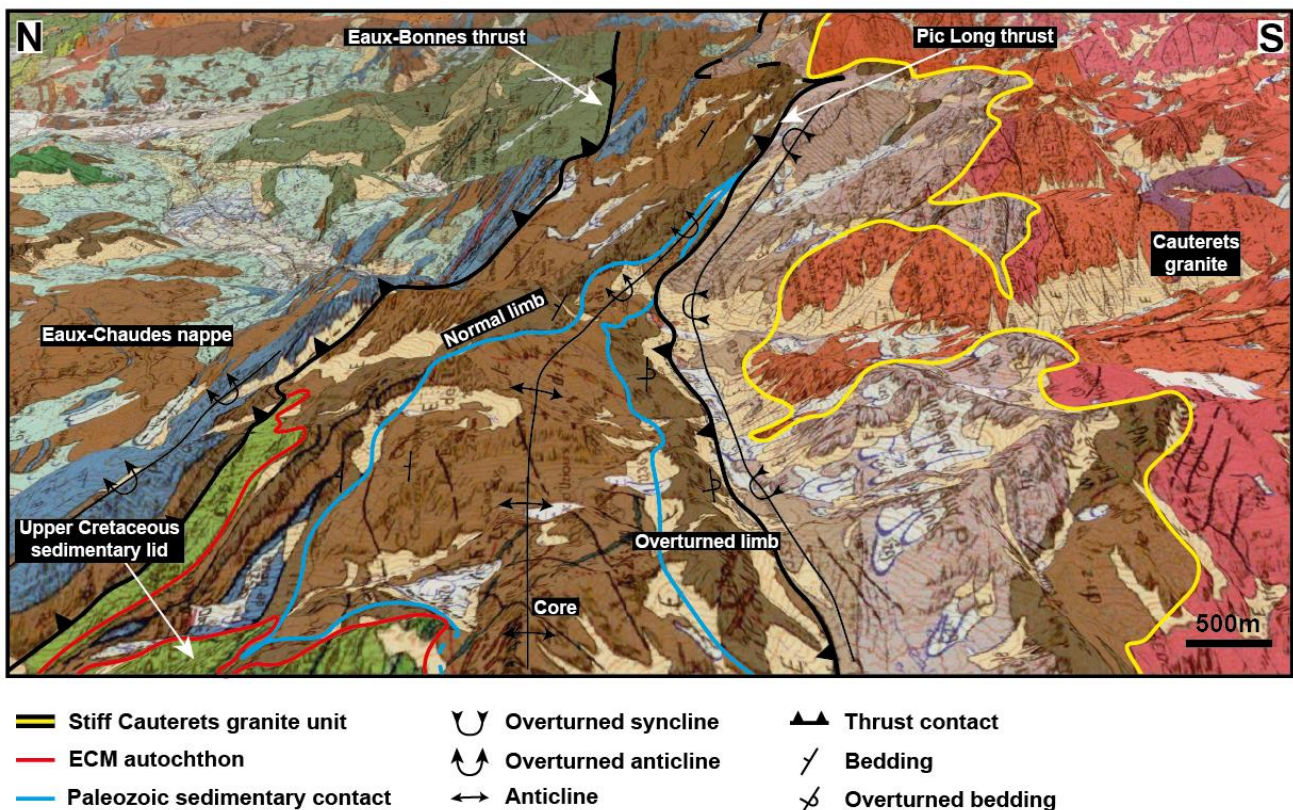
Figure 7.3: *Google Earth N-S view of the BRGM geological map east of the Eaux-Chaudes massif (Ternet et al., 2004) showing analogous structure to the Eaux-Chaudes recumbent fold nappe in the Paleozoic basement.,*

Similar ideas can be extrapolated to the lower weak level. If the viscosity of the lower detachment is in the same order of magnitude such as the UCD panel, the lower detachment is no longer active and nappe initiation/development is terminated. Using the prefactor of Silurian nappe, a viscosity contrast of about ~2-3 is required. Similar contrasts were reported

by Kiss et al. (2020) and Spitz et al. (2020) for the infra-Helvetic nappes of the Alps, reinforcing the comparison between these analogous structures.

The Eaux-Chaudes massif constitutes a unique example of the lateral variation of the structural style during the Alpine orogeny observed thanks to the Upper Cretaceous inlier (e.g., Caldera et al 2023), not observed in other areas of the Axial Zone of the Pyrenees.

However, the involvement of upper Paleozoic rocks in the ECRFN core, and also in the MIN and 5MN above, allows to guess the existence of recumbent folds developed during Alpine times in other places of the Axial Zone of the Pyrenees, where the Mesozoic sedimentary lid has not been preserved. These would also use the Keuper as an upper detachment level, not necessarily tectonically superposed over post-Triassic rocks as at Eaux-Chaudes (e.g., autochthonous or para-autochthonous). The nearby cases of the Montagnon d'Iseye and Cinq-Monts nappes, overturned Buntsandstein (subhorizontal at MIN, up to 35º in 5MN), directly under the Keuper, testifies that (e.g., Fig. 7.5).

The important role of the Silurian as a detachment level has been emphasized for the Variscan geology of the Pyrenees, specifically separating the suprastructure from the infrastructure (upper Paleozoic vs. lower Paleozoic; Matte and Zu-Xhi, 1988, García-Sansegundo, 1990). Recumbent folds are usually reported to exist only in the infrastructure (e.g., de Sitter and Zwart, 1960; Fyson, 1971; Garcia-Sansegundo et al., 2011; Bastida et al., 2014); the Silurian may have played an analogous role as the allochtonous Keuper (the upper detachment level) at Eaux-Chaudes. However, the upper Paleozoic rocks involved and the metamorphic conditions Caldera (2022), indicate that the Eaux-Chaudes fold nappe and other potential recumbent Alpine folds in the Devonian-Carboniferous would be in a position akin to the Variscan suprastructure, where the Silurian acts as the basal decollement level (where Alpine recumbent folds had not been reported before Caldera et al., 2021). For example, in the

213

eastern termination of the ECM the Devonian-Carboniferous metasediments seems to draw an Alpine recumbent fold reproducing similar mechanical conditions (i.e., stiff granite forestop) than those reported for the Eaux-Chaudes recumbent fold nappe (e,g., Fig. 7.3).

I propose that the characteristic non-cylindrical shape of the Alpine Pyrenees resulting from the Mesozoic rifting (e.g., Chevrot et al., 2018; Saspiturry et al., 2020), together with the existence of stiff granite bodies and metasedimentary weak layers within the Paleozoic (oriented favorably for detachment) strongly conditioned the Pyrenean structural style developed by the preservation of mechanical contrasts or heterogeneities. These mechanical inheritances highlight the relevance of the different geological and geodynamic events and processes occurred in a region within the evolution of the Wilson cycles (e.g., Fig. 1.1).

7.3. Sequential evolution of the ECM

7.3.1 The calcite veins of the ECM

We have seen that calcite veins in the ECM are either parallel (i.e., <30°; PFV) or orthogonal (i.e., >30°; OFV) to the main foliation (Figs. 5.5 and 5.6). The cross-cutting relationships established in this thesis indicate that the OFV post-dated the PFV veins (e.g., Fig. 5.8). PFV veins recorded the main deformational folding-thrusting event in the ECM and thus should be considered syn-tectonic with this event. The veins usually display ductile features at the outcrop scale (e.g., folding, stretching and boudinage, sense-of-shear record, etc.) in the high strain domains (e.g., Figs. 5.3A; 5.7C and 5.14A), and in singular outcrops they can define the foliation within discrete shear zones (e.g., Fig. 5.9A) delineating local detachment horizons in a similar way that Teixell et al. (2000) reported further east in the Larra thrust. Following the model from Teixell et al. (2000), the Cenomanian detachment was the result of the fluid assisted linkage of in *en-échelon* vein arrays (developed under applied sub-horizontal shear stress in the footwall of a thrust ramp) that constituted water sills parallel to a thrust

214

zone (equivalent to the PFV veins). Linked vein surfaces constituted zones of no shear strength, accounting for much of the displacement along the thrust. Multievent crack and seal fracturing model has been discarded because of the lack of crack-and-seal textures in the preserved calcite grains (relicts) from thin sections presented in this thesis.

On the other hand, PFV veins also recorded brittle features (e.g., Fig. 5.12A) evidencing therefore brittle-ductile conditions during the deformation as documented by Caldera (2022) for the rocks that host them. In these veins, the fibrous calcite can be found (1) attached and perpendicular to the vein wall, which indicates that the crystals precipitated in mode-I or mode-II fractures (e.g., Fig. 5.19B), (2) in boudin necks (e.g., Fig. 5.11C and 5.23G), or (3) in strain fringes associated to rigid grains (e.g., Fig. 5.11C), corroborating the general top-to-the-south sense of shear. On the other hand, blocky and stretched blocky calcite are most common within these veins, which display ductile features (high temperature mechanical twins, pressure-solution, and dynamic recrystallization) that are locally indicative of crystalline plasticity, consistent with the deformation observed at the outcrop scale. Indeed, in some cases, grain size refinement by intense dynamic recrystallization completely blurred the vein at the micro-scale, despite relicts of coarser grains are still preserved (e.g., Figs. 5.13E and F).

On the other hand, two conjugate sets of OFV calcite veins post-date the PFV and they strike NE-SW to NNE-SSW and NW-SE to WNW-ESE (Fig. 5.8), orientations which coincide with the macro-scale fracture network in the Caureters granite (e.g., Fig. 5.25) and that López-Martínez (1987) and Teixell (1992) reported in the Larra massif. The latter author attributed it to the emplacement of the Gavarnie thrust in Late Eocene (Teixell, 1996; Jolivet et al., 2007; Labaume et al., 2016; Teixell et al., 2016), which produced normal faulting by tangential longitudinal strain. Moreover, the calcite grains from these OFV veins are also deformed, although with less intensity than those of the PFV (pressure solution and relatively low-

temperature mechanical twinning), indicating a decrease in the temperature and strain magnitude (e.g., Figs. 5.11B and 5.13E and F).

7.3.2. Fluid evolution in the ECM

The calcite constitutes the main mineral phase precipitated in the PFV and OFV veins of the ECM, with no evidence of multi-fluid calcite cement growth. In general, the calcite displays homogeneous dull to dark yellow colors because of the large amount of Fe^{2+} (main quencher) concerning the Mn^{2+} (main activator) (e.g., Machel, 1985, 2000; Savard et al., 1995). Moreover, where recrystallization appears more intense in the thin sections, the luminescence is fully quenched and the concentration of Mn (also the other elements) is the lowest, indicating the cleaning of impurities within the crystal lattice (e.g., Fig. 5.15). This suggests that the calcite from the veins and the host rocks could have suffered an extended compositional homogenization due to recrystallisation and dedolomitization. On the other hand, the low luminescence could be also because the fluid precipitating in the fractures has a burial origin rather than meteoric (e.g., Stoppa et al., 2021). A late calcite fluid circulated through the OFV veins and parallel to the vein walls of the PFV calcite veins (e.g., Figs. 5.19A and D; 5.20F), giving a bright yellow color under the CL which is characteristic and extensive along all strain domains, which suggest a meteoric origin of this fluid. However, the available observations cannot unequivocally discriminate between the compositional homogenization and the meteoric origin of the fluids, because recrystallization is not homogeneous along the massif, and more analysis are needed to further investigate the fluid circulation paths in the Eaux-Chaudes massif (e.g., stable isotopes, fluid inclusions), which will be part of the future work.

Finally, dolomite and quartz associations observed in PFV and OFV veins indicate that after the calcite precipitation, Si- (subsaturated) and Mg-rich fluid fluids circulated through the veins

and the host rocks because the crystals from the veins have the same CL response as the rims from the dolomite and quartz from the host rocks.

7.3.3. Time constraints from the geo- and thermochronology

The calcite ages from the PFV and OFV veins presented in this thesis span from the Late Lutetian to the Late Bartonian, which I interpret to record the main folding-thrusting event that constituted the massif (Fig. 7.4 and 7.5). It has been proposed that the Eaux-Chaudes massif records the first stages of the Alpine inversion in the Pyrenees, marked by the deepening of the upper Cretaceous carbonated shelf because of the flexure of the Iberian margin (e.g., Teixell, 1992; Labaume et al., 2016b). The inversion began with the south-directed transport of the fold-and-thrust system of the Chaînons-Bearnais (CBB), carried over the Lakora thrust (Labaume and Teixell, 2020; Teixell et al., 2016; Caldera et al., 2023). Labaume et al. (2016b) discussed from tectonics-sedimentation relationships that the Lakora-Eaux-Chaudes thrust complex was most active during the Early-Mid Eocene, where we interpret that the main foliation and the PFV veins developed (Fig. 7.4B). In the western part of the massif, an upright buckle fold was developed by the buttressing effect exercised by the Eaux-Chaudes pluton (ECP) and the shear transmitted by the upper Paleozoic units (Montagnon d'Iseye -MIN-, Montagne Verte -MVN- and Cinq-Monts -5MN-), while in the east the deformation was mainly accommodated by discrete brittle thrusts in the Upper Cretaceous cover. Also, as the deformation, burial and time advances, the Cenomanian detachment level in the east becomes active by the end of this stage.
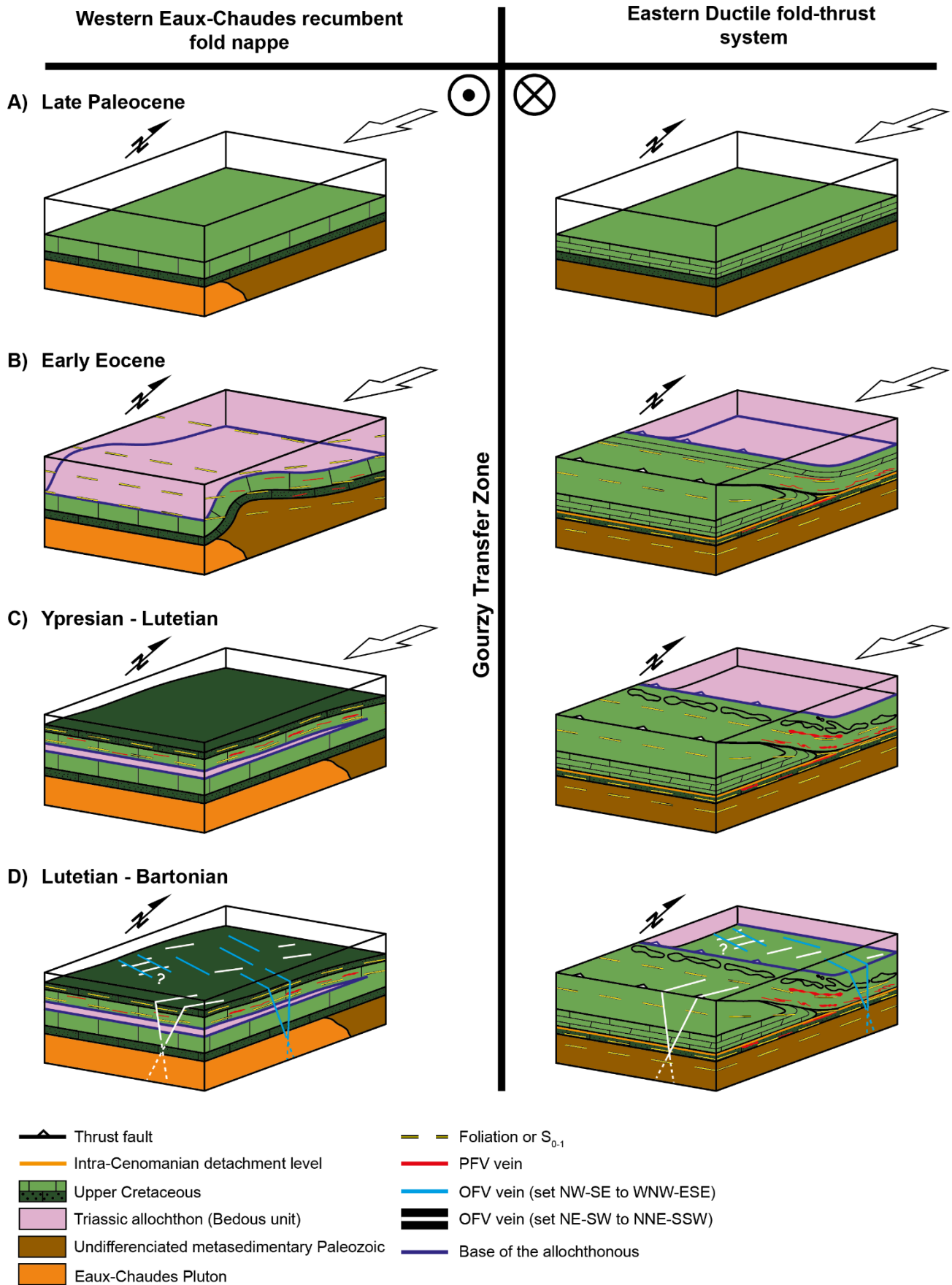
Western Eaux-Chaudes recumbent fold nappe

Eastern Ductile fold-thrust system

Gourzy Transfer Zone

A) **Late Paleocene**

B) **Early Eocene**

C) **Ypresian - Lutetian**

D) **Lutetian - Bartonian**

Thrust fault

Intra-Cenomanian detachment level

Upper Cretaceous

Triassic allochthon (Bedous unit)

Undifferenciated metasedimentary Paleozoic

Eaux-Chaudes Pluton

Foliation or S_{0-1}

PFV vein

OFV vein (set NW-SE to WNW-ESE)

OFV vein (set NE-SW to NNE-SSW)

Base of the allochthonous

During the Ypresian-Lutetian times, the main folding and ductile event occurred (Fig. 7.4C and 7.5). The sedimentary and tectonic burial over the Eaux-Chaudes massif (e.g., Labaume et al., 2016b; Caldera et al., 2023) favoured the ductile conditions and the boudinage of the early PFV veins in both the eastern and western sectors. In the east, this led to the development of tensional fractures where fibrous calcite precipitated (e.g., Fig. 5.23), dating in 48.87±5.66 Ma the main folding-thrusting event. This age coincides with the absolute ages of ca. 48-50 Ma obtained in shear zones within the Paleozoic of the Neouvielle massif further east (connected to the Eaux-Chaudes thrust) by Wayne and McCaig (1998) and Jolivet et al. (2007).

From regional geology it was inferred that last period of activity of the Lakora-Eaux-Chaudes complex was in the Lutetian-Bartonian Labaume et al. (2016b), coinciding with a change in the Jaca turbidite basin provenance (Roigé et al. 2016). In the ECM area, the OFV veins precipitated and recorded this late deformation stage of 38.14 ± 5.99 Ma, which coincides with the onset of the emplacement of the thick-skinned Gavarnie thrust in the footwall of the ECM and puts a constraint on the initiation of the exhumation process in the ECM.

The totally reset mean ZHe thermochronological ages obtained in this thesis indicates that the ECM and overlying units (i.e., MIN, Cinq-Monts and Bois de la Traillère) were tectonically buried under the ZPRZ, and were solidarily exhumed from 36 and 26 Ma (Late Eocene to Early Oligocene), after the main deformation of the ECM. Moreover, the similar ages from samples in different structural positions indicates that the observable E-W tilting of the Eaux-Chaudes fold nappe was developed during or before 30.5 Ma. The exhumation of the ECM happened probably in two main pulses of activity between 39-30 Ma, related to the emplacement of the Gavarnie thrust, and between 30-24 Ma, corresponding to the lower and
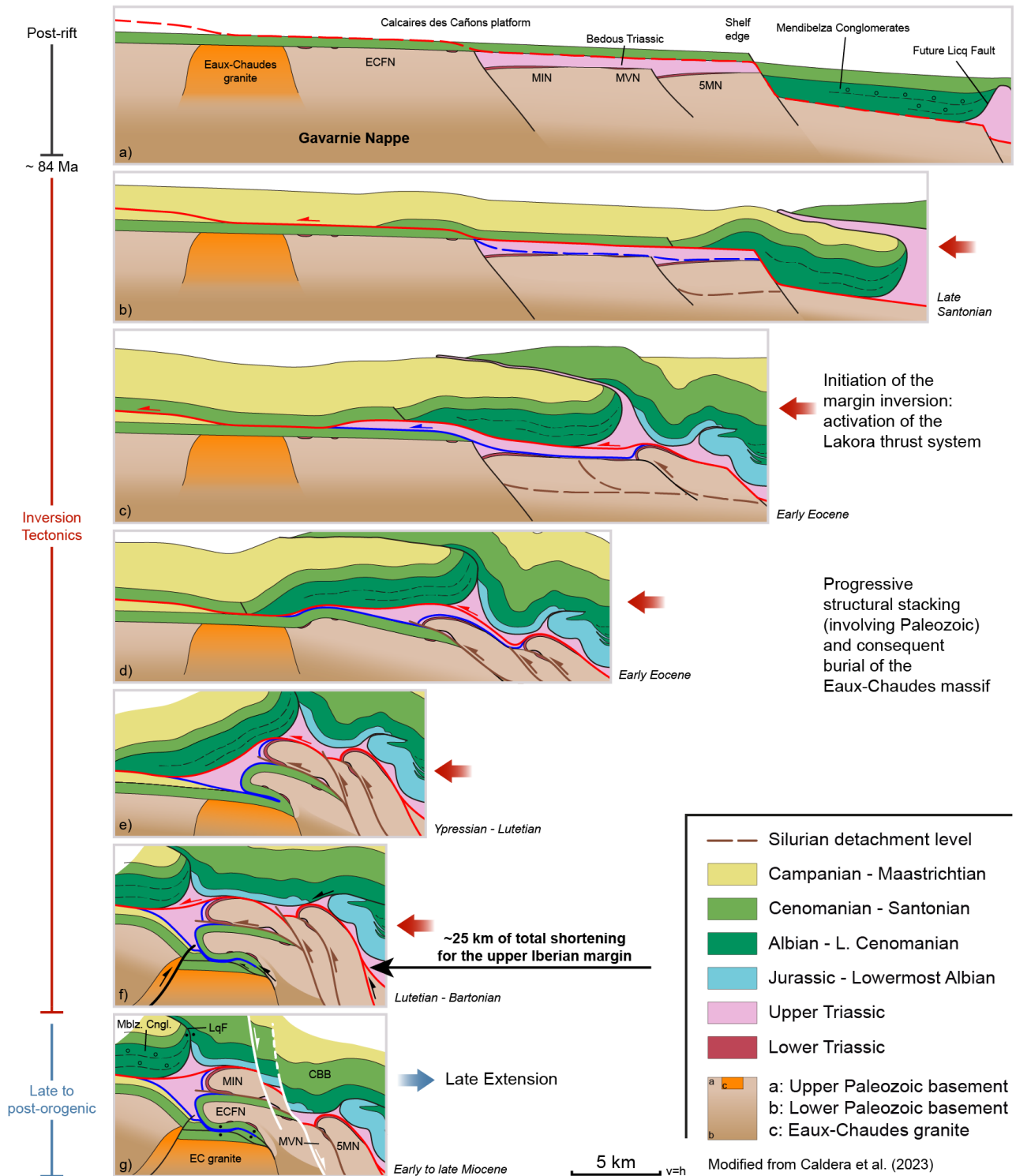
Figure 7.5: *Updated sketch from Caldera et al. (2023) considering the calcite ages and the low-temperature thermochronology results obtained in this thesis. The stages c-f are related to the stages A-D from Fig. 7.4. Red line represents the Lakora thrust carrying Caînons Béarnais fold-and-thrust belt and Mendibelza conglomerates. Blue line is the lower branch of the Lakora thrust (Caldera et al., 2023) carrying the allochthonous Keuper of the Bedous unit over the Eaux-Chaudes fold nappe. Dashed lines indicate the location of future faults in the following*

younger basement thrusts, which further raised the Axial Zone between the Oligocene and Miocene (Teixell, 1996; Jolivet et al., 2007; Labaume et al., 2016b). These cooling pulses are also predicted by the inverse thermal modelling, despite this modelling is not able to detect the RAMAN maximum temperature in the area (~350°C; Caldera et al., 2021) without a the assumption of a constraint in the modelling (48±5; 325±25°C), which unlikely results on a continuous exhumation model. However, the thermochronologic knowledge of the west-central Pyrenees favors the concept of cooling pulses because of the subsequent in-sequence thick-skinned basement thrusts (i.e., Gavarnie, Broto, Fiscal, Guarga) that raised up the Axial Zone of the Pyrenees (e.g., Jolivet et al., 2007; Teixell et al., 2016; Bosch et al., 2016; Labaume et al., 2016b), consistent also with the tectonic-sedimentation relationships observed in the Jaca basin. These pulses were followed by a late stage of more relaxed exhumation activity from ~20 Ma to the present day, as predicted by the thermal modelling and also reported by Bosch et al. (2016). The complex age-elevation relationships between the Cinq-Monts and the Bois de la Traillère units with respect to the ECM, in which the lower elevation samples gave the oldest ZHe ages, lead to the conclusion that normal faulting occurred in this late activity period, probably reactivating basal thrusts from the nappe stack as normal faults, as reported Caldera (2022) (Fig. 6.2B).

7.4. Linking thermomechanical, thermochronology and geochronology results

Considering the results of the different initial temperature gradients applied in the thermomechanical simulations and the results of the QTQt thermochronologic simulations, an important question to be addressed in terms of robustness of the work presented in this study is the compatibility between the results of both systems.
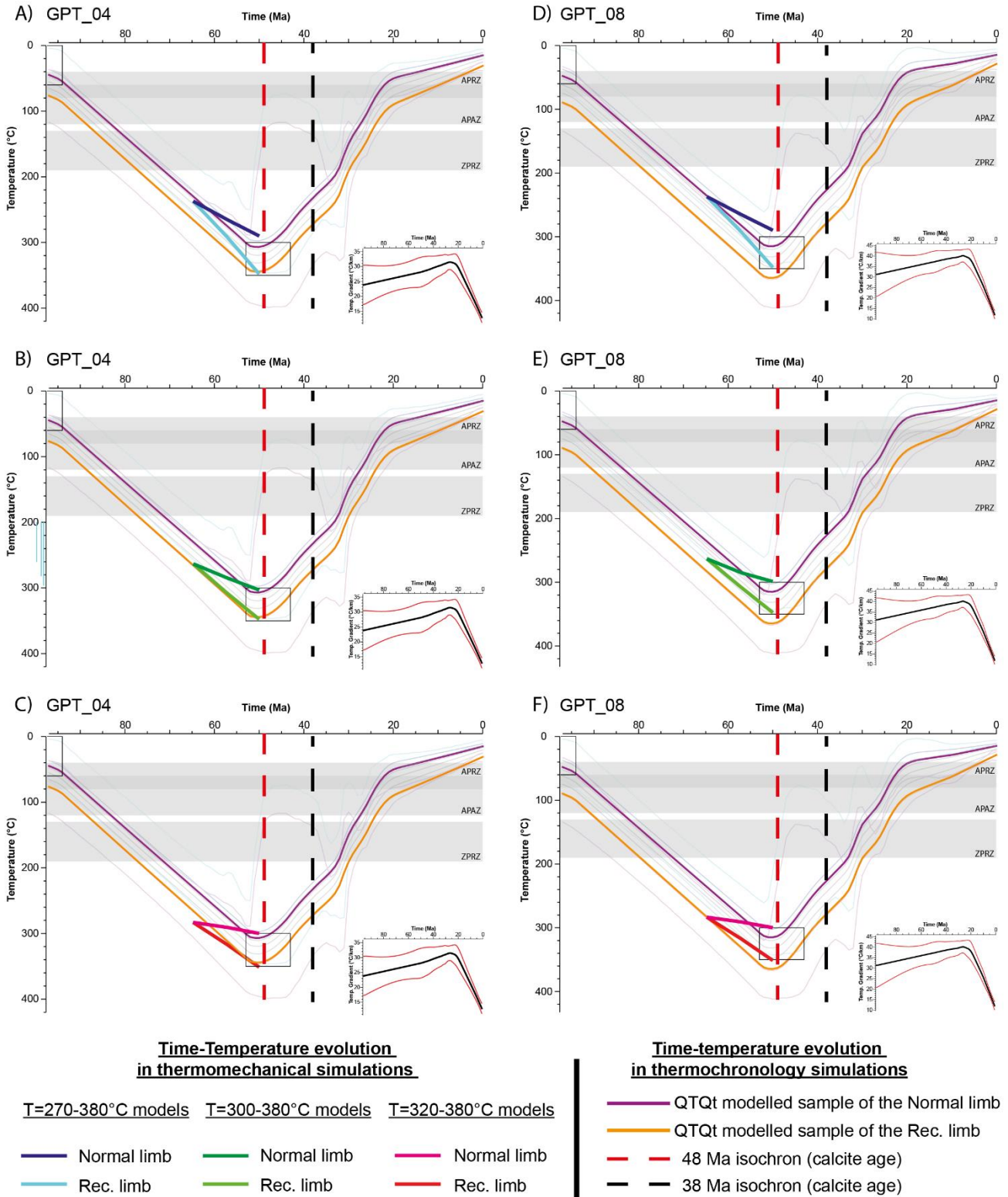
Figure 7.6: *Comparison between the time-temperature paths from the thermochronologic simulations (QTQt) for the sample 21MG155 (orange; recumbent limb) and the thermo-mechanic models (LaMEM) using the temperature extracted from the recumbent limb at 14.75 Ma of simulation time. (**A-C**) Uncorrected QTQt Tt paths at low and variable initial geothermal gradient (i.e., 25 ± 10°C/km) (**D-F**) Uncorrected QTQt Tt paths at high and variable initial geothermal gradient (i.e., 35 ± 10°C/km).*

The comparison between them is displayed in Fig. 7.6 for the thermochronologic simulations GPT_04 and GPT_08 and for the variable-temperature thermomechanic simulations that resulted in recumbent folding with initial temperatures of 270, 300 and 320°C and n = 1 (i.e., those from Fig. 4.10). In these plots, the trajectories from the samples 21MG155 (orange; recumbent limb) and 21MG146 (purple; normal limb) has been highlighted, and the rest of the sample trajectories are shown blurred. In what refers to the thermomechanic simulations, we measured the evolution of the temperature of the normal and recumbent limbs of the Upper Cretaceous layer with time. These simulations were represented after 37.3% of bulk shortening, which is equivalent to 14.75 Ma of simulation time. The time-temperature paths extracted from the different initial temperature models are represented in the QTQt thermochronologic simulations (red, green and blue curves), taking as a common reference point that the maximum temperature from the QTQt thermochronologic system coincides with the maximum temperature of the autochthonous layer (Fig. 7.6).

Note that before the onset of bulk shortening in the termomechanic simulations, the Upper Cretaceous layer is not yet deformed but is located at the same depth, therefore the temperature at the beginning must be the same. This is a condition under which the QTQt cannot reproduce, since the software considers that there is no major disruptions between samples during their burial and exhumation history (Gallagher, 2012; Gallagher et al., 2009). However, assuming that the recumbent limb is at near the same depth as the autochthon, and considering that the isotherms are flat during the deformation (as observed by Caldera (2022) and the zircon data presented in this memoir), several observations can be made.

The comparison between both systems indicates that for thermochronologic simulations using elevated and variable initial geothermal gradients (i.e., 35 ± 10°C/km; Fig. 7.6D-E) the systems are not coupled for none of the initial temperatures proposed in the thermomechanic

simulations since the time-temperature paths of the two systems are oblique between them, especially for low initial temperature in the thermo-mechanic simulations (e.g., Fig. 7.6D-F).

A better coupling arises when a lower geothermal gradient of 25 ± 10°C/km is employed in QTQt (Fig. 7.6A-C), especially for initial temperatures of 300°C and 320°C in thermomechanical simulations (which are those that better model the first-order features of the Eaux-Chaudes recumbent fold nappe), because the time-temperature paths are near parallel to that of the sample belonging to the recumbent limb (i.e., orange path). This suggests that recumbent folding in the ECM is favoured when the initial temperature is relatively high under a moderate initial geothermal gradient of 25-30°C/km, much similar to the geothermal gradients in the thermal peaks of the QTQt simulations GPT-04 (32.6°C/km) (Fig. 6.14). Moreover, the paleodepths displayed by the thermomechanical simulations are in the order of ~12 km, which coincides to those inferred for the thermochronologic simulations GPT-04 (12.3 km) despite uncertainty, as discussed before (see section 6.4.2). Caldera et al. (2021) proposed the combination of an abnormal geothermal gradient and elevated burial deep accounting for the elevated temperatures in the ECM. The comparison between the thermochronologic and thermomechanical simulations presented in this study implies that the elevated burial deep gains weight in front of an abnormal inherited geothermal gradient, not discarding combination of both, as proposed Caldera et al. (2021).

However, this observation needs to be taken with caution because is based on the aforementioned assumptions but also on the uncertainty related to the increase of the geothermal gradient with time predicted in all the QTQt simulations.

Chapter 8: Conclusions

Using a multidisciplinary approach that integrates structural analysis from classical fieldwork, numerical simulations to generate prediction models, novel and recently developed instrumental techniques (*in-situ* LA-ICP-MS U-Pb in calcite), and classical instrumental methods (low temperature (U-Th)/He thermochronology), this thesis presents the following main conclusions on the time evolution and dynamics of the Eaux-Chaudes massif of the Pyrenean Axial Zone:

8.1 Mechanical and thermomechanical controls on recumbent folding:

- The Eaux-Chaudes massif is a unique natural laboratory in the Upper Cretaceous of the collided Iberian margin to study the influence of the mechanical stratigraphy and the geometrical inheritance during the first stages of the alpine inversion in the Pyrenees, which strongly conditioned the style of contractional deformation favoring the differential development of thrust or fold nappe structures.

- The preservation of an inlier of the Upper Cretaceous sedimentary rocks overlying the Paleozoic of the Axial Zone allowed the identification of a kilometer-scale recumbent fold nappe structure, with Devonian and Carboniferous rocks in the core.

- The mechanical simulations and thermomechanical ones with $n = 1$ (linear and temperature-dependent rheology), reproduce the first-order structural elements, burial and temperature conditions, and the scale of the Eaux-Chaudes fold nappe. They also reveal the main mechanical and geometrical factors controlling the formation of thrust nappes vs fold nappes.

- In the numerical models presented in this thesis, the main cause of strain localization is the occurrence of a forestop (which was inspired by an underlying Variscan granite massif in the Eaux-Chaudes natural case) causing stress concentration in the overlying stiff

layers (Devonian and Upper Cretaceous at Eaux-Chaudes). It turns necessary the existence of such a forestop to induce recumbent folding as observed in the natural case. Model runs without a forestop produced detachment buckle folds in the stiff layers, hindering fold nappe development.

- The combination of an upper and a lower weak decoupling units (an allochthonous Keuper sheet and Silurian slates in the Eaux-Chaudes case) are essential features favouring viscous behaviour and spatially distributed deformation (low values and stable paths of the index of localisation, I_{Loc}), enabling the formation of fold nappes by progressive hinge migration (material particles are travelling from the normal to the reverse limb of the fold). The thickness of both weak layers is very relevant to allow the basal detachment of the structure but also to permit the fold to grow and tighten.

- The modelling results presented here emphasize the relevance of mechanical contrasts between stiff and weak layers allowing decoupling in compressional settings. Without a contrast of viscosity between the units involved, upright buckle folds is preferentially developed in the simulated Upper Cretaceous layers.

- The migration of the hinge of the fold nappe structure is required to preserve the thickness of the recumbent limb of the structure, as observed in the natural case, otherwise with a blocked hinge the translation of the nappe causes a strong stretching and faulting of the reverse limb.

- In the different model runs, shallower burial conditions (H), short lengths of the stiff layers (L), lower friction angles of these layers (ϕ) and stiffer upper nappes burying the target structure (η_{AN}) or stiffer simulated Upper Cretaceous layer (η_{UC}) reduce the hinge migration, enhancing the reverse limb stretching and shearing, which eventually results in strain localization and thrusting (i.e., thrust nappes), well tracked by a rapid increase of the I_{Loc}.

- In the case of power-law and temperature-dependent rheology (thermomechanical simulations), the increase of the stress exponent (n) and the temperature (T) causes the occurrence of effective viscosity heterogeneities under the applied strain rates within the key stiff layers. This produces localized surfaces under brittle (at low n and T) or viscous (at $n > 1$ and high T) regimes, resulting also in thrust nappe geometries. On the other hand, at stress exponents of $n = 1$, the behaviour of the Upper Cretaceous and Devonian key layers is homogeneous, and then recumbent folding with an extremely stretched overturned limb is promoted.

- Further work is required to fully constrain the lateral differences of the structural style at the scale of the Eaux-Chaudes massif (i.e., 3D thermomechanical modelling), which could constitute a next step in this project.

- The concepts here achieved may be applicable to other natural examples of recumbent fold nappes (e.g. the Helvetic Alps, with a stiff granite footwall and a weak supra-nappe cover). Similarly, it cannot be discarded that analogous fold nappe structures were also developed during the Alpine orogeny in the upper Paleozoic metasedimentary basement of other parts of the Pyrenean Axial Zone with comparable mechanical and geometrical conditions.

8.2 Calcite veins as kinematic indicators in the Eaux-Chaudes massif

- This work documents for the first time, by means of field analysis, thin section, cathodoluminescence and ICP-MS analysis, systematic data on the calcite veins hosted in the Upper Cretaceous carbonates of the Eaux-Chaudes massif.

- The calcite veins registered the main folding and thrusting event. Veins are found parallel (<30°; PFV) or orthogonal (>30°; OFV) to the main foliation or S_{0-1} developed in the Upper Cretaceous carbonates.

- PFV veins are seen ductilely deformed at the outcrop scale (folded and boudinaged) and show a consistent and characteristic Alpine top-to-the-south sense of shear record. These were post-dated by the OFV veins, attested by systematic offset relationships.

- At the microscopic scale, PFV veins are mainly composed of blocky and stretched blocky calcite displaying ductile features (high-temperature twinning, pressure solution, and dynamic recrystallization) but also brittle cracking in some cases.

- Fibrous calcite also precipitated in the PFV veins (1) orthogonal to the vein walls (indicating that the calcite precipitated in mode-I or mode-II fractures), (2) in the strain shadows of rigid grains (indicating top-to-the-south shear) or (3) in the boudin necks of early PFV veins. PFV veins display a homogeneous dark-to-dull yellow colour under cathodoluminescence, probably because of homogenization at depth due to recrystallization, which is likely the main cause of the abundance of common Pb detected in the geochronological analysis.

- The Gourzy transfer zone inferred by Caldera (2022) and Caldera et al. (2023) has been identified by calcite veins as a sinistral shear zone that accommodated the deformation between the western recumbent fold domain and the eastern ductile fold-and-thrust fan domain.

- The OFV veins registered the last activity of the Eaux-Chaudes thrust/fold and the onset of the exhumation in the Eaux-Chaudes massif. These were deformed under colder and dominant brittle conditions (brittle cracks) than the PFV, and are mainly composed of blocky calcite.

8.3 Timing of deformation and exhumation of the Eaux-Chaudes massif and surrounding units

- Among the objectives of this work were to date directly the main ductile folding and thrusting event affecting the Upper Cretaceous of the Eaux-Chaudes thrust complex in the northern Axial Zone. U-Pb geochronology analytical results of foliation-parallel veins indicate that the main folding/thrusting occurred between the late Ypresian (48.87±5.66 Ma) and the early Bartonian (38.14 ± 5.99 Ma).

- New zircon (U-Th)/He thermochronologic data from the Upper Cretaceous and the upper Paleozoic-bearing structural units (Montagnon d'Iseye, Cinq-Monts and Bois de la Traillère), complementing previous work by Bosch et al. (2016) in the basement (footwall) of the ECM, reveal a complex exhumation history spanning from ~40 to ~6.6 Ma (based on individual aliquot ages).

- The ZHe system was totally reset in the Upper Cretaceous and Paleozoic rocks belonging to the different structural units of the study area. The ECM and the upper nappes (Montagnon d'Iseye, Cinq-Monts) were solidarily exhumed through the zircon closure temperature at ~40-30 Ma (mid-Eocene–Oligocene) over of the thick-skinned Gavarnie thrust, and between ~30-20 Ma as a consequence of in-sequence basement thrust activity, probably the Guarga thrust.

- The referred cooling pulses are detected by the QTQt thermal modelling software preferentially in vertical profiles with higher sample resolution and without the use of the calcite age constraint. The use of the calcite age as the thermal peak produces preferentially continuous exhumation histories.

- From ~20Ma to the present day, the cooling is systematically stable and continuous, constrained by AHe complementary data from Bosch et al. (2016). This episode is

accompanied by late normal faulting which offsets the normal age-elevation relationships

in the Cinq-Monts and Bois de la Traillère units.

Chapter 9: References

Abbey, A., Wildman, M., Stevens Goddard, A. L. and Murray, K.E. (2023): Thermal history modeling techniques and interpretation strategies: Applications using QTQt. *Geosphere, 19 (2),* 493–530. https://doi.org/10.1130/GES02528.1

Aerden, D. and Sayab, M. (2017): Probing the prodigious strain fringes from Lourdes. *Journal of structural Geology, 105*, 88-106. https://doi.org/10.1016/j.jsg.2017.11.001

Alhamawi, M. (1992). Sédimentologie, pétrographie sédimentaire et diagenèse des Calcaires du Crétacé supérieur de la Marge Ibérique: Bordeaux 1, 356 p.

Andò, S. (2020): Gravimetric separation of heavy minerals in sediments and rocks. *Minerals, 10(3)*, 273. https://doi.org/10.3390/min10030273

Argand, E. (1916): Sur l'arc des Alpes Occidentales. *Eclogae Geologicae Helveticae, 14*, 145-191.

Arndt, J., Bartel, T., Scheuber, E. and Schilling, F. (1997): Thermal and rheological properties of granodioritic rocks from the Central Andes, North Chile. *Tectonophysics, 271,* 75-88. https://doi.org/10.1016/S0040-1951(96)00218-1

Badoux, H. (1971): Atlas géologique de la Suisse 1:25000, Feouille 1305: Dents de Morcles. Notice explicative. *Organe de la Société Helvétique des Sciences Naturelles.*

Bastida, F., Aller, J., Fernández, F. J., Lisle. R. J., Bobillo-Ares, N. C. and Menéndez, O. (2014): Recumbent folds: Key structural elements in orogenic belts. *Earth-Science Reviews, 135*, 162-183. https://doi.org/10.1016/j.earscirev.2014.05.002

Bauville, A. and Schmalholz, M. (2015): Transition from thin- to thick-skinned tectonics and consequences for nappe formation: Numerical simulations and applications to the Helvetic nappe system, Switzerland. *Tectonophysics, 665*, 101-117. https://doi.org/10.1016/j.tecto.2015.09.030

Bauville, A. and Schmalholz, S. M. (2017): Tectonic inheritance and kinematic strain localization as trigger for the formation of the Helvetic nappes, Switzerland. *Swiss Journal of Geosciences, 110*, 523-534. https://doi.org/10.1007/s00015-017-0260-9

Beaudoin, N., Lacombe, O., Roberts, N. M., and Koehn, D. (2018): U-Pb dating of calcite veins reveals complex stress evolution and thrust sequence in the Bighorn Basin, Wyoming, USA, *Geology, 46,* 1015–1018. https://doi.org/10.1130/G45379.1

Beaumont, C., Muñoz, J. A., Hamilton, J. and Fullsack, P. (2000): Factors controlling the Alpine evolution of the central Pyrenees inferred from a comparison of observations and geodynamical models. *Journal of Geophysical Research, Solid Earth 105*, 353 8121-8145. https://doi.org/10.1029/1999JB900390

Bellahsen, N., Jolivet, L., Lacombe, O., Bellanger, M., Boutoux, A., Garcia, S., Mouthereau, F., Le Pourhiet, L. and Gumiaux, C. (2012): Mechanisms of margin inversion in the external Western Alps: Implications for crustal rheology. *Tectonophysics, 560-561*, 62-83. https://doi.org/10.1016/j.tecto.2012.06.022

Bellahsen, N., Mouthereau, F., Boutoux, A., Bellanger, M., Lacombe, O., Jolivet, L. and Rolland, Y. (2014): Collision kinematics in the western external Alps. *Tectonics, 33*, 1055-1088. https://doi.org/10.1002/2013TC003453

Bellahsen, N., Bayet, L., Denele, Y., Waldner, M., Airaghi, L., Rosenberg, C., Dubacq, B., Mouthearau, F., Bernet, M., Pik, R., Lahfid, A. Vacherat, A. (2019): Shortening of the axial zone, pyrenees: Shortening sequence, upper crustal mylonites and crustal strength. *Tectonophsics, 766 (5).* 433-452. https://doi.org/10.1016/j.tecto.2019.06.002

Berastegui, X., Garcia, J. M. and Losantos, M. (1990). Structure and sedimentary evolution of the Organyà basin (Central South Pyrenean Unit, Spain) during the lower Cretaceous. *Bulletin de la Société Géologique de France, VI (2).* https://doi.org/10.2113/gssgfbull.VI.2.251

Biteau, J.-J., Le Marrec, A., Le Vot, M. and Masset, J. -M. (2006). The Aquitaine Basin. *Petroleum Geosciences, 12 (3)*, 247-273. http://dx.doi.org/10.1144/1354-079305-674

Bons, P. D., Elburg, M.A. and Gomez-Rivas, E. (2012): A review of the formation of tectonic veins and their microstructures. *Journal of Structural Geology, 43*, 33-62. https://doi.org/10.1016/j.jsg.2012.07.005

Bonini, L., Dallagiovanna, G. and Seno, S. (2010): The role of pre-existing faults in the structural evolution of thrust systems: Insights from the Ligurian Alps (Italy). *Tectonophysics, 480 (1-4)*, 73-87. https://doi.org/10.1016/j.tecto.2009.09.021

Bosch, G. V., Teixell, A., Jolivet, M., Labaume, P., Stockli, D., Domènech, M. and Monié, P. (2016): Timing of Eocene–Miocene thrust activity in the Western Axial Zone and Chaînons Béarnais (west-central Pyrenees) revealed by multi-method thermochronology. *Comptes Rendus Geoscience 348 (3-4),* 246-256. https://doi.org/10.1016/j.crte.2016.01.001

Boutoux, A., Bellashen, N., Lacombe, O., Verlaguet, A. and Mouthereau, F. (2014): Inversion of pre-orogenic extensional basins in the external Western Alps: Structure, microstructures and restoration. *Journal of Structural Geology, 60*, 13-29. https://doi.org/10.1016/j.jsg.2013.12.014

Brennan, C. J., Stockli, D. F. and Patterson, D. D. (2020): Zircon ^{4}He/^{3}He fractional loss step-heating and characterization of parent nuclide distribution. *Chemical Geology, 549.* https://doi.org/10.1016/j.chemgeo.2020.119692

Budd, D. A., Hammes, U. and Ward, W. B. (2000). Cathodoluminescence in calcite cements: New insights on Pb and Zn sensitizing, Mn activation, and Fe quenching at low trace-element concentrations. *Journal of Sedimentary Research, 70 (1)*, 217-226. https://doi.org/10.1306/2DC4090C-0E47-11D7-8643000102C1865D

Burkhard, M. (1993): Calcite twins, their geometry, appearance and significance as stress-strain markers and indicators of tectonic regime: a review, *Journal of Structural Geology, 15 (3-5)*. https://doi.org/10.1016/0191-8141(93)90132-T

Butler, R., Tavarnelli, E. and Grasso, M. (2006): Structural inheritance in mountain belts: An Alpine-Apennine perspective. *Journal of Structural Geology, 28*, 1893-1908. https://doi.org/10.1016/j.jsg.2006.09.006

Butler, R., Bond, C., Cooper M. A. and Watkins, H. (2018): Interpreting structural geometry in fold-thrust belts: Why style matters. *Journal of Structural Geology, 114*, 251-273. https://doi.org/10.1016/j.jsg.2018.06.019

Caldera, N., Teixell, A., Griera, A., Labaume, P. and Lahfid, A. (2021): Recumbent folding in the Upper Cretaceous Eaux-Chaudes massif: A Helvetic-type nappe in the Pyrenees?. *Terra Nova, 33,* 320-331. https://doi.org/10.1111/ter.12517

Caldera, N. (2022): *Ductile deformation of the Pyrenean hinterland during the Alpine collision: The case of the proximal Iberian margin in the Eaux-Chaudes massif (west-central Pyrenees)*. Doctoral dissertation, Universitat Autònoma de Barcelona, 226.

Caldera, N. (2023): Upper Cretaceous cleavage and stretching lineation (Eaux-Chaudes massif) (Version 1) [Dataset]. Mendeley Data. https://doi.org/10.17632/2t2rz4khs4.1

Caldera, N., Teixell, A., Griera, A., Labaume, P. and Guardia, M. (2023): Alpine Ductile Deformation of the Upper Iberian Collided Margin (Eaux-Chaudes Massif, West-Central Pyrenean Hinterland, France). *Tectonics, 42 (11)*. https://doi.org/10.1029/2023TC007828

Carreras, J., Druget, E., Griera, A. (2005): Shear zone-related folds. Journal of Structural Geology, 27, 1229–1251. https://doi.org/10.1016/j.jsg.2004.08.004

Cardozo, N. and Allmendinger, R. (2013): Spherical projections with OSXStereonet. *Computers & Geosciences, 51,* 193-205. https://doi.org/10.1016/j.cageo.2012.07.021

Casey, M. and Dietrich, D. (1997): Overthrust shear in mountain building. In: Sengupta, S. (eds), *Evolution of Geological Structures in Micro- to Macro-scales*. Springer, Dordrecht. https://doi.org/10.1007/978-94-011-5870-1_8

Casteras, M. (1956). Calcaire des Eaux-Chaudes (France, Basses, Pyrénées) – Garumnien – Poudingue de Mendibelza. In *Lexique stratigraphique international, 1*, 4a VI, Crétacé.

Casteras, M. and Souquet, P. (1964). Sur la constitution et sur la structure de la couverture crétacée de la Zone primaire axiale pyrénéenne à l'Ouest du Pic d'Anie. *Comptes Rendus de l'Académie des Scciences, Paris, 259 (17)*, 2881-2886.

Chelalou, R., Nalpas, T., Bousquet, R., Prevost, M., Lahfid, A., Poujol, M., Ringenbach, J.-C. and Ballard, J.-F. (2016). New sedimentological, structural and paleo-thermicity data in the Boucheville Basin (eastern North Pyrenean Zone, France). Comptes Rendus Geoscience, 348 (3-4), 312-321. https://doi.org/10.1016/j.crte.2015.11.008

Chevrot, S., Sylvander, M. Diaz, J., Martin, R., Mouthereau, F., Manatschal, G., Masini, E., Calassou, S., Grimaud, F., Pauchet, H. and Ruiz, M. (2018). The non-cylindrical crustal architecture of the Pyrenees. *Scientific Reports, 8,* 9591. https://doi.org/10.1038/s41598-018-27889-x

Chew, D., Petrus, J. and Kamber, B. (2014): U–Pb LA–ICPMS dating using accessory mineral standards with variable common Pb. *Chemical Geology, 363*, 185-199. https://doi.org/10.1016/j.chemgeo.2013.11.006

Chew, D., Drost, K., Marsh, JH. And Petrus, J.A. (2021): LA-ICP-MS imaging in the geosciences and its applications to geochronology. *Chemical Geology, 559*, 119917. https://doi.org/10.1016/j.chemgeo.2020.119917

Choukroune, P. and ECORS Team. (1989): The ECORS deep seismic profile reflection data and the overall structure of an orogenic belt. Tectonics, 8, 23-29. https://doi.org/10.1029/TC008i001p00023

Clerc, C. (2012): Evolution du domaine nord---pyrénéen au Crétacé. Amincissement crustal extrême et thermicité élevée: un analogue pour les marges passives. Doctoral dissertation, Université Pierre et Marie Curie - Paris VI, 249.

Clerc, C. and Lagabrielle, Y. (2014): Thermal control on the modes of crustal thinning leading to the mantle exhumation: Insights from the Cretaceous Pyrenean hot paleomargins. *Tectonics, 33*, 1340-1359. https://doi.org/10.1002/2013TC003471

Clerc, C., Lahfid, A., Monié, P., Lagabrielle, Y., Chopin, C., Poujol, M., Boulvais, P., Ringenbach, J.-C., Masini, E. and de St Blanquat, M. (2015): High-temperature metamorphism during extreme thinning of the continental crust: a reappraisal of the North Pyrenean passive paleomargin. *Solid Earth, 6 (2)*, 643–668. https://doi.org/10.5194/se-6-643-2015

Clerc, C., Lagabrielle, Y., Labaume, P., Ringenbach, J.-C., Vauchez, A., Nalpas, T., Bousquet, R., Ballard, J.-F., Lahfid, A. and Fourcade, S. (2016). Basement – Cover decoupling and progressive exhumation of metamorphic sediments at hot rifted margin. Insights from the Northeastern Pyrenean analog. *Tectonophysics, 686*, 82-97. https://doi.org/10.1016/j.tecto.2016.07.022

Cloos, H. (1928): Experimenten zur innerenTektonik. *Centralblatt fur Mineralogie and Paleontologie*, 609.

Cloix, A. (2017): Bréchification de la série prérift Nord-Pyrénéenne : Mécanismes tectoniques ou/et sédimentaires et place dans l'histoire tectono-métamorphique de la marge extensive crétacée et de son inversion Pyrénéenne (Chaînons Béarnais, Zone Nord-Pyrénéenne). *Mémoire de recherche Master 2 Géologie de l'Exploration et des Réservoirs.* Université de Montpellier.

Cochelin, B., Chardon, D., Denèle, Y., Gumiaux, C. and Le Bayon, B. (2017): Vertical strain partitioning in hot Variscan crust: Syn-convergence escape of the Pyrenees in the Iberian-Armorican syntax. *Bulletin de la Société Géologique de France, 188 (6)*, 39. https://doi.org/10.1051/bsgf/2017206

Conard, M. and Rioult, M. (1977): Halimeda elliotti nov. sp. Algue calcaire (chlorophyceae) du Turonien des Alpes-Maritimes (Sud-Est de la France). *Géologie Mèditerraneenne, 4 (2)*.

Coogan, L. A., Parrish, R. R., and Roberts, N. M. (2016): Early hydrothermal carbon uptake by the upper oceanic crust: Insight from in situ U-Pb dating, *Geology, 44*, 147–150. https://doi.org/10.1130/G37212.1

Corre, B. (2017): La bordure nord de la plaque ibérique à l'Albo-Cénomanien: architecture d'une marge passive de type ductile (Chaînons Béarnais, Pyrénées Occidentales). *Doctoral dissertation, Rennes 321.*

Cosgrove, J. W. (2015): The association of folds and fractures and the link between folding, fracturing and fluid flow during the evolution of a fold–thrust belt: a brief review. *Geological Society, London, Special Publications, 421*, 41-68. https://doi.org/10.1144/SP421.11

Costa, E. and Vendeville, B. C. (2002): Experimental insights on the geometry and kinematics of fold-and-thrust belts above weak, viscous evaporitic décollement. *Journal of Structural Geology, 24(11),* 1729-1739. https://doi.org/10.1016/S0191-8141(01)00169-9

Crognier, N., hoareau, G., Aubourg, C., Dubois, M., Lacroix, B., Branellec, M., Callot, J. P. and Vennemann, T. (2018): Syn-orogenic fluid flow in the Jaca basin (south Pyrenean fold and thrust belt) from fracture and vein analyses. *Basin Research, 30 (2)*, 187-216. https://doi.org/10.1111/bre.12249

Cruset, D. (2019): Sequential fluid migration along a fold and thrust belt: SE Pyrenees from Late Cretaceous to Oligocene. *Doctoral disetation,* 334pp.

Cruset, D., Vergés, J., Muñoz-López, D., Moragas, M., Cantarero, I. and Travé, A. (2023): Fluid evolution from extension to compression in the Pyrenean Fold Belt and Basque-Cantabrian Basin: A review. *Earth-Science Reviews, 243,* 104494. https://doi.org/10.1016/j.earscirev.2023.104494

Debroas, E. J. (1987): Modele de bassin triangulaire à l'intersection de décrochement divergents pour Ie fossé albo-cénomanien de la Ballongue (zone nord pyrénéenne, France). *Bulletin de la Société Géologique de France, III*. 887-898.

Debroas, E J. (1990): Le Flysch noir albo-cénomanien témoin de la structuration albienne à séronienne de la Zone nord-pyrénénne en Bigorre (Hautes-Pyrénées, France). *Bulletin de la Société Géologique de France, VI*. 273-285.

Dennis, J.G., Price, R. A., Sales, J. K., Hatcher, R., Bally, A. W., Perry, W. J., Laubscher, H. P., Williams, R. E., Elliott, D., Norris, D. K., Hutton, D. W., Emmerr, T. and McClay, K. R. (1981): What is a Thrust? What is a Nappe?, In: Thrust and Nappe Tectonics (McClay, K.R. and Price, N.J., eds.). *Geological Society of London Special Publications, 9*. 7–9. https://doi.org/10.1144/GSL.SP.1981.009.01.02

Déramond, J., Graham, R., Hossack, H., Baby, J. R., Crouzet, P. and Crouzet, G. (1985): Noveau modéle de la chaîne des Pyrénées. *Comptes Rendus de l'Académie des Sciences, Paris, 301,* 1213-1216.

Delvolvé, J. J. (1987). Un basin synorogénique varisque: le Culm des Pyrénées centro-occidentales. *Thèse Doctorel Sciences, Toulouse*, 483 p.

de Sitter, L.U., Zwart, H.J. (1960): Tectonic development in supra and infrastructures of a mountain chain. *Proceedings 21st. International Congress Copenhagen*. 248–256.

Dietrich, D. and Casey, M. (1989): A new tectonic model for the Helvetic nappes. In: Alpine Tectonics (Coward, M.P. and Park, R.G., eds.). *Geological Society London Special Publications 45*, London, 47–63. http://dx.doi.org/10.1144/GSL.SP.1989.045.01.03

Drake, H., Heim, C., Roberts, N. M. W., Zack, T., Tillberg, M., Broman, C., Ivarsson, M., Whitehouse, M. J., and Åström, M. E. (2017): Isotopic evidence for microbial production and consumption of methane in the upper continental crust throughout the Phanerozoic eon, *Earth and Planetary Science Letters, 470*, 108–118. https://doi.org/10.1016/j.epsl.2017.04.034

Drost, K., Chew, D., Petrus, J. A., Scholze, F., Woodhead, J.D., Schneider, J. W. and Harper, D.A. (2018): An Image Mapping Approach to U-Pb LA-ICP-MS Carbonate Dating and Applications to Direct Dating of Carbonate Sedimentation. *Geochemistry, Geophysics, Geosystems, 19 (12)*, 4631-4648. https://doi.org/10.1029/2018GC007850

Ducoux, M. (2017). Structure, thermicité et évolution géodynamique de la Zone Interne Métamorphique des Pyrénées. *Thèse de Doctorat. Université d'Orléans,* 642.

Ducoux, M., Jolivet, L., Callot, J.-P., Aubourg, C., Masini, E., Lahfid, A., Homonnay, E., Cagnard, F. Gumiaux, C. and Baudin, T. (2019). The Nappe des Marbres Unit of the Basque-Cantabrian Basin: the tectono-thermal evolution of a fossil hyperextended rift basin. *Tectonics, 38 (11)*, 3881-3915. https://doi.org/10.1029/2018TC005348

Ducoux, M., Jolivet, L., Masini, E., Augier, R., Lahfid, A., Bernet, M. and Calassou, S. (2021). Distribution and intensity of High-Temperature Low-Pressure metamorphism across the Pyrenean-Cantabrian belt: constraints on the thermal record of the pre-orogenic hyperextension rifting. *Bulletin de la Société Géologique de France, 192 (1)*, 43. https://doi.org/10.1051/bsgf/2021029

Dumont, T., Replumaz, A., Rouméjon, S., Briais, A., Rigo, A. and J-P. (2015): Microseismicity of the Béarn range: Reactivation of inversion and collision structures at the northern edge of the Iberian plate. *Tectonics, 34 (5)*, 934-950. https://doi.org/10.1002/2014TC003816

Epard, J-L. and Groshong, R. H. (1995): Kinematic model of detachment folding including limb rotation, fixed hinges and layer-parallel strain. *Tectonophysics, 247 (1-4)*, 85-103. https://doi.org/10.1016/0040-1951(94)00266-C

Epard, J-L. and Escher, A. (1996): Transition from basement to cover: a geometric model. *Journal of Structural Geology, 5*, 533-548. https://doi.org/10.1016/S0191-8141(96)80022-8

Erickson, S.G. (1996): Influence of mechanical stratigraphy on folding vs. faulting. *Journal of Structural Geology, 18 (4)*, 443-450. https://doi.org/10.1016/0191-8141(95)00064-K

Escher, A., Masson, H. and Steck, A. (1993): Nappe geometry in the Western Swiss Alps. *Journal of Structural Geology, 15*, 501-509. https://doi.org/10.1016/0191-8141(93)90144-Y

Espurt, N., Angrand, P., Teixell, A., Labaume, P., Ford, M., de Saint Blanquart, M. and Chevrot, S. (2019). Crustalscale balanced cross-section and restoration of the Central Pyrenean belt (Nestes-Cinca transect): highlighting the structural control of Variscan belt and Permian-Mesozoic rift systems on mountains building. *Tectonophysics, 764, 25-45*. https://doi.org/10.1016/j.tecto.2019.04.026

Ez, V. (2000): When shearing is the cause of folding. *Earth Science Reviews, 51 (1-4)*, 155-172. https://doi.org/10.1016/S0012-8252(00)00020-9

Farley, K.A., Wolf, R.A. and Silver, L.T. (1996): The effects of long alpha-stopping distances on (U-Th)/He ages. *Geochimica et Cosmochimica Acta, 60 (21)*. 4223-4229. https://doi.org/10.1016/S0016-7037(96)00193-7

Farley, K.A. (2000): Helium diffusion from apatite: General behaviour as illustrated by Durango fluorapatite. *Journal of Geophysical research, 105 (B2)*. https://doi.org/10.1029/1999JB900348

Fernández, F. J., Aller, J. and Bastida, F. (2007): Kinematics of a kilometric recumbent fold: The Courel syncline (Iberian massif, NW Spain). *Journal of Structural Geology, 29*, 1650-1664. https://doi.org/10.1016/j.jsg.2007.05.009

Ferrill, D. A., Morris, A. P., Evans, M. A., Burkhard, M., Groshong Jr., R. H. and Onasch, C. M. (2004): Calcite twin morphology: a low-temperature deformation geothermometer. *Journal of Structural Geology, 26 (8)*. https://doi.org/10.1016/j.jsg.2003.11.028

Fletcher, R. C. (1995): Three-dimensional folding and necking of a power-law layer: are folds cylindrical, and, if so, do we understand why?, *Tectonophysics, 247 (1-4)*. https://doi.org/10.1016/0040-1951(95)00021-E

Flowers, R., Ketcham, R., Shuster, D. and Farley, K. (2009): Apatite (U–Th)/He thermochronometry using a radiation damage accumulation and annealing model. *Geochimica et Cosmochimica Acta, 73 (8),* 2347-2365. https://doi.org/10.1016/j.gca.2009.01.015

France, D. (1987): Recumbent folds. In: *The Encyclopedia of Structural Geology and Plate Tectonics* (Seyfert, C.K., ed.). Van Nostrand Reinhold Company, New York, 650–656.

Frehner, M. (2011): The neutral lines in buckle folds. *Journal of Structural Geology, 33 (10)*. https://doi.org/10.1016/j.jsg.2011.07.005

Fyson, W.K. (1971): Fold attitudes in metamorphic rocks. *American Journal of Science. 270*, 373–382. https://doi.org/10.2475/ajs.270.5.373

Gallagher, K., K. Charvin, S. Nielsen, M. Sambridge, and J. Stephenson (2009): Markov chain Monte Carlo (MCMC) sampling methods to determine optimal models, model resolution and model choice for Earth Science problems. *Marine and Petroleum Geology, 26*, 525–535. https://doi.org/10.1016/j.marpetgeo.2009.01.003

Gallagher, K. (2012): Transdimensional inverse thermal history modeling for quantitative thermochronology. *Journal of Geophysical Research, 117 (B2)*. https://doi.org/10.1029/2011JB008825

Gallagher, K. (2021): QTQt v.5.8.0, User Guide.

García-Sansegundo, J. (1990). Structure of the Paleozoic in the Aran Valley, Axial Zone, central Pyrenees. *Bulletin de la Societe Géologique de France, 2*, 229–239. https://doi.org/10.2113/gssgfbull.VI.2.229

Garcia-Sansegundo, J. (1992): *Estratigrafia y estructura de la Zona Axial pirenaica en la transversal del Valle de Arán y de la Alta Ribagorça*. Doctoral dissertation, Universidad de Oviedo, 167.

García-Sansegundo, J., Poblet, J., Alonso, J. L. and Clariana, P. (2011). Hinterland – foreland zonation of the Variscan orogen in the central Pyrenees: Comparison with the northern part of the Iberian Variscan Massif. *Geological Society, London, Special Publications, 349(1),* 169-184. https://doi.org/10.1144/sp349.9

Garcia-Senz, J., Pedrera, A., Ayala, C., Ruiz-Constán., A., Robador., A. and Rodríguez-Fernández, L. A. (2019): Inversion of the north Iberian hyperextended margin: the role of exhumed mantle indentation during continental collision. In: J. A. Hammerstein (Ed.), *Fold and Thrust Belts: Structural Style, Evolution and Exploration, Geological Society, London, Special Publications,* 490, (177-198) *https://doi.org/10.1144/SP490-2019-112*

Gautheron, C., Tassan-Got, L., Barbarand, J. and Pagel, M. (2009): Effect of alpha damage annealing on apatite (U/Th)/He thermochronology. *Chemical Geology, 266 (3-4).* https://doi.org/10.1016/j.chemgeo.2009.06.001

Gautheron, C., Barbarand, J., Ketcham, R., Tassan-got, L., van der Beek, P., Pagel, M., Pinna-Jamme, R., Couffignal, F. and Fialin, M. (2013): Chemical influence on α-recoil damage annealing in apatite: Implications for (U–Th)/He dating. *Chemical Geology, 351,* 257-267. https://doi.org/10.1016/j.chemgeo.2013.05.027

Gerya, T (2019): Introduction to Numerical Geodynamic Modelling. *Cambridge University Press, 2 edn.*, 345 pp. https://doi.org/10.1017/9781316534243

Gerya, T (2022): Numerical modeling of subduction: State of the art and future directions. *Geosphere, 18 (2)*. 503-561. https://doi.org/10.1130/GES02416.1

Girault, J. B., Bellahsen, N., Boutoux, A., Rosenberg, C. L., Nanni, U., Verlaguet, A. Beyssac, O. (2020): The 3-D Thermal Structure of the Helvetic Nappes of the European Alps: Implications for Collisional Processes. *Tectonics, 39(3).* https://doi.org/10.1029/2018TC005334

Goodfellow, B. W., Viola, G., Bingen, B., Nuriel, P., and KylanderClark, A. R. (2017): Palaeocene faulting in SE Sweden from U–Pb dating of slickenfibre calcite, *Terra Nova, 29,* 321–328. https://doi.org/10.1111/ter.12280

Grool, A. R., Hismans, R. S. and Ford, M. (2019): Salt décollement and rift inheritance controls on crustal deformation in orogens. *Terra Nova, 31*, 562-568. https://doi.org/10.1111/ter.12428

Guardia, M., Griera, A., Kaus, B., Piccolo, A. and Teixell, A. (2023): Conditions favouring fold vs. thrust nappes: insights from the modelling of a Pyrenean example and implications on hinge migration vs. limb stretching mechanisms. *EGU General Assembly 2023*, Vienna, Austria, 24–28 Apr. https://doi.org/10.5194/egusphere-egu23-12099

Guenthner, W. R., Reiners, P.W., Ketcham, R., Nasdala, L. and Giester, G. (2013): Helium diffusion in natural zircon: Radiation damage, anisotropy, and the interpretation of zircon (U-Th)/He thermochronology. *American Journal of Science 313 (3)*, 145-198. https://doi.org/10.2475/03.2013.01

Guerrot, C. (2001): Datation du pluton des Eaux-Chaudes. In: Ternet, Y., Majesté-Menjoulas, C., Canérot, J., Baudin, T., Cocherie, A., Guerrot, C., Rossi, P. (eds) (2004). Notice explicative, Carte géol. France (1/50.000), feuille Laruns-Somport (1069). BRGM, Orléans, pp 185-187.

Habermann, D., Neuser, R. D. and Richter, D. K. (1998). Low limit of Mn2+-activated cathodoluminescence of calcite: state of the art. *Sedimentary Gology, 116 (1-2)*, 13-24. https://doi.org/10.1016/S0037-0738(97)00118-8

Hansman, R. J., Albert, R., Gerdes, A., and Ring, U. (2018): Absolute ages of multiple generations of brittle structures by U-Pb dating of calcite, *Geology, 46,* 207–210. https://doi.org/10.1130/G39822.1

Hatcher, R.D. (1981): Thrusts and nappes in the North American Appalachian Orogen. In: Thrust and Nappe Tectonics (McClay, K.R. and Price, N.J., eds.). *Geological Society London Special Publications, 9.* 491–499. https://doi.org/10.1144/GSL.SP.1981.009.01.44

Heim (1906): Geologische Nachlese Nr. 18. Die vermeintliche «Gewölbeumbiegung des Nordflügels der Glarner Doppelfalte» südlich vom Klausenpass, eine Selbstkorrektur (inkl. Kartenmaterial). *Vierteljahrsschrift der Naturforschenden Gesellschaft in Zürich 51 (2 und 3)*, 403–431.

Heim, A. (1919-1922): Geologie der Schweiz. *Tauchnitz, Leipzig, 2* Bde.

Herlambang, A. and John, C. (2023): Fluid flow evolution revealed by carbonate clumped isotope thermometry along the fractures in a complex salt dome setting: Study case (Jebel Madar, Oman). *Marine and Petroleum Geology, 152,* 106220. https://doi.org/10.1016/j.marpetgeo.2023.106220

Herwegh, M. and Pfiffner, O. A. (2005). Tectono-metamorphic evolution of a nappe stack: A case study of the Swiss Alps. *Tectonophysics, 404 (1-2),* 55-76. https://doi.org/10.1016/j.tecto.2005.05.002

Hiatt, E.E. and Pufahl, P. K. (2014): Cathodoluminiscence petrography of carbonate rocks: a review of applications for understanding diagenesis, reservoir quality, and pore system evolution. In: Coulson, I.M. (ed.). Cathodoluminiscence and its application to geoscience. *Mineralogical Association of Canada Short Course, 45,* 75-96.

Hoareau, G., Claverie, F., Pecheyran, C., Paroisin, C., Grignard, P-A., Motte, G., Chailan, O. and Girard, J-P. (2021): Direct U–Pb dating of carbonates from micron-scale femtosecond laser ablation inductively coupled plasma mass spectrometry images using robust regression. *Geochronology, 3*, 67–87. https://doi.org/10.5194/gchron-3-67-2021

Holdsworth, R. E., McCaffrey, K. J. W., Dempsey, E., Roberts, N. M. W., Hardman, K., Morton, A., Feely, M., Hunt, J., Conway, A., and Robertson, A. (2019): Natural fracture propping and earthquakeinduced oil migration in fractured basement reservoirs, *Geology, 47*, 700–704, https://doi.org/10.1130/G46280.1

Holdsworth, R. E., Trice, R., Hardman, K. McCaffrey, K. J. W., Morton, A., Frei, D., Dempsey, E., Bird, A. and Rogers, D. (2020): The nature and age of basement host rocks and fissure fills in the Lancaster field fractured reservoir, West of Shetland. *Journal of the Geological Society, 177.* https://doi.org/10.1144/jgs2019-142

Hollocher, K. and Ruiz, J. (1995): Major and trace element determinations on NIST glass standard reference materials 611, 612, 614 and 1834 by Inductively Coupled Plasma-Mass Spectrometry. *Geostandards Newsletter, 19 (1),* 27-34. https://doi.org/10.1111/j.1751-908X.1995.tb00149.x

Homza, T. X. and Wallace, W. K. (1995): Geometric and kinematic models for detachment folds with fixed and variable detachment depths. *Journal of Structural geology, 17 (4).* 575-588. https://doi.org/10.1016/0191-8141(94)00077-D

Homza, T. X. and Wallace, W. K. (1997): Detachment folds with fixed hinges and variable detachment depth, northeastern Brooks Range, Alaska. *Journal of Structural geology, 19 (3-4).* 337-354. https://doi.org/10.1016/S0191-8141(96)00118-6

Hopley, P. J., Reade, H., Parrish, R., De Kock, M., and Adams, J.W. (2019): Speleothem evidence for C3 dominated vegetation during the Late Miocene (Messinian) of South Africa, *Review of Palaeobotany and Palynology, 264*, 75–89. https://doi.org/10.1016/j.revpalbo.2019.02.006

Incerpi, N., Martire, L., Manatschal, G., Bernasconi, S. M., Gerdes, A., Czuppon, G., Palcsu, L., Karner, G. D., Johnson, C. A., and Figueredo, P. H. (2020): Hydrothermal fluid flow associated to the extensional evolution of the Adriatic rifted margin: Insights from the pre-to post-rift sedimentary sequence (SE Switzerland, N Italy), *Basin Research, 32*, 91–115. https://doi.org/10.1111/bre.12370

Izquierdo-Llavall, Menant, A., Aubourg, C., Callot, J-P., Hoareau, G., Camps, P. Péré, E. and Lahfid, A. (2020): Preorogenic Folds and Syn-Orogenic Basement Tilts in an Inverted Hyperextended Margin: The Northern Pyrenees Case Study. *Tectonics, 39 (7).* https://doi.org/10.1029/2019TC005719

Jammes, S., Manatschal, G., Lavier, L. and Masini, E. (2009): Tectonosedimentary evolution related to extreme crustal thinning ahead of a propagating ocean: Example of the western Pyrenees. *Tectonics, 28*, 1-24. https://doi.org/10.1029/2008TC002406

Jaquet, Y., Bauville, A. and Schmalholz, M. (2014): Viscous overthrusting versus folding: 2-D quantitative modelling and its application to the Helvetic and Jura fold and thrust belts. *Journal of Structural Geology, 62,* 25-37. https://doi.org/10.1016/j.jsg.2014.01.010

Jolivet, M., Labaume, P., Monié, P., Brunel, M., Arnaud, N. and Campani, M. (2007): Thermochronology constraints for the propagation sequence of the south Pyrenean basement thrust system (France-Spain). *Tectonics, 26 (5),* 1-17. https://doi.org/10.1029/2006TC002080

Karato, S. (2008): Deformation of Earth Materials: An Introduction to the Rheology of Solid Earth. *Cambridge University Press*, 463. https://doi.org/10.1017/CBO9780511804892

Kaus, B.J.P., Popov, A., Baumann, T, Püsök, A., Bauville, A., Fernandez, N. and Collignon, M. (2016): Forward and Inverse Modelling of Lithospheric Deformation on Geological Timescales, in: *NIC Symposium 2016 – Proceedings*, Jülich, Germany, NIC Series, 48, 299-307.

Ketcham, R. A., R. A. Donelick, and W. D. Carlson (1999): Variability of apatite fission-track annealing kinetics: III. Extrapolation to geological timescales. *American Mineralogist*, 84. 1235–1255. https://doi.org/10.2138/am-1999-0903

Ketcham, R. A., A. Carter, R. A. Donelick, J. Barbarand, and A. J. Hurford (2007): Improved modelling of fission-track annealing in apatite. *American Mineralogist, 92*, 799–810. https://doi.org/10.2138/am.2007.2281

Kiss, D., Duretz, T. and Schmalholz, S. M. (2020): Tectonic inheritance controls nappe detachment, transport and stacking in the Helvetic nappe system, Switzerland: insights from thermomechanical simulations. *Solid Earth, 11*, 287-305. https://doi.org/10.5194/se-11-287-2020

Koehn, D., Bons, P., Hilgers, C. and Passchier, C. (2001): Animations of progressive fibrous vein and fringe formation. In: Ailleres, L. and Rawling, T. (eds.). *Animations in Geology. Journal of the Virtual Explorer*, 4.

Kreissl, S., Gerdes, A., Walter, B. F., Neumann, U., Wenzel, T., and Markl, G. (2018): Reconstruction of a > 200 Ma multi-stage "five element" Bi-Co-Ni-Fe-As-S system in the Penninic Alps, Switzerland. *Ore Geology Reviews, 95*, 746–788. https://doi.org/10.1016/j.oregeorev.2018.02.008

Kronenberg, A.K., Kirby, S.H. and Pinkston, J. (1990): Basal slip and mechanical anisotropy of biotite. *Journal of Geophysical Research, 95 (B12),* 19257-19278. https://doi.org/10.1029/JB095iB12p19257

Labaume, P., Meresse, F., Jolivet, M. and Teixell, A. (2016): Exhumation sequence of the basement thrust units in the west-central Pyrenees. Constraints from apatite fission track analysis. *Geogaceta, 60.*

Labaume, P., Meresse, F., Jolivet, M., Teixell, A. and Lahfid, A. (2016b): Tectonothermal history of an exhumed thrust-sheet-top basin: An example from the south Pyrenean thrust belt. Tectonics, 35, 1280-1313. https://doi.org/10.1002/2016TC004192

Labaume, P. and Teixell, A. (2020): Evolution of salt structures of the Pyrenean rift (Chaînons Béarnais, France): From hyper-extension to tectonic inversion. *Tectonophysics,* 785 228451. https://doi.org/10.1016/j.tecto.2020.228451

Lagabrielle, Y., Labaume, P. and S. Blanquat, M. (2010): Mantle exhumation, crustal denudation, and gravity tectonics during Cretaceous rifting in the Pyrenean realm (SW Europe): Insights from the geological setting of the lherzolite bodies. *Tectonics, 29*, 1-26. https://doi.org/10.1029/2009TC002588

Lacombe, O. and Bellahsen, N. (2016): Thick-skinned tectonics and basement-involved fold-thrust belts: insights from selected Cenozoic orogens. *Geological Magazine, 153*, 763-810. https://doi.org/10.1017/S0016756816000078

Lafosse. M., Boutoux, A., Bellahsen, N. and Le Pourhiet, L. (2016): Role of tectonic burial and temperature on the inversion of inherited extensional basins during collision. *Geological Magazine, 153 (5-6)*, 811-826. https://doi.org/10.1017/S0016756816000510

Lawson, M., Shenton, B. ., Stolper, D. A., Eiler, J. M., Rasbury, E. T., Becker, T. P., Phillips-Lander, C. M., Buono, A. S., Becker, S. P., Pottorf, R., and Gray, G. G. (2018): Deciphering the diagenetic history of the El Abra Formation of eastern Mexico using reordered clumped isotope temperatures and U-Pb dating, *GSA Bulletin, 130*, 617–629. https://doi.org/10.1130/B31656.1

Li, S-Y. and Urai, J. (2016): Rheology of rock salt for salt tectonics modelling. *Petroleum Science, 13,* 712-724. https://doi.org/10.1007/s12182-016-0121-6

Llorens, M.-G., Bons, P.D., Griera, A., Gomez-Rivas, E., Evans, L.A. (2013): Single layer folding in simple shear. *Journal of Structural Geology, 50*, 209–220. https://doi.org/10.1016/j.jsg.2012.04.002

Long, J. V. P. and Agrell, S. O. (1965). The cathodo-luminescence of minerals in thin section. *Mineralogical Magazine and Journal of the Mineralogical Society, 34 (268)*, 318-326. https://doi.org/10.1180/minmag.1965.034.268.27

López-Martínez, J. (1987) Relaciones entre la fracturación y el karst en el macizo de la piedra de San Martin (Pirineo Occidental). *Estudios Geologicos, 43*, (217-225). https://doi.org/10.3989/egeol.87433-4591

Lugeon, M. (1902): Les grandes nappes de recouvrement des Alpes du Chablais et de la Suisse. *Bulletin de la Société Geologique Française, 4*, 723-825.

Machel, H.G. (1985): Cathodoluminescence in calcite and dolomite and its chemical interpretation, *Geoscience Canada, 12(4)*, 139–147.

Machel, H.G. (2000). Application of Cathodoluminescence to Carbonate Diagenesis. In: Pagel, M., Barbin, V., Blanc, P., Ohnenstetter, D. (eds). *Cathodoluminescence in Geosciences, 271-301*. Springer, Berlin, Heidelberg. https://doi.org/10.1007/978-3-662-04086-7_11

Majesté-Menjoulas, C. (1979): Evolution alpine d'un segment de chaîne varisque: Nappe de Gavarnie, chevauchement Cinq-Monts-Gentiane (Pyrénées centrales et occidentales). *These Science*, Université Paul Sabatier, Toulouse, 343 pp.

Manatschal G, Chenin P, Lescoutre R, Miró J, Cadenas P, Saspiturry N, Masini E, Chevrot S, Ford M, Jolivet L, Mouthereau F, Thinon I, Issautier B, Calassou S. (2021): The role of inheritance in forming rifts and rifted margins and building collisional orogens: a Biscay-Pyrenean perspective, *Bulletin de la Société Géologique de France, 192(1)*: 55. https://doi.org/10.1051/bsgf/2021042

Mancktelow, N.S. (1999): Finite-element modelling of single-layer folding in elasto-viscous materials: the effect of initial perturbation geometry. *Journal of Structural Geology, 21 (2).* https://doi.org/10.1016/S0191-8141(98)00102-3

Mange, M.A. and Maurer, H.F.W. (1992): Heavy Minerals in Colour. *Chapman & Hall*, London, 147. http://dx.doi.org/10.1007/978-94-011-2308-2

Marcén, M., Casas-Sainz, A. M., Román-Berdiel, T., Oliva-Urcia, B., Soto, R. and Aldega, L. (2018): Kinematics and strain distribution in an orogen-scale shear zone: Insights from structural analyses and magnetic fabrics in the Gavarnie thrust, Pyrenees. *Journal of Structural Geology, 117*, 105–123. https://doi.org/10.1016/j.jsg.2018.09.008

Mares, V. M. and Kronenberg, A. K. (1993): Experimental deformation of muscovite. *Journal of Structural Geology, 15 (9-10),* 1061-1075. https://doi.org/10.1016/0191-8141(93)90156-5

Mase, G. E. and Mase, G.T. (1970): Continuum mechanics. McGraw-Hill, New York, 398.

Mason, R. A. and Mariano, A. N. (1990). Cathodoluminescence activation in manganese-bearing and rare earthbearing synthetic calcites. *Chemical geology, 88 (1-2)*, 191-206. https://doi.org/10.1016/0009-2541(90)90113-L

Martinez-Catalán, J. R., Collett, S., Schulmann, K., Aleksandrowski, P. and Mazur, S. (2020): Correlation of allochthonous terranes and major tectonostratigraphic domains between NW Iberia and the Bohemian Massif, European Variscan belt. *International Journal of Earth Sciences, 109.* 1105-1131. https://doi-org.are.uab.cat/10.1007/s00531-019-01800-z

Matte, P. (1969). Le probleme du passage de la schistosité horizontala la schistosité verticale dans la dôme de la Garonne (Paléozoique des Pyrénées Centrales). *Comptes Rendus de l'Académie des Sciences, 268,* 1841–1844.

Matte, P. and Zhu-Xhi, Q. (1988): Decollements in slate belts, examples from the European variscides and the Qin Ling Belt of Central China. *Geologische Rundschau*, 77 (1), 227-238.

Menant, A., Aubourg, C., Cuyala, J.-B., Hoareau, G., Callot, J.-P., Péré, E., Labaume, P. and Ducoux, M. (2016): Salt tectonics and thermal imprint along an inverted passive margin: the Montacou anticline, Chaînons Béarnais, North Pyrenean Zone. In: Geophysical Research Abstracts, 18, EGU2016-15281, E.G.U. Assembly, 17-22 April 2016, Vienna.

Mercier, E. Rafini, S. and Ahmadi, R. (2007): Folds Kinematics in "Fold-and-Thrust Belts" the "Hinge Migration" Question, a Review. In: Lacombe, O., Roure, F., Lavé, J., Vergés, J. (eds). *Thrust Belts and Foreland Basins*. Frontiers in Earth Sciences. Springer, Berlin, Heidelberg. https://doi-org.are.uab.cat/10.1007/978-3-540-69426-7_7

Methner, K., Mulch, A., Fiebig, J., Wacker, U., Gerdes, A., Graham, S. A., and Chamberlain, C. P. (2016): Rapid middle Eocene temperature change in western North America, *Earth and Planetary Science Letters, 450*, 132–139. https://doi.org/10.1016/j.epsl.2016.05.053

Mirouse, R. (1962). Recherches géologiques dans la partie occidentale de la zone primaire axiale des Pyrénées. Thèse État, Toulousse. *Mémoires pour Servir la Carte Géologique de France, (1966)*, 451 p.

Morris, R.G., Sinclair, H.D., Yelland, A.J. (1998): Exhumation of the Pyrenean orogen: implications for sediment discharge. *Basin Research, 10,* 69-85. https://doi.org/10.1046/j.1365-2117.1998.00053.x

Mouthereau, F., Filleaudeau, P.-Y., Vacherat, A., Pik, R., Lacombe, O., Fellin, M. G., Castelltort, S., Christophoul, F. and Masini, E. (2014). Placing limits to shortening evolution in the Pyrenees: Role of margin architecture and implications for the Iberia/Europe convergence. *Tectonics, 33*, 2283-2314. https://doi.org/10.1002/2014TC003663

Müller, W., Aerden, D. and Halliday, A. N. (2000): Isotopic Dating of Strain Fringe Increments: Duration and Rates of Deformation in Shear Zones, *Science, 288 (5474)*, 2195-2198. https://doi.org/10.1126/science.288.5474.2195

Muñoz, J. A. (1992): Evolution of a continental collision belt: ECORS-Pyrenees crustal balanced cross-section. *Thrust Tectonics*, 235-246. https://doi.org/10.1007/978-94-011-3066-0_21

Muñoz-López, D., Cruset, D., Vergés, J., Cantarero, I., Benedicto, A., Mangenot, X., Albert, R., Gerdes, A., Beranoaguirre, A., and Travé, A. (2023). Spatio-temporal variation of fluid flow behavior along a fold: The Bóixols-Sant Corneli anticline (Southern Pyrenees) from U–Pb dating and structural, petrographic and geochemical constraints. Marine and Petroleum Geology, 143, 105788. https://doi.org/https://doi.org/10.1016/j.marpetgeo.2022.105788

Negrini, M., Smith, S., Scott, J. M. and Tarling, M. D. (2018): Microstructural and rheological evolution of calcite mylonites during shear zone thinning: Constraints from the Mount Irene shear zone, Fiordland, New Zealand. *Journal of Structural Geology, 106,* 86-102. https://doi.org/10.1016/j.jsg.2017.11.013

Nemcok, M., Schamel, S. and Gayer, R. (2005): Thrustbelts. Structural Architecture, Thermal Regimes and Petroleum Systems. *Cambridge University Press*, Cambridge. https://doi.org/10.1017/CBO9780511584244

Nibourel, L., Berger, A., Egli, D., Luensdorf, N. K. and Herwegh, M. (2018). Large vertical displacements of a crystalline massif recorded by Raman thermometry. *Geology, 46,* 879-882. https://doi.org/10.1130/G45121.1

Nicholson, S. L., Pike, A. W., Hosfield, R., Roberts, N. M. W., Sahy, D., Woodhead, J., Cheng, H., Edwards, R. L., Affolter, S., Leuenberger, M., and Burns, S. J. (2020): Pluvial periods in Southern Arabia over the last 1.1 million-years, *Quaternary Science Reviews, 229*, 106112, https://doi.org/10.1016/j.quascirev.2019.106112

Niemeijer, A.R. and Spiers, C.J. (2005): Influence of phyllosilicates on fault strength in the brittle-ductile transition: insights from rock analogue experiments. *Geological Society, London, Special Publications, 245,* 303-327. https://doi.org/10.1144/GSL.SP.2005.245.01.15

Nuriel, P., Weinberger, R., Kylander-Clark, A.R.C., Hacker, B.R., and Craddock, J.P: (2017): The onset of the Dead Sea transform based on calcite age-strain analyses, *Geology,45.* https://doi.org/10.1130/G38903.1

Nuriel, P., Craddock, J., Kylander-Clark, A.R., Uysal, T., Karabacak, V., Dirik, R.K., Hacker, B.R., and Weinberger, R (2019): Reactivation history of the North Anatolian fault zone based on calcite age-strain analyses, *Geology, 47.* https://doi.org/10.1130/G45727.1

Ortí, F., Pérez-López, A. and Salvany, J. M. (2017). Triassic evaporites of Iberia: Sedimentological and palaeogeographical implications for the western Neotethys evolution during the Middle Triassic-Earliest Jurassic. *Palaeogeography, Palaeoclimatology, Palaeoecology, 471*, 157-180. https://doi.org/10.1016/j.palaeo.2017.01.025

Palacios-Garcia, N. B., Fitz-Diaz, E., Stockli, L. Stockli, D. F. (2023): U–Pb calcite dating of brittle deformation in Permian carbonates within the Chicomuselo fold and thrust belt, SE Mexico. *Journal of Structural Geology, 171*, 104863. https://doi.org/10.1016/j.jsg.2023.104863

Parrish, R. R., Parrish, C. M., and Lasalle, S. (2018): Vein calcite dating reveals Pyrenean orogen as cause of Paleogene deformation in southern England, *Journal of the Geological Society, 175*, 425–442. https://doi.org/10.1144/jgs2017-107

Passchier, C.W. and Trouw. R.A.J. (2005): Flow and deformation, in Passchier, C.W. and Trouw. R.A.J. (eds.), *Microtectonics*, Springer Berlin, Heidelberg, 9-23. https://doi.org/10.1007/3-540-29359-0

Paton, C., Hellstrom, J., Paul, B., Woodhead, J. and Hergt, J. (2011): Iolite: freeware for the visualisation and processing of mass spectrometric data. *Journal of Analytical Atomic Spectrometry, 26*, 2508-2518. https://doi.org/10.1039/C1JA10172B

Perrin, C., Clemenzi, L., Malavieille, J., Molli, G., Taboada, A. and Domínguez, S. (2013): Impact of erosion and décollements on large-scale faulting and folding in orogenic wedges: analogue models and case studies. *Journal of the Geological Society, 170.* 893-904. https://doi.org/10.1144/jgs2013-012

Pfiffner, O. A. (1993): The structure of the Helvetic nappes and its relation to the mechanical stratigraphy. *Journal of Structural Geology, 15*, 511-521. https://doi.org/10.1016/0191-8141(93)90145-Z

Pfiffner, O. A., Lehner, P., Heitzmann, P., Mueller, St. and Steck, A. (1997). Deep Structure of the Swiss Alps: Results from NFP 20. *Birkhäuser Verlag, Basel, Switzerland,* 460.

Pfiffner, O. A. (2014): Geology of the Alps. John Wiley and Sons, Chichester, 376.

Pfiffner, O. A. (2017): Thick-Skinned and Thin-Skinned Tectonics: A Global Perspective. *Geosciences, 7(3)*, 71. https://doi.org/10.3390/geosciences7030071

Poblet, J. and McClay, K. (1996): Geometry and kinematics of single-layer detachment folds. *AAPG Bulletin, 80 (7),* 1085-1109. https://doi.org/10.1306/64ED8CA0-1724-11D7-8645000102C1865D

Poblet, J. (2020): Cartographic pattern of terminations of simple, parallel fault-bend folds, fault-propagation folds and detachment folds. *Journal of Structural Geology, 138*, 104135. https://doi.org/10.1016/j.jsg.2020.104135

Pollard, D. D. and Segall, P. (1987): Theoretical displacements and stresses near fractures in rocks: with applications to faults, joints, dikes and solution surfaces. In: Atkinson, B. (ed.), *Fracture Mechanics of Rock, Academic Press, London*, 277-348

Price, N. J. and McClay, K. R. (1981): Thrust and nappe tectonics, *Geological Society of London*, London, 539.

Puigdefàbregas, C. (1975): La sedimentación molásica en la cuenca de Jaca. *Pirineos, 104*. 1-188.

Ramsay, J.G. (1980): Shear zone geometry: a review. *Journal of Structural Geology, 2*, 83-99. https://doi.org/10.1016/0191-8141(80)90038-3

Ramsay, J. G. (1981): Tectonics of the Helvetic Nappes. In: Thrust and Nappe Tectonics (McClay, K.R. and Price, N.J., eds.). *Geological Society London. Special Publications, 9*. 293–309. http://doi.org/10.1144/GSL.SP.1981.009.01.26

Ramsay, J. G. and Huber, M. (1983): Measurement of progressive deformation. In: Ramsay, J.G. and Huber, M. (eds). *The Techniques of Modern Structural Geology, 1*, Academic Press, London

Ramsay,J.G., Casey, M. and Kligfield, R. (1983): Role shear in the development of the Helvetic fold-and-thrust belt of Switzerland. *Geology, 11 (8)*, 439-442. https://doi.org/10.1130/0091-7613(1983)11<439:ROSIDO>2.0.CO;2

Ramsay, J. G. and Huber, M. (1987): *The techniques of modern structural Geology, Volume 2: Folds and Fractures*. Academic Press, London, 391. https://doi.org/10.1017/S0016756800010384

Ranalli, G. (1995): Rheology of the Earth, *Chapman & Hall*, 413.

Rast, M. and Ruh, J. B. (2021): Numerical shear experiments of quartz-biotite aggregates: Insights on strain weakening and two-phase flow laws. *Journal of Structural Geology, 149*, 104375. https://doi.org/10.1016/j.jsg.2021.104375

Reiners, P.W., Farley, K.A. and Hickes, H.J. (2002): He Diffusion and (U-Th)/He thermochronometry of zircon:initial results from Fish Canyon Tuff and Gold Butte. *Tectonophysics, 349 (1-4)*. https://doi.org/10.1016/S0040-1951(02)00058-6

Reiners, P. W., T. L. Spell, S. Nicolescu, and K. A. Zanetti (2004): He diffusion and (U-Th)/He thermochronometry: He diffusion and comparison with ^{40}Ar/^{39}Ar dating. *Geochimica et Cosmochimica Acta, 68.* 1857–1887. https://doi.org/10.1016/j.gca.2003.10.021.

Reiners, P. W. (2005): Zircon (U-Th)/He Thermochronometry. *Reviews in Mineralogy and Geochemistry, 58 (1).* 151–179. https://doi.org/10.2138/rmg.2005.58.6

Renner, J., Evans, B. and Siddiqi, G. (2002): Dislocation creep of calcite. *Journal of Geophysical Research, 107 (B12)*. https://doi.org/10.1029/2001JB001680

Richter, D. K., Götte, T., Götze, J., and Neuser, R. D. (2003): Progress in application of cathodoluminescence (CL) in sedimentary petrology, *Mineralogy and Petrology, 79,* 127–166. https://doi.org/10.1007/s00710-003-0237-4

Riedel, W. (1929): Zurmechanik geologischer brucherscheinungen. *Centralblatt fur Minerologie, Geologie, und Paleontologie*, 354.

Ring, U. and Gerdes, A. (2016): Kinematics of the Alpenrhein-Bodensee graben system in the Central Alps: Oligocene/Miocene transtension due to formation of the Western Alps arc. *Tectonics, 35 (6)*, 1367-1391. https://doi.org/10.1002/2015TC004085

Roberts, N. M. W. and Walker, R. J. (2016): U-Pb geochronology of calcite-mineralized faults: Absolute timing of rift-related fault events on the northeast Atlantic margin, *Geology, 44*, 531–534. https://doi.org/10.1130/G37868.1

Roberts, N. M. W., Rasbury, E. T., Parrish, R, Smith, C., Horstwood, M. and Condon, D. (2017): A calcite reference material for LA-ICP-MS U-Pb geochronology. *Geochemistry, Geophysics, Geosystems, 18 (7)*, 2807-2814. https://doi.org/10.1002/2016GC006784

Roberts, N. M., Drost, K., Horstwood, M. S., Condon, D. J., Chew, D., Drake, H., Milodowski, D. J., McLean, N. M., Smye, , A. J., Walker, R. J., Haslam, R., Hodson, K. Imber, J., Beaudoin, N. and Lee, J. K. (2020): Laser ablation inductively coupled plasma mass spectrometry (LA-ICP-MS) U–Pb carbonate geochronology: strategies, progress, and limitations *Geochronology, 2*, 33–61. https://doi.org/10.5194/gchron-2-33-2020

Roigé, M., Gómez-Gras, D., Remacha, E. Daza, R. and Boya, S. (2016): Tectonic control on sediment sources in the Jaca basin (Middle and Upper Eocene of the South-Central Pyrenees). *Comptes Rendus Geoscience, 348 (3-4),* 236-245. https://doi.org/10.1016/j.crte.2015.10.005

Roure, F., Swennen, R., Schneider, F., Faure, J.L., Ferket, H., Guilhaumou, N., Osadetz, K., Robion, P. and Vandeginste, V. (2005): Incidence and importance of tectonics and natural fluid migration on reservoir evolution in foreland fold-and-thrust belts. *Oil Gas Sci. Technol., 60 (1). https://doi.org/10.2516/ogst:2005006*

Saspiturry, N., Lahfid, A., Baudin, T., Guillon-Frottier, L., Razin, P., Issautier, B., Le Bayon, B., Serrano, O., Lagabrielle, Y. and Corre, B. (2020). Paleogeothermal gradients across an inverted hyperextended rift system: example of the Mauléon fossil rift (western Pyrenees). *Tectonics, 39 (10)*, e2020TC006206. https://doi.org/10.1029/2020TC006206

Saspiturry, N., Allanic, C., Serrano, O., Courrioux, G., Baudin, T., Le Bayon, B., Lahfid, A., Razin, P., Villasenor, A., Cevrot, S. and Issautier, B. (2022). Upper lithospheric transfer zones driving the non-cylindricity of the est-Pyrenean orogenic prism (Mauléon hyperextended basin). *Journal of Structural Geology, 156*, 104535. https://doi.org/10.1016/j.jsg.2022.104535

Savard, M. M., Veizer, J., and Hinton, R. (1995): Cathodoluminescene at low Fe and Mn concentrations; a SIMS study of zones in natural calcites, *Journal of Sedimentary Research, 65*, 208–213. https://doi.org/10.1306/d4268072-2b26-11d7-8648000102c1865d

Shea, W.T. and Kronenberg, A.K. (1989): Experimental deformation of Biotite Shist. *EOS, 70 (15)*. 477. https://doi.org/10.1029/EO070i015p00271

Shea, W.T. and Kronenberg, A.K. (1992): Rheology and deformation mechanisms of anisotropic mica schist. *Journal of Geophysical Research, 97*, 15201–15237. https://doi.org/10.1029/92JB00620

Shea, W.T. and Kronenberg, A.K. (1993): Strength and anisotropy of foliated rocks with varied mica contents. *Journal of Structural Geology, 15 (9-10),* 1097-1121. https://doi.org/10.1016/0191-8141(93)90158-7

Schmid, S.M., Boland, J.N. and Paterson, M.S. (1977): Superplastic flow in finegrained limestone. *Tectonophysics, 43,* 257-291. https://doi.org/10.1016/0040-1951(77)90120-2

Schmid, S.M., Paterson, M.S., Boland, J.N. (1980): High temperature flow and dynamic recrystallization in Carrara marble. *Tectonophysics, 65,* 245-280. https://doi.org/10.1016/0040–1951(80)90077-3

Scholz, C. H. (2002): *The mechanics of earthquakes and faulting.* Cambridge university press. https://doi.org/10.1017/CBO9780511818516

Sippel, R. F. and Glover, E. D. (1965). Structures in carbonate rocks made visible by luminescence petrography. *Science, 150 (3701)*, 1283-1287. https://doi.org/10.1126/science.150.3701.1283

Smeraglia, L., Aldega, L., Billi, A., Carminati, E., Di Fiore, F., Gerdes, A., Albert, R., Rossetti, F. and Vignaroli, G. (2019): Development of an intra-wedge tectonic mélange by out-of-sequence thrusting, buttressing, and intraformational rheological contrast, Mt. Massico ridge, Apennines, Italy, *Tectonics, 38*, 1223–1249. https://doi.org/10.1029/2018TC005243

Soto, J. I., Flinch, J. F. and Tari, G. (2017). Permo-Triassic Salt Provinces of Europe, North Africa and the Atlantic margins: Tectonics and hydrocarbon potential. *Oxford: Elsevier, Print*.

Souquet, P. (1967). Le Crétacé supérieur sud-pyrénéen en Catalogne, Aragon et Navarre. *Thèse Doctorat Sciences*, Université de Toulousse.

Spitz, R., Bauville, A., Epard, J-L., Kaus, B. J. P., Popov, A. and Schmalholz, S. M. (2020): Control of 3D tectonic inheritance on fold-and-thrust belts: insights from 3D numerical models and application to the Helvetic nappe system. *Solid Earth, 11*, 999-1026. https://doi.org/10.5194/se-2019-173

Stoppa, F., Cirilli, S., Sorci, A., Broom-Fendley, S., Principe, C., Grazia Perna, M. and Rosatelli, G. (2021). Igneous and sedimentary 'limestones': the puzzling challenge of a converging classification. *Geological Society, London, Special Publications*, SP520-2021-120. https://doi.org/10.1144/SP520-2021-120

Stockli, D. (2005): Application of low-temperature thermochronology to extensional tectonic setting. *Reviews in Mineralogy and Geochemistry 58 (1)*: 411–448. https://doi.org/10.2138/rmg.2005.58.16

Teixell, A. (1992): *Estructura alpina en la transversal de la terminación occidental de la Zona Axial pirenaica*. Doctoral dissertation, Universitat de Barcelona, 252.

Teixell. A. (1993): Coupe géologique du massif d'Igountze: implications sur l'évolution structural de la bordure sud de la Zone nord-pyrénéenne occidentale. *Comptes Rendus de l'Académie des Sciences, Paris, 316,* 1789-1796.

Teixell, A. (1996): The Ansó transect of the southern Pyrenees: basement and cover thrust geometries. *Journal of the Geological Society, 153(2)*, 301-310. http://dx.doi.org/10.1144/gsjgs.153.2.0301

Teixell, A. (1998): Crustal structure and orogenic material budget in the west central Pyrenees. *Tectonics, 17* (3), 395-406. https://doi.org/10.1029/98TC00561

Teixell, A., Durney, D.W. and Arboleya, M-L. (2000): Stress and fluid control on décollement within competent limestone. *Journal of structural Geology, 22 (3),* 349-371. https://doi.org/10.1016/S0191-8141(99)00159-5

Teixell, A., Labaume, P. and Lagabrielle, Y. (2016): The crustal evolution of the west-central Pyrenees revisited: Inferences from a new kinematic scenario. *Comptes Rendus – Geoscience, 348*, 257-267. https://doi.org/10.1016/j.crte.2015.10.010

Teixell, A., Labaume, P., Ayarza, P., Espurt, N., de Saint Blanquart, M. and Lagabrielle, Y. (2018): Crustal structure and evolution of the Pyrenean-Cantabrian belt: A review and new interpretations from recent concepts and data. *Tectonophysics, 724-725*, 149-170. https://doi.org/10.1016/j.tecto.2018.01.009

ten Have, T. and Heijnen, W. (1985). Cathodoluminescence activation and zonation in carbonate rocks: an experimental approach. *Geologie en Mijnbouw, 64*, 297-310.

Tera, F. and Wasserburg, G.J. (1972): U-Th-Pb systematics in lunar highland samples from the Luna 20 and Apollo 16 missions. *Earth and Planetary Science Letters, 17 (1)*, 36-51. https://doi.org/10.1016/0012-821X(72)90257-9

Termier, P. (1906): La synthèse géologique des Alpes. *Imprimerie Moderne, 29*.

Ternet (1965): Étude du synclinal complexe des Eaux-Chaudes (Basses-Pyrénées), *Thèse Doctorat 3° Cycle: Faculté des sciences de l'Université de Toulouse*, 332 p.

Ternet, Y., Majeste-Menjoulas, C., Canérot, J., Baudin, T., Cocherie, A., Guerrot, C. and Rossi, P. (2004): *Carte géologique de la France: Laruns-Somport.* Bureau des Recherches Géologiques et Minières, scale 1:50000, feuille n°1069.

Travé, A., Labaume, P. Calvet, F. and Soler, A. (1997): Sediment dewatering and pore fluid migration along thrust faults in a foreland basin inferred from isotopic and elemental geochemical analyses (Eocene southern Pyrenees, Spain). *Tectonophysics, 282 (1-4),* 375-398. https://doi.org/10.1016/S0040-1951(97)00225-4

Tugend, J., Manatschal, G., Kusznir, N.J., Masini, E., Mohn, G. and Thinon, I. (2014): Formation and deformation of hyperextended rift systems: Insights from rift domain mapping in the Bay of Biscay-Pyrenees. *Tectonics,* 33 (7), 1239-1276. https://doi.org/10.1002/2014TC003529

Tullis, T. E., Horowitz, F. G. and Tullis, J. (1991): Flow Laws polyphase aggregates from end-member flow laws. *Journal of Geophysical Research, 96 (B5),* 8081-8096. https://doi.org/10.1029/90JB02491

Turcotte, D. and Schubert, J. (2014): Geodynamics. Cambridge University Press, 636 pp.

Vermeesch, P. (2018): IsoplotR: A free and open toolbox for geochronology. *Geoscience Frontiers, 9 (5)*, 1479-1493. https://doi.org/10.1016/j.gsf.2018.04.001

Villard, J. (2016). Déformation et thermicité de la couverture mésozoïque dans une structure salifère des Chaînons Béarnais (Zone Nord Pyrénéenne). Master Géosciences, Mémoire de Master Université de Montpellier, pp. 58. https://rgf.brgm.fr/sites/default/files/upload/documents/productionscientifique/Masters/rgf_amipyr2015_ma7_memoire_villard.pdf

von Tsharner, M., Schmalholz, S.M. and Epard, J-L. (2016): 3-D numerical models of viscous flow applied to fold nappes and the Rawil depression in the Helvetic nappe system (western Switzerland). *Journal of Structural Geology, 86,* 32-46. https://doi.org/10.1016/j.jsg.2016.02.007

Walker, A.N., Rutter, E.H. and Brodie, K. H. (1990): Experimental study of grain-size sensitive flow of synthetic, hot-pressed calcite rocks. *Geological Society, London, Special Publications, 54*, 259-284. https://doi.org/10.1144/GSL.SP.1990.054.01.24

Wallis, D., Lloyd, G. E., Phillips, R. J., Parsons, A. J. and Walshaw, R. D. (2015): Low effective fault strength due to frictional-viscous flow in phyllonites, Karakoram Fault Zone, NW India. *Journal of Structural Geology, 77,* 45-61. https://doi.org/10.1016/j.jsg.2015.05.010

Wang, Z.-C., Bai, Q., Dresen, G., Wirth, R. and Evans, B. (1996): High-temperature deformation of calcite single crystals. *JGR solid earth, 101 (B9)*, 20377-20390. https://doi-org.are.uab.cat/10.1029/96JB01186

Wang, Y., Chevrot, S., Monteiller, V., Komatitsch, D., Mouthereau, F., Manatschal, G., Sylvander, M., Diaz, J., Ruiz, M., Grimaud, F., Benahmed, S., Pauchet, H. and Martin, R. (2016): The deep roots of the western Pyrenees revealed by full waveform inversion of teleseismic P waves. *Geology, 44 (6)*, 475–478. https://doi.org/10.1130/G37812.1

Wawersik, W.R. ans Zeuch, D.H. (1986): Modelling and mechanistic interpretation of creep of rock salt below 200°C. *Tectonophysics, 121,* 125-152. https://doi.org/10.1016/0040-1951(86)90040-5

Wayne, D. M. and McCaig, A. M. (1998): Dating fluid flow in shear zones: Rb-Sr and U-Pb studies of syntectonic veins in the Néouvielle Massif, Pyrenees. *Geological Society, London, Special Publications, 144,* 129-135. https://doi.org/10.1144/GSL.SP.1998.144.01.09

Welbon, A. (1988): The influence of intrabasinal faults on the development of a linked thrust system, *Geologishe Rundschau, 77*, 11-24. https://doi.org/10.1007/BF01848673

Wissing, S. B. and Pfiffner, O. A. (2003): Numerical models for the control of inherited basin geometries on structures and emplacement of the Klippen nappe (Swiss Prealps)*. Journal of Structual Geology, 25*, 1213-1227. https://doi.org/10.1016/S0191-8141(02)00159-1

Wolf, R.A., Farley, K.A. and Kass, D.M. (1998): Modelling of the temperature sensitivity of the apatite (U-Th)/He thermochronometer. *Chemical Geology, 148 (1-2)*. https://doi.org/10.1016/S0009-2541(98)00024-2

Wolfe, M.R. and Stockli, D.F. (2010): Zircon (U–Th)/He thermochronometry in the KTB drill hole, Germany, and its implications for bulk He diffusion kinetics in zircon. *Earth and Planetary Science Letters, 295 (1-2)*. https://doi.org/10.1016/j.epsl.2010.03.025

Zerlauth, M., Ortner, H., Pomella, H., Pfiffner, O. A. and Fügenschuh, B. (2014): Inherited tectonic structures controlling the deformation style: an example from the Helvetic nappes of the Eastern Alps. *Swiss Journal of Geosciences, 107*, 157-175. https://doi.org/10.1007/s00015-014-0167-7

Agraïments/Acknowledgments

Fa 5 anys vaig començar aquest projecte professional i d'enriquiment personal que mai hagués imaginat de poder realitzar, i no m'agradaria finalitzar-lo sense mostrar el meu agraïment a totes les persones que en algun moment han aportat el seu gra de sorra (un bon sac en alguns casos) per a que això hagi estat possible. Demano que em disculpeu si m'oblido d'algú, són les 4 de la matinada del dia que diposito i porto dies sense dormir.

Vaig començar la carrera amb 26 anys (em va agafar una mica tard, sí), només sabia que m'agradava la natura i sobretot, la muntanya. La meva família ve d'un petit poble del Prepirineu, que ara sé que dona nom a una important conca Mesozoica involucrada en la deformació Alpina (al bloc superior de l'encavalcament de Bóixols), que va originar el Pirineu entre finals del Santonià i l'Oligocè inferior, flipa. Els estius de bicicleta al poble, pedalejant i corrent arreu amb llibertat, van despertar la meva curiositat per les muntanyes. Vull destacar, però, el dia que el meu pare em va dir que aquelles muntanyes fa molts anys estaven sota el mar (probablement no ho recordarà). Com podia ser això? Per què hi ha una muntanya de 1000-1500m d'alçada a 158 km del mar si abans estava a sota? I fins aquí hem arribat (de moment).

Als primers a qui vull mostrar el meu profund agraïment és als meus directors de tesi, l'Albert i el Toni. Encara recordo el mail de l'Albert dient-me si m'interessava un doctorat a Suïssa. Vaig pensar que era massa complicat anar cap allà i vaig preguntar-te si el podia fer amb vosaltres a Barcelona. L'endemà ja tenia tota la informació per aplicar a la beca... Vull agrair-vos especialment la confiança que vau dipositar en mi per aquest projecte i per haver-me acompanyat i donat l'oportunitat d'aprendre amb i de vosaltres. Moltes gràcies per la llibertat d'organització, per les discussions científiques de les quals tant n'he après, per les revisions dels articles, dels abstracts, pels congressos, les campanyes de camp, pel vostre temps i per la vostra guia durant tot aquest procés. És molt fàcil treballar amb vosaltres. Albert, et vull agrair especialment el fet d'haver-me introduït al món de la modelització numèrica i a ensenyar-me a integrar el que veiem als models amb el camp a totes les escales, que no és gens senzill. Per ensenyar-me a sistematitzar correcta i lògicament les variables.

També per guiar-me amb el treball amb les venes de calcita, amb les revisions de làmines primes i amb el treball de laboratori. Per sempre estar disponible a qualsevol hora i dia quan he tingut algun dubte. No sé com, però fas que les coses més complicades semblin extremadament senzilles. Toni, et vull agrair infinitament les lliçons que m'has donat de Pirineus i també et vull agrair el fet de posar la teva sobrada experiència i coneixement sempre a disposició. Les facilitats i recolzament que m'has donat durant tot aquest procés i els continus ànims i confiança durant els darrers mesos han significat molt per mi. Sou un exemple tant en el tracte personal com de dedicació a la causa de l'ensenyament i la investigació.

Als meus companys de doctorat amb els que hem compartit tantes alegries i records. A la Laura, per la seva empenta. Al Juan Camilo por sus anécdotas y relatos. Al Guillem, per la seva ajuda amb el Matlab, les equacions diferencials i la mecànica de medis continus quan tot just jo començava (i era un pulpo en un garaje). Al Xavi, per ensenyar-me la metodologia de separació de zircons. Al Gerard, per les converses disteses. Al Sabí, pels migdies de buti i l'empenta que té. A María, por tu alegría y conversación. Moltes gràcies per la vostra ajuda i consell. Finalment al Norbert, per totes les discussions enriquidores, dies de camp (amb vaques i ossos) i despatx.

Gràcies a tots els membres del Departament de Geologia de la Universitat Autònoma de Barcelona per acollir-me i donar-me suport consell i acompanyament quan ho he necessitat. Al Pini, pels bons dinars, els viatges de tornada a casa compartint cotxe quan ha fet falta i per les xerrades disteses i estones compartides. Al David, per sempre tindre un moment per mi quan ho he necessitat, pels ànims durant la "cuesta arriba" i "cuesta abajo", pels caramels post-reunió i per l'alegria que desprens xiulant pel departament. A l'Isaac, pel seu suport, consell i la implantació del "viernes de birra". A l'Eduard per la seva confiança. A Maria Luisa y Paco por las charlas y discusiones enriquecedoras.

A les "secres", Sara, Eva, Lara, Isabel, per la vostra simpatia, alegria, ajuda constant, bona feina i gestió dels mal de caps burocràtics. Als laborants del laboratori de làmines primes, Lluis, Marc i Pepi, moltes gràcies per la vostra simpatia i la bona feina amb les làmines primes i trituració de les roques quan ho he necessitat, especialment quan ha estat urgent, mai heu tingut un "no" com a resposta.

247

I would like to thank Boris Kaus and the Johanes Guttenberg University of Mainz for giving me the opportunity to work together in this project and for giving up their servers for the realisation of numerical modelling simulations.

Vorrei ringraziare in modo particolare Andrea Piccolo, per il suo continuo aiuto, il suo tempo e la sua collaborazione in questo progetto, per aver sempre risolto tutti i miei dubbi e per avermi insegnato pazientemente durante tutto il corso di questa tesi di dottorato.

I would like to extent my gratitude to Daniel Stockli and Lisa Stockli for making things easier for me in Austin and for their help and support with the thermo- and geochronology. Special mention to Rudra for the support and the teaching of the low temperature thermochronology method. I really miss the discussions about football ("soccer").

També m'agradaria agrair a la Gemma la cessió de les seves dades de termocronologia del plutó d'Eaux-Chaudes, que han pogut ser incorporades en aquest treball millorant-ne indubtablement la seva qualitat.

Al Juan Diego, pels consells, el suport i l'ajuda durant les anàlisi de catodoluminescència i el microdrilling a les venes de calcita. Al David per la predisposició i ajuda en els meus primers passos en la geocronologia U-Pb en calcita.

Je tiens à remercier Joseph et Caroline pour leur accueil dans le village de Laruns et des Eaux-Bonnes tout au long des 5 années de campagnes intensives sur le terrain.

I would like to thank Rebecca for welcome me at her house in Austin, for taking me to the Wurstfest and for being so kind and nice person with me. To Layth, for the memories in the Rainey street clubs.

A Fernando, compañero durante la carrera y en Zaragoza y amigo, eres una parte importante de esto. Sin tu apoyo y compañía durante estos años esto no hubiera sido posible. Mención especial a los ratos de biblioteca y jugando con tarros. Inolvidable.

Als meus amics, Eloi, Jordi i Roger per sempre respondre quan ho he necessitat i la vostra comprensió quan no hi he pogut ser. Gracias por facilitarme la desconexión mental durante el doctorado, ya no volveré a decir que no puedo venir al vermut porqué estoy haciendo modelos/trabajando.

Als meus pares, sense la seva guia, el seu recolzament, comprensió i sacrifici al llarg dels anys jo mai hagués arribat aquí ni hagués arribat a ser com soc, us estimo. También me gustaría agradecer a la yaya i el yeye por cuidar de mi cuando más lo necesité y enseñarme a tener curiosidad por cómo funcionan las cosas, sin vosotros tampoco hubiera llegado aquí, os quiero.

A ti, Silvia, compañera de viaje y de vida. Gracias por la paciencia que has tenido a lo largo de todos estos años, por tu comprensión y por tu empatía, especialmente en estos últimos meses de trabajo intenso y poco dormir. Te quiero!

Annexes

Annexes

Annex A3: Complementary mechanical simulations to those

shown in Chapter 3
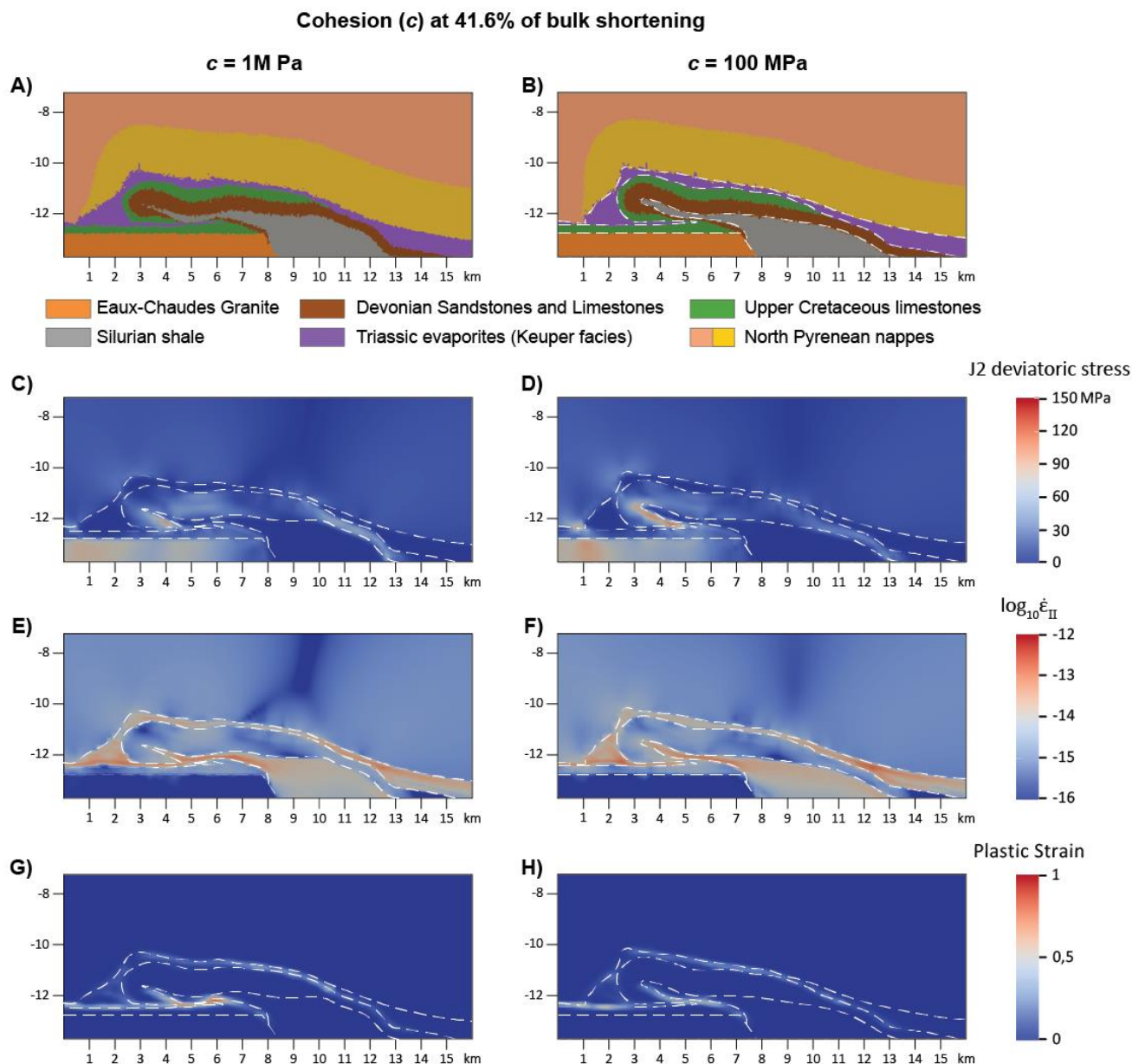
Figure A3.1: *Results of the cohesion variable simulations for c=1MPa -**A)**, **C)**, **E)**, **G)**- and c=100MPa -**B)**, **D)**, **F)**, **H)**- showing the effect of low cohesion, producing an enhancement of the plastic strain and the cross-cutting of a shear zone through the reverse limb.*
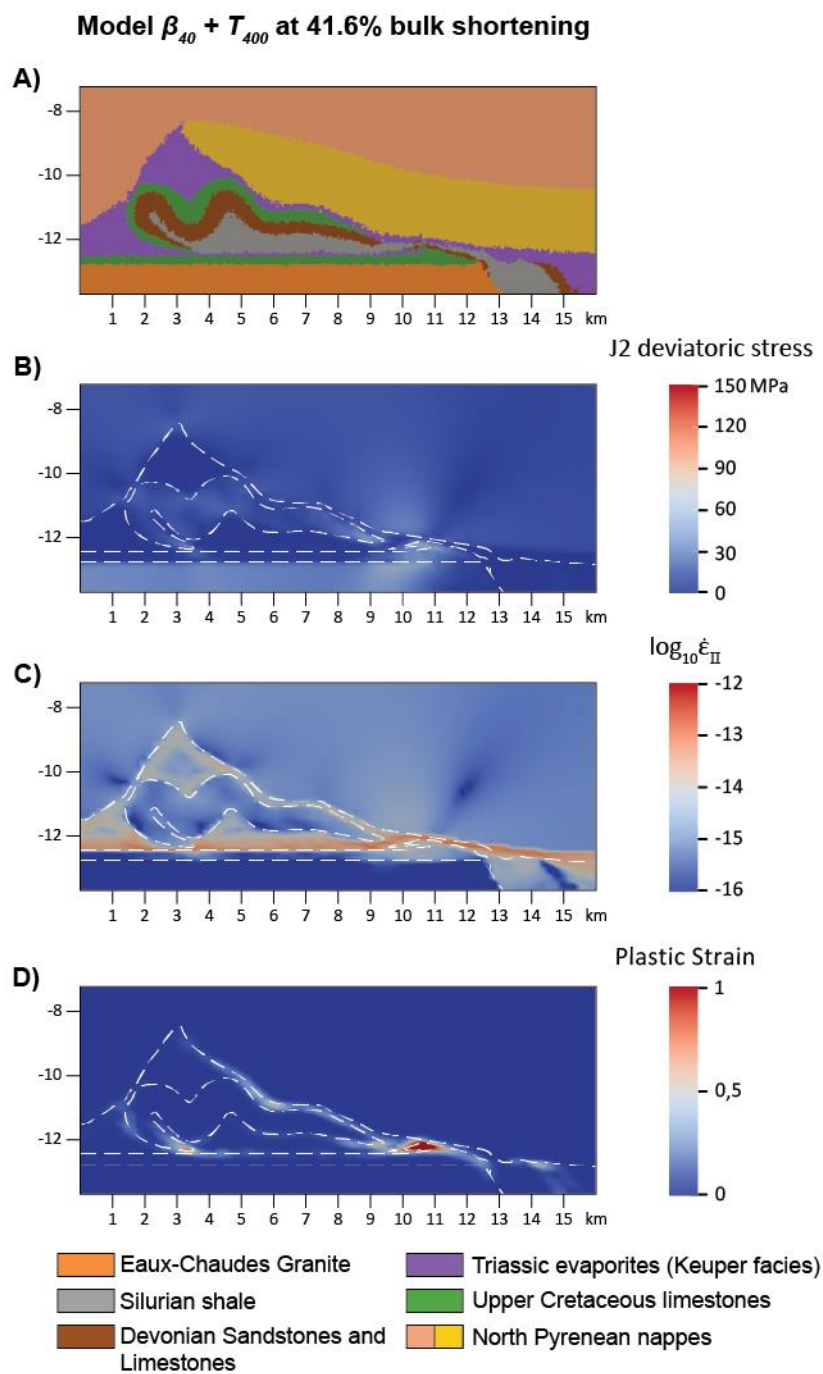
Figure A3.2: *Results of the β_{40}+T_{400} simulation evidencing the development of localization surfaces at $\beta>20°$.*

Annex A4: Complementary thermomechanical simulationsto

those shown in Chapter 4
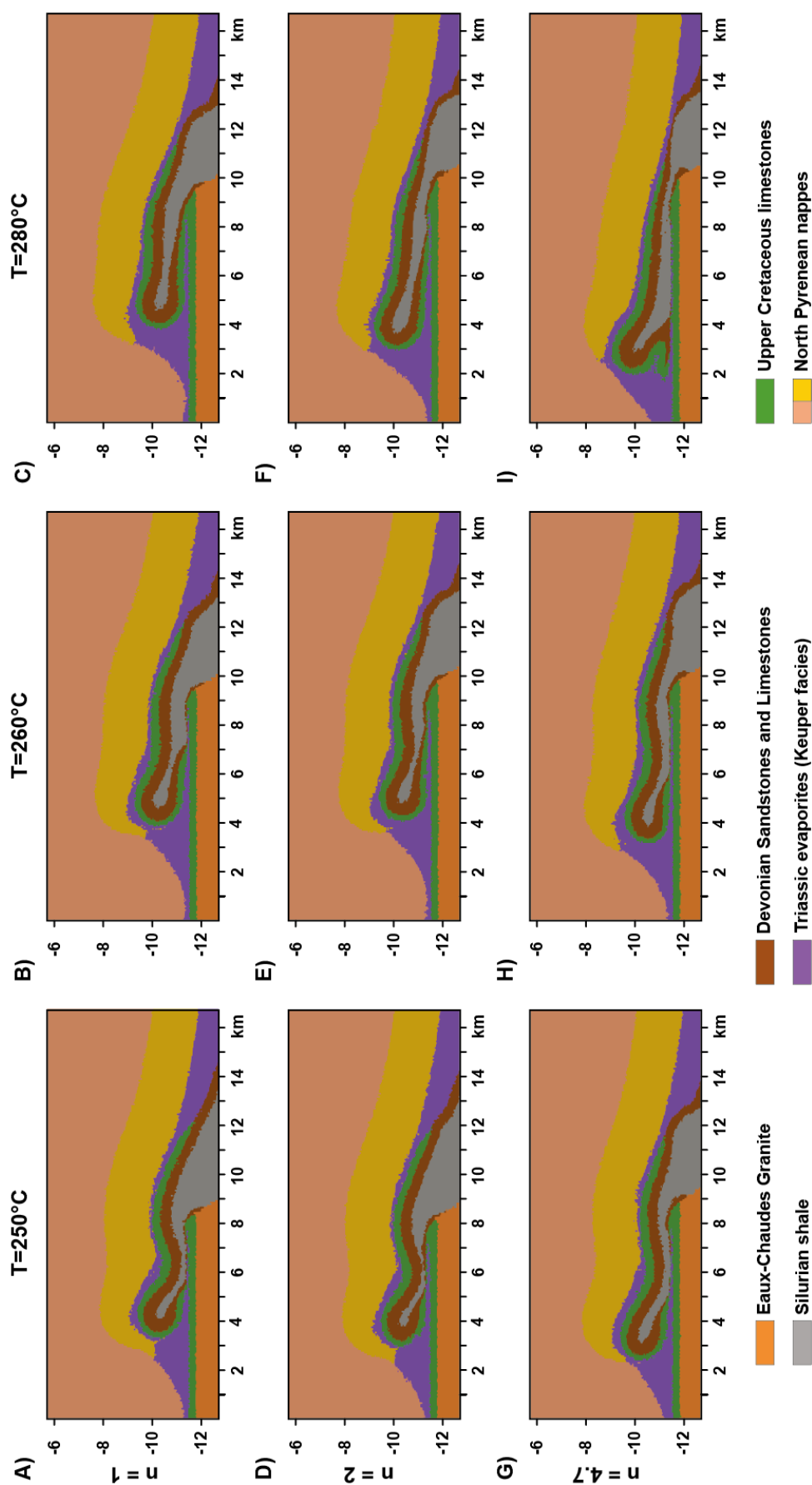
Figure A4.1*: Selected simulations of the systematic model runs under linear media at different constant temperature profiles for different stress exponents (n) at 37.3% of bulk shortening. Each simulation picture correspond to the same interval and area to those shown in Figs. A4.2 and A4.3. The summary of the dominant behaviour under which these modeled structures were developed is shown in Fig. 4.10. Brittle deformation of the overturned limb (i.e. thrusting) is present below 270°C and n ≤ 3. Ductile localization is favored in a wide range of temperatures and at n ≥ 2. In between, a range of situations where recumbent folding (with constant or stretched recumbent limb).*
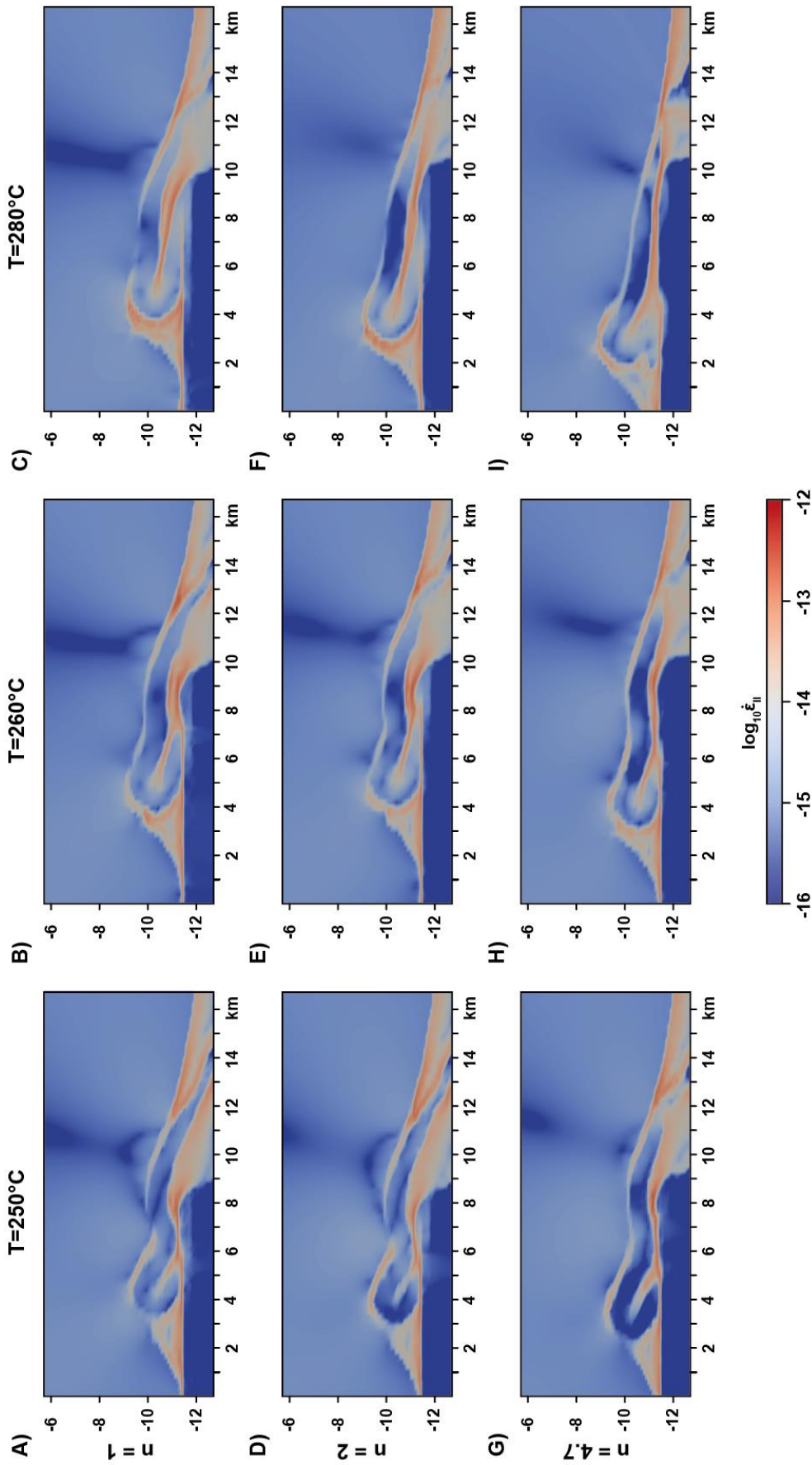
Figure A4.2: *Selected simulations of the second invariant of the strain rate tensor ($\dot{\varepsilon}_{II}$) of the systematic model runs under linear media at different constant temperature profiles for different stress exponents (n) at 37.3% of bulk shortening. Each simulation picture correspond to the same interval and area to those shown in Figs. A4.1 and A4.3. Flat localization surfaces are detected by the elevated strain rate values through the overturned limbs in simulations where no recumbent folding is occurring, showing geometries much resembling a thrust nappe.*
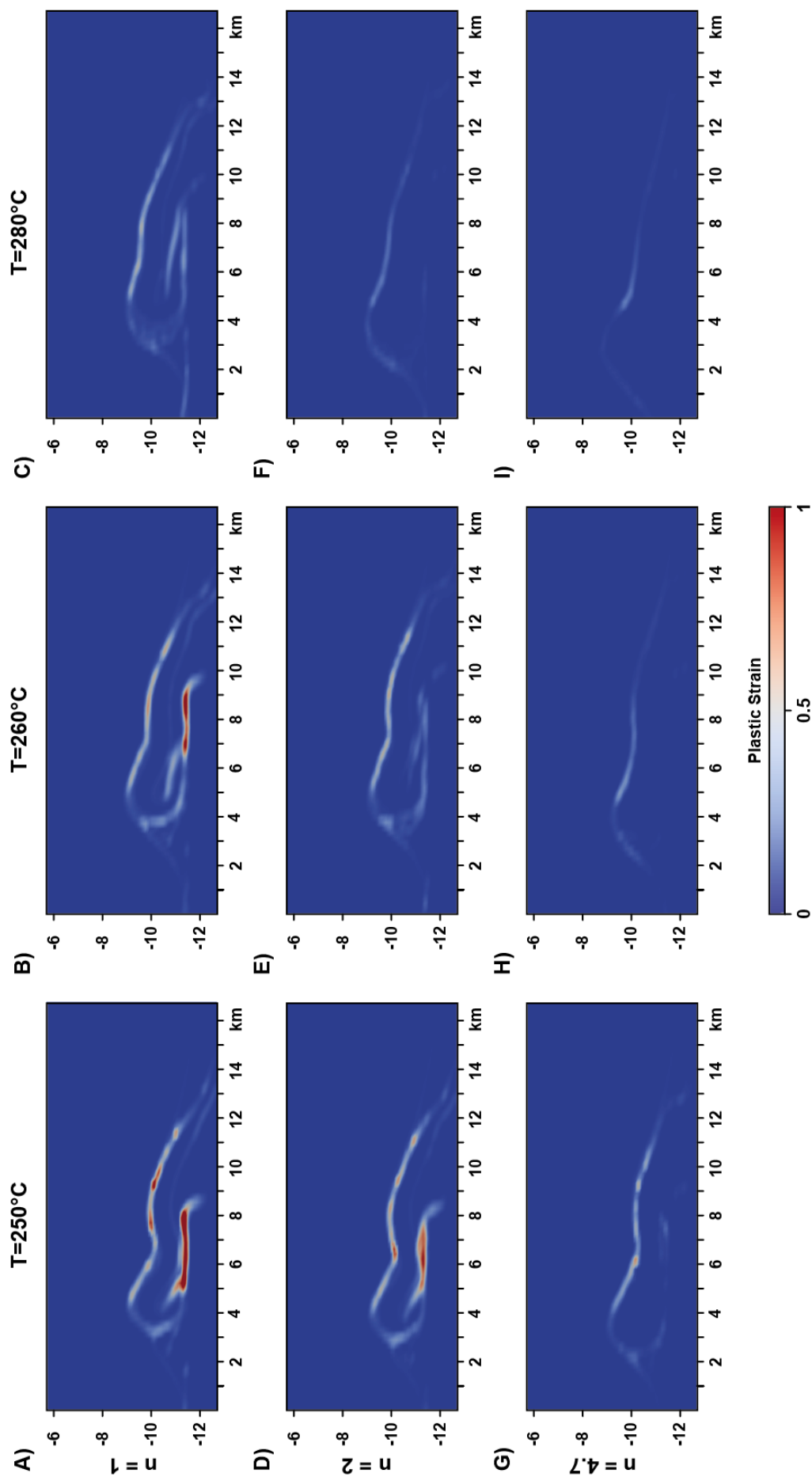
Figure A4.3: *Selected simulations of the natural plastic strain of the systematic model runs under linear media at different constant temperature profiles for different stress exponents (n) at 37.3% of bulk shortening. Each simulation picture correspond to the same interval and area to those shown in Figs. 4.5 and 4.6. Plasticity is favored at low temperatures and stress exponents while the viscous behaviour is dominant at high stress exponent and temperatures.*

Figure A4.4: *Thermo-mechanical simulations results for n = 1 at different applied temperature profiles and linear media (non-dependent on temperature nor strainrate), including the phase (A, B and C), strain-rates (D, E, and F), natural plastic strain (G, H and I) and effective viscosity (J, K and L) plots. T_i : initial temperature at the bottom of the model; T_f : final temperature at the bottom of the model.*

Figure A4.5: *Thermo-mechanical simulations results for n = 2 at different applied temperature profiles and linear media (non-dependent on temperature nor strainrate), including the phase (A, B and C), strain-rates (D, E, and F), natural plastic strain (G, H and I) and effective viscosity (J, K and L) plots. T_i : initial temperature at the bottom of the model; T_f : final temperature at the bottom of the model.*
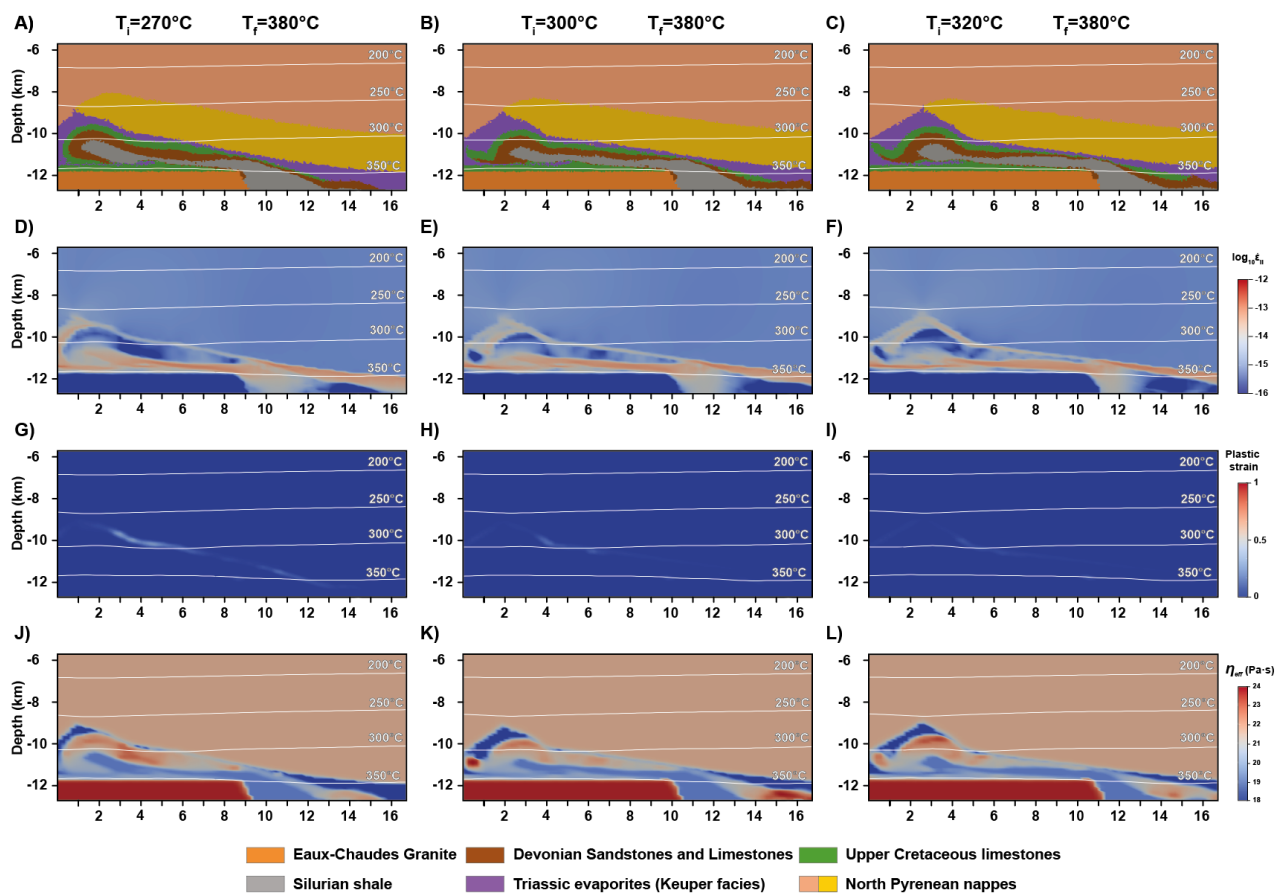
Figure A4.6: *Thermo-mechanical simulations results for n = 4.7 at different applied temperature profiles and linear media (non-dependent on temperature nor strainrate), including the phase (A, B and C), strain-rates (D, E, and F), natural plastic strain (G, H and I) and effective viscosity (J, K and L) plots. T_i : initial temperature at the bottom of the model; T_f : final temperature at the bottom of the model.*

Annex A5: Geochronology data repository from Chapter 5

Table A5.1: U-Pb isotopic data of calcite veins from the ECM obtained during the session 1 (24/09/2021) of LA-ICP-MS U-Pb in calcite. The spot size for all samples is 110 μm. Red labelled data was excluded from the age regression due to evident high error or a point belonging to the host rock.

Spot	Source file (.FIN2)	Sample	$^{238}U/^{206}Pb$	±2σ (abs)	$^{207}Pb/^{206}Pb$	±2σ (abs)	Rho	U (ppm)	Pb (ppm)
Session 1									
WC-1 Calcite reference (Roberts et al., 2017)									
1	WC-1-1	WC-1	25.419	0.388	0.052	0.003	0.14	6.51	0.19
2	WC-1-2	WC-1	24.931	0.404	0.052	0.004	0.10	4.24	0.26
3	WC-1-3	WC-1	24.925	0.391	0.053	0.003	0.13	4.01	0.18
4	WC-1-4	WC-1	25.202	0.451	0.053	0.004	0.10	3.88	0.15
5	WC-1-5	WC-1	24.900	0.434	0.051	0.003	0.41	3.22	0.14
6	WC-1-6	WC-1	24.814	0.369	0.051	0.004	0.14	4.16	0.19
7	WC-1-7	WC-1	24.576	0.429	0.051	0.006	-0.20	3.70	0.31
8	WC-1-8	WC-1	24.783	0.448	0.050	0.005	-0.48	3.90	0.26
9	WC-1-9	WC-1	25.038	0.451	0.047	0.006	-0.55	4.20	0.32
10	WC-1-10	WC-1	24.789	0.369	0.052	0.004	-0.06	4.03	0.25
11	WC-1-11	WC-1	26.110	0.470	0.051	0.004	0.36	3.09	0.17
12	WC-1-12	WC-1	24.814	0.677	0.039	0.011	-0.68	4.52	0.47
13	WC-1-13	WC-1	25.126	0.631	0.047	0.005	-0.57	3.38	0.23
14	WC-1-14	WC-1	24.558	0.428	0.051	0.004	-0.03	3.86	0.22
15	WC-1-15	WC-1	25.381	0.966	0.026	0.013	-0.70	3.61	0.39
16	WC-1-16	WC-1	24.938	0.516	0.043	0.008	-0.68	5.18	0.64
17	WC-1-17	WC-1	24.894	0.483	0.053	0.004	0.30	3.45	0.17
18	WC-1-18	WC-1	24.900	0.502	0.053	0.004	0.23	3.74	0.19
19	WC-1-19	WC-1	25.107	0.454	0.052	0.004	0.07	3.79	0.14
20	WC-1-20	WC-1	24.882	0.458	0.051	0.004	0.08	3.83	0.17
21	WC-1-21	WC-1	24.606	0.430	0.051	0.004	-0.04	3.58	0.24
22	WC-1-22	WC-1	24.931	0.416	0.052	0.003	0.23	3.73	0.18
23	WC-1-23	WC-1	25.681	0.448	0.051	0.003	0.35	3.88	0.12
24	WC-1-24	WC-1	24.777	0.516	0.050	0.010	-0.56	3.77	0.51
25	WC-1-25	WC-1	25.394	0.419	0.051	0.003	0.49	3.62	0.14
26	WC-1-26	WC-1	24.907	0.596	0.041	0.009	-0.67	3.63	0.42
27	WC-1-27	WC-1	25.176	0.425	0.052	0.004	-0.02	4.33	0.19
28	WC-1-28	WC-1	24.038	0.578	0.053	0.006	0.04	3.41	0.28
29	WC-1-29	WC-1	24.789	0.547	0.054	0.007	-0.01	3.69	0.28
30	WC-1-30	WC-1	25.310	0.500	0.049	0.005	-0.36	3.84	0.19
31	WC-1-31	WC-1	24.426	0.424	0.052	0.003	0.31	3.65	0.16
32	WC-1-32	WC-1	25.195	0.495	0.049	0.004	-0.04	3.68	0.14
33	WC-1-33	WC-1	25.278	0.447	0.052	0.004	0.22	3.63	0.20
34	WC-1-34	WC-1	24.704	0.415	0.049	0.005	-0.32	3.75	0.35
35	WC-1-35	WC-1	25.368	0.405	0.051	0.006	-0.34	3.61	0.36
36	WC-1-36	WC-1	25.202	0.603	0.044	0.006	-0.52	5.20	0.53
37	WC-1-37	WC-1	25.063	0.396	0.051	0.004	0.31	3.47	0.21

Spot	Source file (.FIN2)	Sample	^{238}U/^{206}Pb	±2σ (abs)	^{207}Pb/^{206}Pb	±2σ (abs)	Rho	U (ppm)	Pb (ppm)
38	WC-1-38	WC-1	24.814	0.677	0.050	0.014	-0.67	3.77	0.59
39	WC-1-39	WC-1	24.691	0.445	0.053	0.005	0.43	3.78	0.25
40	WC-1-40	WC-1	24.522	0.457	0.052	0.005	-0.25	4.62	0.26
41	WC-1-41	WC-1	24.845	0.556	0.049	0.010	-0.28	3.16	0.31
42	WC-1-42	WC-1	24.814	0.449	0.050	0.004	0.10	3.84	0.16
43	WC-1-43	WC-1	24.558	0.507	0.051	0.005	-0.26	3.54	0.15
44	WC-1-44	WC-1	24.925	0.472	0.051	0.004	0.18	3.47	0.18
45	WC-1-45	WC-1	25.589	0.386	0.051	0.003	0.28	4.14	0.22
46	WC-1-46	WC-1	25.654	0.369	0.051	0.005	-0.31	4.09	0.25
47	WC-1-47	WC-1	25.221	0.382	0.051	0.004	0.04	3.59	0.22
48	WC-1-48	WC-1	24.765	0.393	0.052	0.006	-0.20	3.88	0.32
49	WC-1-49	WC-1	24.876	0.340	0.051	0.003	0.32	3.47	0.17
50	WC-1-50	WC-1	24.552	0.446	0.049	0.007	-0.60	3.93	0.44
51	WC-1-51	WC-1	23.935	0.332	0.050	0.005	-0.30	3.95	0.46
52	WC-1-52	WC-1	25.641	0.421	0.051	0.004	0.21	3.47	0.14
53	WC-1-53	WC-1	25.504	0.377	0.050	0.003	0.10	3.57	0.13
54	WC-1-54	WC-1	24.600	0.430	0.052	0.005	-0.09	3.96	0.26
55	WC-1-55	WC-1	25.394	0.413	0.050	0.003	0.31	3.50	0.13
56	WC-1-56	WC-1	24.704	0.336	0.052	0.004	-0.01	4.05	0.28
57	WC-1-57	WC-1	25.221	0.363	0.052	0.005	0.22	3.51	0.25
58	WC-1-58	WC-1	25.145	0.360	0.052	0.003	0.30	4.36	0.18
59	WC-1-59	WC-1	24.722	0.422	0.055	0.005	0.03	3.44	0.25
60	WC-1-60	WC-1	25.126	0.354	0.050	0.003	0.38	3.67	0.14
61	WC-1-61	WC-1	25.006	0.406	0.052	0.003	0.24	3.80	0.20
62	WC-1-62	WC-1	24.900	0.316	0.051	0.003	0.35	3.53	0.14
63	WC-1-63	WC-1	25.221	0.388	0.052	0.003	-0.02	4.52	0.21
64	WC-1-64	WC-1	25.329	0.340	0.051	0.003	-0.08	3.64	0.14
65	WC-1-65	WC-1	24.313	0.402	0.052	0.004	0.25	3.43	0.17

Soda-lime glass NIST SRM-614

Spot	Source file (.FIN2)	Sample	^{238}U/^{206}Pb	±2σ (abs)	^{207}Pb/^{206}Pb	±2σ (abs)	Rho	U (ppm)	Pb (ppm)
1	NIST614-1	NIST-614	1.414	0.022	0.863	0.012	0.68	0.61	10.84
2	NIST614-2	NIST-614	1.442	0.019	0.877	0.011	0.68	0.60	10.74
3	NIST614-3	NIST-614	1.446	0.020	0.874	0.012	0.57	0.55	9.81
4	NIST614-4	NIST-614	1.446	0.019	0.890	0.012	0.62	0.60	10.56
5	NIST614-5	NIST-614	1.477	0.021	0.874	0.011	0.62	0.57	9.28
6	NIST614-6	NIST-614	1.435	0.023	0.868	0.012	0.64	0.57	9.37
7	NIST614-7	NIST-614	1.421	0.018	0.873	0.011	0.55	0.62	10.31
8	NIST614-8	NIST-614	1.408	0.020	0.873	0.011	0.57	0.59	10.20
9	NIST614-9	NIST-614	1.407	0.018	0.871	0.009	0.56	0.57	10.02
10	NIST614-10	NIST-614	1.391	0.017	0.868	0.009	0.60	0.56	10.21

					19MG21 from DA strain domain				
Spot	**Source file (.FIN2)**	**Sample**	**²³⁸U/²⁰⁶Pb**	**±2σ (abs)**	**²⁰⁷Pb/²⁰⁶Pb**	**±2σ (abs)**	**Rho**	**U (ppm)**	**Pb (ppm)**
	19MG21-1	19MG21-1	2.273	0.723	0.818	0.020	0.03	1.17	6.93
	19MG21-1	19MG21-1	0.585	0.103	0.812	0.036	0.28	0.21	6.56
1	19MG21-1	19MG21-1	0.735	0.135	0.818	0.025	-0.07	1.22	23.80
	19MG21-1	19MG21-1	2.667	0.412	0.809	0.024	0.32	1.49	11.80
	19MG21-1	19MG21-1	0.893	0.167	0.802	0.022	0.21	0.57	12.50
	19MG21-2	19MG21-1	3.704	2.881	0.792	0.037	-0.09	12.60	29.30
2	19MG21-2	19MG21-1	1.727	0.212	0.803	0.017	0.43	1.00	11.45
	19MG21-2	19MG21-1	1.159	0.079	0.818	0.012	0.23	0.65	11.09
	19MG21-3	19MG21-1	0.704	0.119	0.818	0.017	0.20	0.85	19.90
3	19MG21-3	19MG21-1	4.651	1.536	0.792	0.043	-0.52	2.62	7.89
	19MG21-3	19MG21-1	0.952	0.091	0.810	0.012	0.19	0.54	12.60
	19MG21-4	19MG21-1	1.031	0.149	0.799	0.019	-0.29	0.35	6.02
4	19MG21-4	19MG21-1	0.690	0.067	0.804	0.018	-0.07	0.27	8.90
	19MG21-4	19MG21-1	0.508	0.046	0.808	0.019	-0.06	0.16	6.51
5	19MG21-5	19MG21-1	0.169	0.008	0.824	0.016	0.30	0.03	4.07
	19MG21-5	19MG21-1	0.302	0.034	0.819	0.024	0.03	0.06	3.90
6	19MG21-6	19MG21-1	0.228	0.015	0.814	0.022	0.27	0.06	5.93
	19MG21-6	19MG21-1	0.157	0.009	0.805	0.013	0.15	0.04	4.80
7	19MG21-7	19MG21-1	1.075	0.266	0.807	0.049	0.11	0.55	8.37
	19MG21-7	19MG21-1	0.840	0.261	0.832	0.021	-0.14	1.42	12.20
	19MG21-7	19MG21-1	0.806	0.065	0.818	0.015	0.12	0.20	5.42
8	19MG21-8	19MG21-1	2.273	0.723	0.787	0.023	-0.30	2.10	7.99
	19MG21-8	19MG21-1	0.877	0.085	0.817	0.013	0.10	0.56	13.60
9	19MG21-9	19MG21-1	0.344	0.013	0.828	0.015	0.53	0.09	6.10
10	19MG21-10	19MG21-1	0.131	0.011	0.814	0.020	0.46	0.03	5.37
	19MG21-10	19MG21-1	0.204	0.008	0.825	0.016	0.09	0.04	4.88
12	19MG21-12	19MG21-1	0.066	0.005	0.844	0.014	0.13	0.01	4.32
	19MG21-12	19MG21-1	0.171	0.016	0.832	0.038	0.23	0.02	3.75
13	19MG21-13	19MG21-1	0.087	0.005	0.825	0.014	0.15	0.01	4.17
14	19MG21-14	19MG21-1	0.175	0.008	0.805	0.020	0.30	0.03	4.26
	19MG21-14	19MG21-1	0.283	0.016	0.823	0.020	0.39	0.05	4.25
15	19MG21-15	19MG21-1	0.187	0.007	0.819	0.016	0.33	0.03	4.03
16	19MG21-16	19MG21-1	0.101	0.005	0.822	0.013	0.25	0.02	4.40
17	19MG21-17	19MG21-1	0.101	0.005	0.826	0.013	0.27	0.02	4.58
20	19MG21-20	19MG21-1	0.147	0.009	0.811	0.015	-0.03	0.02	3.70
21	19MG21-21	19MG21-1	0.126	0.010	0.816	0.018	0.22	0.03	5.16
	19MG21-21	19MG21-1	0.086	0.005	0.812	0.013	0.19	0.02	4.43
22	19MG21-22	19MG21-1	0.063	0.004	0.823	0.017	0.22	0.01	4.40
	19MG21-22	19MG21-1	0.110	0.009	0.829	0.022	0.16	0.02	3.77
24	19MG21-24	19MG21-1	0.113	0.007	0.826	0.018	-0.06	0.02	4.35
25	19MG21-25	19MG21-1	0.077	0.009	0.820	0.025	-0.03	0.01	3.93

Spot	Source file (.FIN2)	Sample	^{238}U/^{206}Pb	±2σ (abs)	^{207}Pb/^{206}Pb	±2σ (abs)	Rho	U (ppm)	Pb (ppm)
	19MG21-26	19MG21-2	0.090	0.013	0.817	0.030	0.41	0.02	3.92
26	19MG21-26	19MG21-2	0.162	0.018	0.846	0.036	0.05	0.03	4.14
	19MG21-26	19MG21-2	0.081	0.008	0.819	0.024	0.37	0.01	3.69
	19MG21-26	19MG21-2	0.184	0.027	0.820	0.034	0.24	0.03	3.37
27	19MG21-27	19MG21-2	0.137	0.011	0.816	0.020	0.35	0.02	3.78
	19MG21-27	19MG21-2	0.085	0.012	0.789	0.023	0.47	0.01	3.53
	19MG21-28	19MG21-2	0.083	0.008	0.842	0.021	0.46	0.02	4.26
28	19MG21-28	19MG21-2	0.095	0.010	0.846	0.022	-0.06	0.02	3.68
	19MG21-28	19MG21-2	0.152	0.028	0.831	0.043	-0.07	0.02	3.24
29	19MG21-29	19MG21-2	0.132	0.035	0.807	0.039	0.56	0.03	4.00
	19MG21-29	19MG21-2	0.127	0.009	0.829	0.020	0.18	0.02	3.50
30	19MG21-30	19MG21-2	0.058	0.008	0.840	0.069	0.44	0.01	5.25
	19MG21-30	19MG21-2	0.094	0.017	0.822	0.026	0.12	0.03	4.39
31	19MG21-31	19MG21-2	0.071	0.010	0.804	0.023	0.01	0.02	4.71
	19MG21-31	19MG21-2	0.082	0.007	0.813	0.016	0.07	0.02	4.19
	19MG21-32	19MG21-2	0.243	0.025	0.867	0.039	0.12	0.05	5.10
32	19MG21-32	19MG21-2	0.159	0.010	0.825	0.029	0.27	0.03	4.33
	19MG21-32	19MG21-2	0.091	0.007	0.858	0.026	0.32	0.02	4.08
34	19MG21-34	19MG21-2	0.152	0.015	0.817	0.023	0.11	0.03	4.18
	19MG21-35	19MG21-2	0.137	0.010	0.814	0.028	0.25	0.03	4.07
35	19MG21-35	19MG21-2	0.218	0.026	0.836	0.035	0.43	0.04	4.11
	19MG21-35	19MG21-2	0.169	0.015	0.804	0.027	0.34	0.03	4.07
	19MG21-35	19MG21-2	0.248	0.025	0.797	0.028	0.43	0.05	3.73
36	19MG21-36	19MG21-2	0.179	0.011	0.820	0.014	0.26	0.04	4.59
37	19MG21-37	19MG21-2	0.187	0.011	0.823	0.012	0.26	0.04	4.38
38	19MG21-38	19MG21-2	0.186	0.008	0.827	0.017	0.11	0.04	4.41
	19MG21-38	19MG21-2	0.090	0.009	0.832	0.024	0.17	0.02	3.72
39	19MG21-39	19MG21-2	0.138	0.016	0.817	0.030	0.07	0.03	4.93
	19MG21-40	19MG21-2	0.194	0.014	0.836	0.027	0.25	0.04	4.30
40	19MG21-40	19MG21-2	0.510	0.025	0.818	0.016	0.41	0.11	5.09
	19MG21-40	19MG21-2	0.187	0.015	0.807	0.017	0.02	0.05	5.17
	19MG21-41	19MG21-2	0.199	0.013	0.795	0.027	0.13	0.04	4.75
41	19MG21-41	19MG21-2	0.592	0.042	0.831	0.024	0.14	0.14	5.24
	19MG21-41	19MG21-2	0.268	0.027	0.818	0.026	0.12	0.06	4.39
	19MG21-42	19MG21-2	0.243	0.015	0.801	0.027	0.22	0.05	4.71
42	19MG21-42	19MG21-2	0.131	0.008	0.828	0.018	0.15	0.03	4.79
	19MG21-42	19MG21-2	0.103	0.009	0.841	0.030	0.43	0.02	4.30
43	19MG21-43	19MG21-2	0.369	0.015	0.817	0.018	0.37	0.09	5.88
	19MG21-43	19MG21-2	0.249	0.013	0.820	0.015	0.16	0.05	4.68
	19MG21-44	19MG21-2	0.299	0.022	0.826	0.025	0.04	0.06	4.78
44	19MG21-44	19MG21-2	0.529	0.031	0.828	0.032	0.21	0.17	7.60
	19MG21-44	19MG21-2	0.171	0.018	0.827	0.019	0.35	0.05	5.50

Spot	Source file (.FIN2)	Sample	$^{238}U/^{206}Pb$	±2σ (abs)	$^{207}Pb/^{206}Pb$	±2σ (abs)	Rho	U (ppm)	Pb (ppm)
	19MG21-45	19MG21-2	0.149	0.020	0.807	0.038	0.35	0.04	5.48
45	19MG21-45	19MG21-2	0.388	0.021	0.823	0.026	0.47	0.09	5.48
	19MG21-45	19MG21-2	0.271	0.029	0.827	0.020	0.23	0.07	6.01
	19MG21-45	19MG21-2	0.455	0.031	0.812	0.022	0.24	0.10	5.22
	19MG21-46	19MG21-2	0.177	0.017	0.792	0.049	0.37	0.04	5.58
46	19MG21-46	19MG21-2	0.112	0.007	0.795	0.020	0.53	0.02	4.17
	19MG21-46	19MG21-2	0.235	0.016	0.856	0.028	0.19	0.04	4.39
47	19MG21-47	19MG21-2	0.288	0.014	0.822	0.015	0.26	0.07	5.41
	19MG21-47	19MG21-2	0.150	0.020	0.819	0.023	0.05	0.03	4.67
48	19MG21-48	19MG21-2	0.077	0.007	0.825	0.021	-0.10	0.01	4.40
49	19MG21-49	19MG21-2	0.088	0.008	0.833	0.019	-0.05	0.02	3.97
50	19MG21-50	19MG21-2	0.106	0.007	0.826	0.020	0.41	0.02	3.96
	19MG21-50	19MG21-2	0.230	0.017	0.825	0.021	0.40	0.04	3.83
	19MG21-51	19MG21-3	0.301	0.026	0.835	0.037	0.26	0.06	4.39
51	19MG21-51	19MG21-3	0.559	0.034	0.825	0.022	0.14	0.09	3.94
	19MG21-51	19MG21-3	0.355	0.015	0.796	0.023	-0.03	0.05	3.37
	19MG21-52	19MG21-3	0.163	0.011	0.831	0.025	0.44	0.03	4.07
52	19MG21-52	19MG21-3	0.302	0.015	0.817	0.019	0.61	0.05	3.61
	19MG21-52	19MG21-3	0.426	0.031	0.835	0.026	0.37	0.06	3.33
	19MG21-53	19MG21-3	0.408	0.033	0.846	0.035	-0.06	0.07	4.17
	19MG21-53	19MG21-3	0.162	0.013	0.828	0.022	0.15	0.03	4.47
53	19MG21-53	19MG21-3	1.412	0.122	0.839	0.043	-0.05	0.19	3.36
	19MG21-53	19MG21-3	0.294	0.025	0.832	0.027	0.29	0.04	3.49
	19MG21-54	19MG21-3	0.296	0.025	0.831	0.025	0.30	0.06	4.29
54	19MG21-54	19MG21-3	0.979	0.043	0.824	0.027	0.19	0.17	4.29
	19MG21-54	19MG21-3	0.775	0.090	0.825	0.032	0.08	0.12	3.82
	19MG21-54	19MG21-3	0.529	0.028	0.854	0.041	0.40	0.08	3.28
	19MG21-55	19MG21-3	0.229	0.039	0.820	0.033	0.41	0.06	5.35
	19MG21-55	19MG21-3	1.067	0.080	0.802	0.041	-0.44	0.17	4.03
55	19MG21-55	19MG21-3	0.389	0.020	0.842	0.023	0.18	0.07	4.43
	19MG21-55	19MG21-3	0.637	0.057	0.815	0.024	0.20	0.12	4.26
	19MG21-55	19MG21-3	0.369	0.035	0.835	0.022	0.48	0.07	4.13
	19MG21-56	19MG21-3	0.433	0.019	0.836	0.019	0.27	0.08	4.47
56	19MG21-56	19MG21-3	0.642	0.026	0.803	0.022	0.40	0.11	3.93
	19MG21-56	19MG21-3	0.395	0.034	0.833	0.036	0.70	0.06	3.33
	19MG21-57	19MG21-3	0.382	0.039	0.814	0.027	0.02	0.07	4.10
57	19MG21-57	19MG21-3	0.142	0.010	0.821	0.025	0.24	0.02	3.57
	19MG21-57	19MG21-3	0.217	0.017	0.823	0.031	0.02	0.03	3.35
	19MG21-57	19MG21-3	0.345	0.025	0.825	0.029	0.32	0.05	3.28
	19MG21-58	19MG21-3	0.129	0.008	0.837	0.032	0.57	0.02	3.82
58	19MG21-58	19MG21-3	0.153	0.010	0.838	0.039	0.66	0.03	3.85
	19MG21-58	19MG21-3	0.103	0.010	0.830	0.032	0.29	0.02	3.17

Spot	Source file (.FIN2)	Sample	$^{238}U/^{206}Pb$	±2σ (abs)	$^{207}Pb/^{206}Pb$	±2σ (abs)	Rho	U (ppm)	Pb (ppm)
	19MG21-59	19MG21-3	0.671	0.095	0.864	0.068	0.32	0.14	4.86
	19MG21-59	19MG21-3	0.301	0.021	0.812	0.028	0.27	0.06	4.44
59	19MG21-59	19MG21-3	0.435	0.030	0.833	0.031	0.51	0.08	4.06
	19MG21-59	19MG21-3	0.562	0.041	0.829	0.030	0.49	0.10	3.98
	19MG21-59	19MG21-3	0.302	0.021	0.810	0.027	0.31	0.05	3.47
	19MG21-60	19MG21-3	0.183	0.015	0.818	0.026	0.35	0.03	4.17
60	19MG21-60	19MG21-3	0.252	0.029	0.822	0.032	0.46	0.05	3.86
	19MG21-60	19MG21-3	0.088	0.009	0.832	0.020	0.08	0.02	3.37
	19MG21-60	19MG21-3	0.321	0.030	0.814	0.040	0.40	0.04	3.14
61	19MG21-61	19MG21-3	0.113	0.006	0.815	0.013	0.17	0.02	3.84
	19MG21-62	19MG21-3	0.154	0.008	0.840	0.018	0.34	0.03	4.06
62	19MG21-62	19MG21-3	0.217	0.016	0.826	0.026	0.15	0.04	3.93
	19MG21-62	19MG21-3	0.104	0.015	0.796	0.030	0.21	0.02	3.53
63	19MG21-63	19MG21-3	0.140	0.009	0.810	0.018	0.34	0.03	4.00
	19MG21-63	19MG21-3	0.089	0.006	0.839	0.018	0.29	0.02	3.79
64	19MG21-64	19MG21-3	0.082	0.007	0.830	0.024	0.20	0.02	4.04
65	19MG21-65	19MG21-3	0.132	0.017	0.819	0.024	-0.07	0.03	4.13
66	19MG21-66	19MG21-3	0.319	0.023	0.847	0.018	0.06	0.07	3.69
	19MG21-66	19MG21-3	0.098	0.008	0.826	0.023	0.11	0.02	3.18
	19MG21-67	19MG21-3	0.147	0.015	0.799	0.032	0.32	0.04	4.52
67	19MG21-67	19MG21-3	0.818	0.050	0.856	0.059	0.51	0.19	4.59
	19MG21-67	19MG21-3	0.592	0.034	0.820	0.030	0.49	0.13	4.26
	19MG21-67	19MG21-3	0.253	0.027	0.819	0.029	0.43	0.05	3.48
68	19MG21-68	19MG21-3	0.132	0.016	0.842	0.022	0.19	0.03	3.81
	19MG21-68	19MG21-3	0.216	0.018	0.824	0.021	0.11	0.05	3.77
70	19MG21-70	19MG21-3	0.076	0.006	0.810	0.020	0.03	0.02	3.94
	19MG21-70	19MG21-3	0.123	0.011	0.818	0.021	0.26	0.03	3.42
	19MG21-71	19MG21-3	0.813	0.073	0.840	0.028	0.50	0.25	5.24
71	19MG21-71	19MG21-3	0.187	0.019	0.815	0.023	0.09	0.05	4.48
	19MG21-71	19MG21-3	0.085	0.015	0.825	0.017	0.26	0.04	9.60
	19MG21-72	19MG21-3	0.159	0.025	0.834	0.024	0.17	0.04	3.91
72	19MG21-72	19MG21-3	0.190	0.013	0.838	0.028	0.32	0.04	3.75
	19MG21-72	19MG21-3	0.123	0.012	0.829	0.018	0.24	0.03	3.46
73	19MG21-73	19MG21-3			no value	NAN	NaN	0.00	3.51
	19MG21-74	19MG21-3	0.123	0.018	0.822	0.024	-0.02	0.05	3.82
	19MG21-74	19MG21-3	0.676	0.142	0.807	0.029	0.23	0.20	4.05
74	19MG21-74	19MG21-3	1.406	0.081	0.820	0.018	0.29	0.40	4.59
	19MG21-74	19MG21-3	1.205	0.096	0.819	0.031	0.44	0.35	4.63
	19MG21-74	19MG21-3	1.730	0.093	0.835	0.032	0.13	0.47	4.55
76	19MG21-76	19MG21-4	1.439	0.037	0.807	0.014	0.51	0.32	3.83
77	19MG21-77	19MG21-4	1.272	0.050	0.818	0.022	0.42	0.77	10.50
	19MG21-77	19MG21-4	1.016	0.023	0.804	0.011	0.41	0.44	7.26
78	19MG21-78	19MG21-4	1.560	0.066	0.846	0.025	0.56	0.49	5.63
	19MG21-78	19MG21-4	0.433	0.041	0.814	0.021	0.07	0.12	4.32

Spot	Source file (.FIN2)	Sample	^{238}U/^{206}Pb	±2σ (abs)	^{207}Pb/^{206}Pb	±2σ (abs)	Rho	U (ppm)	Pb (ppm)
79	19MG21-79	19MG21-4	0.092	0.006	0.823	0.015	0.00	0.02	4.01
80	19MG21-80	19MG21-4	0.080	0.004	0.818	0.015	0.23	0.02	3.92
	19MG21-81	19MG21-4	0.129	0.015	0.838	0.031	0.09	0.03	4.27
81	19MG21-81	19MG21-4	0.217	0.018	0.820	0.023	0.30	0.05	4.25
	19MG21-81	19MG21-4	0.139	0.011	0.808	0.021	0.30	0.03	3.77
82	19MG21-82	19MG21-4	0.318	0.019	0.820	0.040	0.71	0.07	3.98
	19MG21-82	19MG21-4	0.345	0.018	0.813	0.017	0.20	0.06	3.33
83	19MG21-83	19MG21-4	0.493	0.029	0.831	0.041	0.52	0.08	3.44
	19MG21-83	19MG21-4	0.298	0.015	0.832	0.019	0.18	0.04	2.74
84	19MG21-84	19MG21-4	0.603	0.019	0.812	0.013	0.18	0.14	4.55
85	19MG21-85	19MG21-4	0.105	0.008	0.838	0.028	0.49	0.02	2.97
	19MG21-85	19MG21-4	0.108	0.008	0.835	0.025	0.30	0.02	2.81
87	19MG21-87	19MG21-4	0.138	0.016	0.810	0.037	0.15	0.02	3.18
	19MG21-87	19MG21-4	0.249	0.026	0.827	0.035	0.57	0.04	3.39
88	19MG21-88	19MG21-4	0.302	0.065	0.822	0.069	0.18	0.06	3.82
	19MG21-88	19MG21-4	0.122	0.008	0.814	0.022	0.07	0.02	3.37
	19MG21-89	19MG21-4	0.083	0.008	0.806	0.043	0.13	0.01	3.53
89	19MG21-89	19MG21-4	0.140	0.006	0.820	0.019	0.29	0.02	3.39
	19MG21-89	19MG21-4	0.193	0.021	0.822	0.031	0.34	0.04	3.40
90	19MG21-90	19MG21-4	0.139	0.012	0.820	0.021	0.19	0.03	3.46
	19MG21-91	19MG21-4	0.082	0.007	0.845	0.037	0.15	0.02	4.19
91	19MG21-91	19MG21-4	0.164	0.012	0.808	0.024	0.32	0.03	4.29
	19MG21-91	19MG21-4	0.085	0.005	0.825	0.019	0.16	0.02	4.15
	19MG21-92	19MG21-4	1.605	0.090	0.826	0.033	0.59	0.33	4.46
92	19MG21-92	19MG21-4	1.938	0.101	0.838	0.033	0.70	0.26	3.02
	19MG21-92	19MG21-4	1.715	0.121	0.837	0.042	0.79	0.22	2.87
	19MG21-92	19MG21-4	1.304	0.046	0.827	0.026	0.49	0.15	2.56
	19MG21-93	19MG21-4	0.847	0.051	0.806	0.027	0.51	0.11	3.02
93	19MG21-93	19MG21-4	1.033	0.038	0.813	0.026	0.47	0.14	2.90
	19MG21-93	19MG21-4	0.846	0.034	0.830	0.024	0.43	0.12	2.93
	19MG21-94	19MG21-4	0.333	0.012	0.821	0.013	0.31	0.13	9.07
94	19MG21-94	19MG21-4	0.602	0.073	0.822	0.024	0.35	0.17	5.61
	19MG21-94	19MG21-4	0.441	0.023	0.801	0.019	0.39	0.14	7.02
95	19MG21-95	19MG21-4	0.591	0.030	0.825	0.024	0.26	0.06	2.38
	19MG21-95	19MG21-4	0.739	0.033	0.835	0.025	0.12	0.12	3.45
	19MG21-96	19MG21-4	0.376	0.059	0.827	0.018	0.10	0.03	1.47
	19MG21-96	19MG21-4	0.278	0.049	0.819	0.045	0.18	0.05	3.53
96	19MG21-96	19MG21-4	0.538	0.064	0.815	0.057	0.51	0.08	3.56
	19MG21-96	19MG21-4	0.293	0.038	0.823	0.027	0.14	0.05	3.68
	19MG21-96	19MG21-4	0.166	0.014	0.826	0.019	0.29	0.03	3.76
	19MG21-97	19MG21-4	0.256	0.016	0.831	0.030	0.46	0.04	3.53
97	19MG21-97	19MG21-4	30.303	11.019	0.782	0.079	0.41	7.10	3.68
	19MG21-97	19MG21-4	0.290	0.027	0.827	0.018	0.04	0.05	3.40

Spot	Source file (.FIN2)	Sample	^{238}U/^{206}Pb	±2σ (abs)	^{207}Pb/^{206}Pb	±2σ (abs)	Rho	U (ppm)	Pb (ppm)
98	19MG21-98	19MG21-4	1.669	0.050	0.826	0.018	0.53	0.27	3.79
	19MG21-98	19MG21-4	0.993	0.039	0.814	0.025	0.29	0.21	4.59
	19MG21-99	19MG21-4	0.832	0.032	0.815	0.015	0.49	0.18	4.94
99	19MG21-99	19MG21-4	1.105	0.067	0.832	0.038	0.79	0.21	4.21
	19MG21-99	19MG21-4	1.730	0.099	0.817	0.036	0.51	0.34	4.67
	19MG21-100	19MG21-4	1.088	0.058	0.815	0.039	0.36	0.24	5.02
100	19MG21-100	19MG21-4	1.221	0.072	0.816	0.024	0.25	0.28	5.05
	19MG21-100	19MG21-4	0.973	0.043	0.813	0.019	0.18	0.25	5.50
	19MG21-101	19MG21-5	0.090	0.011	0.844	0.033	0.23	0.02	3.91
101	19MG21-101	19MG21-5	0.110	0.009	0.824	0.019	0.15	0.02	3.26
	19MG21-101	19MG21-5	0.186	0.010	0.855	0.033	0.22	0.03	3.31
	19MG21-102	19MG21-5	0.156	0.011	0.808	0.037	0.15	0.03	3.89
102	19MG21-102	19MG21-5	0.086	0.010	0.815	0.028	0.50	0.02	3.90
	19MG21-102	19MG21-5	0.125	0.022	0.831	0.035	0.20	0.02	3.17
103	19MG21-103	19MG21-5	0.125	0.012	0.810	0.016	0.11	0.02	3.78
105	19MG21-105	19MG21-5	0.370	0.025	0.820	0.026	0.28	0.06	4.25
	19MG21-105	19MG21-5	0.143	0.009	0.826	0.018	0.32	0.02	3.47
106	19MG21-106	19MG21-5	0.091	0.006	0.822	0.019	0.10	0.02	4.07
	19MG21-106	19MG21-5	0.175	0.012	0.813	0.015	0.23	0.03	4.20
	19MG21-107	19MG21-5	0.143	0.014	0.832	0.039	0.50	0.02	3.63
107	19MG21-107	19MG21-5	0.190	0.009	0.822	0.025	0.40	0.03	3.34
	19MG21-107	19MG21-5	0.173	0.010	0.817	0.025	0.25	0.03	3.46
108	19MG21-108	19MG21-5			no value	NAN	NaN	0.00	3.24
109	19MG21-109	19MG21-5	0.117	0.013	0.826	0.033	0.30	0.02	4.20
110	19MG21-110	19MG21-5	0.298	0.021	0.832	0.021	0.36	0.05	3.79
	19MG21-110	19MG21-5	0.166	0.010	0.828	0.019	0.24	0.02	3.36
111	19MG21-111	19MG21-5	0.168	0.015	0.828	0.022	0.36	0.02	3.45
	19MG21-112	19MG21-5	0.106	0.010	0.839	0.039	0.44	0.02	4.35
112	19MG21-112	19MG21-5	0.068	0.005	0.799	0.033	0.11	0.01	3.68
	19MG21-112	19MG21-5	0.077	0.009	0.809	0.028	0.00	0.01	3.42
113	19MG21-113	19MG21-5	0.075	0.007	0.794	0.031	0.00	0.01	3.32
	19MG21-113	19MG21-5	0.220	0.016	0.829	0.020	0.24	0.03	3.49
114	19MG21-114	19MG21-5	0.230	0.012	0.808	0.015	0.34	0.03	3.67
	19MG21-114	19MG21-5	0.459	0.051	0.822	0.023	-0.07	0.06	3.19
115	19MG21-115	19MG21-5	0.230	0.014	0.815	0.016	0.26	0.04	3.82
	19MG21-115	19MG21-5	0.119	0.008	0.819	0.019	0.24	0.02	3.24
116	19MG21-116	19MG21-5	0.262	0.023	0.832	0.021	0.58	0.05	4.79
	19MG21-116	19MG21-5	0.134	0.008	0.825	0.017	0.25	0.02	3.84
	19MG21-117	19MG21-5	0.207	0.016	0.810	0.032	0.04	0.04	4.29
117	19MG21-117	19MG21-5	0.107	0.009	0.827	0.017	0.21	0.02	3.90
	19MG21-117	19MG21-5	0.227	0.022	0.817	0.020	0.27	0.04	3.73
	19MG21-118	19MG21-5	0.232	0.047	0.807	0.035	0.39	0.04	3.96
118	19MG21-118	19MG21-5	0.402	0.027	0.821	0.029	0.47	0.06	4.01
	19MG21-118	19MG21-5	0.211	0.012	0.816	0.018	0.02	0.03	3.65

Spot	Source file (.FIN2)	Sample	^{238}U/^{206}Pb	±2σ (abs)	^{207}Pb/^{206}Pb	±2σ (abs)	Rho	U (ppm)	Pb (ppm)
	19MG21-119	19MG21-5	0.336	0.019	0.824	0.026	-0.43	0.27	20.80
119	19MG21-119	19MG21-5	0.457	0.044	0.799	0.023	0.28	0.20	10.70
	19MG21-119	19MG21-5	0.205	0.024	0.814	0.018	0.02	0.04	3.86
	19MG21-119	19MG21-5	0.444	0.034	0.819	0.019	0.01	0.06	3.42
	19MG21-120	19MG21-5	0.313	0.021	0.821	0.025	0.25	0.05	4.28
120	19MG21-120	19MG21-5	0.543	0.103	0.825	0.041	0.24	0.09	3.99
	19MG21-120	19MG21-5	0.279	0.031	0.807	0.022	0.04	0.07	6.11
	19MG21-120	19MG21-5	0.592	0.070	0.814	0.031	0.40	0.11	4.45
121	19MG21-121	19MG21-5	0.123	0.012	0.822	0.030	0.47	0.02	3.98
	19MG21-121	19MG21-5	0.172	0.006	0.829	0.016	0.35	0.02	3.49
122	19MG21-122	19MG21-5	0.216	0.012	0.828	0.012	0.23	0.04	4.02
123	19MG21-123	19MG21-5	0.115	0.013	0.821	0.020	0.18	0.02	3.98
	19MG21-123	19MG21-5	0.179	0.013	0.821	0.019	0.09	0.03	4.16
	19MG21-123	19MG21-5	0.389	0.027	0.819	0.031	0.31	0.05	3.33
124	19MG21-124	19MG21-5	0.090	0.008	0.818	0.024	0.34	0.01	3.92
	19MG21-124	19MG21-5	0.174	0.012	0.826	0.034	0.35	0.03	3.57
	19MG21-124	19MG21-5	0.142	0.016	0.806	0.019	0.11	0.02	3.54
125	19MG21-125	19MG21-5	0.068	0.008	0.837	0.035	-0.02	0.02	7.02
	19MG21-125	19MG21-5	0.190	0.013	0.827	0.015	0.12	0.03	3.45
126	19MG21-126	19MG21-6	0.178	0.021	0.802	0.025	-0.20	0.03	2.95
	19MG21-126	19MG21-6	0.238	0.013	0.805	0.021	0.26	0.03	2.59
127	19MG21-127	19MG21-6	0.341	0.013	0.833	0.016	0.22	0.04	2.94
128	19MG21-128	19MG21-6	0.106	0.009	0.813	0.021	0.36	0.02	3.24
	19MG21-128	19MG21-6	0.129	0.009	0.834	0.022	0.10	0.02	3.20
129	19MG21-129	19MG21-6	0.099	0.011	0.830	0.042	0.37	0.01	2.74
	19MG21-129	19MG21-6	0.162	0.011	0.826	0.020	0.18	0.02	2.49
130	19MG21-130	19MG21-6	0.144	0.010	0.814	0.019	0.25	0.02	2.85
	19MG21-130	19MG21-6	0.172	0.048	1.500	0.850	0.25	0.04	1.99
131	19MG21-131	19MG21-6	0.108	0.011	0.799	0.027	0.30	0.01	2.91
132	19MG21-132	19MG21-6	1.068	0.065	0.803	0.044	0.54	0.15	3.38
	19MG21-132	19MG21-6	0.462	0.020	0.828	0.021	0.19	0.06	2.90
	19MG21-132	19MG21-6	0.314	0.037	0.838	0.029	0.04	0.04	2.69
133	19MG21-133	19MG21-6	0.268	0.036	0.825	0.034	0.02	0.06	3.78
	19MG21-133	19MG21-6	0.840	0.106	0.776	0.036	0.26	0.15	2.82
	19MG21-133	19MG21-6	15.152	8.035	0.620	0.130	0.49	5.30	2.80
	19MG21-133	19MG21-6	0.521	0.163	0.920	0.180	0.06	0.04	1.75
135	19MG21-135	19MG21-6	0.297	0.013	0.819	0.017	0.07	0.04	2.85
136	19MG21-136	19MG21-6	0.239	0.018	0.792	0.035	0.29	0.03	3.20
	19MG21-136	19MG21-6	0.474	0.025	0.817	0.018	0.29	0.07	2.89
137	19MG21-137	19MG21-6	0.248	0.017	0.853	0.042	0.18	0.04	3.24
	19MG21-137	19MG21-6	0.132	0.007	0.809	0.017	0.13	0.02	2.83
138	19MG21-138	19MG21-6	0.263	0.028	0.846	0.048	0.46	0.03	2.56
	19MG21-138	19MG21-6	0.372	0.013	0.827	0.018	0.30	0.05	2.74

Spot	Source file (.FIN2)	Sample	^{238}U/^{206}Pb	±2σ (abs)	^{207}Pb/^{206}Pb	±2σ (abs)	Rho	U (ppm)	Pb (ppm)
139	19MG21-139	19MG21-6	0.274	0.020	0.838	0.027	0.43	0.04	2.97
	19MG21-139	19MG21-6	0.255	0.013	0.831	0.019	0.23	0.04	2.92
140	19MG21-140	19MG21-6	0.158	0.010	0.822	0.019	0.20	0.02	2.32
141	19MG21-141	19MG21-6	0.179	0.012	0.803	0.017	-0.04	0.02	2.68
	19MG21-142	19MG21-6	0.176	0.026	0.850	0.077	0.48	0.02	2.52
142	19MG21-142	19MG21-6	0.163	0.022	0.841	0.048	0.20	0.02	2.43
	19MG21-142	19MG21-6	0.280	0.023	0.819	0.031	0.20	0.03	2.40
143	19MG21-143	19MG21-6	0.230	0.016	0.804	0.022	0.17	0.03	2.59
	19MG21-143	19MG21-6	0.229	0.016	0.825	0.020	0.28	0.03	2.46
	19MG21-144	19MG21-6	0.375	0.025	0.830	0.024	0.36	0.07	3.48
144	19MG21-144	19MG21-6	0.274	0.017	0.816	0.027	0.44	0.05	3.07
	19MG21-144	19MG21-6	0.166	0.017	0.816	0.031	0.37	0.03	2.59
145	19MG21-145	19MG21-6	0.221	0.013	0.814	0.035	0.55	0.03	2.77
	19MG21-145	19MG21-6	0.196	0.010	0.826	0.017	0.31	0.03	2.78
146	19MG21-146	19MG21-6	0.218	0.019	0.812	0.015	-0.01	0.04	2.96
147	19MG21-147	19MG21-6	0.228	0.028	0.825	0.039	0.18	0.04	3.19
	19MG21-147	19MG21-6	0.148	0.009	0.834	0.020	0.11	0.02	2.88
148	19MG21-148	19MG21-6	0.265	0.015	0.813	0.018	0.21	0.04	3.12
	19MG21-148	19MG21-6	0.251	0.038	0.824	0.026	-0.08	0.06	2.73
	19MG21-149	19MG21-6	0.730	0.069	0.830	0.044	0.22	0.12	3.43
149	19MG21-149	19MG21-6	0.515	0.032	0.799	0.025	0.04	0.08	2.96
	19MG21-149	19MG21-6	0.513	0.026	0.825	0.020	0.17	0.08	2.85
	19MG21-150	19MG21-6	1.361	0.087	0.813	0.022	0.02	0.22	3.42
150	19MG21-150	19MG21-6	0.862	0.104	0.817	0.039	-0.36	0.14	3.14
	19MG21-150	19MG21-6	0.249	0.022	0.815	0.022	0.13	0.04	2.86

19MG74-A from DA strain domain

Spot	Source file (.FIN2)	Sample	^{238}U/^{206}Pb	±2σ (abs)	^{207}Pb/^{206}Pb	±2σ (abs)	Rho	U (ppm)	Pb (ppm)
23	19MG74-1-23	19MG74-A-6B	0.413	0.019	0.802	0.030	0.41	0.08	4.50
	19MG74-1-23	19MG74-A-6B	0.236	0.010	0.826	0.021	0.27	0.05	4.49
24	19MG74-1-24	19MG74-A-6B	0.187	0.009	0.804	0.024	0.43	0.03	3.81
	19MG74-1-24	19MG74-A-6B	0.166	0.008	0.813	0.017	0.51	0.03	3.50
25	19MG74-1-25	19MG74-A-6B	0.539	0.018	0.808	0.022	0.53	0.09	3.86
	19MG74-1-25	19MG74-A-6B	0.483	0.030	0.789	0.021	0.21	0.08	3.54
26	19MG74-1-26	19MG74-A-5B	0.451	0.020	0.828	0.026	0.45	0.09	4.47
	19MG74-1-26	19MG74-A-5B	0.505	0.015	0.816	0.017	0.30	0.10	4.67
27	19MG74-1-27	19MG74-A-5B	0.235	0.016	0.778	0.025	0.26	0.04	3.74
	19MG74-1-27	19MG74-A-5B	0.304	0.014	0.822	0.028	0.27	0.05	3.94
	19MG74-1-27	19MG74-A-5B	0.326	0.032	0.818	0.030	0.26	0.06	3.60
28	19MG74-1-28	19MG74-A-5B	0.282	0.009	0.819	0.013	0.42	0.06	4.62
	19MG74-1-29	19MG74-A-5B	0.200	0.010	0.835	0.031	0.41	0.03	3.42
29	19MG74-1-29	19MG74-A-5B	0.255	0.012	0.829	0.021	0.34	0.04	3.24
	19MG74-1-29	19MG74-A-5B	0.112	0.015	0.793	0.066	0.34	0.01	2.87

Spot	Source file (.FIN2)	Sample	^{238}U/^{206}Pb	±2σ (abs)	^{207}Pb/^{206}Pb	±2σ (abs)	Rho	U (ppm)	Pb (ppm)
30	19MG74-1-30	19MG74-A-5B	0.641	0.023	0.817	0.021	0.52	0.12	4.33
	19MG74-1-30	19MG74-A-5B	0.493	0.029	0.816	0.020	0.32	0.09	3.92
31	19MG74-1-31	19MG74-A-5B	0.514	0.022	0.848	0.033	0.48	0.08	3.92
	19MG74-1-31	19MG74-A-5B	0.266	0.012	0.816	0.021	0.27	0.04	3.66
32	19MG74-1-32	19MG74-A-5B	0.135	0.008	0.853	0.023	0.15	0.02	3.57
	19MG74-1-32	19MG74-A-5B	0.172	0.013	0.820	0.023	0.25	0.03	3.54
33	19MG74-1-33	19MG74-A-5B	0.523	0.015	0.812	0.014	0.26	0.09	3.76
34	19MG74-1-34	19MG74-A-5B	0.539	0.015	0.818	0.014	0.50	0.10	4.19
35	19MG74-1-35	19MG74-A-5B	0.191	0.010	0.823	0.024	0.49	0.03	3.36
	19MG74-1-35	19MG74-A-5B	0.141	0.008	0.834	0.024	0.24	0.02	2.95
36	19MG74-1-36	19MG74-A-5B	0.216	0.012	0.817	0.025	0.24	0.03	3.50
	19MG74-1-36	19MG74-A-5B	0.357	0.011	0.809	0.022	0.39	0.05	3.20
37	19MG74-1-37	19MG74-A-5B	0.285	0.023	0.830	0.024	0.41	0.05	3.97
	19MG74-1-37	19MG74-A-5B	0.282	0.017	0.822	0.019	0.31	0.05	3.64
38	19MG74-1-38	19MG74-A-5B	0.425	0.015	0.830	0.024	0.33	0.09	4.75
	19MG74-1-38	19MG74-A-5B	0.281	0.010	0.830	0.020	0.39	0.05	4.21
39	19MG74-1-39	19MG74-A-5B	0.422	0.027	0.808	0.038	0.43	0.08	4.45
	19MG74-1-39	19MG74-A-5B	0.562	0.023	0.824	0.026	0.43	0.09	3.56
	19MG74-1-39	19MG74-A-5B	0.382	0.017	0.809	0.027	0.34	0.06	3.35
40	19MG74-1-40	19MG74-A-5B	0.534	0.014	0.824	0.014	0.40	0.09	4.02
41	19MG74-1-41	19MG74-A-5B	0.436	0.011	0.811	0.015	0.47	0.07	3.58
42	19MG74-1-42	19MG74-A-5B	0.379	0.016	0.801	0.030	0.59	0.06	3.73
	19MG74-1-42	19MG74-A-5B	0.362	0.017	0.824	0.021	0.08	0.06	3.69
43	19MG74-1-43	19MG74-A-5B	0.264	0.010	0.830	0.019	0.39	0.04	3.12
44	19MG74-1-44	19MG74-A-5B	0.498	0.020	0.823	0.026	0.46	0.07	3.45
	19MG74-1-44	19MG74-A-5B	0.752	0.090	0.829	0.029	0.02	0.12	3.47
45	19MG74-1-45	19MG74-A-5B	0.296	0.018	0.816	0.027	0.38	0.05	3.65
	19MG74-1-45	19MG74-A-5B	0.246	0.011	0.815	0.018	0.16	0.04	3.37
46	19MG74-1-46	19MG74-A-5B	0.294	0.022	0.818	0.033	0.41	0.04	3.24
	19MG74-1-46	19MG74-A-5B	0.476	0.019	0.800	0.017	0.40	0.07	3.59
47	19MG74-1-47	19MG74-A-5B	0.461	0.034	0.822	0.033	0.26	0.08	3.81
	19MG74-1-47	19MG74-A-5B	0.433	0.019	0.803	0.019	0.36	0.07	3.87
48	19MG74-1-48	19MG74-A-5B	0.375	0.017	0.824	0.025	0.55	0.06	3.81
	19MG74-1-48	19MG74-A-5B	0.355	0.015	0.821	0.019	0.49	0.06	3.64
49	19MG74-1-49	19MG74-A-5B	0.213	0.007	0.801	0.017	0.20	0.03	3.10
51	19MG74-1-51	19MG74-A-3	0.352	0.015	0.821	0.022	0.26	0.06	4.66
	19MG74-1-51	19MG74-A-3	0.444	0.026	0.823	0.016	0.09	0.08	4.05
52	19MG74-1-52	19MG74-A-3	1.264	0.075	0.828	0.039	0.55	0.04	0.86
	19MG74-1-52	19MG74-A-3	0.752	0.102	0.821	0.063	0.00	0.05	1.75
	19MG74-1-52	19MG74-A-3	1.181	0.100	0.827	0.086	0.77	0.05	1.00
	19MG74-1-52	19MG74-A-3	0.606	0.118	0.839	0.043	0.18	0.04	1.76

Spot	Source file (.FIN2)	Sample	^{238}U/^{206}Pb	±2σ (abs)	^{207}Pb/^{206}Pb	±2σ (abs)	Rho	U (ppm)	Pb (ppm)
	19MG74-1-53	19MG74-A-3	0.333	0.024	0.819	0.036	0.58	0.07	5.02
53	19MG74-1-53	19MG74-A-3	0.436	0.016	0.825	0.024	0.32	0.08	4.34
	19MG74-1-53	19MG74-A-3	0.418	0.023	0.820	0.032	0.34	0.07	4.17
	19MG74-1-53	19MG74-A-3	0.561	0.026	0.814	0.027	0.41	0.08	3.74
	19MG74-1-54	19MG74-A-3	0.614	0.026	0.828	0.019	0.49	0.10	4.10
54	19MG74-1-54	19MG74-A-3	0.760	0.032	0.803	0.030	0.42	0.10	3.39
	19MG74-1-54	19MG74-A-3	1.110	0.105	0.859	0.048	0.46	0.12	2.48
55	19MG74-1-55	19MG74-A-3	1.374	0.055	0.846	0.038	0.62	0.06	1.03
	19MG74-1-55	19MG74-A-3	1.340	0.088	0.829	0.042	-0.04	0.04	0.82
	19MG74-1-56	19MG74-A-3	1.808	0.108	0.781	0.050	0.60	0.06	0.84
56	19MG74-1-56	19MG74-A-3	2.247	0.167	0.809	0.058	0.68	0.09	0.91
	19MG74-1-56	19MG74-A-3	1.733	0.096	0.770	0.053	0.61	0.04	0.58
57	19MG74-1-57	19MG74-A-3	1.131	0.077	0.873	0.052	0.62	0.03	0.59
	19MG74-1-57	19MG74-A-3	1.147	0.075	0.812	0.038	0.63	0.03	0.59
58	19MG74-1-58	19MG74-A-3	0.978	0.037	0.826	0.026	0.25	0.07	1.70
	19MG74-1-58	19MG74-A-3	1.111	0.040	0.815	0.025	0.52	0.08	1.74
	19MG74-1-59	19MG74-A-3	0.531	0.025	0.840	0.022	0.48	0.07	3.35
59	19MG74-1-59	19MG74-A-3	0.435	0.021	0.805	0.025	0.32	0.06	3.20
	19MG74-1-59	19MG74-A-3	0.541	0.032	0.810	0.022	0.11	0.06	2.71
	19MG74-1-60	19MG74-A-3	2.370	0.163	0.919	0.058	0.55	0.04	0.44
60	19MG74-1-60	19MG74-A-3	3.906	0.687	0.768	0.051	0.03	0.22	1.09
	19MG74-1-60	19MG74-A-3	2.849	0.244	0.752	0.073	0.77	0.06	0.50
	19MG74-1-61	19MG74-A-3	2.513	0.170	0.801	0.059	0.73	0.11	1.05
61	19MG74-1-61	19MG74-A-3	2.137	0.187	0.821	0.068	0.49	0.09	0.87
	19MG74-1-61	19MG74-A-3	2.907	0.237	0.855	0.078	0.82	0.11	0.88
	19MG74-1-61	19MG74-A-3	1.164	0.061	0.826	0.038	0.74	0.08	1.62
	19MG74-1-62	19MG74-A-3	2.257	0.168	0.908	0.079	0.75	0.06	0.66
62	19MG74-1-62	19MG74-A-3	2.188	0.292	0.817	0.079	0.45	0.06	0.62
	19MG74-1-62	19MG74-A-3	2.762	0.168	0.912	0.090	0.47	0.08	0.69
	19MG74-1-62	19MG74-A-3	1.855	0.127	0.866	0.056	0.67	0.05	0.57
63	19MG74-1-63	19MG74-A-3	2.725	0.156	0.838	0.056	0.50	0.06	0.56
	19MG74-1-63	19MG74-A-3	2.283	0.146	0.841	0.046	0.53	0.06	0.59
	19MG74-1-64	19MG74-A-3	2.770	0.215	0.839	0.059	0.60	0.09	0.82
64	19MG74-1-64	19MG74-A-3	2.558	0.118	0.801	0.043	0.61	0.09	0.82
	19MG74-1-64	19MG74-A-3	3.012	0.318	0.806	0.063	-0.01	0.09	0.66
	19MG74-1-65	19MG74-A-3	4.032	0.472	0.800	0.065	0.69	0.21	1.27
	19MG74-1-65	19MG74-A-3	3.067	0.169	0.802	0.038	0.51	0.22	1.56
65	19MG74-1-65	19MG74-A-3	3.802	0.246	0.823	0.047	0.71	0.18	1.11
	19MG74-1-65	19MG74-A-3	3.205	0.216	0.776	0.063	0.55	0.10	0.66
	19MG74-1-65	19MG74-A-3	3.247	0.337	0.890	0.120	0.51	0.07	0.53
	19MG74-1-66	19MG74-A-3	1.282	0.062	0.805	0.036	0.56	0.06	1.07
66	19MG74-1-66	19MG74-A-3	1.300	0.081	0.795	0.045	0.33	0.06	1.00
	19MG74-1-66	19MG74-A-3	1.634	0.077	0.825	0.046	0.51	0.06	0.78

Spot	Source file (.FIN2)	Sample	$^{238}U/^{206}Pb$	±2σ (abs)	$^{207}Pb/^{206}Pb$	±2σ (abs)	Rho	U (ppm)	Pb (ppm)
	19MG74-1-67	19MG74-A-3	0.452	0.023	0.806	0.032	0.42	0.06	3.14
67	19MG74-1-67	19MG74-A-3	0.543	0.038	0.812	0.035	0.42	0.07	2.86
	19MG74-1-67	19MG74-A-3	0.580	0.019	0.821	0.020	0.28	0.07	2.86
68	19MG74-1-68	19MG74-A-3	1.773	0.113	0.868	0.063	0.73	0.04	0.51
	19MG74-1-68	19MG74-A-3	1.751	0.098	0.840	0.046	0.78	0.05	0.63
69	19MG74-1-69	19MG74-A-3	0.439	0.018	0.817	0.021	0.17	0.06	3.11
	19MG74-1-69	19MG74-A-3	0.341	0.015	0.829	0.020	0.33	0.05	2.91
70	19MG74-1-70	19MG74-A-3	0.481	0.023	0.812	0.024	0.37	0.07	3.26
	19MG74-1-70	19MG74-A-3	0.626	0.034	0.809	0.016	0.42	0.10	3.26
71	19MG74-1-71	19MG74-A-3	3.367	0.238	0.775	0.046	0.72	0.27	1.76
	19MG74-1-71	19MG74-A-3	3.968	0.189	0.832	0.045	0.48	0.11	0.61
	19MG74-1-71	19MG74-A-3	4.425	0.568	0.882	0.095	0.59	0.09	0.42
	19MG74-1-72	19MG74-A-3	1.789	0.150	0.840	0.100	0.42	0.04	0.51
72	19MG74-1-72	19MG74-A-3	2.849	0.235	0.807	0.090	0.49	0.06	0.41
	19MG74-1-72	19MG74-A-3	4.630	0.579	0.867	0.077	0.63	0.09	0.39
	19MG74-1-72	19MG74-A-3	3.058	0.281	0.931	0.089	0.72	0.04	0.33
	19MG74-1-73	19MG74-A-3	1.692	0.115	0.826	0.049	0.62	0.08	1.02
	19MG74-1-73	19MG74-A-3	9.901	2.549	0.754	0.054	-0.06	0.57	1.62
73	19MG74-1-73	19MG74-A-3	2.294	0.263	0.797	0.051	-0.17	0.11	1.02
	19MG74-1-73	19MG74-A-3	1.010	0.122	0.798	0.034	0.35	0.08	1.79
	19MG74-1-73	19MG74-A-3	1.961	0.384	0.845	0.051	0.02	0.12	1.22
74	19MG74-1-74	19MG74-A-3	0.901	0.058	0.803	0.023	0.20	0.15	3.69
	19MG74-1-74	19MG74-A-3	0.959	0.040	0.813	0.018	0.54	0.17	3.51
	19MG74-1-75	19MG74-A-3	0.833	0.090	0.832	0.053	-0.12	0.13	3.52
75	19MG74-1-75	19MG74-A-3	0.604	0.031	0.836	0.029	0.26	0.08	2.99
	19MG74-1-75	19MG74-A-3	0.534	0.019	0.818	0.017	0.48	0.08	3.05
76	19MG74-1-76	19MG74-A-4	1.832	0.054	0.828	0.024	0.51	0.27	3.18
	19MG74-1-76	19MG74-A-4	1.795	0.048	0.829	0.019	0.35	0.30	3.51
	19MG74-1-77	19MG74-A-4	1.832	0.074	0.844	0.025	0.56	0.34	4.21
77	19MG74-1-77	19MG74-A-4	2.924	0.145	0.844	0.030	0.57	0.57	4.12
	19MG74-1-77	19MG74-A-4	2.725	0.119	0.806	0.017	0.29	0.58	4.35
	19MG74-1-78	19MG74-A-4	0.490	0.043	0.837	0.035	0.28	0.09	3.51
78	19MG74-1-78	19MG74-A-4	2.494	0.168	0.809	0.031	0.56	0.45	3.79
	19MG74-1-78	19MG74-A-4	2.710	0.132	0.814	0.020	0.40	0.43	3.27
	19MG74-1-79	19MG74-A-4	2.618	0.206	0.838	0.024	0.18	0.48	3.79
79	19MG74-1-79	19MG74-A-4	1.996	0.084	0.828	0.021	0.28	0.39	4.15
	19MG74-1-79	19MG74-A-4	1.570	0.086	0.809	0.027	0.66	0.30	3.74
	19MG74-1-80	19MG74-A-4	3.106	0.145	0.819	0.028	0.47	0.46	3.10
80	19MG74-1-80	19MG74-A-4	3.401	0.150	0.827	0.029	0.40	0.56	3.52
	19MG74-1-80	19MG74-A-4	2.370	0.140	0.805	0.020	0.30	0.40	3.39
81	19MG74-1-81	19MG74-A-4	2.849	0.146	0.825	0.025	0.39	0.42	3.09
	19MG74-1-81	19MG74-A-4	2.538	0.135	0.815	0.024	0.35	0.40	3.23

Spot	Source file (.FIN2)	Sample	$^{238}U/^{206}Pb$	±2σ (abs)	$^{207}Pb/^{206}Pb$	±2σ (abs)	Rho	U (ppm)	Pb (ppm)
	19MG74-1-82	19MG74-A-4	2.558	0.150	0.809	0.054	0.70	0.32	2.61
	19MG74-1-82	19MG74-A-4	3.279	0.215	0.820	0.057	0.61	0.46	2.99
82	19MG74-1-82	19MG74-A-4	4.444	0.277	0.861	0.038	0.61	0.61	2.90
	19MG74-1-82	19MG74-A-4	3.096	0.211	0.788	0.019	0.42	0.52	3.35
	19MG74-1-82	19MG74-A-4	4.000	0.208	0.861	0.029	0.09	0.59	3.08
	19MG74-1-83	19MG74-A-4	2.740	0.165	0.813	0.043	0.14	0.44	3.34
83	19MG74-1-83	19MG74-A-4	2.000	0.084	0.829	0.025	0.52	0.29	3.16
	19MG74-1-83	19MG74-A-4	2.358	0.089	0.808	0.018	0.19	0.37	3.13
	19MG74-1-84	19MG74-A-4	1.764	0.065	0.808	0.025	0.44	0.30	3.58
84	19MG74-1-84	19MG74-A-4	2.571	0.119	0.804	0.021	0.08	0.43	3.42
	19MG74-1-84	19MG74-A-4	2.188	0.134	0.800	0.031	0.42	0.34	3.18
	19MG74-1-85	19MG74-A-4	2.801	0.149	0.814	0.028	0.50	0.43	3.19
85	19MG74-1-85	19MG74-A-4	1.938	0.068	0.828	0.021	0.24	0.31	3.46
	19MG74-1-85	19MG74-A-4	1.942	0.072	0.821	0.023	0.36	0.30	3.12
	19MG74-1-86	19MG74-A-4	2.488	0.111	0.782	0.039	0.73	0.45	3.71
86	19MG74-1-86	19MG74-A-4	2.994	0.179	0.803	0.032	0.24	0.54	3.52
	19MG74-1-86	19MG74-A-4	1.961	0.104	0.834	0.023	-0.14	0.38	3.85
	19MG74-1-86	19MG74-A-4	1.395	0.076	0.806	0.027	0.44	0.25	3.46
	19MG74-1-87	19MG74-A-4	2.558	0.177	0.794	0.025	0.15	0.48	3.72
	19MG74-1-87	19MG74-A-4	2.907	0.177	0.823	0.028	0.05	0.55	3.78
87	19MG74-1-87	19MG74-A-4	2.262	0.082	0.827	0.030	0.62	0.43	3.90
	19MG74-1-87	19MG74-A-4	3.289	0.151	0.871	0.035	0.43	0.56	3.52
	19MG74-1-87	19MG74-A-4	2.070	0.090	0.807	0.027	0.64	0.37	3.42
88	19MG74-1-88	19MG74-A-4	2.427	0.082	0.827	0.022	0.41	0.42	3.62
	19MG74-1-88	19MG74-A-4	2.387	0.074	0.785	0.018	0.53	0.43	3.54
89	19MG74-1-89	19MG74-A-4	2.070	0.073	0.842	0.021	0.38	0.37	3.61
	19MG74-1-89	19MG74-A-4	1.383	0.048	0.820	0.017	0.53	0.26	3.63
90	19MG74-1-90	19MG74-A-4	2.646	0.091	0.808	0.023	0.49	0.42	3.22
	19MG74-1-90	19MG74-A-4	3.801	0.134	0.822	0.018	0.46	0.66	3.45
91	19MG74-1-91	19MG74-A-4	2.674	0.200	0.836	0.024	-0.06	0.47	3.40
	19MG74-1-91	19MG74-A-4	2.545	0.084	0.817	0.020	0.51	0.44	3.30
	19MG74-1-92	19MG74-A-4	1.779	0.114	0.810	0.041	0.71	0.30	3.13
92	19MG74-1-92	19MG74-A-4	2.041	0.183	0.885	0.083	0.82	0.32	3.35
	19MG74-1-92	19MG74-A-4	3.003	0.126	0.825	0.024	0.37	0.53	3.39
	19MG74-1-92	19MG74-A-4	3.925	0.137	0.817	0.017	0.39	0.66	3.15
	19MG74-1-93	19MG74-A-4	1.961	0.108	0.811	0.034	0.29	0.40	3.98
93	19MG74-1-93	19MG74-A-4	2.342	0.132	0.819	0.027	0.25	0.47	3.74
	19MG74-1-93	19MG74-A-4	4.016	0.306	0.842	0.033	0.24	0.73	3.32
	19MG74-1-94	19MG74-A-4	2.907	0.118	0.848	0.039	0.52	0.55	3.65
94	19MG74-1-94	19MG74-A-4	2.268	0.113	0.816	0.027	0.27	0.47	3.94
	19MG74-1-94	19MG74-A-4	2.584	0.100	0.808	0.020	0.44	0.54	3.96
	19MG74-1-95	19MG74-A-4	2.660	0.120	0.819	0.029	0.24	0.46	3.26
95	19MG74-1-95	19MG74-A-4	2.028	0.115	0.830	0.032	0.23	0.40	3.51
	19MG74-1-95	19MG74-A-4	1.346	0.053	0.811	0.018	0.44	0.26	3.45

Spot	Source file (.FIN2)	Sample	^{238}U/^{206}Pb	±2σ (abs)	^{207}Pb/^{206}Pb	±2σ (abs)	Rho	U (ppm)	Pb (ppm)
96	19MG74-1-96	19MG74-A-4	2.000	0.088	0.842	0.028	0.41	0.38	3.57
	19MG74-1-96	19MG74-A-4	1.502	0.041	0.819	0.020	0.58	0.31	3.68
97	19MG74-1-97	19MG74-A-4	1.473	0.069	0.837	0.032	0.51	0.28	3.44
	19MG74-1-97	19MG74-A-4	2.732	0.224	0.836	0.024	0.14	0.56	3.71
	19MG74-1-97	19MG74-A-4	1.656	0.082	0.818	0.019	0.20	0.36	3.58
98	19MG74-1-98	19MG74-A-4	2.012	0.101	0.796	0.022	0.39	0.42	3.65
	19MG74-1-98	19MG74-A-4	2.439	0.095	0.823	0.021	0.42	0.48	3.36
99	19MG74-1-99	19MG74-A-4	1.368	0.060	0.815	0.016	0.36	0.29	3.68
	19MG74-1-99	19MG74-A-4	1.838	0.135	0.824	0.030	0.55	0.40	3.79
100	19MG74-1-100	19MG74-A-4	1.704	0.073	0.807	0.025	0.34	0.36	3.62
	19MG74-1-100	19MG74-A-4	2.786	0.050	0.834	0.018	0.41	0.52	3.37
101	19MG74-1-101	19MG74-A-5	1.667	0.069	0.853	0.030	0.54	0.34	3.50
	19MG74-1-101	19MG74-A-5	2.169	0.089	0.825	0.022	0.43	0.43	3.32
102	19MG74-1-102	19MG74-A-5	2.865	0.189	0.822	0.030	0.49	0.53	3.25
	19MG74-1-102	19MG74-A-5	2.899	0.118	0.801	0.025	0.17	0.57	3.38
	19MG74-1-102	19MG74-A-5	2.632	0.173	0.830	0.024	0.21	0.61	3.66
103	19MG74-1-103	19MG74-A-5	1.034	0.094	0.844	0.036	0.45	0.21	3.46
	19MG74-1-103	19MG74-A-5	1.976	0.211	0.809	0.028	0.56	0.42	3.40
	19MG74-1-103	19MG74-A-5	0.592	0.056	0.792	0.020	0.22	0.17	4.52
104	19MG74-1-104	19MG74-A-5	2.941	0.130	0.838	0.025	0.42	0.55	3.29
	19MG74-1-104	19MG74-A-5	2.519	0.070	0.812	0.021	0.57	0.46	3.05
105	19MG74-1-105	19MG74-A-5	2.488	0.192	0.829	0.026	0.06	0.57	3.55
	19MG74-1-105	19MG74-A-5	3.448	0.131	0.825	0.019	0.40	0.68	3.26
106	19MG74-1-106	19MG74-A-5	1.490	0.073	0.816	0.018	0.33	0.37	4.23
	19MG74-1-106	19MG74-A-5	2.257	0.143	0.810	0.023	0.02	0.56	3.90
107	19MG74-1-107	19MG74-A-5	0.435	0.015	0.837	0.025	0.41	0.11	4.23
	19MG74-1-107	19MG74-A-5	0.303	0.018	0.840	0.024	0.50	0.08	4.49
	19MG74-1-107	19MG74-A-5	0.535	0.046	0.802	0.026	0.25	0.15	4.47
	19MG74-1-107	19MG74-A-5	1.049	0.088	0.804	0.039	0.17	0.25	4.20
108	19MG74-1-108	19MG74-A-5	1.091	0.055	0.802	0.029	0.38	0.25	3.99
	19MG74-1-108	19MG74-A-5	1.931	0.093	0.824	0.016	0.27	0.47	3.93
109	19MG74-1-109	19MG74-A-5	2.421	0.106	0.820	0.021	0.20	0.55	3.84
	19MG74-1-109	19MG74-A-5	2.028	0.058	0.825	0.023	0.61	0.48	3.93
110	19MG74-1-110	19MG74-A-5	2.268	0.072	0.820	0.022	0.49	0.46	3.52
	19MG74-1-110	19MG74-A-5	1.767	0.081	0.831	0.022	0.27	0.35	3.43
111	19MG74-1-111	19MG74-A-5	1.855	0.079	0.811	0.021	0.32	0.39	3.63
	19MG74-1-111	19MG74-A-5	1.333	0.057	0.817	0.019	0.36	0.27	3.47
112	19MG74-1-112	19MG74-A-5	2.625	0.103	0.803	0.024	0.54	0.55	3.67
	19MG74-1-112	19MG74-A-5	1.730	0.069	0.814	0.024	0.53	0.39	3.76
113	19MG74-1-113	19MG74-A-5	1.969	0.066	0.826	0.021	0.56	0.40	3.66
	19MG74-1-113	19MG74-A-5	1.923	0.067	0.827	0.022	0.52	0.39	3.38
114	19MG74-1-114	19MG74-A-5	2.404	0.087	0.825	0.018	0.44	0.48	3.54
	19MG74-1-114	19MG74-A-5	1.934	0.112	0.813	0.028	0.50	0.41	3.49

Spot	Source file (.FIN2)	Sample	$^{238}U/^{206}Pb$	±2σ (abs)	$^{207}Pb/^{206}Pb$	±2σ (abs)	Rho	U (ppm)	Pb (ppm)
	19MG74-1-115	19MG74-A-5	1.085	0.068	0.823	0.027	0.26	0.27	4.28
115	19MG74-1-115	19MG74-A-5	1.389	0.060	0.821	0.025	0.51	0.37	4.69
	19MG74-1-115	19MG74-A-5	1.563	0.054	0.822	0.023	0.59	0.38	4.28
116	19MG74-1-116	19MG74-A-5	1.942	0.083	0.802	0.023	0.61	0.37	3.35
	19MG74-1-116	19MG74-A-5	1.541	0.064	0.815	0.020	0.51	0.30	3.36
117	19MG74-1-117	19MG74-A-5	3.676	0.311	0.833	0.028	0.37	0.68	3.30
	19MG74-1-117	19MG74-A-5	1.984	0.059	0.819	0.017	0.60	0.39	3.43
	19MG74-1-118	19MG74-A-5	1.536	0.092	0.824	0.031	0.42	0.28	3.39
118	19MG74-1-118	19MG74-A-5	2.105	0.075	0.820	0.020	0.38	0.38	3.18
	19MG74-1-118	19MG74-A-5	2.899	0.252	0.831	0.035	0.39	0.53	3.35
	19MG74-1-119	19MG74-A-5	1.779	0.076	0.808	0.026	0.43	0.33	3.40
119	19MG74-1-119	19MG74-A-5	2.198	0.082	0.823	0.023	0.44	0.41	3.41
	19MG74-1-119	19MG74-A-5	2.632	0.166	0.796	0.024	0.28	0.53	3.51
	19MG74-1-120	19MG74-A-5	0.784	0.041	0.820	0.029	0.43	0.13	3.17
120	19MG74-1-120	19MG74-A-5	0.611	0.024	0.808	0.016	0.40	0.12	3.38
	19MG74-1-120	19MG74-A-5	0.962	0.080	0.807	0.045	0.25	0.18	3.16
	19MG74-1-121	19MG74-A-5	1.808	0.128	0.820	0.050	0.72	0.34	3.77
121	19MG74-1-121	19MG74-A-5	1.258	0.046	0.821	0.025	0.36	0.24	3.51
	19MG74-1-121	19MG74-A-5	1.745	0.052	0.820	0.019	0.47	0.33	3.51
122	19MG74-1-122	19MG74-A-5	2.146	0.055	0.821	0.015	0.55	0.36	3.14
	19MG74-1-123	19MG74-A-5	1.733	0.087	0.810	0.020	0.36	0.38	4.09
123	19MG74-1-123	19MG74-A-5	0.725	0.053	0.816	0.024	0.24	0.20	4.97
	19MG74-1-123	19MG74-A-5	0.405	0.023	0.807	0.027	0.40	0.11	5.01
	19MG74-1-124	19MG74-A-5	1.577	0.107	0.782	0.031	0.40	0.30	3.74
124	19MG74-1-124	19MG74-A-5	2.004	0.056	0.820	0.020	0.43	0.39	3.94
	19MG74-1-124	19MG74-A-5	1.462	0.049	0.835	0.025	0.33	0.28	3.70
125	19MG74-1-125	19MG74-A-5	1.215	0.065	0.805	0.031	0.48	0.22	3.78
	19MG74-1-125	19MG74-A-5	1.513	0.041	0.826	0.016	0.53	0.27	3.55
	19MG74-1-126	19MG74-A-6	0.944	0.048	0.833	0.032	0.14	0.17	3.63
126	19MG74-1-126	19MG74-A-6	0.759	0.029	0.812	0.023	0.04	0.14	3.56
	19MG74-1-126	19MG74-A-6	1.224	0.075	0.812	0.033	0.56	0.23	3.57
127	19MG74-1-127	19MG74-A-6	1.083	0.040	0.818	0.021	0.12	0.19	3.68
	19MG74-1-127	19MG74-A-6	0.880	0.031	0.817	0.021	0.60	0.16	3.69
128	19MG74-1-128	19MG74-A-6	0.896	0.039	0.806	0.023	0.27	0.16	3.80
	19MG74-1-128	19MG74-A-6	0.861	0.032	0.815	0.019	0.37	0.16	3.94
129	19MG74-1-129	19MG74-A-6	1.374	0.040	0.829	0.020	0.32	0.24	3.84
	19MG74-1-129	19MG74-A-6	1.200	0.035	0.817	0.017	0.20	0.23	4.07
130	19MG74-1-130	19MG74-A-6	1.339	0.045	0.815	0.019	0.33	0.22	3.64
	19MG74-1-130	19MG74-A-6	1.318	0.062	0.813	0.022	0.23	0.20	3.39
131	19MG74-1-131	19MG74-A-6	1.266	0.045	0.816	0.014	0.30	0.24	4.23
	19MG74-1-131	19MG74-A-6	0.922	0.057	0.826	0.029	-0.07	0.17	4.19
132	19MG74-1-132	19MG74-A-6	2.083	0.065	0.818	0.022	0.62	0.22	2.48
	19MG74-1-132	19MG74-A-6	2.247	0.167	0.822	0.024	0.03	0.27	2.64

Spot	Source file (.FIN2)	Sample	$^{238}U/^{206}Pb$	±2σ (abs)	$^{207}Pb/^{206}Pb$	±2σ (abs)	Rho	U (ppm)	Pb (ppm)
133	19MG74-1-133	19MG74-A-6	1.222	0.045	0.817	0.016	0.34	0.20	3.88
	19MG74-1-133	19MG74-A-6	0.930	0.040	0.808	0.025	0.48	0.13	3.24
134	19MG74-1-134	19MG74-A-6	1.695	0.092	0.825	0.018	0.29	0.25	3.50
	19MG74-1-134	19MG74-A-6	1.321	0.073	0.841	0.023	0.17	0.18	3.34
135	19MG74-1-135	19MG74-A-6	0.837	0.035	0.815	0.031	0.46	0.11	3.16
	19MG74-1-135	19MG74-A-6	1.381	0.063	0.834	0.020	0.30	0.19	3.43
	19MG74-1-135	19MG74-A-6	1.427	0.116	0.831	0.023	0.25	0.22	3.63
136	19MG74-1-136	19MG74-A-6	1.174	0.081	0.806	0.041	0.24	0.13	2.89
	19MG74-1-136	19MG74-A-6	0.732	0.035	0.812	0.022	0.49	0.09	2.92
	19MG74-1-136	19MG74-A-6	0.838	0.034	0.802	0.025	0.45	0.10	2.72
137	19MG74-1-137	19MG74-A-6	1.736	0.130	0.816	0.020	0.11	0.23	3.33
	19MG74-1-137	19MG74-A-6	1.965	0.151	0.785	0.026	0.29	0.27	3.21
	19MG74-1-137	19MG74-A-6	1.103	0.053	0.809	0.032	0.56	0.14	3.16
138	19MG74-1-138	19MG74-A-6	0.891	0.056	0.809	0.028	0.29	0.11	3.02
	19MG74-1-138	19MG74-A-6	1.555	0.053	0.822	0.019	0.32	0.19	3.05
139	19MG74-1-139	19MG74-A-6	1.332	0.053	0.825	0.025	0.30	0.16	3.02
	19MG74-1-139	19MG74-A-6	2.012	0.073	0.828	0.021	0.23	0.22	2.72
140	19MG74-1-140	19MG74-A-6	1.067	0.035	0.797	0.024	0.36	0.14	3.30
	19MG74-1-140	19MG74-A-6	0.983	0.040	0.831	0.019	0.44	0.13	3.19
141	19MG74-1-141	19MG74-A-6	1.215	0.047	0.814	0.020	0.37	0.16	3.46
	19MG74-1-141	19MG74-A-6	1.230	0.045	0.815	0.020	0.43	0.16	3.16
142	19MG74-1-142	19MG74-A-6	0.998	0.048	0.836	0.022	0.51	0.12	3.13
	19MG74-1-142	19MG74-A-6	1.224	0.045	0.807	0.022	0.36	0.14	2.94
143	19MG74-1-143	19MG74-A-6	0.513	0.017	0.828	0.017	0.29	0.07	3.53
	19MG74-1-143	19MG74-A-6	0.577	0.021	0.802	0.018	0.43	0.08	3.48
144	19MG74-1-144	19MG74-A-6	0.829	0.031	0.818	0.018	0.62	0.12	3.91
	19MG74-1-144	19MG74-A-6	0.672	0.024	0.787	0.027	0.31	0.10	3.79
	19MG74-1-144	19MG74-A-6	0.939	0.040	0.826	0.031	0.18	0.14	3.65
145	19MG74-1-145	19MG74-A-6	0.864	0.048	0.809	0.039	0.58	0.13	3.92
	19MG74-1-145	19MG74-A-6	0.524	0.030	0.824	0.021	0.27	0.08	3.65
	19MG74-1-145	19MG74-A-6	0.641	0.041	0.817	0.027	0.47	0.10	3.92
146	19MG74-1-146	19MG74-A-6	1.019	0.059	0.871	0.048	-0.07	0.13	3.70
	19MG74-1-146	19MG74-A-6	0.760	0.039	0.830	0.041	0.44	0.10	3.42
	19MG74-1-146	19MG74-A-6	0.958	0.048	0.793	0.023	-0.01	0.14	3.80
	19MG74-1-146	19MG74-A-6	0.673	0.032	0.805	0.017	0.36	0.10	3.76
147	19MG74-1-147	19MG74-A-6	0.603	0.029	0.825	0.030	0.23	0.08	3.59
	19MG74-1-147	19MG74-A-6	0.795	0.040	0.818	0.032	0.51	0.11	3.47
	19MG74-1-147	19MG74-A-6	0.978	0.040	0.806	0.023	0.44	0.13	3.39
148	19MG74-1-148	19MG74-A-6	0.617	0.033	0.821	0.030	0.29	0.08	3.50
	19MG74-1-148	19MG74-A-6	0.636	0.019	0.805	0.016	0.48	0.09	3.63
149	19MG74-1-149	19MG74-A-6	0.615	0.022	0.823	0.023	0.45	0.09	3.65
	19MG74-1-149	19MG74-A-6	0.724	0.025	0.829	0.018	0.46	0.11	3.78
150	19MG74-1-150	19MG74-A-6	0.512	0.018	0.815	0.022	0.32	0.08	3.80
	19MG74-1-150	19MG74-A-6	0.455	0.021	0.816	0.027	0.54	0.06	3.54

19MG74-B from DA strain domain

Spot	Source file (.FIN2)	Sample	$^{238}U/^{206}Pb$	±2σ (abs)	$^{207}Pb/^{206}Pb$	±2σ (abs)	Rho	U (ppm)	Pb (ppm)
	19MG74-2-1	19MG74-B	3.333	0.200	0.852	0.058	0.72	0.197	1.372
1	19MG74-2-1	19MG74-B	2.571	0.178	0.810	0.050	0.69	0.138	1.167
	19MG74-2-1	19MG74-B	2.315	0.091	0.842	0.031	0.71	0.106	1.002
	19MG74-2-2	19MG74-B	3.040	0.148	0.815	0.044	0.73	0.172	1.320
2	19MG74-2-2	19MG74-B	2.625	0.152	0.797	0.047	0.68	0.134	1.134
	19MG74-2-2	19MG74-B	1.577	0.090	0.762	0.044	0.64	0.072	0.895
	19MG74-2-3	19MG74-B	1.401	0.112	0.829	0.053	0.51	0.095	1.484
3	19MG74-2-3	19MG74-B	1.727	0.075	0.818	0.033	0.64	0.104	1.279
	19MG74-2-3	19MG74-B	1.953	0.095	0.878	0.044	0.55	0.106	1.169
4	19MG74-2-4	19MG74-B	2.049	0.160	0.812	0.049	0.61	0.127	1.295
	19MG74-2-4	19MG74-B	1.011	0.047	0.820	0.034	0.41	0.059	1.154
5	19MG74-2-5	19MG74-B	2.933	0.172	0.810	0.038	0.54	0.190	1.321
	19MG74-2-5	19MG74-B	2.506	0.126	0.789	0.032	0.67	0.145	1.160
6	19MG74-2-6	19MG74-B	3.759	0.155	0.835	0.030	0.54	0.237	1.287
	19MG74-2-6	19MG74-B	2.611	0.150	0.795	0.037	0.66	0.144	1.055
7	19MG74-2-7	19MG74-B	5.516	0.228	0.810	0.035	0.12	0.372	1.365
	19MG74-2-7	19MG74-B	5.319	0.204	0.799	0.029	0.51	0.345	1.218
8	19MG74-2-8	19MG74-B	1.140	0.072	0.820	0.037	0.50	0.072	1.262
	19MG74-2-8	19MG74-B	1.650	0.084	0.819	0.033	0.51	0.092	1.073
9	19MG74-2-9	19MG74-B	0.383	0.021	0.792	0.031	-0.03	0.029	1.479
	19MG74-2-9	19MG74-B	0.275	0.029	0.809	0.034	-0.11	0.018	1.229
10	19MG74-2-10	19MG74-B	1.172	0.069	0.821	0.027	0.35	0.094	1.555
	19MG74-2-10	19MG74-B	0.465	0.037	0.804	0.041	0.52	0.034	1.347
	19MG74-2-11	19MG74-B	1.130	0.077	0.800	0.044	0.25	0.073	1.273
11	19MG74-2-11	19MG74-B	1.323	0.063	0.847	0.033	0.58	0.078	1.199
	19MG74-2-11	19MG74-B	1.786	0.108	0.804	0.055	0.35	0.101	1.153
12	19MG74-2-12	19MG74-B	2.049	0.067	0.816	0.026	0.58	0.104	1.005
13	19MG74-2-13	19MG74-B	1.050	0.063	0.818	0.030	0.51	0.060	1.201
	19MG74-2-13	19MG74-B	1.527	0.063	0.836	0.030	0.35	0.084	1.062
	19MG74-2-14	19MG74-B	0.893	0.120	0.867	0.056	0.46	0.044	1.119
14	19MG74-2-14	19MG74-B	1.167	0.106	0.808	0.051	0.72	0.045	0.842
	19MG74-2-14	19MG74-B	0.710	0.038	0.845	0.037	0.19	0.027	0.759
	19MG74-2-15	19MG74-B	2.481	0.154	0.802	0.036	0.34	0.138	1.229
15	19MG74-2-15	19MG74-B	3.650	0.280	0.854	0.053	0.62	0.152	0.902
	19MG74-2-15	19MG74-B	3.367	0.193	0.825	0.052	0.75	0.144	0.892
	19MG74-2-16	19MG74-B	7.097	0.363	0.804	0.040	0.47	0.598	1.880
16	19MG74-2-16	19MG74-B	6.761	0.265	0.836	0.029	0.72	0.494	1.575
	19MG74-2-16	19MG74-B	6.028	0.243	0.762	0.037	0.64	0.453	1.510
	19MG74-2-17	19MG74-B	1.616	0.089	0.806	0.047	0.57	0.090	1.158
17	19MG74-2-17	19MG74-B	1.927	0.145	0.835	0.057	0.71	0.095	1.090
	19MG74-2-17	19MG74-B	1.565	0.081	0.827	0.042	0.24	0.076	1.030
18	19MG74-2-18	19MG74-B	2.703	0.110	0.821	0.028	0.66	0.190	1.527
	19MG74-2-18	19MG74-B	3.390	0.126	0.827	0.032	0.68	0.180	1.165

Spot	Source file (.FIN2)	Sample	$^{238}U/^{206}Pb$	±2σ (abs)	$^{207}Pb/^{206}Pb$	±2σ (abs)	Rho	U (ppm)	Pb (ppm)
	19MG74-2-19	19MG74-B	3.900	0.138	0.795	0.033	0.44	0.295	1.747
19	19MG74-2-19	19MG74-B	4.342	0.138	0.805	0.028	0.53	0.288	1.459
	19MG74-2-19	19MG74-B	5.556	0.340	0.844	0.061	0.78	0.334	1.310
20	19MG74-2-20	19MG74-B	2.740	0.135	0.844	0.037	0.70	0.164	1.416
	19MG74-2-20	19MG74-B	2.994	0.117	0.811	0.031	0.65	0.160	1.214
	19MG74-2-21	19MG74-B	2.725	0.171	0.849	0.055	0.40	0.156	1.490
21	19MG74-2-21	19MG74-B	2.045	0.130	0.829	0.038	0.51	0.129	1.517
	19MG74-2-21	19MG74-B	1.678	0.065	0.829	0.030	0.62	0.100	1.382
	19MG74-2-22	19MG74-B	2.381	0.170	0.797	0.055	0.63	0.087	0.880
22	19MG74-2-22	19MG74-B	2.770	0.184	0.890	0.052	0.69	0.083	0.714
	19MG74-2-22	19MG74-B	2.941	0.173	0.818	0.042	0.66	0.087	0.675
23	19MG74-2-23	19MG74-B	4.742	0.196	0.792	0.034	0.72	0.242	1.195
	19MG74-2-23	19MG74-B	5.711	0.219	0.860	0.041	0.68	0.249	1.112
24	19MG74-2-24	19MG74-B	0.448	0.032	0.807	0.038	0.53	0.030	1.578
	19MG74-2-25	19MG74-B	0.342	0.022	0.822	0.041	0.23	0.027	2.040
25	19MG74-2-25	19MG74-B	0.680	0.034	0.825	0.029	0.40	0.055	2.017
	19MG74-2-25	19MG74-B	0.571	0.033	0.821	0.028	0.47	0.049	2.025
26	19MG74-2-26	19MG74-B	2.611	0.123	0.811	0.043	0.66	0.098	0.925
	19MG74-2-26	19MG74-B	2.427	0.118	0.797	0.037	0.70	0.086	0.835
27	19MG74-2-27	19MG74-B	1.845	0.071	0.779	0.026	0.56	0.071	0.970
	19MG74-2-27	19MG74-B	1.912	0.110	0.831	0.044	0.64	0.067	0.784
28	19MG74-2-28	19MG74-B	3.571	0.179	0.826	0.048	0.65	0.093	0.673
	19MG74-2-28	19MG74-B	3.717	0.221	0.855	0.051	0.68	0.098	0.639
29	19MG74-2-29	19MG74-B			no value	NAN	NaN	0.004	0.768
30	19MG74-2-30	19MG74-B			no value	NAN	NaN	0.001	0.865
31	19MG74-2-31	19MG74-B	0.714	0.087	0.852	0.057	0.29	0.026	0.893
	19MG74-2-31	19MG74-B	1.221	0.055	0.835	0.037	0.58	0.039	0.773
32	19MG74-2-32	19MG74-B	1.575	0.087	0.842	0.044	0.66	0.058	0.962
	19MG74-2-32	19MG74-B	1.441	0.066	0.836	0.034	0.35	0.053	0.863
33	19MG74-2-33	19MG74-B	3.226	0.177	0.812	0.041	0.61	0.102	0.754
	19MG74-2-33	19MG74-B	1.608	0.119	0.782	0.042	0.97	0.051	0.742
34	19MG74-2-34	19MG74-B	2.183	0.138	0.810	0.040	0.53	0.070	0.782
	19MG74-2-34	19MG74-B	1.919	0.103	0.829	0.034	0.33	0.060	0.758
	19MG74-2-35	19MG74-B	1.355	0.116	0.855	0.062	0.42	0.043	0.744
35	19MG74-2-35	19MG74-B	2.179	0.114	0.830	0.038	0.61	0.065	0.745
	19MG74-2-35	19MG74-B	1.650	0.237	0.900	0.130	0.65	0.046	0.616
36	19MG74-2-36	19MG74-B	3.311	0.197	0.852	0.052	0.68	0.104	0.754
	19MG74-2-36	19MG74-B	3.096	0.173	0.833	0.038	0.51	0.091	0.713
37	19MG74-2-37	19MG74-B	2.899	0.168	0.847	0.045	0.65	0.096	0.799
	19MG74-2-37	19MG74-B	2.513	0.107	0.793	0.036	0.56	0.087	0.798
38	19MG74-2-38	19MG74-B	0.559	0.031	0.824	0.039	0.41	0.019	0.810
	19MG74-2-38	19MG74-B	0.610	0.045	0.869	0.052	0.65	0.019	0.705
39	19MG74-2-39	19MG74-B	0.395	0.027	0.832	0.036	0.38	0.015	0.864
	19MG74-2-39	19MG74-B	0.990	0.062	0.826	0.059	0.63	0.036	0.851

Spot	Source file (.FIN2)	Sample	^{238}U/^{206}Pb	±2σ (abs)	^{207}Pb/^{206}Pb	±2σ (abs)	Rho	U (ppm)	Pb (ppm)
	19MG74-2-40	19MG74-B	3.096	0.163	0.846	0.036	0.65	0.102	0.785
40	19MG74-2-40	19MG74-B	6.024	0.544	0.910	0.170	-0.02	0.166	0.649
	19MG74-2-40	19MG74-B	3.521	0.273	0.862	0.055	0.58	0.106	0.671
42	19MG74-2-42	19MG74-B	1.368	0.065	0.804	0.036	0.57	0.051	0.861
	19MG74-2-42	19MG74-B	1.852	0.117	0.865	0.038	0.24	0.067	0.786
43	19MG74-2-43	19MG74-B			no value	NAN	NaN	0.004	0.968
44	19MG74-2-44	19MG74-B	2.119	0.211	0.824	0.040	0.29	0.097	1.016
	19MG74-2-44	19MG74-B	3.165	0.170	0.827	0.031	0.53	0.125	0.927
	19MG74-2-45	19MG74-B	3.774	0.271	0.842	0.063	0.60	0.165	0.944
45	19MG74-2-45	19MG74-B	2.653	0.169	0.793	0.045	0.49	0.130	1.085
	19MG74-2-45	19MG74-B	2.415	0.128	0.841	0.036	0.67	0.106	0.979
	19MG74-2-46	19MG74-B	2.513	0.114	0.841	0.041	0.45	0.095	0.810
46	19MG74-2-46	19MG74-B	3.247	0.179	0.853	0.047	0.77	0.122	0.837
	19MG74-2-46	19MG74-B	3.906	0.519	0.800	0.100	0.77	0.147	0.775
47	19MG74-2-47	19MG74-B	8.673	0.391	0.799	0.037	0.56	0.300	0.790
	19MG74-2-47	19MG74-B	4.444	0.277	0.790	0.038	0.47	0.197	0.928
48	19MG74-2-48	19MG74-B	1.672	0.084	0.818	0.040	0.62	0.060	0.760
	19MG74-2-48	19MG74-B	1.912	0.124	0.776	0.048	0.66	0.061	0.609
	19MG74-2-49	19MG74-B	6.711	0.495	0.829	0.074	0.62	0.276	0.878
49	19MG74-2-49	19MG74-B	4.717	0.334	0.805	0.046	0.27	0.208	0.959
	19MG74-2-49	19MG74-B	3.676	0.203	0.867	0.040	0.41	0.143	0.837
50	19MG74-2-50	19MG74-B	0.398	0.021	0.811	0.032	0.41	0.017	0.961
	19MG74-2-50	19MG74-B	0.585	0.038	0.820	0.037	0.36	0.023	0.791
51	19MG74-2-51	19MG74-B	0.619	0.029	0.823	0.026	0.32	0.063	2.273
	19MG74-2-51	19MG74-B	1.656	0.244	0.825	0.070	0.41	0.184	2.360
	19MG74-2-52	19MG74-B	0.674	0.029	0.805	0.022	0.11	0.062	2.001
52	19MG74-2-52	19MG74-B	5.000	0.825	0.788	0.035	0.36	0.600	2.040
	19MG74-2-52	19MG74-B	1.546	0.155	0.784	0.041	0.37	0.142	1.965
	19MG74-2-53	19MG74-B	0.853	0.034	0.799	0.025	0.61	0.102	2.657
53	19MG74-2-53	19MG74-B	0.533	0.028	0.811	0.029	0.15	0.069	2.800
	19MG74-2-53	19MG74-B	0.298	0.019	0.785	0.029	0.20	0.037	2.648
	19MG74-2-54	19MG74-B	2.273	0.160	0.835	0.070	0.48	0.167	1.675
54	19MG74-2-54	19MG74-B	1.894	0.136	0.792	0.037	0.36	0.134	1.572
	19MG74-2-54	19MG74-B	1.267	0.040	0.818	0.020	0.40	0.084	1.460
55	19MG74-2-55	19MG74-B	0.322	0.012	0.806	0.020	0.54	0.053	3.670
	19MG74-2-55	19MG74-B	0.455	0.017	0.814	0.016	0.33	0.067	3.263
56	19MG74-2-56	19MG74-B	0.773	0.029	0.796	0.023	0.28	0.116	3.400
	19MG74-2-56	19MG74-B	0.722	0.028	0.828	0.020	0.31	0.098	3.075
	19MG74-2-57	19MG74-B	0.918	0.051	0.790	0.047	0.36	0.108	2.760
57	19MG74-2-57	19MG74-B	1.466	0.092	0.792	0.046	0.72	0.139	2.040
	19MG74-2-57	19MG74-B	1.267	0.058	0.812	0.031	0.61	0.126	2.247
	19MG74-2-57	19MG74-B	1.037	0.059	0.806	0.036	0.36	0.110	2.290
58	19MG74-2-58	19MG74-B	1.441	0.069	0.817	0.034	0.40	0.073	1.199
	19MG74-2-58	19MG74-B	2.755	0.152	0.787	0.035	0.34	0.150	1.228

Spot	Source file (.FIN2)	Sample	^{238}U/^{206}Pb	±2σ (abs)	^{207}Pb/^{206}Pb	±2σ (abs)	Rho	U (ppm)	Pb (ppm)
59	19MG74-2-59	19MG74-B	2.433	0.101	0.819	0.029	0.48	0.145	1.433
	19MG74-2-59	19MG74-B	2.500	0.106	0.800	0.032	0.61	0.144	1.350
60	19MG74-2-60	19MG74-B	2.618	0.144	0.827	0.040	0.52	0.173	1.681
	19MG74-2-60	19MG74-B	3.690	0.177	0.825	0.033	0.54	0.268	1.673
	19MG74-2-60	19MG74-B	2.387	0.108	0.831	0.036	0.55	0.178	1.748
61	19MG74-2-61	19MG74-B	2.817	0.119	0.854	0.038	0.59	0.164	1.501
	19MG74-2-61	19MG74-B	2.288	0.105	0.829	0.039	0.66	0.142	1.493
	19MG74-2-61	19MG74-B	2.809	0.142	0.818	0.039	0.64	0.175	1.487
62	19MG74-2-62	19MG74-B	1.529	0.091	0.858	0.037	0.79	0.150	2.620
	19MG74-2-62	19MG74-B	1.033	0.045	0.820	0.027	0.62	0.092	2.140
	19MG74-2-62	19MG74-B	1.190	0.040	0.837	0.025	0.50	0.094	1.889
63	19MG74-2-63	19MG74-B	4.484	0.342	0.777	0.055	0.46	0.352	1.930
	19MG74-2-63	19MG74-B	3.279	0.193	0.807	0.040	0.47	0.239	1.860
	19MG74-2-63	19MG74-B	2.415	0.292	0.779	0.036	0.20	0.210	2.010
	19MG74-2-63	19MG74-B	2.994	0.161	0.790	0.028	0.52	0.208	1.654
64	19MG74-2-64	19MG74-B	2.000	0.072	0.825	0.025	0.52	0.137	1.827
	19MG74-2-64	19MG74-B	2.165	0.061	0.793	0.024	0.46	0.152	1.712
65	19MG74-2-65	19MG74-B	2.237	0.150	0.802	0.051	0.61	0.137	1.600
	19MG74-2-65	19MG74-B	1.529	0.087	0.783	0.048	0.39	0.092	1.502
	19MG74-2-65	19MG74-B	0.965	0.040	0.807	0.026	0.58	0.053	1.372
66	19MG74-2-66	19MG74-B	1.645	0.065	0.814	0.027	0.57	0.112	1.788
	19MG74-2-66	19MG74-B	1.466	0.049	0.789	0.024	0.37	0.092	1.553
67	19MG74-2-67	19MG74-B	1.029	0.039	0.823	0.024	0.40	0.063	1.567
	19MG74-2-67	19MG74-B	0.759	0.043	0.799	0.027	0.40	0.046	1.465
68	19MG74-2-68	19MG74-B	1.499	0.058	0.811	0.024	0.56	0.104	1.826
	19MG74-2-68	19MG74-B	1.321	0.056	0.802	0.024	0.57	0.090	1.671
69	19MG74-2-69	19MG74-B	0.769	0.044	0.773	0.050	0.52	0.043	1.458
	19MG74-2-69	19MG74-B	1.043	0.052	0.843	0.037	0.38	0.046	1.171
	19MG74-2-69	19MG74-B	0.793	0.042	0.818	0.037	0.49	0.039	1.261
70	19MG74-2-70	19MG74-B	2.079	0.095	0.803	0.029	0.24	0.102	1.228
	19MG74-2-70	19MG74-B	1.229	0.059	0.820	0.029	0.36	0.064	1.308
71	19MG74-2-71	19MG74-B	0.832	0.064	0.781	0.038	0.50	0.056	1.713
	19MG74-2-71	19MG74-B	1.326	0.065	0.820	0.032	0.18	0.079	1.523
	19MG74-2-71	19MG74-B	1.074	0.046	0.804	0.033	0.48	0.071	1.597
72	19MG74-2-72	19MG74-B	1.664	0.091	0.804	0.043	0.55	0.084	1.255
	19MG74-2-72	19MG74-B	1.942	0.113	0.820	0.041	0.75	0.090	1.110
	19MG74-2-72	19MG74-B	2.252	0.142	0.814	0.038	0.75	0.105	1.107
73	19MG74-2-73	19MG74-B	1.230	0.059	0.831	0.036	0.55	0.063	1.311
	19MG74-2-73	19MG74-B	1.555	0.065	0.808	0.031	0.39	0.079	1.188
74	19MG74-2-74	19MG74-B	0.265	0.025	0.826	0.036	-0.02	0.015	1.263
	19MG74-2-74	19MG74-B	0.305	0.029	0.825	0.037	0.00	0.017	1.208
75	19MG74-2-75	19MG74-B	0.417	0.056	0.829	0.042	0.34	0.028	1.640
	19MG74-2-75	19MG74-B	0.916	0.050	0.838	0.043	0.45	0.051	1.350
	19MG74-2-75	19MG74-B	0.714	0.056	0.827	0.057	-0.01	0.037	1.287

Spot	**Source file (.FIN2)**	**Sample**	**^{238}U/^{206}Pb**	**±2σ (abs)**	**^{207}Pb/^{206}Pb**	**±2σ (abs)**	**Rho**	**U (ppm)**	**Pb (ppm)**

19MG79 from DA strain domain

Spot	**Source file (.FIN2)**	**Sample**	**^{238}U/^{206}Pb**	**±2σ (abs)**	**^{207}Pb/^{206}Pb**	**±2σ (abs)**	**Rho**	**U (ppm)**	**Pb (ppm)**
1	19MG79-1	19MG79-1	16.077	1.499	0.813	0.072	0.69	0.120	0.174
	19MG79-1	19MG79-1	16.722	2.517	0.749	0.061	0.43	0.157	0.219
	19MG79-2	19MG79-1	1.605	0.232	0.812	0.079	0.51	0.025	0.408
2	19MG79-2	19MG79-1	3.534	0.275	0.822	0.066	0.57	0.040	0.275
	19MG79-2	19MG79-1	4.292	0.479	0.860	0.110	0.76	0.040	0.232
	19MG79-3	19MG79-1	3.846	0.488	0.940	0.130	0.78	0.030	0.174
3	19MG79-3	19MG79-1	3.356	0.360	0.865	0.090	0.48	0.031	0.223
	19MG79-3	19MG79-1	2.315	0.268	0.871	0.086	0.55	0.020	0.183
	19MG79-4	19MG79-1	9.434	1.068	0.868	0.091	0.61	0.060	0.162
4	19MG79-4	19MG79-1	6.897	2.521	1.110	0.490	0.79	0.035	0.132
	19MG79-4	19MG79-1	5.435	0.709	1.000	0.190	0.78	0.023	0.106
	19MG79-4	19MG79-1	7.246	1.943	0.820	0.330	0.22	0.022	0.073
5	19MG79-5	19MG79-1	4.762	0.476	0.838	0.071	0.60	0.065	0.371
	19MG79-5	19MG79-1	6.329	0.481	0.830	0.067	0.62	0.078	0.306
	19MG79-6	19MG79-1	7.143	1.071	0.950	0.130	0.51	0.047	0.193
6	19MG79-6	19MG79-1	17.606	2.666	1.020	0.150	0.65	0.095	0.129
	19MG79-6	19MG79-1	6.757	1.096	0.841	0.083	0.38	0.052	0.229
	19MG79-7	19MG79-1	3.289	0.249	0.791	0.062	0.71	0.043	0.307
7	19MG79-7	19MG79-1	2.169	0.188	0.790	0.080	0.55	0.031	0.309
	19MG79-7	19MG79-1	3.125	0.254	0.831	0.079	0.64	0.047	0.348
	19MG79-8	19MG79-1	4.274	0.749	0.736	0.057	-0.04	0.203	0.835
8	19MG79-8	19MG79-1	4.149	0.517	0.772	0.044	0.19	0.176	0.786
	19MG79-8	19MG79-1	4.367	0.953	0.762	0.073	-0.03	0.210	0.623
	19MG79-9	19MG79-1	2.717	0.510	0.842	0.082	0.49	0.039	0.347
9	19MG79-9	19MG79-1	4.049	0.508	1.000	0.140	0.74	0.039	0.234
	19MG79-9	19MG79-1	2.732	0.299	0.750	0.060	0.66	0.036	0.305
10	19MG79-10	19MG79-1	6.061	0.478	0.795	0.074	0.53	0.058	0.231
	19MG79-10	19MG79-1	6.211	0.463	0.873	0.073	0.67	0.069	0.281
11	19MG79-11	19MG79-1	8.000	0.768	0.754	0.060	0.62	0.100	0.289
	19MG79-11	19MG79-1	7.874	0.515	0.781	0.050	0.51	0.119	0.398
12	19MG79-12	19MG79-1	1.582	0.220	0.830	0.059	0.22	0.033	0.610
	19MG79-12	19MG79-1	4.115	0.356	0.894	0.087	0.64	0.042	0.270
13	19MG79-13	19MG79-1	1.600	0.136	0.795	0.049	0.57	0.030	0.490
	19MG79-13	19MG79-1	2.041	0.162	0.793	0.058	0.64	0.034	0.377
14	19MG79-14	19MG79-1	3.745	0.365	0.812	0.060	0.39	0.041	0.279
	19MG79-14	19MG79-1	4.950	0.515	0.920	0.100	0.70	0.054	0.283
	19MG79-15	19MG79-1	2.770	0.361	0.838	0.085	0.52	0.031	0.297
15	19MG79-15	19MG79-1	3.289	0.368	0.765	0.064	0.11	0.056	0.411
	19MG79-15	19MG79-1	6.494	0.675	0.807	0.074	0.42	0.079	0.362

Spot	Source file (.FIN2)	Sample	^{238}U/^{206}Pb	±2σ (abs)	^{207}Pb/^{206}Pb	±2σ (abs)	Rho	U (ppm)	Pb (ppm)
	19MG79-16	19MG79-1	1.618	0.175	0.822	0.054	0.32	0.035	0.600
16	19MG79-16	19MG79-1	1.517	0.203	0.769	0.047	0.41	0.037	0.620
	19MG79-16	19MG79-1	2.375	0.339	0.810	0.100	0.43	0.047	0.471
	19MG79-16	19MG79-1	2.203	0.301	0.864	0.077	0.71	0.045	0.533
17	19MG79-17	19MG79-1	12.165	1.021	0.866	0.073	0.48	0.123	0.264
	19MG79-17	19MG79-1	11.614	0.890	0.861	0.068	0.70	0.098	0.218
18	19MG79-18	19MG79-1	3.165	0.180	0.850	0.053	0.61	0.054	0.453
	19MG79-18	19MG79-1	3.891	0.348	0.816	0.055	0.38	0.068	0.418
19	19MG79-19	19MG79-1	6.410	0.534	0.868	0.082	0.65	0.053	0.238
	19MG79-19	19MG79-1	4.878	0.500	0.788	0.088	0.70	0.040	0.195
	19MG79-20	19MG79-1	2.203	0.311	0.877	0.065	0.51	0.056	0.697
20	19MG79-20	19MG79-1	3.623	0.381	0.839	0.088	0.30	0.063	0.471
	19MG79-20	19MG79-1	2.770	0.299	0.798	0.048	0.24	0.057	0.558
21	19MG79-21	19MG79-1	3.155	0.537	0.864	0.055	0.45	0.077	0.620
	19MG79-21	19MG79-1	5.405	0.380	0.801	0.052	0.64	0.089	0.425
22	19MG79-22	19MG79-1	5.319	0.594	0.827	0.065	0.51	0.061	0.335
	19MG79-22	19MG79-1	5.435	0.354	0.788	0.062	0.64	0.055	0.273
23	19MG79-23	19MG79-1	1.401	0.114	0.786	0.029	0.46	0.074	1.330
	19MG79-23	19MG79-1	1.701	0.171	0.810	0.043	0.61	0.064	0.990
	19MG79-24	19MG79-1	1.031	0.553	0.910	0.100	0.47	0.015	0.360
24	19MG79-24	19MG79-1	2.000	0.200	0.893	0.083	0.76	0.014	0.195
	19MG79-24	19MG79-1	3.145	0.554	1.020	0.170	0.31	0.014	0.143
	19MG79-25	19MG79-1	1.631	0.192	0.832	0.079	0.42	0.018	0.276
25	19MG79-25	19MG79-1	1.149	0.172	0.745	0.061	0.40	0.021	0.432
	19MG79-25	19MG79-1	1.395	0.150	0.796	0.076	0.49	0.021	0.367
	19MG79-26	19MG79-1	7.463	0.724	0.866	0.071	0.53	0.119	0.423
26	19MG79-26	19MG79-1	5.376	0.520	0.811	0.068	0.48	0.098	0.444
	19MG79-26	19MG79-1	2.513	0.606	0.849	0.056	0.39	0.095	0.810
27	19MG79-27	19MG79-1	2.899	0.235	0.797	0.052	0.59	0.080	0.705
	19MG79-27	19MG79-1	5.405	0.409	0.806	0.050	0.60	0.094	0.467
	19MG79-28	19MG79-1	2.294	0.295	0.798	0.044	0.44	0.074	0.820
28	19MG79-28	19MG79-1	3.731	0.668	0.878	0.071	0.49	0.074	0.514
	19MG79-28	19MG79-1	3.534	0.375	0.805	0.061	0.65	0.066	0.443
	19MG79-29	19MG79-1	0.870	0.590	0.810	0.110	-0.31	0.021	0.540
	19MG79-29	19MG79-1	0.541	0.178	0.791	0.054	0.38	0.017	0.750
29	19MG79-29	19MG79-1	1.333	0.356	0.900	0.190	0.73	0.021	0.329
	19MG79-29	19MG79-1	2.041	0.541	0.790	0.120	0.20	0.034	0.400
	19MG79-29	19MG79-1	1.190	0.241	0.920	0.110	0.29	0.022	0.456
30	19MG79-30	19MG79-1	4.425	0.411	0.850	0.110	0.26	0.028	0.138
	19MG79-30	19MG79-1	6.803	0.555	0.850	0.100	0.63	0.036	0.124

Spot	Source file (.FIN2)	Sample	^{238}U/^{206}Pb	±2σ (abs)	^{207}Pb/^{206}Pb	±2σ (abs)	Rho	U (ppm)	Pb (ppm)
	19MG79-31	19MG79-1	6.211	0.887	0.990	0.150	0.73	0.035	0.143
31	19MG79-31	19MG79-1	8.475	1.221	1.050	0.150	0.62	0.034	0.115
	19MG79-31	19MG79-1	6.993	1.369	0.800	0.240	0.75	0.039	0.109
32	19MG79-32	19MG79-1	7.752	1.082	0.870	0.150	0.70	0.037	0.124
	19MG79-32	19MG79-1	6.173	0.724	0.870	0.100	0.75	0.045	0.168
33	19MG79-33	19MG79-1	1.661	0.119	0.817	0.036	0.51	0.046	0.685
	19MG79-33	19MG79-1	2.825	0.375	0.970	0.170	0.66	0.040	0.363
34	19MG79-34	19MG79-1	2.577	0.226	0.792	0.063	0.47	0.032	0.308
36	19MG79-36	19MG79-1	2.667	0.398	0.891	0.095	0.63	0.027	0.259
	19MG79-36	19MG79-1	3.226	0.354	0.930	0.120	0.86	0.022	0.140
37	19MG79-37	19MG79-1	2.506	0.201	0.793	0.054	0.47	0.041	0.400
	19MG79-37	19MG79-1	2.551	0.247	0.800	0.069	0.51	0.050	0.458
38	19MG79-38	19MG79-1	5.319	0.396	0.844	0.067	0.72	0.058	0.238
	19MG79-38	19MG79-1	5.988	0.574	0.805	0.076	0.61	0.064	0.237
39	19MG79-39	19MG79-1	4.098	0.370	0.823	0.077	0.47	0.061	0.330
	19MG79-39	19MG79-1	5.804	0.269	0.749	0.038	0.63	0.093	0.336
40	19MG79-40	19MG79-1	1.130	0.105	0.814	0.061	0.18	0.025	0.508
	19MG79-40	19MG79-1	1.412	0.134	0.770	0.039	0.23	0.045	0.728
	19MG79-40	19MG79-1	2.370	0.281	0.828	0.077	0.79	0.050	0.454
41	19MG79-41	19MG79-1	0.800	0.160	0.902	0.098	0.49	0.018	0.508
	19MG79-41	19MG79-1	2.288	0.225	0.843	0.060	0.68	0.037	0.344
42	19MG79-42	19MG79-1	4.695	0.441	0.883	0.083	0.44	0.075	0.386
	19MG79-42	19MG79-1	6.711	0.991	0.870	0.150	0.69	0.063	0.202
	19MG79-42	19MG79-1	4.808	0.693	0.850	0.100	0.52	0.039	0.175
43	19MG79-43	19MG79-1	4.310	0.502	0.830	0.074	0.75	0.107	0.598
	19MG79-43	19MG79-1	8.475	0.934	0.792	0.050	0.37	0.194	0.501
44	19MG79-44	19MG79-1	3.597	0.440	0.799	0.071	0.81	0.036	0.226
	19MG79-44	19MG79-1	4.329	0.412	0.866	0.075	0.54	0.036	0.205
45	19MG79-45	19MG79-1	4.184	0.333	0.813	0.065	0.75	0.063	0.359
	19MG79-45	19MG79-1	6.219	0.309	0.854	0.051	0.65	0.112	0.411
46	19MG79-46	19MG79-1	3.546	0.415	0.785	0.054	0.48	0.099	0.623
	19MG79-46	19MG79-1	5.405	0.351	0.837	0.066	0.73	0.095	0.410
47	19MG79-47	19MG79-1	7.407	0.768	0.890	0.100	0.62	0.046	0.133
	19MG79-47	19MG79-1	6.711	1.081	0.840	0.180	0.66	0.033	0.099
48	19MG79-48	19MG79-1			no value	NAN	NaN	0.002	0.544
49	19MG79-49	19MG79-1	2.941	0.450	0.747	0.076	0.43	0.053	0.355
	19MG79-49	19MG79-1	2.179	0.460	0.762	0.088	0.53	0.037	0.400
50	19MG79-50	19MG79-1	5.682	0.678	1.010	0.120	0.60	0.069	0.276
	19MG79-50	19MG79-1	7.407	0.658	0.885	0.066	0.68	0.092	0.269

Table A5.2: U-Pb isotopic data of calcite veins from the ECM obtained during the session 2 (08-10-2021) of LA-ICP-MS U-Pb in calcite. The spot size for all samples were 85 µm. Red labelled data was excluded from the age regression due to evident high error or a point belonging to the host rock.

Spot	Source file (.FIN2)	Sample	²³⁸U/²⁰⁶Pb	±2σ (abs)	²⁰⁷Pb/²⁰⁶Pb	±2σ (abs)	Rho	U (ppm)	Pb (ppm)
				Session 2					
			WC-1 Calcite reference (Roberts et al., 2017)						
1	WC1-1	WC-1	24.564	0.422	0.053	0.004	-0.01	3.320	0.184
2	WC1-2	WC-1	24.857	0.414	0.051	0.004	0.18	3.650	0.129
3	WC1-3	WC-1	25.233	0.363	0.051	0.004	0.15	3.593	0.204
4	WC1-4	WC-1	25.088	0.516	0.045	0.007	-0.62	3.600	0.212
5	WC1-5	WC-1	25.126	0.574	0.044	0.009	-0.73	4.344	0.280
6	WC1-7	WC-1	25.069	0.402	0.053	0.005	0.31	3.453	0.212
7	WC1-8	WC-1	25.056	0.396	0.053	0.005	0.22	3.552	0.204
8	WC1-10	WC-1	25.278	0.403	0.050	0.004	0.18	3.775	0.198
9	WC1-12	WC-1	24.649	0.401	0.052	0.006	-0.01	3.676	0.157
10	WC1-14	WC-1	24.863	0.371	0.052	0.005	0.26	3.637	0.198
11	WC1-15	WC-1	24.728	0.428	0.053	0.006	0.35	3.479	0.158
12	WC1-16	WC-1	25.387	0.374	0.050	0.005	0.34	3.941	0.204
13	WC1-18	WC-1	24.272	1.002	0.049	0.017	-0.81	3.679	0.189
14	WC1-20	WC-1	25.132	0.436	0.052	0.005	0.23	3.611	0.157
15	WC1-22	WC-1	24.925	0.447	0.052	0.005	0.13	3.700	0.139
16	WC1-24	WC-1	25.063	0.415	0.054	0.006	-0.01	4.500	0.258
17	WC1-26	WC-1	24.649	0.565	0.051	0.007	-0.34	3.445	0.221
18	WC1-27	WC-1	24.857	0.433	0.051	0.005	0.40	3.651	0.210
19	WC1-28	WC-1	25.355	0.463	0.052	0.007	-0.48	3.933	0.202
20	WC1-29	WC-1	24.988	0.493	0.052	0.005	0.34	3.580	0.133
21	WC1-32	WC-1	25.094	0.460	0.049	0.005	0.40	4.001	0.193
22	WC1-34	WC-1	24.450	0.478	0.051	0.005	0.38	3.648	0.158
23	WC1-36	WC-1	25.214	0.420	0.051	0.005	0.30	3.768	0.173
24	WC1-38	WC-1	25.381	1.031	0.023	0.009	-0.75	3.772	0.220
25	WC1-40	WC-1	24.474	0.449	0.051	0.006	0.14	3.742	0.252
26	WC1-41	WC-1	25.407	0.484	0.052	0.005	0.16	3.592	0.188
27	WC1-42	WC-1	25.164	0.570	0.052	0.007	-0.26	3.744	0.194
28	WC1-44	WC-1	25.069	0.490	0.052	0.006	-0.25	3.411	0.128
29	WC1-46	WC-1	25.107	0.403	0.049	0.004	0.29	4.117	0.232
30	WC1-49	WC-1	24.534	0.494	0.052	0.007	0.50	3.284	0.150
31	WC1-45	WC-1	24.278	0.477	0.050	0.007	0.09	4.756	0.321
32	WC1-52	WC-1	25.833	0.487	0.048	0.005	-0.25	4.030	0.150
33	WC1-54	WC-1	25.038	0.458	0.051	0.006	0.28	3.569	0.217
34	WC1-56	WC-1	25.013	0.413	0.051	0.005	0.29	4.152	0.304
35	WC1-58	WC-1	24.765	0.534	0.051	0.005	0.12	3.474	0.104
36	WC1-53	WC-1	24.869	0.476	0.053	0.007	0.23	3.872	0.471
37	WC1-60	WC-1	25.272	0.556	0.052	0.004	0.28	3.664	0.116
38	WC1-62	WC-1	24.963	0.499	0.053	0.004	-0.26	5.700	0.157

Spot	Source file (.FIN2)	Sample	$^{238}U/^{206}Pb$	±2σ (abs)	$^{207}Pb/^{206}Pb$	±2σ (abs)	Rho	U (ppm)	Pb (ppm)
39	WC1-64	WC-1	24.588	0.550	0.052	0.007	0.28	3.431	0.143
40	WC1-66	WC-1	25.543	0.528	0.052	0.005	0.14	3.769	0.164
41	WC1-67	WC-1	25.202	0.470	0.051	0.005	0.46	3.411	0.215
42	WC1-68	WC-1	24.685	0.439	0.049	0.006	0.24	4.025	0.383
43	WC1-69	WC-1	24.789	0.473	0.053	0.006	0.34	3.466	0.311
44	WC1-65	WC-1	25.246	0.535	0.052	0.005	0.02	4.038	0.204
45	WC1-63	WC-1	24.876	0.501	0.052	0.004	0.15	3.680	0.070
46	WC1-61	WC-1	25.145	0.525	0.053	0.005	0.23	3.591	0.200
47	WC1-11	WC-1	24.826	0.419	0.050	0.005	-0.20	4.096	0.261
48	WC1-6	WC-1	25.297	0.390	0.051	0.004	0.08	4.860	0.172
49	WC1-9	WC-1	24.432	0.466	0.051	0.008	0.08	3.413	0.533
50	WC1-13	WC-1	25.381	0.464	0.051	0.005	0.00	4.062	0.139
51	WC1-21	WC-1	24.752	0.613	0.051	0.008	-0.33	3.719	0.524

Soda-lime glass NIST SRM-614

Spot	Source file (.FIN2)	Sample	$^{238}U/^{206}Pb$	±2σ (abs)	$^{207}Pb/^{206}Pb$	±2σ (abs)	Rho	U (ppm)	Pb (ppm)
1	NIST614-1	NIST-614	1.370	0.018	0.866	0.011	0.60	0.517	5.240
2	NIST614-2	NIST-614	1.377	0.019	0.860	0.011	0.55	0.509	5.020
3	NIST614-3	NIST-614	1.397	0.019	0.857	0.011	0.61	0.454	3.453
4	NIST614-4	NIST-614	1.406	0.022	0.861	0.012	0.64	0.448	3.380
5	NIST614-5	NIST-614	1.418	0.024	0.872	0.013	0.57	0.570	3.666
6	NIST614-6	NIST-614	1.431	0.023	0.856	0.011	0.73	0.594	3.669
7	NIST614-7	NIST-614	1.387	0.023	0.856	0.014	0.53	0.581	6.800
8	NIST614-8	NIST-614	1.399	0.025	0.874	0.014	0.55	0.584	6.910
9	NIST614-9	NIST-614	1.403	0.024	0.863	0.012	0.53	0.493	7.120
10	NIST614-10	NIST-614	1.395	0.023	0.861	0.013	0.68	0.481	7.010

19MG21 from DA strain domain

Spot	Source file (.FIN2)	Sample	$^{238}U/^{206}Pb$	±2σ (abs)	$^{207}Pb/^{206}Pb$	±2σ (abs)	Rho	U (ppm)	Pb (ppm)
1	19MG21-1	19MG21-1B	0.699	0.088	0.810	0.013	0.01	0.447	9.250
	19MG21-1	19MG21-1B	4.444	0.988	0.757	0.017	0.00	3.710	8.050
	19MG21-2	19MG21-1B	1.754	0.400	0.784	0.042	-0.12	0.570	4.180
	19MG21-2	19MG21-1B	0.758	0.109	0.793	0.020	-0.05	0.400	7.400
2	19MG21-2	19MG21-1B	1.471	0.216	0.787	0.020	0.15	0.610	5.390
	19MG21-2	19MG21-1B	0.391	0.044	0.809	0.013	-0.11	0.409	17.500
	19MG21-2	19MG21-1B	1.667	0.417	0.816	0.024	0.02	0.950	7.300
	19MG21-3	19MG21-1B	0.741	0.093	0.808	0.042	0.38	0.150	3.280
	19MG21-3	19MG21-1B	0.392	0.060	0.803	0.036	-0.27	0.172	7.080
3	19MG21-3	19MG21-1B	0.709	0.116	0.808	0.019	-0.09	0.450	8.300
	19MG21-3	19MG21-1B	1.053	0.288	0.779	0.028	-0.01	0.560	4.600
	19MG21-3	19MG21-1B	0.549	0.094	0.788	0.027	-0.26	0.247	6.430
	19MG21-3	19MG21-1B	0.345	0.054	0.824	0.025	-0.19	0.134	6.490

287

Spot	Source file (.FIN2)	Sample	^{238}U/^{206}Pb	±2σ (abs)	^{207}Pb/^{206}Pb	±2σ (abs)	Rho	U (ppm)	Pb (ppm)
	19MG21-4	19MG21-1B	0.326	0.042	0.794	0.021	0.00	0.470	21.500
	19MG21-4	19MG21-1B	0.196	0.028	0.831	0.015	-0.01	0.574	41.400
4	19MG21-4	19MG21-1B	0.461	0.174	0.806	0.023	-0.17	1.500	31.500
	19MG21-4	19MG21-1B	0.332	0.049	0.789	0.025	-0.03	0.315	14.200
	19MG21-4	19MG21-1B	0.794	0.094	0.787	0.013	0.07	0.510	7.850
	19MG21-5	19MG21-1B	0.248	0.055	0.827	0.026	-0.40	0.520	37.000
5	19MG21-5	19MG21-1B	1.017	0.102	0.800	0.017	-0.38	0.500	5.020
	19MG21-5	19MG21-1B	0.233	0.059	0.811	0.018	0.34	0.410	20.500
	19MG21-5	19MG21-1B	0.556	0.340	0.838	0.025	-0.16	0.580	12.800
	19MG21-6	19MG21-1B	0.800	0.141	0.810	0.023	0.07	0.368	5.170
6	19MG21-6	19MG21-1B	1.176	0.104	0.810	0.016	0.13	0.684	8.020
	19MG21-6	19MG21-1B	2.174	0.473	0.777	0.018	0.02	1.930	9.800
	19MG21-7	19MG21-1B	1.585	0.163	0.808	0.020	0.05	0.750	5.500
7	19MG21-7	19MG21-1B	0.752	0.096	0.794	0.025	-0.08	0.250	4.150
	19MG21-7	19MG21-1B	1.124	0.151	0.807	0.026	-0.12	0.356	4.580
8	19MG21-8	19MG21-1B	1.449	0.200	0.811	0.019	0.14	0.631	6.030
	19MG21-8	19MG21-1B	1.163	0.162	0.794	0.011	-0.12	0.940	7.240
	19MG21-9	19MG21-1B	0.806	0.104	0.803	0.025	0.08	0.225	3.070
9	19MG21-9	19MG21-1B	1.053	0.488	0.785	0.029	-0.17	1.210	3.860
	19MG21-9	19MG21-1B	0.353	0.051	0.798	0.020	-0.01	0.444	16.300
	19MG21-9	19MG21-1B	1.235	0.168	0.814	0.015	0.30	0.630	6.630
	19MG21-10	19MG21-1B	0.806	0.091	0.801	0.019	-0.11	0.434	7.000
	19MG21-10	19MG21-1B	0.490	0.072	0.823	0.022	0.11	0.371	9.420
10	19MG21-10	19MG21-1B	0.781	0.146	0.790	0.017	0.21	0.920	12.900
	19MG21-10	19MG21-1B	0.699	0.054	0.813	0.028	0.06	0.363	7.180
	19MG21-10	19MG21-1B	1.250	0.234	0.778	0.017	-0.17	0.760	6.260
11	19MG21-11	19MG21-1B	0.455	0.054	0.800	0.013	0.15	0.333	8.700
	19MG21-11	19MG21-1B	0.775	0.108	0.814	0.016	-0.01	0.320	4.010
	19MG21-12	19MG21-1B	1.205	0.247	0.808	0.027	-0.07	0.810	4.960
12	19MG21-12	19MG21-1B	0.864	0.058	0.802	0.026	0.42	0.294	4.020
	19MG21-12	19MG21-1B	0.971	0.132	0.802	0.016	0.02	0.593	6.450
	19MG21-13	19MG21-1B	0.341	0.026	0.816	0.017	-0.06	0.334	12.000
	19MG21-13	19MG21-1B	0.813	0.271	0.787	0.021	-0.23	1.260	14.660
13	19MG21-13	19MG21-1B	0.251	0.018	0.806	0.016	-0.02	0.229	11.400
	19MG21-13	19MG21-1B	0.397	0.058	0.851	0.059	0.22	0.235	6.970
	19MG21-13	19MG21-1B	0.368	0.036	0.818	0.023	0.03	0.171	5.590
	19MG21-13	19MG21-1B	0.833	0.146	0.807	0.016	-0.04	0.580	5.560
14	19MG21-14	19MG21-1B	1.220	0.223	0.801	0.020	-0.17	2.570	6.650
	19MG21-14	19MG21-1B	0.595	0.050	0.802	0.010	0.02	0.319	6.250
	19MG21-15	19MG21-1B	1.370	0.263	0.808	0.030	-0.05	0.470	3.510
	19MG21-15	19MG21-1B	0.806	0.117	0.825	0.036	0.23	0.170	2.490
15	19MG21-15	19MG21-1B	2.217	0.393	0.794	0.025	-0.21	0.860	3.790
	19MG21-15	19MG21-1B	0.139	0.019	0.805	0.009	-0.17	0.268	20.100
	19MG21-15	19MG21-1B	0.413	0.067	0.806	0.016	-0.29	0.315	8.120

Spot	Source file (.FIN2)	Sample	$^{238}U/^{206}Pb$	±2σ (abs)	$^{207}Pb/^{206}Pb$	±2σ (abs)	Rho	U (ppm)	Pb (ppm)
	19MG21-16	19MG21-1B	0.758	0.138	0.805	0.031	0.20	0.920	11.700
16	19MG21-16	19MG21-1B	1.447	0.170	0.813	0.042	0.29	0.497	3.570
	19MG21-16	19MG21-1B	0.493	0.066	0.813	0.013	-0.12	0.580	14.200
	19MG21-16	19MG21-1B	0.450	0.032	0.809	0.013	-0.11	0.184	5.300
	19MG21-17	19MG21-1B	0.901	0.089	0.795	0.023	0.11	0.580	6.690
17	19MG21-17	19MG21-1B	0.420	0.078	0.811	0.018	0.02	0.382	10.200
	19MG21-17	19MG21-1B	1.408	0.238	0.790	0.022	-0.14	0.620	3.890
	19MG21-17	19MG21-1B	0.334	0.035	0.802	0.021	0.31	0.435	14.930
18	19MG21-18	19MG21-1B	0.578	0.037	0.800	0.014	0.08	0.315	6.100
	19MG21-18	19MG21-1B	0.299	0.024	0.814	0.015	0.03	0.107	3.947
19	19MG21-19	19MG21-1B	0.286	0.016	0.804	0.011	0.11	0.091	3.580
20	19MG21-20	19MG21-1B	0.202	0.008	0.814	0.014	0.20	0.075	4.383
	19MG21-20	19MG21-1B	0.164	0.010	0.819	0.018	0.24	0.055	3.952
	19MG21-21	19MG21-1B	0.248	0.015	0.799	0.021	0.42	0.052	2.258
21	19MG21-21	19MG21-1B	0.364	0.034	0.807	0.031	0.43	0.070	2.173
	19MG21-21	19MG21-1B	0.334	0.028	0.817	0.026	0.55	0.059	2.069
	19MG21-22	19MG21-1B	0.351	0.041	0.812	0.024	-0.05	0.087	2.374
22	19MG21-22	19MG21-1B	0.223	0.014	0.834	0.017	0.14	0.064	3.280
	19MG21-22	19MG21-1B	0.298	0.043	0.781	0.022	0.35	0.117	3.940
	19MG21-23	19MG21-1B	0.446	0.026	0.804	0.023	0.54	0.092	2.253
23	19MG21-23	19MG21-1B	0.538	0.040	0.804	0.031	0.35	0.114	2.350
	19MG21-23	19MG21-1B	0.311	0.017	0.812	0.023	0.28	0.054	1.956
	19MG21-24	19MG21-1B	0.671	0.077	0.819	0.019	-0.04	0.203	3.110
24	19MG21-24	19MG21-1B	1.163	0.270	0.793	0.033	0.35	0.307	2.290
	19MG21-24	19MG21-1B	0.498	0.074	0.801	0.021	-0.09	0.199	4.030
25	19MG21-25	19MG21-1B	1.340	0.128	0.802	0.017	0.02	0.412	2.710
	19MG21-25	19MG21-1B	0.592	0.060	0.809	0.015	-0.28	0.360	6.260
	19MG21-26	19MG21-1B	1.190	0.156	0.789	0.021	0.14	0.580	4.650
26	19MG21-26	19MG21-1B	0.962	0.120	0.817	0.018	0.11	0.606	6.610
	19MG21-26	19MG21-1B	0.472	0.109	0.797	0.013	0.14	0.565	11.500
	19MG21-27	19MG21-1B	0.144	0.013	0.801	0.013	0.06	0.311	22.120
27	19MG21-27	19MG21-1B	0.575	0.073	0.829	0.022	-0.02	0.323	5.720
	19MG21-27	19MG21-1B	1.176	0.166	0.814	0.025	-0.30	0.334	2.870
28	19MG21-28	19MG21-1B	1.431	0.129	0.814	0.016	0.08	0.633	4.310
	19MG21-28	19MG21-1B	0.752	0.085	0.807	0.017	0.13	0.490	6.430
30	19MG21-30	19MG21-1B	0.171	0.009	0.811	0.016	0.20	0.029	1.776
	19MG21-30	19MG21-1B	0.110	0.012	0.838	0.032	-0.05	0.017	1.588
32	19MG21-32	19MG21-1B	0.115	0.009	0.846	0.043	0.27	0.018	1.704
	19MG21-32	19MG21-1B	0.181	0.015	0.828	0.019	0.14	0.029	1.518
	19MG21-33	19MG21-1B	0.210	0.017	0.806	0.029	0.33	0.042	1.941
	19MG21-33	19MG21-1B	0.265	0.057	0.830	0.051	-0.19	0.053	1.885
33	19MG21-33	19MG21-1B	0.201	0.014	0.835	0.037	0.00	0.034	1.796
	19MG21-33	19MG21-1B	0.382	0.086	0.828	0.047	0.49	0.069	1.630
	19MG21-33	19MG21-1B	0.207	0.021	0.820	0.040	0.12	0.032	1.573

Spot	Source file (.FIN2)	Sample	^{238}U/^{206}Pb	±2σ (abs)	^{207}Pb/^{206}Pb	±2σ (abs)	Rho	U (ppm)	Pb (ppm)
	19MG21-34	19MG21-1B	0.100	0.011	0.813	0.051	0.18	0.018	1.595
34	19MG21-34	19MG21-1B	0.120	0.010	0.826	0.033	-0.01	0.019	1.629
	19MG21-34	19MG21-1B	0.119	0.018	0.811	0.053	0.05	0.018	1.548
	19MG21-36	19MG21-1B	0.146	0.016	0.822	0.021	0.30	0.033	1.870
36	19MG21-36	19MG21-1B	0.448	0.125	0.795	0.035	0.41	0.094	1.495
	19MG21-36	19MG21-1B	0.182	0.083	0.797	0.050	-0.12	0.034	1.480
	19MG21-37	19MG21-1B	0.095	0.012	0.809	0.034	0.31	0.018	1.753
37	19MG21-37	19MG21-1B	0.102	0.010	0.828	0.030	0.36	0.018	1.748
	19MG21-37	19MG21-1B	0.191	0.020	0.811	0.044	0.01	0.031	1.605
	19MG21-37	19MG21-1B	0.150	0.013	0.812	0.022	0.17	0.025	1.582
	19MG21-38	19MG21-1B	0.169	0.032	0.808	0.044	0.42	0.033	1.841
38	19MG21-38	19MG21-1B	0.267	0.023	0.833	0.027	0.44	0.048	1.794
	19MG21-38	19MG21-1B	0.155	0.020	0.818	0.033	0.23	0.030	1.802
	19MG21-39	19MG21-1B	0.120	0.020	0.786	0.042	0.37	0.027	1.980
39	19MG21-39	19MG21-1B	0.138	0.019	0.813	0.028	0.33	0.028	1.810
	19MG21-39	19MG21-1B	0.079	0.008	0.825	0.037	-0.13	0.014	1.694
	19MG21-39	19MG21-1B	0.146	0.018	0.806	0.047	0.32	0.024	1.499
	19MG21-40	19MG21-1B	0.091	0.009	0.828	0.034	0.47	0.018	1.915
40	19MG21-40	19MG21-1B	0.116	0.008	0.802	0.027	0.13	0.021	1.804
	19MG21-40	19MG21-1B	0.140	0.013	0.801	0.029	0.23	0.033	2.189
	19MG21-40	19MG21-1B	0.141	0.015	0.828	0.026	-0.12	0.029	1.946
	19MG21-41	19MG21-1B	0.103	0.008	0.799	0.022	0.30	0.020	1.770
41	19MG21-41	19MG21-1B	0.242	0.027	0.826	0.026	0.23	0.042	1.546
	19MG21-41	19MG21-1B	0.166	0.015	0.808	0.033	0.37	0.026	1.511
	19MG21-41	19MG21-1B	0.184	0.021	0.823	0.030	0.25	0.026	1.293
	19MG21-42	19MG21-1B	0.330	0.057	0.842	0.046	-0.36	0.063	1.650
42	19MG21-42	19MG21-1B	0.529	0.106	0.787	0.038	0.20	0.100	1.521
	19MG21-42	19MG21-1B	0.256	0.016	0.812	0.019	0.24	0.038	1.412
	19MG21-42	19MG21-1B	0.166	0.021	0.827	0.035	0.38	0.026	1.384
43	**19MG21-43**	**19MG21-1B**			**no value**	**NAN**	**NaN**	**0.000**	**1.345**
44	19MG21-44	19MG21-1B	0.105	0.010	0.817	0.029	0.33	0.019	1.759
	19MG21-45	19MG21-1B	0.137	0.030	0.846	0.032	0.36	0.034	1.642
45	19MG21-45	19MG21-1B	0.181	0.010	0.821	0.020	0.27	0.028	1.511
	19MG21-45	19MG21-1B	0.275	0.038	0.863	0.052	0.72	0.040	1.410
	19MG21-46	19MG21-1B	0.081	0.007	0.820	0.034	0.37	0.015	1.912
46	19MG21-46	19MG21-1B	0.078	0.009	0.811	0.039	0.21	0.014	1.738
47	**19MG21-47**	**19MG21-1B**			**no value**	**NAN**	**NaN**	**0.004**	**1.304**
49	**19MG21-49**	**19MG21-1B**			**no value**	**NAN**	**NaN**	**0.000**	**1.440**
50	19MG21-50	19MG21-1B	0.115	0.008	0.832	0.030	0.23	0.017	1.502
52	19MG21-52	19MG21-4B	0.382	0.034	0.816	0.019	0.20	0.071	1.468
	19MG21-52	19MG21-4B	0.172	0.012	0.809	0.037	0.08	0.019	1.051
54	19MG21-54	19MG21-4B	0.541	0.021	0.812	0.018	0.41	0.064	1.185
55	19MG21-55	19MG21-4B	0.776	0.032	0.820	0.018	0.40	0.203	2.670
	19MG21-55	19MG21-4B	0.428	0.016	0.810	0.013	0.02	0.132	3.010

Spot	Source file (.FIN2)	Sample	^{238}U/^{206}Pb	±2σ (abs)	^{207}Pb/^{206}Pb	±2σ (abs)	Rho	U (ppm)	Pb (ppm)
56	19MG21-56	19MG21-4B	0.488	0.024	0.799	0.018	0.34	0.092	1.852
	19MG21-56	19MG21-4B	0.508	0.021	0.798	0.020	0.35	0.097	1.912
57	19MG21-57	19MG21-4B	0.876	0.042	0.802	0.017	0.10	0.280	3.093
	19MG21-57	19MG21-4B	0.703	0.020	0.800	0.013	0.23	0.176	2.479
58	19MG21-58	19MG21-4B	0.329	0.011	0.831	0.018	0.26	0.041	1.244
	19MG21-59	19MG21-4B	0.193	0.023	0.877	0.041	0.22	0.023	1.200
59	19MG21-59	19MG21-4B	0.330	0.021	0.796	0.028	0.35	0.038	1.121
	19MG21-59	19MG21-4B	0.323	0.033	0.823	0.029	0.03	0.039	1.094
60	19MG21-60	19MG21-4B	0.463	0.064	0.824	0.040	0.49	0.056	1.030
	19MG21-60	19MG21-4B	1.002	0.063	0.806	0.031	0.31	0.110	1.055
62	19MG21-62	19MG21-4B	0.283	0.023	0.831	0.023	0.46	0.036	1.236
	19MG21-63	19MG21-4B	0.361	0.039	0.815	0.029	0.35	0.050	1.316
63	19MG21-63	19MG21-4B	0.676	0.050	0.798	0.030	0.18	0.088	1.233
	19MG21-63	19MG21-4B	0.405	0.031	0.834	0.035	0.48	0.045	1.063
64	19MG21-64	19MG21-4B	0.338	0.038	0.808	0.022	0.18	0.059	1.375
66	19MG21-66	19MG21-4B	0.481	0.039	0.804	0.016	0.30	0.073	1.380
	19MG21-66	19MG21-4B	0.301	0.037	0.820	0.041	0.37	0.048	1.530
67	19MG21-67	19MG21-4B	0.166	0.010	0.822	0.019	0.19	0.022	1.209
68	19MG21-68	19MG21-4B	0.917	0.039	0.811	0.017	0.21	0.149	1.566
69	19MG21-69	19MG21-4B	1.198	0.062	0.815	0.016	0.08	0.218	1.716
70	19MG21-70	19MG21-4B	0.218	0.010	0.804	0.017	0.34	0.032	1.366
73	19MG21-73	19MG21-4B	0.143	0.009	0.813	0.018	0.39	0.023	1.492
74	19MG21-74	19MG21-4B	0.117	0.007	0.821	0.019	0.17	0.018	1.392
75	19MG21-75	19MG21-4B	0.150	0.009	0.814	0.012	0.14	0.017	0.929
	19MG21-75	19MG21-4B	0.204	0.010	0.813	0.012	0.31	0.052	2.357
76	19MG21-76	19MG21-4B	0.317	0.015	0.808	0.012	0.18	0.093	2.663
77	19MG21-77	19MG21-4B	2.857	0.090	0.806	0.016	0.33	0.384	1.281
78	19MG21-78	19MG21-4B	1.838	0.057	0.819	0.018	0.42	0.212	1.095
79	19MG21-79	19MG21-4B	0.154	0.019	0.805	0.024	0.02	0.027	1.580
	19MG21-79	19MG21-4B	0.104	0.008	0.809	0.022	0.20	0.018	1.673
80	19MG21-80	19MG21-4B	4.742	0.124	0.791	0.014	0.11	0.877	1.764
81	19MG21-81	19MG21-4B	3.831	0.078	0.794	0.013	0.28	0.901	2.262
82	19MG21-82	19MG21-4B	1.267	0.055	0.805	0.019	0.41	0.270	2.130
	19MG21-82	19MG21-4B	0.993	0.040	0.804	0.029	0.58	0.131	1.339
83	19MG21-83	19MG21-4B	0.424	0.017	0.814	0.017	0.38	0.055	1.209
84	19MG21-84	19MG21-4B	0.581	0.023	0.803	0.012	0.20	0.155	2.562
85	19MG21-85	19MG21-4B	2.315	0.075	0.808	0.015	0.36	0.334	1.444
86	19MG21-86	19MG21-4B	1.832	0.057	0.788	0.016	0.47	0.319	1.694
	19MG21-86	19MG21-4B	0.730	0.165	0.809	0.010	-0.17	1.860	14.300
87	19MG21-87	19MG21-4B	2.058	0.072	0.812	0.015	0.27	0.305	1.455
88	19MG21-88	19MG21-4B	1.255	0.033	0.808	0.017	0.51	0.171	1.364
89	19MG21-89	19MG21-4B	0.673	0.028	0.812	0.021	0.40	0.074	1.061
90	19MG21-90	19MG21-4B	0.467	0.020	0.821	0.017	0.23	0.056	1.165

Spot	Source file (.FIN2)	Sample	^{238}U/^{206}Pb	±2σ (abs)	^{207}Pb/^{206}Pb	±2σ (abs)	Rho	U (ppm)	Pb (ppm)
91	19MG21-91	19MG21-4B	0.715	0.028	0.821	0.026	0.32	0.091	1.270
	19MG21-91	19MG21-4B	0.418	0.032	0.797	0.023	0.13	0.057	1.269
92	19MG21-92	19MG21-4B	1.377	0.076	0.801	0.012	0.18	0.304	2.150
93	19MG21-93	19MG21-4B	1.013	0.031	0.796	0.016	0.25	0.157	1.558
	19MG21-93	19MG21-4B	1.451	0.078	0.808	0.034	-0.07	0.261	1.894
94	19MG21-94	19MG21-4B	1.279	0.057	0.814	0.026	0.34	0.242	1.930
	19MG21-94	19MG21-4B	1.172	0.055	0.814	0.020	0.40	0.200	1.660
95	19MG21-95	19MG21-4B	1.412	0.048	0.802	0.013	0.31	0.283	2.019
96	19MG21-96	19MG21-4B	1.972	0.058	0.814	0.017	0.49	0.264	1.339
97	19MG21-97	19MG21-4B	0.611	0.032	0.804	0.018	0.23	0.078	1.157
98	19MG21-98	19MG21-4B	1.431	0.074	0.811	0.015	0.16	0.272	1.940
99	19MG21-99	19MG21-4B	2.123	0.077	0.808	0.014	0.47	0.341	1.659
	19MG21-1B00	19MG21-4B	0.783	0.032	0.811	0.018	0.36	0.326	4.360
100	19MG21-1B00	19MG21-4B	1.099	0.098	0.812	0.020	0.24	0.385	3.350
	19MG21-1B00	19MG21-4B	1.122	0.047	0.805	0.019	0.47	0.329	2.960
101	19MG21-1B01	19MG21-4B	0.237	0.011	0.824	0.014	0.36	0.051	2.097
102	19MG21-1B02	19MG21-4B	0.163	0.018	0.795	0.030	0.07	0.032	1.820
103	19MG21-1B03	19MG21-4B	0.992	0.031	0.803	0.011	0.27	0.355	3.740

19MG46 from DA strain domain

Spot	Source file (.FIN2)	Sample	^{238}U/^{206}Pb	±2σ (abs)	^{207}Pb/^{206}Pb	±2σ (abs)	Rho	U (ppm)	Pb (ppm)
1	19MG46-1	19MG46-1	9.407	0.823	0.920	0.100	0.70	0.046	0.050
2	19MG46-2	19MG46-1	2.439	0.595	0.770	0.130	0.72	0.019	0.069
	19MG46-2	19MG46-1	6.211	1.620	0.830	0.230	0.97	0.022	0.024
3	19MG46-3	19MG46-1	7.692	1.716	0.910	0.130	0.75	0.075	0.094
	19MG46-3	19MG46-1	14.815	2.151	1.230	0.300	0.98	0.087	0.051
4	19MG46-4	19MG46-1	5.236	0.822	0.800	0.150	0.43	0.031	0.054
	19MG46-4	19MG46-1	11.494	4.360	0.850	0.140	0.55	0.103	0.071
5	19MG46-5	19MG46-1	11.236	2.020	0.749	0.081	0.81	0.121	0.100
	19MG46-5	19MG46-1	10.417	1.302	0.860	0.130	0.83	0.067	0.058
6	19MG46-6	19MG46-1	9.804	1.057	0.940	0.120	0.95	0.064	0.068
7	19MG46-7	19MG46-1	13.870	1.250	0.940	0.099	0.60	0.085	0.063
8	19MG46-8	19MG46-1	17.575	1.853	0.950	0.110	0.63	0.095	0.051
9	19MG46-9	19MG46-1	11.494	1.097	1.100	0.130	0.78	0.038	0.035
	19MG46-9	19MG46-1	7.752	1.562	0.900	0.190	0.87	0.061	0.093
	19MG46-9	19MG46-1	8.403	1.130	1.200	0.230	0.92	0.048	0.054
11	19MG46-11	19MG46-1	18.382	3.244	0.770	0.170	0.13	0.102	0.052
	19MG46-11	19MG46-1	12.987	2.530	0.970	0.200	0.53	0.080	0.071
	19MG46-11	19MG46-1	17.241	2.438	0.970	0.260	0.99	0.088	0.047
12	**19MG46-12**	**19MG46-1**	**11.494**	**1.850**	**0.800**	**0.170**	**0.80**	**0.066**	**0.049**
	19MG46-12	19MG46-1	17.544	3.386	1.300	0.560	0.93	0.068	0.044
	19MG46-12	**19MG46-1**	**16.920**	**2.691**	**0.900**	**0.190**	**0.90**	**0.093**	**0.058**
13	19MG46-13	19MG46-1	14.749	1.675	0.880	0.120	0.74	0.070	0.035

Spot	Source file (.FIN2)	Sample	^{238}U/^{206}Pb	±2σ (abs)	^{207}Pb/^{206}Pb	±2σ (abs)	Rho	U (ppm)	Pb (ppm)
14	19MG46-14	19MG46-1	1.587	0.428	0.800	0.120	0.86	0.050	0.287
	19MG46-14	19MG46-1	10.000	1.100	1.040	0.170	0.96	0.088	0.065
15	19MG46-15	19MG46-1	22.624	3.378	0.900	0.200	0.96	0.098	0.042
	19MG46-15	19MG46-1	11.905	1.842	1.030	0.350	0.93	0.050	0.035
16	19MG46-16	19MG46-1	7.937	1.323	0.830	0.100	0.58	0.103	0.114
	19MG46-16	19MG46-1	11.236	1.262	0.960	0.140	0.78	0.067	0.053
17	19MG46-17	19MG46-1	6.410	2.835	0.760	0.180	0.29	0.048	0.055
18	19MG46-18	19MG46-1	2.915	0.374	0.790	0.100	0.74	0.043	0.115
	19MG46-18	19MG46-1	6.250	0.820	0.900	0.110	0.52	0.073	0.075
19	19MG46-19	19MG46-1	7.407	0.878	0.840	0.120	0.67	0.099	0.101
	19MG46-19	19MG46-1	7.246	0.945	0.910	0.170	0.62	0.095	0.099
	19MG46-19	19MG46-1	6.711	0.856	1.010	0.150	0.73	0.047	0.048
20	19MG46-20	19MG46-1	9.524	1.542	1.180	0.370	0.97	0.061	0.049
	19MG46-20	19MG46-1	10.101	1.428	0.900	0.130	0.86	0.061	0.046
21	19MG46-21	19MG46-1	10.204	1.145	0.990	0.110	0.88	0.088	0.060
23	19MG46-23	19MG46-2	4.975	0.792	0.930	0.140	0.79	0.053	0.091
	19MG46-23	19MG46-2	9.259	1.029	1.010	0.150	0.78	0.064	0.059
24	19MG46-24b	19MG46-2	6.494	0.548	1.020	0.110	0.86	0.053	0.060
25	19MG46-25	19MG46-2	3.774	0.698	1.090	0.250	0.80	0.044	0.076
	19MG46-25	19MG46-2	6.897	0.713	0.870	0.130	0.81	0.049	0.051
26	**19MG46-26**	**19MG46-2**	**3.289**	**0.801**	**1.030**	**0.270**	**0.81**	**0.034**	**0.062**
	19MG46-26	**19MG46-2**	**1.923**	**0.851**	**0.670**	**0.110**	**0.52**	**0.023**	**0.060**
	19MG46-26	**19MG46-2**	**7.092**	**1.257**	**1.270**	**0.350**	**0.78**	**0.042**	**0.045**
	19MG46-26	**19MG46-2**	**6.135**	**3.237**	**0.760**	**0.140**	**0.75**	**0.077**	**0.115**
	19MG46-26	**19MG46-2**	**5.747**	**2.808**	**0.660**	**0.130**	**0.78**	**0.088**	**0.107**
	19MG46-26	**19MG46-2**	**6.452**	**3.413**	**1.280**	**0.410**	**0.41**	**0.085**	**0.097**
27	19MG46-27	19MG46-2	7.092	0.805	0.870	0.230	0.74	0.053	0.055
29	19MG46-29	19MG46-2	4.878	0.500	0.980	0.100	0.78	0.040	0.062
30	19MG46-30	19MG46-2	3.247	0.464	0.880	0.150	0.51	0.027	0.062
31	19MG46-31	19MG46-2	2.703	0.643	0.890	0.160	0.77	0.052	0.140
	19MG46-31	19MG46-2	1.124	0.353	0.710	0.120	0.35	0.025	0.230
32	19MG46-32	19MG46-2	2.924	0.522	1.070	0.210	0.68	0.026	0.094
	19MG46-32	19MG46-2	2.950	0.383	0.900	0.200	0.82	0.025	0.055
	19MG46-32	19MG46-2	4.065	1.091	1.040	0.470	1.00	0.030	0.047
	19MG46-32	19MG46-2	7.194	1.294	0.750	0.210	0.42	0.038	0.036
35	19MG46-35	19MG46-2	8.977	0.580	1.095	0.088	0.94	0.032	0.036
33	19MG46-33	19MG46-2	11.403	1.066	0.890	0.390	0.95	0.063	0.046
35	19MG46-35	19MG46-2	9.709	1.131	0.850	0.110	0.82	0.090	0.082
	19MG46-35	19MG46-2	11.236	1.894	1.080	0.250	0.99	0.082	0.059
36	19MG46-36	19MG46-2	3.676	0.608	0.657	0.098	0.46	0.070	0.124
	19MG46-36	19MG46-2	14.472	1.885	0.980	0.140	0.81	0.111	0.067
	19MG46-36	19MG46-2	13.889	2.315	1.010	0.210	0.67	0.088	0.050
37	19MG46-37	19MG46-2	11.364	1.291	1.020	0.220	0.64	0.079	0.062
	19MG46-37	19MG46-2	11.111	1.235	0.970	0.160	0.25	0.063	0.061

Spot	Source file (.FIN2)	Sample	$^{238}U/^{206}Pb$	±2σ (abs)	$^{207}Pb/^{206}Pb$	±2σ (abs)	Rho	U (ppm)	Pb (ppm)
38	19MG46-38	19MG46-2	10.101	2.143	0.830	0.150	0.64	0.099	0.078
	19MG46-38	19MG46-2	13.831	1.263	0.940	0.110	0.66	0.090	0.057
39	19MG46-39	19MG46-2	3.831	0.705	1.020	0.220	0.68	0.034	0.071
	19MG46-39	19MG46-2	8.333	0.972	1.120	0.210	0.99	0.063	0.067
40	19MG46-40	19MG46-2	7.353	0.919	0.910	0.120	0.74	0.067	0.089
	19MG46-40	19MG46-2	7.813	0.916	0.980	0.150	0.87	0.042	0.045
41	19MG46-41	19MG46-3	6.579	0.779	0.850	0.120	0.71	0.061	0.075
	19MG46-41	19MG46-3	6.098	1.227	0.770	0.180	0.77	0.052	0.068
	19MG46-41	19MG46-3	6.369	0.933	0.940	0.180	0.88	0.041	0.052
42	19MG46-42	19MG46-3	8.475	2.011	0.940	0.220	0.75	0.072	0.088
	19MG46-42	19MG46-3	16.863	2.133	1.030	0.190	0.65	0.081	0.042
43	19MG46-43	19MG46-3	8.197	0.806	1.060	0.130	0.72	0.065	0.082
44	19MG46-44	19MG46-3	12.453	1.210	1.240	0.230	0.82	0.078	0.059
45	19MG46-45	19MG46-3	2.778	0.772	0.870	0.170	0.73	0.058	0.147
	19MG46-45	19MG46-3	12.690	1.433	1.200	0.180	0.99	0.058	0.052
46	19MG46-46	19MG46-3	5.051	1.530	0.970	0.260	0.39	0.060	0.078
	19MG46-46	19MG46-3	12.987	1.855	0.940	0.160	0.75	0.082	0.063
	19MG46-46	19MG46-3	9.434	1.958	0.880	0.200	0.79	0.081	0.099
	19MG46-46	19MG46-3	6.494	1.096	0.720	0.150	0.77	0.046	0.058
	19MG46-46	19MG46-3	5.495	1.238	0.800	0.200	1.00	0.032	0.055
47	**19MG46-47**	**19MG46-3**	**2.500**	**1.063**	**0.760**	**0.150**	**0.57**	**0.032**	**0.147**
	19MG46-47	**19MG46-3**	**6.250**	**1.289**	**1.190**	**0.250**	**0.99**	**0.034**	**0.062**
	19MG46-47	**19MG46-3**	**4.762**	**2.268**	**0.760**	**0.280**	**0.55**	**0.046**	**0.092**
	19MG46-47	**19MG46-3**	**12.658**	**2.564**	**1.180**	**0.400**	**0.61**	**0.045**	**0.036**
48	19MG46-48	19MG46-3	5.348	0.601	0.867	0.075	0.57	0.051	0.086
49	19MG46-49	19MG46-3	2.933	0.396	0.890	0.120	0.66	0.025	0.085
50	19MG46-50	19MG46-3	7.519	0.735	0.910	0.090	0.62	0.049	0.062
51	**19MG46-51**	**19MG46-3**			**no value**	**NAN**	**NaN**	**0.003**	**0.093**
52	19MG46-52	19MG46-3	6.757	1.415	0.790	0.180	0.73	0.053	0.061
	19MG46-52	19MG46-3	12.048	2.177	0.710	0.180	0.87	0.075	0.053
	19MG46-52	19MG46-3	10.417	1.519	1.060	0.310	0.87	0.034	0.035
53	19MG46-53	19MG46-3	6.757	0.913	1.240	0.230	0.91	0.041	0.057
54	19MG46-54	19MG46-3	11.364	1.291	0.740	0.410	0.81	0.039	0.031
55	19MG46-55	19MG46-3	3.289	1.060	0.830	0.220	0.55	0.034	0.098
	19MG46-55	19MG46-3	7.813	0.977	1.130	0.320	0.97	0.047	0.073
	19MG46-55	19MG46-3	4.386	1.000	0.657	0.094	0.59	0.040	0.083
56	19MG46-56	19MG46-3	4.115	1.236	0.940	0.150	0.70	0.041	0.129
	19MG46-56	19MG46-3	8.591	0.672	0.881	0.098	0.66	0.055	0.071
57	19MG46-57	19MG46-3	11.099	0.998	0.950	0.140	0.98	0.093	0.084
58	19MG46-58	19MG46-3	5.848	1.094	1.240	0.260	0.37	0.057	0.120
	19MG46-58	19MG46-3	9.091	1.736	0.920	0.200	0.63	0.061	0.072
	19MG46-58	19MG46-3	7.299	2.824	0.800	0.170	0.95	0.047	0.060
	19MG46-58	19MG46-3	6.452	0.957	0.950	0.200	0.68	0.031	0.045
	19MG46-58	19MG46-3	7.353	1.460	1.020	0.240	0.72	0.026	0.040

Spot	Source file (.FIN2)	Sample	^{238}U/^{206}Pb	±2σ (abs)	^{207}Pb/^{206}Pb	±2σ (abs)	Rho	U (ppm)	Pb (ppm)
59	19MG46-59	19MG46-3	12.903	1.365	0.940	0.200	0.82	0.064	0.051
60	19MG46-60	19MG46-3	10.101	1.122	0.920	0.110	0.77	0.061	0.054
	19MG46-61	19MG46-4	7.092	1.358	0.740	0.390	0.67	0.031	0.035
61	19MG46-61	19MG46-4	5.618	1.515	0.650	0.210	0.29	0.019	0.022
	19MG46-61	19MG46-4	13.889	3.665	0.730	0.260	0.97	0.035	0.024
62	19MG46-62	19MG46-4	5.988	1.649	1.000	0.300	0.90	0.057	0.088
	19MG46-62	19MG46-4	6.897	1.189	0.100	0.760	0.73	0.027	0.034
63	19MG46-63	19MG46-4	12.821	1.808	0.530	0.440	0.75	0.049	0.039
64	19MG46-64	19MG46-4	8.475	1.436	0.610	0.420	0.90	0.036	0.036
	19MG46-65	**19MG46-4**	**5.376**	**1.330**	**0.960**	**0.250**	**0.25**	**0.037**	0.067
65	**19MG46-65**	**19MG46-4**	**8.000**	**1.472**	**-0.040**	**0.880**	**0.87**	**0.025**	0.032
	19MG46-65	**19MG46-4**	**15.152**	**3.903**	**0.470**	**0.680**	**0.73**	**0.044**	0.023
66	19MG46-66	19MG46-4	4.292	1.308	0.300	1.100	0.63	0.033	0.064
	19MG46-66	19MG46-4	9.901	2.059	0.100	1.300	0.91	0.022	0.024
67	**19MG46-67**	**19MG46-4**	**5.618**	**1.357**	**-0.100**	**1.400**	**0.85**	**0.017**	**0.030**
	19MG46-67	**19MG46-4**	**20.325**	**4.049**	**0.080**	**0.770**	**0.69**	**0.039**	**0.022**
	19MG46-68	**19MG46-4**	**19.608**	**4.229**	**0.960**	**0.360**	**0.99**	**0.096**	**0.038**
	19MG46-68	**19MG46-4**	**17.241**	**3.864**	**1.170**	**0.400**	**0.99**	**0.051**	**0.031**
68	**19MG46-68**	**19MG46-4**	**16.393**	**3.762**	**0.300**	**1.000**	**0.86**	**0.040**	**0.021**
	19MG46-68	**19MG46-4**	**18.868**	**6.408**	**0.700**	**0.280**	**0.93**	**0.049**	**0.028**
	19MG46-68	**19MG46-4**	**15.385**	**4.260**	**-0.400**	**1.800**	**0.88**	**0.061**	**0.031**
69	**19MG46-69**	**19MG46-4**	**20.243**	**3.442**	**-1.400**	**1.100**	**0.79**	**0.057**	**0.026**
	19MG46-70	19MG46-4	9.434	2.136	0.880	0.220	0.96	0.037	0.046
70	19MG46-70	19MG46-4	0.676	0.169	0.744	0.065	-0.09	0.037	0.500
	19MG46-70	19MG46-4	7.299	1.865	0.700	0.210	0.18	0.035	0.046
	19MG46-70	19MG46-4	2.041	0.541	0.700	0.130	0.89	0.018	0.067
71	**19MG46-71**	**19MG46-4**	**11.111**	**2.099**	**-0.900**	**1.000**	**0.81**	**0.022**	**0.022**
	19MG46-72	19MG46-4	5.051	1.199	0.860	0.230	0.73	0.042	0.084
72	19MG46-72	19MG46-4	7.752	2.464	1.000	0.290	0.52	0.039	0.044
	19MG46-72	19MG46-4	17.007	2.603	1.130	0.230	0.98	0.066	0.039
	19MG46-72	19MG46-4	7.937	2.016	0.870	0.230	0.72	0.047	0.057
73	19MG46-73	19MG46-4	18.762	2.358	0.770	0.350	0.75	0.069	0.032
74	19MG46-74	19MG46-4	4.255	1.177	0.870	0.240	0.45	0.019	0.034
75	19MG46-75	19MG46-4	11.628	1.622	0.550	0.680	0.77	0.043	0.035
	19MG46-76	19MG46-5	5.102	1.145	0.780	0.190	0.73	0.052	0.080
76	19MG46-76	19MG46-5	8.696	2.722	0.810	0.260	0.55	0.043	0.051
	19MG46-76	19MG46-5	7.463	1.170	0.970	0.140	0.98	0.053	0.052
	19MG46-77	19MG46-5	10.101	1.224	0.710	0.150	0.59	0.081	0.074
77	19MG46-77	19MG46-5	11.364	2.066	1.020	0.250	0.50	0.068	0.053
	19MG46-77	19MG46-5	8.065	1.431	0.930	0.260	0.43	0.035	0.036
	19MG46-77	19MG46-5	16.129	3.382	1.180	0.360	0.99	0.060	0.045

Spot	Source file (.FIN2)	Sample	^{238}U/^{206}Pb	±2σ (abs)	^{207}Pb/^{206}Pb	±2σ (abs)	Rho	U (ppm)	Pb (ppm)
	19MG46-78	19MG46-5	8.547	1.972	0.760	0.140	0.80	0.170	0.167
	19MG46-78	19MG46-5	18.051	2.672	0.810	0.110	0.61	0.289	0.142
78	19MG46-78	19MG46-5	9.901	1.470	0.790	0.140	0.60	0.149	0.108
	19MG46-78	19MG46-5	13.333	5.867	0.605	0.089	-0.43	0.620	0.114
	19MG46-78	19MG46-5	6.757	0.959	0.740	0.094	0.75	0.081	0.110
	19MG46-79	19MG46-5	3.571	1.276	0.670	0.130	-0.13	0.055	0.111
79	19MG46-79	19MG46-5	6.494	1.434	0.840	0.260	0.79	0.029	0.038
	19MG46-79	19MG46-5	5.587	2.715	0.690	0.290	1.00	0.026	0.023
80	19MG46-80	19MG46-5	5.435	1.241	0.980	0.310	0.56	0.042	0.069
	19MG46-80	19MG46-5	13.514	1.826	0.830	0.430	0.90	0.107	0.059
81	19MG46-81	19MG46-5	5.376	0.607	1.100	0.180	0.97	0.035	0.047
	19MG46-82	19MG46-5	4.739	1.235	0.860	0.100	0.32	0.166	0.278
82	19MG46-82	19MG46-5	12.195	2.082	0.950	0.130	0.24	0.215	0.154
	19MG46-82	19MG46-5	11.905	2.126	0.780	0.120	-0.03	0.290	0.095
	19MG46-83	19MG46-5	6.289	0.831	0.731	0.085	0.79	0.103	0.119
83	19MG46-83	19MG46-5	7.463	1.726	0.940	0.120	0.68	0.126	0.186
	19MG46-83	19MG46-5	9.615	1.479	0.680	0.130	0.15	0.126	0.096
	19MG46-83	19MG46-5	14.286	2.449	1.010	0.210	0.88	0.145	0.095
84	19MG46-84	19MG46-5	10.204	1.145	0.890	0.140	1.00	0.076	0.059
	19MG46-84	19MG46-5	14.286	2.857	1.010	0.280	0.84	0.059	0.039
	19MG46-85	19MG46-5	4.484	0.623	1.030	0.250	0.94	0.029	0.049
85	19MG46-85	19MG46-5	10.101	2.959	0.870	0.370	1.00	0.044	0.024
	19MG46-85	**19MG46-5**	**16.393**	**3.225**	**0.150**	**0.970**	**0.75**	**0.049**	**0.031**
	19MG46-85	19MG46-5	2.778	1.929	1.060	0.240	0.14	0.036	0.110
86	19MG46-86	19MG46-5	5.464	1.284	0.710	0.150	0.58	0.067	0.099
	19MG46-86	19MG46-5	16.313	2.502	0.970	0.130	0.77	0.130	0.046
	19MG46-87	19MG46-5	10.417	1.953	0.900	0.200	0.68	0.074	0.083
	19MG46-87	19MG46-5	10.417	1.736	1.030	0.490	0.90	0.052	0.043
87	19MG46-87	19MG46-5	8.333	2.153	0.720	0.270	0.99	0.043	0.045
	19MG46-87	19MG46-5	11.765	5.121	0.740	0.300	0.99	0.031	0.023
	19MG46-87	19MG46-5	14.925	5.124	1.020	0.370	0.89	0.058	0.027
88	19MG46-88	19MG46-5	6.803	1.111	0.900	0.210	0.53	0.066	0.053
	19MG46-89	19MG46-5	4.065	1.058	0.940	0.210	0.80	0.050	0.089
89	19MG46-89	19MG46-5	13.333	1.778	1.180	0.220	0.96	0.057	0.038
	19MG46-89	19MG46-5	21.930	4.761	0.750	0.200	0.96	0.125	0.043
90	19MG46-90	19MG46-5	11.494	1.189	0.720	0.480	0.91	0.061	0.051
91	19MG46-91	19MG46-6	15.175	1.773	0.390	0.700	0.87	0.050	0.028
92	19MG46-92	19MG46-6	11.403	1.248	0.500	0.590	0.85	0.051	0.043
93	19MG46-93	19MG46-6	19.455	2.157	0.580	0.630	0.75	0.070	0.038
94	19MG46-94	19MG46-6	19.646	2.277	0.940	0.340	0.90	0.065	0.031

Spot	Source file (.FIN2)	Sample	^{238}U/^{206}Pb	±2σ (abs)	^{207}Pb/^{206}Pb	±2σ (abs)	Rho	U (ppm)	Pb (ppm)
	19MG46-95	19MG46-6	19.231	4.068	1.150	0.220	0.35	0.126	0.080
	19MG46-95	19MG46-6	33.898	9.767	0.600	0.130	0.09	0.440	0.044
95	19MG46-95	19MG46-6	35.587	5.319	0.910	0.230	0.74	0.187	0.049
	19MG46-95	19MG46-6	28.986	8.318	0.870	0.250	0.20	0.199	0.037
	19MG46-95	19MG46-6	19.231	4.808	0.910	0.290	0.86	0.069	0.038
	19MG46-96	19MG46-6	8.850	1.410	1.110	0.210	0.78	0.048	0.062
96	19MG46-96	19MG46-6	10.204	1.874	0.800	0.170	0.79	0.053	0.047
	19MG46-96	19MG46-6	11.364	1.679	1.200	0.650	0.91	0.037	0.037
97	19MG46-97	19MG46-6	5.556	0.586	1.140	0.210	0.73	0.029	0.047
98	19MG46-98	19MG46-6	21.277	5.885	0.970	0.300	1.00	0.113	0.060
	19MG46-98	19MG46-6	32.154	3.929	0.670	0.480	0.91	0.118	0.034
	19MG46-99	19MG46-6	7.634	1.690	0.850	0.240	0.57	0.072	0.098
99	19MG46-99	19MG46-6	29.412	10.381	0.680	0.170	0.41	0.410	0.075
	19MG46-99	19MG46-6	5.556	3.086	1.060	0.420	0.98	0.096	0.250
	19MG46-99	19MG46-6	0.338	0.030	0.797	0.027	0.06	0.076	2.090
100	19MG46-100	19MG46-6	7.353	1.352	0.660	0.210	0.74	0.026	0.028

19MG74-A from DA strain domain

Spot	Source file (.FIN2)	Sample	^{238}U/^{206}Pb	±2σ (abs)	^{207}Pb/^{206}Pb	±2σ (abs)	Rho	U (ppm)	Pb (ppm)
	19MG74-1-1	19MG74-A-6B	2.304	0.122	0.790	0.033	0.61	0.360	1.630
1	19MG74-1-1	19MG74-A-6B	1.715	0.076	0.805	0.025	0.43	0.287	1.714
	19MG74-1-1	19MG74-A-6B	2.041	0.104	0.827	0.041	0.41	0.306	1.622
	19MG74-1-1	19MG74-A-6B	2.907	0.228	0.809	0.030	0.49	0.426	1.600
	19MG74-1-2	**19MG74-A-6B**	**2.933**	**0.129**	**0.793**	**0.037**	**0.51**	**0.473**	**1.668**
2	**19MG74-1-2**	**19MG74-A-6B**	**4.739**	**0.629**	**0.811**	**0.055**	**0.58**	**0.560**	**1.260**
	19MG74-1-2	**19MG74-A-6B**	**1.923**	**0.518**	**1.260**	**0.270**	**0.09**	**0.276**	**1.650**
	19MG74-1-2	**19MG74-A-6B**	**0.794**	**0.315**	**1.710**	**0.440**	**0.24**	**0.152**	**0.760**
	19MG74-1-3	19MG74-A-6B	0.971	0.104	0.815	0.041	0.74	0.167	1.623
3	19MG74-1-3	19MG74-A-6B	0.799	0.045	0.816	0.039	0.10	0.131	1.725
	19MG74-1-3	19MG74-A-6B	0.976	0.080	0.797	0.032	0.15	0.156	1.574
	19MG74-1-3	19MG74-A-6B	1.466	0.196	0.784	0.040	0.06	0.234	1.570
	19MG74-1-4	19MG74-A-6B	2.123	0.099	0.816	0.039	0.56	0.314	1.487
4	19MG74-1-4	19MG74-A-6B	1.721	0.080	0.796	0.022	0.23	0.256	1.493
	19MG74-1-4	19MG74-A-6B	3.311	0.219	0.826	0.042	0.56	0.458	1.396
	19MG74-1-4	19MG74-A-6B	1.880	0.177	0.809	0.039	0.14	0.276	1.351
	19MG74-1-5	19MG74-A-6B	0.518	0.027	0.822	0.032	0.50	0.095	1.873
5	19MG74-1-5	19MG74-A-6B	0.625	0.029	0.821	0.026	0.31	0.106	1.690
	19MG74-1-5	19MG74-A-6B	0.676	0.073	0.825	0.040	0.61	0.109	1.630
	19MG74-1-5	19MG74-A-6B	0.541	0.044	0.791	0.037	0.65	0.089	1.580

Spot	Source file (.FIN2)	Sample	^{238}U/^{206}Pb	±2σ (abs)	^{207}Pb/^{206}Pb	±2σ (abs)	Rho	U (ppm)	Pb (ppm)
	19MG74-1-6	19MG74-A-6B	2.288	0.115	0.806	0.032	0.30	0.461	1.920
	19MG74-1-6	19MG74-A-6B	2.924	0.180	0.800	0.045	0.58	0.608	2.040
	19MG74-1-6	19MG74-A-6B	2.513	0.126	0.792	0.051	0.25	0.464	1.849
6	19MG74-1-6	19MG74-A-6B	3.247	0.253	0.775	0.086	0.67	0.555	1.690
	19MG74-1-6	19MG74-A-6B	2.445	0.102	0.817	0.029	0.48	0.441	1.820
	19MG74-1-6	19MG74-A-6B	3.003	0.225	0.827	0.051	0.49	0.539	1.797
	19MG74-1-6	19MG74-A-6B	2.959	0.333	0.806	0.039	0.33	0.561	1.713
	19MG74-1-7	19MG74-A-6B	0.926	0.094	0.809	0.049	0.30	0.179	1.740
	19MG74-1-7	19MG74-A-6B	0.885	0.094	0.785	0.053	0.30	0.185	1.880
7	19MG74-1-7	19MG74-A-6B	1.185	0.101	0.821	0.032	0.30	0.226	1.855
	19MG74-1-7	19MG74-A-6B	1.095	0.054	0.789	0.026	0.46	0.196	1.679
	19MG74-1-7	19MG74-A-6B	1.681	0.085	0.810	0.027	0.67	0.274	1.588
	19MG74-1-8	19MG74-A-6B	1.672	0.115	0.787	0.060	0.23	0.370	1.960
	19MG74-1-8	19MG74-A-6B	2.092	0.245	0.814	0.049	0.17	0.468	1.920
	19MG74-1-8	19MG74-A-6B	1.901	0.195	0.738	0.064	0.75	0.415	2.040
8	19MG74-1-8	19MG74-A-6B	2.439	0.107	0.835	0.038	0.46	0.494	1.883
	19MG74-1-8	19MG74-A-6B	2.347	0.138	0.798	0.037	0.49	0.485	1.910
	19MG74-1-8	19MG74-A-6B	2.375	0.130	0.875	0.041	0.46	0.465	1.870
	19MG74-1-8	19MG74-A-6B	1.961	0.211	0.742	0.062	0.50	0.421	1.940
	19MG74-1-8	19MG74-A-6B	3.077	0.246	0.832	0.055	0.65	0.598	1.783
	19MG74-1-9	19MG74-A-6B	2.375	0.248	0.810	0.035	0.02	0.440	1.590
9	19MG74-1-9	19MG74-A-6B	1.567	0.057	0.805	0.026	0.60	0.302	1.666
	19MG74-1-9	19MG74-A-6B	2.288	0.141	0.821	0.036	0.74	0.417	1.574
	19MG74-1-9	19MG74-A-6B	1.608	0.090	0.829	0.031	0.31	0.271	1.501
	19MG74-1-10	19MG74-A-6B	1.996	0.147	0.811	0.048	0.49	0.400	1.697
	19MG74-1-10	19MG74-A-6B	2.865	0.378	0.788	0.035	0.45	0.624	1.880
	19MG74-1-10	19MG74-A-6B	2.342	0.176	0.797	0.044	0.71	0.504	1.921
10	19MG74-1-10	19MG74-A-6B	2.268	0.298	0.799	0.053	0.05	0.522	1.980
	19MG74-1-10	19MG74-A-6B	1.613	0.057	0.832	0.026	0.65	0.343	1.882
	19MG74-1-10	19MG74-A-6B	1.319	0.061	0.806	0.028	0.41	0.292	1.991
	19MG74-1-10	19MG74-A-6B	1.618	0.139	0.850	0.056	0.64	0.374	2.086
	19MG74-1-11	19MG74-A-6B	1.786	0.140	0.831	0.028	0.05	0.357	1.677
	19MG74-1-11	19MG74-A-6B	1.362	0.110	0.811	0.034	0.69	0.271	1.682
11	19MG74-1-11	19MG74-A-6B	1.953	0.233	0.811	0.028	0.24	0.369	1.510
	19MG74-1-11	19MG74-A-6B	1.368	0.116	0.839	0.030	0.37	0.227	1.480
	19MG74-1-11	19MG74-A-6B	1.730	0.099	0.834	0.036	0.49	0.320	1.631
	19MG74-1-12	19MG74-A-6B	2.342	0.214	0.867	0.058	0.65	0.417	1.550
	19MG74-1-12	19MG74-A-6B	3.067	0.216	0.833	0.043	0.58	0.538	1.480
12	19MG74-1-12	19MG74-A-6B	2.500	0.194	0.775	0.040	0.55	0.454	1.441
	19MG74-1-12	19MG74-A-6B	2.747	0.121	0.800	0.030	0.40	0.690	2.070
	19MG74-1-12	19MG74-A-6B	1.965	0.282	0.836	0.053	0.58	0.679	2.990
	19MG74-1-12	19MG74-A-6B	2.959	0.149	0.810	0.034	0.46	0.503	1.490

Spot	Source file (.FIN2)	Sample	^{238}U/^{206}Pb	±2σ (abs)	^{207}Pb/^{206}Pb	±2σ (abs)	Rho	U (ppm)	Pb (ppm)
	19MG74-1-13	19MG74-A-6B	1.297	0.165	0.823	0.079	0.28	0.311	2.050
	19MG74-1-13	19MG74-A-6B	1.379	0.105	0.783	0.042	0.33	0.365	2.120
13	19MG74-1-13	19MG74-A-6B	2.392	0.223	0.794	0.037	0.42	0.559	1.822
	19MG74-1-13	19MG74-A-6B	1.684	0.094	0.825	0.032	0.47	0.367	1.757
	19MG74-1-13	19MG74-A-6B	2.445	0.143	0.797	0.035	0.55	0.498	1.703
	19MG74-1-14	19MG74-A-6B	2.525	0.230	0.771	0.028	0.30	0.635	1.828
	19MG74-1-14	19MG74-A-6B	1.912	0.069	0.811	0.031	0.66	0.376	1.625
14	19MG74-1-14	19MG74-A-6B	2.488	0.099	0.816	0.039	0.73	0.487	1.623
	19MG74-1-14	19MG74-A-6B	3.521	0.136	0.806	0.035	0.46	0.612	1.487
	19MG74-1-14	19MG74-A-6B	3.247	0.369	0.794	0.064	0.73	0.581	1.520
	19MG74-1-15	19MG74-A-6B	3.846	0.325	0.805	0.046	0.53	0.827	1.670
	19MG74-1-15	19MG74-A-6B	3.344	0.313	0.812	0.048	0.06	0.584	1.450
15	19MG74-1-15	19MG74-A-6B	3.861	0.268	0.844	0.062	0.74	0.606	1.274
	19MG74-1-15	19MG74-A-6B	3.484	0.255	0.783	0.047	0.87	0.534	1.246
	19MG74-1-15	19MG74-A-6B	3.636	0.264	0.824	0.051	0.71	0.571	1.314
	19MG74-1-15	19MG74-A-6B	2.463	0.158	0.841	0.029	0.24	0.406	1.371
	19MG74-1-16	19MG74-A-6B	1.639	0.161	0.812	0.040	0.47	0.377	1.809
	19MG74-1-16	19MG74-A-6B	1.890	0.257	0.775	0.059	0.67	0.503	2.140
	19MG74-1-16	19MG74-A-6B	3.236	0.367	0.794	0.049	0.42	0.850	2.004
16	19MG74-1-16	19MG74-A-6B	2.660	0.127	0.817	0.040	0.40	0.635	1.975
	19MG74-1-16	19MG74-A-6B	2.119	0.144	0.797	0.035	0.71	0.462	1.753
	19MG74-1-16	19MG74-A-6B	2.584	0.093	0.793	0.030	0.50	0.494	1.587
	19MG74-1-16	19MG74-A-6B	2.817	0.254	0.840	0.049	0.62	0.462	1.282
	19MG74-1-17	19MG74-A-6B	2.096	0.123	0.821	0.043	0.52	0.529	2.200
	19MG74-1-17	19MG74-A-6B	1.934	0.071	0.815	0.034	0.59	0.479	2.028
	19MG74-1-17	19MG74-A-6B	2.494	0.174	0.810	0.035	0.15	0.541	1.816
17	19MG74-1-17	19MG74-A-6B	2.865	0.181	0.803	0.049	0.60	0.630	1.845
	19MG74-1-17	19MG74-A-6B	2.770	0.261	0.810	0.050	0.36	0.586	1.642
	19MG74-1-17	19MG74-A-6B	3.077	0.199	0.865	0.052	0.77	0.607	1.704
	19MG74-1-17	19MG74-A-6B	2.551	0.143	0.820	0.035	0.67	0.522	1.792
18	19MG74-1-18	19MG74-A-6B	1.789	0.253	0.783	0.034	0.41	0.594	2.400
	19MG74-1-18	19MG74-A-6B	1.020	0.034	0.807	0.018	0.48	0.250	2.070
	19MG74-1-19	19MG74-A-6B	1.592	0.109	0.832	0.047	0.43	0.340	1.980
	19MG74-1-19	19MG74-A-6B	1.675	0.149	0.752	0.048	0.53	0.373	1.820
19	19MG74-1-19	19MG74-A-6B	2.160	0.131	0.812	0.050	0.77	0.419	1.691
	19MG74-1-19	19MG74-A-6B	2.725	0.141	0.819	0.035	0.76	0.496	1.659
	19MG74-1-19	19MG74-A-6B	2.294	0.116	0.815	0.033	0.39	0.391	1.590
20	19MG74-1-20	19MG74-A-6B	3.300	0.120	0.831	0.027	0.56	0.661	1.815
	19MG74-1-20	19MG74-A-6B	2.370	0.090	0.806	0.027	0.49	0.461	1.744
	19MG74-1-21	19MG74-A-6B	1.852	0.230	0.864	0.044	0.27	0.410	2.064
21	19MG74-1-21	19MG74-A-6B	2.257	0.076	0.795	0.020	0.41	0.443	1.793
	19MG74-1-21	19MG74-A-6B	2.237	0.130	0.807	0.050	0.69	0.382	1.590

Spot	Source file (.FIN2)	Sample	^{238}U/^{206}Pb	±2σ (abs)	^{207}Pb/^{206}Pb	±2σ (abs)	Rho	U (ppm)	Pb (ppm)
	19MG74-1-22	19MG74-A-6B	1.067	0.071	0.787	0.050	0.59	0.252	2.180
	19MG74-1-22	19MG74-A-6B	1.418	0.095	0.808	0.048	0.66	0.273	1.800
22	19MG74-1-22	19MG74-A-6B	1.202	0.098	0.782	0.054	0.80	0.227	1.730
	19MG74-1-22	19MG74-A-6B	1.208	0.063	0.792	0.034	0.52	0.218	1.780
	19MG74-1-22	19MG74-A-6B	1.701	0.095	0.819	0.023	0.38	0.291	1.660
	19MG74-1-23	19MG74-A-6B	1.942	0.083	0.770	0.028	0.55	0.372	1.819
23	19MG74-1-23	19MG74-A-6B	2.364	0.179	0.791	0.044	0.60	0.463	1.820
	19MG74-1-23	19MG74-A-6B	2.577	0.113	0.819	0.027	0.40	0.487	1.914
	19MG74-1-23	19MG74-A-6B	3.135	0.167	0.797	0.029	0.52	0.542	1.719
	19MG74-1-24	19MG74-A-6B	2.865	0.148	0.799	0.028	0.65	0.533	1.853
24	19MG74-1-24	19MG74-A-6B	2.309	0.176	0.782	0.038	0.56	0.468	1.990
	19MG74-1-24	19MG74-A-6B	1.721	0.136	0.812	0.054	0.89	0.302	1.824
	19MG74-1-24	19MG74-A-6B	1.037	0.071	0.811	0.030	0.32	0.189	1.854
	19MG74-1-25	19MG74-A-6B	3.040	0.194	0.820	0.049	0.65	0.658	2.200
25	19MG74-1-25	19MG74-A-6B	3.125	0.146	0.814	0.033	0.35	0.596	1.950
	19MG74-1-25	19MG74-A-6B	2.370	0.084	0.813	0.026	0.58	0.426	1.888
26	19MG74-1-26	19MG74-A-6B	0.803	0.059	0.812	0.030	0.30	0.163	2.054
	19MG74-1-26	19MG74-A-6B	2.294	0.089	0.840	0.022	0.33	0.365	1.778
	19MG74-1-27	19MG74-A-6B	1.070	0.077	0.819	0.026	0.34	0.202	1.996
27	19MG74-1-27	19MG74-A-6B	2.105	0.160	0.839	0.035	0.38	0.335	1.679
	19MG74-1-27	19MG74-A-6B	1.667	0.142	0.785	0.047	0.70	0.258	1.570
	19MG74-1-27	19MG74-A-6B	2.008	0.085	0.843	0.040	0.86	0.292	1.652
	19MG74-1-28	19MG74-A-6B	2.538	0.129	0.796	0.031	0.35	0.514	2.298
	19MG74-1-28	19MG74-A-6B	2.538	0.174	0.815	0.036	0.01	0.447	1.993
28	19MG74-1-28	19MG74-A-6B	2.105	0.137	0.814	0.048	0.41	0.366	1.990
	19MG74-1-28	19MG74-A-6B	1.984	0.114	0.801	0.032	0.75	0.325	1.835
	19MG74-1-28	19MG74-A-6B	2.994	0.170	0.779	0.028	0.45	0.490	1.861
	19MG74-1-29	19MG74-A-5B	3.145	0.148	0.774	0.036	-0.03	0.505	1.712
	19MG74-1-29	19MG74-A-5B	4.762	0.590	0.799	0.053	0.55	0.778	1.740
29	19MG74-1-29	19MG74-A-5B	3.115	0.252	0.823	0.044	0.36	0.494	1.820
	19MG74-1-29	19MG74-A-5B	2.874	0.124	0.800	0.025	0.64	0.379	1.527
	19MG74-1-29	19MG74-A-5B	1.821	0.096	0.843	0.035	0.50	0.203	1.410
	19MG74-1-30	19MG74-A-5B	2.232	0.095	0.797	0.027	0.47	0.352	1.772
	19MG74-1-30	19MG74-A-5B	2.353	0.183	0.754	0.045	0.32	0.364	1.848
30	19MG74-1-30	19MG74-A-5B	1.992	0.099	0.825	0.046	0.79	0.287	1.742
	19MG74-1-30	19MG74-A-5B	2.415	0.175	0.815	0.053	0.20	0.355	1.751
	19MG74-1-30	19MG74-A-5B	2.967	0.150	0.779	0.048	0.45	0.426	1.733
	19MG74-1-30	19MG74-A-5B	3.597	0.233	0.812	0.054	0.78	0.488	1.650
	19MG74-1-31	19MG74-A-5B	2.770	0.200	0.809	0.040	0.14	0.502	1.911
31	19MG74-1-31	19MG74-A-5B	2.882	0.125	0.803	0.038	0.55	0.467	1.941
	19MG74-1-31	19MG74-A-5B	2.959	0.140	0.811	0.031	0.45	0.443	1.751
	19MG74-1-31	19MG74-A-5B	2.160	0.107	0.818	0.036	0.49	0.313	1.768

Spot	Source file (.FIN2)	Sample	^{238}U/^{206}Pb	±2σ (abs)	^{207}Pb/^{206}Pb	±2σ (abs)	Rho	U (ppm)	Pb (ppm)
32	19MG74-1-32	19MG74-A-5B	2.421	0.129	0.840	0.035	0.17	0.381	1.960
	19MG74-1-32	19MG74-A-5B	4.717	0.823	0.817	0.064	0.24	0.770	1.900
	19MG74-1-32	19MG74-A-5B	2.488	0.087	0.807	0.031	0.43	0.371	1.920
	19MG74-1-32	19MG74-A-5B	2.667	0.114	0.819	0.025	0.35	0.351	1.649
33	19MG74-1-33	19MG74-A-5B	1.730	0.093	0.833	0.030	0.23	0.271	1.974
	19MG74-1-33	19MG74-A-5B	2.506	0.170	0.874	0.039	0.33	0.363	1.854
	19MG74-1-33	19MG74-A-5B	2.294	0.116	0.814	0.027	0.30	0.329	1.739
	19MG74-1-33	19MG74-A-5B	1.838	0.084	0.838	0.025	0.21	0.239	1.591
34	19MG74-1-34	19MG74-A-5B	2.967	0.273	0.838	0.046	0.42	0.471	2.020
	19MG74-1-34	19MG74-A-5B	2.551	0.254	0.755	0.051	0.55	0.500	2.510
	19MG74-1-34	19MG74-A-5B	3.226	0.135	0.811	0.027	0.51	0.497	1.900
	19MG74-1-34	19MG74-A-5B	2.674	0.186	0.778	0.037	0.38	0.428	1.910
	19MG74-1-34	19MG74-A-5B	3.472	0.121	0.835	0.032	0.36	0.459	1.700
35	19MG74-1-35	19MG74-A-5B	2.353	0.111	0.887	0.061	0.52	0.344	2.033
	19MG74-1-35	19MG74-A-5B	2.155	0.121	0.827	0.037	0.33	0.313	1.830
	19MG74-1-35	19MG74-A-5B	2.907	0.237	0.839	0.041	0.60	0.436	2.020
	19MG74-1-35	19MG74-A-5B	3.390	0.276	0.783	0.033	0.48	0.554	1.928
	19MG74-1-35	19MG74-A-5B	2.625	0.138	0.811	0.032	0.67	0.384	1.844
36	19MG74-1-36	19MG74-A-5B	1.531	0.082	0.817	0.021	0.35	0.231	1.839
	19MG74-1-36	19MG74-A-5B	3.774	0.256	0.844	0.035	0.42	0.479	1.710
37	19MG74-1-37	19MG74-A-5B	2.451	0.150	0.826	0.037	0.29	0.345	1.859
	19MG74-1-37	19MG74-A-5B	3.247	0.211	0.836	0.045	0.67	0.482	1.960
	19MG74-1-37	19MG74-A-5B	2.519	0.127	0.796	0.029	0.39	0.377	1.918
	19MG74-1-37	19MG74-A-5B	1.727	0.107	0.808	0.031	0.34	0.282	2.040
38	19MG74-1-38	19MG74-A-5B	1.669	0.123	0.808	0.025	0.24	0.295	1.976
	19MG74-1-38	19MG74-A-5B	2.558	0.203	0.833	0.034	0.41	0.410	2.008
	19MG74-1-38	19MG74-A-5B	2.667	0.171	0.803	0.034	-0.04	0.403	2.019
39	19MG74-1-39	19MG74-A-5B	2.695	0.211	0.803	0.031	0.38	0.500	2.385
	19MG74-1-39	19MG74-A-5B	1.502	0.061	0.811	0.018	0.36	0.260	2.262
40	19MG74-1-40	19MG74-A-5B	2.591	0.114	0.825	0.028	0.53	0.430	2.303
	19MG74-1-40	19MG74-A-5B	2.198	0.058	0.828	0.020	0.52	0.318	2.039
41	19MG74-1-41	19MG74-A-5B	1.304	0.083	0.820	0.043	0.56	0.233	2.390
	19MG74-1-41	19MG74-A-5B	1.724	0.155	0.792	0.038	0.56	0.286	2.160
	19MG74-1-41	19MG74-A-5B	2.024	0.143	0.830	0.043	0.67	0.316	2.228
	19MG74-1-41	19MG74-A-5B	1.253	0.047	0.810	0.023	0.40	0.184	2.020
42	19MG74-1-42	19MG74-A-5B	2.415	0.228	0.813	0.057	0.61	0.450	2.470
	19MG74-1-42	19MG74-A-5B	2.924	0.291	0.784	0.040	0.23	0.547	2.650
	19MG74-1-42	19MG74-A-5B	2.500	0.094	0.813	0.034	0.63	0.412	2.320
	19MG74-1-42	19MG74-A-5B	3.968	0.189	0.819	0.027	0.52	0.609	2.120
43	19MG74-1-43	19MG74-A-5B	2.475	0.061	0.809	0.020	0.60	0.381	2.188
	19MG74-1-43	19MG74-A-5B	3.226	0.260	0.833	0.040	0.46	0.481	1.993

Spot	Source file (.FIN2)	Sample	^{238}U/^{206}Pb	±2σ (abs)	^{207}Pb/^{206}Pb	±2σ (abs)	Rho	U (ppm)	Pb (ppm)
44	19MG74-1-44	19MG74-A-5B	1.208	0.067	0.817	0.031	0.52	0.259	3.100
	19MG74-1-44	19MG74-A-5B	1.381	0.088	0.768	0.029	0.52	0.278	2.720
	19MG74-1-44	19MG74-A-5B	1.238	0.031	0.806	0.018	0.61	0.232	2.654
	19MG74-1-44	19MG74-A-5B	1.100	0.054	0.804	0.032	0.38	0.182	2.372
45	19MG74-1-45	19MG74-A-5B	3.135	0.147	0.776	0.042	0.55	0.512	2.380
	19MG74-1-45	19MG74-A-5B	3.165	0.240	0.836	0.049	0.48	0.449	2.090
	19MG74-1-45	19MG74-A-5B	2.278	0.368	0.798	0.039	0.37	0.493	3.090
	19MG74-1-45	19MG74-A-5B	4.425	0.274	0.778	0.037	0.63	0.675	2.200
	19MG74-1-45	19MG74-A-5B	3.205	0.154	0.825	0.033	0.35	0.478	2.206
46	19MG74-1-46	19MG74-A-5B	2.564	0.296	0.800	0.033	0.08	0.494	2.220
	19MG74-1-46	19MG74-A-5B	1.653	0.060	0.823	0.033	0.48	0.244	2.160
	19MG74-1-46	19MG74-A-5B	2.299	0.169	0.793	0.041	0.25	0.313	1.937
	19MG74-1-46	19MG74-A-5B	3.268	0.310	0.829	0.040	0.23	0.436	1.940
47	19MG74-1-47	19MG74-A-5B	2.681	0.259	0.833	0.049	0.45	0.398	2.170
	19MG74-1-47	19MG74-A-5B	2.193	0.202	0.819	0.033	0.29	0.325	2.220
	19MG74-1-47	19MG74-A-5B	1.499	0.045	0.809	0.025	0.33	0.215	2.127
	19MG74-1-47	19MG74-A-5B	2.278	0.202	0.799	0.043	0.36	0.321	2.060
48	19MG74-1-48	19MG74-A-5B	1.799	0.165	0.836	0.053	0.50	0.270	2.200
	19MG74-1-48	19MG74-A-5B	2.551	0.137	0.877	0.055	0.69	0.378	2.250
	19MG74-1-48	19MG74-A-5B	2.288	0.120	0.789	0.037	0.33	0.380	2.440
	19MG74-1-48	19MG74-A-5B	4.049	0.377	0.820	0.036	0.48	0.597	2.190
	19MG74-1-48	19MG74-A-5B	2.604	0.224	0.798	0.033	0.17	0.371	2.005
49	19MG74-1-49	19MG74-A-5B	2.242	0.151	0.829	0.024	0.12	0.422	2.640
	19MG74-1-49	19MG74-A-5B	3.096	0.182	0.828	0.029	0.13	0.564	2.705
	19MG74-1-49	19MG74-A-5B	2.020	0.175	0.801	0.032	0.42	0.362	2.578
50	19MG74-1-50	19MG74-A-5B	1.410	0.078	0.824	0.037	0.56	0.282	3.020
	19MG74-1-50	19MG74-A-5B	2.747	0.264	0.794	0.023	0.04	0.612	2.710
	19MG74-1-50	19MG74-A-5B	1.362	0.165	0.807	0.038	0.28	0.260	2.636
51	19MG74-1-51	19MG74-A-5B	0.510	0.031	0.786	0.033	0.09	0.090	2.490
	19MG74-1-51	19MG74-A-5B	0.610	0.041	0.818	0.031	-0.03	0.107	2.683
	19MG74-1-51	19MG74-A-5B	0.592	0.032	0.811	0.027	0.17	0.106	2.682
	19MG74-1-51	19MG74-A-5B	1.020	0.100	0.800	0.050	0.45	0.196	2.650
52	19MG74-1-52	19MG74-A-5B	1.511	0.135	0.828	0.042	0.60	0.279	2.710
	19MG74-1-52	19MG74-A-5B	2.188	0.124	0.812	0.029	0.44	0.414	2.756
	19MG74-1-52	19MG74-A-5B	2.326	0.119	0.816	0.025	0.27	0.425	2.724
53	19MG74-1-53	19MG74-A-5B	0.415	0.040	0.863	0.040	0.27	0.069	2.370
	19MG74-1-53	19MG74-A-5B	1.656	0.129	0.820	0.033	0.50	0.278	2.610
	19MG74-1-53	19MG74-A-5B	1.764	0.236	0.810	0.043	0.29	0.317	2.560
	19MG74-1-53	19MG74-A-5B	1.524	0.204	0.765	0.052	0.75	0.265	2.640
	19MG74-1-53	19MG74-A-5B	2.070	0.154	0.787	0.051	0.43	0.362	2.600
	19MG74-1-53	19MG74-A-5B	2.538	0.122	0.795	0.030	0.25	0.418	2.410

Spot	Source file (.FIN2)	Sample	^{238}U/^{206}Pb	±2σ (abs)	^{207}Pb/^{206}Pb	±2σ (abs)	Rho	U (ppm)	Pb (ppm)
	19MG74-1-54	19MG74-A-5B	3.145	0.188	0.804	0.040	0.51	0.551	2.590
	19MG74-1-54	19MG74-A-5B	2.070	0.317	0.791	0.039	0.55	0.432	2.920
54	19MG74-1-54	19MG74-A-5B	3.534	0.187	0.846	0.038	0.39	0.546	2.300
	19MG74-1-54	19MG74-A-5B	2.933	0.146	0.775	0.054	0.07	0.488	2.450
	19MG74-1-54	19MG74-A-5B	4.444	0.257	0.830	0.028	0.59	0.723	2.419
55	19MG74-1-55	19MG74-A-5B	3.356	0.180	0.795	0.023	0.43	0.621	2.695
	19MG74-1-55	19MG74-A-5B	1.972	0.109	0.827	0.025	0.48	0.330	2.449
	19MG74-1-56	19MG74-A-5B	4.115	0.254	0.854	0.048	0.43	0.780	2.940
56	19MG74-1-56	19MG74-A-5B	2.564	0.256	0.827	0.036	0.05	0.675	4.160
	19MG74-1-56	19MG74-A-5B	2.924	0.188	0.804	0.020	0.36	0.607	2.843
	19MG74-1-57	19MG74-A-5B	4.854	0.377	0.809	0.048	0.29	0.836	2.550
57	19MG74-1-57	19MG74-A-5B	4.032	0.260	0.851	0.029	0.05	0.792	3.180
	19MG74-1-57	19MG74-A-5B	4.386	0.308	0.815	0.039	0.31	0.854	2.970
	19MG74-1-57	19MG74-A-5B	3.509	0.271	0.811	0.021	0.34	0.671	2.900
	19MG74-1-58	19MG74-A-5B	2.632	0.139	0.837	0.030	0.42	0.397	2.360
58	19MG74-1-58	19MG74-A-5B	3.058	0.318	0.795	0.052	0.53	0.543	2.900
	19MG74-1-58	19MG74-A-5B	2.841	0.145	0.818	0.035	0.41	0.504	2.660
	19MG74-1-58	19MG74-A-5B	2.347	0.083	0.817	0.030	0.65	0.362	2.532
	19MG74-1-59	19MG74-A-5B	1.745	0.113	0.834	0.032	0.49	0.340	3.140
59	19MG74-1-59	19MG74-A-5B	3.534	0.312	0.804	0.038	0.27	0.546	2.440
	19MG74-1-59	19MG74-A-5B	2.381	0.074	0.793	0.022	0.48	0.379	2.510
	19MG74-1-60	19MG74-A-5B	2.688	0.130	0.822	0.044	0.54	0.514	3.110
60	19MG74-1-60	19MG74-A-5B	2.710	0.140	0.829	0.042	0.49	0.473	2.810
	19MG74-1-60	19MG74-A-5B	3.257	0.223	0.893	0.068	0.72	0.543	2.790
	19MG74-1-60	19MG74-A-5B	2.849	0.097	0.814	0.033	0.63	0.440	2.612
	19MG74-1-61	19MG74-A-5B	2.232	0.125	0.777	0.038	0.43	0.439	3.050
61	19MG74-1-61	19MG74-A-5B	3.984	0.238	0.806	0.041	0.43	0.674	2.730
	19MG74-1-61	19MG74-A-5B	3.021	0.080	0.816	0.018	0.52	0.493	2.726
	19MG74-1-62	19MG74-A-5B	3.367	0.215	0.821	0.043	0.48	0.525	2.730
62	19MG74-1-62	19MG74-A-5B	2.584	0.140	0.823	0.044	0.69	0.411	2.710
	19MG74-1-62	19MG74-A-5B	4.032	0.244	0.815	0.035	0.25	0.689	3.030
	19MG74-1-62	19MG74-A-5B	3.601	0.115	0.818	0.028	0.50	0.548	2.613
	19MG74-1-63	19MG74-A-5B	1.748	0.138	0.805	0.034	0.58	0.298	2.830
	19MG74-1-63	19MG74-A-5B	1.912	0.102	0.812	0.040	0.49	0.329	2.960
63	19MG74-1-63	19MG74-A-5B	1.346	0.065	0.809	0.027	0.33	0.226	2.850
	19MG74-1-63	19MG74-A-5B	1.143	0.090	0.802	0.045	0.45	0.191	2.750
	19MG74-1-63	19MG74-A-5B	1.580	0.145	0.835	0.048	0.69	0.249	2.580
	19MG74-1-64	19MG74-A-5B	2.825	0.160	0.812	0.026	0.20	0.541	3.200
64	19MG74-1-64	19MG74-A-5B	2.222	0.202	0.813	0.034	0.20	0.436	3.160
	19MG74-1-64	19MG74-A-5B	1.129	0.056	0.813	0.020	0.23	0.220	3.227
	19MG74-1-65	19MG74-A-5B	3.115	0.243	0.862	0.061	0.75	0.504	2.750
65	19MG74-1-65	19MG74-A-5B	2.320	0.140	0.786	0.023	0.45	0.428	3.030
	19MG74-1-65	19MG74-A-5B	3.378	0.171	0.822	0.025	0.26	0.570	2.870
	19MG74-1-65	19MG74-A-5B	2.198	0.169	0.821	0.041	0.43	0.338	2.690

Spot	Source file (.FIN2)	Sample	$^{238}U/^{206}Pb$	±2σ (abs)	$^{207}Pb/^{206}Pb$	±2σ (abs)	Rho	U (ppm)	Pb (ppm)
	19MG74-1-66	19MG74-A-5B	1.976	0.133	0.834	0.048	0.56	0.336	2.850
66	19MG74-1-66	19MG74-A-5B	1.976	0.145	0.800	0.033	0.11	0.358	3.110
	19MG74-1-66	19MG74-A-5B	1.570	0.064	0.824	0.022	0.30	0.259	2.815
67	19MG74-1-67	19MG74-A-5B	0.613	0.026	0.812	0.020	0.18	0.103	2.864
	19MG74-1-67	19MG74-A-5B	1.490	0.158	0.814	0.036	0.42	0.255	2.850
68	19MG74-1-68	19MG74-A-4B	2.786	0.209	0.914	0.076	0.52	0.042	0.260
69	19MG74-1-69	19MG74-A-4B	2.653	0.176	0.881	0.060	0.60	0.060	0.411
	19MG74-1-69	19MG74-A-4B	1.502	0.176	0.861	0.097	0.58	0.030	0.315
	19MG74-1-70	19MG74-A-4B	1.321	0.099	0.819	0.063	0.53	0.041	0.526
70	19MG74-1-70	19MG74-A-4B	1.333	0.196	0.807	0.080	0.30	0.048	0.618
	19MG74-1-70	19MG74-A-4B	1.414	0.182	0.920	0.120	0.69	0.035	0.414
	19MG74-1-71	19MG74-A-4B	1.391	0.145	0.801	0.081	0.72	0.049	0.581
71	19MG74-1-71	19MG74-A-4B	1.529	0.138	0.932	0.086	0.68	0.035	0.397
	19MG74-1-71	19MG74-A-4B	3.125	0.273	0.838	0.074	0.43	0.062	0.361
72	19MG74-1-72	19MG74-A-4B	1.429	0.224	0.785	0.054	0.07	0.075	0.840
	19MG74-1-72	19MG74-A-4B	1.534	0.172	0.842	0.061	0.40	0.057	0.554
73	19MG74-1-73	19MG74-A-4B	2.066	0.213	0.826	0.076	0.01	0.050	0.404
	19MG74-1-73	19MG74-A-4B	1.786	0.159	0.929	0.091	0.81	0.037	0.356
74	19MG74-1-74	19MG74-A-4B	3.448	0.202	0.880	0.057	0.69	0.057	0.256
	19MG74-1-75	19MG74-A-4B	0.644	0.030	0.784	0.028	0.50	0.139	3.410
75	19MG74-1-75	19MG74-A-4B	0.455	0.029	0.789	0.024	0.52	0.089	3.010
	19MG74-1-75	19MG74-A-4B	0.448	0.024	0.797	0.029	0.43	0.076	2.656
76	19MG74-1-76	19MG74-A-4B	0.370	0.013	0.826	0.015	0.48	0.075	3.078
77	19MG74-1-77	19MG74-A-4B	2.976	0.221	0.822	0.041	0.47	0.088	0.412
	19MG74-1-78	19MG74-A-4B	2.976	0.221	0.849	0.063	0.59	0.075	0.368
78	19MG74-1-78	19MG74-A-4B	2.967	0.229	0.832	0.061	0.59	0.075	0.366
	19MG74-1-78	19MG74-A-4B	2.941	0.285	0.762	0.077	0.65	0.080	0.347
	19MG74-1-78	19MG74-A-4B	0.917	0.168	0.860	0.062	0.21	0.095	1.540
	19MG74-1-79	19MG74-A-4B	1.342	0.160	0.851	0.091	0.28	0.092	0.910
79	19MG74-1-79	19MG74-A-4B	1.838	0.203	0.798	0.082	0.34	0.098	0.770
	19MG74-1-79	19MG74-A-4B	2.577	0.173	0.841	0.041	0.32	0.122	0.669
80	19MG74-1-80	19MG74-A-4B	1.422	0.081	0.839	0.043	0.40	0.050	0.464
81	19MG74-1-81	19MG74-A-4B	0.930	0.063	0.845	0.049	0.51	0.063	0.846
	19MG74-1-81	19MG74-A-4B	1.229	0.053	0.842	0.038	0.54	0.079	0.813
82	19MG74-1-82	19MG74-A-4B	1.786	0.134	0.859	0.078	0.48	0.068	0.483
	19MG74-1-82	19MG74-A-4B	2.959	0.184	0.829	0.043	0.56	0.156	0.626
83	19MG74-1-83	19MG74-A-4B	2.695	0.232	0.855	0.052	0.35	0.094	0.440
	19MG74-1-83	19MG74-A-4B	1.992	0.278	0.849	0.095	0.55	0.042	0.236
84	19MG74-1-84	19MG74-A-4B	1.984	0.240	0.796	0.043	0.09	0.146	0.523
	19MG74-1-84	19MG74-A-4B	2.179	0.271	0.878	0.078	0.34	0.061	0.288
85	19MG74-1-85	19MG74-A-4B	3.356	0.259	0.926	0.070	0.69	0.068	0.236
	19MG74-1-86	19MG74-A-4B	1.779	0.209	0.797	0.059	-0.01	0.112	0.548
86	19MG74-1-86	19MG74-A-4B	1.099	0.362	0.754	0.051	0.20	0.159	1.340
	19MG74-1-86	19MG74-A-4B	1.116	0.095	0.809	0.049	0.49	0.109	1.026

Spot	Source file (.FIN2)	Sample	^{238}U/^{206}Pb	±2σ (abs)	^{207}Pb/^{206}Pb	±2σ (abs)	Rho	U (ppm)	Pb (ppm)
	19MG74-1-87	19MG74-A-4B	2.564	0.276	0.790	0.054	0.52	0.085	0.299
87	19MG74-1-87	19MG74-A-4B	2.083	0.174	0.930	0.100	0.65	0.066	0.377
	19MG74-1-87	19MG74-A-4B	1.675	0.230	0.818	0.094	0.67	0.058	0.343
88	19MG74-1-88	19MG74-A-4B	2.747	0.204	0.887	0.058	0.47	0.178	0.739
	19MG74-1-88	19MG74-A-4B	1.767	0.181	0.822	0.051	0.48	0.091	0.478
89	19MG74-1-89	19MG74-A-4B	0.591	0.022	0.818	0.022	0.44	0.102	1.688
90	19MG74-1-90	19MG74-A-4B	1.795	0.113	0.835	0.044	0.55	0.070	0.363
91	19MG74-1-91	19MG74-A-4B	1.695	0.103	0.867	0.050	0.68	0.051	0.295
92	19MG74-1-92	19MG74-A-4B	1.064	0.095	0.815	0.049	0.41	0.061	0.563
	19MG74-1-92	19MG74-A-4B	1.437	0.109	0.849	0.048	0.73	0.061	0.410
93	19MG74-1-93	19MG74-A-4B	1.340	0.079	0.854	0.057	0.73	0.039	0.286
	19MG74-1-94	19MG74-A-4B	0.758	0.109	0.877	0.081	0.61	0.036	0.513
94	19MG74-1-94	19MG74-A-4B	2.584	0.441	0.766	0.054	0.02	0.430	0.757
	19MG74-1-94	19MG74-A-4B	1.250	0.089	0.838	0.059	0.58	0.068	0.559
	19MG74-1-95	19MG74-A-4B	1.832	0.148	0.809	0.069	0.69	0.054	0.302
95	19MG74-1-95	19MG74-A-4B	1.266	0.192	0.797	0.079	0.21	0.060	0.494
	19MG74-1-95	19MG74-A-4B	1.821	0.123	0.883	0.064	0.72	0.054	0.363
96	19MG74-1-96	19MG74-A-4B	1.021	0.041	0.833	0.031	0.58	0.067	0.715
97	19MG74-1-97	19MG74-A-4B	4.695	0.419	0.892	0.069	0.89	0.128	0.294
	19MG74-1-97	19MG74-A-4B	2.681	0.295	0.827	0.059	0.56	0.072	0.293
98	19MG74-1-98	19MG74-A-4B	2.433	0.172	0.841	0.050	0.52	0.061	0.303
	19MG74-1-99	19MG74-A-4B	0.992	0.083	0.812	0.057	0.45	0.054	0.606
99	19MG74-1-99	19MG74-A-4B	1.364	0.134	0.803	0.095	0.65	0.045	0.369
	19MG74-1-99	19MG74-A-4B	0.987	0.085	0.839	0.058	0.37	0.042	0.502
100	19MG74-1-100	19MG74-A-4B	1.214	0.062	0.854	0.042	0.47	0.057	0.556
	19MG74-1-100	19MG74-A-4B	2.066	0.145	0.821	0.053	0.36	0.083	0.488

19MG79 from DA strain domain

Spot	Source file (.FIN2)	Sample	^{238}U/^{206}Pb	±2σ (abs)	^{207}Pb/^{206}Pb	±2σ (abs)	Rho	U (ppm)	Pb (ppm)
1	19MG79-1	19MG79-1B			no value	NAN	NaN	0.010	0.190
2	19MG79-2	19MG79-1B	5.556	0.494	0.917	0.092	0.79	0.080	0.164
	19MG79-2	19MG79-1B	11.905	1.417	0.880	0.110	0.35	0.139	0.152
	19MG79-3	19MG79-1B	2.950	0.235	0.825	0.051	0.60	0.088	0.371
3	19MG79-3	19MG79-1B	4.673	0.415	0.844	0.055	0.20	0.100	0.292
	19MG79-3	19MG79-1B	3.145	0.445	0.761	0.067	0.32	0.118	0.434
4	19MG79-4	19MG79-1B	2.457	0.362	0.800	0.062	0.71	0.061	0.292
	19MG79-4	19MG79-1B	1.923	0.340	0.851	0.078	0.82	0.044	0.291
5	19MG79-5	19MG79-1B	1.613	0.312	0.750	0.140	0.90	0.021	0.173
6	19MG79-6	19MG79-1B	4.098	0.873	0.898	0.084	0.16	0.084	0.249
	19MG79-6	19MG79-1B	3.040	0.351	0.920	0.110	0.88	0.048	0.203
7	19MG79-7	19MG79-1B	2.208	0.361	0.752	0.074	0.65	0.070	0.408
	19MG79-7	19MG79-1B	3.185	0.446	0.859	0.074	0.56	0.057	0.234
8	**19MG79-8**	**19MG79-1B**			**no value**	**NAN**	**NaN**	**0.006**	**0.251**

Spot	Source file (.FIN2)	Sample	^{238}U/^{206}Pb	±2σ (abs)	^{207}Pb/^{206}Pb	±2σ (abs)	Rho	U (ppm)	Pb (ppm)
9	19MG79-9	19MG79-1B	3.021	0.383	0.807	0.090	0.64	0.073	0.345
	19MG79-9	19MG79-1B	2.577	0.173	0.842	0.047	0.54	0.072	0.380
10	19MG79-10	19MG79-1B	4.310	0.725	0.802	0.088	0.55	0.089	0.227
	19MG79-10	19MG79-1B	9.009	0.812	0.845	0.083	0.61	0.089	0.134
11	19MG79-11	19MG79-1B	2.770	0.315	0.890	0.100	0.65	0.062	0.316
	19MG79-11	19MG79-1B	2.933	0.335	0.908	0.099	0.58	0.060	0.296
	19MG79-11	19MG79-1B	1.149	0.238	0.776	0.039	0.25	0.085	0.970
12	19MG79-12	19MG79-1B	2.809	0.387	1.020	0.150	0.75	0.035	0.171
	19MG79-12	19MG79-1B	2.096	0.272	0.860	0.100	1.00	0.023	0.146
13	19MG79-13	19MG79-1B	5.495	0.392	0.839	0.081	0.53	0.096	0.234
	19MG79-13	19MG79-1B	8.130	0.661	0.902	0.075	0.66	0.124	0.231
14	19MG79-14	19MG79-1B	3.030	0.230	0.786	0.045	0.36	0.119	0.554
	19MG79-14	19MG79-1B	1.695	0.575	0.765	0.072	0.13	0.097	0.670
	19MG79-14	19MG79-1B	4.878	0.880	0.797	0.077	0.56	0.110	0.326
15	19MG79-15	19MG79-1B	2.123	0.334	0.752	0.086	0.84	0.042	0.266
	19MG79-15	19MG79-1B	0.980	0.231	0.824	0.060	0.60	0.055	0.860
	19MG79-15	19MG79-1B	5.102	1.874	0.980	0.190	0.47	0.085	0.245
16	19MG79-16	19MG79-1B	3.788	0.445	0.820	0.100	0.76	0.067	0.235
	19MG79-16	19MG79-1B	4.386	0.731	0.930	0.220	0.57	0.068	0.203
	19MG79-16	19MG79-1B	5.348	0.886	0.840	0.180	0.52	0.064	0.186
	19MG79-16	19MG79-1B	3.968	0.866	1.160	0.390	0.98	0.044	0.174
	19MG79-16	19MG79-1B	3.906	0.671	0.810	0.094	0.41	0.040	0.164
17	19MG79-17	19MG79-1B	2.577	0.458	0.780	0.079	0.41	0.089	0.505
	19MG79-17	19MG79-1B	5.051	0.536	0.850	0.120	0.76	0.059	0.143
	19MG79-17	19MG79-1B	3.906	0.351	0.852	0.078	0.66	0.054	0.192
18	19MG79-18	19MG79-1B	3.436	0.248	0.871	0.074	0.66	0.047	0.202
	19MG79-18	19MG79-1B	2.381	0.737	0.840	0.120	0.20	0.047	0.294
	19MG79-18	19MG79-1B	4.762	0.726	0.930	0.190	0.69	0.049	0.163
19	19MG79-19	19MG79-1B	1.585	0.196	0.886	0.096	0.77	0.020	0.192
20	19MG79-20	19MG79-1B	2.222	0.321	0.880	0.150	0.89	0.022	0.128
	19MG79-20	19MG79-1B	2.326	0.384	0.820	0.120	0.15	0.020	0.102
21	19MG79-21	19MG79-1B	4.115	0.423	0.854	0.075	0.79	0.067	0.211
	19MG79-21	19MG79-1B	4.049	0.770	0.960	0.150	0.95	0.045	0.156
	19MG79-21	19MG79-1B	3.546	0.704	0.860	0.160	0.94	0.030	0.118
22	19MG79-22	19MG79-1B	2.066	0.320	0.768	0.066	0.26	0.077	0.443
	19MG79-22	19MG79-1B	1.190	0.156	0.743	0.083	0.62	0.042	0.451
	19MG79-22	19MG79-1B	0.581	0.061	0.773	0.034	0.38	0.065	1.620
	19MG79-22	19MG79-1B	0.948	0.087	0.819	0.052	0.41	0.105	1.520
	19MG79-22	19MG79-1B	2.564	0.237	0.813	0.073	0.27	0.135	0.780
23	19MG79-23	19MG79-1B	3.534	0.462	0.990	0.160	0.79	0.037	0.133
	19MG79-23	19MG79-1B	2.564	0.460	0.810	0.110	0.77	0.028	0.159
24	19MG79-24	19MG79-1B	7.692	0.710	0.815	0.072	0.72	0.118	0.209
	19MG79-24	19MG79-1B	5.051	0.689	0.842	0.080	0.95	0.076	0.196

Spot	Source file (.FIN2)	Sample	$^{238}U/^{206}Pb$	±2σ (abs)	$^{207}Pb/^{206}Pb$	±2σ (abs)	Rho	U (ppm)	Pb (ppm)
	19MG79-25	19MG79-1B	4.673	0.611	0.817	0.092	0.70	0.087	0.263
25	19MG79-25	19MG79-1B	5.952	0.638	0.990	0.120	0.64	0.065	0.170
	19MG79-25	19MG79-1B	4.016	0.710	0.880	0.150	0.66	0.061	0.232
	19MG79-25	19MG79-1B	2.525	0.281	0.856	0.085	0.75	0.057	0.341
26	19MG79-26	19MG79-1B	1.678	0.121	0.852	0.053	0.63	0.034	0.284
	19MG79-27	19MG79-1B	3.096	0.393	0.840	0.120	0.86	0.035	0.161
27	19MG79-27	19MG79-1B	1.818	0.661	1.000	0.180	0.52	0.041	0.350
	19MG79-27	19MG79-1B	3.831	0.470	0.825	0.079	0.81	0.058	0.202
	19MG79-28	19MG79-1B	4.785	0.847	0.848	0.063	0.78	0.155	0.455
28	19MG79-28	19MG79-1B	7.042	0.893	0.819	0.075	0.58	0.228	0.438
	19MG79-28	19MG79-1B	4.237	0.610	0.848	0.057	0.56	0.152	0.570
	19MG79-29	19MG79-1B	0.980	0.173	0.806	0.072	0.55	0.057	0.690
29	19MG79-29	19MG79-1B	1.299	0.169	0.825	0.054	0.30	0.075	0.723
	19MG79-29	19MG79-1B	1.873	0.126	0.769	0.044	0.62	0.108	0.749
	19MG79-30	19MG79-1B	2.155	0.181	0.903	0.084	0.69	0.045	0.298
30	19MG79-30	19MG79-1B	3.597	0.311	0.945	0.087	0.70	0.076	0.343
	19MG79-30	19MG79-1B	5.181	0.966	0.900	0.130	0.60	0.133	0.364
	19MG79-31	19MG79-1B	4.695	0.419	0.827	0.062	0.68	0.139	0.432
31	19MG79-31	19MG79-1B	3.745	0.912	0.820	0.079	0.47	0.124	0.429
	19MG79-31	19MG79-1B	5.780	0.668	0.880	0.130	0.42	0.084	0.188
32	19MG79-32	19MG79-1B	2.079	0.225	0.868	0.098	0.81	0.040	0.281
	19MG79-32	19MG79-1B	2.985	0.258	0.868	0.076	0.66	0.055	0.245
33	**19MG79-33**	**19MG79-1B**			**no value**	**NAN**	**NaN**	**0.006**	**0.158**
	19MG79-34	19MG79-1B	2.688	0.188	0.839	0.072	0.66	0.082	0.453
34	19MG79-34	19MG79-1B	3.663	0.483	0.950	0.140	0.89	0.053	0.193
	19MG79-34	19MG79-1B	2.315	0.305	0.830	0.110	0.76	0.045	0.292
	19MG79-35	19MG79-1B	4.785	0.595	0.840	0.110	0.80	0.068	0.227
35	19MG79-35	19MG79-1B	4.000	1.600	0.860	0.130	0.71	0.076	0.270
	19MG79-35	19MG79-1B	4.367	0.496	0.804	0.099	0.72	0.061	0.186
	19MG79-36	19MG79-1B	3.436	0.661	0.878	0.098	0.83	0.097	0.461
36	19MG79-36	19MG79-1B	2.268	0.283	0.940	0.130	0.74	0.039	0.234
	19MG79-36	19MG79-1B	4.274	0.402	0.912	0.086	0.73	0.049	0.190
37	19MG79-37	19MG79-1B	7.353	0.595	0.954	0.066	0.81	0.090	0.186
38	19MG79-38	19MG79-1B	3.012	0.299	0.897	0.087	0.93	0.050	0.248
	19MG79-38	19MG79-1B	3.125	0.479	0.876	0.098	0.36	0.050	0.223
	19MG79-39	19MG79-1B	2.500	0.750	0.804	0.094	0.49	0.061	0.390
39	19MG79-39	19MG79-1B	2.632	0.298	0.830	0.081	0.61	0.055	0.321
	19MG79-39	19MG79-1B	3.690	0.626	0.980	0.170	0.79	0.047	0.184
40	19MG79-40	19MG79-1B	1.953	0.328	0.820	0.140	0.28	0.030	0.203
	19MG79-41	19MG79-1B	1.277	0.155	0.835	0.050	0.38	0.088	0.988
41	19MG79-41	19MG79-1B	2.667	0.256	0.834	0.069	0.52	0.090	0.536
	19MG79-41	19MG79-1B	5.128	0.657	0.850	0.110	0.52	0.073	0.197
42	19MG79-42	19MG79-1B	1.739	0.230	0.830	0.110	0.38	0.036	0.305
	19MG79-42	19MG79-1B	2.681	0.237	0.925	0.095	0.73	0.032	0.199

Spot	Source file (.FIN2)	Sample	$^{238}U/^{206}Pb$	±2σ (abs)	$^{207}Pb/^{206}Pb$	±2σ (abs)	Rho	U (ppm)	Pb (ppm)
43	19MG79-43	19MG79-1B	1.773	0.302	0.830	0.130	0.64	0.030	0.245
	19MG79-43	19MG79-1B	3.030	0.294	0.876	0.072	0.60	0.048	0.239
	19MG79-44	19MG79-1B	2.016	0.248	0.808	0.069	0.49	0.051	0.394
44	19MG79-44	19MG79-1B	0.333	0.144	0.740	0.057	0.42	0.028	1.260
	19MG79-44	19MG79-1B	2.646	0.413	0.857	0.086	0.10	0.049	0.323
45	19MG79-45	19MG79-1B	2.488	0.464	0.900	0.110	0.46	0.061	0.409
	19MG79-45	19MG79-1B	4.808	0.439	0.891	0.092	0.81	0.060	0.210
	19MG79-46	19MG79-1B	1.786	0.201	0.883	0.099	0.65	0.051	0.470
46	19MG79-46	19MG79-1B	1.706	0.224	0.880	0.140	0.69	0.035	0.335
	19MG79-46	19MG79-1B	2.053	0.261	0.870	0.110	0.87	0.036	0.317
	19MG79-46	19MG79-1B	1.408	0.357	1.010	0.130	0.75	0.025	0.327
	19MG79-47	19MG79-1B	2.387	0.205	0.779	0.072	0.67	0.074	0.494
47	19MG79-47	19MG79-1B	2.262	0.409	0.806	0.091	0.83	0.062	0.450
	19MG79-47	19MG79-1B	3.367	0.363	0.910	0.120	0.60	0.059	0.311
	19MG79-47	19MG79-1B	2.747	0.506	0.820	0.110	0.89	0.046	0.271
	19MG79-48	19MG79-1B	9.901	2.843	0.850	0.140	0.65	0.137	0.250
48	19MG79-48	19MG79-1B	6.211	0.887	0.830	0.110	0.70	0.103	0.292
	19MG79-48	19MG79-1B	9.709	0.943	0.850	0.110	0.87	0.105	0.179
	19MG79-49	19MG79-1B	4.587	0.779	0.860	0.120	0.36	0.073	0.273
49	19MG79-49	19MG79-1B	3.846	0.488	0.790	0.110	0.77	0.058	0.266
	19MG79-49	19MG79-1B	3.546	0.843	0.690	0.170	0.68	0.053	0.247
	19MG79-49	19MG79-1B	4.831	0.513	0.865	0.083	0.61	0.074	0.257
	19MG79-50	19MG79-1B	2.500	1.250	0.930	0.150	0.54	0.053	0.390
50	19MG79-50	19MG79-1B	2.976	0.487	0.830	0.120	0.35	0.040	0.195
	19MG79-50	19MG79-1B	3.497	0.513	0.940	0.170	0.83	0.040	0.219
	19MG79-50	19MG79-1B	4.405	0.505	0.990	0.140	0.91	0.040	0.166

Table A5.3: *U-Pb isotopic data of calcite veins from the ECM obtained during the session 3 (05-11-2021) of LA-ICP-MS U-Pb in calcite. The spot size for samples 19MG20, 19MG21 and 19MG43 was 85 µm and 135 µm for the sample 19MG46. Red labelled data was excluded from the age regression due to evident high error or a point belonging to the host rock.*

			Session 3						
			WC-1 Calcite reference (Roberts et al., 2017)						
Spot	**Source file (.FIN2)**	**Sample**	**^{238}U/^{206}Pb**	**±2σ (abs)**	**^{207}Pb/^{206}Pb**	**±2σ (abs)**	**Rho**	**U (ppm)**	**Pb (ppm)**
1	WC1-2	WC-1	24.888	0.390	0.051	0.004	0.17	3.479	0.140
2	WC1-3	WC-1	24.857	0.395	0.051	0.005	-0.11	3.988	0.172
3	WC1-4	WC-1	25.233	0.382	0.050	0.005	0.28	4.015	0.199
4	WC1-5	WC-1	25.069	0.522	0.052	0.007	-0.02	3.433	0.183
5	WC1-6	WC-1	24.802	0.480	0.049	0.007	0.15	3.770	0.217
6	WC1-7	WC-1	25.452	0.486	0.052	0.007	0.00	3.689	0.218
7	WC1-8	WC-1	25.259	0.383	0.052	0.006	0.05	3.725	0.174
8	WC1-9	WC-1	24.624	0.424	0.051	0.006	0.25	3.340	0.180
9	WC1-30	WC-1	24.390	0.595	0.050	0.012	-0.54	3.961	0.324
10	WC1-10	WC-1	25.523	0.456	0.049	0.006	-0.49	3.682	0.182
11	WC1-11	WC-1	24.552	0.410	0.052	0.004	0.01	3.762	0.155
12	WC1-31	WC-1	24.994	0.462	0.052	0.005	0.36	3.678	0.150
13	WC1-12	WC-1	24.969	0.493	0.047	0.007	-0.47	3.702	0.289
14	WC1-13	WC-1	24.746	0.410	0.052	0.003	0.23	3.696	0.186
15	WC1-14	WC-1	24.851	0.414	0.053	0.006	-0.43	3.760	0.168
16	WC1-33	WC-1	24.826	0.468	0.052	0.006	0.34	3.592	0.307
17	WC1-15	WC-1	25.227	0.592	0.045	0.007	-0.70	3.966	0.197
18	WC1-16	WC-1	25.132	0.417	0.051	0.004	0.01	3.680	0.112
19	WC1-17	WC-1	25.484	0.494	0.051	0.008	-0.07	3.705	0.222
20	WC1-34	WC-1	25.075	0.459	0.052	0.006	0.28	3.693	0.169
21	WC1-18	WC-1	24.225	0.446	0.054	0.007	0.29	3.702	0.206
22	WC1-19	WC-1	25.240	0.484	0.051	0.007	0.15	3.698	0.216
23	WC1-35	WC-1	25.195	0.533	0.054	0.007	0.08	3.702	0.227
24	WC1-20	WC-1	25.381	0.509	0.051	0.008	0.24	3.699	0.145
25	WC1-21	WC-1	25.189	0.634	0.052	0.010	-0.51	3.700	0.170
26	WC1-22	WC-1	24.981	0.362	0.052	0.005	0.32	3.699	0.210
27	WC1-23	WC-1	24.981	0.424	0.052	0.005	-0.08	3.721	0.129
28	WC1-36	WC-1	25.227	0.458	0.054	0.006	0.25	3.660	0.178
29	WC1-24	WC-1	24.938	0.423	0.052	0.005	0.19	3.704	0.243
30	WC1-25	WC-1	25.094	0.390	0.050	0.004	-0.19	3.695	0.137
31	WC1-26	WC-1	25.157	0.367	0.050	0.004	0.25	3.738	0.167
32	WC1-37	WC-1	24.225	0.563	0.052	0.010	-0.18	3.023	0.264
33	WC1-38	WC-1	24.882	0.489	0.046	0.008	-0.49	5.689	0.349
34	WC1-39	WC-1	24.851	0.593	0.051	0.007	0.46	2.996	0.151

	Soda-lime glass NIST SRM-614							
Spot	Source file (.FIN2)	Sample	$^{238}U/^{206}Pb$	±2σ (abs)	$^{207}Pb/^{206}Pb$	±2σ (abs)	Rho	U (ppm)	Pb (ppm)
1	NIST614-85-1	NIST-614	1.474	0.018	0.861	0.010	0.29	0.903	5.030
2	NIST614-85-2	NIST-614	1.478	0.019	0.861	0.009	0.54	0.906	5.070
3	NIST614-85-3	NIST-614	1.483	0.019	0.862	0.010	0.33	0.908	5.030
4	NIST614-85-4	NIST-614	1.477	0.022	0.862	0.011	0.63	0.607	5.820
5	NIST614-85-5	NIST-614	1.443	0.020	0.865	0.011	0.60	0.657	5.900
6	NIST614-85-6	NIST-614	1.450	0.019	0.858	0.011	0.54	0.948	4.420
7	NIST614-85-7	NIST-614	1.444	0.019	0.857	0.010	0.29	0.632	4.760
8	NIST614-85-8	NIST-614	1.461	0.020	0.859	0.011	0.46	0.917	7.410
9	NIST614-85-9	NIST-614	1.445	0.021	0.863	0.011	0.29	1.001	7.650
10	NIST614-85-10	NIST-614	1.441	0.019	0.866	0.010	0.57	1.014	7.830

	19MG20 from DA strain domain							
Spot	Source file (.FIN2)	Sample	$^{238}U/^{206}Pb$	±2σ (abs)	$^{207}Pb/^{206}Pb$	±2σ (abs)	Rho	U (ppm)	Pb (ppm)
1	19MG20-1	19MG20-T1	2.294	0.258	0.814	0.053	0.30	0.122	0.258
	19MG20-1	19MG20-T1	1.739	0.188	0.821	0.063	0.47	0.049	0.141
2	19MG20-2	19MG20-T1	7.353	0.703	0.792	0.074	0.31	0.598	0.393
	19MG20-2	19MG20-T1	4.065	0.364	0.862	0.054	0.66	0.218	0.307
3	19MG20-2	19MG20-T1	7.092	1.207	0.786	0.089	-0.13	0.189	0.120
3	19MG20-3	19MG20-T1	0.833	0.160	0.869	0.085	-0.11	0.064	0.399
4	19MG20-3	19MG20-T1	1.101	0.073	0.832	0.049	0.29	0.054	0.221
4	19MG20-4	19MG20-T1	1.828	0.110	0.887	0.049	0.53	0.066	0.187
5	19MG20-5	19MG20-T1	1.608	0.121	0.866	0.047	0.28	0.068	0.199
6	19MG20-6	19MG20-T1	5.780	0.735	0.840	0.055	0.32	1.420	1.210
6	19MG20-6	19MG20-T1	5.917	1.330	0.788	0.058	-0.24	2.020	1.590
	19MG20-6	19MG20-T1	5.814	0.811	0.773	0.048	0.39	0.965	0.801
7	19MG20-6	19MG20-T1	2.660	0.375	0.809	0.026	0.09	1.413	2.650
7	19MG20-7	19MG20-T1	1.908	0.229	0.836	0.072	0.22	0.101	0.252
8	19MG20-7	19MG20-T1	2.747	0.385	0.859	0.065	0.22	0.103	0.196
	19MG20-7	19MG20-T1	4.115	0.559	0.866	0.071	0.19	0.166	0.198
9	19MG20-8	19MG20-T1	2.222	0.207	0.918	0.062	0.13	0.073	0.168
9	19MG20-9	19MG20-T1	1.053	0.155	0.838	0.039	0.03	0.386	2.370
10	19MG20-9	19MG20-T1	1.031	0.191	0.829	0.036	-0.11	0.267	1.500
	19MG20-9	19MG20-T1	0.446	0.074	0.832	0.040	0.01	0.260	3.910
11	19MG20-9	19MG20-T1	0.926	0.197	0.819	0.069	0.02	0.194	1.270
	19MG20-9	19MG20-T1	2.101	0.238	0.817	0.056	0.21	0.224	0.650
12	19MG20-10	19MG20-T1	1.122	0.106	0.854	0.031	0.08	0.309	1.360
	19MG20-10	19MG20-T1	2.577	0.418	0.785	0.033	0.28	1.050	2.320
13	19MG20-10	19MG20-T1	1.473	0.154	0.790	0.026	-0.08	0.750	3.030
	19MG20-10	19MG20-T1	1.942	0.294	0.817	0.033	0.29	0.719	2.430
14	19MG20-11	19MG20-T1	2.755	0.235	0.803	0.067	0.03	0.176	0.367
	19MG20-11	19MG20-T1	3.509	0.283	0.839	0.044	0.01	0.151	0.253

Spot	Source file (.FIN2)	Sample	$^{238}U/^{206}Pb$	±2σ (abs)	$^{207}Pb/^{206}Pb$	±2σ (abs)	Rho	U (ppm)	Pb (ppm)
15	19MG20-12	19MG20-T1	1.248	0.128	0.818	0.054	0.53	0.051	0.242
	19MG20-12	19MG20-T1	4.808	0.832	0.787	0.079	0.27	0.216	0.244
16	19MG20-12	19MG20-T1	8.696	1.210	0.708	0.065	0.56	0.343	0.230
13	19MG20-13	19MG20-T1	1.393	0.103	0.887	0.047	0.30	0.044	0.201
17	19MG20-14	19MG20-T1	0.813	0.079	0.894	0.079	0.70	0.017	0.156
15	19MG20-15	19MG20-T1	20.790	1.815	0.950	0.075	0.14	0.482	0.177
18	19MG20-16	19MG20-T1	2.262	0.302	0.858	0.051	0.33	0.126	0.413
	19MG20-16	19MG20-T1	1.136	0.181	0.839	0.025	0.01	0.256	1.790
19	19MG20-17	19MG20-T1	1.453	0.114	0.831	0.045	0.34	0.060	0.344
	19MG20-17	19MG20-T1	0.704	0.034	0.859	0.052	-0.02	0.104	1.296
20	19MG20-18	19MG20-T1	1.319	0.165	0.897	0.076	0.26	0.074	0.424
	19MG20-18	19MG20-T1	0.901	0.068	0.837	0.050	0.03	0.027	0.252
21	19MG20-19	19MG20-T1	0.901	0.089	0.804	0.068	0.47	0.023	0.198
	19MG20-19	19MG20-T1	1.333	0.249	0.850	0.110	0.01	0.027	0.179
22	19MG20-19	19MG20-T1	1.149	0.132	0.819	0.091	0.66	0.021	0.168
20	19MG20-20	19MG20-T1	1.754	0.157	0.788	0.054	0.59	0.034	0.168
	19MG20-20	19MG20-T1	1.808	0.177	0.865	0.083	0.69	0.031	0.148
21	19MG20-21	19MG20-T2	1.656	0.151	0.762	0.063	0.51	0.040	0.253
	19MG20-21	19MG20-T2	3.413	0.303	0.841	0.055	0.45	0.063	0.189
22	19MG20-22	19MG20-T2	5.102	0.390	0.803	0.025	0.08	2.440	5.710
	19MG20-22	19MG20-T2	4.505	0.588	0.779	0.021	-0.26	1.770	4.030
	19MG20-22	19MG20-T2	3.922	0.185	0.801	0.017	0.34	0.923	2.720
23	19MG20-23	19MG20-T2	1.969	0.132	0.809	0.032	0.71	2.000	10.900
	19MG20-23	19MG20-T2	2.959	0.123	0.795	0.028	-0.04	1.873	7.040
	19MG20-23	19MG20-T2	2.994	0.143	0.798	0.053	0.22	1.387	5.260
	19MG20-23	19MG20-T2	3.378	0.228	0.823	0.025	0.64	1.790	5.880
	19MG20-23	19MG20-T2	3.650	0.293	0.793	0.021	0.15	1.198	3.710
24	19MG20-24	19MG20-T2	2.415	0.257	0.835	0.049	0.47	0.451	2.170
	19MG20-24	19MG20-T2	1.805	0.287	0.824	0.047	-0.13	0.528	3.490
	19MG20-24	19MG20-T2	5.128	0.394	0.854	0.051	0.37	0.345	0.793
	19MG20-24	19MG20-T2	0.621	0.096	0.818	0.019	0.49	0.629	13.100
25	19MG20-25	19MG20-T2	2.114	0.139	0.843	0.049	0.33	0.048	0.249
26	19MG20-26	19MG20-T2	10.309	1.807	0.740	0.140	0.74	0.289	0.330
	19MG20-26	19MG20-T2	21.231	2.885	0.713	0.063	-0.28	0.880	0.200
	19MG20-26	19MG20-T2	8.772	1.385	0.760	0.110	0.57	0.312	0.357
	19MG20-26	19MG20-T2	21.459	3.500	0.662	0.063	0.55	0.595	0.232
27	19MG20-27	19MG20-T2	6.803	0.740	0.809	0.053	0.40	0.680	1.270
	19MG20-27	19MG20-T2	9.091	1.405	0.831	0.064	0.47	0.146	0.156
28	19MG20-28	19MG20-T2	2.899	0.185	0.830	0.047	0.46	0.053	0.217
	19MG20-28	19MG20-T2	13.850	1.611	0.750	0.065	0.56	0.238	0.187
29	19MG20-29	19MG20-T2	15.432	1.334	0.784	0.051	0.17	0.476	0.341
	19MG20-29	19MG20-T2	2.703	0.541	0.834	0.037	0.21	0.326	1.490

Spot	Source file (.FIN2)	Sample	$^{238}U/^{206}Pb$	±2σ (abs)	$^{207}Pb/^{206}Pb$	±2σ (abs)	Rho	U (ppm)	Pb (ppm)
30	19MG20-30	19MG20-T2	2.611	0.307	0.802	0.056	-0.03	1.880	8.430
	19MG20-30	19MG20-T2	3.497	0.257	0.789	0.022	0.33	1.364	4.630
	19MG20-30	19MG20-T2	4.545	0.537	0.808	0.031	0.24	1.460	3.400
	19MG20-30	19MG20-T2	5.319	0.707	0.810	0.028	0.21	1.570	3.150
	19MG20-30	19MG20-T2	4.425	0.313	0.784	0.028	0.18	0.761	2.000
	19MG20-30	19MG20-T2	4.831	0.700	0.804	0.028	-0.09	1.550	3.390
31	19MG20-31	19MG20-T2	4.425	0.607	0.784	0.021	0.48	5.530	11.500
	19MG20-31	19MG20-T2	6.817	0.339	0.816	0.029	0.59	5.700	7.740
	19MG20-31	19MG20-T2	7.246	0.578	0.804	0.021	0.33	5.670	7.250
	19MG20-31	19MG20-T2	2.212	0.416	0.819	0.023	-0.24	4.410	18.700
	19MG20-31	19MG20-T2	2.625	0.220	0.793	0.018	0.08	6.020	20.800
	19MG20-31	19MG20-T2	2.976	0.257	0.819	0.015	0.14	3.200	10.200
	19MG20-31	19MG20-T2	4.167	0.347	0.805	0.023	0.39	3.950	8.350
32	19MG20-32	19MG20-T2	5.025	0.404	0.819	0.045	0.46	0.894	1.620
	19MG20-32	19MG20-T2	1.299	0.186	0.814	0.028	0.55	0.765	5.600
	19MG20-32	19MG20-T2	3.135	0.275	0.801	0.030	0.24	0.666	1.930
	19MG20-32	19MG20-T2	7.246	1.418	0.789	0.039	0.30	1.550	1.510
	19MG20-32	19MG20-T2	8.264	0.888	0.782	0.030	0.10	1.640	1.740
33	19MG20-33	19MG20-T2	1.475	0.174	0.847	0.051	-0.04	0.640	3.910
	19MG20-33	19MG20-T2	3.378	0.605	0.783	0.042	0.05	0.409	1.240
	19MG20-33	19MG20-T2	1.416	0.165	0.831	0.034	0.39	0.344	2.160
	19MG20-33	19MG20-T2	2.488	0.254	0.828	0.046	0.25	0.206	0.765
34	19MG20-34	19MG20-T2	27.933	2.497	0.710	0.048	-0.32	3.070	0.861
	19MG20-34	19MG20-T2	4.739	1.146	0.810	0.085	-0.20	2.040	3.510
	19MG20-34	19MG20-T2	18.519	3.429	0.717	0.093	0.02	1.730	0.770
	19MG20-34	19MG20-T2	7.246	1.155	0.765	0.035	0.50	2.050	2.440
	19MG20-34	19MG20-T2	15.898	2.022	0.712	0.035	0.21	1.423	0.738
35	19MG20-35	19MG20-T2	19.960	2.709	0.665	0.027	0.04	4.390	1.830
	19MG20-35	19MG20-T2	21.978	4.782	0.714	0.061	0.35	5.350	2.100
	19MG20-35	19MG20-T2	12.255	0.661	0.719	0.040	-0.22	3.350	2.530
	19MG20-35	19MG20-T2	24.096	2.787	0.644	0.031	0.12	4.070	1.300
	19MG20-35	19MG20-T2	45.872	3.998	0.602	0.053	0.31	4.580	0.821
	19MG20-35	19MG20-T2	38.610	3.280	0.630	0.048	0.05	4.150	0.780
	19MG20-35	19MG20-T2	30.303	2.571	0.671	0.051	0.80	3.940	1.080
	19MG20-35	19MG20-T2	37.313	3.898	0.631	0.051	0.27	4.370	0.950
36	19MG20-36	19MG20-T2	14.409	1.080	0.709	0.054	0.67	0.953	0.690
	19MG20-36	19MG20-T2	15.244	1.673	0.682	0.088	0.87	0.759	0.392
	19MG20-36	19MG20-T2	19.920	2.103	0.673	0.087	0.47	0.849	0.367
	19MG20-36	19MG20-T2	19.920	3.413	0.715	0.073	0.20	0.860	0.283
	19MG20-36	19MG20-T2	25.253	3.252	0.679	0.083	0.49	0.910	0.281
	19MG20-36	19MG20-T2	18.868	3.916	0.740	0.110	0.59	0.497	0.218
37	19MG20-37	19MG20-T2	2.545	0.317	0.813	0.055	0.46	0.077	0.252
	19MG20-37	19MG20-T2	3.049	0.260	0.812	0.056	0.08	0.064	0.190

Spot	Source file (.FIN2)	Sample	$^{238}U/^{206}Pb$	±2σ (abs)	$^{207}Pb/^{206}Pb$	±2σ (abs)	Rho	U (ppm)	Pb (ppm)
39	19MG20-39	19MG20-T2	4.255	0.398	0.827	0.058	0.49	0.133	0.320
	19MG20-39	19MG20-T2	2.564	0.217	0.872	0.057	-0.11	0.057	0.248
40	19MG20-40	19MG20-T2	14.184	1.147	0.793	0.040	0.31	0.375	0.248
	19MG20-41	19MG20-T3	4.167	0.486	0.800	0.100	0.75	0.061	0.187
41	19MG20-41	19MG20-T3	5.618	0.694	0.847	0.083	0.61	0.084	0.206
	19MG20-41	19MG20-T3	9.872	0.809	0.820	0.077	-0.07	0.125	0.158
	19MG20-43	19MG20-T3	4.049	0.459	0.813	0.079	0.15	0.139	0.451
43	19MG20-43	19MG20-T3	2.070	0.214	0.817	0.045	0.22	0.176	1.300
	19MG20-43	19MG20-T3	4.132	0.563	0.819	0.039	0.01	0.162	0.540
	19MG20-44	19MG20-T3	2.506	0.251	0.880	0.080	0.43	0.037	0.236
44	19MG20-44	19MG20-T3	2.083	0.156	0.796	0.071	0.34	0.028	0.196
	19MG20-44	19MG20-T3	5.376	0.780	0.744	0.076	0.39	0.082	0.183
	19MG20-45	19MG20-T3	1.887	1.104	0.740	0.240	0.49	0.080	0.338
	19MG20-45	19MG20-T3	6.410	0.657	0.804	0.072	-0.01	0.159	0.396
45	19MG20-45	19MG20-T3	4.695	0.331	0.740	0.048	0.64	0.211	0.669
	19MG20-45	19MG20-T3	8.850	1.331	0.743	0.069	-0.17	0.242	0.382
	19MG20-45	19MG20-T3	5.405	0.380	0.765	0.061	0.71	0.107	0.291
	19MG20-45	19MG20-T3	6.803	0.926	0.752	0.065	-0.26	0.142	0.278
	19MG20-46	19MG20-T3	4.717	1.557	0.760	0.130	0.35	0.093	0.238
46	19MG20-46	19MG20-T3	6.757	0.593	0.860	0.067	0.45	0.093	0.204
	19MG20-46	19MG20-T3	10.989	1.570	0.780	0.100	0.26	0.115	0.201
47	19MG20-47	19MG20-T3	6.494	0.590	0.982	0.071	0.43	0.084	0.190
	19MG20-47	19MG20-T3	8.621	1.263	0.900	0.110	0.34	0.086	0.191
	19MG20-48	19MG20-T3	7.143	5.612	0.890	0.180	-0.01	0.267	0.397
	19MG20-48	19MG20-T3	13.333	2.311	0.770	0.110	0.43	0.400	0.447
	19MG20-48	19MG20-T3	14.085	2.182	0.707	0.085	0.69	0.322	0.341
48	19MG20-48	19MG20-T3	13.699	1.877	0.820	0.120	0.40	0.281	0.383
	19MG20-48	19MG20-T3	16.694	2.648	0.707	0.080	0.35	0.308	0.275
	19MG20-48	19MG20-T3	12.407	1.062	0.729	0.072	0.77	0.201	0.234
	19MG20-48	19MG20-T3	10.417	1.628	0.573	0.099	0.20	0.172	0.251
	19MG20-48	19MG20-T3	62.500	42.969	0.640	0.100	-0.06	6.000	0.463
	19MG20-49	19MG20-T3	10.309	1.594	0.733	0.072	0.40	0.328	0.509
	19MG20-49	19MG20-T3	10.638	2.037	0.667	0.077	0.00	0.940	1.500
49	19MG20-49	19MG20-T3	15.456	2.198	0.712	0.091	0.15	0.307	0.295
	19MG20-49	19MG20-T3	13.889	5.787	0.600	0.140	0.42	0.338	0.410
	19MG20-49	19MG20-T3	6.667	1.467	0.704	0.073	0.19	0.188	0.388
50	19MG20-50	19MG20-T3	8.772	1.770	0.903	0.065	0.31	0.440	0.760
51	19MG20-51	19MG20-T3	8.772	1.539	0.940	0.086	0.02	0.198	0.267
52	19MG20-52	19MG20-T3	3.257	0.308	0.970	0.093	-0.02	0.044	0.226
53	19MG20-53	19MG20-T3	3.356	0.338	0.899	0.060	0.32	0.049	0.251
54	19MG20-54	19MG20-T3	1.261	0.135	0.863	0.062	0.28	0.020	0.312

313

Spot	Source file (.FIN2)	Sample	$^{238}U/^{206}Pb$	±2σ (abs)	$^{207}Pb/^{206}Pb$	±2σ (abs)	Rho	U (ppm)	Pb (ppm)
	19MG20-55	19MG20-T3	5.291	0.644	0.733	0.085	0.04	0.248	0.760
	19MG20-55	19MG20-T3	5.464	1.254	0.694	0.062	-0.12	0.267	0.900
55	19MG20-55	19MG20-T3	7.463	0.947	0.688	0.059	-0.26	0.540	1.080
	19MG20-55	19MG20-T3	8.333	1.319	0.669	0.054	0.18	0.376	0.843
	19MG20-55	19MG20-T3	11.223	1.247	0.740	0.061	0.36	0.432	0.705
	19MG20-55	19MG20-T3	8.929	1.355	0.645	0.043	0.60	0.618	1.200
56	19MG20-56	19MG20-T3	4.405	0.485	0.889	0.065	0.16	0.059	0.199
57	19MG20-57	19MG20-T3	1.898	0.302	0.840	0.065	0.10	0.076	0.840
	19MG20-57	19MG20-T3	1.984	0.189	0.839	0.045	0.38	0.049	0.450
58	19MG20-58	19MG20-T3	1.429	0.100	0.863	0.053	0.58	0.021	0.279
	19MG20-59	19MG20-T3	3.472	0.470	0.833	0.068	0.15	0.062	0.279
	19MG20-59	19MG20-T3	16.835	1.644	0.651	0.037	0.57	0.830	0.850
59	19MG20-59	19MG20-T3	17.575	1.205	0.676	0.068	0.83	1.000	0.950
	19MG20-59	19MG20-T3	14.577	1.381	0.731	0.063	0.39	0.423	0.518
	19MG20-59	19MG20-T3	11.236	1.389	0.768	0.095	0.65	0.256	0.380
	19MG20-60	19MG20-T3	2.008	0.379	0.799	0.089	0.16	0.066	0.356
60	19MG20-60	19MG20-T3	3.125	1.270	0.770	0.120	0.29	0.073	0.245
	19MG20-60	19MG20-T3	4.739	0.651	0.940	0.120	-0.03	0.084	0.282

19MG21 from DA strain domain

Spot	Source file (.FIN2)	Sample	$^{238}U/^{206}Pb$	±2σ (abs)	$^{207}Pb/^{206}Pb$	±2σ (abs)	Rho	U (ppm)	Pb (ppm)
1	19MG21-1B	19MG21-1C	2.320	0.065	0.798	0.014	0.34	1.058	3.245
	19MG21-1B	19MG21-1C	2.801	0.094	0.795	0.017	0.33	1.158	2.737
2	19MG21-2	19MG21-1C	2.667	0.121	0.802	0.023	0.40	0.924	1.916
	19MG21-2	19MG21-1C	1.567	0.101	0.816	0.022	0.17	0.508	1.578
3	19MG21-3	19MG21-1C	0.400	0.018	0.819	0.015	0.11	0.203	2.155
4	19MG21-4	19MG21-1C	0.684	0.019	0.806	0.015	-0.09	0.337	1.870
	19MG21-5	19MG21-1C	0.895	0.046	0.805	0.022	0.25	0.670	2.771
5	19MG21-5	19MG21-1C	1.555	0.077	0.768	0.021	0.36	1.021	2.455
	19MG21-5	19MG21-1C	0.919	0.035	0.806	0.023	0.45	0.583	2.409
	19MG21-6	19MG21-1C	1.340	0.124	0.812	0.030	0.25	0.931	2.930
6	19MG21-6	19MG21-1C	1.266	0.160	0.783	0.032	-0.14	1.220	3.990
	19MG21-6	19MG21-1C	1.041	0.055	0.811	0.014	0.10	1.130	4.150
7	19MG21-7	19MG21-1C	1.042	0.056	0.804	0.024	-0.01	0.229	0.953
8	19MG21-8	19MG21-1C	0.407	0.016	0.821	0.014	0.23	0.141	1.860
9	19MG21-9	19MG21-1C	0.156	0.014	0.813	0.024	0.15	0.042	1.677
	19MG21-9	19MG21-1C	0.649	0.020	0.827	0.018	0.38	0.183	1.771
10	19MG21-10	19MG21-1C	0.776	0.036	0.823	0.021	0.47	0.271	2.343
	19MG21-10	19MG21-1C	0.422	0.037	0.790	0.027	0.26	0.123	1.792
	19MG21-11	19MG21-1C	2.294	0.110	0.804	0.016	0.19	0.910	3.170
11	19MG21-11	19MG21-1C	2.653	0.106	0.799	0.030	0.58	0.799	2.410
	19MG21-11	19MG21-1C	2.950	0.104	0.787	0.025	0.54	0.775	2.087
12	19MG21-12	19MG21-1C	3.049	0.121	0.796	0.019	0.07	0.772	2.057
	19MG21-12	19MG21-1C	2.283	0.068	0.812	0.022	0.58	0.551	1.999

Spot	Source file (.FIN2)	Sample	^{238}U/^{206}Pb	±2σ (abs)	^{207}Pb/^{206}Pb	±2σ (abs)	Rho	U (ppm)	Pb (ppm)
13	19MG21-13	19MG21-1C	2.653	0.077	0.797	0.022	0.50	0.627	2.060
	19MG21-13	19MG21-1C	2.882	0.108	0.797	0.023	0.46	0.590	1.780
14	19MG21-14	19MG21-1C	4.632	0.165	0.803	0.023	0.41	1.066	2.133
	19MG21-14	19MG21-1C	4.153	0.133	0.805	0.018	0.40	0.866	1.886
	19MG21-15	19MG21-1C	2.907	0.169	0.766	0.024	0.19	0.651	2.002
15	19MG21-15	19MG21-1C	2.950	0.096	0.797	0.024	0.39	0.581	1.871
	19MG21-15	19MG21-1C	2.268	0.098	0.789	0.023	0.46	0.419	1.783
16	19MG21-16	19MG21-1C	3.186	0.096	0.804	0.013	0.19	0.563	1.695
17	19MG21-17	19MG21-1C	2.058	0.174	0.799	0.020	0.78	0.745	3.500
	19MG21-17	19MG21-1C	2.457	0.085	0.799	0.017	0.48	0.602	2.454
18	19MG21-18	19MG21-1C	1.739	0.127	0.781	0.022	0.21	0.423	2.400
	19MG21-18	19MG21-1C	1.447	0.057	0.800	0.018	0.17	0.302	2.152
19	19MG21-19	19MG21-1C	0.875	0.030	0.823	0.015	0.28	0.136	1.644
20	19MG21-20	19MG21-1C	1.493	0.058	0.811	0.022	0.09	0.258	1.868
	19MG21-20	19MG21-1C	0.719	0.052	0.837	0.023	0.09	0.127	1.849
21	19MG21-21	19MG21-1C	1.678	0.062	0.796	0.032	0.78	0.333	1.997
	19MG21-21	19MG21-1C	1.890	0.068	0.815	0.019	0.48	0.344	1.838
22	19MG21-22	19MG21-1C	3.165	0.441	0.743	0.036	0.10	1.120	2.660
	19MG21-22	19MG21-1C	0.935	0.049	0.795	0.018	0.03	0.211	2.020
23	19MG21-23	19MG21-1C	0.221	0.019	0.807	0.014	0.01	0.063	1.911
24	19MG21-24	19MG21-1C	1.873	0.077	0.806	0.023	0.58	0.820	3.740
	19MG21-24	19MG21-1C	2.564	0.055	0.807	0.015	0.58	0.832	2.805
	19MG21-25	19MG21-1C	0.649	0.031	0.786	0.030	0.51	0.221	2.630
25	19MG21-25	19MG21-1C	0.878	0.066	0.778	0.024	0.46	0.241	2.120
	19MG21-25	19MG21-1C	0.546	0.033	0.811	0.028	0.39	0.127	1.846
26	19MG21-26	19MG21-1C	1.144	0.065	0.817	0.031	0.47	0.329	2.130
	19MG21-26	19MG21-1C	1.264	0.099	0.799	0.017	0.13	0.570	2.260
	19MG21-27	19MG21-1C	0.908	0.036	0.794	0.022	0.37	0.296	2.336
27	19MG21-27	19MG21-1C	0.685	0.061	0.823	0.030	0.11	0.210	2.280
	19MG21-27	19MG21-1C	1.416	0.128	0.804	0.030	0.49	0.375	1.934
	19MG21-27	19MG21-1C	0.909	0.091	0.776	0.028	-0.01	0.290	2.099
28	19MG21-28	19MG21-1C	1.475	0.074	0.795	0.029	0.38	0.465	2.290
	19MG21-28	19MG21-1C	1.828	0.057	0.806	0.017	0.29	0.545	2.244
29	19MG21-29	19MG21-1C	1.372	0.083	0.821	0.034	0.51	0.466	2.502
	19MG21-29	19MG21-1C	1.600	0.123	0.821	0.016	0.17	0.800	3.990
30	19MG21-30	19MG21-1C	0.187	0.009	0.805	0.016	0.20	0.051	2.243
31	19MG21-31	19MG21-1C	2.105	0.071	0.804	0.018	0.51	0.413	2.709
	19MG21-31	19MG21-1C	1.590	0.071	0.800	0.025	0.53	0.353	3.038
32	19MG21-32	19MG21-1C	2.681	0.072	0.821	0.015	0.33	0.411	2.314
33	19MG21-33	19MG21-1C	2.237	0.080	0.820	0.024	0.55	0.239	1.670
	19MG21-33	19MG21-1C	1.362	0.058	0.821	0.027	0.37	0.115	1.347
	19MG21-34	19MG21-1C	2.933	0.086	0.804	0.028	0.61	0.376	2.095
34	19MG21-34	19MG21-1C	3.262	0.101	0.805	0.026	0.62	0.392	2.035
	19MG21-34	19MG21-1C	3.356	0.124	0.795	0.028	0.70	0.418	2.056

Spot	Source file (.FIN2)	Sample	^{238}U/^{206}Pb	±2σ (abs)	^{207}Pb/^{206}Pb	±2σ (abs)	Rho	U (ppm)	Pb (ppm)
35	19MG21-35	19MG21-1C	4.484	0.111	0.791	0.025	0.54	0.652	2.411
	19MG21-35	19MG21-1C	4.255	0.120	0.805	0.020	0.55	0.568	2.193
36	19MG21-36	19MG21-1C	3.096	0.153	0.817	0.024	0.33	0.432	2.426
	19MG21-36	19MG21-1C	2.882	0.091	0.815	0.022	0.44	0.339	2.006
37	19MG21-37	19MG21-1C	2.101	0.071	0.781	0.019	0.32	0.558	4.320
	19MG21-37	19MG21-1C	2.674	0.071	0.821	0.016	0.25	0.438	2.719
38	19MG21-38	19MG21-1C	1.029	0.052	0.815	0.029	0.55	0.178	2.790
	19MG21-38	19MG21-1C	1.205	0.061	0.811	0.020	0.22	0.227	2.940
39	19MG21-39	19MG21-1C	0.704	0.060	0.845	0.029	0.12	0.142	2.950
	19MG21-39	19MG21-1C	0.556	0.040	0.833	0.044	0.47	0.099	2.900
	19MG21-39	19MG21-1C	0.759	0.037	0.820	0.020	0.25	0.136	2.883
40	19MG21-40	19MG21-1C	1.639	0.086	0.816	0.019	0.12	0.494	4.580
	19MG21-40	19MG21-1C	1.587	0.101	0.798	0.020	-0.05	0.521	5.060

19MG43 from DA strain domain

Spot	Source file (.FIN2)	Sample	^{238}U/^{206}Pb	±2σ (abs)	^{207}Pb/^{206}Pb	±2σ (abs)	Rho	U (ppm)	Pb (ppm)
1	19MG43-1	19MG43-1	1.515	0.161	0.807	0.023	0.26	0.094	0.967
	19MG43-1	19MG43-1	2.674	0.293	0.805	0.044	0.19	0.166	0.900
2	19MG43-2	19MG43-1	3.650	0.240	0.789	0.039	0.29	0.253	1.161
	19MG43-2	19MG43-1	2.584	0.140	0.820	0.029	0.36	0.170	1.005
3	19MG43-3	19MG43-1	2.481	0.166	0.822	0.035	0.50	0.085	0.540
4	19MG43-4	19MG43-1	2.653	0.218	0.814	0.022	0.25	0.176	0.978
5	19MG43-5	19MG43-1	2.222	0.202	0.853	0.068	0.47	0.069	0.510
	19MG43-5	19MG43-1	1.087	0.118	0.828	0.033	0.27	0.094	1.490
6	19MG43-6	19MG43-1	1.221	0.067	0.825	0.027	0.22	0.058	0.795
7	19MG43-7	19MG43-1	3.378	0.274	0.814	0.040	0.25	0.089	0.439
	19MG43-7	19MG43-1	2.747	0.355	0.846	0.065	0.42	0.111	0.710
8	19MG43-8	19MG43-1	1.692	0.123	0.806	0.039	0.29	0.105	1.034
	19MG43-8	19MG43-1	2.959	0.184	0.860	0.040	0.52	0.092	0.576
9	19MG43-9	19MG43-1	1.698	0.182	0.806	0.045	0.42	0.096	0.990
	19MG43-9	19MG43-1	2.703	0.482	0.779	0.022	-0.12	0.331	1.960
	19MG43-9	19MG43-1	3.401	0.231	0.817	0.050	0.05	0.187	0.913
10	19MG43-10	19MG43-1	2.841	0.266	0.765	0.062	0.45	0.136	0.764
	19MG43-10	19MG43-1	2.857	0.180	0.805	0.032	0.15	0.129	0.762
	19MG43-10	19MG43-1	1.289	0.091	0.828	0.044	-0.17	0.098	1.290
11	19MG43-11	19MG43-1	1.773	0.129	0.801	0.040	0.25	0.180	1.083
	19MG43-11	19MG43-1	1.736	0.109	0.787	0.028	0.01	0.148	0.947
	19MG43-11	19MG43-1	1.157	0.086	0.811	0.056	0.62	0.109	1.022
12	19MG43-12	19MG43-1	0.131	0.009	0.818	0.020	0.19	0.037	2.910
	19MG43-12	19MG43-1	0.287	0.022	0.815	0.024	0.13	0.047	1.700
13	19MG43-13	19MG43-1	1.048	0.089	0.819	0.055	0.56	0.071	0.722
	19MG43-13	19MG43-1	0.625	0.043	0.864	0.034	0.37	0.063	1.132
14	19MG43-14	19MG43-1	0.302	0.025	0.809	0.016	0.00	0.067	2.042
15	19MG43-15	19MG43-1	2.151	0.129	0.821	0.023	0.45	0.166	0.914

Spot	Source file (.FIN2)	Sample	$^{238}U/^{206}Pb$	±2σ (abs)	$^{207}Pb/^{206}Pb$	±2σ (abs)	Rho	U (ppm)	Pb (ppm)
16	19MG43-16	19MG43-1	1.890	0.111	0.844	0.035	0.52	0.056	0.366
17	19MG43-17	19MG43-1	5.952	0.602	0.848	0.072	0.26	0.178	0.393
	19MG43-17	19MG43-1	3.521	0.236	0.824	0.035	0.31	0.170	0.635
18	19MG43-18	19MG43-1	0.469	0.033	0.821	0.028	0.34	0.031	0.929
	19MG43-18	19MG43-1	1.183	0.080	0.841	0.053	0.43	0.041	0.500
19	19MG43-19	19MG43-1	0.205	0.028	0.804	0.041	0.01	0.020	1.318
	19MG43-19	19MG43-1	0.483	0.035	0.804	0.027	0.28	0.027	0.878
	19MG43-19	19MG43-1	0.294	0.041	0.880	0.080	-0.05	0.015	0.804
20	19MG43-20	19MG43-1			no value	NAN	NaN	0.007	1.402
21	19MG43-21	19MG43-1	0.714	0.061	0.818	0.046	0.56	0.028	0.684
	19MG43-21	19MG43-1	1.284	0.105	0.818	0.045	0.64	0.031	0.401
22	19MG43-22	19MG43-1			no value	NAN	NaN	0.006	0.205
24	19MG43-24	19MG43-1			no value	NAN	NaN	0.003	0.141
25	19MG43-25	19MG43-1			no value	NAN	NaN	0.002	0.365
26	19MG43-26	19MG43-1	0.348	0.038	0.829	0.081	0.44	0.009	0.527
27	19MG43-27	19MG43-1	1.136	0.107	0.836	0.049	0.15	0.039	0.657
	19MG43-27	19MG43-1	0.395	0.033	0.809	0.037	0.26	0.016	0.753
28	19MG43-28	19MG43-1	0.995	0.090	0.825	0.030	0.30	0.034	0.658
29	19MG43-29	19MG43-1	3.077	0.199	0.867	0.043	0.29	0.060	0.390
30	19MG43-30	19MG43-1	0.418	0.046	0.825	0.080	0.39	0.021	0.953
	19MG43-30	19MG43-1	0.568	0.042	0.811	0.035	0.47	0.023	0.828
	19MG43-30	19MG43-1	0.524	0.049	0.795	0.034	0.24	0.018	0.655
31	19MG43-31	19MG43-1	0.284	0.036	0.789	0.031	0.14	0.020	1.223
32	19MG43-32	19MG43-1	0.339	0.049	0.798	0.030	0.18	0.017	0.832
33	19MG43-33	19MG43-1	0.562	0.063	0.822	0.019	0.20	0.075	2.350
	19MG43-33	19MG43-1	1.220	0.208	0.806	0.025	0.15	0.116	1.640
	19MG43-33	19MG43-1	0.588	0.066	0.809	0.049	0.27	0.043	1.370
34	19MG43-34	19MG43-1	0.943	0.049	0.825	0.028	0.38	0.049	0.984
35	19MG43-35	19MG43-1	1.792	0.222	0.811	0.077	0.52	0.134	1.257
	19MG43-35	19MG43-1	2.571	0.496	0.757	0.023	0.43	0.181	1.530
	19MG43-35	19MG43-1	1.984	0.110	0.838	0.030	0.45	0.136	1.331
	19MG43-35	19MG43-1	3.215	0.269	0.803	0.035	0.23	0.183	1.045
36	19MG43-36	19MG43-1	1.124	0.303	0.799	0.036	0.41	0.114	1.380
	19MG43-36	19MG43-1	3.279	0.441	0.818	0.031	0.14	0.195	0.950
	19MG43-36	19MG43-1	1.316	0.126	0.827	0.044	0.49	0.056	0.810
37	19MG43-37	19MG43-1	0.645	0.042	0.799	0.040	0.19	0.072	1.920
	19MG43-37	19MG43-1	2.564	0.920	0.755	0.048	-0.58	0.490	1.518
	19MG43-37	19MG43-1	2.105	0.310	0.831	0.057	0.37	0.133	1.050
	19MG43-37	19MG43-1	1.242	0.099	0.819	0.031	-0.19	0.086	1.160
38	19MG43-38	19MG43-1	1.934	0.198	0.784	0.039	-0.07	0.092	0.722
	19MG43-38	19MG43-1	4.405	0.854	0.752	0.048	0.09	0.300	0.800
	19MG43-38	19MG43-1	3.704	1.646	0.735	0.084	-0.76	0.940	0.900
	19MG43-38	19MG43-1	1.919	0.365	0.785	0.076	0.31	0.066	0.542

Spot	Source file (.FIN2)	Sample	$^{238}U/^{206}Pb$	±2σ (abs)	$^{207}Pb/^{206}Pb$	±2σ (abs)	Rho	U (ppm)	Pb (ppm)
	19MG43-39	19MG43-1	5.208	0.814	0.798	0.033	0.41	0.420	1.100
39	19MG43-39	19MG43-1	3.534	0.275	0.799	0.032	0.56	0.231	1.051
	19MG43-39	19MG43-1	5.000	0.300	0.834	0.039	0.21	0.263	0.889
	19MG43-40	19MG43-1	0.290	0.025	0.815	0.041	0.16	0.029	1.539
40	19MG43-40	19MG43-1	0.505	0.036	0.827	0.036	0.42	0.043	1.316
	19MG43-40	19MG43-1	0.370	0.021	0.835	0.024	0.35	0.029	1.212
	19MG43-41	19MG43-1	0.412	0.042	0.787	0.045	0.24	0.039	1.017
41	19MG43-41	19MG43-1	0.827	0.061	0.828	0.034	0.33	0.060	0.795
	19MG43-41	19MG43-1	0.649	0.067	0.843	0.079	-0.23	0.055	1.060
	19MG43-41	19MG43-1	1.235	0.145	0.801	0.033	0.02	0.250	1.360
	19MG43-42	19MG43-1	0.207	0.018	0.823	0.037	0.34	0.030	1.472
42	19MG43-42	19MG43-1	0.262	0.016	0.792	0.033	0.19	0.032	1.224
	19MG43-42	19MG43-1	0.184	0.019	0.827	0.027	0.22	0.027	1.313
	19MG43-43	19MG43-1	1.887	0.203	0.767	0.026	0.01	0.204	0.779
43	19MG43-43	19MG43-1	3.774	0.527	0.795	0.079	0.34	0.294	0.671
	19MG43-43	19MG43-1	1.453	0.127	0.834	0.040	0.20	0.121	0.684
44	19MG43-44	19MG43-1	2.755	0.152	0.844	0.028	0.51	0.429	1.382
	19MG43-44	19MG43-1	3.344	0.313	0.777	0.025	0.04	0.543	1.173
45	19MG43-45	19MG43-1	2.123	0.257	0.811	0.023	0.14	0.538	1.500
	19MG43-45	19MG43-1	0.495	0.049	0.808	0.019	0.42	0.377	5.870
46	19MG43-46	19MG43-1	0.448	0.038	0.823	0.025	0.08	0.068	1.151
	19MG43-46	19MG43-1	0.981	0.058	0.807	0.032	0.49	0.080	0.566
47	19MG43-47	19MG43-1	0.223	0.011	0.812	0.019	0.25	0.041	1.285
48	19MG43-48	19MG43-1	1.256	0.112	0.883	0.093	0.25	0.204	0.925
49	19MG43-49	19MG43-1			no value	NAN	NaN	0.014	1.101
	19MG43-50	19MG43-1	1.156	0.120	0.801	0.040	0.40	0.143	1.102
50	19MG43-50	19MG43-1	0.565	0.054	0.827	0.045	0.15	0.064	1.070
	19MG43-50	19MG43-1	0.709	0.070	0.811	0.033	0.24	0.069	0.859
53	19MG43-53	19MG43-2	10.417	1.302	0.747	0.097	0.37	1.950	2.910
	19MG43-53	19MG43-2	1.163	0.149	0.750	0.100	0.37	0.025	0.307
	19MG43-54	19MG43-2	5.650	0.543	0.754	0.093	0.55	1.280	3.500
54	19MG43-54	19MG43-2	9.606	0.581	0.845	0.062	0.20	0.709	1.145
	19MG43-54	19MG43-2	8.969	0.434	0.778	0.035	0.56	0.718	1.340
55	19MG43-55	19MG43-2	10.309	2.126	0.700	0.180	0.77	0.548	0.520
	19MG43-55	19MG43-2	3.831	0.558	0.894	0.079	0.06	0.123	0.328
58	19MG43-58	19MG43-2	2.841	0.307	0.838	0.030	0.20	0.601	3.250
	19MG43-58	19MG43-2	8.032	0.606	0.780	0.110	0.58	0.426	0.696
59	19MG43-59	19MG43-2	17.331	1.562	0.885	0.066	0.65	0.747	0.592
	19MG43-60	19MG43-2	15.873	3.023	0.740	0.110	0.77	1.480	1.300
60	19MG43-60	19MG43-2	27.248	2.005	0.891	0.072	0.77	0.767	0.343
	19MG43-60	19MG43-2	19.231	4.068	0.870	0.120	0.75	0.443	0.246
	19MG43-63	19MG43-2	0.020	0.003	0.841	0.023	-0.06	0.095	39.100
63	19MG43-63	19MG43-2	0.459	0.059	0.887	0.051	-0.07	0.172	2.830

Spot	Source file (.FIN2)	Sample	$^{238}U/^{206}Pb$	±2σ (abs)	$^{207}Pb/^{206}Pb$	±2σ (abs)	Rho	U (ppm)	Pb (ppm)
72	19MG43-72	19MG43-2	8.772	1.000	0.682	0.052	0.22	0.893	0.523
	19MG43-72	19MG43-2	11.377	0.712	0.870	0.069	-0.06	0.741	0.477
	19MG43-72	19MG43-2	11.682	0.751	0.800	0.063	0.82	0.641	0.418
	19MG43-72	19MG43-2	10.299	0.700	0.904	0.072	0.54	0.615	0.429
78	19MG43-78	19MG43-3	5.747	0.562	0.792	0.029	0.18	0.428	0.488
79	19MG43-79	19MG43-3	4.525	0.307	0.829	0.041	0.05	0.198	0.267
80	19MG43-80	19MG43-3	2.933	0.344	0.910	0.066	0.40	0.121	0.242
81	19MG43-81	19MG43-3	0.518	0.054	0.825	0.019	0.24	0.710	8.590
	19MG43-81	19MG43-3	3.597	0.505	0.791	0.047	0.49	0.432	0.642
	19MG43-81	19MG43-3	6.452	0.583	0.808	0.035	0.33	0.453	0.431
82	19MG43-82	19MG43-3	1.389	0.164	0.991	0.096	0.34	0.037	0.145
83	19MG43-83	19MG43-3	2.817	0.309	0.894	0.083	0.04	0.105	0.166
	19MG43-83	19MG43-3	16.667	8.889	0.683	0.062	-0.09	3.300	0.806
	19MG43-83	19MG43-3	2.475	0.607	0.841	0.052	-0.36	0.673	1.610
	19MG43-83	19MG43-3	2.326	0.595	0.770	0.043	-0.51	1.090	2.390
	19MG43-83	19MG43-3	1.269	0.129	0.838	0.035	0.25	0.499	2.560
84	19MG43-84	19MG43-3	5.236	0.521	0.817	0.062	0.58	0.156	0.162
	19MG43-84	19MG43-3	7.837	0.559	0.850	0.059	0.56	0.267	0.213
85	19MG43-85	19MG43-3	4.587	0.337	0.825	0.047	0.42	0.160	0.223
	19MG43-85	19MG43-3	6.024	0.581	0.809	0.045	0.20	0.324	0.330
86	19MG43-86	19MG43-3	5.051	1.326	0.717	0.065	-0.21	0.217	0.159
	19MG43-86	19MG43-3	2.398	0.408	0.710	0.110	0.62	0.081	0.167
	19MG43-86	19MG43-3	5.291	0.588	0.890	0.058	0.43	0.171	0.206
	19MG43-86	19MG43-3	5.682	1.001	0.727	0.059	0.02	0.325	0.283
	19MG43-86	19MG43-3	7.698	0.516	0.817	0.089	0.43	0.289	0.245
87	19MG43-87	19MG43-3	4.348	0.586	0.792	0.064	0.30	0.094	0.123
	19MG43-87	19MG43-3	13.038	1.122	0.788	0.095	0.43	0.354	0.176
	19MG43-87	19MG43-3	15.949	1.730	0.712	0.049	0.10	0.625	0.194
88	19MG43-88	19MG43-3	12.987	2.024	0.781	0.076	0.33	0.390	0.174
	19MG43-88	19MG43-3	11.655	1.182	0.867	0.074	0.48	0.436	0.233
	19MG43-88	19MG43-3	17.007	1.186	0.800	0.054	0.49	0.788	0.270
89	19MG43-89	19MG43-3	0.935	0.087	0.816	0.073	-0.03	0.027	0.175
	19MG43-89	19MG43-3	1.718	0.201	0.821	0.070	0.26	0.065	0.197
90	19MG43-90	19MG43-3	6.098	0.632	0.766	0.052	0.28	0.313	0.286
	19MG43-90	19MG43-3	5.917	1.225	0.735	0.079	0.16	0.560	0.395
	19MG43-90	19MG43-3	9.671	0.898	0.826	0.058	0.06	0.492	0.293
	19MG43-90	19MG43-3	5.917	0.665	0.817	0.041	0.38	1.100	1.210
91	19MG43-91	19MG43-3	6.944	0.868	0.809	0.071	0.06	0.477	0.418
	19MG43-91	19MG43-3	18.215	2.986	0.731	0.072	0.16	1.420	0.488
	19MG43-91	19MG43-3	7.463	0.613	0.774	0.025	0.50	0.853	0.737
92	19MG43-92	19MG43-3	4.292	0.313	0.850	0.044	0.64	0.141	0.220
	19MG43-92	19MG43-3	5.525	0.580	0.806	0.045	0.14	0.413	0.449
93	19MG43-93	19MG43-3	2.445	0.203	0.839	0.037	0.35	0.118	0.264

Spot	Source file (.FIN2)	Sample	$^{238}U/^{206}Pb$	±2σ (abs)	$^{207}Pb/^{206}Pb$	±2σ (abs)	Rho	U (ppm)	Pb (ppm)
	19MG43-94	19MG43-3	3.546	0.528	0.819	0.070	0.46	0.173	0.284
94	19MG43-94	19MG43-3	7.553	0.542	0.815	0.050	0.22	0.315	0.267
	19MG43-94	19MG43-3	11.710	1.316	0.785	0.051	0.02	0.694	0.393
	19MG43-95	19MG43-3	2.183	0.310	0.868	0.066	0.24	0.097	0.218
95	19MG43-95	19MG43-3	10.101	1.122	0.794	0.060	0.17	0.407	0.237
	19MG43-95	19MG43-3	39.683	6.141	0.514	0.057	-0.44	4.480	0.344
	19MG43-95	19MG43-3	28.736	1.982	0.730	0.110	0.49	1.680	0.343
96	19MG43-96	19MG43-3	3.115	0.175	0.842	0.038	0.30	0.134	0.256
97	19MG43-97	19MG43-3	3.165	0.190	0.854	0.047	0.12	0.153	0.288
	19MG43-97	19MG43-3	4.000	0.624	0.807	0.053	-0.05	0.277	0.339
98	19MG43-98	19MG43-3	2.252	0.188	0.874	0.060	0.34	0.111	0.264
99	19MG43-99	19MG43-3	1.969	0.174	0.950	0.100	0.13	0.088	0.227
	19MG43-99	19MG43-3	2.545	0.363	0.803	0.054	-0.14	0.340	0.387
100	19MG43-100	19MG43-3	2.513	0.240	0.898	0.070	0.12	0.128	0.238

WC-1 Calcite reference (Roberts et al., 2017)

Spot	Source file (.FIN2)	Sample	$^{238}U/^{206}Pb$	±2σ (abs)	$^{207}Pb/^{206}Pb$	±2σ (abs)	Rho	U (ppm)	Pb (ppm)
1	WC1-1	WC-1	24.546	0.386	0.050	0.003	0.13	3.704	0.192
2	WC1-2	WC-1	25.119	0.303	0.051	0.003	0.40	3.768	0.170
3	WC1-3	WC-1	25.006	0.313	0.051	0.004	0.01	3.490	0.200
4	WC1-4	WC-1	25.094	0.290	0.052	0.003	-0.02	3.971	0.233
5	WC1-5	WC-1	24.492	0.330	0.051	0.003	0.30	3.327	0.173
6	WC1-6	WC-1	25.368	0.296	0.052	0.003	0.39	3.852	0.201
7	WC1-7	WC-1	25.278	0.281	0.051	0.002	0.22	3.706	0.166
20	WC1-20	WC-1	24.408	0.435	0.049	0.008	-0.49	3.695	0.382
8	WC1-8	WC-1	25.400	0.316	0.051	0.002	0.12	3.705	0.126
21	WC1-21	WC-1	23.883	0.405	0.051	0.005	0.06	3.641	0.333
9	WC1-9	WC-1	25.183	0.336	0.051	0.003	0.11	3.750	0.188
10	WC1-10	WC-1	24.826	0.333	0.052	0.004	-0.20	3.682	0.243
22	WC1-22	WC-1	25.265	0.281	0.051	0.002	0.08	3.693	0.181
11	WC1-11	WC-1	24.808	0.320	0.051	0.002	0.08	3.864	0.197
23	WC1-23	WC-1	24.679	0.335	0.052	0.003	0.17	3.384	0.166
12	WC1-12	WC-1	25.556	0.320	0.051	0.002	0.11	4.271	0.167
24	WC1-24	WC-1	25.063	0.352	0.052	0.003	0.11	3.646	0.170
13	WC1-13	WC-1	24.679	0.341	0.052	0.003	0.07	3.767	0.133
16	WC1-16	WC-1	25.013	0.350	0.051	0.004	0.04	3.655	0.157
17	WC1-17	WC-1	24.254	0.318	0.051	0.003	-0.12	4.543	0.189
14	WC1-14	WC-1	24.938	0.417	0.050	0.006	0.11	3.656	0.223
15	WC1-15	WC-1	25.240	0.344	0.051	0.003	0.00	3.708	0.175
19	WC1-19	WC-1	25.063	0.446	0.052	0.008	-0.58	4.634	0.328
25	WC1-25	WC-1	24.944	0.392	0.047	0.008	-0.04	3.391	0.187
26	WC1-26	WC-1	25.195	0.317	0.052	0.003	-0.17	6.020	0.212
28	WC1-28	WC-1	25.208	0.356	0.053	0.010	-0.37	3.694	0.412

Soda-lime glass NIST SRM-614

Spot	Source file (.FIN2)	Sample	$^{238}U/^{206}Pb$	±2σ (abs)	$^{207}Pb/^{206}Pb$	±2σ (abs)	Rho	U (ppm)	Pb (ppm)
1	NIST614-135-1	NIST-614	1.513	0.023	0.867	0.009	0.15	0.436	9.680
2	NIST614-135-2	NIST-614	1.474	0.019	0.875	0.009	0.26	0.435	9.700
3	NIST614-135-3	NIST-614	1.439	0.017	0.871	0.009	0.43	0.457	9.810
4	NIST614-135-4	NIST-614	1.489	0.017	0.860	0.009	0.45	1.873	7.550
5	NIST614-135-5	NIST-614	1.444	0.018	0.858	0.009	-0.03	0.383	7.250
6	NIST614-135-6	NIST-614	1.473	0.018	0.855	0.009	0.25	0.412	7.190
7	NIST614-135-7	NIST-614	1.455	0.018	0.865	0.009	0.30	0.464	7.120

Sample 19MG46 from DA domain

Spot	Source file (.FIN2)	Sample	$^{238}U/^{206}Pb$	±2σ (abs)	$^{207}Pb/^{206}Pb$	±2σ (abs)	Rho	U (ppm)	Pb (ppm)
1	19MG46-1	19MG46-4B	5.348	2.116	0.870	0.100	0.56	0.058	0.560
	19MG46-1	19MG46-4B	7.692	1.302	0.865	0.089	0.14	0.044	0.130
	19MG46-2	19MG46-4B	6.173	1.143	1.000	0.270	0.54	0.032	0.156
2	19MG46-2	19MG46-4B	10.753	2.428	0.630	0.130	0.38	0.055	0.096
	19MG46-2	19MG46-4B	12.151	1.019	0.939	0.095	0.61	0.044	0.097
3	19MG46-3	19MG46-4B	20.492	1.764	0.865	0.073	0.83	0.063	0.097
4	19MG46-4	19MG46-4B	8.197	1.008	0.910	0.100	0.46	0.028	0.095
	19MG46-4	19MG46-4B	16.779	1.745	0.838	0.098	0.83	0.052	0.090
	19MG46-5	19MG46-4B	9.804	1.250	0.860	0.120	0.17	0.032	0.090
5	19MG46-5	19MG46-4B	0.505	0.224	0.819	0.080	0.59	0.031	1.750
	19MG46-5	19MG46-4B	9.804	1.442	0.810	0.110	0.00	0.032	0.095
	19MG46-5	19MG46-4B	2.273	0.671	0.820	0.100	0.45	0.030	0.350
6	19MG46-6	19MG46-4B	15.974	1.480	0.918	0.086	0.83	0.048	0.083
7	19MG46-7	19MG46-4B	7.519	0.848	0.810	0.110	0.50	0.033	0.132
	19MG46-7	19MG46-4B	10.299	0.732	0.863	0.073	0.43	0.033	0.100
8	19MG46-8	19MG46-4B	1.176	0.595	0.813	0.079	0.76	0.020	0.510
	19MG46-8	19MG46-4B	13.755	1.173	0.990	0.130	0.82	0.033	0.073
	19MG46-9	19MG46-4B	9.709	1.037	0.832	0.074	0.50	0.030	0.100
9	19MG46-9	19MG46-4B	11.364	1.420	0.870	0.100	0.73	0.042	0.119
	19MG46-9	19MG46-4B	14.556	1.377	0.937	0.098	0.75	0.044	0.108
10	19MG46-10	19MG46-4B	11.628	2.028	0.890	0.110	0.44	0.036	0.084
11	19MG46-11	19MG46-4B	29.412	4.671	0.710	0.130	0.60	0.107	0.059
	19MG46-11	19MG46-4B	25.381	4.380	0.620	0.140	0.40	0.089	0.057
	19MG46-12	19MG46-4B	12.469	1.104	0.828	0.073	0.35	0.123	0.187
12	19MG46-12	19MG46-4B	2.653	0.528	0.808	0.051	0.42	0.178	1.350
	19MG46-12	19MG46-4B	13.514	2.191	0.730	0.130	0.64	0.106	0.126
	19MG46-12	19MG46-4B	13.699	1.877	0.780	0.110	0.55	0.089	0.122
13	19MG46-13	19MG46-4B	0.752	0.158	0.786	0.043	0.62	0.088	2.630
	19MG46-13	19MG46-4B	13.316	1.294	0.764	0.061	0.07	0.101	0.116
14	19MG46-14	19MG46-4B	9.346	0.873	0.890	0.120	0.07	0.044	0.098
	19MG46-14	19MG46-4B	11.198	1.091	0.860	0.130	0.99	0.033	0.057

Spot	Source file (.FIN2)	Sample	^{238}U/^{206}Pb	±2σ (abs)	^{207}Pb/^{206}Pb	±2σ (abs)	Rho	U (ppm)	Pb (ppm)
	19MG46-15	19MG46-4B	18.587	3.075	0.800	0.130	0.65	0.145	0.300
	19MG46-15	19MG46-4B	12.658	3.685	0.590	0.160	0.60	0.059	0.067
15	19MG46-15	19MG46-4B	16.556	2.522	0.740	0.110	0.70	0.056	0.060
	19MG46-15	19MG46-4B	21.882	3.735	0.950	0.190	0.76	0.068	0.073
	19MG46-15	19MG46-4B	4.695	1.697	0.670	0.150	0.27	0.063	0.230
	19MG46-15	19MG46-4B	5.618	2.399	0.800	0.120	0.46	0.060	0.220
16	19MG46-16	19MG46-4B	18.939	1.614	0.831	0.063	0.69	0.078	0.078
17	19MG46-17	19MG46-4B	16.892	1.084	0.896	0.078	0.94	0.078	0.092
	19MG46-18	19MG46-4B	3.704	1.509	0.820	0.130	-0.10	0.083	0.480
18	19MG46-18	19MG46-4B	9.346	3.232	0.760	0.200	0.61	0.051	0.118
	19MG46-18	19MG46-4B	27.933	2.887	0.930	0.120	0.60	0.073	0.052
	19MG46-19	19MG46-4B	10.753	1.387	0.800	0.120	0.49	0.058	0.150
19	19MG46-19	19MG46-4B	20.040	3.012	1.010	0.170	0.78	0.062	0.077
	19MG46-19	19MG46-4B	16.949	4.022	0.730	0.120	0.20	0.070	0.073
20	19MG46-20	19MG46-4B	7.246	1.628	0.580	0.160	0.94	0.034	0.082
	19MG46-20	19MG46-4B	17.889	1.568	0.913	0.091	0.68	0.061	0.064
	19MG46-21	19MG46-4B	14.771	1.745	0.810	0.120	0.48	0.078	0.144
21	19MG46-21	19MG46-4B	20.000	1.840	0.840	0.100	0.55	0.065	0.064
	19MG46-21	19MG46-4B	26.525	3.448	0.810	0.150	0.94	0.076	0.070
	19MG46-22	19MG46-4B	18.382	1.994	0.880	0.120	0.33	0.110	0.110
22	19MG46-22	19MG46-4B	40.984	9.574	0.730	0.160	-0.28	0.350	0.100
	19MG46-22	19MG46-4B	15.699	1.922	0.765	0.090	0.57	0.111	0.127
	19MG46-22	19MG46-4B	19.194	3.352	0.640	0.140	0.73	0.094	0.078
23	19MG46-23	19MG46-4B	19.608	2.307	1.000	0.140	0.71	0.056	0.050
	19MG46-23	19MG46-4B	19.231	3.698	0.760	0.120	0.33	0.082	0.064
24	19MG46-24	19MG46-4B	18.149	1.746	0.850	0.110	0.53	0.085	0.069
	19MG46-24	19MG46-4B	29.940	4.034	0.800	0.150	0.88	0.111	0.049
25	19MG46-25	19MG46-4B	2.083	0.694	0.697	0.095	0.48	0.073	0.400
	19MG46-25	19MG46-4B	17.857	1.626	0.929	0.093	0.98	0.115	0.490
26	19MG46-26	19MG46-4B	16.287	1.326	0.873	0.079	0.56	0.100	0.086
	19MG46-26	19MG46-4B	6.667	2.933	0.710	0.082	0.63	0.078	0.096
	19MG46-27	19MG46-4B	16.393	2.956	0.780	0.120	0.63	0.127	0.128
27	19MG46-27	19MG46-4B	21.459	2.809	0.940	0.140	0.92	0.136	0.089
	19MG46-27	19MG46-4B	15.748	1.885	0.870	0.140	0.70	0.090	0.065
	19MG46-27	19MG46-4B	20.000	5.200	0.770	0.160	0.00	0.230	0.071
	19MG46-28	19MG46-4B	11.494	2.642	0.780	0.110	0.15	0.317	0.360
28	19MG46-28	19MG46-4B	19.685	1.899	0.803	0.075	0.59	0.128	0.070
	19MG46-28	19MG46-4B	36.101	8.080	0.600	0.120	0.08	0.287	0.065
	19MG46-29	19MG46-4B	14.144	1.560	0.868	0.091	0.73	0.101	0.101
29	19MG46-29	19MG46-4B	3.425	0.669	0.820	0.180	0.87	0.119	0.510
	19MG46-29	19MG46-4B	19.231	4.438	0.640	0.180	0.99	0.107	0.055
30	19MG46-30	19MG46-4B	14.124	1.476	0.830	0.082	0.64	0.108	0.111
	19MG46-30	19MG46-4B	28.653	2.791	0.770	0.100	0.44	0.166	0.074

Spot	Source file (.FIN2)	Sample	$^{238}U/^{206}Pb$	±2σ (abs)	$^{207}Pb/^{206}Pb$	±2σ (abs)	Rho	U (ppm)	Pb (ppm)
	19MG46-31	19MG46-5B	6.803	1.064	0.790	0.110	0.57	0.034	0.109
31	19MG46-31	19MG46-5B	12.500	2.344	1.010	0.320	0.77	0.051	0.079
	19MG46-31	19MG46-5B	16.611	2.290	0.833	0.079	0.63	0.088	0.097
	19MG46-32	19MG46-5B	11.494	1.453	0.970	0.120	0.64	0.059	0.124
	19MG46-32	19MG46-5B	4.695	1.367	0.680	0.140	0.72	0.059	0.247
32	19MG46-32	19MG46-5B	14.085	2.380	0.940	0.160	0.46	0.052	0.096
	19MG46-32	19MG46-5B	4.484	1.367	0.760	0.100	0.31	0.053	0.241
	19MG46-32	19MG46-5B	12.195	2.528	0.800	0.100	0.09	0.085	0.116
	19MG46-33	19MG46-5B	8.772	1.077	0.866	0.097	0.56	0.042	0.117
	19MG46-33	19MG46-5B	15.152	4.821	0.800	0.140	-0.04	0.069	0.074
33	19MG46-33	19MG46-5B	16.611	2.732	0.990	0.240	0.40	0.047	0.059
	19MG46-33	19MG46-5B	1.282	0.345	0.785	0.083	0.06	0.043	0.710
	19MG46-33	19MG46-5B	16.129	3.642	1.000	0.220	0.59	0.041	0.052
	19MG46-34	19MG46-5B	9.615	1.202	0.990	0.130	0.63	0.040	0.112
34	19MG46-34	19MG46-5B	2.128	1.222	0.860	0.270	0.56	0.035	0.470
	19MG46-34	19MG46-5B	10.417	1.302	0.730	0.120	0.66	0.041	0.072
	19MG46-34	19MG46-5B	13.947	1.595	0.870	0.120	0.79	0.039	0.049
	19MG46-35	19MG46-5B	8.547	0.804	0.940	0.110	0.04	0.043	0.102
35	19MG46-35	19MG46-5B	8.403	1.554	0.890	0.150	0.76	0.037	0.092
	19MG46-35	19MG46-5B	14.859	1.700	0.800	0.110	0.99	0.043	0.059
	19MG46-36	19MG46-5B	8.929	2.073	0.698	0.091	-0.08	0.095	0.330
36	19MG46-36	19MG46-5B	6.098	2.268	0.730	0.110	0.01	0.121	0.330
	19MG46-36	19MG46-5B	19.268	1.782	0.960	0.110	0.77	0.065	0.062
37	19MG46-37	19MG46-5B	6.135	0.677	0.693	0.061	0.45	0.050	0.154
	19MG46-37	19MG46-5B	15.504	1.274	0.829	0.085	0.70	0.072	0.085
38	19MG46-38	19MG46-5B	4.000	0.368	0.820	0.075	0.67	0.040	0.181
	19MG46-38	19MG46-5B	9.852	0.854	0.816	0.077	0.72	0.053	0.101
39	19MG46-39	19MG46-5B	4.785	0.962	0.794	0.085	0.35	0.063	0.235
	19MG46-39	19MG46-5B	12.642	1.263	0.768	0.090	0.65	0.063	0.075
	19MG46-40	19MG46-5B	6.329	1.001	0.840	0.110	0.22	0.061	0.134
40	19MG46-40	19MG46-5B	7.874	0.992	0.846	0.084	0.06	0.111	0.207
	19MG46-40	19MG46-5B	9.901	2.255	0.721	0.060	-0.05	0.227	0.271
	19MG46-41	19MG46-5B	8.258	0.614	0.915	0.083	0.12	0.030	0.136
41	19MG46-41	19MG46-5B	6.897	0.951	0.870	0.100	0.62	0.027	0.159
	19MG46-41	19MG46-5B	10.638	3.056	0.660	0.120	-0.23	0.084	0.101
	19MG46-42	19MG46-5B	8.000	3.584	0.800	0.082	0.54	0.073	0.430
42	19MG46-42	19MG46-5B	11.111	1.235	0.900	0.110	0.75	0.024	0.103
	19MG46-42	19MG46-5B	15.873	6.299	0.610	0.130	-0.39	0.107	0.141
	19MG46-42	19MG46-5B	5.747	0.628	0.816	0.097	0.70	0.014	0.098
	19MG46-43	19MG46-5B	6.623	0.921	1.010	0.200	0.91	0.009	0.064
43	19MG46-43	19MG46-5B	2.381	1.020	0.820	0.150	0.14	0.014	0.231
	19MG46-43	19MG46-5B	7.813	0.916	0.920	0.140	0.83	0.014	0.061

Spot	Source file (.FIN2)	Sample	$^{238}U/^{206}Pb$	±2σ (abs)	$^{207}Pb/^{206}Pb$	±2σ (abs)	Rho	U (ppm)	Pb (ppm)
	19MG46-44	19MG46-5B	6.250	1.602	1.040	0.220	0.73	0.012	0.097
44	19MG46-44	19MG46-5B	20.000	5.600	0.830	0.200	0.15	0.095	0.081
	19MG46-44	19MG46-5B	8.403	3.037	0.760	0.120	-0.28	0.052	0.127
	19MG46-44	19MG46-5B	13.680	1.722	0.990	0.140	0.36	0.020	0.073
45	19MG46-45	19MG46-5B	7.692	0.769	0.921	0.099	0.09	0.020	0.111
	19MG46-46	19MG46-5B	7.692	0.651	0.979	0.092	0.28	0.015	0.095
46	19MG46-46	19MG46-5B	3.984	1.063	0.830	0.120	0.58	0.023	0.255
	19MG46-46	19MG46-5B	8.475	1.580	0.730	0.150	0.77	0.021	0.100
47	19MG46-47	19MG46-5B	13.072	0.837	0.874	0.063	0.31	0.027	0.086
	19MG46-48	19MG46-5B	7.407	1.591	0.850	0.180	0.34	0.016	0.061
48	19MG46-48	19MG46-5B	3.521	1.203	0.770	0.110	0.43	0.024	0.268
	19MG46-48	19MG46-5B	9.434	2.136	0.720	0.110	-0.18	0.050	0.109
	19MG46-48	19MG46-5B	8.065	0.845	0.855	0.094	0.53	0.016	0.085
49	19MG46-49	19MG46-5B	15.873	3.023	0.960	0.120	0.73	0.023	0.050
50	19MG46-50	19MG46-5B	4.608	0.998	0.827	0.083	0.39	0.022	0.157
	19MG46-50	19MG46-5B	20.367	2.572	0.850	0.140	0.87	0.035	0.052
	19MG46-51	19MG46-5B	3.922	0.461	0.747	0.073	0.50	0.062	0.226
	19MG46-51	19MG46-5B	3.096	0.882	0.750	0.110	0.03	0.079	0.222
51	19MG46-51	19MG46-5B	3.788	0.344	0.669	0.057	0.49	0.051	0.164
	19MG46-51	19MG46-5B	6.135	1.355	0.720	0.110	0.25	0.076	0.112
	19MG46-51	19MG46-5B	10.000	2.100	0.930	0.190	0.31	0.076	0.092
52	19MG46-52	19MG46-5B	6.061	0.588	0.940	0.120	0.00	0.061	0.086
	19MG46-53	19MG46-5B	6.289	1.622	0.740	0.110	-0.38	0.260	0.171
	19MG46-53	19MG46-5B	1.370	0.732	0.781	0.065	0.65	0.089	0.440
53	19MG46-53	19MG46-5B	12.195	1.933	0.788	0.072	0.06	0.344	0.185
	19MG46-53	19MG46-5B	33.333	14.444	0.580	0.170	-0.20	0.820	0.161
	19MG46-53	19MG46-5B	10.638	1.924	0.820	0.110	-0.08	0.164	0.155
	19MG46-53	19MG46-5B	6.329	1.402	0.765	0.082	0.47	0.162	0.244
	19MG46-54	19MG46-5B	5.236	1.234	0.850	0.230	0.53	0.066	0.138
54	19MG46-54	19MG46-5B	13.158	3.289	0.740	0.120	-0.31	0.320	0.137
	19MG46-54	19MG46-5B	5.882	0.796	0.791	0.052	0.43	0.120	0.246
	19MG46-54	19MG46-5B	10.309	4.889	0.626	0.071	0.48	0.510	0.251
	19MG46-55	19MG46-5B	8.065	0.911	0.809	0.067	0.43	0.072	0.121
55	19MG46-55	19MG46-5B	2.439	0.892	0.830	0.130	0.29	0.071	0.440
	19MG46-55	19MG46-5B	8.333	1.319	0.880	0.150	0.84	0.044	0.066
	19MG46-55	19MG46-5B	17.241	4.756	0.770	0.150	-0.06	0.109	0.075
	19MG46-56	19MG46-5B	4.202	0.424	0.754	0.087	0.50	0.027	0.120
56	19MG46-56	19MG46-5B	7.042	0.843	0.780	0.093	0.32	0.041	0.103
	19MG46-56	19MG46-5B	10.989	3.381	0.780	0.140	0.51	0.052	0.104
	19MG46-56	19MG46-5B	18.587	2.315	0.900	0.180	0.93	0.060	0.074

Spot	Source file (.FIN2)	Sample	$^{238}U/^{206}Pb$	±2σ (abs)	$^{207}Pb/^{206}Pb$	±2σ (abs)	Rho	U (ppm)	Pb (ppm)
	19MG46-57	19MG46-5B	8.696	1.512	0.790	0.180	0.27	0.059	0.163
	19MG46-57	19MG46-5B	23.256	17.847	0.430	0.140	-0.59	3.800	0.284
	19MG46-57	19MG46-5B	10.309	3.614	0.696	0.071	-0.08	0.134	0.280
57	19MG46-57	19MG46-5B	5.917	2.101	0.747	0.086	-0.55	0.259	0.830
	19MG46-57	19MG46-5B	4.545	1.529	0.642	0.086	-0.01	0.135	0.460
	19MG46-57	19MG46-5B	17.857	4.145	0.720	0.130	-0.03	0.233	0.209
	19MG46-57	19MG46-5B	20.161	3.943	0.796	0.085	0.25	0.225	0.196
	19MG46-57	19MG46-5B	12.500	2.188	0.741	0.045	0.32	0.144	0.208
	19MG46-58	19MG46-5B	13.889	3.086	0.760	0.110	0.57	0.187	0.306
	19MG46-58	19MG46-5B	7.042	1.190	0.731	0.062	0.31	0.072	0.246
	19MG46-58	19MG46-5B	9.434	2.136	0.770	0.110	0.22	0.135	0.284
	19MG46-58	19MG46-5B	12.048	3.193	0.747	0.088	0.44	0.151	0.251
58	19MG46-58	19MG46-5B	8.264	1.229	0.729	0.055	0.53	0.079	0.193
	19MG46-58	19MG46-5B	9.346	1.572	0.688	0.080	0.35	0.104	0.199
	19MG46-58	19MG46-5B	10.753	1.734	0.647	0.058	-0.21	0.113	0.207
	19MG46-58	19MG46-5B	24.331	4.736	0.670	0.100	0.02	0.245	0.202
	19MG46-58	19MG46-5B	18.868	5.340	0.750	0.150	0.00	0.230	0.176
	19MG46-59	19MG46-5B	8.696	1.210	0.728	0.042	0.30	0.135	0.364
	19MG46-59	19MG46-5B	4.405	1.669	0.780	0.054	-0.32	0.200	1.020
	19MG46-59	19MG46-5B	10.000	2.600	0.722	0.048	-0.40	0.490	1.220
59	19MG46-59	19MG46-5B	5.464	0.747	0.715	0.060	0.13	0.128	0.610
	19MG46-59	19MG46-5B	0.694	0.246	0.827	0.053	0.26	0.139	3.500
	19MG46-59	19MG46-5B	16.393	4.569	0.686	0.065	-0.67	0.362	0.416
	19MG46-59	19MG46-5B	13.699	3.002	0.704	0.076	0.53	0.264	0.460
	19MG46-59	19MG46-5B	6.024	0.762	0.780	0.073	0.27	0.096	0.417
	19MG46-60	19MG46-5B	4.785	1.236	0.800	0.150	0.39	0.044	0.192
60	19MG46-60	19MG46-5B	9.174	1.431	0.842	0.097	0.02	0.042	0.087
	19MG46-60	19MG46-5B	9.615	2.219	0.716	0.074	-0.03	0.057	0.114
	19MG46-60	19MG46-5B	9.091	1.074	0.890	0.100	0.58	0.039	0.105
	19MG46-61	19MG46-6B	9.434	2.136	1.260	0.410	0.98	0.027	0.051
	19MG46-61	19MG46-6B	0.613	0.211	0.860	0.150	0.74	0.030	0.570
61	19MG46-61	19MG46-6B	8.403	1.765	0.950	0.380	0.82	0.029	0.042
	19MG46-61	19MG46-6B	9.709	2.168	0.750	0.100	-0.09	0.056	0.039
	19MG46-61	19MG46-6B	25.000	12.500	0.610	0.140	-0.07	0.840	0.071
	19MG46-61	19MG46-6B	3.333	2.111	0.677	0.095	0.72	0.060	0.260
	19MG46-62	19MG46-6B	9.259	1.543	0.806	0.099	0.30	0.136	0.129
	19MG46-62	19MG46-6B	5.181	2.121	0.787	0.092	-0.08	0.360	0.640
	19MG46-62	19MG46-6B	1.282	0.444	0.766	0.069	-0.19	0.690	3.410
62	19MG46-62	19MG46-6B	0.893	0.096	0.772	0.048	0.04	0.290	2.980
	19MG46-62	19MG46-6B	5.650	0.766	0.700	0.110	0.43	0.320	0.422
	19MG46-62	19MG46-6B	20.408	7.497	0.670	0.110	-0.12	0.660	0.219
	19MG46-62	19MG46-6B	5.000	1.400	0.703	0.092	0.36	0.224	0.324
	19MG46-62	19MG46-6B	15.873	4.535	0.730	0.110	0.20	0.540	0.177

Spot	Source file (.FIN2)	Sample	^{238}U/^{206}Pb	±2σ (abs)	^{207}Pb/^{206}Pb	±2σ (abs)	Rho	U (ppm)	Pb (ppm)
	19MG46-63	19MG46-6B	8.696	2.344	0.840	0.140	0.12	0.147	0.115
63	19MG46-63	19MG46-6B	14.286	2.653	0.860	0.150	0.75	0.101	0.051
	19MG46-63	19MG46-6B	18.975	2.520	0.960	0.160	0.94	0.099	0.041
	19MG46-64	19MG46-6B	1.205	0.595	0.920	0.150	0.56	0.053	0.330
64	19MG46-64	19MG46-6B	9.259	1.115	0.833	0.097	0.64	0.077	0.054
	19MG46-64	19MG46-6B	6.897	1.712	0.810	0.140	0.79	0.136	0.185
	19MG46-65	19MG46-6B	3.831	0.778	0.850	0.140	0.51	0.045	0.112
65	19MG46-65	19MG46-6B	6.173	0.533	0.830	0.100	0.83	0.079	0.110
	19MG46-65	19MG46-6B	6.757	0.593	0.860	0.110	0.20	0.084	0.108
66	19MG46-66	19MG46-6B	13.495	1.730	0.980	0.250	0.49	0.068	0.052
67	19MG46-67	19MG46-6B	13.158	2.251	0.920	0.190	0.81	0.046	0.037
	19MG46-67	19MG46-6B	22.222	3.951	0.980	0.310	0.83	0.057	0.028
	19MG46-68	19MG46-6B	12.346	1.829	1.030	0.200	1.00	0.040	0.044
68	19MG46-68	19MG46-6B	3.497	1.051	0.660	0.110	0.65	0.027	0.107
	19MG46-68	19MG46-6B	22.321	3.587	0.750	0.660	0.88	0.047	0.032
	19MG46-69	19MG46-6B	8.929	1.435	0.870	0.190	0.89	0.028	0.049
69	19MG46-69	19MG46-6B	30.303	13.774	0.600	0.220	-0.08	0.480	0.037
	19MG46-69	19MG46-6B	14.205	1.876	0.980	0.200	0.78	0.029	0.031
	19MG46-69	19MG46-6B	8.264	2.595	0.650	0.150	0.29	0.030	0.054
70	19MG46-70	19MG46-6B	26.738	2.860	1.020	0.360	0.75	0.050	0.031
71	19MG46-71	19MG46-6B	25.641	6.377	0.670	0.150	-0.07	0.240	0.049
	19MG46-71	19MG46-6B	15.974	2.092	0.910	0.180	0.91	0.036	0.029
	19MG46-72	19MG46-6B	12.658	1.763	0.900	0.160	0.16	0.060	0.067
72	19MG46-72	19MG46-6B	12.092	1.389	0.910	0.150	1.00	0.031	0.049
	19MG46-72	19MG46-6B	14.706	5.190	1.700	1.100	0.78	0.023	0.030
	19MG46-72	19MG46-6B	30.303	18.365	0.470	0.200	-0.25	0.460	0.035
73	19MG46-73	19MG46-6B	18.315	1.811	0.950	0.110	0.72	0.042	0.043
	19MG46-74	19MG46-6B	10.870	1.654	1.080	0.260	0.02	0.039	0.082
	19MG46-74	19MG46-6B	10.417	1.736	0.980	0.210	0.49	0.034	0.077
74	19MG46-74	19MG46-6B	1.887	0.498	0.786	0.070	0.90	0.079	0.890
	19MG46-74	19MG46-6B	10.309	1.382	0.870	0.110	0.65	0.045	0.109
	19MG46-74	19MG46-6B	2.941	0.545	0.832	0.085	-0.11	0.065	0.555
	19MG46-74	19MG46-6B	10.309	2.232	0.930	0.160	0.78	0.055	0.149

Spot	Source file (.FIN2)	Sample	$^{238}U/^{206}Pb$	±2σ (abs)	$^{207}Pb/^{206}Pb$	±2σ (abs)	Rho	U (ppm)	Pb (ppm)
	19MG46-75	19MG46-6B	2.381	1.644	0.704	0.060	0.50	1.000	4.200
	19MG46-75	19MG46-6B	3.125	1.563	0.709	0.041	-0.30	0.370	1.600
	19MG46-75	19MG46-6B	10.010	0.661	0.768	0.060	0.41	0.099	0.304
	19MG46-75	19MG46-6B	19.608	6.920	0.660	0.130	-0.76	0.238	0.267
	19MG46-75	19MG46-6B	17.241	4.459	0.710	0.110	-0.32	0.205	0.285
75	19MG46-75	19MG46-6B	11.236	2.146	0.750	0.180	-0.03	0.089	0.145
	19MG46-75	19MG46-6B	10.417	1.736	0.703	0.069	0.08	0.146	0.347
	19MG46-75	19MG46-6B	33.898	6.205	0.672	0.093	-0.19	0.317	0.199
	19MG46-75	19MG46-6B	12.987	3.205	0.680	0.064	0.04	0.121	0.214
	19MG46-75	19MG46-6B	16.393	6.987	0.680	0.100	0.40	0.208	0.182
	19MG46-75	19MG46-6B	21.277	6.790	0.580	0.110	0.30	0.161	0.145
	19MG46-75	19MG46-6B	13.021	1.373	0.800	0.120	0.48	0.092	0.194
76	19MG46-76	19MG46-6B	17.731	1.760	1.050	0.160	0.91	0.027	0.048
77	19MG46-77	19MG46-6B	11.862	1.281	1.010	0.170	1.00	0.027	0.069
	19MG46-77	19MG46-6B	7.353	2.109	0.740	0.240	-0.06	0.014	0.045
	19MG46-78	19MG46-6B	11.236	1.641	0.774	0.067	0.01	0.084	0.156
	19MG46-78	19MG46-6B	7.353	1.622	0.672	0.071	0.20	0.052	0.199
78	19MG46-78	19MG46-6B	27.778	13.889	0.500	0.160	-0.66	0.290	0.072
	19MG46-78	19MG46-6B	16.667	4.722	0.620	0.160	-0.20	0.126	0.080
	19MG46-79	19MG46-6B	8.929	2.392	0.730	0.130	0.70	0.024	0.063
	19MG46-79	19MG46-6B	4.310	1.040	0.760	0.130	0.63	0.033	0.205
79	19MG46-79	19MG46-6B	14.472	1.927	0.810	0.150	1.00	0.022	0.038
	19MG46-79	19MG46-6B	0.699	0.200	0.703	0.056	0.81	0.016	0.630
	19MG46-79	19MG46-6B	7.576	2.009	0.750	0.250	0.85	0.012	0.038
	19MG46-80	19MG46-6B	15.748	2.058	0.870	0.150	0.84	0.028	0.040
80	19MG46-80	19MG46-6B	11.236	2.525	0.680	0.200	0.77	0.020	0.023
	19MG46-80	19MG46-6B	18.904	3.145	0.880	0.200	0.79	0.026	0.028
	19MG46-80	19MG46-6B	12.346	2.439	1.020	0.370	0.93	0.022	0.036
	19MG46-81	19MG46-6B	10.204	4.998	0.640	0.290	0.65	0.626	0.086
81	19MG46-81	19MG46-6B	25.000	6.875	0.800	0.290	0.66	0.619	0.036
	19MG46-81	19MG46-6B	24.814	4.125	0.870	0.280	0.97	0.853	0.022
	19MG46-81	19MG46-6B	20.000	5.600	0.990	0.200	0.59	2.850	0.042
	19MG46-82	19MG46-6B	10.989	2.294	0.870	0.210	0.94	-0.253	0.038
	19MG46-82	19MG46-6B	9.524	2.902	0.640	0.200	1.00	-0.230	0.043
82	19MG46-82	19MG46-6B	16.129	3.382	0.800	0.130	0.09	-0.580	0.045
	19MG46-82	19MG46-6B	16.129	4.683	0.970	0.290	0.87	-0.252	0.042
	19MG46-82	19MG46-6B	8.696	2.268	0.740	0.170	0.92	-0.210	0.055
	19MG46-82	19MG46-6B	18.868	3.560	0.920	0.240	0.59	-0.260	0.036
	19MG46-83	19MG46-6B	18.868	5.696	0.735	0.092	-0.15	-1.420	0.178
	19MG46-83	19MG46-6B	11.905	1.417	0.776	0.067	0.47	-0.588	0.183
83	19MG46-83	19MG46-6B	0.526	0.144	0.775	0.024	-0.49	-0.610	4.300
	19MG46-83	19MG46-6B	8.547	2.118	0.750	0.080	0.30	-0.723	0.345
	19MG46-83	19MG46-6B	14.706	2.595	0.800	0.100	0.33	-0.690	0.179

Spot	Source file (.FIN2)	Sample	^{238}U/^{206}Pb	±2σ (abs)	^{207}Pb/^{206}Pb	±2σ (abs)	Rho	U (ppm)	Pb (ppm)
	19MG46-84	19MG46-6B	7.194	2.277	0.777	0.059	0.01	-1.660	0.572
	19MG46-84	19MG46-6B	8.475	2.011	0.758	0.068	0.20	-1.300	0.537
84	19MG46-84	19MG46-6B	4.651	1.514	0.729	0.047	-0.02	-0.950	0.730
	19MG46-84	19MG46-6B	2.193	0.365	0.755	0.038	0.07	-0.648	1.180
	19MG46-84	19MG46-6B	4.545	1.198	0.749	0.037	0.06	-0.880	0.600
	19MG46-84	19MG46-6B	1.852	0.480	0.726	0.037	0.41	-0.540	1.050
	19MG46-85	19MG46-6B	6.803	0.879	0.930	0.120	0.20	-0.153	0.093
	19MG46-85	19MG46-6B	14.706	10.381	0.580	0.120	-0.48	-3.700	0.430
85	19MG46-85	19MG46-6B	1.389	0.386	0.830	0.120	0.67	-0.094	0.280
	19MG46-85	19MG46-6B	15.385	7.574	0.700	0.220	-0.36	-0.650	0.083
	19MG46-85	19MG46-6B	10.309	1.275	0.890	0.140	0.75	-0.159	0.062
	19MG46-86	19MG46-6B	3.846	0.355	0.864	0.065	0.43	-0.152	0.119
86	19MG46-86	19MG46-6B	7.576	0.746	0.920	0.099	0.65	-0.304	0.105
	19MG46-86	19MG46-6B	8.333	2.500	0.730	0.190	0.21	-0.520	0.098
	19MG46-87	19MG46-6B	12.500	4.531	0.700	0.100	-0.15	-6.700	0.242
	19MG46-87	19MG46-6B	3.831	1.306	0.707	0.044	0.05	-6.800	0.710
	19MG46-87	19MG46-6B	14.286	2.449	0.760	0.120	0.16	-5.070	0.161
	19MG46-87	19MG46-6B	0.962	0.250	0.757	0.053	-0.21	-8.100	3.600
87	19MG46-87	19MG46-6B	16.667	6.944	0.770	0.130	0.51	-21.800	0.310
	19MG46-87	19MG46-6B	15.385	4.497	0.757	0.088	-0.37	-14.900	0.205
	19MG46-87	19MG46-6B	10.204	2.395	0.790	0.110	0.43	-11.300	0.236
	19MG46-87	19MG46-6B	1.515	0.551	0.734	0.056	0.46	-21.400	1.650
	19MG46-87	19MG46-6B	10.101	1.735	0.710	0.044	0.15	-31.000	0.329
	19MG46-88	19MG46-6B	4.673	1.266	0.712	0.048	0.02	0.910	0.430
	19MG46-88	19MG46-6B	9.709	2.168	0.817	0.087	0.23	1.600	0.321
88	19MG46-88	19MG46-6B	7.407	1.481	0.725	0.035	0.29	3.100	0.790
	19MG46-88	19MG46-6B	13.333	2.489	0.750	0.120	0.00	1.390	0.214
	19MG46-88	19MG46-6B	7.692	2.130	0.679	0.044	-0.22	1.380	0.333
	19MG46-89	19MG46-6B	3.984	0.540	0.698	0.049	0.21	0.850	1.004
	19MG46-89	19MG46-6B	5.155	1.249	0.693	0.083	0.60	0.580	0.550
	19MG46-89	19MG46-6B	8.850	0.940	0.684	0.073	0.17	0.680	0.362
89	19MG46-89	19MG46-6B	6.452	1.332	0.704	0.042	0.16	1.360	0.810
	19MG46-89	19MG46-6B	5.405	0.935	0.767	0.049	0.63	0.815	0.813
	19MG46-89	19MG46-6B	8.772	1.616	0.782	0.085	0.43	0.980	0.556
	19MG46-89	19MG46-6B	6.623	0.658	0.772	0.063	0.54	0.484	0.401
	19MG46-89	19MG46-6B	6.250	1.758	0.750	0.059	0.19	0.830	0.670
	19MG46-90	19MG46-6B	2.632	0.900	0.749	0.067	0.84	0.325	1.000
	19MG46-90	19MG46-6B	30.303	11.938	0.580	0.130	-0.59	1.650	0.213
	19MG46-90	19MG46-6B	3.610	1.030	0.789	0.064	0.15	0.267	0.590
90	19MG46-90	19MG46-6B	9.804	1.826	0.686	0.083	0.43	0.344	0.239
	19MG46-90	19MG46-6B	2.857	0.898	0.774	0.064	0.37	0.312	0.900
	19MG46-90	19MG46-6B	7.194	0.828	0.686	0.064	0.73	0.228	0.254
	19MG46-90	19MG46-6B	10.417	4.557	0.663	0.092	-0.30	1.270	0.850
	19MG46-90	19MG46-6B	1.250	0.453	0.711	0.062	0.67	0.450	2.650

***Table A5.4:** U-Pb isotopic data of calcite veins from the ECM obtained during the session 4 (29-11-2021) of LA-ICP-MS U-Pb in calcite. The spot size for samples 19MG20, 19MG32 and 19MG67 was 85 µm and 65 µm for the sample 19MG43. Red labelled data was excluded from the age regression due to evident high error or a point belonging to the host rock.*

Spot	Source file (.FIN2)	Sample	$^{238}U/^{206}Pb$	±2σ (abs)	$^{207}Pb/^{206}Pb$	±2σ (abs)	Rho	U (ppm)	Pb (ppm)
			Session 2						
			WC-1 Calcite reference (Roberts et al., 2017)						
1	WC1-1	WC-1	24.839	0.432	0.051	0.007	0.04	4.170	0.189
2	WC1-2	WC-1	24.931	0.448	0.050	0.005	-0.05	3.202	0.129
3	WC1-3	WC-1	24.963	0.467	0.051	0.005	0.10	3.603	0.151
4	WC1-4	WC-1	24.207	0.416	0.053	0.005	-0.16	4.649	0.258
5	WC1-5	WC-1	25.497	0.442	0.050	0.006	0.17	3.433	0.248
6	WC1-6	WC-1	24.975	0.561	0.051	0.009	0.35	3.142	0.135
7	WC1-7	WC-1	25.907	0.570	0.050	0.008	0.40	4.033	0.221
8	WC1-8	WC-1	24.618	0.503	0.053	0.008	0.08	3.400	0.210
9	WC1-9	WC-1	25.208	0.470	0.051	0.005	0.38	3.286	0.223
10	WC1-10	WC-1	25.304	0.455	0.051	0.005	0.25	3.988	0.240
11	WC1-11	WC-1	25.310	0.404	0.051	0.004	0.16	3.688	0.097
12	WC1-12	WC-1	24.661	0.426	0.051	0.004	0.32	3.632	0.170
13	WC1-14	WC-1	25.157	0.449	0.051	0.006	-0.34	3.716	0.165
14	WC1-15	WC-1	25.214	0.401	0.052	0.005	0.32	3.740	0.155
15	WC1-16	WC-1	25.157	0.500	0.049	0.006	-0.58	3.662	0.220
16	WC1-17	WC-1	25.056	0.496	0.052	0.008	-0.52	3.857	0.204
17	WC1-19	WC-1	24.546	0.512	0.052	0.009	-0.32	3.674	0.236
18	WC1-20	WC-1	23.941	0.493	0.053	0.011	-0.20	3.496	0.329
19	WC1-21	WC-1	25.504	0.436	0.050	0.007	-0.23	3.811	0.213
20	WC1-22	WC-1	25.478	0.519	0.052	0.008	0.50	3.437	0.182
21	WC1-23	WC-1	24.120	0.489	0.051	0.008	0.31	4.100	0.221
22	WC1-24	WC-1	25.304	0.557	0.052	0.008	0.38	3.852	0.169
23	WC1-26	WC-1	24.432	0.531	0.051	0.007	0.16	3.583	0.144
24	WC1-27	WC-1	24.125	0.495	0.051	0.008	0.44	3.791	0.315
25	WC1-28	WC-1	24.925	0.466	0.051	0.005	0.08	3.754	0.172
26	WC1-29	WC-1	24.938	0.435	0.050	0.004	0.27	3.881	0.141
27	WC1-30	WC-1	24.219	0.504	0.054	0.007	0.14	2.890	0.237
28	WC1-31	WC-1	25.733	0.457	0.051	0.004	0.28	3.748	0.127
29	WC1-32	WC-1	25.323	0.481	0.051	0.004	0.21	3.940	0.223
30	WC1-33	WC-1	25.253	0.453	0.051	0.003	0.25	3.772	0.163
31	WC1-34	WC-1	25.126	0.499	0.051	0.005	0.14	3.436	0.240
			Soda-lime glass NIST SRM-614						
1	NIST614-1	NIST-614	1.425	0.024	0.842	0.012	0.66	1.138	4.927
2	NIST614-2	NIST-614	1.438	0.020	0.843	0.011	0.61	1.062	4.808

Spot	Source file (.FIN2)	Sample	^{238}U/^{206}Pb	±2σ (abs)	^{207}Pb/^{206}Pb	±2σ (abs)	Rho	U (ppm)	Pb (ppm)
3	NIST614-3	NIST-614	1.420	0.022	0.831	0.010	0.62	1.017	4.733
4	NIST614-4	NIST-614	1.437	0.020	0.847	0.011	0.59	0.973	4.781
5	NIST614-5	NIST-614	1.437	0.019	0.866	0.010	0.59	0.932	3.381
6	NIST614-6	NIST-614	1.479	0.022	0.861	0.011	0.58	0.939	3.271
7	NIST614-7	NIST-614	1.455	0.021	0.858	0.011	0.58	1.018	3.544
8	NIST614-8	NIST-614	1.467	0.021	0.853	0.010	0.49	0.462	6.610
9	NIST614-9	NIST-614	1.418	0.022	0.850	0.010	0.54	0.460	6.900
10	NIST614-10	NIST-614	1.418	0.022	0.858	0.011	0.59	0.467	7.090

19MG20 from DA strain domain

Spot	Source file (.FIN2)	Sample	^{238}U/^{206}Pb	±2σ (abs)	^{207}Pb/^{206}Pb	±2σ (abs)	Rho	U (ppm)	Pb (ppm)
22	19MG20-22	19MG20-2	1.133	0.097	0.885	0.065	0.22	0.036	0.225
23	19MG20-23	19MG20-2	2.778	0.231	0.990	0.100	0.16	0.081	0.243
24	19MG20-24	19MG20-2	1.031	0.102	0.780	0.031	0.19	0.550	3.180
	19MG20-24	19MG20-2	3.155	0.229	0.828	0.053	0.39	0.157	0.372
28	19MG20-28	19MG20-2	0.154	0.014	0.836	0.034	0.11	0.037	1.930
	19MG20-28	19MG20-2	0.474	0.049	0.812	0.035	0.12	0.063	1.108
29	19MG20-29	19MG20-2			no value	NAN	NaN	0.006	0.228
31	19MG20-31	19MG20-2			no value	NAN	NaN	0.005	0.253
32	19MG20-32	19MG20-2			no value	NAN	NaN	0.005	0.223
33	19MG20-33	19MG20-2	1.250	0.203	0.891	0.073	0.33	0.046	0.273
34	19MG20-34	19MG20-2	1.229	0.091	0.910	0.066	0.37	0.024	0.283
35	19MG20-35	19MG20-2	0.735	0.092	0.859	0.089	0.65	0.020	0.276
	19MG20-35	19MG20-2	1.163	0.149	0.860	0.110	0.02	0.017	0.152
36	19MG20-36	19MG20-2	1.351	0.201	0.850	0.110	0.48	0.022	0.189
37	19MG20-37	19MG20-2	0.606	0.081	0.840	0.110	0.51	0.013	0.233
38	19MG20-38	19MG20-2	0.870	0.144	0.903	0.091	-0.04	0.024	0.294
	19MG20-38	19MG20-2	1.449	0.210	0.840	0.110	0.92	0.016	0.136
39	19MG20-39	19MG20-2	1.053	0.266	0.923	0.091	0.00	0.027	0.193
40	19MG20-40	19MG20-2	1.285	0.152	0.833	0.067	0.48	0.018	0.150
41	19MG20-41	19MG20-2	1.486	0.135	0.893	0.055	0.46	0.022	0.183
42	19MG20-42	19MG20-3	0.493	0.029	0.819	0.018	0.25	0.297	7.580
	19MG20-43	19MG20-3	0.474	0.079	0.789	0.023	0.01	0.960	27.500
43	19MG20-43	19MG20-3	1.138	0.105	0.798	0.032	0.28	0.375	3.880
	19MG20-43	19MG20-3	0.402	0.044	0.787	0.018	0.15	0.535	15.600
	19MG20-43	19MG20-3	1.168	0.074	0.801	0.014	-0.04	0.888	8.860
	19MG20-44	19MG20-3	1.190	0.198	0.805	0.039	0.45	0.280	3.200
44	19MG20-44	19MG20-3	2.404	0.306	0.837	0.055	0.67	0.211	1.060
	19MG20-44	19MG20-3	4.000	0.672	0.760	0.046	0.04	0.560	1.200
45	19MG20-45	19MG20-3	0.735	0.054	0.828	0.043	0.21	1.310	20.600
	19MG20-45	19MG20-3	1.104	0.065	0.810	0.032	0.35	0.341	3.940
	19MG20-46	19MG20-3	0.474	0.031	0.816	0.023	0.16	0.545	13.800
46	19MG20-46	19MG20-3	0.351	0.018	0.806	0.012	0.10	0.715	24.560
	19MG20-46	19MG20-3	0.540	0.029	0.803	0.016	0.23	0.815	17.800

Spot	Source file (.FIN2)	Sample	^{238}U/^{206}Pb	±2σ (abs)	^{207}Pb/^{206}Pb	±2σ (abs)	Rho	U (ppm)	Pb (ppm)
	19MG20-47	19MG20-3	0.789	0.049	0.808	0.021	0.18	3.160	49.100
47	19MG20-47	19MG20-3	2.941	0.952	0.772	0.017	-0.35	3.200	13.400
	19MG20-47	19MG20-3	4.098	0.336	0.765	0.022	0.13	2.120	5.860
	19MG20-47	19MG20-3	9.709	1.885	0.726	0.045	0.01	3.800	2.920
	19MG20-48	19MG20-3	1.887	0.463	0.785	0.037	0.30	3.600	25.700
	19MG20-48	19MG20-3	2.257	0.433	0.788	0.028	0.25	5.790	27.600
	19MG20-48	19MG20-3	1.333	0.178	0.797	0.026	0.37	4.380	38.300
48	19MG20-48	19MG20-3	1.010	0.143	0.813	0.026	0.32	4.630	51.500
	19MG20-48	19MG20-3	0.800	0.070	0.796	0.016	0.43	4.700	70.400
	19MG20-48	19MG20-3	1.395	0.060	0.813	0.013	0.07	4.980	43.300
	19MG20-48	19MG20-3	1.314	0.121	0.774	0.037	0.19	2.520	24.200
	19MG20-49	19MG20-3	0.392	0.037	0.826	0.033	0.36	0.190	6.300
49	19MG20-49	19MG20-3	0.599	0.036	0.809	0.022	0.30	0.119	2.560
	19MG20-49	19MG20-3	0.934	0.084	0.809	0.040	0.16	0.083	1.180
	19MG20-50	19MG20-3	2.288	0.356	0.779	0.050	0.10	1.030	5.480
	19MG20-50	19MG20-3	4.525	0.471	0.787	0.027	0.30	1.170	2.870
50	19MG20-50	19MG20-3	2.591	0.248	0.796	0.020	0.52	0.898	4.470
	19MG20-50	19MG20-3	1.684	0.162	0.804	0.024	0.04	0.710	5.200
	19MG20-50	19MG20-3	7.042	1.537	0.755	0.039	0.09	1.320	1.840
	19MG20-50	19MG20-3	3.717	0.525	0.777	0.052	0.39	0.400	1.370
51	19MG20-51	19MG20-3	0.204	0.046	0.845	0.030	0.34	0.092	6.000
	19MG20-51	19MG20-3	1.957	0.134	0.821	0.041	0.28	0.085	0.494
52	19MG20-52	19MG20-3	0.202	0.022	0.825	0.020	-0.03	1.039	60.100
	19MG20-52	19MG20-3	0.483	0.026	0.802	0.033	0.54	0.820	19.500
	19MG20-53	19MG20-3	0.268	0.027	0.810	0.031	0.27	1.300	56.900
53	19MG20-53	19MG20-3	7.463	0.613	0.793	0.033	-0.31	35.200	56.200
	19MG20-53	19MG20-3	0.397	0.022	0.803	0.014	0.05	0.769	23.300
	19MG20-54	19MG20-3	0.905	0.071	0.842	0.038	0.08	0.508	7.100
54	19MG20-54	19MG20-3	0.625	0.063	0.803	0.022	0.18	0.753	13.700
	19MG20-54	19MG20-3	0.314	0.020	0.809	0.010	0.23	0.643	25.130
55	19MG20-55	19MG20-3	11.236	1.641	0.669	0.045	-0.03	4.230	3.080
56	19MG20-56	19MG20-3	0.323	0.026	0.830	0.051	0.21	0.147	4.920
	19MG20-56	19MG20-3	0.518	0.040	0.888	0.056	0.12	0.050	1.310
57	19MG20-57	19MG20-3	1.351	0.119	0.846	0.047	0.33	0.469	3.930
	19MG20-57	19MG20-3	2.358	0.278	0.844	0.072	0.10	0.275	1.350
58	19MG20-58	19MG20-3	0.966	0.064	0.864	0.062	0.18	0.386	5.400
	19MG20-58	19MG20-3	0.813	0.035	0.825	0.015	0.23	1.212	18.200
	19MG20-59	19MG20-3	2.604	0.115	0.836	0.037	0.49	6.760	35.000
	19MG20-59	19MG20-3	3.086	0.191	0.782	0.029	0.52	6.660	26.900
	19MG20-59	19MG20-3	4.651	0.281	0.783	0.024	0.26	6.090	15.520
59	19MG20-59	19MG20-3	6.452	0.624	0.812	0.030	0.26	7.240	12.810
	19MG20-59	19MG20-3	4.808	0.393	0.795	0.019	0.14	8.790	22.000
	19MG20-59	19MG20-3	4.880	0.174	0.780	0.021	0.18	7.060	17.400
	19MG20-59	19MG20-3	4.902	1.129	0.779	0.051	0.59	5.300	10.800

Spot	Source file (.FIN2)	Sample	$^{238}U/^{206}Pb$	±2σ (abs)	$^{207}Pb/^{206}Pb$	±2σ (abs)	Rho	U (ppm)	Pb (ppm)
	19MG20-60	19MG20-3	3.534	0.437	0.808	0.028	0.42	2.720	10.400
60	19MG20-60	19MG20-3	5.376	0.809	0.776	0.034	0.56	2.460	5.600
	19MG20-60	19MG20-3	2.227	0.238	0.794	0.015	0.26	4.340	25.300
	19MG20-60	19MG20-3	9.174	0.631	0.770	0.033	0.64	3.440	4.630
61	19MG20-61	19MG20-3	0.498	0.037	0.857	0.039	0.23	0.217	4.850
	19MG20-62	19MG20-3	1.361	0.080	0.801	0.020	0.20	0.938	8.610
62	19MG20-62	19MG20-3	1.835	0.104	0.794	0.016	0.31	1.011	6.980
	19MG20-62	19MG20-3	1.661	0.113	0.803	0.015	0.38	0.935	6.610
63	19MG20-63	19MG20-3	1.010	0.153	0.851	0.036	0.25	0.048	0.474
64	19MG20-64	19MG20-3	0.637	0.101	0.855	0.035	0.34	0.023	0.610
	19MG20-65	19MG20-3	1.563	0.293	0.858	0.044	0.36	0.085	0.720
65	19MG20-65	19MG20-3	1.675	0.157	0.776	0.063	0.69	0.031	0.217
	19MG20-65	19MG20-3	3.367	0.419	0.787	0.065	0.30	0.094	0.290
66	19MG20-66	19MG20-3	0.240	0.032	0.904	0.071	0.55	0.026	1.390
	19MG20-66	19MG20-3	0.917	0.126	0.864	0.055	0.11	0.026	0.247
67	19MG20-67	19MG20-3	1.266	0.256	0.831	0.037	0.08	0.083	0.640
	19MG20-67	19MG20-3	3.215	0.558	0.803	0.031	-0.23	0.350	0.740
	19MG20-68	19MG20-3	0.870	0.151	0.870	0.045	0.46	0.073	1.050
68	19MG20-68	19MG20-3	3.226	0.281	0.877	0.054	0.38	0.084	0.305
	19MG20-68	19MG20-3	4.831	0.420	0.844	0.076	0.48	0.098	0.229
69	19MG20-69	19MG20-3	0.282	0.040	0.810	0.071	0.46	0.033	1.610
	19MG20-69	19MG20-3	0.709	0.101	0.838	0.074	0.64	0.015	0.263
70	19MG20-70	19MG20-3	0.417	0.052	0.852	0.076	0.58	0.012	0.314
	19MG20-70	19MG20-3	1.185	0.104	0.890	0.052	0.62	0.019	0.196
71	19MG20-71	19MG20-3	0.467	0.083	0.806	0.045	0.05	0.050	1.400
	19MG20-71	19MG20-3	3.311	0.340	0.855	0.042	0.05	0.101	0.292
	19MG20-72	19MG20-3	0.826	0.178	0.880	0.150	0.54	0.016	0.175
72	19MG20-72	19MG20-3	1.842	0.220	0.869	0.076	0.53	0.025	0.147
	19MG20-72	19MG20-3	2.513	0.328	0.890	0.120	0.46	0.026	0.113
73	19MG20-73	19MG20-4	0.493	0.029	0.874	0.024	0.35	0.101	2.490
	19MG20-73	19MG20-4	0.795	0.046	0.896	0.024	0.36	0.063	0.881
	19MG20-74	19MG20-4	0.258	0.026	0.864	0.025	0.24	0.051	2.400
74	19MG20-74	19MG20-4	0.991	0.064	0.880	0.029	0.27	0.172	2.130
	19MG20-74	19MG20-4	1.645	0.127	0.878	0.031	0.44	0.126	0.843
	19MG20-75	19MG20-4	0.452	0.035	0.876	0.025	0.21	0.072	1.860
75	19MG20-75	19MG20-4	0.671	0.090	0.884	0.031	0.33	0.108	1.760
	19MG20-75	19MG20-4	0.173	0.021	0.871	0.019	0.15	0.032	1.772
76	19MG20-76	19MG20-4	0.703	0.034	0.863	0.025	0.30	0.066	1.069
	19MG20-76	19MG20-4	0.424	0.038	0.883	0.029	0.17	0.031	0.752
77	19MG20-77	19MG20-4	0.908	0.038	0.885	0.021	0.35	0.062	0.828
78	19MG20-78	19MG20-4	1.045	0.055	0.878	0.033	0.48	0.024	0.269
79	19MG20-79	19MG20-4	0.728	0.051	0.841	0.032	0.37	0.084	1.180
	19MG20-79	19MG20-4	1.236	0.061	0.906	0.033	0.44	0.047	0.422
80	19MG20-80	19MG20-4	0.639	0.033	0.896	0.022	0.33	0.045	0.804

Spot	Source file (.FIN2)	Sample	$^{238}U/^{206}Pb$	±2σ (abs)	$^{207}Pb/^{206}Pb$	±2σ (abs)	Rho	U (ppm)	Pb (ppm)
81	19MG20-81	19MG20-4	2.571	0.159	0.946	0.053	0.84	0.045	0.193
82	19MG20-82	19MG20-4	7.937	0.945	0.826	0.053	-0.14	0.540	0.490
83	19MG20-83	19MG20-4	0.488	0.050	0.908	0.031	0.33	0.025	0.468
84	19MG20-84	19MG20-4	0.227	0.016	0.894	0.013	0.23	0.060	2.760
85	19MG20-85	19MG20-4	2.849	0.227	0.905	0.038	0.05	0.139	0.479
86	19MG20-86	19MG20-4	0.993	0.078	0.877	0.050	0.30	0.040	0.345
	19MG20-87	19MG20-4	0.289	0.026	0.901	0.043	0.39	0.082	2.860
87	19MG20-87	19MG20-4	0.535	0.034	0.893	0.021	0.17	0.118	2.387
	19MG20-87	19MG20-4	0.257	0.015	0.893	0.016	0.22	0.088	3.690
	19MG20-88	19MG20-4	1.786	0.415	0.886	0.076	0.54	0.047	0.237
88	19MG20-88	19MG20-4	3.610	0.209	0.840	0.060	0.31	0.081	0.223
	19MG20-88	19MG20-4	2.571	0.185	0.853	0.051	0.49	0.063	0.242

19MG32 from WDA strain domain

Spot	Source file (.FIN2)	Sample	$^{238}U/^{206}Pb$	±2σ (abs)	$^{207}Pb/^{206}Pb$	±2σ (abs)	Rho	U (ppm)	Pb (ppm)
	19MG32-1	19MG32-1	0.091	0.006	0.806	0.032	0.11	0.033	2.220
1	19MG32-1	19MG32-1	0.108	0.007	0.807	0.021	0.21	0.030	1.603
	19MG32-1	19MG32-1	0.121	0.014	0.821	0.054	0.31	0.022	1.179
2	19MG32-2	19MG32-1	0.088	0.009	0.798	0.015	0.09	0.062	3.080
	19MG32-2	19MG32-1	0.074	0.006	0.805	0.021	0.38	0.030	2.490
	19MG32-4	19MG32-1	0.075	0.015	0.786	0.058	0.56	0.023	2.110
4	19MG32-4	19MG32-1	0.163	0.013	0.838	0.031	0.10	0.027	1.251
	19MG32-4	19MG32-1	0.117	0.012	0.831	0.053	0.40	0.022	1.399
	19MG32-4	19MG32-1	0.116	0.010	0.818	0.050	0.14	0.019	1.225
5	19MG32-5	19MG32-1	0.144	0.011	0.835	0.026	0.41	0.022	1.109
	19MG32-5	19MG32-1	0.132	0.021	0.828	0.056	0.40	0.021	1.169
	19MG32-6	19MG32-1	0.105	0.007	0.838	0.024	-0.59	0.028	2.087
6	19MG32-6	19MG32-1	0.080	0.008	0.816	0.038	0.22	0.020	1.970
	19MG32-6	19MG32-1	0.108	0.007	0.815	0.034	0.15	0.020	1.431
7	19MG32-7	19MG32-1	0.412	0.030	0.819	0.023	0.11	0.101	2.000
	19MG32-7	19MG32-1	0.178	0.009	0.815	0.020	0.22	0.035	1.591
8	19MG32-8	19MG32-1	0.101	0.012	0.829	0.036	0.28	0.018	1.554
10	19MG32-10	19MG32-1	0.142	0.011	0.818	0.026	-0.04	0.026	1.750
	19MG32-10	19MG32-1	0.323	0.028	0.829	0.023	0.16	0.051	1.376
11	19MG32-11	19MG32-1	0.395	0.027	0.821	0.015	0.05	0.062	1.302
12	19MG32-12	19MG32-1	0.077	0.006	0.835	0.019	0.04	0.029	4.140
	19MG32-12	19MG32-1	0.086	0.004	0.826	0.017	0.23	0.020	2.586
13	19MG32-13	19MG32-1	0.182	0.012	0.831	0.017	0.18	0.044	2.570
	19MG32-13	19MG32-1	0.257	0.021	0.844	0.023	0.24	0.040	1.732
14	19MG32-14	19MG32-1	0.176	0.014	0.834	0.023	0.24	0.036	2.260
	19MG32-14	19MG32-1	0.372	0.023	0.813	0.019	0.06	0.078	2.330
15	19MG32-15	19MG32-1	0.217	0.020	0.825	0.024	0.10	0.032	1.668
	19MG32-15	19MG32-1	0.148	0.008	0.834	0.017	0.20	0.020	1.521

Spot	Source file (.FIN2)	Sample	$^{238}U/^{206}Pb$	±2σ (abs)	$^{207}Pb/^{206}Pb$	±2σ (abs)	Rho	U (ppm)	Pb (ppm)
16	19MG32-16	19MG32-2	0.139	0.013	0.821	0.019	0.07	0.031	2.320
	19MG32-16	19MG32-2	0.196	0.018	0.836	0.024	-0.01	0.029	1.680
17	19MG32-17	19MG32-2	0.169	0.011	0.856	0.020	0.31	0.028	1.925
18	19MG32-18	19MG32-2	0.353	0.041	0.481	0.041	-0.95	0.491	0.462
19	19MG32-19	19MG32-2	0.167	0.016	0.841	0.026	0.11	0.030	2.004
	19MG32-19	19MG32-2	0.294	0.036	0.839	0.033	0.12	0.048	1.570
20	19MG32-20	19MG32-2	0.104	0.006	0.854	0.018	0.08	0.018	2.113
	19MG32-20	19MG32-2	0.091	0.013	0.817	0.040	0.37	0.015	2.006
22	19MG32-22	19MG32-2	0.184	0.020	0.849	0.039	0.15	0.015	1.024
23	19MG32-23	19MG32-2	0.101	0.011	0.848	0.023	0.17	0.004	0.621
24	19MG32-24	19MG32-2	0.071	0.008	0.814	0.038	0.28	0.014	2.380
25	19MG32-25	19MG32-2			no value	NAN	NaN	0.006	1.810
29	19MG32-29	19MG32-2			no value	NAN	NaN	0.001	0.645
31	19MG32-31	19MG32-3	0.402	0.040	0.821	0.009	0.19	0.590	20.300
	19MG32-31	19MG32-3	0.347	0.029	0.823	0.016	0.06	0.209	7.990
32	19MG32-32	19MG32-3	0.370	0.036	0.815	0.014	0.00	0.538	18.550
	19MG32-32	19MG32-3	0.402	0.012	0.817	0.010	0.27	0.436	15.990
33	19MG32-33	19MG32-3	0.171	0.016	0.818	0.014	0.12	0.176	15.630
	19MG32-33	19MG32-3	0.324	0.056	0.827	0.014	-0.07	0.393	12.070
	19MG32-33	19MG32-3	0.143	0.009	0.815	0.011	0.25	0.105	10.730
34	19MG32-34	19MG32-3	0.426	0.025	0.819	0.013	0.16	0.351	12.800
	19MG32-34	19MG32-3	0.219	0.014	0.814	0.014	0.21	0.124	8.460
35	19MG32-35	19MG32-3	0.254	0.027	0.827	0.020	0.20	0.150	9.600
	19MG32-35	19MG32-3	0.437	0.040	0.843	0.021	-0.10	0.294	10.030
36	19MG32-36	19MG32-3	0.009	0.002	0.819	0.023	0.04	0.024	28.500
37	19MG32-37	19MG32-3	0.187	0.012	0.819	0.010	0.31	0.674	55.500
	19MG32-37	19MG32-3	0.182	0.018	0.815	0.008	0.11	0.484	36.900
38	19MG32-38	19MG32-3	0.028	0.004	0.804	0.026	-0.05	0.026	13.900
	19MG32-38	19MG32-3	0.021	0.002	0.810	0.017	0.12	0.015	11.830
40	19MG32-40	19MG32-3	0.793	0.059	0.815	0.009	0.01	0.966	18.260
41	19MG32-41	19MG32-3	0.685	0.052	0.812	0.009	0.13	0.634	14.820
42	19MG32-42	19MG32-3	0.082	0.017	0.809	0.032	-0.02	0.035	5.810
	19MG32-42	19MG32-3	0.105	0.016	0.833	0.019	0.35	0.047	7.560
	19MG32-42	19MG32-3	0.259	0.034	0.830	0.018	0.19	0.152	9.720
	19MG32-42	19MG32-3	0.102	0.008	0.834	0.024	-0.07	0.041	7.450
	19MG32-42	19MG32-3	0.260	0.030	0.818	0.052	0.22	0.049	3.380
43	19MG32-43	19MG32-3	0.205	0.038	0.813	0.028	0.16	0.030	1.870
44	19MG32-44	19MG32-3	0.203	0.018	0.814	0.019	0.33	0.084	6.840
	19MG32-44	19MG32-3	0.120	0.007	0.838	0.012	0.03	0.065	10.100
45	19MG32-45	19MG32-3	0.147	0.039	0.829	0.014	-0.11	0.197	12.540
	19MG32-45	19MG32-3	0.532	0.028	0.829	0.016	0.15	0.342	12.680

	19MG67 from OL strain domain								
Spot	Source file (.FIN2)	Sample	$^{238}U/^{206}Pb$	±2σ (abs)	$^{207}Pb/^{206}Pb$	±2σ (abs)	Rho	U (ppm)	Pb (ppm)
	19MG67-1	19MG67-1	0.106	0.012	0.865	0.045	0.20	0.025	2.199
1	19MG67-1	19MG67-1	0.227	0.052	0.915	0.054	0.10	0.063	2.039
	19MG67-1	19MG67-1	0.182	0.018	0.862	0.049	0.48	0.035	1.956
	19MG67-1	19MG67-1	0.344	0.022	0.898	0.021	0.23	0.058	1.762
2	19MG67-2	19MG67-1	0.114	0.006	0.902	0.015	0.34	0.020	1.774
3	19MG67-3	19MG67-1	0.101	0.004	0.887	0.014	0.23	0.018	1.823
4	19MG67-4	19MG67-1	0.102	0.008	0.870	0.019	-0.04	0.023	2.070
	19MG67-4	19MG67-1	0.078	0.005	0.890	0.021	0.35	0.013	1.679
6	19MG67-6	19MG67-1	0.185	0.008	0.879	0.014	0.17	0.037	1.908
8	19MG67-8	19MG67-1	0.108	0.012	0.891	0.042	0.36	0.017	1.560
	19MG67-8	19MG67-1	0.100	0.014	0.869	0.040	0.19	0.018	1.441
9	19MG67-9	19MG67-1	0.143	0.009	0.881	0.022	0.04	0.029	1.831
	19MG67-9	19MG67-1	0.163	0.010	0.854	0.021	0.41	0.030	1.708
14	19MG67-14	19MG67-1	0.077	0.014	0.808	0.096	0.33	0.019	2.130
	19MG67-14	19MG67-1	0.160	0.015	0.866	0.014	-0.11	0.042	1.826
	19MG67-15	19MG67-1	0.060	0.009	0.859	0.038	0.16	0.015	2.032
15	19MG67-15	19MG67-1	0.089	0.006	0.888	0.027	0.31	0.019	1.857
	19MG67-15	19MG67-1	0.071	0.007	0.847	0.056	0.21	0.014	1.569
	19MG67-15	19MG67-1	0.120	0.015	0.877	0.045	0.25	0.021	1.489
	19MG67-16	19MG67-1	0.129	0.012	0.867	0.026	0.18	0.032	2.088
16	19MG67-16	19MG67-1	0.154	0.011	0.867	0.021	0.08	0.032	1.764
	19MG67-16	19MG67-1	0.164	0.011	0.866	0.028	0.48	0.033	1.656
	19MG67-16	19MG67-1	0.123	0.011	0.863	0.032	0.15	0.021	1.449
21	19MG67-21	19MG67-1			no value	NAN	NaN	0.006	1.982
23	19MG67-23	19MG67-1			no value	NAN	NaN	0.004	1.511
24	19MG67-24	19MG67-1	0.166	0.007	0.850	0.016	0.20	0.041	1.990
	19MG67-24	19MG67-1	0.192	0.011	0.884	0.022	0.43	0.038	1.603
	19MG67-25	19MG67-1	0.147	0.011	0.860	0.019	0.25	0.040	2.150
25	19MG67-25	19MG67-1	0.187	0.010	0.854	0.023	0.38	0.039	1.695
	19MG67-25	19MG67-1	0.208	0.016	0.856	0.025	0.21	0.042	1.618
26	19MG67-26	19MG67-1	0.088	0.005	0.856	0.017	0.33	0.021	1.881
	19MG67-26	19MG67-1	0.117	0.012	0.868	0.038	0.04	0.024	1.722
27	19MG67-27	19MG67-1	0.075	0.005	0.853	0.018	0.24	0.021	2.231
	19MG67-27	19MG67-1	0.094	0.020	0.864	0.034	-0.40	0.027	1.886
	19MG67-28	19MG67-1	0.233	0.028	0.863	0.032	0.19	0.081	2.710
28	19MG67-28	19MG67-1	0.192	0.011	0.866	0.022	0.08	0.055	2.314
	19MG67-28	19MG67-1	0.133	0.008	0.856	0.020	0.36	0.034	1.969
29	19MG67-29	19MG67-1	0.171	0.009	0.849	0.017	-0.58	0.051	2.330
	19MG67-29	19MG67-1	0.209	0.012	0.879	0.021	0.48	0.047	1.727
30	19MG67-30	19MG67-1	0.369	0.020	0.869	0.029	0.17	0.110	2.350
	19MG67-30	19MG67-1	0.485	0.207	0.910	0.120	-0.02	0.157	1.550

Spot	Source file (.FIN2)	Sample	^{238}U/^{206}Pb	±2σ (abs)	^{207}Pb/^{206}Pb	±2σ (abs)	Rho	U (ppm)	Pb (ppm)
	19MG67-31	19MG67-2	2.950	0.087	0.839	0.021	0.55	0.972	2.610
31	19MG67-31	19MG67-2	2.681	0.086	0.855	0.024	0.68	0.656	1.996
	19MG67-31	19MG67-2	2.404	0.092	0.840	0.034	0.70	0.547	1.776
	19MG67-31	19MG67-2	2.740	0.113	0.841	0.027	0.55	0.546	1.520
	19MG67-32	19MG67-2	3.497	0.183	0.843	0.017	0.25	1.181	2.510
32	19MG67-32	19MG67-2	3.833	0.141	0.858	0.025	0.54	0.981	2.010
	19MG67-32	19MG67-2	3.571	0.166	0.858	0.033	0.04	0.895	1.960
33	19MG67-33	19MG67-2	1.712	0.144	0.851	0.017	0.02	0.536	2.350
	19MG67-33	19MG67-2	2.941	0.112	0.857	0.020	0.44	0.606	1.505
	19MG67-34	19MG67-2	2.755	0.144	0.853	0.016	0.18	1.122	2.960
34	19MG67-34	19MG67-2	4.329	0.225	0.857	0.046	0.91	0.990	1.650
	19MG67-34	19MG67-2	3.610	0.085	0.841	0.019	0.49	1.044	2.055
	19MG67-35	19MG67-2	3.311	0.318	0.842	0.035	0.14	0.780	1.900
35	19MG67-35	19MG67-2	3.356	0.124	0.828	0.029	0.56	0.872	1.800
	19MG67-35	19MG67-2	3.049	0.093	0.824	0.020	0.43	0.922	2.072
	19MG67-35	19MG67-2	2.882	0.166	0.850	0.033	0.19	0.862	2.160
	19MG67-36	19MG67-2	3.731	0.139	0.844	0.021	0.44	1.001	1.861
36	19MG67-36	19MG67-2	2.577	0.173	0.830	0.021	0.13	0.716	1.803
	19MG67-36	19MG67-2	1.261	0.092	0.865	0.021	0.10	0.389	2.052
	19MG67-37	19MG67-2	2.703	0.088	0.817	0.018	0.19	1.172	2.807
37	19MG67-37	19MG67-2	3.275	0.090	0.842	0.023	0.49	1.005	2.060
	19MG67-37	19MG67-2	2.004	0.161	0.815	0.025	0.48	0.544	1.660
	19MG67-38	19MG67-2	0.191	0.032	0.820	0.016	0.09	0.075	0.760
38	19MG67-38	19MG67-2	0.112	0.009	0.826	0.026	0.29	0.054	2.903
	19MG67-38	19MG67-2	0.102	0.015	0.798	0.032	-0.34	0.048	2.700
39	19MG67-39	19MG67-2	0.189	0.031	0.830	0.010	0.04	0.177	1.220
38	19MG67-38	19MG67-2	0.081	0.006	0.832	0.016	0.26	0.031	2.309
	19MG67-39	19MG67-2	1.629	0.125	0.826	0.015	0.25	0.707	2.400
39	19MG67-39	19MG67-2	0.204	0.046	0.847	0.019	-0.23	0.134	2.458
	19MG67-40	19MG67-2	0.829	0.066	0.827	0.017	0.21	0.444	2.810
40	19MG67-40	19MG67-2	0.260	0.034	0.843	0.025	0.01	0.134	2.624
	19MG67-40	19MG67-2	0.080	0.015	0.821	0.028	0.01	0.040	2.483
41	19MG67-41	19MG67-2			no value	NAN	NaN	0.005	3.152
43	19MG67-43	19MG67-2	3.185	0.112	0.810	0.015	0.39	1.427	2.132
	19MG67-43	19MG67-2	1.099	0.121	0.805	0.018	-0.01	0.565	2.141
45	19MG67-45	19MG67-3	1.883	0.071	0.810	0.012	0.16	1.716	4.260
	19MG67-45	19MG67-3	0.877	0.063	0.808	0.014	0.08	0.892	4.790
46	19MG67-46	19MG67-3	1.266	0.046	0.806	0.011	0.25	2.042	7.950
	19MG67-46	19MG67-3	1.370	0.032	0.784	0.013	0.43	1.662	5.750
47	19MG67-47	19MG67-3	1.209	0.025	0.809	0.011	0.18	2.271	9.250
	19MG67-47	19MG67-3	1.229	0.027	0.800	0.011	0.56	1.877	7.380
	19MG67-48	19MG67-3	1.414	0.054	0.798	0.013	0.34	2.391	8.430
48	19MG67-48	19MG67-3	1.264	0.032	0.809	0.010	0.37	2.043	7.920
	19MG67-48	19MG67-3	1.079	0.073	0.783	0.028	0.50	1.340	5.700

Spot	Source file (.FIN2)	Sample	$^{238}U/^{206}Pb$	±2σ (abs)	$^{207}Pb/^{206}Pb$	±2σ (abs)	Rho	U (ppm)	Pb (ppm)
	19MG67-49	19MG67-3	1.767	0.131	0.799	0.020	0.04	1.700	4.720
49	19MG67-49	19MG67-3	1.206	0.028	0.792	0.012	0.46	1.995	8.020
	19MG67-49	19MG67-3	1.057	0.053	0.809	0.017	0.36	1.522	6.940
	19MG67-49	19MG67-3	1.096	0.044	0.807	0.017	0.47	1.420	6.210
50	19MG67-50	19MG67-3	2.500	0.113	0.800	0.015	0.12	1.962	3.740
	19MG67-50	19MG67-3	1.661	0.102	0.785	0.012	0.24	1.789	4.900
51	19MG67-51	19MG67-3	1.269	0.019	0.802	0.008	0.51	1.940	7.350
52	19MG67-52	19MG67-3	0.654	0.039	0.797	0.016	0.08	0.712	4.580
	19MG67-52	19MG67-3	0.338	0.016	0.788	0.016	0.30	0.212	2.911
54	19MG67-54	19MG67-3			no value	NAN	NaN	0.005	1.677
56	19MG67-56	19MG67-3	0.571	0.042	0.798	0.011	0.02	0.730	4.070
	19MG67-57	19MG67-3	1.287	0.041	0.799	0.014	0.34	2.350	8.980
57	19MG67-57	19MG67-3	1.718	0.044	0.798	0.015	0.28	1.524	4.180
	19MG67-57	19MG67-3	1.202	0.052	0.804	0.022	0.05	1.150	4.460
58	19MG67-58	19MG67-3	1.420	0.042	0.798	0.012	0.43	2.501	8.260
	19MG67-58	19MG67-3	1.592	0.033	0.790	0.011	0.47	1.910	5.620
60	19MG67-60	19MG67-3	0.065	0.008	0.822	0.037	0.61	0.037	2.550
	19MG67-60	19MG67-3	0.052	0.009	0.809	0.034	0.03	0.031	2.550
61	19MG67-61	19MG67-3			no value	NAN	NaN	0.002	1.695
62	19MG67-62	19MG67-3	1.271	0.071	0.793	0.016	0.24	2.210	9.200
	19MG67-62	19MG67-3	1.325	0.096	0.795	0.012	0.23	1.216	4.190
63	19MG67-63	19MG67-3	0.955	0.066	0.807	0.014	0.37	2.160	12.900
	19MG67-63	19MG67-3	0.902	0.020	0.796	0.008	0.19	2.144	12.550
64	19MG67-64	19MG67-3	1.217	0.038	0.797	0.016	0.41	1.299	6.090
	19MG67-64	19MG67-3	1.013	0.060	0.810	0.015	0.15	0.814	4.394

WC-1 Calcite reference (Roberts et al., 2017) (65 µm spot)

Spot	Source file (.FIN2)	Sample	$^{238}U/^{206}Pb$	±2σ (abs)	$^{207}Pb/^{206}Pb$	±2σ (abs)	Rho	U (ppm)	Pb (ppm)
1	WC1-1	WC-1	25.214	0.547	0.051	0.008	-0.18	3.460	0.158
2	WC1-2	WC-1	25.394	0.574	0.059	0.008	-0.09	4.090	0.180
3	WC1-3	WC-1	24.366	0.445	0.053	0.008	-0.01	3.500	0.214
4	WC1-4	WC-1	25.088	0.548	0.052	0.007	-0.27	3.960	0.159
6	WC1-6	WC-1	24.931	0.609	0.045	0.009	-0.50	3.887	0.220
7	WC1-7	WC-1	25.145	0.525	0.050	0.008	0.03	3.674	0.173
8	WC1-8	WC-1	25.767	0.564	0.048	0.010	-0.03	3.565	0.188
9	WC1-9	WC-1	24.631	0.540	0.051	0.006	0.38	3.505	0.181
10	WC1-10	WC-1	24.789	0.535	0.051	0.007	0.08	3.971	0.177
11	WC1-11	WC-1	24.552	0.555	0.050	0.006	0.16	3.652	0.179
14	WC1-14	WC-1	25.069	0.528	0.052	0.006	0.08	4.060	0.181
15	WC1-15	WC-1	25.432	0.576	0.046	0.008	-0.57	3.540	0.147
16	WC1-16	WC-1	24.931	0.553	0.046	0.007	0.09	4.070	0.247
17	WC1-17	WC-1	25.075	0.503	0.054	0.005	0.04	3.480	0.158
18	WC1-18	WC-1	24.564	0.465	0.052	0.006	-0.02	3.802	0.175
19	WC1-19	WC-1	25.063	0.628	0.051	0.005	0.25	3.693	0.155

Spot	Source file (.FIN2)	Sample	^{238}U/^{206}Pb	±2σ (abs)	^{207}Pb/^{206}Pb	±2σ (abs)	Rho	U (ppm)	Pb (ppm)
21	WC1-21	WC-1	24.925	0.491	0.052	0.008	-0.05	3.821	0.231
22	WC1-22	WC-1	25.445	0.589	0.052	0.008	0.14	3.420	0.187

Soda-lime glass NIST SRM-614 (65 µm spot)

Spot	Source file (.FIN2)	Sample	^{238}U/^{206}Pb	±2σ (abs)	^{207}Pb/^{206}Pb	±2σ (abs)	Rho	U (ppm)	Pb (ppm)
1	NIST614-1	NIST-614	1.445	0.025	0.850	0.012	0.61	0.651	3.555
2	NIST614-2	NIST-614	1.443	0.025	0.851	0.012	0.53	0.663	3.640
3	NIST614-3	NIST-614	1.466	0.026	0.855	0.012	0.50	0.684	3.745
4	NIST614-4	NIST-614	1.464	0.024	0.847	0.012	0.60	0.701	3.790
5	NIST614-5	NIST-614	1.429	0.022	0.845	0.012	0.48	0.660	5.860
6	NIST614-6	NIST-614	1.451	0.025	0.868	0.014	0.61	0.659	5.930
7	NIST614-7	NIST-614	1.439	0.023	0.860	0.013	0.50	0.653	6.010
8	NIST614-8	NIST-614	1.449	0.029	0.881	0.013	0.56	0.532	6.630
9	NIST614-9	NIST-614	1.431	0.029	0.876	0.014	0.64	0.528	6.370
10	NIST614-10	NIST-614	1.471	0.026	0.891	0.014	0.57	0.560	6.110

19MG43 from DA domain

Spot	Source file (.FIN2)	Sample	^{238}U/^{206}Pb	±2σ (abs)	^{207}Pb/^{206}Pb	±2σ (abs)	Rho	U (ppm)	Pb (ppm)
	19MG43-1	19MG43-1	14.104	1.154	0.756	0.093	0.32	0.303	0.164
1	19MG43-1	19MG43-1	22.573	1.783	0.722	0.069	0.54	0.445	0.149
	19MG43-1	19MG43-1	32.573	4.987	0.694	0.093	0.19	1.060	0.169
2	19MG43-2	19MG43-1	13.755	1.154	0.767	0.056	0.15	0.367	0.191
3	19MG43-3	19MG43-1	12.755	1.009	0.749	0.054	0.14	0.397	0.225
4	19MG43-4	19MG43-1	11.364	1.291	0.800	0.072	0.49	0.275	0.161
	19MG43-4	19MG43-1	5.952	1.488	0.746	0.046	0.87	0.486	0.480
5	19MG43-5	19MG43-1	7.246	0.525	0.804	0.047	0.27	0.314	0.311
	19MG43-6	19MG43-1	5.848	0.581	0.762	0.044	0.11	0.418	0.464
6	19MG43-6	19MG43-1	6.250	0.586	0.761	0.049	0.19	0.719	0.869
	19MG43-6	19MG43-1	4.425	0.587	0.785	0.055	0.01	0.832	1.450
	19MG43-6	19MG43-1	7.855	0.562	0.773	0.054	0.49	0.789	0.757
7	19MG43-7	19MG43-1	5.650	0.415	0.841	0.053	0.63	0.167	0.202
8	19MG43-8	19MG43-1	2.915	0.212	0.795	0.035	0.43	0.112	0.254
9	19MG43-9	19MG43-1	6.211	0.656	0.806	0.055	0.29	0.254	0.273
	19MG43-9	19MG43-1	5.587	0.468	0.773	0.040	0.10	0.337	0.443
10	19MG43-10	19MG43-1	2.020	0.131	0.792	0.040	0.47	0.064	0.224
11	19MG43-11	19MG43-1	4.367	0.477	0.810	0.055	0.50	0.182	0.291
	19MG43-11	19MG43-1	5.747	0.694	0.758	0.034	-0.07	0.483	0.395
12	19MG43-12	19MG43-1	1.639	0.148	0.865	0.061	0.43	0.055	0.247
	19MG43-12	19MG43-1	3.497	0.342	0.766	0.049	0.14	0.244	0.476
13	19MG43-13	19MG43-1	1.684	0.196	0.766	0.052	-0.06	0.175	0.722
	19MG43-13	19MG43-1	3.745	0.224	0.810	0.027	0.22	0.404	0.857
14	19MG43-14	19MG43-1	1.969	0.112	0.821	0.041	0.54	0.061	0.246
15	19MG43-15	19MG43-1	2.227	0.139	0.815	0.036	0.53	0.101	0.347
16	19MG43-16	19MG43-1	2.020	0.204	0.802	0.029	0.08	0.237	0.819

Spot	Source file (.FIN2)	Sample	$^{238}U/^{206}Pb$	±2σ (abs)	$^{207}Pb/^{206}Pb$	±2σ (abs)	Rho	U (ppm)	Pb (ppm)
21	19MG43-21	19MG43-1	4.049	0.426	0.870	0.110	0.85	0.062	0.145
22	19MG43-22	19MG43-1	2.551	0.176	0.806	0.036	0.20	0.197	0.783
	19MG43-22	19MG43-1	5.525	0.580	0.767	0.031	0.14	0.700	0.996
23	19MG43-23	19MG43-1	2.703	0.234	0.827	0.054	-0.02	0.124	0.419
24	19MG43-24	19MG43-1	1.408	0.155	0.761	0.084	0.27	0.028	0.193
	19MG43-24	19MG43-1	3.460	0.838	0.794	0.086	0.40	0.159	0.320
	19MG43-24	19MG43-1	1.538	0.260	0.827	0.035	0.26	0.282	1.770
25	19MG43-25	19MG43-1			no value	NAN	NaN	0.008	0.117
26	19MG43-26	19MG43-1	2.033	0.149	0.845	0.054	0.74	0.077	0.417
	19MG43-26	19MG43-1	2.188	0.124	0.833	0.039	0.59	0.170	0.864
27	19MG43-27	19MG43-1	2.062	0.276	0.834	0.054	0.08	0.064	0.236
28	19MG43-28	19MG43-1	1.754	0.139	0.781	0.067	0.51	0.095	0.702
29	19MG43-29	19MG43-1	1.946	0.269	0.689	0.092	0.39	0.033	0.190
	19MG43-29	19MG43-1	1.672	0.207	0.826	0.077	0.90	0.074	0.541
30	19MG43-30	19MG43-1	2.141	0.303	0.780	0.140	0.72	0.030	0.137
31	19MG43_31	19MG43-4	3.413	0.326	0.860	0.052	-0.03	0.83	2.150
32	19MG43_32	19MG43-4	4.329	0.375	0.755	0.031	0.54	0.72	1.963
	19MG43_32	19MG43-4	5.618	0.347	0.817	0.031	0.46	0.68	1.532
	19MG43_32	19MG43-4	5.376	0.289	0.796	0.040	0.36	0.60	1.515
33	19MG43_33	19MG43-4	5.618	0.473	0.800	0.040	0.14	0.89	1.964
	19MG43_33	19MG43-4	7.042	0.595	0.766	0.035	0.10	1.00	1.689
	19MG43_33	19MG43-4	5.464	0.328	0.805	0.033	0.38	0.57	1.379
34	19MG43_34	19MG43-4	5.495	0.392	0.765	0.030	0.15	0.96	2.180
	19MG43_34	19MG43-4	5.348	0.315	0.806	0.045	0.29	0.71	1.706
	19MG43_34	19MG43-4	6.854	0.432	0.808	0.032	0.24	0.79	1.567
	19MG43_34	19MG43-4	7.576	1.205	0.784	0.043	0.22	1.02	1.543
35	19MG43_35	19MG43-4	57.143	14.367	0.568	0.037	-0.27	23.90	3.900
	19MG43_35	19MG43-4	10.204	1.145	0.755	0.042	-0.05	1.48	1.712
	19MG43_35	19MG43-4	7.813	0.610	0.764	0.036	0.35	0.95	1.630
	19MG43_35	19MG43-4	9.643	0.446	0.793	0.030	0.47	0.93	1.340
36	19MG43_36	19MG43-4	8.264	0.820	0.758	0.037	0.12	1.33	2.000
	19MG43_36	19MG43-4	7.353	1.081	0.781	0.033	0.27	1.15	1.848
	19MG43_36	19MG43-4	9.346	0.873	0.792	0.036	0.58	1.06	1.502
	19MG43_36	19MG43-4	7.576	0.574	0.805	0.036	0.12	0.75	1.448
37	19MG43_37	19MG43-4	5.236	0.740	0.801	0.043	0.46	0.95	2.340
	19MG43_37	19MG43-4	9.579	0.725	0.793	0.033	0.20	1.09	1.458
	19MG43_37	19MG43-4	15.152	3.214	0.751	0.062	-0.42	1.79	1.180
	19MG43_37	19MG43-4	6.410	0.493	0.805	0.059	0.44	0.47	1.000
38	19MG43_38	19MG43-4	8.703	0.523	0.774	0.051	0.22	1.73	2.620
	19MG43_38	19MG43-4	6.944	0.772	0.790	0.034	0.48	1.35	2.490
	19MG43_38	19MG43-4	6.757	0.361	0.807	0.033	0.49	0.80	1.687
	19MG43_38	19MG43-4	2.825	0.303	0.789	0.040	0.11	0.61	3.060

Spot	Source file (.FIN2)	Sample	^{238}U/^{206}Pb	±2σ (abs)	^{207}Pb/^{206}Pb	±2σ (abs)	Rho	U (ppm)	Pb (ppm)
	19MG43_39	19MG43-4	6.135	0.715	0.771	0.047	0.39	1.12	2.480
39	19MG43_39	19MG43-4	6.536	0.555	0.814	0.032	0.27	0.87	1.845
	19MG43_39	19MG43-4	6.959	0.446	0.781	0.030	0.41	0.74	1.443
	19MG43_40	19MG43-4	10.870	1.300	0.744	0.021	0.20	7.17	8.240
	19MG43_40	19MG43-4	6.173	0.610	0.794	0.021	-0.19	6.40	14.490
	19MG43_40	19MG43-4	11.765	1.661	0.762	0.028	0.27	7.68	8.710
40	19MG43_40	19MG43-4	10.753	1.156	0.761	0.023	0.28	5.38	6.760
	19MG43_40	19MG43-4	11.779	1.179	0.765	0.038	-0.09	5.97	7.040
	19MG43_40	19MG43-4	7.457	0.423	0.760	0.027	0.48	3.76	7.260
	19MG43_40	19MG43-4	9.416	0.514	0.766	0.020	0.12	5.41	8.120
	19MG43_40	19MG43-4	7.087	0.462	0.760	0.032	0.59	4.01	7.400
	19MG43_41	19MG43-4	21.231	1.037	0.741	0.055	0.52	2.12	1.352
	19MG43_41	19MG43-4	46.296	3.858	0.650	0.042	-0.05	5.74	1.505
41	19MG43_41	19MG43-4	27.322	3.509	0.684	0.051	0.31	2.63	1.105
	19MG43_41	19MG43-4	21.505	1.434	0.722	0.051	0.73	1.43	0.949
	19MG43_41	19MG43-4	31.056	4.629	0.695	0.066	0.01	3.10	0.948
42	19MG43_42	19MG43-4	4.202	0.194	0.835	0.023	0.42	0.40	1.411
43	19MG43_43	19MG43-4	5.952	0.461	0.812	0.033	0.26	0.78	1.950
	19MG43_43	19MG43-4	7.794	0.413	0.806	0.034	0.32	0.80	1.630
44	19MG43_44	19MG43-4	5.917	0.595	0.810	0.033	0.14	0.79	1.994
	19MG43_44	19MG43-4	3.759	0.212	0.823	0.028	0.36	0.35	1.527
	19MG43_45	19MG43-4	1.855	0.207	0.815	0.031	0.16	0.56	4.500
45	19MG43_45	19MG43-4	3.077	0.227	0.777	0.031	0.02	0.57	2.800
	19MG43_45	19MG43-4	5.405	0.351	0.791	0.031	0.36	0.65	1.714
	19MG43_46	19MG43-4	3.436	0.201	0.776	0.028	0.35	0.49	2.100
46	19MG43_46	19MG43-4	5.348	0.400	0.829	0.034	0.27	0.61	1.885
	19MG43_46	19MG43-4	4.386	0.346	0.821	0.044	0.55	0.43	1.618
47	19MG43_47	19MG43-4	2.874	0.198	0.805	0.032	0.12	0.30	1.669
	19MG43_47	19MG43-4	3.472	0.205	0.825	0.033	0.47	0.27	1.190
	19MG43_48	19MG43-4	6.289	0.435	0.821	0.050	0.47	0.84	2.140
48	19MG43_48	19MG43-4	9.174	1.431	0.823	0.056	0.51	0.93	1.477
	19MG43_48	19MG43-4	8.000	0.704	0.803	0.038	0.28	0.81	1.528
	19MG43_48	19MG43-4	7.874	0.496	0.808	0.040	0.50	0.76	1.651
	19MG43_49	19MG43-4	4.132	0.546	0.802	0.030	0.26	0.57	2.150
49	19MG43_49	19MG43-4	6.614	0.407	0.812	0.036	0.65	0.67	1.680
	19MG43_49	19MG43-4	6.711	0.676	0.784	0.046	0.01	0.76	1.675
	19MG43_49	19MG43-4	2.381	0.624	0.814	0.029	0.25	0.65	4.000
50	19MG43_50	19MG43-4	1.802	0.084	0.828	0.022	0.35	0.17	1.598
	19MG43_51	19MG43-4	7.299	1.279	0.783	0.051	0.25	1.51	3.150
51	19MG43_51	19MG43-4	6.373	0.366	0.816	0.035	0.23	0.77	2.078
	19MG43_51	19MG43-4	7.837	0.479	0.815	0.029	0.42	0.79	1.729
	19MG43_52	19MG43-4	3.367	0.249	0.871	0.042	0.44	0.29	1.550
52	19MG43_52	19MG43-4	4.717	0.467	0.793	0.047	0.33	0.42	1.390
	19MG43_52	19MG43-4	3.861	0.417	0.812	0.050	0.32	0.24	1.082

Spot	Source file (.FIN2)	Sample	$^{238}U/^{206}Pb$	±2σ (abs)	$^{207}Pb/^{206}Pb$	±2σ (abs)	Rho	U (ppm)	Pb (ppm)
53	19MG43_53	19MG43-4	1.550	0.137	0.842	0.044	0.53	0.24	2.730
	19MG43_53	19MG43-4	2.222	0.168	0.840	0.024	0.12	0.27	2.036
54	19MG43_54	19MG43-4	1.362	0.132	0.813	0.028	0.30	0.84	11.050
	19MG43_54	19MG43-4	4.717	0.334	0.802	0.028	0.56	0.76	2.800
	19MG43_54	19MG43-4	6.173	0.572	0.796	0.056	0.58	0.45	1.376
	19MG43_54	19MG43-4	2.232	0.419	0.814	0.030	0.65	0.45	3.840
55	19MG43_55	19MG43-4	3.636	0.317	0.821	0.082	0.69	0.40	2.000
	19MG43_55	19MG43-4	4.950	0.613	0.800	0.056	0.62	0.51	1.825
	19MG43_55	19MG43-4	2.591	0.148	0.836	0.028	0.43	0.21	1.547
56	19MG43_56	19MG43-4	2.933	0.310	0.816	0.049	0.46	0.35	2.010
	19MG43_56	19MG43-4	2.681	0.144	0.837	0.030	0.32	0.23	1.615
57	19MG43_57	19MG43-4	4.202	0.353	0.838	0.036	0.11	0.39	1.590
	19MG43_57	19MG43-4	3.311	0.230	0.787	0.036	0.56	0.24	1.388
	19MG43_57	19MG43-4	5.291	0.448	0.834	0.046	0.19	0.39	1.502
58	19MG43_58	19MG43-4	0.289	0.029	0.842	0.013	0.07	0.14	6.280
59	19MG43_59	19MG43-4	0.122	0.018	0.877	0.087	-0.22	0.02	3.970
60	19MG43_60	19MG43-4			no value	NAN	NaN	0.00	6.110

A) **19MG21**

1 cm

B) **19MG46**

1 cm

C) **19MG74A**

1 cm

D) **19MG74B**

1 cm
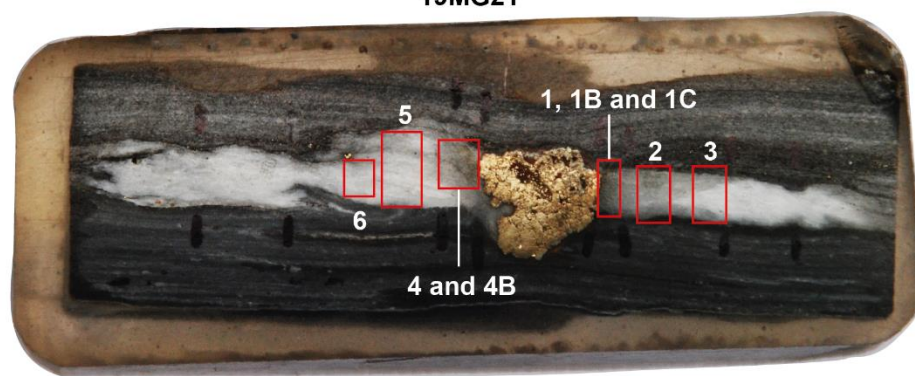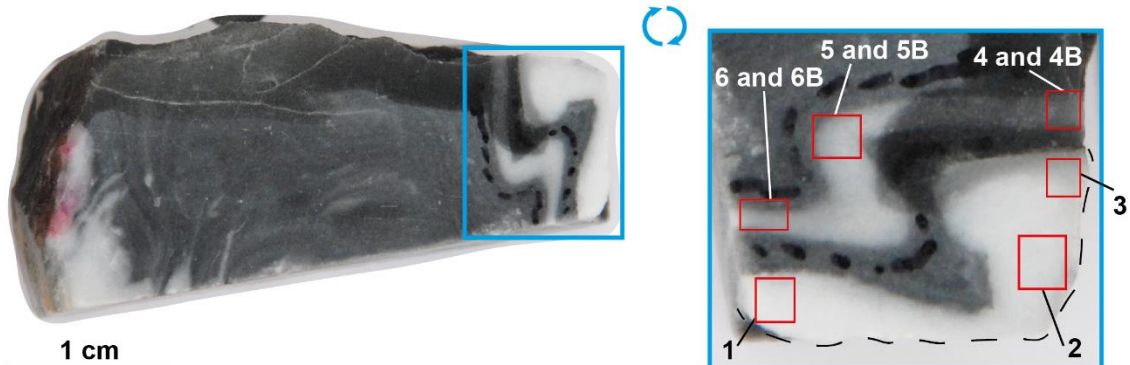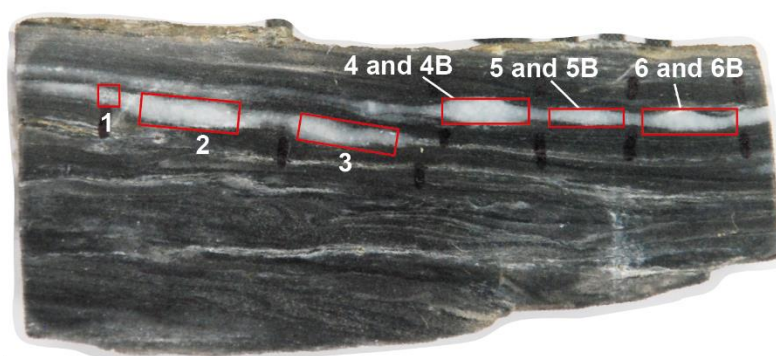
Figure A5.1: Polished billets from the different calcite veins of the samples 19MG21, 19MG46, 19MG74A and 19MG74B which were analyzed by in situ LA-ICP-MS U-Pb. Labelled spots as -B corresponds to the re-analyzed spots with higher U concentration in a former session. The corresponding Tera-Wasserburg age plots can be found in Figs. A5.3, A5.4 and A5.5.
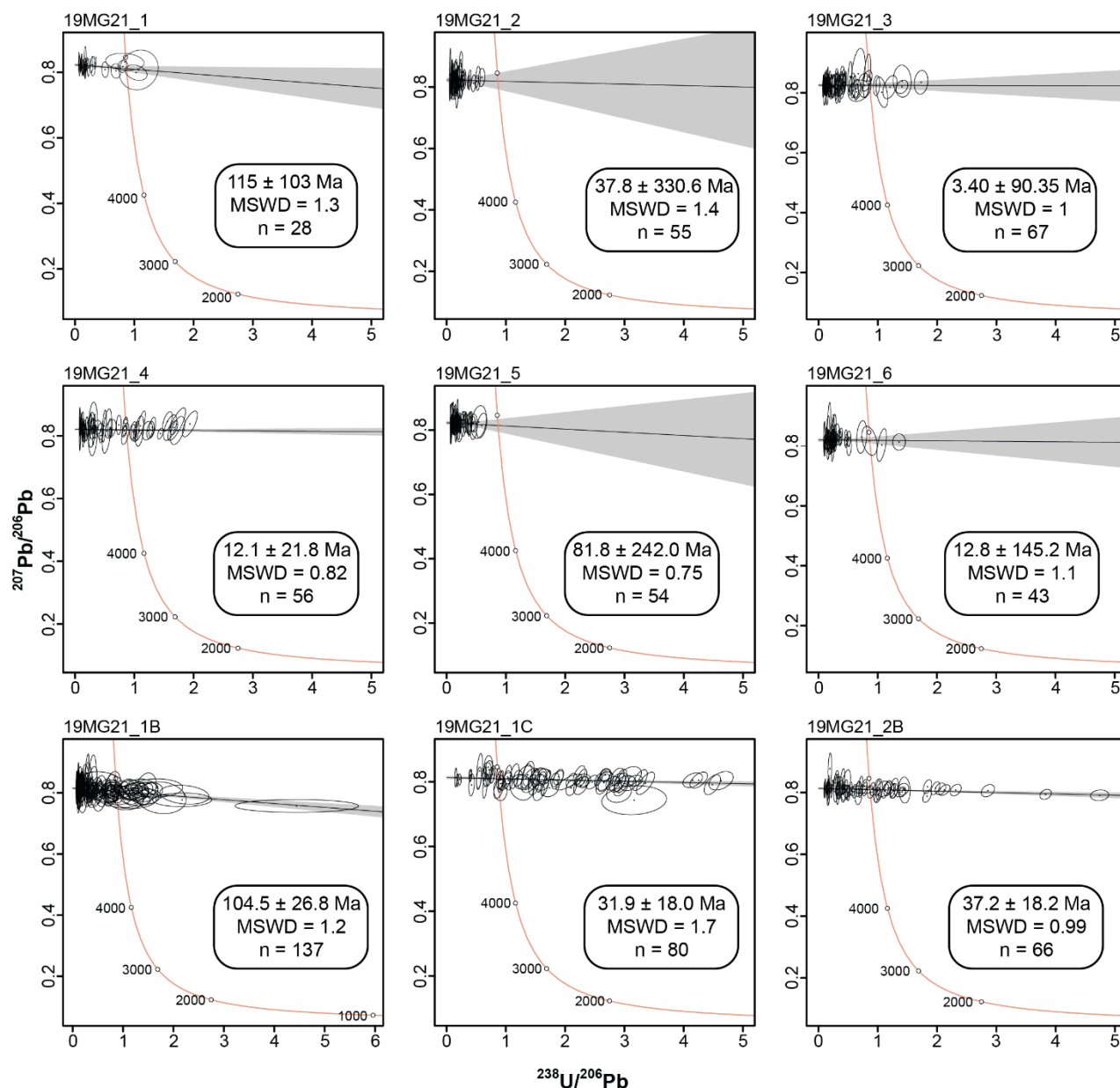
A)

19MG32

B)

19MG67

C)
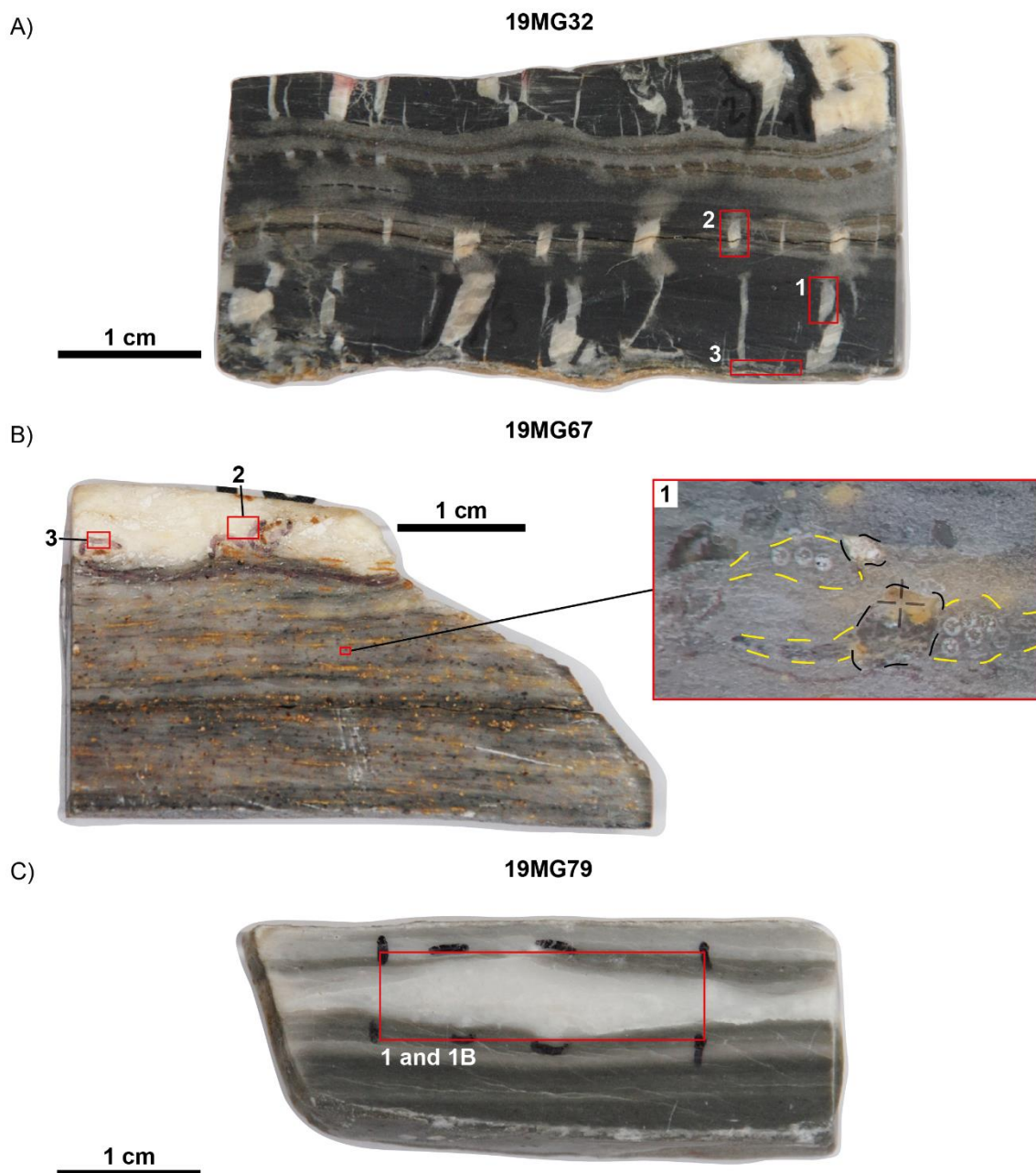
19MG79

Figure A5.2: Polished billets from the different calcite veins of the samples samples 19MG32, 19MG67 and 19MG79 which were analyzed by in situ LA-ICP-MS U-Pb. Labelled spots as -B corresponds to the re-analyzed spots with higher U concentration in a former session. The corresponding Tera-Wasserburg age plots can be found in Figs. A5.6.

Figure A5.3: *Tera-Wasserburg plots (Tera and Wasserburg, 1972) from the analyzed calcite cements of the sample 19MG21 (age±2σ). Lower intercept ages were calculated using IsoplotR (Vermeesch, 2018). Each diagram corresponds to an analyzed area of the sample, labelled in Fig. A5.1A.*
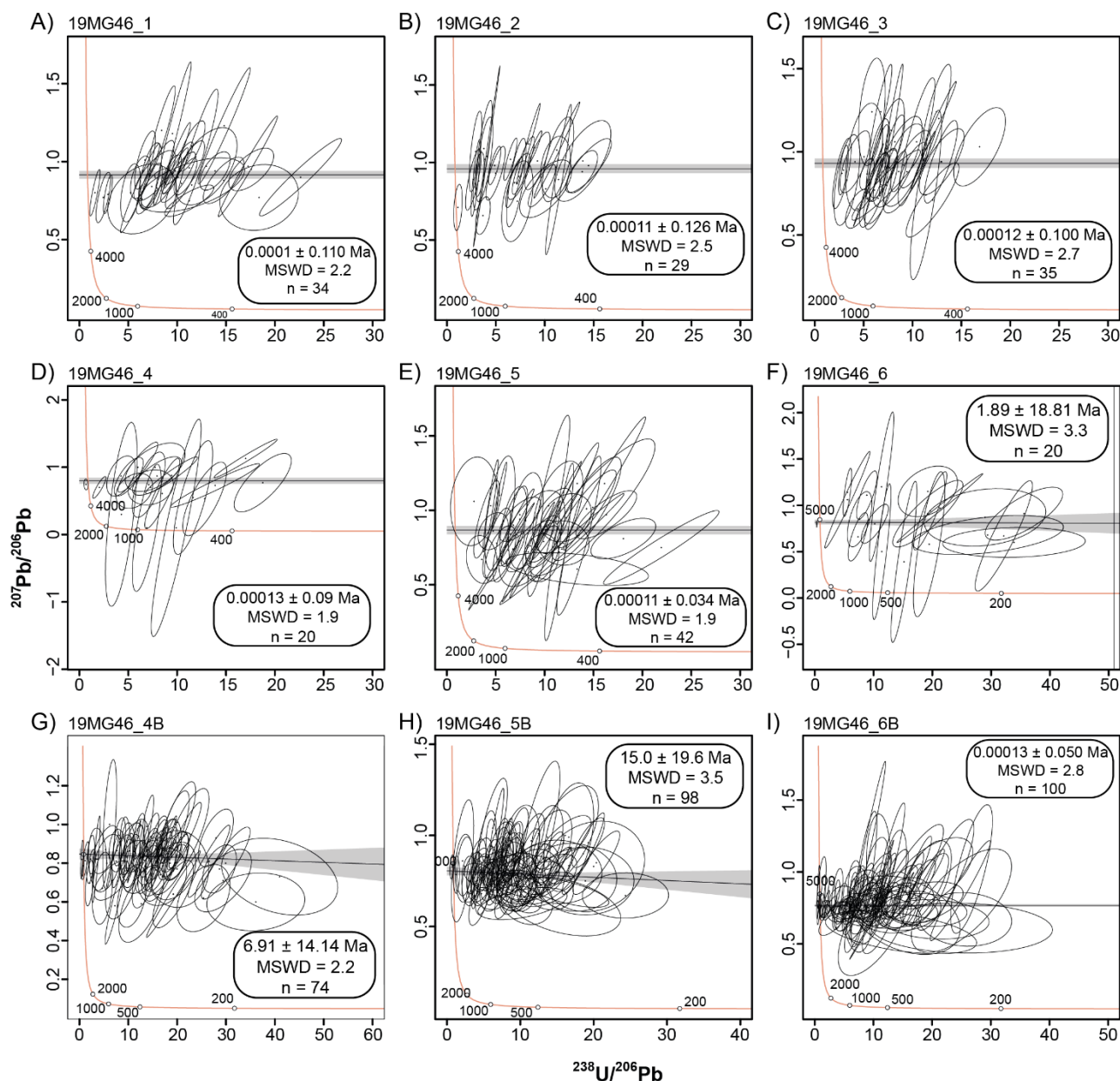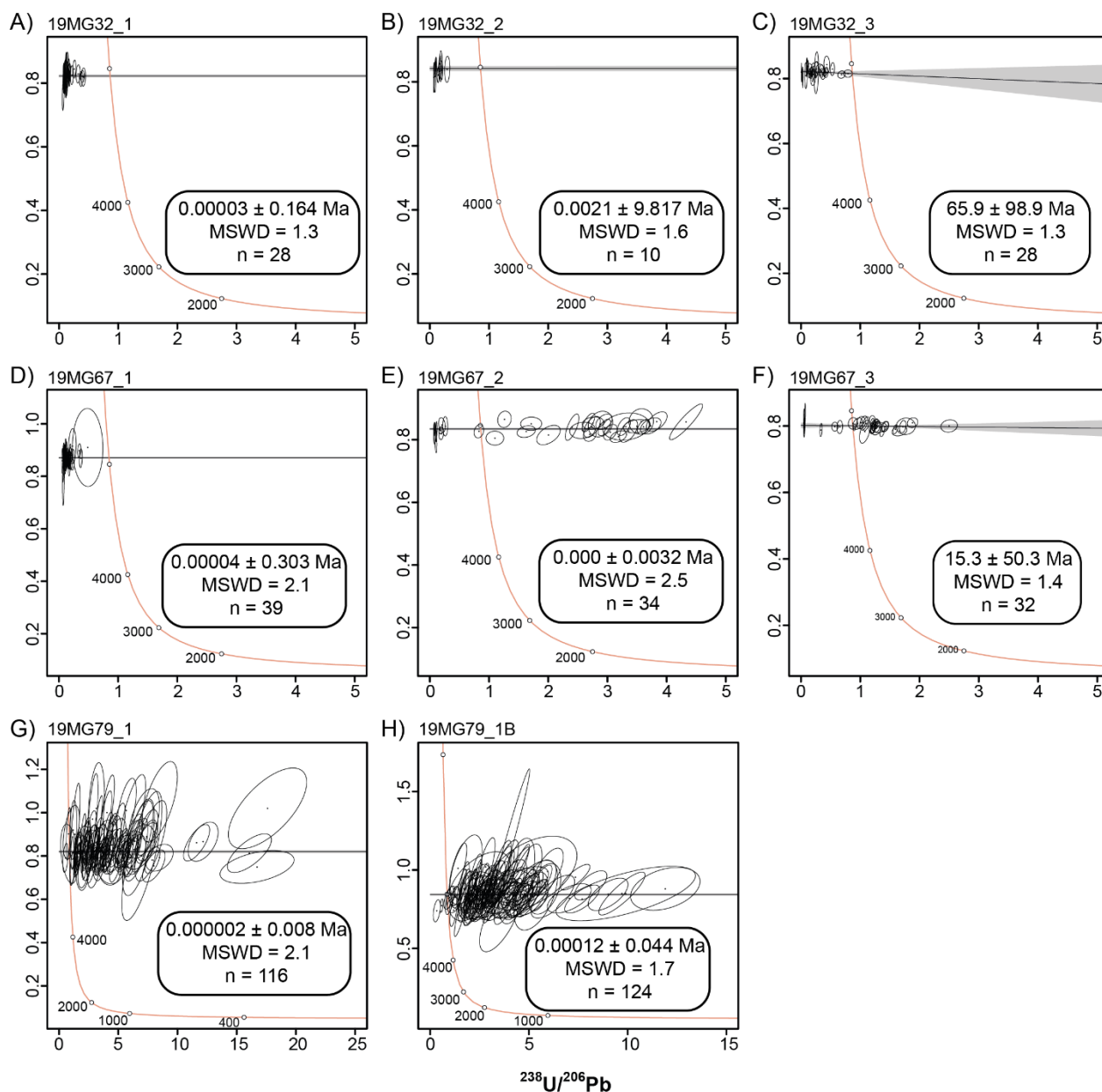
Figure A5.4: *Tera-Wasserburg plots from the analyzed calcite cements of the sample 19MG46 (age±2σ). Lower intercept ages were calculated using IsoplotR (Vermeesch, 2018). Each diagram corresponds to an analyzed area of the sample, labelled in Fig. A5.1B.*
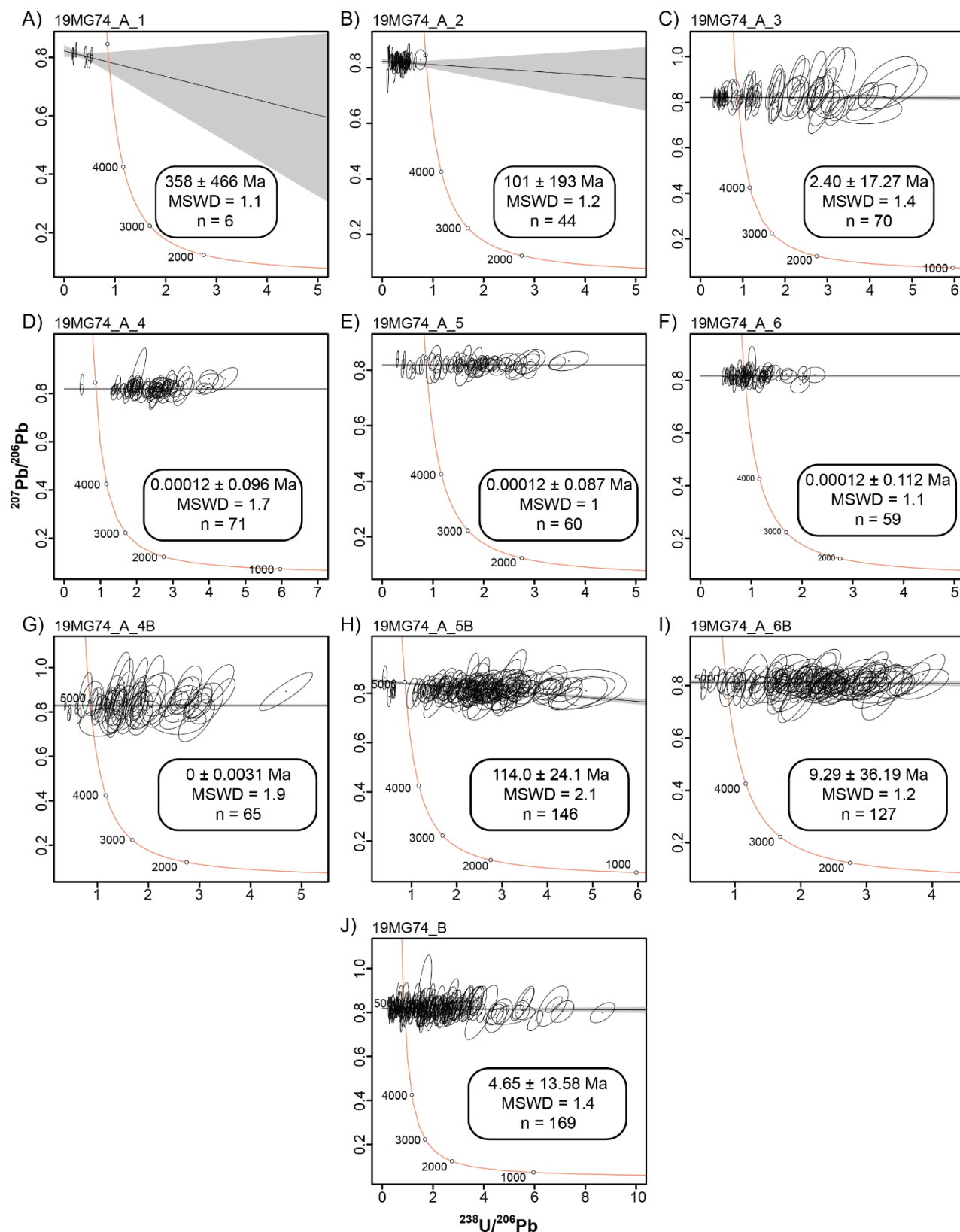
Figure A5.5: *Tera-Wasserburg plots from the analyzed calcite cements of the samples 19MG74A and B (age±2σ). Lower intercept ages were calculated using IsoplotR (Vermeesch, 2018). Each diagram corresponds to an analyzed area of the sample, labelled in Fig. A5.1C and D.*

Figure A5.5: *Tera-Wasserburg plots from the analyzed calcite cements of the samples 19MG32, 19MG67 and 19MG79 (age±2σ). Lower intercept ages were calculated using IsoplotR (Vermeesch, 2018). Each diagram corresponds to an analyzed area of the sample, labelled in Fig. A5.2A-C.*

Annex A6. Complete series of model runs with QTQt software, which complement those shown in Chapter 6.

A) EPT_02

C) EPT_06

E) EPT_10

G) EPT_14

B)

D)

F)

H)

Legend:
- ▲ ZHe Age Obs
- ▼ ZHe Age Pred
- ✳ Sampled Pred. Zr
- ✕ Sampled ZHe Obs.
- ▲ AHe Age Obs
- ▼ AHe Age Pred
- ✶ Sampled Pred. Ap
- ✚ Sampled AHe Obs.
- ● FT Age Obs
- ╌ FT Age Pred
- ━ Sampled FTA Pred
- ◆ MTL Obs
- ┈ MTL Pred
- ━ Sampled MTL Pred.
- ◻ Kin In
- ┈ Kin Pred
- ◼ Kin Sampled
- ━ z19MG40
- ━ z19MG66
- ━ zGPY11
- ━ zGPY09
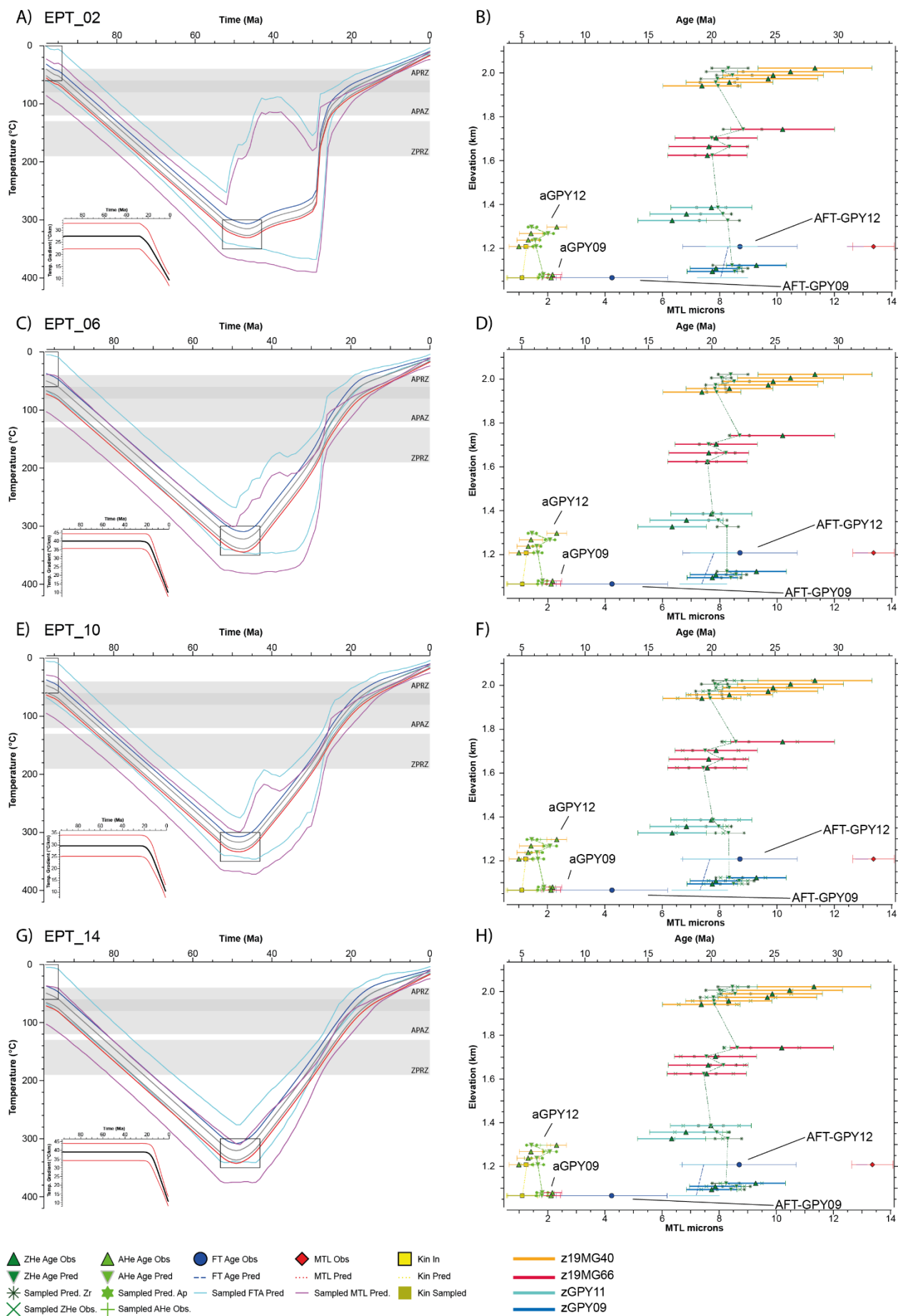
Figure A6.7: *Representative thermal simulations for the East vertical profile with fixed geothermal gradient over time. These simulations complements those shown in Fig. 6.7 with variable geothermal gradient over time.* **A-D)** *modelled T-t path, geothermal gradient and age-elevation profiles of the observed ages (uncorrected) for low (A and B) and high (C and D) geothermal gradient.* **E-H)** *modelled T-t path, geothermal gradient and age-elevation profiles of the resampled ages (uncorrected) for low (E and F) and high geothermal gradient (G and H). MTL: Mean track lengths; Red and blue curves corresponds to the bottom (hot) and top (cold) samples together with its 95% credible interval; APRZ: Apatite partial retention zone; APAZ: Apatite partial annealing zone; ZPRZ: Zircon partial retention zone. Prefix z refers to a zircon sample, a to apatite sample and AFT to apatite fission track.*
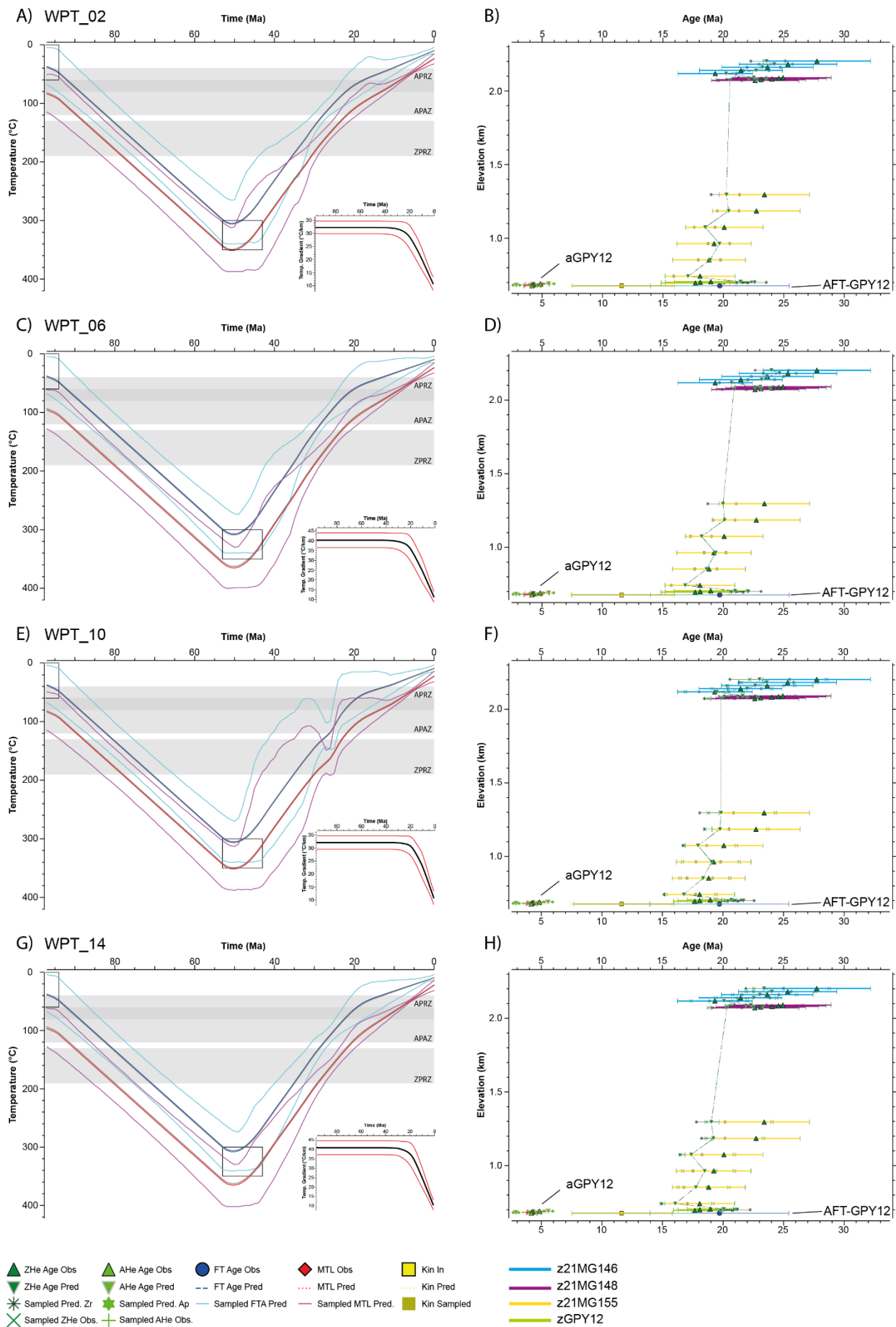
Figure A6.8: *Representative thermal simulations for the East vertical profile with fixed geothermal gradient over time. These simulations complements those shown in Fig. 6.8 with variable geothermal gradient over time. **A-D)** modelled T-t path, geothermal gradient and age-elevation profiles of the observed ages (uncorrected) for low (A and B) and high (C and D) geothermal gradient. **E-H)** modelled T-t path, geothermal gradient and age-elevation profiles of the resampled ages (uncorrected) for low (E and F) and high geothermal gradient (G and H). MTL: Mean track lengths; Red and blue curves corresponds to the bottom (hot) and top (cold) samples together with its 95% credible interval; APRZ: Apatite partial retention zone; APAZ: Apatite partial annealing zone; ZPRZ: Zircon partial retention zone. Prefix **z** refers to a zircon sample, a to apatite sample and AFT to apatite fission track.*
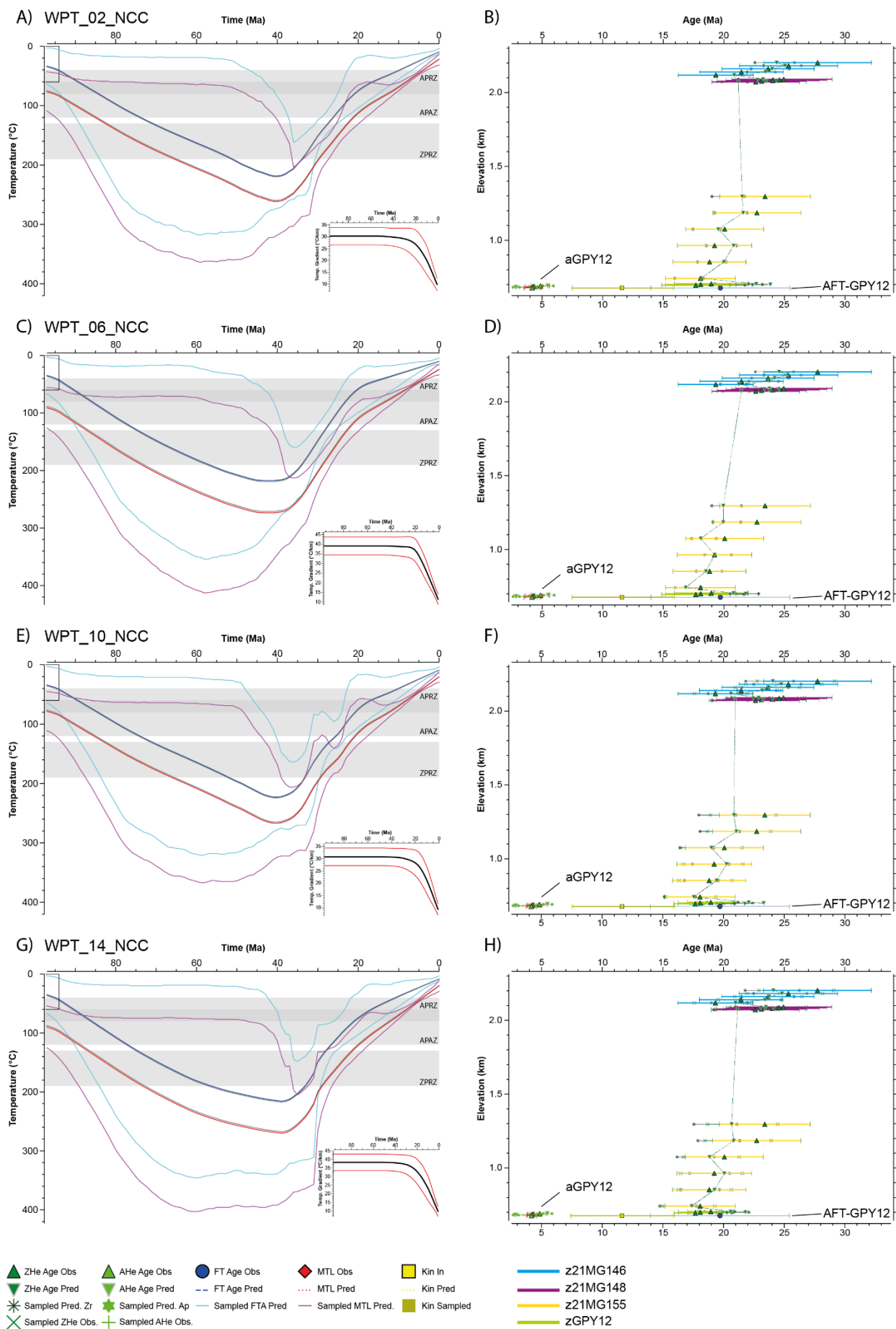
Figure A6.9: Representative thermal simulations for the West vertical profile with fixed geothermal gradient over time. These simulations complements those shown in Fig. 6.9 with variable geothermal gradient over time. *A-D)* modelled T-t path, geothermal gradient and age-elevation profiles of the observed ages (uncorrected) for low (A and B) and high (C and D) geothermal gradient. *E-H)* modelled T-t path, geothermal gradient and age-elevation profiles of the resampled ages (uncorrected) for low (E and F) and high geothermal gradient (G and H). MTL: Mean track lengths; Red and blue curves corresponds to the bottom (hot) and top (cold) samples together with its 95% credible interval; APRZ: Apatite partial retention zone; APAZ: Apatite partial annealing zone; ZPRZ: Zircon partial retention zone. Prefix z refers to a zircon sample, a to apatite sample and AFT to apatite fission track.

Figure A6.10: *Representative thermal simulations for the West vertical profile with fixed geothermal gradient over time. These simulations complements those shown in Fig. 6.10 with variable geothermal gradient over time. **A-D)** modelled T-t path, geothermal gradient and age-elevation profiles of the observed ages (uncorrected) for low (A and B) and high (C and D) geothermal gradient. **E-H)** modelled T-t path, geothermal gradient and age-elevation profiles of the resampled ages (uncorrected) for low (E and F) and high geothermal gradient (G and H). MTL: Mean track lengths; Red and blue curves corresponds to the bottom (hot) and top (cold) samples together with its 95% credible interval; APRZ: Apatite partial retention zone; APAZ: Apatite partial annealing zone; ZPRZ: Zircon partial retention zone. Prefix z refers to a zircon sample, a to apatite sample and AFT to apatite fission track.*
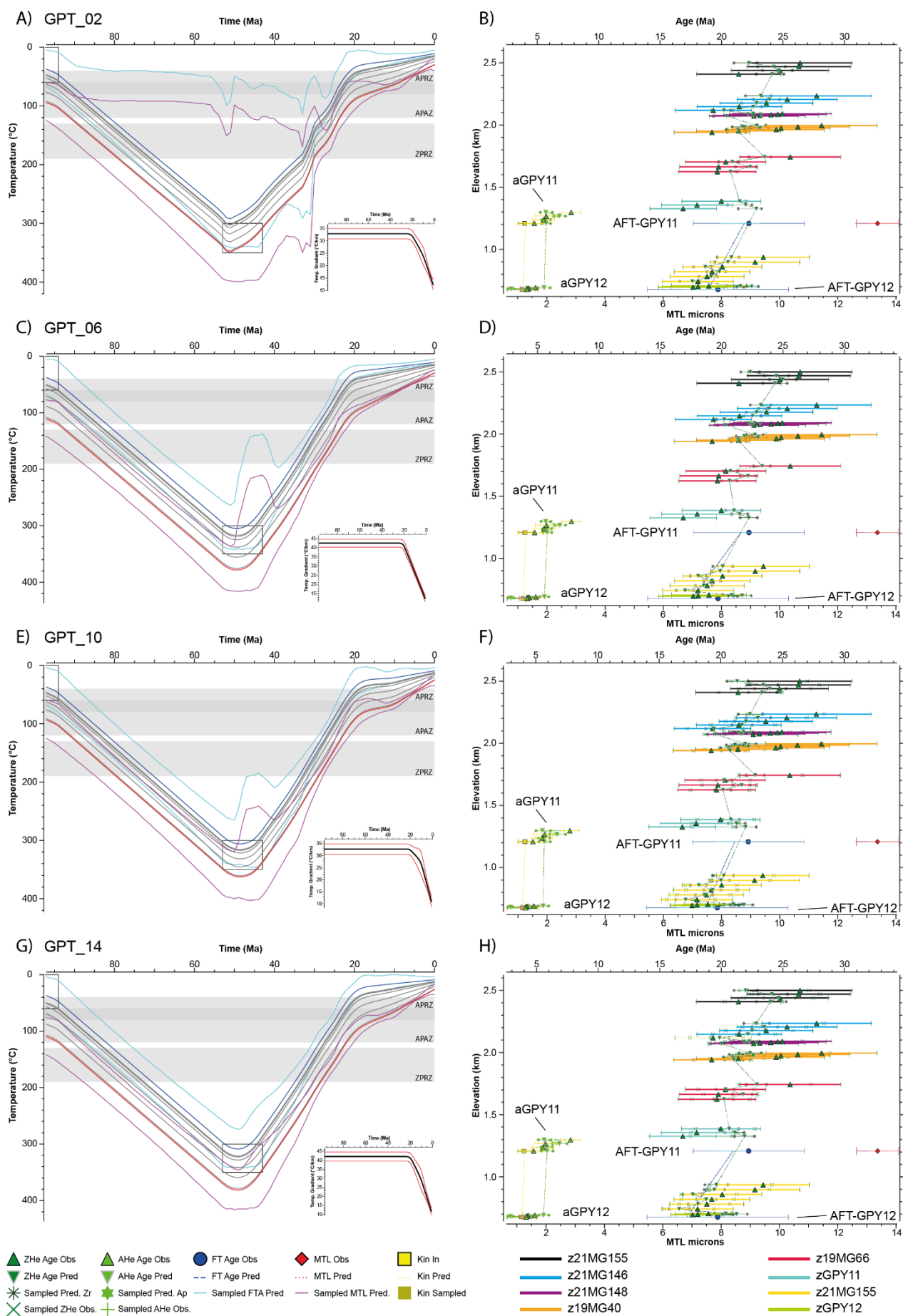
Figure A6.11: *Representative thermal simulations for the E-W vertical profile with fixed geothermal gradient over time. These simulations complements those shown in Fig. 6.11 with variable geothermal gradient over time.* **A-D)** *modelled T-t path, geothermal gradient and age-elevation profiles of the observed ages (uncorrected) for low (A and B) and high (C and D) geothermal gradient.* **E-H)** *modelled T-t path, geothermal gradient and age-elevation profiles of the resampled ages (uncorrected) for low (E and F) and high geothermal gradient (G and H). MTL: Mean track lengths; Red and blue curves corresponds to the bottom (hot) and top (cold) samples together with its 95% credible interval; APRZ: Apatite partial retention zone; APAZ: Apatite partial annealing zone; ZPRZ: Zircon partial retention zone. Prefix z refers to a zircon sample, a to apatite sample and AFT to apatite fission track.*
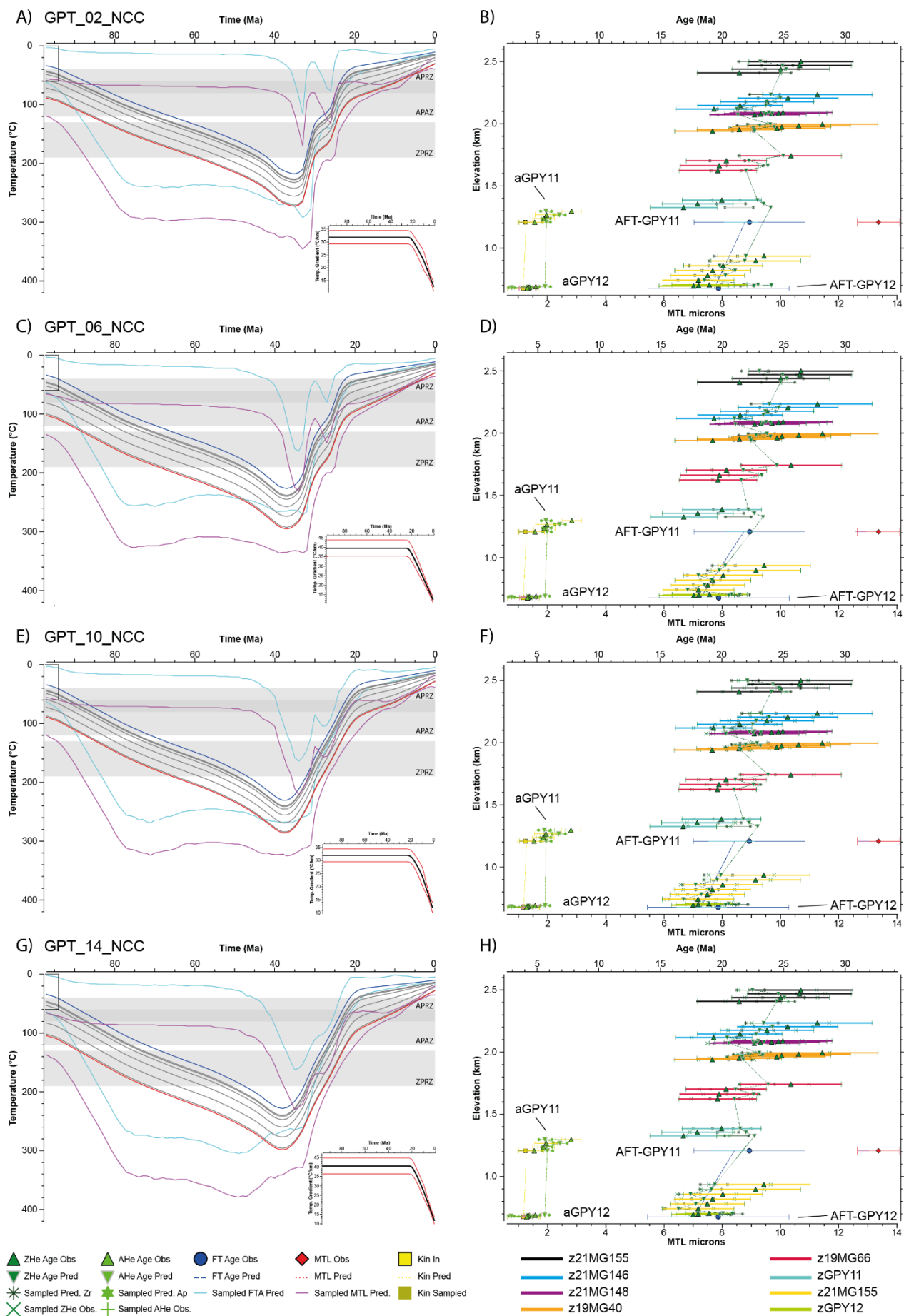
Figure A6.12*: Representative thermal simulations for the E-W vertical profile with fixed geothermal gradient over time. These simulations complements those shown in Fig. 6.12 with variable geothermal gradient over time. **A-D)** modelled T-t path, geothermal gradient and age-elevation profiles of the observed ages (uncorrected) for low (A and B) and high (D and E) geothermal gradient. **E-H)** modelled T-t path, geothermal gradient and age-elevation profiles of the resampled ages (uncorrected) for low (E and F) and high geothermal gradient (G and H). MTL: Mean track lengths; Red and blue curves corresponds to the bottom (hot) and top (cold) samples together with its 95% credible interval; APRZ: Apatite partial retention zone; APAZ: Apatite partial annealing zone; ZPRZ: Zircon partial retention zone. Prefix **z** refers to a zircon sample, **a** to apatite sample and AFT to apatite fission track.*